246
Topics in Current Chemistry

Topics in Current Chemistry

Recently Published and Forthcoming Volumes

New Techniques in Solid-State NMR

Volume Editor: Jacek Klinowski

With contributions by
O. N. Antzutkin · T. Anupõld · H. Eckert · S. Elbers · J. D. Epping ·
C. Fernandez · I. Heinmaa · J. W. Hennel · A. V. Ivanov · M. Janssen ·
M. Kalwei · S. Kazmierski · J. Klinowski · W. Kolodziejski ·
P. K. Madhu · C. M. Morais · J. Past · M. J. Potrzebowski · A. Reinhold ·
J. Rocha · A. Samoson · W. Strojek · T. Tuherm · E. Vinogradov ·
S. Vega · U. Voigt

 Springer

The series *Topics in Current Chemistry* presents critical reviews of the present and future trends in modern chemical research. The scope of coverage includes all areas of chemical science including the interfaces with related disciplines such as biology, medicine and materials science. The goal of eaxch thematic volume is to give the nonspecialist reader, whether at the university or in industry, a comprehensive overview of an area where new insights are emerging that are of interest to a larger scientific audience.

As a rule, contributions are specially commissioned. The editors and publishers will, however, always be pleased to receive suggestions and supplementary information. Papers are accepted for *Topics in Current Chemistry* in English.

In references *Topics in Current Chemistry* is abbreviated Top Curr Chem and is cited as a journal.

Visit the TCC content at http://www.springerlink.com/

The use of general descriptive names, registered names, trademarks, etc. in this publication does not imply, even in the absence of a specific statement, that such names are exempt from the relevant protective laws and regulations and therefore free for general use.

Topics in Current Chemistry
also Available Electronically

For all customers who have a standing order to Topics in Current Chemistry, we offer the electronic version via SpringerLink free of charge. Please contact your librarian who can receive a password for free access to the full articles by registration at:

springerlink.com

If you do not have a subscription, you can still view the tables of contents of the volumes and the abstract of each article by going to the SpringerLink Homepage, clicking on "Browse by Online Libraries", then "Chemical Sciences", and finally choose Topics in Current Chemistry.

You will find information about the

– Editorial Board
– Aims and Scope
– Instructions for Authors
– Sample Contribution

at http://www.springeronline.com using the search function.

Preface

After the discovery of nuclear magnetic resonance, [1, 2] the new spectroscopy was used for the study of ^{1}H nuclei in liquids, but then the signal from copper in the receiver coil itself, the first observation of NMR in the solid state, was found. "Wide-line NMR", named thus because of the line-broadening effects of dipolar interaction and chemical shift anisotropy, was not far behind, and soon led to significant advances through the analysis of spectral lineshapes. In this way Richards and Smith [3] demonstrated the presence of H_3O^+ cations in solid hydrates of strong acids, while Andrew and Eades [4] investigated the details of molecular motion in three solid benzenes. Even now, 50 years later, it is difficult to think of a technique which would provide a more convincing demonstration of the reality of these effects.

The development of magic angle spinning (MAS)[5, 6] initiated a new era in the structural study of solids, greatly enhancing our knowledge of a wide range of materials encountered in chemistry, physics, biology, earth sciences and technology. The introduction of Fourier-transform NMR, [7] cross-polarization [8] and high-field superconducting magnets, improved the sensitivity of the spectra. MAS was combined with cross-polarization for ^{13}C NMR of organics, [9] and this approach greatly contributed to the study of ^{29}Si and ^{27}Al in molecular sieve catalysts, minerals and many other materials. High-resolution spectra of solids are now routinely obtained using a combination of MAS and cross-polarization. However, MAS does not eliminate the quadrupolar interaction, and since 74% of all magnetically active naturally occurring isotopes are quadrupolar, the main effort in solid-state NMR is now directed towards methods for the observation of high-resolution spectra of such nuclei.

Springer, the publishers of this volume, originally asked me to edit a book on advances in magic-angle spinning. Aware that, while there have been significant advances in MAS itself, strategies developed for increasing the resolution of NMR spectra almost invariably combine MAS with various radiofrequency pulse trains, I invited several leading modern practitioners of solid-state NMR to describe their recent work. I am grateful to them for their contributions, and I hope that the volume will be of interest to readers in various fields involving the physics and chemistry of solids.

Jacek Klinowski   Cambridge, July 2004

[1] Purcell, E. M.; Torrey, H. C.; Pound, R. V. *Phys. Rev.* **1946**, *69*, 37.

[2] Bloch, F.; Hansen, W. W.; Packard, M. *Phys. Rev.* **1946**, *69*, 127.

[3] Richards, R. E.; Smith, J. A. S. *Trans. Faraday Soc.* **1951**, *47*, 1261.

[4] Andrew, E. R.; Eades, R. G. *Proc. Royal Soc. London* **1953**, *A218*, 537.

[5] Andrew, E. R.; Bradbury, A.; Eades, R. G. *Nature* **1959**, *183*, 1802.

[6] Lowe, I. J.; Norberg, R. E. *Phys. Rev.* **1957**, *107*, 46.

[7] Ernst, R. R.; Anderson, W. A. *Rev. Sci. Inst.* **1966**, *37*, 93.

[8] Pines, A.; Gibby, M. G.; Waugh, J. S. *J. Chem. Phys.* **1972**, *56*, 1776.

[9] Schaefer, J.; Stejskal, E. O. *J. Am. Chem. Soc.* **1976**, *98*, 1031.

Contents

Contents of volume 225
Modern Mass Spectrometry

Volume Editor: Christoph A. Schalley
ISBN 3-540-00098-4

Magic-Angle Spinning: a Historical Perspective

Jacek W. Hennel[1] · Jacek Klinowski[2] (✉)

[1] The Niewodniczanski Institute of Nuclear Physics, 31-342 Kraków, Radzikowskiego 152,
Poland
jhennel@vsb02.ifj.edu.pl
[2] Department of Chemistry, University of Cambridge, Lensfield Road, Cambridge CB2 1EW,
UK
jk18@cam.ac.uk

At the time of its discovery in 1945 [1, 2], NMR was hailed as a new method for the accurate measurement of nuclear magnetic moments. However, several years later Dickinson [3], Proctor and Yu [4], and Hahn [5], found that the resonance frequency of a nucleus depends on its chemical environment. While the discovery of the chemical shift disappointed many physicists, it enabled NMR to be a very powerful tool for the study of molecular structure. Although it still took 20 years to convince chemists that NMR was widely applicable to their problems, by the mid-1960s NMR spectrometers had penetrated most chemical laboratories, thanks to good textbooks [6–11] and to the commercial availability of high-resolution spectrometers.

Unfortunately, the usefulness of NMR for the investigation of chemical problems was strictly limited to liquid samples, so solid samples first had to be dissolved or melted. This is because of the anisotropic nuclear interactions which strongly depend on molecular orientation, and are therefore averaged by molecular motion. In liquids, the molecules reorient randomly very quickly: a water molecule requires ca. 10^{-11} s for complete reorientation. Although certain solids have sufficient molecular motion for their NMR spectra to be obtainable without resorting to special techniques, in the general case of a 'true solid,' there is no such motion, and conventional NMR, instead of sharp spectral lines, yields a broad hump which conceals most information of interest to chemists. For example, the width of the ^1H NMR resonance in the spectrum of water is ca. 0.1 Hz, while the line from a static sample of ice is ca. 100 kHz wide, i.e., a million times broader. Andrew et al. [12], and independently Lowe [13], had the idea of substituting the insufficient molecular motion in solids for the macroscopic rotation of the sample.

Consider a pair of protons, separated by distance r, in a rigid crystal immersed in an external magnetic field $\mathbf{B}_o$. Each nuclear magnetic dipole produces a magnetic field in its neighbourhood. Therefore, depending on its quan-

tum state (1/2 or –1/2), each of the two protons slightly increases or decreases the magnetic field acting on its neighbour, and the NMR line splits into a doublet. The splitting expressed in frequency units is $-\frac{3}{2} dh^{-1} (1 - 3\cos^2\theta)$, where d is the dipolar coupling constant proportional to r^{-3}, and γ^2, where γ is the gyromagnetic ratio of the proton and θ is the angle between the direction of the magnetic field $\mathbf{B}_o$ and the vector connecting the two protons.

The factor $(1-3\cos^2\theta)$, known as the second-order Legendre polynomial, comes from the secular part of the Hamiltonian of the dipolar interaction [14], which has the form

$$H = -\frac{1}{2} d \left[I^{(1)} I^{(2)} - 3I_z^{(1)} I_z^{(2)} \right] (1 - 3\cos^2\theta)$$

where the upper indices refer to the two interacting protons. The isotropic reorientation of molecules in liquids reduces the spectral effects of the dipolar interaction because the integral

$$\int (1 - 3\cos^2\theta) \, d\Omega$$

over the sphere vanishes. Here $d\Omega = \sin\theta d\theta d\phi$ is the element of the spherical angle.

It might seem, at first glance, that similar reduction could be easily obtained in solids by orienting a monocrystalline sample in such a manner that $(1-3\cos^2\theta)=0$, by adjusting the angle θ to be equal to arccos $\frac{1}{\sqrt{3}}$ 54°44'8,4" (the "magic angle"). No rotation would then be necessary. Unfortunately, other differently situated pairs of nuclei in the crystal would still broaden the spectrum.

Imagine that the sample rotates with an axis inclined to magnetic field $\mathbf{B}_o$ at an angle α. Denote the running angle of rotation by φ, so that $\frac{d\varphi}{dt} = \Omega$. As a result of the rotation the angle θ varies periodically. The relationship between $\cos\theta$ and φ can be obtained from a spherical triangle formed by the directions of $\mathbf{B}_o$, the proton–proton vector r and the axis of rotation (Fig. 1). Application of the 'cosine theorem' of spherical trigonometry to the triangle APQ gives

$$\cos\theta = \cos\beta \cos\alpha + \sin\alpha \cos\varphi$$

Introducing this expression into $(3\cos^2\theta-1)$ we obtain after some rearrangement

$$3\cos^2\theta - 1 = \frac{1}{2} (3\cos^2\alpha - 1)(3\cos^2\beta - 1) + \frac{3}{2} \sin^2\alpha \sin^2\beta \cos 2\varphi$$

$$= \frac{3}{2} \sin 2\alpha \sin 2\beta \cos\varphi .$$
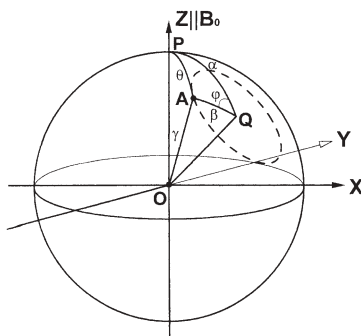
Fig. 1 The spherical triangle QAP formed by the direction OP of the magnetic field, the axis of sample rotation OQ and the interproton line OA. The proton pair is marked by *two heavy dots* (points O and A). By sample rotation the position A of one of the protons moves along the *dashed circle*. φ is the running angle of rotation

The angles α and β are constant and the time dependence resides only in φ. The mean *value* of the functions of φ is $\overline{\cos 2\varphi} = 0$ and $\overline{\cos \varphi} = 0$. We have therefore

$$\overline{3\cos^2\theta - 1} = \frac{1}{2}\,(3\cos^2\alpha - 1)\,(3\cos^2\beta - 1)$$

If the angle α between the axis of rotation and the direction of the magnetic field is 'magic', then $3\cos^2\theta - 1 = 0$, independently of the value of β which may differ for different pairs of protons. All dipolar interactions between protons within the sample are then reduced to zero permitting more subtle interactions to be observed. The same applies to the dipolar interaction from nuclei other than protons and to pairs composed of not necessarily the same spins. The name 'magic-angle spinning' was coined by the late Professor Gorter of Leiden when he learned about the method at the AMPERE Congress in Pisa in 1960. MAS imposes an average axial symmetry on an otherwise asymmetric environment. The magic angle is simply the angle between the body diagonal of a cube and each of the faces, equal to a half of the 'tetrahedral angle' (109°22′) known from organic chemistry.

The most common interactions, such as chemical shift anisotropy and dipole-dipole coupling, all transform as second-rank spherical harmonics. To average these interactions, we do not need to move the sample over a whole sphere, as nature does in liquids; we need only to impose cubic symmetry, and this is what MAS does. An early ^{31}P spectrum of zinc phosphide obtained with "magic-angle spinning" (MAS) is shown in Fig. 2 [15].

The chemical shift in a non-rotating single crystal depends on the orientation of the crystal with respect to the external magnetic field. Rotation of the sample, so effective in removing the effects of dipolar interaction, also averages
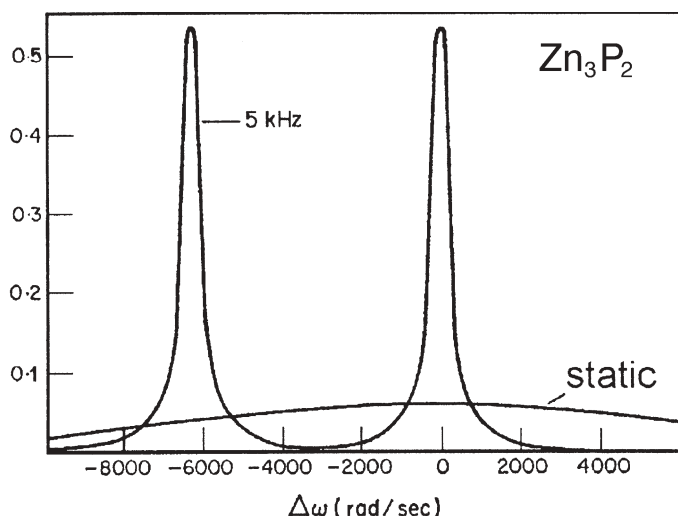
Fig. 2 ^{31}P NMR spectrum of rotating and static sample of polycrystalline zinc phosphide Zn$_3$P$_2$. The *two lines* are attributed to crystallographically inequivalent phosphorus sites in the tetragonal unit cell. Reproduced with permission from [15]

the anisotropy of the chemical shift to the isotropic value. The angular dependence of the chemical shift is described by a tensor, the elements of which can be calculated from measurements performed at different orientations. If the crystal is rotated under the magic angle, the observed chemical shift no longer depends on the orientation and – as for a liquid – its value is equal to the trace of the tensor. The anisotropy of the chemical shift is removed, and even a polycrystalline sample rotating under the magic angle gives a set of narrow lines corresponding to inequivalent crystal sites of the nucleus being observed. This feature of MAS is specially important when the solid is studied by NMR of nuclei other than protons. Chemical shifts of heavier nuclei are usually much larger and the perturbation due to dipolar interaction is weaker. The dipolar interaction has only a slight effect on the spectrum, and if a monocrystalline sample is available, the components of the chemical shift tensor can be readily measured. On the other hand, the spectra of polycrystalline samples appear as broad lines because the randomly oriented crystallites give their contributions at different positions on the frequency scale. If there is more than one inequivalent site, such a broad line is difficult or even impossible to interpret in terms of individual values of the tensor elements. The application of MAS then offers the only chance of obtaining useful information.

MAS requires high sample rotation speeds. If the sample rotates too slowly, satellite lines at integer multiples of the rotation frequency appear in the spectrum (Fig. 3) [16]. The rate of rotation must thus be at least comparable (in Hz) with the width of the spectrum of a static sample, since only then are the satellite spectra detached from the narrowed central line and separately resolved.

spinning rate
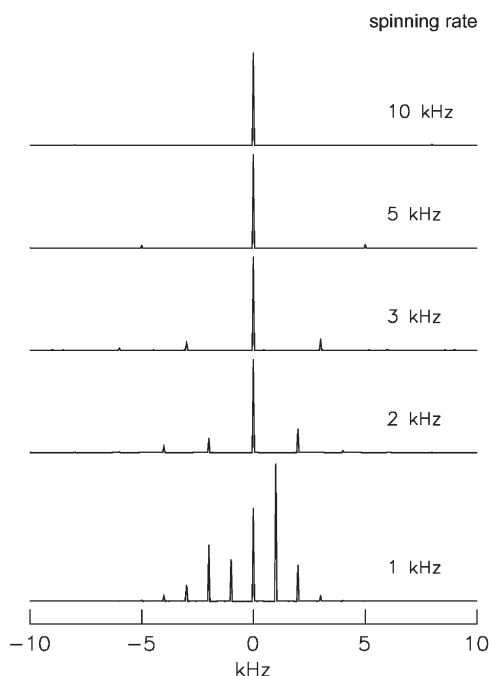
Fig. 3 The effect of slow magic-angle spinning. A set of spinning sidebands appears with a centre-band at the isotropic chemical shift and further lines spaced at the spinning frequency. The intensities of the sidebands change with spinning speed with higher-order sidebands (i.e., those further away from the centre-band) becoming less intense as the spinning speed increases. The chemical shift parameters used in the calculation of these sideband patterns are: isotropic chemical shift offset 0 Hz; chemical shift anisotropy 5 kHz; asymmetry 0. Reproduced with permission from [16]

In some cases observation of the satellites may also be useful since their intensities contain information on chemical shift anisotropy [17]. Rigorous mathematical description of MAS, particularly for the more complex slow-spinning case, with spinning satellites and rotor echoes, has been given by Schmidt-Rohr and Spiess [18].

The requirement of MAS for high frequencies poses a considerable practical challenge, and requires the use of gas-driven turbines with gas bearings. Rotation frequencies of the order of 5 kHz are often sufficient, but sometimes much higher speeds are needed. The spinning rate is limited by the strength of the rotor material to withstand the vast centrifugal forces. In addition, it was believed for a long time that the velocity of the surface of the rotor cannot exceed the velocity of sound in the driving gas. To deal with this, rotors were spun in helium, in which sound travels 2.7 times faster than in air. However, in the last ten years it has been shown that supersonic MAS frequencies can in fact be achieved. This topic is dealt with in the chapter by Samoson and his colleagues. Suffice it to say here, that the spinning rate record now stands at over 70 kHz.

While still insufficient to remove the very strong dipolar interactions between protons in organic solids, this spinning rate allows the acquisition of ^{19}F spectra of perfluorinated polymers, such as Teflon.

There are three main designs for the gas-bearing turbines used in MAS. The original design of Andrew, Bradbury and Eades is shown in Fig. 4a,b. The cylindrical part of the rotor contains the sample and is ca. 8 mm in outer diameter. The bottom part of the rotor has the form of a cone, with tiny flutes machined on the conical surface. The rotor is inserted into a double-walled stator in the shape of a conical bowl, the cone angle being slightly sharper than the rotor. The driving gas (air, nitrogen, or helium), under pressure of a few atmospheres, is conducted through the wall of the stator and reaches the rotor through small orifices, thus making it rotate. The rotor never touches the stator, but is firmly held inside it by the effect known as the 'hydrodynamic paradox'. This enables the adjustment of the rotation axis to the magic angle by orienting the stator
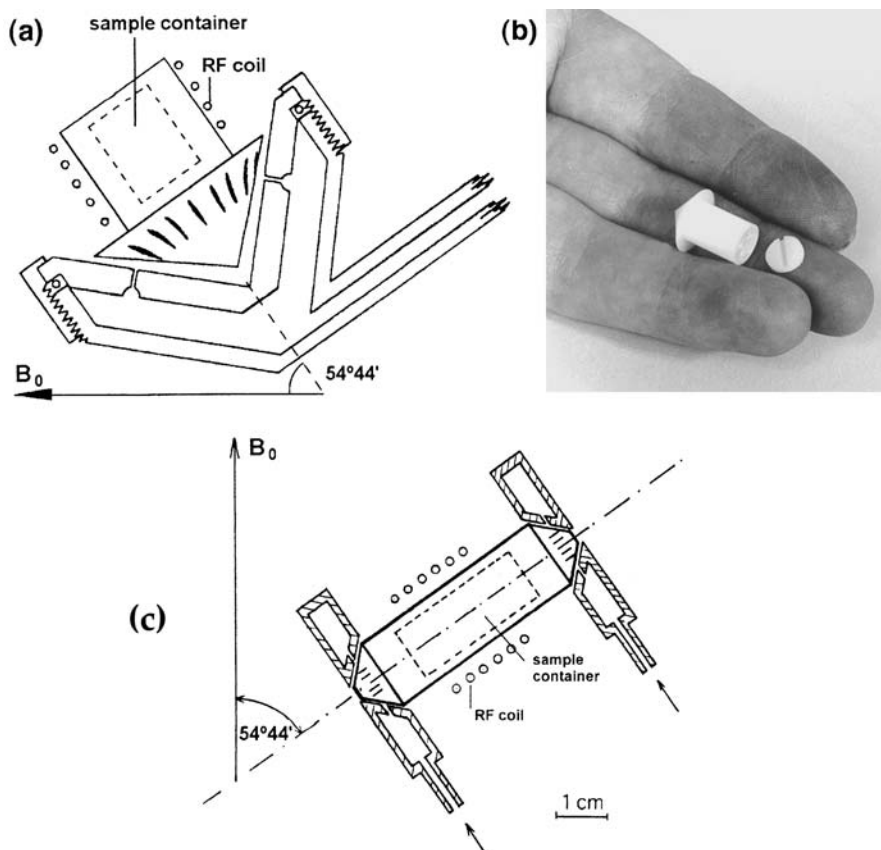
Fig. 4a–c Gas-bearing turbines used in MAS: **a** the original design of Andrew, Bradbury and Eades; **b** an Andrew-Beams rotor; **c** a modern MAS turbine with two gas bearings

precisely. Modern MAS turbines use two gas bearings (Fig. 4c), which provide better stability of the magic angle. In the third type of turbine (not shown) the rotor is supported by an axle [19].

By 1970 all important problems of MAS, both theoretical and experimental, seemed to have been solved. Spinning rates up to 15 kHz were attainable. Physicists made a number of successful applications of MAS to inorganic substances, including metals, and comprehensive reviews were published [18, 20]. Despite this, MAS was not gaining popularity comparable to that of high-resolution NMR of liquids. Physicists, disappointed by MAS, developed a competing method of line narrowing [21]. The idea was to average the term $[I^{(1)}I^{(2)} - 3I_z^{(1)}I_z^{(2)}]$ appearing in the secular Hamiltonian (1) instead of the term $(1 - 3\cos^2\theta)$. Special chains of radio frequency pulses were designed for the purpose, and interest in MAS seemed to decline.

However, the low period did not last long. In 1967–1970 two physical chemists in Prague, D. Doskocilová and B. Schneider, applied MAS to the study of polymers [22–24]. They found that to obtain line narrowing at practically attainable spinning speeds, the static linewidth must be partially narrowed by internal motion which is anisotropic and retains some residual static dipolar interactions. The resulting residual linewidth in the MAS spectrum is limited by the frequency of the internal motion, which causes partial narrowing of the spectrum [25]. Nevertheless, at perfect settings of the magic angle Doskocilová and Schneider could reach a resolution of 3 Hz, not only demonstrating the applicability of MAS to chemical problems but also showing that the method is not too difficult even for chemists, unlike the multiple pulse method which, incidentally, turned out to be less versatile than expected.

The pioneering work of Doskocilová and Schneider renewed interest in MAS just at the time when all branches of NMR were rapidly benefiting from the progress in technology. Solid-state electronics, superconducting magnets and cheap computers entered the laboratories to change NMR completely. Some old and unexploited ideas, such as Fourier transform NMR, could now be realized and soon replaced the old-fashioned and much less sensitive method of sweeping through the spectrum with a continuous wave. This conceptual and technological explosion affected MAS, adding new momentum to its further development. New advances were not long in coming.

In 1975, Schaefer and Stejskal [26] combined MAS with a method of magnetization transfer known as cross-polarization (CP), developed by Pines et al. [27]. The combined method, known as CP/MAS, can be applied to organic substances and permits high-resolution spectra of ^{13}C at its natural low abundance (1.1%) to be obtained. CP/MAS makes use of the fact that such substances contain protons at rather high concentration. A specially designed double-resonance procedure transfers the strong polarization of protons to ^{13}C, enabling those magnetically weak and low-abundance spins to give a sufficiently strong signal. At the same time, magic angle spinning removes the broadening caused in polycrystalline samples by chemical shift anisotropy. A spectrum is then obtained which is as well resolved and readily interpretable as in the case of liq-

uid samples. CP/MAS soon gained recognition by chemists and became a routine method for investigating organic and inorganic solids.

^{29}Si was, after ^{13}C, the next nucleus to become extensively studied by high-resolution NMR in solids. It appears at 4.7% abundance and has spin 1/2. The first highly resolved ^{29}Si CP/MAS and MAS spectra of solid silicates and organosilicon compounds were obtained by the Tallinn group led by E. Lippmaa, in collaboration with G. Engelhardt from the then East Berlin [28]. They showed that the five environments of a silicon atom $Si(OAl)_{4-n}(OSi)_n$ (where n=0, 1, 2, 3, or 4) have different ^{29}Si chemical shifts. Soon several other research groups, notably those at Cambridge University (Klinowski), EXXON (Melchior), Shell-Amsterdam, Leipzig (Pfeifer and Freude), Namur (Derouane and Nagy), and Nijmegen (Veeman) embarked on their own investigations. In highly siliceous zeolites, ^{29}Si signals from $(OSi)_4$ units correspond quantitatively to inequivalent sites for silicon [29]. Extensive ^{1}H MAS measurements of zeolites by the Leipzig group led to the assignment of various proton resonances [30]. ^{13}C MAS studies by the Cambridge group identified 29 different organic species in the intracrystalline environment of zeolite ZSM-5 during the catalytic conversion of methanol to gasoline, and monitored their fate as a function of time and temperature [31, 32].

MAS works very well with spin 1/2 nuclei such as ^{13}C, ^{15}N, ^{29}Si, and ^{31}P, but is less successful with quadrupolar nuclei, such as ^{11}B, ^{17}O, ^{23}Na, and ^{27}Al, which have an asymmetric distribution of the nuclear charge. This is because the second-order quadrupolar interaction is not averaged to zero by MAS alone. Although MAS does reduce the linewidth of the NMR spectra of such nuclei, this is often insufficient for the spectra to be chemically interpretable. The MAS NMR spectrum then consists of a number of satellite resonances symmetrically situated on the frequency scale with respect to the central line appearing at the main resonance frequency, $\gamma B_o/2\pi$ (Fig. 5). Since the positions of the satellites are strongly orientation-dependent, in polycrystalline samples the satellites form a line so broad as to be practically invisible, because they are spread over a very wide range of frequencies. Although chemical shift information can in principle be inferred from the exact position of the central line, this is not easy, because the central line is broadened – and shifted – not only by the chemical shift anisotropy, but also by second-order quadrupolar effects which cannot be averaged out by spinning the sample about a single axis.

In particular, ^{27}Al MAS NMR in solids has, in the past, been something of a disappointment in comparison with, for example, ^{29}Si, a sister nucleus which gives highly resolved MAS spectra. This was very unfortunate, since aluminium is the second most abundant element in the Earth's crust, and over half of all known minerals are silicates and aluminosilicates. It is thus highly desirable for chemists, mineralogists, metallurgists, and materials scientists to be able to obtain high-resolution spectra of this nucleus.

Strategies developed for increasing the resolution of quadrupolar NMR spectra invariably combine MAS with various radiofrequency pulse trains. They include two-dimensional quadrupole nutation, which uses the correlation
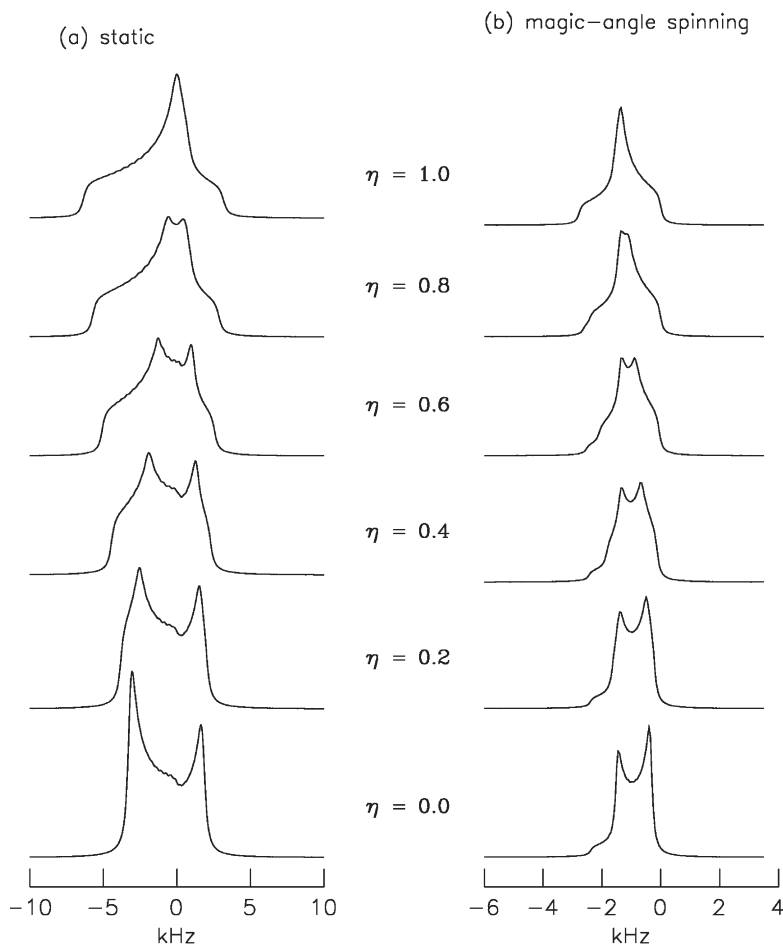
Fig. 5 The effect of magic-angle spinning on the central transition lineshape for a half-integer spin quadrupolar nucleus. *Left*: central transition lineshape under static, i.e., non-spinning conditions. *Right*: the same transition under magic-angle spinning. The asymmetry parameter η is given with each spectrum. Reproduced with permission from [61])

between the quadrupolar parameters and the precession frequencies induced by the pulses [33–35]; satellite transition spectroscopy (SATRAS), which can determine the quadrupole and chemical shift parameters [36–39], and quadrupolar phase alternated sideband suppression (QPASS), which suppresses the overlapping spinning sidebands in the MAS spectra of quadrupolar nuclei [40]. Dipolar interactions between the quadrupolar and spin-1/2 nuclei have been measured using cross-polarization (CP), rotational echo double resonance (REDOR) [41–44], transferred echo double resonance (TEDOR) [42, 45], transfer of populations double resonance (TRAPDOR) [44, 46], and rotational echo adiabatic passage double resonance (REAPDOR) [43, 44].
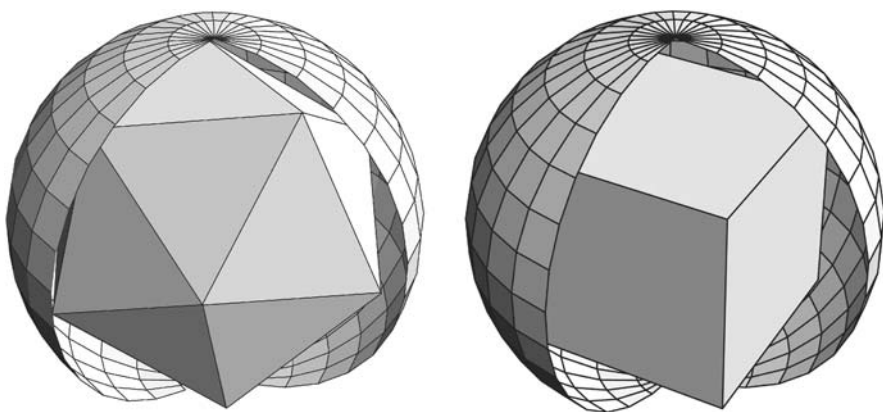
Fig. 6 DOR has icosahedral symmetry (*left*) and DAS has cubic symmetry (*right*)

Group theory tells us that the quadrupolar interaction transforms as fourth-rank spherical harmonics, and is averaged by motion conforming to icosahedral symmetry. The icosahedron is a better approximation to a sphere than a cube (Fig. 6), and the question of inscribing an icosahedron into the sphere is the famous "Euclid's last problem". However, icosahedral symmetry cannot be achieved by rotating the sample about a single axis [47, 48]. Pines and his group, working together with Samoson and Lippmaa in Tallinn, Estonia, realized that there were two different ways of spatial averaging of the second-order quadrupolar broadening of the central transition. The argument goes as follows.

The second-order quadrupole interaction depends on the Wigner rotation matrices, which become time-dependent when the sample is rotated about an angle θ with respect to $\mathbf{B}_0$. The average second-order quadrupolar shift then depends on the Legendre polynomials

$$P_2(\cos\theta) = \frac{1}{2}\,(3\cos^2\theta - 1) \quad \text{and} \quad P_4(\cos\theta) = \frac{1}{8}\,(35\cos^4\theta - 30\cos^2\theta + 3)$$

There is clearly no value of θ for which both the $P_2(\cos\theta)$ and the $P_4(\cos\theta)$ terms are zero. One way of satisfying both the above equations together, known as "Double Rotation" (DOR) [49, 50], is to spin the sample *simultaneously* about two axes: the first axis is inclined to the magnetic field at the magic angle (the zero of the second-order Legendre polynomial); the second at the angle which is the zero of the fourth-order Legendre polynomial (Fig. 7). The sample is placed in a small inner rotor, which is rotating inside an outer rotor [48]. We then have

$$P_2(\cos\theta_1) = 0 \quad \text{and} \quad P_4(\cos\theta_2) = 0$$

with solutions $\theta_1=54.74°$ (the conventional "magic angle") and $\theta_2=30.56°$ or $70.12°$. The resulting complicated sample trajectory averages the anisotropic broadening to zero.
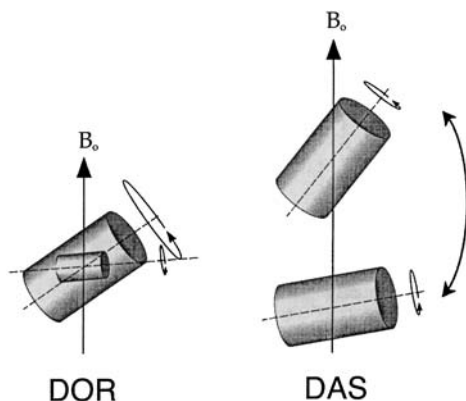
Fig. 7 DOR and DAS

But how does one supply the driving gas to a rotor which is itself embedded in another rotor? An awesome engineering task, but not one which could not be successfully solved. It turns out that, if the centres of gravity of the two rotors exactly coincide, there is no net torque acting on the inner rotor which contains the sample. DOR signals are greatly reduced in width in comparison with MAS, and are not much broader than those measured in liquids. The greater spectral resolution is accompanied by an improvement in sensitivity. It is interesting to note that the principle of DOR is similar to that of the "Gandolfi camera" [51, 52], used by crystallographers for obtaining X-ray *powder* patterns of very small *single* crystals, which also rotates about two independent axes.

In 'Dynamic Angle Spinning' (DAS) [53–55], the sample is rotated *sequentially* about two different axes, θ'_1 and θ'_2, which are chosen so that

$$P_2(\cos\theta'_1) = -P_2(\cos\theta'_2) \quad \text{and} \quad P_4(\cos\theta'_1) = -P_4(\cos\theta'_2)$$

with the solutions $\theta'_1 = 37.38°$ and $\theta'_2 = 79.19°$. The sample is rotated about the first axis, reoriented, rotated about the second axis and so on (Fig. 7). As switching the rotation axis cannot be performed instantaneously, an echo pulse sequence must be used to preserve the transverse magnetization during the angle-switching period.

DOR and DAS achieve resolution enhancement by one or two orders of magnitude [56]. For example, the ^{17}O DOR NMR spectrum of the mineral diopside clearly reveals the presence of three crystallographically inequivalent oxygen sites [53]. Both techniques have been used for the study of minerals, heterogeneous catalysts, zeolites, glasses, polymers, and superconductors.

In 1995 Frydman et al. realized that the line narrowing of the central transition can be achieved by changing the coherence state of the spins instead of spatial reorientation of the spinning axis [57, 58], and proposed a third method of avoiding second-order quadrupolar broadening, known as Multiple-Quantum MAS (MQ-MAS). This two-dimensional method uses fast MAS and cor-

relates the phase evolutions of the multiple-quantum and single-quantum co-herences, permitting the observation of a purely isotropic echo. The coherence state of half-integer quadrupolar spins is controlled by using strong radiofre-quency irradiation [59, 60]. MQ-MAS does not suffer from the closely-spaced spinning sidebands in DOR and the loss of magnetization through relaxation during the reorientation of the spinner axis in DAS, and is of considerable value in studies of catalysts, glasses and of amorphous and crystalline inorganic solids in general. The technique is fully discussed in the chapter by Rocha, Morais, and Fernandez.

It is interesting to note that MAS NMR was not the initial goal of its inven-tor, Professor Andrew. When beginning to work with rotating samples, he was interested in the relationship between the second moment of NMR lines and molecular motion in solids, aiming to solve a paradox which intrigued physi-cists in the 1950s. This is as follows. On the one hand, it was known from the Van Vleck theory that the second moment of an NMR spectrum is invariant to orientation. On the other, experiments showed that in many solids the second moment decreases as a result of random molecular rotations, especially at el-evated temperatures. Andrew's calculations indicated that coherent rotation of the sample should split the spectrum into a set of satellites separated from the central line by multiples of the spinning frequency. He suspected that the sec-ond moment of such a spectrum is constant, independent of the speed of ro-tation. In the case of incoherent random molecular rotations caused by inter-nal thermal excitations, the satellites would be invisible, being spread over a broad frequency range. The central line alone would remain, representing only a part of the second moment. Andrew confirmed this hypothesis by examining spectra of rotating samples, which led him to the idea of MAS. This story shows how research on a purely academic problem may unexpectedly produce results of great practical value.

References

1. Purcell EM, Torrey HC, Pound RV (1946) Phys Rev 69:37
2. Bloch F, Hansen WW, Packard M (1946) Phys Rev 69:127
3. Dickinson WC (1950) Phys Rev 77:736
4. Proctor WG, Yu FC (1950) Phys Rev 77:717
5. Hahn EL (1950) Phys Rev 80:580
6. Andrew ER (1956) Nuclear magnetic resonance. Cambridge University Press, Cambridge
7. Saha AK; Das TP (1957)Theory and applications of nuclear induction. Saha Institute of Nuclear Physics, Calcutta, India
8. Pople JA, Schneider WG, Bernstein HJ (1959) High-resolution nuclear magnetic reso-nance. McGraw-Hill, New York
9. Jackman LM (1959) Applications of nuclear magnetic resonance spectroscopy in organic chemistry. Pergamon Press, Oxford
10. Roberts JD (1959) Nuclear magnetic resonance: applications to organic chemistry. McGraw-Hill, New York
11. Abragam A (1983) The principles of nuclear magnetism. Clarendon Press, Oxford

12. Andrew ER, Bradbury A, Eades RG (1959) Nature 183:1802
13. Lowe IJ (1959) Phys Rev Lett 2:285
14. Hennel JW, Klinowski J (1993) Fundamentals of nuclear magnetic resonance. Longman, Harlow, UK
15. Kessemeier H, Norberg RE (1967) Phys Rev 155:321
16. Duer MJ (2002) Essential techniques for spin-1/2 nuclei. In: Duer MJ (ed) Solid-state NMR spectroscopy: principles and applications. Blackwell Science, Oxford, pp 73
17. Maricq MM, Waugh JS (1979) J Chem Phys 70:3300
18. Schmidt-Rohr K, Spiess HW (1994) Multidimensional solid-state NMR and polymers. Academic Press, London
19. Andrew ER (1970) Progress in nuclear magnetic resonance spectroscopy 8, part I
20. Mansfield P (1970) Progress in nuclear magnetic resonance spectroscopy 8, part I, p 41
21. Haeberlen U (1976) High resolution NMR in solids. Selective averaging. Supplement 1 to Advances in magnetic resonance. Academic Press, New York
22. Doskocilová D, Schneider B (1970) Chem Phys Lett 6:381
23. Schneider B, Doskocilová D, Babka J, Ruzicka J (1980) J Magn Reson 37:41
24. Doskocilová D, Schneider B (1982) Pure Appl Chem 54:575
25. Andrew ER, Jasinski A (1971) J Phys C 4391
26. Schaefer J, Stejskal EO (1976) J Am Chem Soc 98:1031
27. Pines A, Gibby MG, Waugh JS (1973) J Chem Phys 59:569
28. Lippmaa E, Alla MA, Pehk TJ, Engelhardt G (1978) J Am Chem Soc 100:1929
29. Ramdas S, Klinowski J (1984) Nature 308:521
30. Freude D, Hunger M, Pfeifer H, Schwieger W (1986) Chem Phys Lett 128:62
31. Anderson MW, Klinowski J (1989) Nature 339:200
32. Anderson MW, Klinowski J (1990) J Am Chem Soc 1990 112:10
33. Samoson A, Lippmaa E (1988) J Magn Reson 79:255
34. Nielsen NC, Bildsøe H, Jakobsen HJ (1992) J Magn Reson 97:149
35. Kentgens APM (1993) J Magn Reson A104:302
36. Samoson A (1985) Chem Phys Lett 119:29
37. Jakobsen HJ, Skibsted J, Bildsøe H, Nielsen NC (1989) J Magn Reson 85:173
38. Jäger CJ (1992) Magn Reson 99:353
39. Jäger C (1994) Satellite transition spectroscopy of quadrupolar nuclei. In: Solid-state NMR II: inorganic matter, vol 31. Springer, Berlin Heidelberg New York
40. Massiot D, Montouillout V, Fayon F, Florian P, Bessada C (1997) Chem Phys Lett 272:295
41. Gullion T, Schaefer J (1989) J Magn Reson 81:196
42. Fyfe CA, Mueller KT, Grondey H, Wong-Moon KC (1992) Chem Phys Lett 199:198
43. Gullion T (1995) J Magn Reson A117:326
44. Gullion T (1995) Chem Phys Lett 246:325
45. Hing AW, Vega S, Schaefer J (1992) J Magn Reson 96:205
46. Grey CP, Vega AJ (1995) J Am Chem Soc 117:8232
47. Llor A, Virlet J (1988) Chem Phys Lett 152:248
48. Samoson A, Lippmaa E, Pines A (1988) Mol Phys 65:1013
49. Chmelka BF, Pines A (1989) Science 246:71
50. Chmelka BF, Zwanziger JW (1994) In: Solid-state NMR II: inorganic matter, vol 33. Springer, Berlin Heidelberg New York
51. Gandolfi G (1967) Mineral Petr Acta 13:67
52. Graeber EJ, Jelinek DA (1966) Norelco Rep 13:91
53. Chmelka BF, Mueller KT, Pines A, Stebbins J, Wu Y, Zwanziger JW (1989) Nature 339:42
54. Mueller KT, Sun BQ, Chingas GC, Zwanziger JW, Terao T, Pines A (1990) J Magn Res 86:470
55. Mueller KT, Wooten EW, Pines A (1991) J Magn Res 92:620

56. Mueller KT, Wu Y, Chmelka BF, Stebbins J, Pines A (1991) J Am Chem Soc 113:32
57. Frydman L, Harwood JS (1995) J Am Chem Soc 117:5367
58. Medek A, Harwood JS, Frydman L (1995) J Am Chem Soc 117:12779
59. Vega S, Naor Y (1981) J Chem Phys 75:75
60. Nielsen NC, Bildsøe H, Jakobsen HJ (1992) Chem Phys Lett 191:205
61. Duer MJ (2002) Quadrupole coupling. In: Duer MJ (ed) Solid-state NMR spectroscopy: principles and applications. Blackwell Science, Oxford, p 179

New Horizons for Magic-Angle Spinning NMR

Ago Samoson (✉) · Tiit Tuherm · Jaan Past · Andres Reinhold ·
Tiit Anupõld · Ivo Heinmaa

National Institute of Chemical Physics and Biophysics, Akadeemia Tee 23, Tallinn Estonia
ago@kbfi.ee

Abstract   Recent developments in sample rotation technology have had a profound impact
on magic-angle-spinning NMR. First, rotation frequencies approaching, and even exceed-
ing, strong homonuclear spin interactions have made high-resolution solid-state ^1H spec-
troscopy much more accessible. Second, the new concept of fast rotation sweep spectroscopy
has emerged. Third, high-resolution NMR at cryogenic temperatures has become feasible,
offering an enormous sensitivity gain and the opportunity to study a wide range of physi-
cal phenomena.

Keywords   Magic-Angle Spinning NMR · Sample rotation · Rotor size · Selectivity ·
Sensitivity · Spectral resolution

1
Introduction

Magic-angle-spinning (MAS) NMR is one of the most fascinating experimental
techniques in modern science, offering unprecedented cross-disciplinary appli-
cations. MAS NMR, with rotors routinely spinning at subsonic rates, is being used
across the world by physicists, chemists, biologists and materials scientists. Al-
though the technique was invented in the late 1950s, it became widely used only
about 25 years later, due to advances in spectrometer hardware and ceramics
technology. The sample spinning systems now use much more stable double-

bearing designs than the prototype mushroom-shaped Andrew-Beams rotors. The rotors are fixed in a shaft by gas-lubricated bearings, while the driving momentum is provided by one or more separate sets of high speed gas jets.

Originally designed with the aim of eliminating internuclear interactions, MAS spectroscopy was concerned with a systematic study of cross-polarization between abundant and rare spin systems. Subsequent developments have introduced many sophisticated manipulations of spin interactions to unravel the structure and dynamics of solid materials. The latest advances described in this contribution illustrate the new methods of tackling the problems of selectivity, sensitivity and spectral resolution.

2
Basic Theory

The product of maximum sustained rotation frequency and rotor diameter, obtained from the well-known relationship

$$v = \frac{\sqrt{3}}{\pi} \sqrt{\frac{T\Delta}{\varrho}} \frac{1}{D}$$

where T is the tensile strength of the material, Δ the relative wall thickness of the rotor, ϱ density of the material and D the rotor diameter, is at present ~90 Hz m, so that the external surface of the rotor travels at ca. 85% of the speed of sound. The actual limit depends primarily on the tensile strength of the rotor material, provided that the necessary precautions concerning rotor balancing and bearing lubrication are taken [1].

Not only the ultimate speed but also the safety of operation are very important considerations in MAS NMR. For example, isotopically labelled biopolymers are not only very expensive, but may also pose a serious health hazard if a rotor containing a sample such as amyloid fibril protein disintegrates in the laboratory.

Reliable operation of MAS requires a reasonable understanding of the principles of mechanics, careful rotor handling and a stable supply of very clean compressed gas. The performance and stability of the experiment depend on the quality of rotor filling, which can be conveniently tested by a histogram of the rotor speed. The alignment of the rotor with respect to its bearings can be described in terms of harmonic oscillations. To a good approximation, the deviation of the axis of the rotor from the ideal position is countered by a force proportional to the deviation at low spinning frequencies. The rotor then experiences two mechanical resonances, characteristic of translational and conical whirl modes, at the respective frequencies

$$\omega_T = \sqrt{\frac{2K}{M}} \tag{1}$$

$$\omega_C = \sqrt{\frac{K}{2(I_\perp - I_A)}} L_B \qquad (2)$$

where K is the bearing force constant and L_B is the length of the bearing. Transverse and axial inertial moments depend on the diameter, length and mass of the rotor:

$$I_\perp = \left(\frac{D^2}{16} + \frac{L^2}{12}\right) M \qquad (3)$$

$$I_A = \frac{D^2}{8} M \qquad (4)$$

The frequency of the conical resonance is ca. 1.4 times higher than the translational resonance for a typical aspect ratio $a=L/D$ of the rotor. Demand for the rotor drive energy increases on approaching the mechanical resonance frequency. The increasing amplitude of the rotor deviation from the symmetry axis on approaching the frequency of mechanical resonance directs part of the drive energy to vibration of the rotor housing. Figure 1 shows a set of rotation speed spectrograms for different bearing pressures, with a slow gradual in-
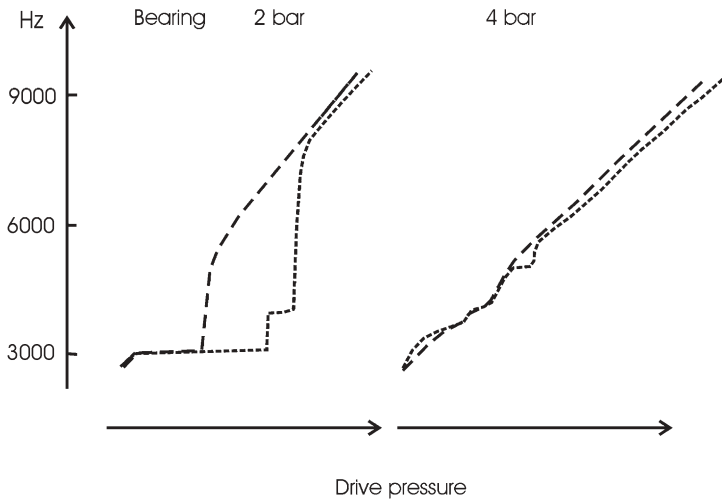
Fig. 1 Mechanical resonances of a 4-µL rotor filled with a specially shaped solid, simulating cylindrical and conical asymmetry. Rotation speed was slowly increased by servo-controlled drive pressure. Cylindrical imbalance (*long dash*) enables corresponding modes of resonance to be identified. The ratio of jerk positions closely corresponds to the theoretical ratio of two different resonance modes. Higher bearing pressure increases the force constant and the frequencies of the mechanical resonances

crease in the drive pressure. The mechanical resonance parameters can be readily identified by using a test rotor with deliberately simulated asymmetric rotor filling. The increase in rotor speed almost disappears on approaching the resonance condition. After passing the resonance threshold, the rotor picks up speed very quickly, following a virtually linear curve. The force constant is larger and mechanical resonances shift to higher frequencies for higher bearing pressures (right hand graphs). The plot also shows the splitting of translational resonance positions, indicating that different conditions apply at opposite ends of the rotor. Part of the energy which is absorbed by the stator is proportional to the deviation of the rotor and thus to the imbalance. The eccentricity may become too large for the rotor-bearing geometry, or residual drive energy may become insufficient for a further rotor acceleration. Reduction of the force constant by lowering the bearing pressure brings resonance frequencies down and, by doing so sufficiently quickly, rotor motion may 'tunnel' beyond the critical resonance barrier. This procedure is frequently used to spin up poorly balanced rotors.
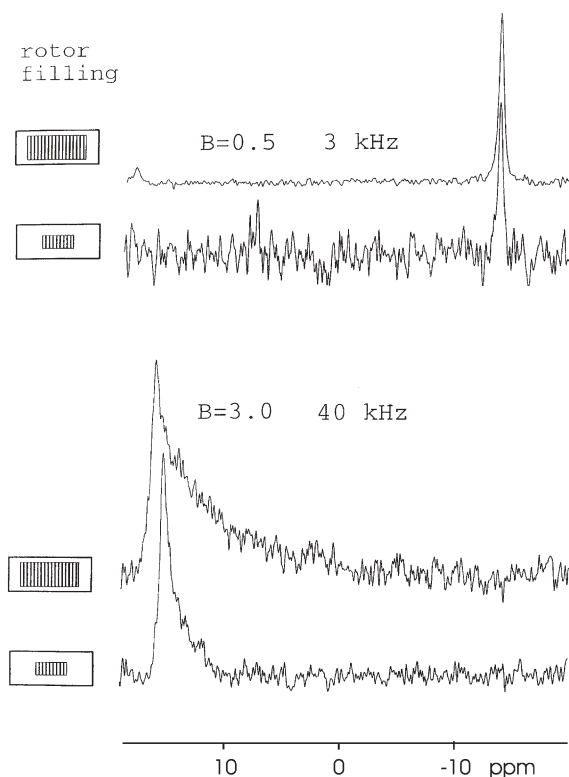
Fig. 2 ^{207}Pb signal of lead nitrate at 3 kHz and 40 kHz rotation frequencies. The profile of the signal reflects temperature distribution in the rotor, as tested with two filling configurations

Another common problem with fast rotation is rotor warming. Surface friction heats rotors proportionally to the second power of the speed [2]. Lead nitrate is a convenient compound to monitor the temperature via the change of chemical shift [3]. A peak shift of ca. 30 ppm, corresponding to a ca. 40 °C temperature increase, is observed as the rotation speed is increased to 40 kHz (Fig. 2). The distribution of the recorded signal is associated with the heating profile. This is a manifestation of the rotor size scaling. The ratio of the rotor surface area to the bulk volume scales up with the reduction of linear dimension, thus amplifying the temperature distribution. A very similar scaling effect applies to the inhomogeneity of the magnetic field induced by the coil and the stator. We have also observed a measurable increase in sample temperature in a poorly balanced rotor, indicating increased friction caused by reduction of the clearance between the rotor wall and the bearing surface. The spinning system is then more sensitive to other fluctuations, such as contamination of the driving gas by dust particles, and the probability of mechanical damage is thus increased.

3
Spectroscopy at High Speed Limits

One of the major problems in solid-state NMR is homogeneous line broadening of the spectra of abundant spin systems. Multiple-pulse suppression methods work only within a very limited range of rotation frequency and require extremely careful setup. Even then, results suffer from quantitative distortions by the frequency offset and by the relaxation and mobility properties of atoms at different positions within the solid. The offset and chemical shift anisotropy become even more of a problem at higher magnetic fields. A straightforward non-scaled Bloch decay measurement may be the most convenient and reliable solution in many cases. In addition, various 2D experiments benefit from direct suppression of the ^{1}H dipolar interaction. A combination of high rotation frequencies with increased chemical shift range at high magnetic fields is especially attractive [4]. While the homogeneous broadening remains constant on the frequency scale, line separation increases on the ppm scale. A "quadratic" effect can thus be obtained with a combined increase in mechanical spinning and in spin precession frequencies.

We have found that the dependence of the linewidth on rotor speed for the aminoacid alanine is almost linear (Fig. 3). Although the residual homogeneous dipolar line broadening is the dominant resolution-limiting factor even at 70 kHz, a much more detailed study of the individual lines and spin relaxation properties becomes feasible. For example, a rotation speed dependent relaxation has been observed and discussed by Gil and Alberti [5]. A site selective study will be available due to suppression of spin diffusion. Figure 3 also shows that the width of the lines from the amine protons converges to a quite different value than that from the aliphatic and methyl protons (see below).

Alanine 600 MHz 1H: NH$_3$, CH$_3$, CH
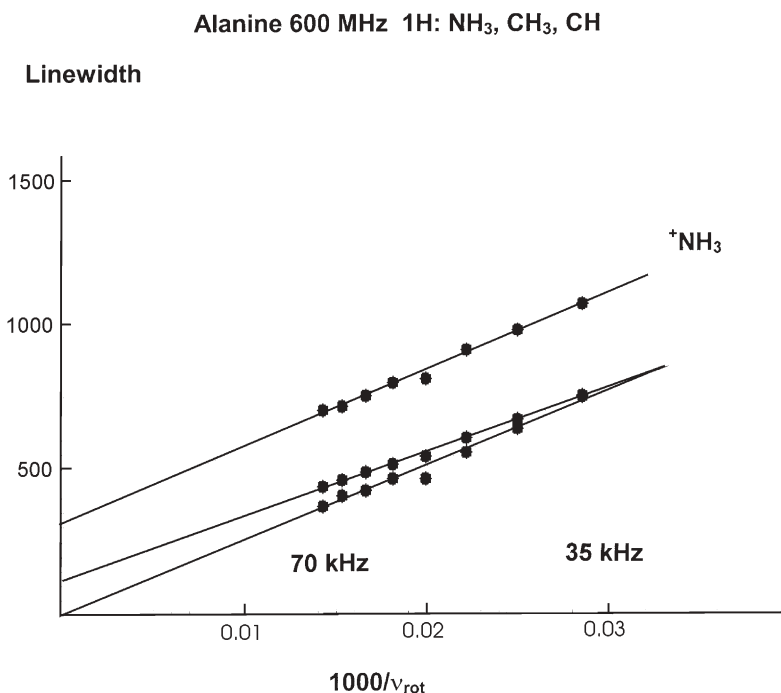
Fig. 3 Dependence of the linewidth of the ^1H spectrum of alanine on rotation speed, measured at 600 MHz. The sample was cooled to compensate for rotation-induced heating

Multi-spin behaviour in an abundant spin system can be observed indirectly by studying the linewidth dependence of a rare spin as a function of the amplitude of the decoupling radiofrequency. Figure 4 shows the efficiency of the proton decoupling on the amplitude of the alpha carbon line in glycine. Well known recoupling conditions, where the proton rf amplitude matches the double and single spinning frequency, are complemented by evidence of the recoupling at a third of the rotation frequency. This phenomenon becomes observable only at very high rotation frequencies (above 35 kHz) and implies a three-quantum overtone process in the proton spin system. Three-spin interactions have been theoretically analysed as the ultimate mechanism of homogeneous line-broadening at high rotation frequencies [6].

As is clear from Fig. 4, CW decoupling and resolution enhancement are more effective at the low end of decoupler power for a given range of ca 200 W. Low-power decoupling is a completely new situation in standard MAS. Theoretically, the order of spin interaction averaging is reversed, and mechanical reorientation has to be considered first. More sophisticated decoupling schemes have been proposed and analysed by Ernst et al. [7, 8]. Although the CH$_2$ lines were still narrower at high decoupling powers, the low power option constitutes a very competitive, if not better, alternative for the rest of the spectrum. In the
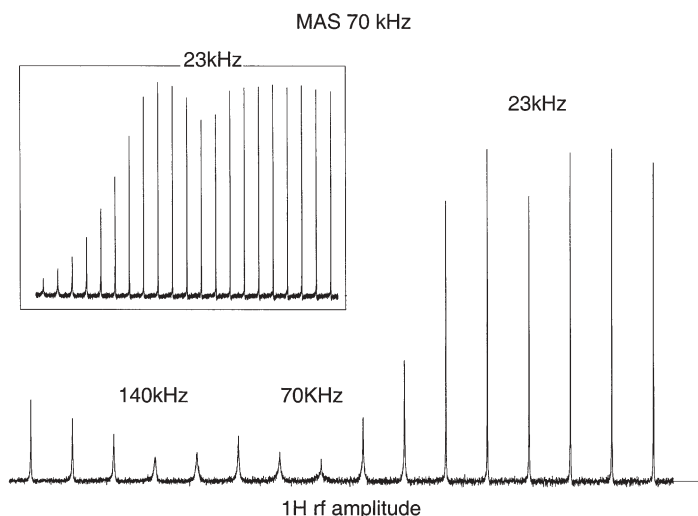
Fig. 4 Sequence of 150 MHz Cα lines of glycine with progressively decreasing decoupling power, step –1 dB and –0.25 dB (*insert*). Rotational resonances occur at double, single and fractional (1/3) rotation frequency

case of temperature-sensitive biological samples, low power decoupling may well become established as the method of choice.

Various correlation and internuclear distance measurements are based on zero- or double quantum spin flips. The most efficient correlation methods are based on the adiabatic process, which is relatively insensitive to actual, orientation-dependent coupling strength. A double-quantum spin flip is generated by a sweep of the rf field amplitude, centred at half rotation frequency (the HORROR condition [9]). The increased rotation frequency leads to a crucial improvement in the broad-band character of the DREAM method [10]. The zero-quantum adiabatic spin flip process is considered in the next section.

Various 1D and 2D experiments related to first-order quadrupole broadening also benefit from the fast rotation frequency. For heavier nuclei, quadrupole interaction and chemical shift anisotropy averaging at higher speeds results in better focusing of signal intensity to the remaining rotation sidebands (Fig. 5).

4
Rotation Sweep

The recently introduced rotation sweep spectroscopy [11] is based on the realization that decreased rotor size provides acceleration proportional to the inverse cube of the rotor diameter
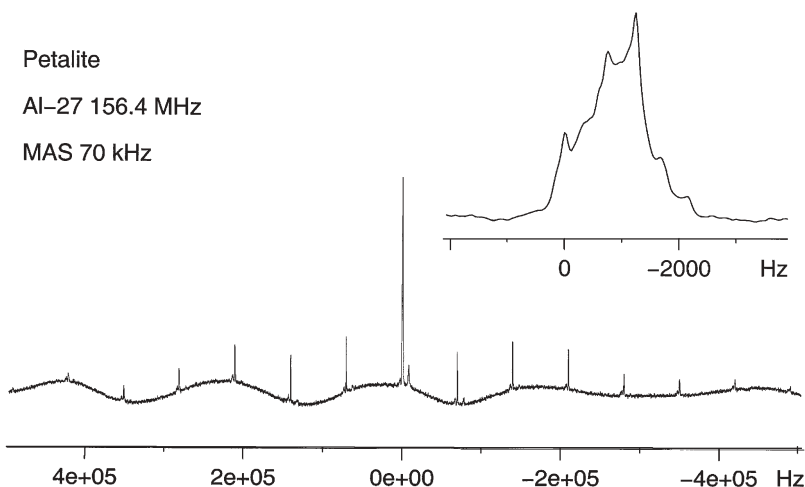
Fig. 5 [27]Al spectrum of the mineral petalite measured at 156 MHz. Quadrupole coupling can be estimated at 4.8 MHz, and the set of first-order satellite transition sidebands spans ca. 1 MHz

$$\dot{v} = \frac{16f}{\pi a \varrho} \frac{1}{D^3}$$

where, in addition to the definitions given earlier, f is the driving force per unit circumference. A stator with two 5-bar drive rings at opposite ends of the rotor provided acceleration rates up to 1 MHz for a 10 µL sample in our experimental setup. A rapid change of speed over 10 kHz is then performed in a timescale much shorter than typical spin-lattice relaxation, and even shorter than spin-lock relaxation in many cases. This experimental degree of freedom permits diverse real-time combinations of radiofrequency field amplitude and rotation frequency. For example, a robust broad-band cross-polarization approach was experimentally demonstrated [12]. Generally, efficient thermal contact between two spin species during sample spinning is provided only if the respective rf field amplitudes differ by a single or double rotation speed value. However, the rf field falls across the (regular pitch) solenoidal coil towards the coil ends in proportion to the maximum value, whereas spinning frequency is uniform. Therefore, whole sample cross-polarization is not possible if the two fields and sample spinning are kept constant. Fast acceleration is allowed to ramp the initially stationary sample to a regular high-resolution speed during the cross-polarization process. The resulting signal intensity is immune to variations of radiofrequency amplitude over the length of the coil and to a mismatch of the Hartmann-Hahn condition, thus providing maximum available polarization transfer over the entire sample.

A very useful class of solid-state experiments exploits the rotational resonance condition, where the rotation frequency is set to be equal to a multiple

of the difference between the isotropic line positions. Selective homonuclear re-coupling is generated, providing information on the internuclear configuration. By changing the rotation speed, the rotational resonance condition can be passed adiabatically. A formal description can be given in terms of the inter-change of phase (=identity) information of the two nuclear spins. The site-spe-cific coherent phase, acquired during the evolution period, is stored in level population density matrix elements ϱ_{nn}. The sweep through the rotational res-onance condition swaps populations ϱ_{11} and ϱ_{22} of the inner energy levels, which on the basis of the direct product can be written as:

$$M_{S1}(t) = Tr\{S1_z\varrho(t)\} = \frac{1}{2}\left(\varrho_{00} + \varrho_{11} - \varrho_{22} - \varrho_{33}\right) \rightarrow M_{S2}(t) \tag{5}$$

$$M_{S2}(t) = Tr\{S2_z\varrho(t)\} = \frac{1}{2}\left(\varrho_{00} + \varrho_{22} - \varrho_{11} - \varrho_{33}\right) \rightarrow M_{S1}(t) \tag{6}$$

The physical picture of the experiment is analogous to the adiabatic passage in the rotating frame, as in the case of a strong Zeman field and a small perturb-ing transverse field, which is scanned over the resonance condition of a two-level system by changing the carrier frequency. Here, a two-level system is com-posed of the inner pair of energy levels of a two-spin system, and the radiofrequency field is formed by the perpendicular component of a dipolar field, modulated by the sample rotation at the 'radio frequency', typically in the range of 10 kHz. If the rotation frequency approaches the difference between the energy levels, here equal to the difference in chemical shifts, spins start to follow the change of the dipolar field modulated by the rotor frequency sweep. An alternative description uses the avoidance of level crossing of the so-called dressed states [13], where each spin energy level is flanked with a swarm of vir-tual levels, displaced by multiples of the rotation frequency.

Unlike correlation spectroscopy based on spin diffusion, the adiabatic ver-sion enables, in principle, almost full exchange of magnetization between the two spins. As a result, the entire signal intensity will reside in the cross-peaks. Violation of the adiabaticity is characterized by the appearance of a diagonal peak and can be expected to occur if the rotation sweep is too fast compared to the interaction between spins. While numerical simulations indicate possi-ble linear dependencies of the polarization transfer coefficient on spin coupling and the rate of the sweep over a range of practical values, the validity of this as-sumption remains to be tested. Here we present a semi-quantitative example of a relayed polarization transfer process.

The model test sample is uniformly ^{13}C enriched *trans*-crotonic acid. The methyl (S1) resonance is well separated from the two carbonyl lines. The clos-est carbonyl, S2, is spatially two bonds away, while S3 is directly bonded (Fig. 6). The usual spin phase encoding is stored after t_1 evolution in the z direction, whereupon the rotation speed is changed to sweep, in this case sequentially over the rotational resonance between methyl and both carbonyl sites. The mix-ing flowchart is thus composed of a sequence of passing rotational resonance

conditions. Assuming an initial rotation speed of ca. 10 kHz, which is then increased, the first contact is made between S1 and S2. For the sake of generality, only part of the exchange is expected. Once the frequency of rotation has reached 13–14 kHz, position S2 is labelled dominantly by the phase of S1. Since the distance is two bonds, the adiabatic condition may not be completely fulfilled and some residual original S2 phase is left on S2 too. Position S1 acquires phase information from S2 (plus some residual S1) in a complementary fashion. The next event is the exchange between S1 (which now actually carries new
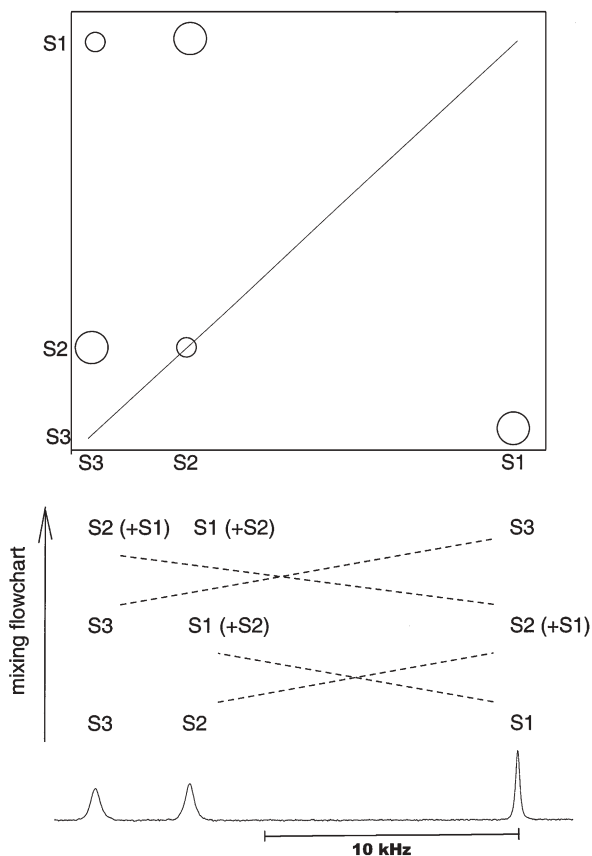

Fig. 6 Schematic presentation of events during a rotation sweep. The mixing flowchart presents a two-step relayed mixing process. Original populations along F_1 in sites S_3, S_2 and S_1 end up in positions as shown in *the top line*. The *rectangle* presents the resulting 2D spectrum, where original populations project to F_1 and final populations to F_2. 2D correlation is derived from labels of mixing flowchart top line (F_1 coordinate) and positions (F_2 coordinate). The relayed process of semi-adiabatic polarization transfer renders the cross-peak pattern asymmetric about the diagonal. The *bottom figure* represents the 1D spectrum of transcrotonic acid as a reference. The sideband of S_1 crosses the positions of S_2 and S_3 during the rotation sweep described

information from S2!) and S3. Here we assume full adiabatic exchange as a reflection of the much stronger one-bond dipolar interaction of the model sample. As a result, the two-dimensional spectrum shows migration from the original Sn positions (F1 dimension) to new locations. The signal from S3 resides at S1 in the final F2 dimension, S1 (+S2) at S2, and S2 (+S1) at S3. This is shown schematically by respectively larger and smaller circles in an illustrative 2D plot. The relayed transfer is characterized by a single cross-peak, i.e. a peak on one side of the diagonal only. Assigning transfer coefficients, Kmn, to the various rotational resonance exchange processes, a simple equation cascade can be written as

$$Sm_{i+1} = KmnSn_i + (1 - Kmn)Sm_i \qquad (7)$$

The dynamics of the rotor speed can be conveniently analysed and adjusted by feeding a signal from the rotor motion monitor (via an optical fibre) to a console ADC (Fig. 7). The corresponding spectra are shown in Fig. 8. The faster sweep clearly reduces K12, and to a lesser extent K13. Both direct complementary peaks (1–Kmn) and relayed peaks depend on the product of complementary transfer coefficients, and correlate well with the expected influence of the sweep rate variation. The observed relay process can be shorted by proton-driven spin diffusion. Consequently, efficient rotation-speed independent (or carefully synchronized) decoupling is required during the entire mixing period.

The ^{13}C spectra of proteins consist of three separate bands, with the backbone carbons separated by 15–20 kHz in medium-field spectrometers, thereby enabling NMR sequencing of small peptides. On passing through rotational resonances in the aliphatic region, the carbonyl carbon will transfer magnetization from one adjacent α-carbon to the other, generating correlation peaks between sequential aminoacids. Figure 9 shows the results of NMR "Edman degradation" [14], where aminoacid sequencing can be directly inferred from the spectrum of a small model peptide.
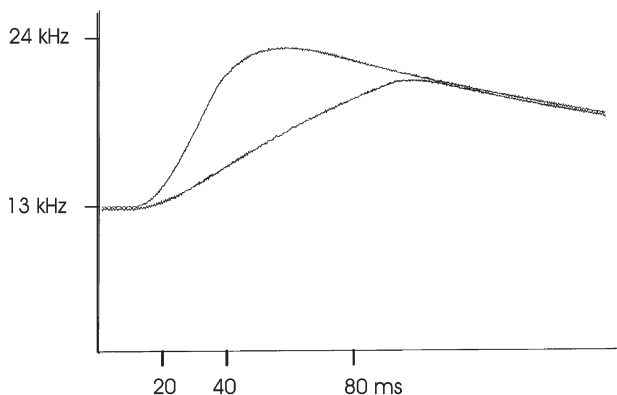
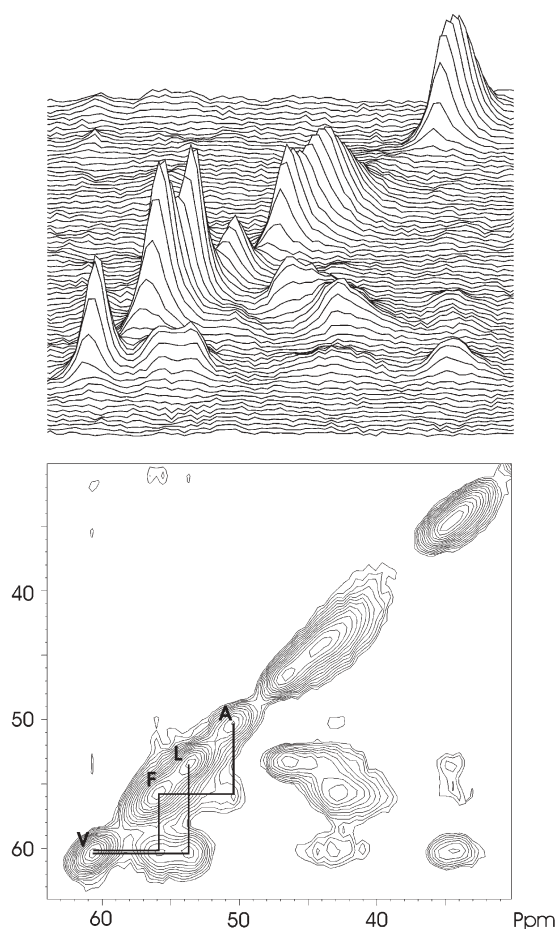**Fig. 7** Rotor speed profile for the two experiments in Fig. 8
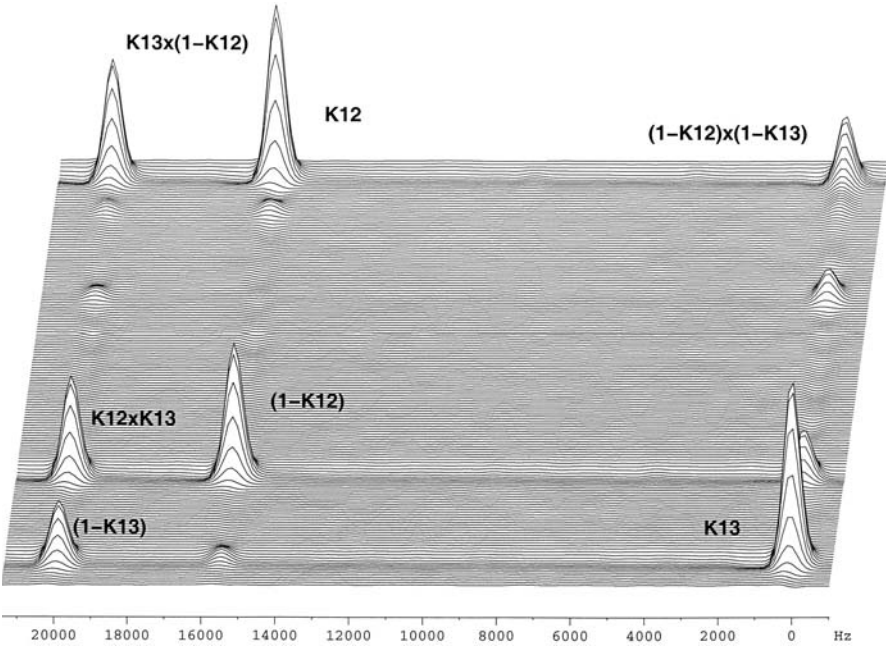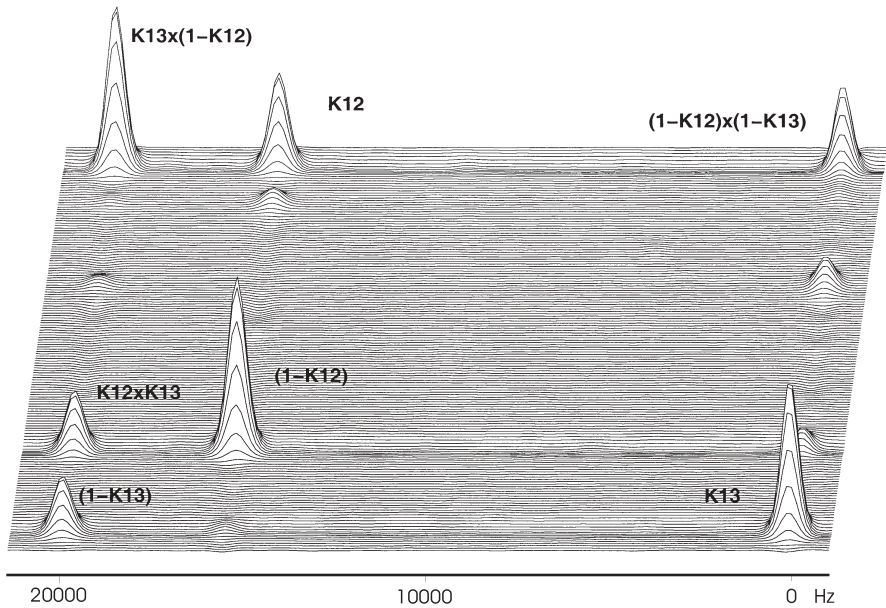
Fig. 8 Rotation sweep spectra of *trans*-crotonic acid at two different sweep rates

Fig. 9 NMR peptide sequencing by rotation sweep illustrated with a ^{13}C spectrum of the fully isotopically labelled peptide LVFFA. Carbonyl sites mediate polarization transfer between neighbouring alpha-carbons. The sequential ordering of amino acids can be directly inferred from the spectrum

5
Cryo-MAS™ [1]

The new potential of MAS comes mainly from a reduction in rotor size. The fastest rotors (70 kHz rotation frequency) currently hold 4 µL of sample, while ca. 10 µL samples can be rotated up to 50 kHz. If the filling factor is maintained, down-scaling leads to better mass sensitivity. On the one hand, increased mass sensitivity is welcome in cases where the availability of the sample is a problem,

---

[1] CRYOMAS is a registered trademark (NICPB, Tallinn, Estonia, 2004)

as is the case with isotopically labelled biopolymers. In addition, reduced rotor dimensions enable the construction of more efficient radiofrequency circuits at high frequencies. On the other hand, the absolute sensitivity decreases with the decreasing number of resonating nuclei. This disadvantage can be compensated for by working at lower temperatures. The effect of radiofrequency noise reduction has been exploited by using cryoprobes from high-resolution NMR (a term invented to annoy solid-state NMR spectroscopists), where the radiofrequency circuit is carefully isolated from the sample and cooled to ca. 20–30 K. A three- to fourfold improvement in the signal-to-noise ratio has been reported by commercial manufacturers. The same idea works much more effectively in solid-state NMR, since the sample generally does not need thermal isolation, being typically "frozen" already. Considering both major contributions, the increase in equilibrium magnetization and the reduction in thermal noise, a gain in sensitivity of an order of magnitude can already be expected at ~70 K. The theoretical factor of 30 in the signal-to-noise ratio can be reached when the temperature is reduced from 293 K to 30 K. The ideal gain, however, may be reduced by instrumental factors as well as by long relaxation times, if relaxation agents are not used.

Such obvious benefits have stimulated solid-state MAS experiments at cryogenic temperatures in several research laboratories. In the most successful and reproducible case, a sealed sample with a liquid-nitrogen temperature spinning module was cooled in a helium bath, but rotation speeds did not exceed 2 kHz at 40 K and 1 kHz at 5 K [15]. This is a serious limitation for practical applications.

The design features of the cooling technique harmonize perfectly with the general down-scaling. The requirements for lubrication and drive gas refrigeration power will be far less demanding, as will the thermal isolation of the probehead. The combined effect on power of heat extraction is thus very nonlinear. Moreover, the small mass of the sample enables the use of fast temperature ramps. Correlation spectroscopy of phase transitions and polarization enhancement using the Haupt effect [16], where dynamic proton polarization upon a rapid change of temperature is induced by the relaxation of the coupled nuclear spin and the methyl group rotation levels, are among potential applications.

Our prototype experiment, capitalizing on the new generation of fast rotors, demonstrated a promising perspective. At the lowest temperature, a 10-μL rotor was driven by helium gas at a rate of 3 m^3/h, cooled to 7 K by a heat exchanger located in the probehead. The heat exchanger was cooled by liquid helium at ca. 2–3 l/h. The temperature was measured by a thermometer in the exit gas flow. The rotor heating in the He atmosphere was controlled to within a few degrees. For a given rotor speed, the lowest temperature is determined mainly by the effectiveness of the heat exchanger. 7 K can be reached at 5 kHz, 13 K at 10 kHz, and 20 K at 20 kHz sample spinning. As an example, Fig. 10 shows the freezing of a H_2 molecule in a fullerene cage [17, 18].

The principal resolution may depend on the sample temperature. Understanding the interference of molecular motion with rotation and line narrow-
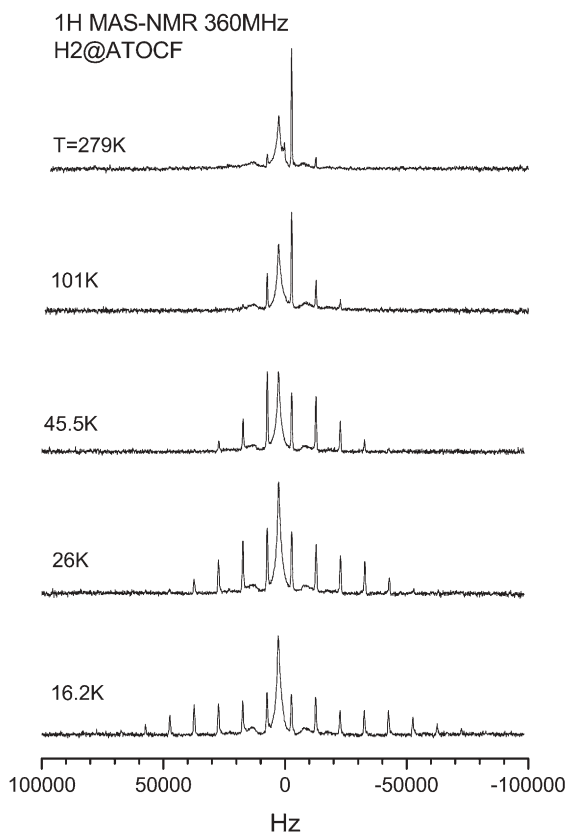
Fig. 10 Variable-temperature ^{1}H MAS spectra of H$_2$@ATOCF at 360 MHz, 10 kHz sample spinning speed. The spectrum at 279 K consists of a broad line from the protons at the fullerene opening region and of a sharp line corresponding to the hydrogen molecule which is rotating nearly freely inside the fullerene cage. The span of spinning sidebands is caused by the residual dipolar interaction between the protons of the hydrogen molecule. Below 100 K the sideband pattern broadens with decreasing temperature. Saturation of this broadening below 20 K indicates the freezing of the molecular rotation. The sample was synthesized by K. Komatsu and brought to our attention by M. Levitt and M. Carravetta

ing is essential for the design of multi-pulse line-narrowing techniques. In the case of alanine, reducing the temperature by ca. 50 K resulted in a significant broadening of the ^{1}H line from the amino group (higher field and higher rotation speed, Fig. 11). Measurements in a wide-bore magnet at lower temperatures confirm the broadening. Although the resolution is much lower because of the lower field and lower rotation speed, a reversal of the line-broadening effect could still be observed at the lowest temperature of 27 K. The central band and sidebands sharpen up, indicating different relative dynamics of the molecular motion. This phenomenon may also explain the failure of certain pulse narrowing techniques to maintain quantitatively correct intensity ratios of dif-

600 MHz

MAS 60 kHz

300K   350 K

360 MHz

MAS 21 kHz

295K

148K

27K

5e+04   0e+00   −5e+04   Hz
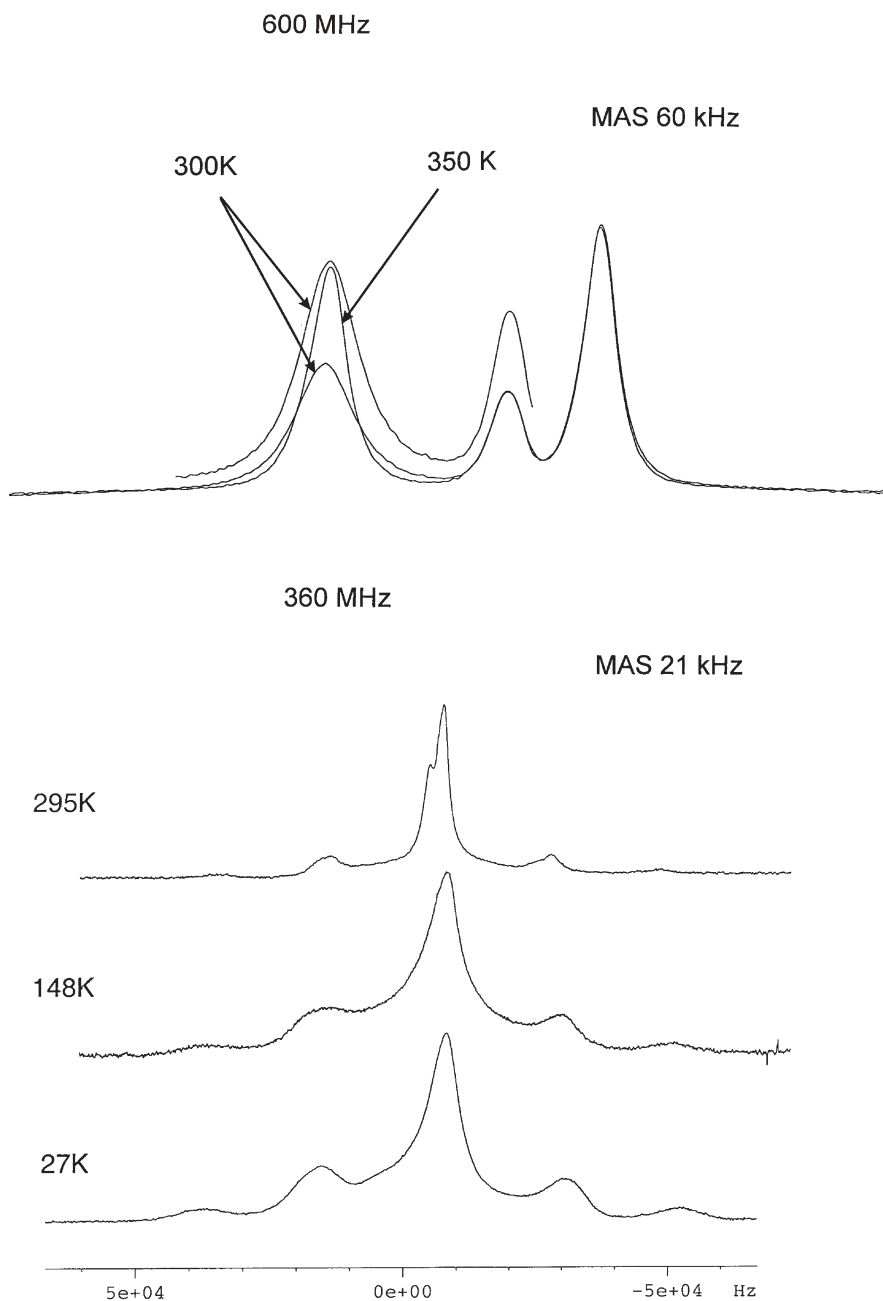
Fig. 11 Variable-temperature ¹H MAS spectra of alanine at 600 and 360 MHz. Low temperature spectra are registered for instrumental reasons at lower field; nevertheless sharpening of the signal can be observed at the lowest temperature

ferently moving molecular units and different convergences of linewidth on increasing rotation speed (Fig. 3).

6
Conclusions

Reduction of the rotor size opens up several hitherto unexplored avenues for study of the principles of MAS NMR and for practical applications. Exploitation of these new possibilities and features may sometimes reward the observant investigator with unexpected associations and nodes of seemingly unrelated regularities.

References

1. Samoson A (2002) Extended magic-angle spinning. In: The encyclopedia of nuclear magnetic resonance, vol 9. Advances in NMR. Wiley, pp 59–64
2. Geropp D (1969) Ing-Arch 38:195
3. Bielecki A, Burum DP (1995) J Magn Reson A116:215–220
4. Samoson A, Tuherm T, Gan Z (2001) Solid State NMR 20:130–136
5. Gil AM, Alberti E (1998) Solid State Magn Reson 11:203–209
6. Filip C, Filip X, Demco DE, Hafner S (1997) Mol Phys 92:757–771
7. Ernst M, Samoson A, Meier BH (2001) Chem Phys Lett 348:293–302
8. Ernst M, Samoson A, Meier BH (2003) J Mag Reson 163:332–339
9. Nielsen NC, Creuzet F, Griffin RG, Levitt MH (1992) J Chem Phys 9:5668
10. Ernst M, Meier MA, Samoson A, Meier BH (2004) J Am Chem Soc (in press)
11. Samoson A, Tuherm T, Past J (2002) Rotation sweep NMR. Chem Phys Lett 365:292–299
12. Samoson A, Tuherm T, Past J (2001) J Magn Reson 149:264–267
13. Shirley JH (1965) Phys Rev 138B:979
14. Edman P (1950) Acta Chem Scand 4:283
15. Myhre PC, Webb GG, Yannoni CS (1990) J Am Chem Soc 112:8991–8995
16. Haupt J (1972) Phys Lett 38A:389–390
17. Murata Y, Murata M, Komatsu K (2003) J Am Chem Soc 125:7142–7153
18. Carravetta M, Murata Y, Murata M, Heinmaa I, Stern R, Tontcheva A, Samoson A, Rubin Y, Komatsu K, Levitt MH (2004) Chem Soc (in press)

Strategies for High-Resolution Proton Spectroscopy in Solid-State NMR

Elena Vinogradov[1] · P.K. Madhu[2] (✉) · Shimon Vega[3]

[1] Radiology Department, The Beth Israel Deaconess Medical Center,
330 Brookline Avenue, Boston, MA 02215, USA

[2] Department of Chemical Sciences, Tata Institute of Fundamental Research,
Homi Bhabha Road, Colaba, Mumbai 400 005, India
madhu@tifr.res.in

[3] Department of Chemical Physics, Weizmann Institute of Science, 76100 Rehovot, Israel
shimon.vega@weizmann.ac.il

Abstract We describe radiofrequency (RF) pulse schemes in solid-state NMR applied to samples rotating at the magic angle (MAS) to obtain high-resolution ^{1}H spectra. Without combined RF schemes and MAS, ^{1}H spectra are normally severely broadened by the strong homonuclear proton-proton dipolar couplings. This review gives an outline of a representative class of multiple-pulse sequences, designed to work with and without MAS, and commonly used for high-resolution proton spectroscopy in solid-state NMR. We give a theoretical treatment of these sequences based on Floquet theory, both single-mode and bimodal. Using this approach, we define first-order homonuclear decoupling efficiency parameters which provide the line-narrowing characteristics of the various pulse sequences when applied to fast rotating samples. These parameters are used to compare the line-narrowing efficiencies of the multiple-pulse schemes.

Keywords Solid-state NMR · Proton spectra · Multiple-pulse schemes · PMLG and FSLG · Bimodal Floquet theory

1
Introduction

Solid-state NMR has found applications in fields such as materials science [1], polymer science [2], and biological science [3–5]. Spectral resolution and signal sensitivity enhancement schemes have been primarily responsible for making solid-state NMR a powerful tool for resonance assignment, measuring distances and angles and for structural characterisation [5]. The most commonly observed spin-1/2 nuclei are ^{13}C, ^{15}N, ^{31}P and ^{29}Si and ^{23}Na, ^{27}Al, and ^{17}O are the most popular quadrupolar nuclei. Resolution and sensitivity enhancement of the NMR spectra of these nuclei can be achieved using the following techniques, either alone or in combination: magic-angle spinning (MAS) [6,7],heteronuclear dipolar decoupling [8–10], cross-polarisation [11–13], multiple-quantum NMR [5,14], double-rotation [15], dynamic-angle spinning [16,17], multiple-quantum magic-angle spinning [18], and satellite transition magic-angle spinning [19]. The techniques used to obtain high-resolution spectra involve full or partial averaging of the various anisotropic spin interactions present in the solid-state, either in the coordinate space or in the spin space [2,14,20,21]. Spatial averaging is brought about by mechanical manipulation of the spins, as in MAS, and spin-space averaging by radiofrequency (RF) manipulation of the spins, as in heteronuclear dipolar decoupling [5,14].

One of the most popular spin-1/2 nuclei in NMR is ^{1}H, which is particularly widely studied in solution-state NMR [22]. Probing protons in the solid-state is difficult because of the strong homonuclear dipolar interactions (DD$_{homo}$) among them that result in broad spectral lines. This is caused by the 100% natural abundance of protons and their high gyromagnetic ratio. While chemical shift anisotropy (CSA) and heteronuclear dipolar interactions (DD$_{het}$) are inhomogeneous in nature, the DD$_{homo}$ couplings are homogeneous [23]. Hence, MAS is most effective for averaging CSA and DD$_{het}$. A narrowing of ^{1}H spectral lines is possible only if the MAS frequencies are greater than the strength of the dipolar interactions, which are usually of the order of tens of kHz. RF irra-

diation schemes must therefore be used to overcome the homonuclear dipolar line-broadening effects.

The first attempt at line-narrowing of ^{1}H spectral lines in solid-state NMR used the Lee-Goldburg (LG) decoupling scheme [24]. In the early days of solid-state NMR it was realised that averaging in spin-space is the solution to removing the strong DD_{homo} couplings. This heralded the concept of multiple-pulse schemes, starting with the four-pulse WHH4 sequence introduced by Waugh, Huber and Haeberlen [25]. Such sequences were first aimed at removing the strong DD_{homo} couplings among ^{1}H or ^{19}F spins and retaining CS interactions [25, 26]. Following the LG scheme and the WHH sequence, several schemes were later introduced to obtain high-resolution ^{1}H spectra in the solid-state [24–55]. The field continues to be developed with applications of ^{1}H NMR spectroscopy in the solid-state [56–68]. The development of this field has been a consequence of the improved theoretical understanding of decoupling strategy and advances in spectrometer hardware which make it possible to implement sophisticated pulse sequences.

Initially, the decoupling schemes were applied to static samples and averaged only the DD_{homo} couplings to zero. The spectra were still broadened by CSA. A combination of multiple-pulse schemes with MAS is necessary to obtain truly high-resolution spectra, and the so-called combined rotation and multiple-pulse sequences (CRAMPS) were introduced [31, 36, 40, 69]. Since both RF and MAS are external periodic modulations with their own characteristic periods, their interference often leads to a deterioration of spectral resolution [42, 43, 46, 51, 52, 69–71]. The advent of high MAS probeheads with spinning frequencies of up to $\omega_r/2\pi = 50$ kHz has made possible the acquisition of ^{1}H spectra with reasonable resolution employing MAS alone [72–76]. However, the achievable resolution was still insufficient for systems with strong and proton-rich networks, such as biomolecules. Although MAS-driven modulation rates of spin systems have become comparable to those which could earlier only be attained with pulse schemes, a combination of both is still vital for obtaining high-resolution ^{1}H spectra.

The efficient combination of RF pulses with MAS requires theoretical tools. While the initial multiple-pulse sequences were based on the average Hamiltonian theory (AHT) [14, 25, 26, 32, 33], some of the later schemes were more effectively formulated on the basis of Floquet theory [52], combinations of both AHT and Floquet theory [51], synchronisation arguments [42, 43, 46, 55], and numerical methods [50]. A combination of RF pulses with MAS was also visualised in terms of certain symmetry conditions based on AHT [77]. An attempt to present all these in a unified picture is perhaps not out of place for a better understanding of the underlying phenomena.

In this review, the following issues will be addressed:

– An overview of homonuclear dipolar decoupling sequences.
– The bimodal Floquet theory representation of the time-dependent spin Hamiltonian describing coupled proton systems.

– Derivation of zero- and first-order contributions to the effective Hamiltonian.
– Comparison of various sequences based on first-order contributions and spectral simulations to obtain a broad perspective of the line-broadening mechanism in ^{1}H spectra.

2
Homonuclear Dipolar Decoupling Sequences

In this section we list some of the homonuclear dipolar decoupling multiple-pulse sequences for high-resolution ^{1}H NMR in the solid-state which we will analyse explicitly later. Almost all were designed for experiments on non-spinning samples. We broadly classify them into four classes: sequences based on solid-echo pulse trains [78–81] sequences derived from magic-echo sandwich pulses [28], sequences based on Lee-Goldburg irradiation [24], and rotor-synchronised sequences [42, 43, 46, 51, 53, 77]. The sequences belonging to each of the classes which we will analyse are:
Class I: WHH4, MREV8, BR24, BLEW12, DUMBO
Class II: TREV8, MSHOT3
Class III: LG, FSLG, PMLGn
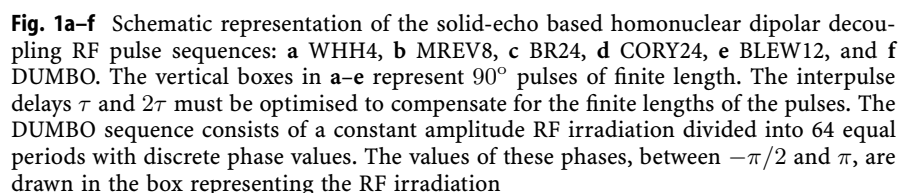Class IV: semi-windowed WHH4, CN$_k^\chi$, RN$_\kappa^\chi$[1]
    The decoupling efficiency of most of these RF irradiation schemes was described using AHT on non-spinning coupled spin-1/2 nuclei. Only in the case of Class IV samples was spinning taken into account during the basic pulse sequence design.

2.1
Solid-Echo Based Sequences

On-resonance pulse schemes based on a combination of solid-echoes are built upon 90_x-τ-90_y- pulse pairs, where τ is the interpulse delay. Figure 1 shows a schematic of such sequences, (a) WHH4 [25], (b) MREV8 [27, 30], (c) BR24 [32, 33], and (d) CORY24 [39]. Experiments involve application of these sequences following a $90°$ excitation pulse and acquisition of data points at the end of each pulse cycle. These cycles are sequentially repeated and a ^{1}H free induction decay is obtained. Details of the setting up of these sequences are well documented [25–27, 30, 32, 33, 39, 70, 71]. Two additional sequences shown in Fig. 1 are (e) BLEW12 [34] and (f) DUMBO [50]. BLEW12 is a windowless sequence and DUMBO is a numerically optimised sequence based on BLEW12. Since both sequences are windowless, experiments need to be performed in a two-dimensional (2D) way by incrementing the RF cycle, one cycle at a time, in the t_1 dimension following a $90°$ pulse. A projection onto the indirect dimension gives a high-resolution ^{1}H spectrum. It has recently been shown that acquisition

---

[1] To be consistent with our Floquet theory notation we denote the symmetry-adapted sequences from Levitt's group as CN$_\kappa^\chi$ and RN$_\kappa^\chi$, instead of CN$_n^\nu$ and RN$_n^\nu$, as detailed later.

Fig. 1a–f Schematic representation of the solid-echo based homonuclear dipolar decoupling RF pulse sequences: **a** WHH4, **b** MREV8, **c** BR24, **d** CORY24, **e** BLEW12, and **f** DUMBO. The vertical boxes in **a–e** represent 90° pulses of finite length. The interpulse delays τ and 2τ must be optimised to compensate for the finite lengths of the pulses. The DUMBO sequence consists of a constant amplitude RF irradiation divided into 64 equal periods with discrete phase values. The values of these phases, between $-\pi/2$ and π, are drawn in the box representing the RF irradiation

windows can be inserted between DUMBO cycles, permitting one-dimensional (1D) experiments [82].

The total Hamiltonian of a dipolar coupled spin system may be written as

$$\mathcal{H}(t) = \mathcal{H}_{DD}(t) + \mathcal{H}_{CS}(t) + \mathcal{H}_{J}(t) + \mathcal{H}_{RF}(t) + \mathcal{H}_{E}(t) \tag{1}$$

where $\mathcal{H}_{DD}, \mathcal{H}_{CS}, \mathcal{H}_{J}, \mathcal{H}_{RF}$, and $\mathcal{H}_{E}$ are the Hamiltonians for homonuclear dipolar interaction, chemical shift interaction, scalar coupling, ideal RF pulse schemes and experimental errors of the pulses, such as incorrect pulse lengths, phase glitches and RF inhomogeneity. Transforming $\mathcal{H}(t)$ to the toggling frame of $\mathcal{H}_{RF}(t)$ and using AHT, an effective Hamiltonian $\mathcal{H}_{eff}$, describing the synchronous evolution of the spin system, can be derived and expanded in terms of increasing order of perturbation [34]:

Table 1. Properties of solid-echo based pulse sequences[2]

Sequence	$\tilde{\mathcal{H}}_{DD}^{(0)}$	$\tilde{\mathcal{H}}_{DD}^{(1)}$	$\tilde{\mathcal{H}}_{DD\times CS}^{(1)}$	$\tilde{\mathcal{H}}_{DD}^{(2)}$	$\tilde{\mathcal{H}}_{DD\times CS}^{(2)}$	Scale Factor	Tilt Angle
WHH4	0^*	0	0^*	$\neq 0$	$\neq 0$	0.63	$55.6°$
MREV8	0	0	0^*	$\neq 0$	$\neq 0$	0.50	$45.0°$
BR24	0	0	0	0	$\neq 0$	0.41	$54.7°$
CORY24	0	0	0	0	$\neq 0$	0.34	$90°$
BLEW12	0	0	0	0	$\neq 0$	0.48	$63.4°$

*(Only for $90°$ $\delta-$pulses)

$$\mathcal{H}_{eff} = \tilde{\mathcal{H}}_{eff}^{(0)} + \tilde{\mathcal{H}}_{eff}^{(1)} + \tilde{\mathcal{H}}_{eff}^{(2)} + \cdots \tag{2a}$$

$$\tilde{\mathcal{H}}_{eff}^{(0)} = \tilde{\mathcal{H}}_{DD}^{(0)} + \tilde{\mathcal{H}}_{CS}^{(0)} \tag{2b}$$

$$\tilde{\mathcal{H}}_{eff}^{(1)} = \tilde{\mathcal{H}}_{DD}^{(1)} + \tilde{\mathcal{H}}_{CS}^{(1)} + \tilde{\mathcal{H}}_{DD\times CS}^{(1)} \tag{2c}$$

$$\tilde{\mathcal{H}}_{eff}^{(2)} = \tilde{\mathcal{H}}_{DD}^{(2)} + \tilde{\mathcal{H}}_{CS}^{(2)} + \tilde{\mathcal{H}}_{DD\times CS}^{(2)} + \cdots \tag{2d}$$

where the upper indices give the order of perturbation. In general, the higher the order the lower the magnitude. Lower indices refer to interactions involved in the derivation of the expansion terms, which include cross-terms between various spin interactions. The finite lengths of the pulses are taken into account in $\mathcal{H}_{RF}(t)$, ignoring all other pulse parameters contributing to $\mathcal{H}_E(t)$. This does not mean that pulse imperfections are unimportant. The ability of a sequence to compensate for pulse errors can determine the choice of the experiment. This issue has been exhaustively discussed in the literature [26, 32, 33, 39, 70, 83]. The order of importance of the contribution of different terms in Eq. 2 to the residual line-broadening in homonuclear dipolar decoupling experiments on non-spinning samples is approximately $\tilde{\mathcal{H}}_{DD}^{(0)}$, $\tilde{\mathcal{H}}_{DD}^{(1)}$, $\tilde{\mathcal{H}}_{DD\times CS}^{(1)}$, $\tilde{\mathcal{H}}_{DD}^{(2)}$, and $\tilde{\mathcal{H}}_{DD\times CS}^{(2)}$. $\tilde{\mathcal{H}}_{CS}^{(0)}$ determines the isotropic chemical shift Hamiltonian scaled by a factor as a result of the application of the pulses. The averaging properties of the solid-echo-based pulse sequences applied to non-spinning samples are given in Table 1.

Terms such as $\tilde{\mathcal{H}}_{DD}^{(1)}$ and $\tilde{\mathcal{H}}_{DD\times CS}^{(1)}$ vanish for all sequences in Table 1, since all of them except MREV8 possess internal reflection symmetry [26]. The scale factors of these sequences decrease with increasing number of pulses. Thus, line narrowing must compensate for the scaling of the spectral width in order to increase the resolution on a corrected *ppm* scale.

A combination of the sequences in Table 1 with MAS is also necessary to average out the CSA interaction. Such a combination is not straightforward, given the possible interference effects from the simultaneous presence of both RF and MAS. Such problems forced the above sequences to be applied in the quasi-static limit, where the MAS period τ_r is much longer than the cycle time of the sequence

---

[2] The scale factors and tilt angles were evaluated assuming the pulse parameters given in Section 7.3.
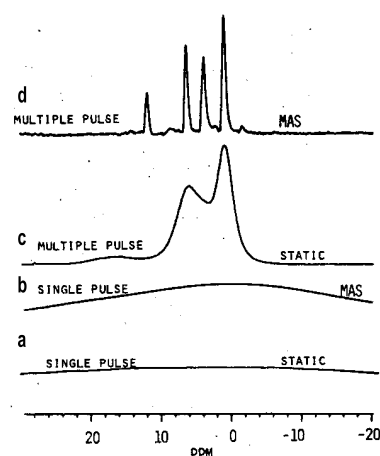
Fig. 2a–d ^{1}H spectra of monoethyl fumarate at a Larmor frequency of 187 MHz obtained after a single-pulse excitation without any additional RF irradiation of **a** a static sample and **b** a sample rotating at the magic angle; and with stroboscopic detection during BR24 decoupling applied to **c** a static sample and **d** a sample rotating at the magic-angle with a spinning frequency $\omega_r/2\pi = 2.0$ kHz (Reproduced with permission from Ref. [36])

τ_c. This also meant that only very low MAS rates could be used [36]. In fact, the best performance of the sequences in Table 1 is at MAS rates from 500 to 4000 Hz. BR24 has been widely used, giving the best results at low spinning speeds of ca. 2000 Hz, with a τ_c of 100–150 μs [36, 70].

The BLEW12 sequence consists of three units of symmetric four $90°$ pulses. Despite its sensitivity to RF fluctuations, it performs better than MREV8 at relatively low RF power values. An extension to BLEW48 [34] resulted in a sequence comparable with BR24.

The DUMBO decoupling scheme has been derived by optimising seven complex Fourier coefficients of a Fourier expansion of a phase modulated, constant amplitude RF field [50]. This procedure generated an RF waveform with an improved performance over BLEW12 in terms of its RF amplitude stability. No AHT analysis was used to derive it, and hence the sequence does not appear in Table 1. The scale factor for the DUMBO sequence is 0.52 and the tilt angle is $38°$. Due to the short cycle times, BLEW12 and DUMBO perform better than others at high spinning speeds [50]. Figures 2–4 show representative spectra of MREV8, BR24, and DUMBO sequences.

2.2
Magic-Echo Sandwich Based Sequences

Rhim et al. have shown that application of a suitable sequence of strong RF pulses can reverse the time evolution of the coherent spin state caused by the homonuclear dipolar interaction [28]. Consequently, the influence of the dipo-
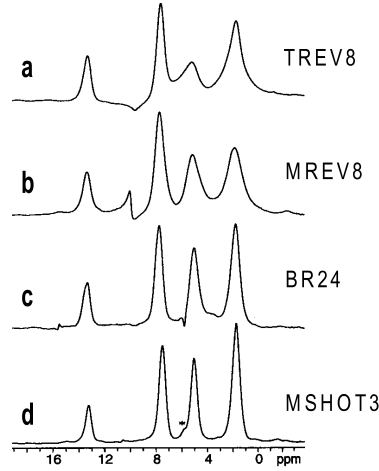
Fig. 3a–d ^{1}H spectra obtained with **a** TREV8 ($\tau_r = 10\tau_c, \omega_r/2\pi = 1595\,\mathrm{Hz}$), **b** MREV8 ($\tau_r = 12\tau_c, \omega_r/2\pi = 1543\,\mathrm{Hz}$), **c** BR24 ($\tau_r = 4\tau_c, \omega_r/2\pi = 1543\,\mathrm{Hz}$), and **d** MSHOT3 ($\tau_r = 5\tau_c, \omega_r/2\pi = 2101\,\mathrm{Hz}$) homonuclear dipolar decoupling sequences on a sample of monoethyl fumarate with an RF intensity $\omega_1/2\pi$ of about $100\,\mathrm{kHz}$ (Reproduced with permission from Ref. [45])

lar interaction on the spins can be eliminated, giving rise to a high-resolution spectrum of the abundant spins. The original sequence involved a large number of RF pulses with sequentially reversed phases and off-sets required to minimise RF inhomogeneity effects. The sequence is demanding in terms of the RF field strength and sensitive to pulse imperfections and RF inhomogeneity. TREV4, a simpler version, based on time reversal echoes, was extended to the TREV8 decoupling scheme [35]. A combination of three TREV4 magic-echo sandwiches with a relative phase difference of $120°$ resulted in the MSHOT3 sequence [44,45]. The TREV8 and MSHOT3 sequences are shown in Fig. 5.

The basic symmetric magic-echo sandwich can be represented by

$$\{\tau - 90°_y - \beta_x - \beta_{\bar{x}} - 90°_{\bar{y}} - \tau\} \tag{3}$$

where β_x and $\beta_{\bar{x}}$ correspond to RF irradiation of intensity $\omega_1/2\pi$ and duration $2\pi/\omega_1$ and τ a delay of length π/ω_1. The scale factor of this sequence is 1/3, assuming $90°$ δ-pulses.

TREV8, originally designed for static samples [35], was later adapted for MAS [40]. The spectral resolution obtained by TREV8 was not as good as that of BR24. Nonetheless, TREV8 has several advantages: (i) it has a higher bandwidth compared with BR24 because of the short cycle times, (ii) it is robust over a large range of off-set values, and (iii) the duration of the sampling window can be made sufficiently large without substantial loss of resolution [40].

The MSHOT3 (magic-sandwich higher-order truncation) sequence comprises three magic-sandwich units phase shifted by $120°$ with respect to one another.
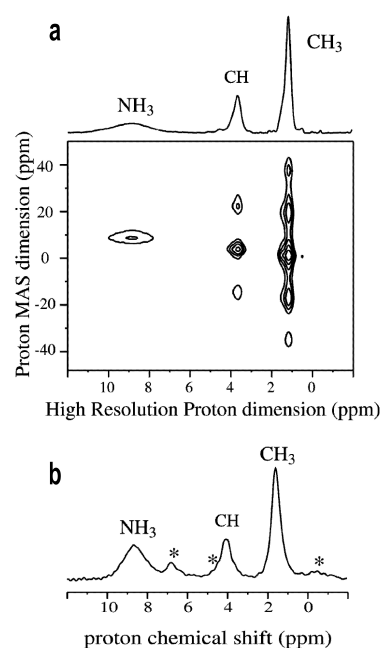
Fig. 4a,b ^{1}H spectra of natural abundance L-alanine obtained with the DUMBO decoupling sequence in **a** a 2D experiment and **b** a 1D experiment with observation windows inserted between the DUMBO cycles. In **a** and **b** $\omega_r/2\pi$ was 9 kHz and 12 kHz, respectively, $\omega_1/2\pi$ = 100 kHz and the external field corresponded to a ^{1}H Larmor frequency of 500 MHz. The observation window in **b** was 5 μs. The stars in **b** are quadrature images (Reproduced with permission from Ref. [82])
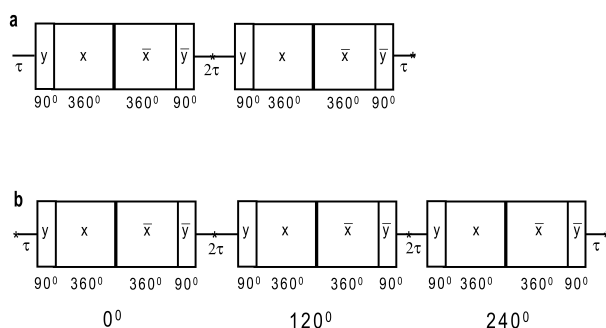
Fig. 5a,b Schematic drawings of the **a** TREV8 and **b** MSHOT3 pulse sequences. Asterisks show possible data sampling points. For $90°$ δ-pulses the interpulse delay 2τ is equal to the length of a $360°$ pulse. In actual experiments, finite pulse lengths require a modification of the τ value from their ideal values. In **b** the overall phase of the three TREV4 units composing the MSHOT3 sequence is given below each unit
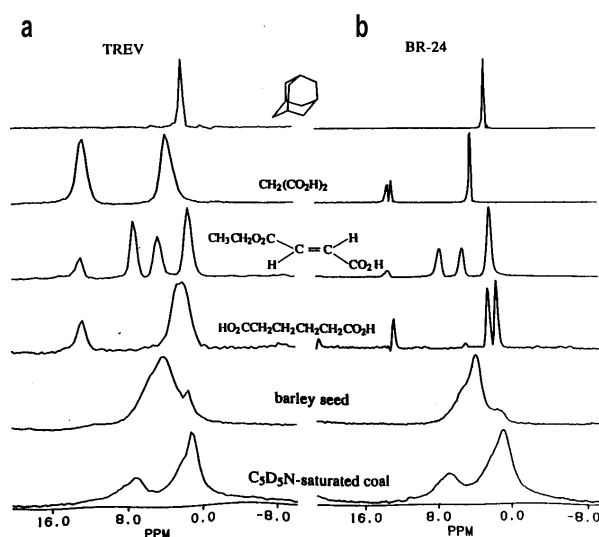
Fig. 6a,b ^{1}H spectra obtained from **a** TREV8 and **b** BR24 decoupling experiments at a [1]H Larmor frequency of 187 MHz of adamantane, malonic acid, monoethyl fumarate, adipic acid, barley seed, and saturated coal. The interpulse delays τ in the TREV8 and BR24 sequences were 8 μs and 3 μs, respectively. In all the experiments the spinning frequency $\omega_r/2\pi$ was between 1 and 1.5 kHz, and the RF intensity $\omega_1/2\pi$ was ≈ 190 kHz (Reproduced with permission from Ref. [40])

For finite $90°$ pulses, the scale factor of MSHOT3 is about 0.35. Both TREV8 and MSHOT3 are effective z-rotation sequences. This leads to relatively artifact-free spectra with respect to a wide range of off-set values. MSHOT3 eliminates expansion terms of the Hamiltonian that are proportional to first- and second-rank irreducible tensor operators $T_m^{(1)}$ and $T_m^{(2)}$. In this way, for static samples, fourth-order terms with $m \neq 0$ vanish for $\delta-$pulses and third-order terms for finite $90°$ pulses [44, 45]. In fact, when four BLEW12 are concatenated with consecutive phase shifts of $90°$, one achieves a higher-oder truncation up to fourth-order for $m \neq 0$, but the scale factor becomes only 0.18 [47]. MSHOT3 was successfully used to study ^{1}H chemical shielding anisotropies [84, 85].

Figures 3 and 6 show representative spectra with the application of TREV8 and MSHOT3 sequences, some of which are compared with solid-echo based sequences such as MREV8 and BR24.

2.3
Lee-Goldburg Based Sequences

The Lee-Goldburg (LG) irradiation scheme achieves spin-space averaging by an off-resonance irradiation, such that the spins rotate in the off-resonance rotating frame around a direction inclined at an angle $\theta_m = 54.7°$ with respect to the direction of the external magnetic field. In effect, the same angle is achieved
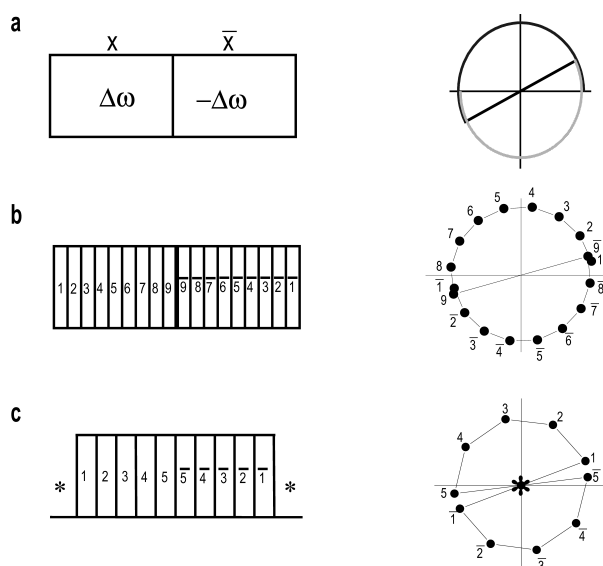
Fig. 7a–c The pulse schemes and time dependent RF irradiation field profiles in the xy-plane of the on-resonance rotating frame of **a** FSLG, **b** PMLG9, and **c** wPMLG5. Asterisks denote possible data sampling points. The rotation frequencies $\Delta\omega$ (black) and $-\Delta\omega$ (grey) of the irradiation vector in the case of FSLG obey the relation $\Delta\omega = \omega_1/\sqrt{2}$, where ω_1 is the RF intensity. The continuous time-dependent phase in FSLG is replaced in PMLGn by n discrete phases (shown by dots in **b** and **c**). One possible set of phase values for PMLG9 in **b** are: $\phi_1 = 11.54°$, $\phi_2 = 34.63°$, $\phi_3 = 57.72°$, $\phi_4 = 80.81°$, $\phi_5 = 103.9°$, $\phi_6 = 126.99°$, $\phi_7 = 150.08°$, $\phi_8 = 173.17°$, $\phi_9 = 196.26°$, $\phi_{\bar{9}} = 16.26°$, $\phi_{\bar{8}} = 353.17°$, $\phi_{\bar{7}} = 330.08°$, $\phi_{\bar{6}} = 306.99°$, $\phi_{\bar{5}} = 283.9°$, $\phi_{\bar{4}} = 260.81°$, $\phi_{\bar{3}} = 237.72°$, $\phi_{\bar{2}} = 214.63°$, $\phi_{\bar{1}} = 191.54°$, and for wPMLG5 in **c** are: $\phi_1 = 20.78°$, $\phi_2 = 62.34°$, $\phi_3 = 103.9°$, $\phi_4 = 145.46°$, $\phi_5 = 187.02°$, $\phi_{\bar{5}} = 7.02°$, $\phi_{\bar{4}} = 325.46°$, $\phi_{\bar{3}} = 283.9°$, $\phi_{\bar{2}} = 242.34°$, $\phi_{\bar{1}} = 200.78°$

with the WHH4 sequence using ideal pulses. The off-resonance value of the RF irradiation is given by $\Delta\omega = \omega_1 \cot\theta_m$, the LG condition. The duration of an LG cycle corresponds to a 2π rotation of the proton magnetisation about the effective field direction, and is given by $\tau_{LG} = 2\pi/\omega_{eff}$, where the effective nutation frequency of the spins $\omega_{eff} = \sqrt{\omega_1^2 + \Delta\omega^2}$. The LG scheme only averages out the homonuclear dipolar interaction to zero-order, and as such is not effective for homonuclear dipolar decoupling. Symmetrisation and thus an improvement in the averaging of the LG scheme can be achieved by a sequence shown in Fig. 7a. This involves application of an off-resonance RF field at $+\Delta\omega$ for a duration of τ_{LG} with phase x, immediately followed by the application of another off-resonance RF field at -$\Delta\omega$ for a duration of τ_{LG} with phase $\bar{x}$ [29, 37, 38, 41]. This involves simultaneous switching of both the phase and the frequency of the RF irradiation, making it experimentally demanding. This sequence is called frequency-switched LG (FSLG) which is finding more and more applications

currently with advances made in the hardware of NMR spectrometers [56–67]. As in the case of WHH4, the scale factor of FSLG is 0.571. Although the original implementation of FSLG was in a 1D way by inserting observation windows [37, 38, 41], a better way of doing the experiment is in a 2D way. For a RF nutation frequency of 100 kHz, $\tau_{LG} = 8.2\mu s$, and the cycle time is around 16 μs, making the combination of FSLG with MAS even more feasible than the sequences discussed so far.

An on-resonance version of FSLG was introduced by Vinogradov et al. [48]. The sequence, phase-modulated LG (PMLG), consists of a series of pulses in which the phase is changed, while the frequency is kept constant. This, as FSLG, averages out both the zero- and the first-order homonuclear dipolar interactions. This is accomplished by modulating the phases of the pulses in a discrete manner. A PMLGn cycle approximates an LG unit by n on-resonance pulses, each with duration of τ_{LG}/n, with $n =3,5,9 \cdots$. The symmetrisation required to average a out the odd-order terms in the dipolar average Hamiltonian in the static case is the same as for FSLG. Hence, the experiment involves n pulses each of duration τ_{LG}/n and a phase increment of $\Delta\phi = 207.8/n$ between successive pulses, again followed by the same set of pulses in the reverse order with an overall phase shift of 180° with respect to the first set. The pulse sequence and the RF profile in the on-resonance rotating frame are shown in Fig. 7b. The scale factors of PMLG9, PMLG5 and PMLG3 for a constant RF amplitude of 100 kHz are 0.580, 0.585 and 0.597, with $\tau_{LG} = 8.2\,\mu s$, the duration of each of the pulses being 0.91 μs, 1.64 μs, and 2.73 μs respectively.

Experiments involving PMLG were initially implemented in a 2D way [48, 49, 52]. High-resolution ^{1}H spectral lines were reported with the use of this in combination with MAS in a variety of samples [48, 49, 52]. It has been found that higher MAS rates from 15 kHz to 20 kHz are possible with PMLG, provided the nutation frequency is also increased accordingly. Short cycle time and ease of implementation are some of the reasons for the increasing applications of PMLG. High-resolution ^{1}H spectral lines can be obtained in a 1D way by inserting observation windows in the PMLG cycle, wPMLGn [54]. The RF schematic of this approach is shown in Fig. 7c. Such 1D methods open up new avenues in ^{1}H NMR spectroscopy in the solid-state. Heterocorrelation experiments may be envisaged with ^{1}H detection to improve sensitivity and multiple-quantum ^{1}H experiments may be performed for connectivity information with proton homonuclear decoupling in both the dimensions of a 2D experiment giving high-resolution ^{1}H spectra in both the dimensions.

Figures 8 and 9 depict representative spectra with the application of FSLG and PMLG sequences.

2.4
MAS Synchronised Sequences

Developing sequences with both MAS and RF taken into account are of prime importance in solid-state NMR. Probably the first attempt in synchronising RF and
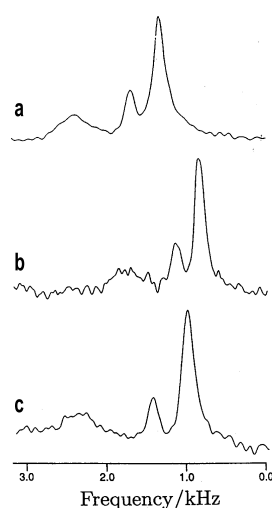
Fig. 8a–c ^{1}H spectra of natural abundant L-alanine acquired with **a** MREV8, **b** BR24, and **c** the first windowed FSLG sequence with $\omega_r/2\pi = 3\,\text{kHz}$ (Reproduced with permission from Ref. [41])
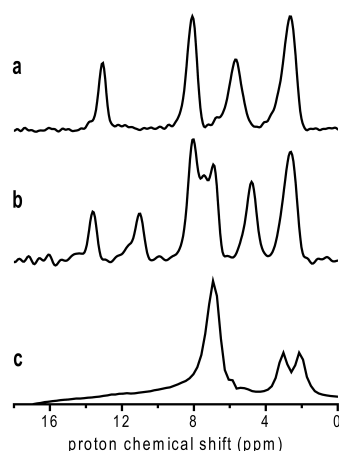
Fig. 9a–c ^{1}H spectra of **a** monoethyl fumarate, **b** histidine.HCl, and **c** glycine, employing wPMLG5 with $\omega_r/2\pi = 10\,\text{kHz}$ and $\omega_1/2\pi = 82\,\text{kHz}$. The ^{1}H Larmor frequencies of the spectra in **a** and **b** were 300 MHz, and in **c** 600 MHz. The samples were confined to about 1 mm in the centre of the rotor to reduce B_1 inhomogeneity effects

MAS for homonuclear dipolar decoupling was made by Hafner et al. [46, 51]. A synchronisation strategy was suggested, using windowless and semi-windowless sequences to minimise cycle times, to avoid destructive interference between RF pulses and sample spinning. For example, when four WHH4 cycles are applied during one rotor cycle, as in Fig. 10a, it can be shown graphically that the
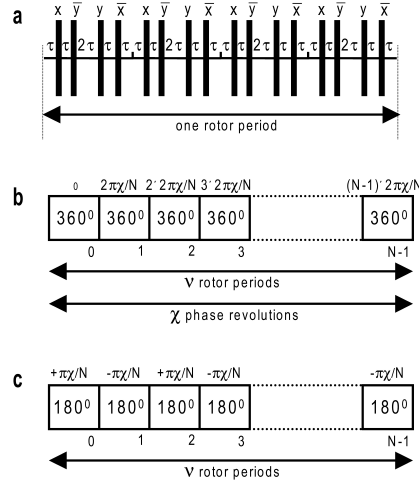
Fig. 10a–c Schematic representation of rotor-synchronised pulse sequences: **a** a synchronised WHH4 sequence, employing four WHH4 cycles per rotor cycle, **b** the CN_κ^χ sequence consisting of N consecutive pulses each performing an effective $360°$ rotation of the spins and each differing in their overall phase by $2\pi\chi/N$, the N pulses span κ rotor periods, **c** the RN_κ^χ sequence consisting of $N/2$ equal pairs of effective $180°$ pulses with overall phases flipping between $+\pi\chi/N$ and $-\pi\chi/N$, a total of $N/2$ pulse pairs span κ rotor periods

zero-order average dipolar Hamiltonian vanishes. This approach allows high-spinning frequencies, making it possible to eliminate CSA and DD_{homo} effects by a synchronisation of the RF and MAS cycles. It was shown that the application of standard, windowless, and semi-windowless WHH4 sequences is possible at high spinning speeds.

Symmetry arguments have been proposed by Levitt and coworkers [77,86–88] that enable a constructive combination of both MAS and RF based on certain symmetry properties of the internal spin Hamiltonians. Two classes of symmetry sequences have been proposed, CN_κ^χ [86] and RN_κ^χ [87,88]. Selective recoupling or decoupling of spin interactions is possible with a suitable combination of the symmetry numbers, N, κ and χ. An example of $R18_2^9$ for homonuclear dipolar decoupling will be discussed later.

Figures 11 and 12 show representative spectra with the application of synchronous sequences, namely WHH4, and $R18_2^9$.

3
The Spin Hamiltonians

In this section we introduce bimodal Floquet theory (BMFT), based on which we represent the spin Hamiltonians and analyse the various homonuclear dipolar decoupling sequences.
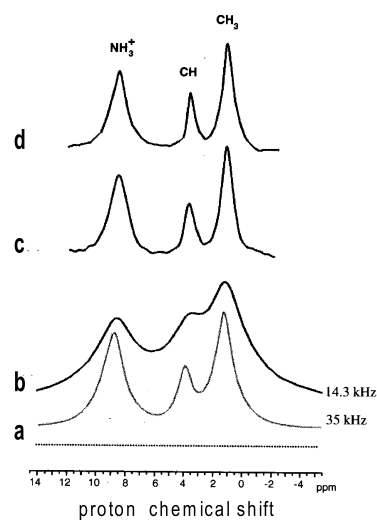
Fig. 11a–d ^{1}H spectra of L-alanine obtained with **a** only MAS at $\omega_r/2\pi = 35\,\text{kHz}$, **b** with only MAS at $\omega_r/2\pi = 14.3\,\text{kHz}$, **c** with indirect (2D) detection employing a rotor-synchronised semi-windowless WHH4 sequence with $\omega_r/2\pi = 14.3\,\text{kHz}$, and **d** the same as **c** but with direct stroboscopic (1D) detection (Reproduced with permission from Ref. [55])
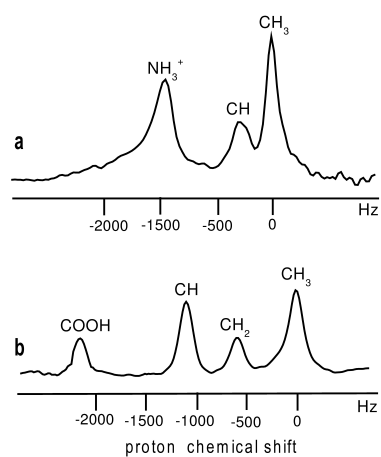
Fig. 12a,b ^{1}H spectra of **a** L-alanine and **b** monoethyl fumarate obtained with the pulse sequence R18$_2^9$, with $\omega_1/2\pi = 135\,\text{kHz}$ and $\omega_r/2\pi = 20\,\text{kHz}$. The ^{1}H Larmor frequency was 400 MHz (Reproduced with permission from Ref. [53])

3.1
RF Interaction Representation

The quantum description of N coupled protons in Hilbert space is given by a spin Hamiltonian of dimension 2^N equalling the number of direct product spin-$\frac{1}{2}$ states. Two experimental tools have been used for the decoupling of spin interactions, RF irradiation and MAS. In the following, any discussion of sample spinning assumes MAS conditions. MAS effectively eliminates the CSA and DD_{hetero} interaction between protons and other spin-$\frac{1}{2}$ nuclei.

A system of coupled nuclei with spin-$\frac{1}{2}$ rotating at the magic-angle in an external magnetic field under RF irradiation has a Hamiltonian in the rotating frame of the form:

$$\mathcal{H}(t) = \mathcal{H}_{ISO} + \mathcal{H}_{CSA}(t) + \mathcal{H}_{DD}(t) + \mathcal{H}_J + \mathcal{H}_{RF}(t) \tag{4}$$

The forms of the first four terms are well known [14,89]. The isotropic chemical shift ($\mathcal{H}_{ISO}$) and chemical shift anisotropy ($\mathcal{H}_{CSA}$) terms are [89]

$$\mathcal{H}_{ISO} + \mathcal{H}_{CSA}(t) = \sum_{a=1}^{N} \left\{ -\Delta\omega_a I_{za} + \sum_{n=-2}^{2} -\omega_a g_n(\Omega_a; \eta_a) e^{in\omega_r t} I_{za} \right\} \tag{5}$$

where for spin a, $\Delta\omega_a$ is the isotropic chemical shift, ω_a is the CSA frequency parameter, and η_a is the CSA asymmetry parameter. The geometric parameters g_n are functions of the Euler angles $\Omega_a \equiv (\alpha_a, \beta_a, \gamma_a)$ that define the transformation of the initial principal axis systems of the CSA tensors to the rotor frame. Expressions for these g-coefficients can be found in Appendix 1. ω_r is the spinning frequency and $\tau_r = 2\pi/\omega_r$ is the rotor period.

The proton-proton dipolar interaction term is [89]

$$\mathcal{H}_{DD}(t) = \sum_{a<b=1}^{N} \sum_{n=-2}^{2} \omega_{ab} G_n(\Omega_{ab}) e^{in\omega_r t} (3I_{za} I_{zb} - \bar{I}_a \cdot \bar{I}_b) \tag{6}$$

Explicit expressions for the G_n-parameters in terms of the Euler angles $\Omega_{ab} \equiv (\alpha_{ab}, \beta_{ab}, \gamma_{ab})$ between the initial dipolar tensor frame and the rotor frame are also given in Appendix 1, as well as the distance dependence, $1/r_{ab}^3$, of the dipolar frequency coefficient ω_{ab}. The $G_{n,ab}$ and $g_{n,a}$ coefficients satisfy

$$G_{n,ab} \equiv G_n(\Omega_{ab}) = G_{-n}^*(\Omega_{ab}) \tag{7a}$$

$$g_{n,a} \equiv g_n(\Omega_a; \eta_a) = g_{-n}^*(\Omega_a; \eta_a) \tag{7b}$$

The time independent isotropic spin-spin scalar coupling Hamiltonian is

$$\mathcal{H}_J = J_{ab}\bar{I}_a \cdot \bar{I}_b \tag{8}$$

This term is of the order of a few Hz in the homonuclear proton case and will be ignored in the following.

The last term in Eq. 4 represents the time dependent RF irradiation field in the rotating frame, which can be written in terms of two perpendicular time dependent amplitudes as

$$\mathcal{H}_{RF}(t) = \omega_{1x}(t)I_x + \omega_{1y}(t)I_y \tag{9}$$

In homonuclear dipolar decoupling experiments this RF sequence is applied to accomplish efficient decoupling, leaving the isotropic chemical shifts at least partially intact. The actual time dependence of the RF coefficients varies for each experiment. Here we will assume that the $\mathcal{H}_{RF}(t)$ term is periodic in time with an RF cycle time τ_c:

$$\mathcal{H}_{RF}(t + k\tau_c) = \mathcal{H}_{RF}(t) \tag{10}$$

for all positive integers k and for $0 < t < \tau_c$. Corresponding to this cycle time we define a characteristic RF frequency, $\omega_c = 2\pi/\tau_c$. In most of the experiments the RF pulse sequences that are used are also cyclic, namely

$$U_{RF}(k\tau_c) = Te^{-i\int_0^{\tau_c} dt' \mathcal{H}_{RF}(t')} = 1. \tag{11}$$

However, RF sequences exist that exhibit non-cyclic behavior. In the following we will refer to cyclic cases only.

In the cyclic case it is most convenient to transform the spin system to the RF interaction frame, defined by the transformation operator $U_{RF}(t)$. The total Hamiltonian in the RF interaction frame becomes [26]

$$\mathcal{H}_{int}(t) = U_{RF}^{-1}(t)\left\{\mathcal{H}_{ISO} + H_{CSA}(t) + \mathcal{H}_{DD}(t)\right\}U_{RF}(t) \tag{12}$$

It is convenient to write the Hamiltonian terms in the curly brackets in terms of irreducible tensor operators (ITO), $T_m^{(l)}$, given in Appendix 1, where the $T_{m,a}^{(1)}$ components, with $m = -1, 0, 1$, appear in the chemical-shift terms and the $T_{m,ab}^{(2)}$ components, with $m = -2, -1, 0, 1, 2$, appear in the dipole-dipole interactions terms. Starting in the rotating frame with operators truncated according to the high-field approximation [14], the transformation of the spin operators may be written as

$$U_{RF}^{-1}(t)T_0^{(l)}U_{RF}(t) = \sum_{m=-l}^{l} d_m^{(l)}(t)T_m^{(l)} \tag{13a}$$

$$= \sum_{m=-l}^{l}\sum_{k=-\infty}^{\infty} d_{mk}^{(l)}T_m^{(l)}e^{ik\omega_c t} \tag{13b}$$

where $d_m^{(l)}(t)$ are time-dependent coefficients resulting from the transformation to the RF interaction frame and $d_{mk}^{(l)}$ are their Fourier components. Combining this with the expansion in Eqs. 5 and 6 our interaction Hamiltonian consists of two combined Fourier series, one induced by the sample spinning and one by the RF irradiation. Since the forms of $g_{n,a}$ and $G_{n,ab}$ in a powder sample are fixed, the $d_{mk}^{(l)}$'s are the only parameters that can be modified for a fixed characteristic frequency ω_c.

3.2
The Fourier Space Representation

Evaluation of the response of the spin system to a time dependent Hamiltonian requires an appropriate mathematical framework. This framework must deal with Hamiltonians that are periodically time dependent with at least two characteristic frequencies, ω_r and ω_c, that are not necessarily commensurate. We choose bimodal Floquet theory (BMFT) towards this, and in this Section we will set the basis of this theory. The approach is very similar to the single mode Floquet theory (SMFT) approach adapted by others to NMR spectroscopy [91].

Following Eqs. 5, 6 and 13b the RF interaction Hamiltonian can be expressed as

$$\mathcal{H}_{int}(t) = \sum_{n,k} H_{nk} e^{in\omega_r t} e^{ik\omega_c t} \tag{14}$$

where the Fourier operator coefficients H_{nk} are defined in the same Hilbert space as the Hamiltonian itself. These time independent operator coefficients contain all parameters $d_{mk}^{(l)}$, $g_{n,a}$ and $G_{n,ab}$, as well as the spin operators $T_m^{(l)}$, and can only be manipulated by changing the RF irradiation scheme.

Floquet theory provides a generalised form for the propagators of systems with periodically time dependent Hamiltonians [90, 91]. The propagator for a doubly periodic Hamiltonian in the BMFT representation may be written as [92, 93]

$$U_{int}(t) = U(t)e^{-i\Lambda t}U^{-1}(0) \tag{15}$$

where the unitary operator $U(t)$ is periodic according to

$$U(t) = \sum_{n,k} u_{nk} e^{in\omega_r t} e^{ik\omega_c t} \tag{16}$$

and Λ is diagonal. In the Hilbert space this diagonal operator is not unique, because subtracting from the diagonal elements of Λ, n' multiples of ω_r and k' of ω_c, and multiplying $U(t)$ with a diagonal matrix with elements $\exp\{-i(n'\omega_r + k'\omega_c)t\}$ does not modify $U_{int}(t)$. In this review we will almost always deal with Hamiltonians that have off-diagonal matrix elements smaller than ω_r and ω_c and therefore with corrections of the diagonal elements of Λ that are also smaller than ω_r and ω_c. In all our discussions we will choose the initial time of our experiments to occur at $t_0 = 0$. Thus, here the more general dependence $U_{int}(t; t_0)$ is replaced by a simpler form $U_{int}(t)$. The operators u_{nk} are of course functions of the initial state of $\mathcal{H}(t_0)$.

The fact that we can express the propagator in this form allows us also to expand the reduced density operator in the RF interaction frame as

$$\sigma_{int}(t) = U_{int}(t)\sigma_{int}(0)U_{int}^{-1}(t) = \sum_{n,k} \sigma_{nk}(t) e^{in\omega_r t} e^{ik\omega_c t} \tag{17}$$
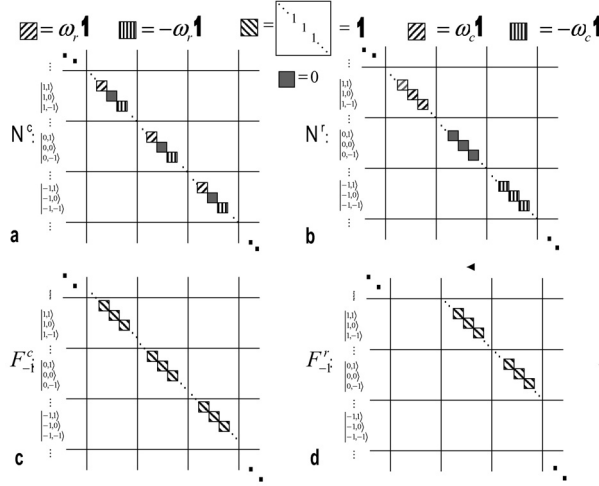
Fig. 13a–d The number operators **a** N^c and **b** N^r, and the ladder operators **c** F_1^c and **d** F_1^r in the manifold of Floquet states $\{|nk\rangle\}$ with $\{|n\rangle\}$ the Fourier states corresponding to the spinning frequency ω_r and $\{|k\rangle\}$ the Fourier states corresponding to the characteristic RF frequency ω_c

At this stage in our discussion it becomes convenient to represent the Hamiltonian and the density operator in a Fourier matrix representation defined by a set of dressed Fourier states $\{|n,k>\}_{n,k=-\infty}^{\infty}$. In this infinite representation we can use the ladder operators defined earlier by Boender et al. [94,95]:

$$< n'+n,k'|F_n^r|n',k'> = 1 \tag{18a}$$

$$< n',k'+k|F_k^c|n',k'> = 1 \tag{18b}$$

and the number operators [94,95]:

$$< n',k'|N^r|n'',k''> = n'\delta_{n'n''}\delta_{k'k''} \tag{19a}$$

$$< n',k'|N^c|n'',k''> = k'\delta_{n'n''}\delta_{k'k''} \tag{19b}$$

for all n' and k' ($-\infty,\dots,\infty$). The total basis set is now $\{|p,n,k>\}$ with $|p>$ the spin product states. Hence, the "matrix block element" between $< n',k'|$ and $|n'',k''>$ has the dimension of the Hilbert space of the spin system. In the case of F_n^r, F_k^c, N^r and N^c all the non-zero block elements are diagonal. The ladder and number operators are shown schematically in Fig. 13.

These operators enable a compact Fourier matrix representation of the Hamiltonian and the density matrix:

$$H_{int}^F(t) = \sum_{n,k} H_{nk}F_n^r F_k^c e^{in\omega_r t}e^{ik\omega_c t} \tag{20a}$$

$$\sigma_{int}^F(t) = \sum_{n,k} \sigma_{nk}(t)F_n^r F_k^c e^{in\omega_r t}e^{ik\omega_c t} \tag{20b}$$

a Fourier space   **b** Floquet space

■ H_{00} ■ $H_{00} + n\omega_r + k\omega_c$

☑ $H_{0k}e^{ik\omega_c t}$ ☑ H_{0k}

◩ $H_{0-k}e^{-ik\omega_c t}$ ◩ H_{0-k}

⊞ $H_{1k}e^{i\omega_r t}e^{ik\omega_c t}$ ⫸ ⊞ H_{1k}

⊞ $H_{-1k}e^{-i\omega_r t}e^{ik\omega_c t}$ ⊞ H_{-1k}

⊟ $H_{2k}e^{i2\omega_r t}e^{ik\omega_c t}$ ⊟ H_{2k}

⊠ $H_{-2k}e^{-i2\omega_r t}e^{ik\omega_c t}$ ⊠ H_{-2k}
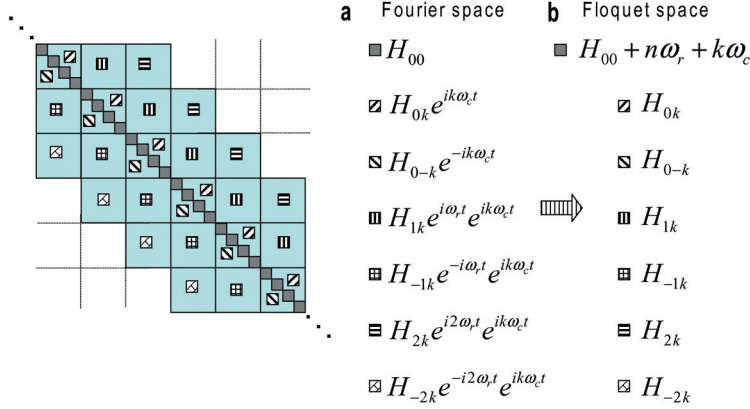
Fig. 14a,b The Hamiltonian of the spin system during MAS and a periodic RF irradiation in Fourier and Floquet space. The definitions of the different block-elements are given in **a** for the Fourier representation and in **b** for the Floquet representation. The Hamiltonians retain the same general form, but the time-dependent elements in **a** become time-independent in **b** with the addition of the number operator elements on the diagonal

A schematic of the Fourier representation is given in Fig. 14. The fact that the Hamiltonian is still time dependent does not show any advantage of this representation. However, things can be simplified when we use the commutation relations between the number and ladder operators:

$$[N^r, F_n^r] = n F_n^r \tag{21a}$$
$$[N^c, F_k^c] = k F_k^c \tag{21b}$$

and as a consequence

$$e^{i\omega_r N^r t} F_n^r e^{-i\omega_r N^r t} = F_n^r e^{in\omega_r t} \tag{22a}$$
$$e^{i\omega_c N^c t} F_k^c e^{-i\omega_c N^c t} = F_k^c e^{ik\omega_c t} \tag{22b}$$

With $[F_n^r, F_k^c] = 0$ it is now possible to express the Hamiltonian as well as the density operator as

$$H_{int}^F(t) = e^{i\omega_r N^r t} e^{i\omega_c N^c t} \left\{ \sum_{n,k} H_{nk} F_n^r F_k^c \right\} e^{-i\omega_r N^r t} e^{-i\omega_c N^c t} \tag{23a}$$

$$\sigma_{int}^F(t) = e^{i\omega_r N^r t} e^{i\omega_c N^c t} \left\{ \sum_{n,k} \sigma_{nk}(t) F_n^r F_k^c \right\} e^{-i\omega_r N^r t} e^{-i\omega_c N^c t} \tag{23b}$$

Before using these expressions and transforming the spin system to Floquet space, we should discuss some features of the evolution operator $U_{int}(t)$ and introduce the effective Hamiltonian.

3.3
The Effective Hamiltonian

The propagator in Eq. 15 can also be written in terms of the ladder operators. However, before doing so we insert the unit operator $U^{-1}(0)U(0)$ and obtain

$$U_{int}(t) = \sum_{n,k} \left\{ U_{nk} e^{in\omega_r t} e^{ik\omega_c t} \right\} e^{-i\mathcal{H}_{eff}t} \tag{24}$$

where an effective Hamiltonian $\mathcal{H}_{eff}$ is defined in the same Hilbert space as the total Hamiltonian in Eq. 4:

$$\mathcal{H}_{eff} = U(0)\Lambda U^{-1}(0) \tag{25}$$

and the operator coefficients U_{nk} are obtained by the expansion using Eq. 16

$$U(t)U^{-1}(0) = \sum_{n,k} U_{nk} e^{in\omega_r t} e^{ik\omega_c t} \tag{26}$$

In Fourier space the propagator is given the form

$$U_{int}^F(t) = \sum_{n,k} \left\{ U_{nk} F_n^r F_k^c e^{in\omega_r t} e^{ik\omega_c t} \right\} e^{-i\mathcal{H}_{eff}F_0^r F_0^c t} \tag{27}$$

This demonstrates again the special form of the propagator, a doubly periodic operator times an unitary operator defined by a time independent effective Hamiltonian.

The inverse transformation of operators from Fourier space to Hilbert space can be performed straightforwardly. Using the fact that all operators O^F (except the number operators in the Hamiltonian) satisfy the diagonal property

$$< n' + n, k' + k|O^F|n', k' > = < n'' + n, k'' + k|O^F|n'', k'' > \tag{28}$$

for all n', n'', k' and k'', the transformation of Fourier operators to Hilbert space operators is given by

$$\sigma_{int}(t) = \sum_{n,k} < n, k|\sigma_{int}^F(t)|0, 0 > \tag{29a}$$

$$U_{int}(t) = \sum_{n,k} < n, k|U_{int}^F(t)|0, 0 > \tag{29b}$$

At this point we have expressed the Hamiltonian, the density operator and the evolution operator in Fourier space. We have introduced an effective Hamiltonian, defined in the Hilbert space of the same dimension 2^N as the total time-dependent Hamiltonian itself, and we have shown how to transform operators between the two representations. The definition of the effective Hamiltonian enables us to predict the overall evolution of the spin system, despite the fact that we can *not* find time-points for synchronous detection, t', where $U_{int}(t') = \exp\{-i\mathcal{H}_{eff}t'\}$. In actual experiments the time dependent signals are monitored and after Fourier transformation they result in frequency sideband

patterns with two characteristic frequencies. The centreband will be mainly determined by the effective Hamiltonian, especially when the sideband intensities are small. In the following, the expression for $\mathcal{H}_{eff}$ will be derived and parameters determining its magnitude will be calculated for the evaluation of the linewidth of the (centreband) spectra.

3.4
The Floquet Space Representation

The form of the RF interaction Hamiltonian in Fourier space in Eq. 23a suggests that we can transform it to a space where it becomes time independent. Transforming the Fourier density operator to a new interaction frame defined by

$$\sigma_F(t) = \sum_{n,k} e^{-i\omega_r N^r t} e^{-i\omega_c N^c t} \sigma_{int}^F(t) e^{i\omega_r N^r t} e^{i\omega_c N^c t} \tag{30}$$

and inserting it in the Liouville-von Neumann equation, we get a new representation of our spin system with a time independent Hamiltonian

$$\mathcal{H}_F = \sum_{n,k} H_{nk} F_n^r F_k^c + \omega_r N^r + \omega_c N^c \tag{31}$$

This new representation is the Floquet space representation, which is the N-interaction representation of $\mathcal{H}_{int}^F(t)$, and is still defined by the Fourier states $\{|n,k>\}$. A schematic of the Floquet Hamiltonian is shown in Fig. 14. The time evolution of the density operator in this frame is again governed by

$$\frac{d}{dt}\sigma_F(t) = i[\sigma_F(t), \mathcal{H}_F] \tag{32}$$

and the solution of the propagator is now simply

$$U_F(t) = e^{-i\mathcal{H}_F t} \tag{33}$$

Since $\mathcal{H}_F$ is time independent, it is, in principle, possible to diagonalise it for an evaluation of $U_F(t)$. It also becomes possible to use standard perturbation theory or van Vleck perturbation theory [96] to estimate the eigenvalues of $\mathcal{H}_F$. In the Floquet space, the time dependent problem is transferred to a (although infinite) discrete energy level problem [97]. This is convenient, in particular, when resonance conditions are derived for recoupling and decoupling experiments. In the rest of our discussion, the time independent Floquet energy levels and the matrix elements between them will guide us to understand decoupling methodologies. The actual diagonalisation of the Floquet Hamiltonian is in many cases difficult and the evaluation of the propagator *impractical*. However, as we will show, the use of perturbation theory to estimate the Floquet energies is very helpful to understand the spin evolution.

The definition of the matrix elements of the BMFT Hamiltonian is straightforward, as well as the definition of the initial density operator:

$$\sigma_F(0) = \sigma_{int}^F(0) = \sigma(0) F_0^r F_0^c \tag{34}$$

The choice of this form for the initial density matrix is in line with the above definitions of the Fourier and Floquet space, and maintains the form of all operators in Floquet space as in Eq. 28.

The back transformation of operators from Floquet space to Hilbert space results in the expression originally derived by Chu et al. [92,93]. Using the expressions for $U_{int}^F(t)$ and $\sigma_{int}^F(t)$ in Eq. 29:

$$O_{int}(t) = \sum_{n,k} < n,k|O_F(t)|0,0 > e^{in\omega_r t} e^{ik\omega_c t} \tag{35}$$

where the Floquet operator $O_F(t)$ can be $U_F(t)$ or $\sigma_F(t)$, and $O_{int}(t)$ their Hilbert space analogues.

We now will derive the form of the effective Hamiltonian by block-diagonalising $\mathcal{H}_F$.

3.5
Diagonalisation of the Floquet Hamiltonian

The diagonalisation of the matrix representation of $\mathcal{H}_F$ can formally be represented by the transformation

$$\Lambda_F = D_F^{-1} \mathcal{H}_F D_F \tag{36}$$

The matrix Λ_F is diagonal in spin space *and* in Fourier space, and the block matrix elements of D_F are

$$D_{nk} = < n,k|D_F|0,0 > \tag{37a}$$
$$D_{nk}^{-1} = < n,k|D_F^{-1}|0,0 > \tag{37b}$$

Thus, as a result of the diagonalisation, we get a diagonal spin-Hamiltonian Λ_{00} and

$$\Lambda_F = \Lambda_{00} F_0^r F_0^c + \omega_r N^r + \omega_c N^c \tag{38}$$

Using these definitions we can write the propagator of our spin system in Hilbert space, using Eq. 35, as

$$U_{int}(t) = \sum_{n,k} < n,k|D_F e^{-i\Lambda_F t} D_F^{-1}|0,0 > e^{in\omega_r t} e^{ik\omega_c t} \tag{39}$$

This expression has the same form as Eq. 24, when we define

$$U^{-1}(0) = \sum_{n,k} D_{nk}^{-1} \quad ; \quad U(0) = \sum_{n,k} D_{nk} \tag{40}$$

and

$$\mathcal{H}_{eff} = U(0)\Lambda_{00}U^{-1}(0) \tag{41a}$$
$$U_{nk} = D_{nk}U^{-1}(0) \tag{41b}$$

resulting again in
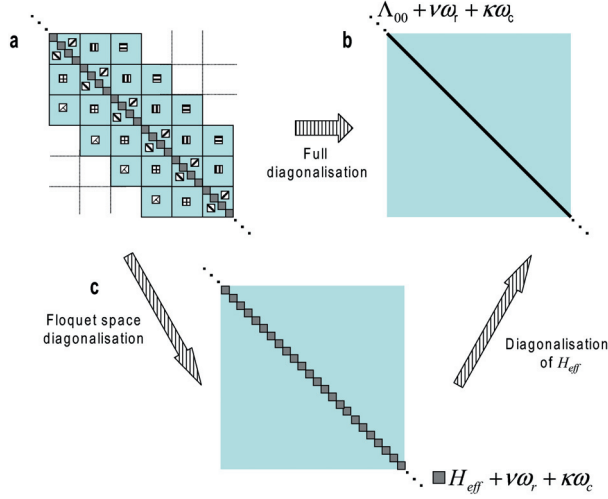
Fig. 15a–c Schematic representation of the diagonalisation of the Floquet Hamiltonian. The Floquet Hamiltonian in **a** can be diagonalised fully resulting in a diagonal Floquet Hamiltonian **b** with elements $\Lambda_{00} + \nu\omega_r + \kappa\omega_c$ and Λ_{00} diagonal in spin space. Block diagonalisation in Floquet space only results in a block diagonal Hamiltonian **c** with an effective spin space Hamiltonian $\mathcal{H}_{eff}$ that could be diagonalised to give again Λ_{00}

$$U_{int}(t) = \sum_{n,k} U_{nk} e^{in\omega_r t} e^{ik\omega_c t} e^{-i\mathcal{H}_{eff}t} \tag{42}$$

From the diagonalisation of the Floquet Hamiltonian one can thus derive the effective Hamiltonian, as well as the operator coefficients of the propagator. The diagonalisation of the Floquet Hamiltonian is illustrated in Fig. 15.

In conclusion we summarise the protocol for evaluating the propagator as:

- Define the periodic Hamiltonian in the Hilbert space and transform it to the time independent Floquet Hamiltonian.
- Diagonalise the Floquet Hamiltonian, to yield Λ_F, D_F and D_F^{-1}.
- Extract the diagonal matrix in Hilbert space equal to Λ_{00}.
- Determine the matrices $U^{-1}(0) = \left\{ \sum_{n,k} D_{nk}^{-1} \right\}$ and $U(0) = \left\{ \sum_{n,k} D_{nk} \right\}$.
- Calculate the effective Hamiltonian $U(0)\Lambda_{00}U^{-1}(0)$ and the coefficients of the periodic matrix $U_{nk} = D_{nk}U^{-1}(0)$.

This procedure could be followed, when possible, analytically, or by truncating the Floquet Hamiltonian and using computer calculations. However, because this numerical approach can become cumbersome, it is almost always more practical to perform exact time ordering for actual numerical spin evolution calculations. The Floquet approach is then only used when physical insight is required and when perturbation theory can be utilised to estimate $\mathcal{H}_{eff}$ and the D_{nk}'s.

3.6
The Floquet Hamiltonian

To finalise the discussion let us have a closer look at the Floquet Hamiltonian of our spin system. Its general form is:

$$\mathcal{H}_F = \sum_{n,k} H_{nk} F_n^r F_k^c + \omega_r N^r + \omega_c N^c \tag{43}$$

with a block diagonal matrix

$$H_{00} = \sum_{a<b} \sum_m -\Delta\omega_a d_{m0}^{(1)} T_{m,a}^{(1)} \tag{44}$$

and off-diagonal block matrices

$$H_{nk} = \sum_{a,b} \sum_{m=-1}^{1} -(\Delta\omega_a \delta_{n0} + \omega_a g_{n,a}) d_{mk}^{(1)} T_{m,a}^{(1)} + \sum_{m=-2}^{2} \sqrt{6}\omega_{ab} G_{n,ab} d_{mk}^{(2)} T_{m,ab}^{(2)} \tag{45}$$

k and n are allowed to be zero in these elements, and $g_{0,a} = G_{0,ab} = 0$. For $n = 0$ the elements contain isotropic chemical shift off-resonance terms with $k \neq 0$ and for $n = \pm 1, \pm 2$, CSA and DD_{homo} terms. This Hamiltonian is shown schematically in Fig. 14. The diagonalisation of $\mathcal{H}_F$ is strongly dependent on the relative magnitudes of the off-diagonal elements with respect to the difference between the diagonal elements they connect. The magnitude of the block diagonal matrix elements of $\mathcal{H}_F$ is mainly determined by $n\omega_r + k\omega_c$ and thus the most significant off-diagonal matrix coefficients $\omega_{ab} G_{\nu,ab} d_{m-\kappa}^{(2)}$ must be compared to Floquet energy differences $\nu\omega_r - \kappa\omega_c$, when diagonalisation via perturbation theory is considered.

The schematic of Floquet energy levels is shown in Fig. 16. For certain characteristic frequencies these energy differences can become zero and a Floquet energy level crossing occurs:

$$n'\omega_r + k'\omega_c = n''\omega_r + k''\omega_c \tag{46}$$

for $\nu = n' - n''$ and $\kappa = k'' - k'$. These crossings are shown in Fig. 17. In that case even small off-diagonal elements $H_{\nu-\kappa}$ can become very significant to finding $\mathcal{H}_{eff}$. At the non-degenerate conditions all off-diagonal elements can be treated as perturbations as long as

$$|H_{\nu-\kappa}| << |\nu\omega_r - \kappa\omega_c| \tag{47}$$

This, of course, is not always the case, and when Eq. 47 fails, an exact diagonalisation should be performed. At the non-crossing conditions perturbation approaches are justified when $\omega_a g_{n,a} d_{m\kappa}^{(1)}$ and $\omega_{ab} G_{n,ab} d_{m\kappa}^{(2)}$ of the CSA and the DD_{homo} interaction tensor elements are relatively small. For example, for the elimination of the DD_{homo} influence on the effective Hamiltonian we should require at least
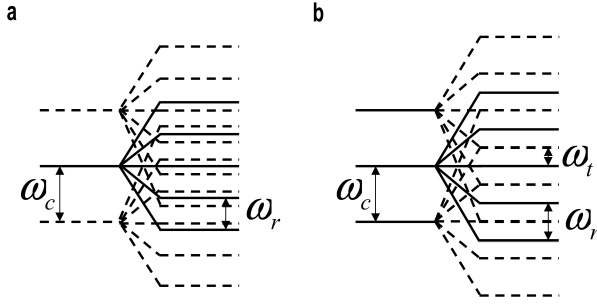
Fig. 16a,b A schematic representation of the Floquet energy levels (the $n\omega_r + k\omega_c$ diagonal elements of the Floquet Hamiltonian, ignoring the values of the spin space energies of Λ_{00}) of a spin system with a spinning frequency ω_r under the influence of a periodic RF field with a characteristic frequency ω_c. The two frequencies ω_r and ω_c can be incommensurate, as shown in **a**, or commensurate, as shown in **b**. In the later case energy level crossings occur and a single characteristic frequency, ω_t, can be defined
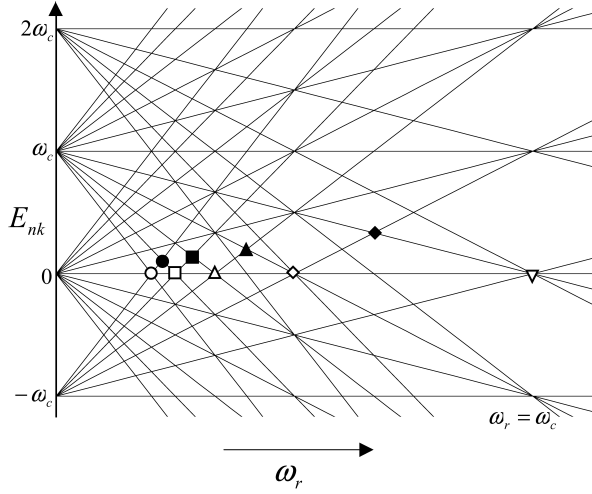
Fig. 17 The Floquet energy levels $E_{nk} = n\omega_r + k\omega_c$ as a function of the spinning frequency ω_r for a constant ω_c value for $\omega_r < \omega_c$. Level crossings are indicated by symbols $\{\nu,\kappa\}$: open circle for $\{5,1\}$; filled circle for $\{9,2\}$; open square for $\{4,1\}$; filled square for $\{7,2\}$; open triangle for $\{3,1\}$, filled triangle for $\{5,2\}$; open diamond for $\{2,1\}$; filled diamond for $\{3,2\}$ and inverted triangle for $\{1,1\}$

$$\left| \omega_{ij} G_{\nu,ab} d_{m0}^{(2)} \right| \ll \left| \nu\omega_r \right| \tag{48a}$$

$$\left| \omega_{ij} G_{\nu,ab} d_{m-\kappa}^{(2)} \right| \ll \left| \nu\omega_r - \kappa\omega_c \right| \tag{48b}$$

The conditions for CSA terms are more problematic because in many instances the CSA frequency is larger than the spinning frequency, $\omega_a > \omega_r$, and

strong sidebands appear in spectra, indicating that real diagonalisation is necessary. The values of the CSA frequency parameters ω_a for protons reach about 15 ppm, which is 12 kHz in a 800 MHz spectrometer. The g_ν and $d_{m\kappa}^{(1)}$ values reduce the corresponding matrix elements by at least a factor of 4. Thus for reasonable spinning frequencies they introduce no real problems for the application of perturbation theory. This last argument would not hold for coupled nuclei, such as ^{13}C, with large CSA tensors. Then, prediagonalisation of the CSA terms would be necessary before perturbation can be applied. The isotropic chemical shifts, proportional to $\Delta\omega_a d_{m\kappa}^{(1)}$, can almost always be assumed to be smaller than $\kappa\omega_c$. In the following sections we will come back to the arguments of the relative intensities of matrix elements.

With the constraints of Eq. 47 we can, in general, use perturbation theory to find the approximate eigenvalues of $\mathcal{H}_F$. In the coming sections we will do so by using van Vleck perturbation theory, but only after discussing Floquet energy level crossings.

In addition to degeneracies described in Eq. 46, for certain experimental conditions, accidental degeneracies can occur of the type

$$\nu\omega_r - \kappa\omega_c + \Delta\omega_a s d_{m0}^{(1)} = 0 \tag{49}$$

where s is the scale factor (see Section 6).

The level anti-crossings due to the off-diagonal elements can give rise to line shifts and to sharp frequency responses, the so-called rotor-RF lines in the spectrum. These effects are observed in many spectra and are discussed extensively elsewhere [52]. The positions of these sharp features, ω_{RRFL}, are

$$\omega_{RRFL} = \nu\omega_r - \kappa\omega_c \tag{50}$$

and they can be expected close to the normal lines in any spectra.

4
The Single-Mode Floquet Hamiltonian

4.1
Floquet Level Crossings

The propagator given in Eq. 16 becomes periodic in time only when the two characteristic frequencies, ω_r and ω_c, are commensurate. Then Floquet energy level crossings occur (see Figs. 16 and 17) under the condition [52]:

$$\nu\omega_r = \kappa\omega_c \tag{51}$$

In that case a new characteristic frequency can be defined that is equal to

$$\omega_t = \frac{\omega_r}{\kappa} = \frac{\omega_c}{\nu} \tag{52}$$

This new characteristic frequency enables the BMFT representation to be reduced to a single mode Floquet (SMFT) representation. An effective Hamiltonian can be

derived by diagonalising the Floquet matrix span by single-index Fourier states. Here, we will therefore present a separate discussion of homonuclear dipolar decoupling experiments, where sample spinning and RF pulse sequences are synchronised.

At any Floquet energy level crossing condition all states $|n',k'>$ with the same Floquet state energy $n'\omega_r + k'\omega_c = l\omega_t$ obey

$$n'\kappa + k'\nu = l \tag{53}$$

as shown in Fig. 17. The Hamiltonian then becomes

$$\mathcal{H}_{int}(t) = \sum_{n,k} H_{nk} e^{in\omega_r t} e^{ik\omega_c t} = \sum_{n,k} H_{nk} e^{i(n\kappa + k\nu)\omega_t t} = \sum_l H_l e^{il\omega_r t} \tag{54}$$

Replacing $n\kappa + k\nu$ by l and combining all the elements with equal l for all possible integers

$$k(n,l) = \frac{l - n\kappa}{\nu} \tag{55}$$

we get for $n = 0, \pm 1, \pm 2$

$$H_l = H_{-2k(-2l)} + H_{-1k(-1l)} + H_{0k(0l)} + H_{1k(1l)} + H_{2k(2l)} \tag{56}$$

The BMFT Hamiltonian representation can then be reduced to a SMFT Hamiltonian

$$\mathcal{H}_F = \sum_l H_l F_l^t + \omega_t N^t \tag{57}$$

where the ladder operators F_l^t and the number operator N^t have their standard definitions in the manifold of Fourier states $\{|l>\}$, defined by the characteristic frequency ω_t and the characteristic time interval $\tau_t = 2\pi/\omega_t$. The SMFT Hamiltonian has matrix elements H_l that can be correlated with the BMFT elements H_{nk}, using Eq. 56. In this equation BMFT elements have two sub-indices n,k and SMFT elements have one sub-index l. For each l there can be a maximum of five different H_{nk} elements to be summed. For $n = 0$ the possible values of l are $\nu k(0,l)$. Thus only l values that are a multiple k of ν have terms H_{0k}. When $n \neq 0$ $l = \nu k(n,l) + n\kappa$ and each k value will contribute to some l-element.

4.2
The Zero- and Higher-Order Effective Hamiltonians

To obtain the effective Hamiltonian we need to diagonalise the SMFT Hamiltonian in Floquet space. When this is not practical we should consider perturbation expansions. The van Vleck transformation [96] will be the most convenient approach in this case. The result will be an expansion of the effective Hamiltonian $\mathcal{H}_{eff}$ in terms of higher-order terms[3], with

---

[3] We index the various orders from 0 while the group of Levitt and Nielsen index the various orders from 1.

$$\mathcal{H}_{eff} = \tilde{U}(0)\tilde{\mathcal{H}}_{eff}\tilde{U}^{-1}(0) \tag{58}$$

and

$$\tilde{U}(t) = \sum_n <n|e^{iS^{(1)}}e^{iS^{(2)}}e^{iS^{(3)}}\dots|0> e^{in\omega_t t} \tag{59a}$$

$$\tilde{\mathcal{H}}_{eff} = \tilde{\mathcal{H}}_{eff}^{(0)} + \tilde{\mathcal{H}}_{eff}^{(1)} + \tilde{\mathcal{H}}_{eff}^{(2)} + \dots \tag{59b}$$

in

$$U_{int}(t) = \tilde{U}(t)\tilde{U}^{-1}(0)e^{-i\tilde{U}(0)\tilde{\mathcal{H}}_{eff}\tilde{U}^{-1}(0)} \tag{60}$$

At this point of the discussion the zero- and higher-order terms will not be derived explicitly, but we will return to the van Vleck approach at a later stage, where we will treat the BMFT case. Following Goldman's derivation [98, 99] and Mehring's secular averaging theory [14] the result of the van Vleck transformation yields

$$\tilde{\mathcal{H}}_{eff}^{(0)} = H_0 \tag{61a}$$

$$\tilde{\mathcal{H}}_{eff}^{(1)} = -\frac{1}{2}\sum_{l\neq 0}\frac{[H_l,H_{-l}]}{l\omega_t} \tag{61b}$$

$$\tilde{\mathcal{H}}_{eff}^{(2)} = \frac{1}{3}\sum_{l\neq 0,l'\neq 0}\frac{[H_{-l},[H_{l-l'},H_{l'}]]}{(l-l')l'\omega_t^2} - \frac{1}{2}\sum_{l\neq 0}\frac{[H_0,[H_l,H_{-l}]]}{l^2\omega_t^2} \tag{61c}$$

and

$$S^{(1)} = i\sum_{l\neq 0}\frac{H_l}{l\omega_t} \tag{62}$$

If $|H_l| < l\omega_t$ and we approximate $\tilde{U}(0) \simeq 1$, the effective Hamiltonian to first-order becomes

$$\mathcal{H}_{eff} \simeq \tilde{\mathcal{H}}_{eff}^{(0)} + \tilde{\mathcal{H}}_{eff}^{(1)} \tag{63}$$

The zero-order contribution to $\mathcal{H}_{eff}$ is thus just equal to the diagonal term H_0, and depends on the matrix elements H_{nk} as in Eq. 56. We will discuss briefly which bimodal Floquet elements H_{nk} can contribute to the diagonal block H_0 in the single-mode representation. According to Eq. 55, in order to obtain $l = 0$ the integer k must be equal to $-n\kappa/\nu$. There is always a possibility that $n = 0$ and $k = 0$ and hence H_{00} will always contribute to H_0.

For spinning frequencies slower than or equal to the characteristic RF frequency ($\omega_r < \omega_c$ with $\nu \geq \kappa$), κ/ν is less then 1. Since $n = \pm 1, \pm 2$ and k is an integer (it is an index), only when κ/ν equals 1 or 1/2 elements $H_{n\ -n\kappa/\nu}$ exist that can contribute to H_0. This corresponds to the synchronisation conditions with $\tau_r/\tau_c = \nu/\kappa = 1,2$. For all other τ_r/τ_c ratios the only element contributing to H_0 is H_{00}. The possible k and n values defining H_{nk} that contribute to H_0 are illustrated graphically in Fig. 18a for $\nu \geq \kappa$.

For the opposite case, i.e., spinning frequencies higher than the characteristic RF frequency, $\omega_r > \omega_c$, with $\nu < \kappa$ and $\tau_r/\tau_c < 1$ k, is still equal to $-n\kappa/\nu$, but
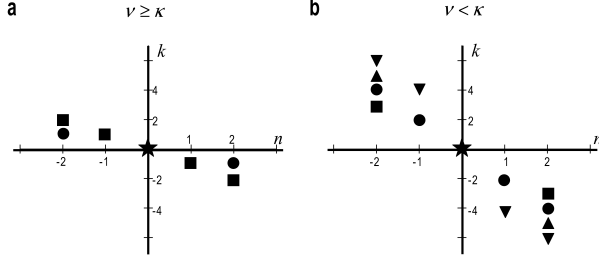
Fig. 18a,b Values of n and k such that $l = n\kappa + k\nu = 0$. In **a** for $\nu \geq \kappa$ the filled squares correspond to a κ/ν ratio equal to 1 and the filled circles to $\kappa/\nu = 1/2$. For $\kappa/\nu \leq 1/3$ no k and n values exist that fulfill the requirement $l = 0$. In **b** for $\nu < \kappa$ the filled squares correspond to $\kappa/\nu = 3/2$, the filled circles to $\kappa/\nu = 2$, the filled triangles to $\kappa/\nu = 5/2$ and the inverted filled triangles to $\kappa/\nu = 3$. For any other ratio $\kappa/\nu = i/2$ (i being any integer) k,n values can be found that satisfy $l = 0$

this time κ/ν is bigger than 1, and can be written in general as $\kappa/\nu = i/2$, with integer $i > 2$. Hence, the diagonal block is equal to the sum of the contributions from bimodal Floquet blocks $H_{n\,ni/2}$ according to:

$$i \; odd \; : \; H_0 = H_{-2i} + H_{00} + H_{2-i} \tag{64a}$$

$$i \; even \; : \; H_0 = H_{-2i} + H_{-1i/2} + H_{00} + H_{1-i/2} + H_{2-i} \tag{64b}$$

This is illustrated in Fig. 18b. Because the DD_{homo} and CSA terms in the Hamiltonian have no elements with $n = 0$ ($H_{00}^{CSA} = H_{00}^{DD} = 0$) they contribute to the diagonal terms only when $\kappa/\nu = i/2$, $i = 1,2,3,\ldots$

Based on the previous discussion, during homonuclear dipolar decoupling experiments, the zero-order effective Hamiltonian is at least equal to

$$\tilde{\mathcal{H}}_{eff,a}^{(0)} = H_0 \simeq -\Delta\omega_i \left(d_{00}^{(1)} I_{za} + \frac{1}{\sqrt{2}}(d_{-10}^{(1)} - d_{+10}^{(1)}) I_{xa} + \frac{i}{\sqrt{2}}(d_{+10}^{(1)} + d_{-10}^{(1)}) I_{ya} \right) \tag{65}$$

This can be rewritten as

$$\tilde{\mathcal{H}}_{eff,a}^{(0)} = -s \, \Delta\omega_a \, I_{\bar{e}} \tag{66}$$

where $\bar{e}$ represents a direction in the rotating frame with polar angles (θ,φ) and a scale factor s determining the scaling of the off-resonance values during the proton evolution:

$$s = \left\{ (d_{00}^{(1)})^2 + (d_{-10}^{(1)})^2 + (d_{+10}^{(1)})^2 \right\}^{1/2} \tag{67}$$

The direction of the effective field $\bar{e}$ with respect to the z-direction of the rotating frame is defined by

$$\tan\theta = \frac{\sqrt{\left(d_{+10}^{(1)}\right)^2 + \left(d_{-10}^{(1)}\right)^2}}{d_{00}^{(1)}} \tag{68a}$$

$$\tan\varphi = i\frac{d_{+10}^{(1)} - d_{-10}^{(1)}}{d_{+10}^{(1)} + d_{-10}^{(1)}} \tag{68b}$$

A discussion about the effects of the higher-order van Vleck correction terms will be given at a later stage, where we deal with the BMFT approach. However, a comment about Average Hamiltonian Theory (AHT) must be made at this point. This powerful theoretical approach is valid for single frequency periodic Hamiltonians.

4.3
Average Hamiltonian Theory

The Average Hamiltonian Theory (AHT) [23, 26] is applied to express the propagator of a periodic Hamiltonian $\mathcal{H}_{int}(t + k\tau_t) = \mathcal{H}_{int}(t)$ in terms of a time independent effective Hamiltonian $\langle\mathcal{H}\rangle$. When the Hamiltonian is also cyclic and $U_{int}(k\tau_t) = U_{int}(0) = 1$, the propagator gets the generalised form

$$U_{int}(k\tau_t) = e^{-ik\langle\mathcal{H}\rangle\tau_t} \tag{69}$$

This effective Hamiltonian is again not unique but can be chosen such that its eigenvalue differences are smaller than $1/2\omega_t$. Maricq [100–102] and others [14, 103] have demonstrated that the Magnus expansion of the effective Hamiltonian in AHT and the van Vleck transformation approach of the Floquet Hamiltonian are equivalent. At the time points $k\tau_t$ the Floquet solution for the propagator in Eq. 24 has the form

$$U_{int}(k\tau_t) = e^{-i\mathcal{H}_{eff}k\tau_t} \tag{70}$$

and the van Vleck transformation results according to Eq. 58 in

$$< \mathcal{H} >= \mathcal{H}_{eff} \cong \tilde{U}(0)\tilde{\mathcal{H}}_{eff}\tilde{U}^{-1}(0) \tag{71}$$

with $\tilde{U}(0)$ and $\tilde{\mathcal{H}}_{eff}$ given above (Eq. 59). Insertion of the expression for $\tilde{H}_{eff}^{(0)}$, $\tilde{H}_{eff}^{(1)}$, and considering only the first two terms of the Taylor expansion of $\tilde{U}(0)$, Eq. 59a, we get for $< \mathcal{H} >$

$$< \mathcal{H} >= H_0 - \frac{1}{2}\sum_{l\neq 0}\frac{[H_l,H_{-l}]}{l\omega_t} - \frac{1}{2}\sum_{l\neq 0}\frac{[H_0,H_l]}{l\omega_t} + \dots \tag{72}$$

This expression is identical to the zero and first AHT terms obtained when the first-order Magnus expansion terms are calculated using the integral expressions and the Fourier expansion of $\mathcal{H}_{int}(t)$. Thus the effective Hamiltonian to first-order in AHT differs from the first-order van Vleck expansion, Eq. 61b. This difference has been discussed by Goldman [98], Mehring [14] and others [103, 104] and it was shown that the additional term in $< \mathcal{H} >$ should be discarded

when calculations are performed to first-order with this Hamiltonian. A reason for this is that the approximated $\tilde{U}(0)$ is not unitary, as will be discussed later.

In the rest of this review we will mainly restrict ourselves to first-order effects and will therefore use only the van Vleck perturbation approach. As mentioned already, we will not present derivations of the decoupling schemes but rather present a comparative study in the case of magic-angle spinning. As will be discussed later, at high spinning rates the magnitude of the first-order contributions to the effective Hamiltonian is an indication of the homonuclear dipolar decoupling efficiency.

5
Floquet Treatment of MAS and RF Synchronisation

In this section we will deal with homonuclear dipolar decoupling sequences where the RF irradiation is synchronised with MAS.

Special classes of multiple-pulse sequences were designed by Levitt et al., using the symmetry principles of internal spin Hamiltonians [77, 86–88] where an integer number of RF pulse units spans a certain number of rotor cycles. These sequences are classified as CN_κ^χ and RN_κ^χ sequences [77].

5.1
C-Sequences

In the CN_κ^χ-sequence N consecutive pulse segments of duration τ_s, with each pulse segment differing in their overall phase by $\varphi_q = 2\pi q\chi/N$ ($q = 0,1,\ldots,(N-1)$), are applied on a rotating spin system, such that $N\tau_s = \kappa\tau_r$ and $\tau_c = \kappa\tau_r$, where τ_c is the total duration of the N segments (see Fig. 10b). Here, both κ and χ are integers. Each segment performs an overall 2π rotation with the total propagator equal to one. In the nomenclature of the above discussion we are dealing with the crossing conditions at $\nu = 1$ and $\kappa = 1,2,\ldots$ (depending on the RF cycle) and $\omega_t = \omega_c$. For zero-order homonuclear dipolar decoupling we have to concentrate on H_0 of Eq. 64b:

$$\tilde{\mathcal{H}}_{eff}^{(0)} = H_{-22\kappa} + H_{-1\kappa} + H_{00} + H_{1-\kappa} + H_{2-2\kappa} \tag{73}$$

The dipolar interaction and CSA contribute to $H_{-22\kappa}, H_{-1\kappa}, H_{1\kappa}, H_{2-2\kappa}$, but not to H_{00}. On the contrary, the isotropic chemical shift contributes only to H_{00}. Hence, in order to achieve zero-order decoupling, all the terms in Eq. 73 must vanish, except H_{00}. This can be accomplished when, according to the definition of H_{nk}, the coefficients $d_{m2\kappa}^{(l)}$, $d_{m\kappa}^{(l)}$, $d_{m-\kappa}^{(l)}$ and $d_{m-2\kappa}^{(l)}$ are made zero for all m. For H_{nk} to contribute to H_0 ($l = 0$) its k-index must be equal to $k = (l - n\kappa)/\nu = -n\kappa$ ($n = -2, -1, 1, 2$), hence, we must find RF sequences that result in a set of non-zero $d_{mk}^{(l)}$ coefficients with

$$k \neq -n\kappa \tag{74}$$

The residual H_{00} term determines the scaled isotropic chemical shifts. In Appendix 2 it is shown that for the CN_κ^χ sequences the non-zero $d_{mk}^{(l)}$ coefficients for all $T_m^{(l)}$ components in the Hamiltonian have k values

$$k = k'N - m\chi \tag{75}$$

with k' an integer. Combining the last equation with Eq. 74 results in

$$-n\kappa \neq k'N - m\chi \tag{76}$$

which agrees with Levitt's selection rules to zero-order [77].

Table 2 shows examples of CN_κ^χ homonuclear dipolar decoupling sequences with values of k according to Eq. 76. The k values are tabulated for both homonuclear dipolar (with interaction terms proportional to $T_{\pm 2}^{(2)}$, $T_{\pm 1}^{(2)}$ and $T_0^{(2)}$) and CSA (with interaction terms proportional to $T_{\pm 1}^{(1)}$ and $T_0^{(1)}$) interactions. If the resulting k values are not equal to $-n\kappa$, then the corresponding interaction terms are symmetry-forbidden to zero-order, $\tilde{\mathcal{H}}_{eff}^{(0)} = 0$.

As a specific case, consider the sequence $C9_1^3$ which has 9 pulse elements during one rotor period with phase increments $\varphi = 2\pi/3$ and $n\kappa = \pm 1, \pm 2$. For DD_{homo} with terms proportional to $T_{\pm 2}^{(2)}$ one gets $k = \pm 6$ for $k' = 0$ and $k = \pm 3$ for $k' = \pm 1$. Similarly, for DD_{homo} with terms proportional to $T_{\pm 1}^{(2)}$ and for the CSA interaction with terms proportional to $T_{\pm 1}^{(1)}$ the values become ± 6 for $k' = \pm 1$ and ± 3 for $k' = 0$. Finally, the $T_0^{(2)}$ and $T_0^{(1)}$ terms contribute to the values $k = \pm 9, 0$. All these values differ from $-n\kappa = \pm 1, \pm 2$, and hence these interaction terms do not contribute to line-broadening to zero-order. The isotropic chemical-shift interaction is independent of the sample spinning ($n = 0$) and has only diagonal contributions for $k = 0$, and hence will be retained as long as the zero-order Hamiltonian terms themselves are non-zero. Unfortunately, the scale factor for CN_κ^χ sequences appropriate for homonuclear dipolar decoupling is zero with the basic C element corresponding to a 2π rotation (see Appendix 2), and hence such sequences are not practical for obtaining high-resolution ^{1}H spectra.

Table 2. Examples of CN_κ^χ homonuclear dipolar decoupling sequences ($|k| \leq 10$)

CN_κ^χ	$k = k'N - m\chi$						$-n\kappa$
$C8_1^4$	± 8	± 4	0				$\pm 1, \pm 2$
$C9_1^3$	± 9	± 6	± 3	0			$\pm 1, \pm 2$
$C10_1^5$	± 10	± 5	0				$\pm 1, \pm 2$
$C10_1^3$	± 10	± 7	± 6	± 4	± 3	0	$\pm 1, \pm 2$
$C11_1^3$	± 8	± 6	± 5	± 3	0		$\pm 1, \pm 2$

5.2
R-Sequences

The pulse schemes based on Levitt's R-sequences [77, 87, 88] can be treated in a similar fashion as the C-sequences and result in slightly different selection rules, making a distinction between first- and second-rank tensors.

A RN_κ^χ sequence consists of $N/2$ contiguous and equal pulse pairs $\{R_\varphi, R'_{-\varphi}\}$ with R_φ corresponding to an effective π rotation around an axis making a φ angle with the x-direction in the rotating frame, and R' is obtained from R by inverting all its phases. The total duration of $N/2$ pulse pairs is $\tau_c = \kappa\tau_r$ and $\varphi = \pi\chi/N$, as illustrated in Fig. 10c. If the duration of each R element is τ_R, $N\tau_R = \kappa\tau_r$.

Selection rules for RN_κ^χ are derived in Appendix 2. The result is that the non-zero $d_{mk}^{(1)}$ coefficients have k-values

$$k = (2k' + 1)N/2 - m\chi \tag{77}$$

and the non-zero $d_{mk}^{(2)}$ coefficients have k-values

$$k = 2k'N/2 - m\chi \tag{78}$$

with k' any integer.

When these values are not equal to $-n\kappa$ we get the selection rules for R-sequences.

[1]H experiments were performed using $R18_2^9$ [53]. Table 3 shows examples of RN_κ^χ homonuclear dipolar decoupling sequences with values of k according to Eqs. 77 and 78. The k values are tabulated for both homonuclear dipolar (with interaction terms proportional to $T_{\pm 2}^{(2)}$, $T_{\pm 1}^{(2)}$ and $T_0^{(2)}$) and CSA (with interaction terms proportional to $T_{\pm 1}^{(1)}$ and $T_0^{(1)}$) interactions. If the resulting k values are not equal to $-n\kappa$, then the corresponding interaction terms are symmetry-forbidden to zero-order, $\tilde{\mathcal{H}}_{eff}^{(0)} = 0$.

Table 3. Examples of RN_κ^χ homonuclear dipolar decoupling sequences ($|k| \leq 18$)

RN_κ^χ	$DD:$ $2k'N/2 - m\chi$			$CSA:$ $(2k' + 1)N/2 - m\chi$			$-n\kappa$		scale factor
$R10_1^5$	± 10	± 5	0	± 10	± 5	0	± 2	± 1	0.45
$R10_2^5$	± 10	± 5	0	± 10	± 5	0	± 4	± 2	0.45
$R14_1^7$	± 14	± 7	0	± 14	± 7	0	± 2	± 1	0.45
$R14_2^7$	± 14	± 7	0	± 14	± 7	0	± 4	± 2	0.45
$R14_3^7$	± 14	± 7	0	± 14	± 7	0	± 6	± 3	0.45
$R18_1^9$	± 18	± 9	0	± 18	± 9	0	± 2	± 1	0.45
$R18_2^9$	± 18	± 9	0	± 18	± 9	0	± 4	± 2	0.45

Although both CN_κ^χ and RN_κ^χ symmetry numbers indicate the nature of the spin interactions that are symmetry-allowed and symmetry-forbidden, they do not reflect the magnitudes of the zero- and higher-order terms of $\tilde{\mathcal{H}}_{eff}$.

5.3
The WHH4 Decoupling Scheme

Many different pulse sequences have been used for homonuclear dipolar decoupling under MAS conditions. As mentioned in the introduction, most were developed for non-spinning samples and were later combined with sample spinning; the first to minimise the dipolar interactions and the second to eliminate the CSA effects. Because we are interested in high MAS frequencies it is necessary to treat the spinning and the periodic time dependence of $T_0^{(1)}$ (Eq. 13b) in the interaction frame simultaneously. Hafner et al. [42,43,46,51] showed experimental results of high-resolution proton spectra that were obtained at relatively high spinning frequencies. Their RF schemes, based on the original four pulse WHH4 sequence, were semi windowless sequences to enable stroboscopic data sampling. The RF pulse cycles were applied synchronous with the spinning and they demonstrated graphically that applying four WHH4 cycles during one spinning period results in a zero average Hamiltonian [42,43,46]. In our nomenclature this corresponds to $\kappa = 1$ and $\nu = 4$. Insertion of acquisition windows between four equivalent decoupling units was also investigated successfully. With short WHH4 cycles a quasi-static limit ($\tau_r/\tau_c \gg 1$) can be considered, and only the detection windows have to be chosen appropriately in order to achieve $\mathcal{H}_{DD}^{(0)} = 0$. A combination of AHT and Floquet theory was applied for an analysis of these experiments [51].

Because we are dealing with $\omega_c = \nu\omega_r$ and $\nu > 2$ the diagonal SMFT Hamiltonian term H_0 in Eq. 56 equals H_{00}, which is determined solely by isotropic chemical shift terms as long as $d_{m0}^{(2)} \simeq 0$ for the DD interactions. The non-zero H_l terms of the Hamiltonian, with $l = \nu k(n,l) + n$ according to Eq. 56, must be inserted in Eq. 61b in order to obtain the first-order corrections to $\mathcal{H}_{eff}$. As we will show later, for $\nu = 3,4$, these correction terms contribute directly to H_0, while for non-synchronous cases their influence diminishes. Thus, one can expect at least the same line narrowing between and beyond the $\nu = 3,4$ crossing as at the crossings themselves. Filip et al. indeed showed experimentally that minimum line widths were obtained in the whole regime $3\omega_r < \omega_c < 5\omega_r$ [51].

Finally, Hafner et al. showed that at slow spinning conditions the insertion of four detection windows between efficient decoupling sequences maintains the spectral resolution in decoupled proton spectra. This was accomplished by choosing the four detection windows such that

$$\sum_{i=1}^{4} \int_{t_i}^{t_i+t_p} G_{n,ab} e^{in\omega_r t} dt = 0 \tag{79}$$

where t_i are the beginning points of the windows during one spinning period and t_p their lengths, while assuming that during the decoupling cycles the DD_{homo} interactions are zero [42, 43, 46].

6
Non-Synchronous Schemes

6.1
The Van Vleck Transformation

In this section, we describe decoupling sequences that have characteristic RF frequencies ω_c which are larger than the spinning frequency ω_r without being their integer multiples. We continue using the BMFT approach. Other approaches, such as a combination of SMFT and AHT, are also possible candidates to treat the incommensurate cases, but they are more suitable for $\omega_c >> \omega_r$. While most RF schemes were first derived for non-spinning experiments and later combined with MAS in CRAMPS experiments, we will immediately consider the simultaneous presence of MAS and RF irradiation. As we are particularly interested in experiments at high spinning frequencies, we will mainly concentrate on the high-spinning limit where the efficiency of the decoupling experiment is not determined by the "quasi-static" performance of the RF sequence and where first-order effects can be significant. In the following we will use the van Vleck transformation to estimate the effective Hamiltonians.

Since here we are excluding Floquet level-crossing conditions, we can assume that the general BMFT Hamiltonian $\mathcal{H}_F$ does not have block matrix elements that connect degenerate states with Floquet energy differences $\nu\omega_r - \kappa\omega_c = 0$. To evaluate the effective Hamiltonian it is necessary to at least block diagonalise the Floquet Hamiltonian. The transformation that generates the block diagonal Hamiltonian $\tilde{\mathcal{H}}_{eff}$ can be represented by some unitary transformation

$$D_F^{-1}\mathcal{H}_F D_F = \tilde{\mathcal{H}}_{eff} F_0^r F_0^c + \omega_r N^r + \omega_c N^c \tag{80}$$

with $\mathcal{H}_F$ defined in Eq. 31. Following the discussion in Section 3.5 the diagonalisation matrix can be expanded as

$$D_F = \sum_{n,k} D_{nk} \, F_n^r F_k^c \tag{81}$$

and the effective Hamiltonian in Hilbert spin space is again of the form

$$\mathcal{H}_{eff} = \tilde{U}(0)\tilde{\mathcal{H}}_{eff}\tilde{U}^{-1}(0) \tag{82a}$$

$$\tilde{U}(0) = \sum_{n,k} D_{nk} \tag{82b}$$

where $\tilde{U}(0)$ is a unitary transformation.

For the block diagonalisation procedure we can use the van Vleck transformation. This procedure eliminates off-diagonal blocks of the Floquet Hamiltonian modifying the diagonal blocks. A first-order transformation removes

$H_{nk}F_n^r F_k^c$, with n and k not simultaneously zero, from $\mathcal{H}_F$ and corrects $H_{00}F_0^r F_0^c + \omega_r N^r + \omega_c N^c$. The unitary transformation matrix D_F can be defined by a Hermitian operator S_F as

$$D_F = e^{iS_F} = 1 + iS_F - \frac{1}{2}S_F^2 + \ldots \tag{83}$$

and

$$D_F^{-1}\mathcal{H}_F D_F = \mathcal{H}_F + i[\mathcal{H}_F, S_F] - \frac{1}{2}[[\mathcal{H}_F, S_F], S_F] + \ldots \tag{84}$$

When S_F is chosen to first-order such that

$$S_F^{(1)} = \sum_{n'k'} \frac{iH_{n'k'}}{n'\omega_r + k'\omega_c} F_{n'}^r F_{k'}^c \tag{85}$$

D_F removes the off-diagonal terms of $\mathcal{H}_F$ with

$$i[\omega_r N^r + \omega_c N^c, S_F^{(1)}] = -\sum_{n',k'} H_{nk} F_{n'}^r F_{k'}^c \tag{86}$$

and leaves the terms $i[H_{nk}F_n^r F_k^c, S_F^{(1)}]$, resulting in

$$\begin{aligned} D_F^{-1}\mathcal{H}_F D_F =\ & H_{00}F_0^r F_0^c + \omega_r N^r + \omega_c N^c - \\ & \frac{1}{2}\sum_{n,k,n',k'}(1 + \delta_{n0}\delta_{k0})\frac{[H_{nk}, H_{n'k'}]}{n'\omega_r + k'\omega_c}F_{n+n'}^r F_{k+k'}^c + \ldots \end{aligned} \tag{87}$$

Here, the sum, again with n' and k' not simultaneously zero, contains diagonal as well as off-diagonal terms. When we add the diagonal terms that are proportional to $(n'\omega_r + k'\omega_c)^{-1}$ to H_{00} and ignore all the off-diagonal terms with $n + n' \neq 0$ and $k + k' \neq 0$, as well as higher-order terms, the first-order block diagonal Hamiltonian becomes

$$\tilde{\mathcal{H}}_{eff} \simeq \tilde{\mathcal{H}}_{eff}^{(0)} + \tilde{\mathcal{H}}_{eff}^{(1)} = H_{00} - \frac{1}{2}\sum_{n',k'}\frac{[H_{-n'-k'}, H_{n'k'}]}{n'\omega_r + k'\omega_c} \tag{88}$$

To the same order of approximation the diagonalisation matrix equals $D_F = 1 + iS_F$ and the Hilbert space $\tilde{U}(0)$ operator becomes

$$\tilde{U}(0) \simeq 1 - \sum_{n',k'}\frac{H_{n'k'}}{n'\omega_r + k'\omega_c} \tag{89}$$

Notice that this $\tilde{U}(0)$ operator is not unitary. Thus, in order to maintain the eigenvalues of the first-order corrected $\tilde{\mathcal{H}}_{eff}$ in Eq. 88 this operator has to be modified and made unitary before it can be inserted in Eq. 82a. This can be accomplished by orthonormalisation of the columns of the $\tilde{U}(0)$ matrix, as is done in standard perturbation theory, or by maintaining all terms of D_F and defining

$$\tilde{U}(0) = \sum_{n,k} <n,k|e^{+iS_F^{(1)}}|0,0> \tag{90}$$

The effective spin Hamiltonian $\mathcal{H}_{eff}$ can then be approximated by $\tilde{U}(0)\tilde{\mathcal{H}}_{eff}\tilde{U}^{-1}(0)$. Only when we assume that $\tilde{U}(0) \simeq 1$ can we equalise $\mathcal{H}_{eff}$ and $\tilde{\mathcal{H}}_{eff}$.

The frequency response of the spin system to the combined sample spinning and RF perturbation irradiation is determined by the differences $\Delta\omega_{pq}$ between the eigenvalues of $\mathcal{H}_{eff}$ and linear combinations of multiples of ω_c and ω_r : $\Delta\omega_{pq} + k\omega_c + n\omega_r$. The eigenvalues of $\mathcal{H}_{eff}$ are the same for $\tilde{\mathcal{H}}_{eff}$. By changing the eigenvalues of $\mathcal{H}_{eff}$ the frequency response of the density operator will be modified. Thus, when we are interested in lineshifts and powder linewidths it is sufficient to consider $\tilde{\mathcal{H}}_{eff}$ instead of $\mathcal{H}_{eff}$. On the other hand for the evaluation of the intensities and the lineshapes of centrebands and sidebands we must estimate $\mathcal{H}_{eff}$ itself and take $\exp(+iS_F^{(1)})$ into account. Because we are mainly interested in decoupling efficiencies in terms of linewidths, we will restrict ourselves to the evaluation of $\tilde{\mathcal{H}}_{eff}$. The actual calculation of the spectra that will be shown later will not rely on these effective Hamiltonian expressions, but rather on stepwise integration methods.

When the approximate expression for $\tilde{U}(0)$ in Eq. 89, despite not being unitary, is used to evaluate the effective Hamiltonian the result is

$$\mathcal{H}_{eff} = \tilde{\mathcal{H}}_{eff}^{(0)} + \tilde{\mathcal{H}}_{eff}^{(1)} + \sum_{n'k'} \frac{[H_0, H_{n'k'}]}{n'\omega_r + k'\omega_c} \tag{91}$$

This addition changes the eigenvalues of the first-order corrected Hamiltonian and therefore the frequency response of the spins, when used to calculate the time dependence of density operators. Using AHT a similar term is obtained in the expression of the first-order correction of the average Hamiltonian. As was discussed by Goldman, Bruishvili, Mehring and others [14, 98–102, 104] using this additional term can result in invalid spin responses, and thus it has been advised to discard this term.

For the evaluation of the higher-order correction terms of $\tilde{\mathcal{H}}_{eff}$ we must first find the diagonal second-order terms in Eq. 87. A straightforward expansion then results in

$$\mathcal{H}_{eff}^{(2)} = \sum_{n',n'',k',k''} \left(\frac{1}{3} + \frac{1}{6}\delta_{0n'}\delta_{0k'}\right) \frac{[[H_{-n'-n'' \ -k'-k''}, H_{n'k'}], H_{n''k''}]}{(n'\omega_r + k'\omega_c)(n''\omega_r + k''\omega_c)} \tag{92}$$

In the sum above the values of n' and k' as well as n'' and k'' are not simultaneously zero. This second-order correction term must be added to the effective Hamiltonian in Eq. 88. To obtain this result it was not necessary to change $S^{(1)}$ defining D_F. Thus to obtain the effective Hamiltonian in the original spin Hilbert space, it is again sufficient to apply $\exp(+iS_F^{(1)})$. Only when we are interested in higher-order terms is an additional van Vleck transformation with $\exp(+iS_F^{(2)})$ required. This is, however, outside the scope of our discussion here.

The $H_{n'k'}$ terms in $\mathcal{H}_F$ themselves, and thus the $d_{mk'}^{(l)}$ coefficients, determine the magnitudes of the terms in the first- and second-order corrections to

the effective Hamiltonian $\tilde{\mathcal{H}}_{eff}$. Therefore we will now concentrate on these co-efficients and check their influence on the decoupling performances. However, before doing so, we should discuss some aspects concerning level crossing conditions.

6.2
Level Crossings

The crossing conditions of the Floquet energy levels were defined before as

$$\nu\omega_r = \kappa\omega_c \tag{93}$$

and they can be assigned by $\{\nu,\kappa\}$ values (see Fig. 17). At these conditions the first-order van Vleck transformation cannot be performed as long as there are $H_{n'k'} \neq 0$ Floquet elements that directly connect the degenerate Floquet states. Because n' is constrained between -2 and 2, level crossings involving these terms can only occur at $\{\pm 1,\kappa\}$ or $\{\pm 2,\kappa\}$ with $H_{\pm 1 \mp \kappa/\nu} \neq 0$ or $H_{\pm 2 \mp 2\kappa/\nu} \neq 0$, respectively. At these crossings the directly connecting (dipolar) Hamiltonian terms can cause severe line-broadening. Thus for a fixed rotor period τ_r and RF cycle times shorter than or equal to τ_r the ratio κ/ν is smaller than 1 and the crossings that should be avoided are $\{1,1\}$ and $\{2,1\}$ with $\tau_c = \tau_r$ and $\tau_c = 1/2\tau_r$. When $\tau_c > \tau_r$ and $\kappa/\nu > 1$, as discussed in Section 5 for the symmetry-based decoupling schemes, direct dipolar contributions are possible at all crossings, as can be seen from Eq. 64b.

For $\tau_c < \tau_r$ and avoiding $\tau_c = \tau_r$ and $\tau_c = 1/2\tau_r$, the effective Hamiltonian $\tilde{\mathcal{H}}_{eff}$ determines the line-broadening in the decoupling experiments. This Hamiltonian is approximated by truncating the expansion of $D_F^{-1}\mathcal{H}_F D_F$ as in Eq. 88, taking only the diagonal terms, $F_0^r F_0^c$, into account. However, when the $F_{n+n'}^r F_{k+k'}^c$ terms in $\tilde{\mathcal{H}}_{eff}$ of Eq. 87 connect degenerate states with $(n + n')\omega_r + (k + k')\omega_c = 0$ their coefficients, proportional to $[H_{nk}, H_{n'k'}]$, must also be added to the first-order Hamiltonian. To avoid this situation we must refrain from crossing conditions $\nu\omega_r = \kappa\omega_c$ with $\nu = |n + n'| = 0,1,2,3,4$ and in particular $\tau_c \neq 1/3\tau_r$ and $\tau_c \neq 1/4\tau_c$. When $1 > \tau_c > 1/2\tau_r$, crossings with $\tau_c = 2/3\tau_r$ at $\{3,2\}$ and $\tau_c = 3/4\tau_r$ at $\{4,3\}$ can also cause dipolar line-broadening. In all other instances, and for small off-diagonal blocks $|H_{nk}| << (n\omega_r + k\omega_c)$, the elements proportional to $[H_{nk}, H_{n'k'}]$ do not connect diagonal Floquet energies and will change the effective Hamiltonians only by amounts of the order of $|H_{n'k'}|^2 / (n'\omega_r + k'\omega_c)$.

Thus, as long as we are not close to the crossings $\{1,1\}, \{2,1\}, \{3,1\}, \{4,1\}, \{3,2\}$, and $\{4,3\}$, the first-order van Vleck transformation is sufficient for analysing proton spectra to the first-order.

6.3
The First-Order Effective Hamiltonian

The $\tilde{\mathcal{H}}_{eff}^{(0)} = H_{00}$ contribution to the effective Hamiltonian $\mathcal{H}_{eff}$ contains only scaled isotropic chemical-shift terms. The first-order correction to the effective Hamiltonian requires the evaluation of commutators between DD elements, CSA elements and cross-terms DD$\times$ CSA. We should remind ourselves that the basic justification for using the van Vleck transformation is that the off-diagonal elements of the interactions are small with respect to the differences between the diagonal elements (see Eqs. 48a and 48b). When that is the case

$$\tilde{\mathcal{H}}_{eff}^{(1)} = -\frac{1}{2}\sum_{n',k'}\frac{[H_{-n'-k'},H_{n'k'}]}{n'\omega_r + k'\omega_c} = \mathcal{H}_{DD}^{(1)} + \mathcal{H}_{CSA}^{(1)} + \mathcal{H}_{DD\times CSA}^{(1)} \qquad (94)$$

The first term is the dominant one in the expansion and must be considered first. Insertion of the explicit expressions for the dipole-dipole Hamiltonian results in

$$\mathcal{H}_{DD}^{(1)} = -\frac{1}{2}\sum_{a<b,b<c}\sum_{n,k}\sum_{m,m'}\omega_{ab}\omega_{bc}G_{n,ab}G_{-n,bc}\frac{d_{mk}^{(2)}d_{m'-k}^{(2)}}{n\omega_r + k\omega_c}[T_{m,ab}^{(2)},T_{m',bc}^{(2)}] \quad (95)$$

and the coefficients of the commutators $[T_{m,ab}^{(2)},T_{m',bc}^{(2)}]$ are

$$\omega_{ab}\omega_{bc}\sum_{n}G_{n,ab}G_{-n,bc}\sum_{k}\frac{d_{mk}^{(2)}d_{m'-k}^{(2)}}{n\omega_r + k\omega_c} \qquad (96)$$

In the non-spinning case these coefficients become zero when the dipolar Hamiltonian is symmetric, with $d_{mk}^{(2)} = d_{m-k}^{(2)}$, and the n dependence is absent. However, in the spinning case these coefficients are different from zero, and they at least partly determine the dipolar broadening of the decoupled proton lines in the spectra. We cannot be sure whether these contributions are smaller or larger than the second-order contributions for all lines in the spectrum. For strongly dipolar coupled pairs (a,b), like the protons in CH_2 groups, coupled to at least one additional proton **c** the linewidth is at least partially governed by $\mathcal{H}_{DD}^{(1)}$. To stress this point further, simulation of a five-proton system was performed assuming a PMLG9-MAS experiment. The model compound is shown in Fig. 19a and its proton coordinates and chemical shift values are given in Table 4. The simulations were performed using the SPINEVOLUTION program [105]. Single crystal spectra were simulated and the widths of the $H_{3,4}-$ bands, corresponding to the two protons of the CH_2 group, and the H_2-proton of the adjacent CH group were measured as a function of the strength of the dipolar interaction by scaling all dipolar parameters ω_{ab} in the molecule by a factor s_D. Thus in the calculations all ω_{ab} coefficients were replaced by $s_D\omega_{ab}$. The results of these simulations at different magnetic fields are shown in Fig. 19c–e. The first-order dipole-dipole correction term, Eq. 95, is proportional to the multiple of two dipolar interaction parameters and hence to the square of the dipolar scaling factor s_D:
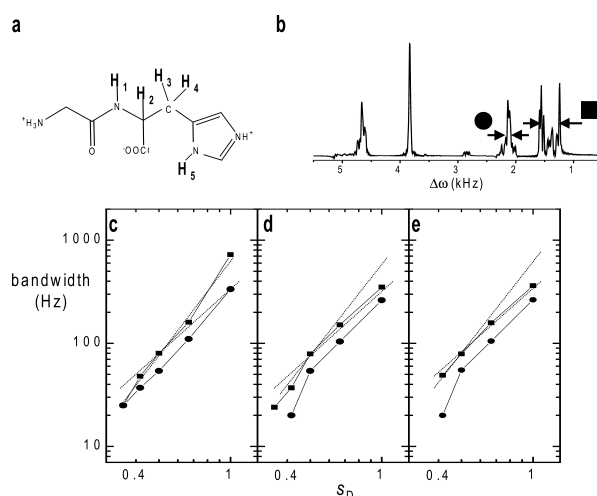
Fig. 19a–e a The five-proton model compound used for spectral simulations. The chemical shift values of the five numbered protons and their coordinates are given in Table 4. **b** A simulated single crystal spectrum of the five-proton system, assuming a PMLG9 irradiation on a rotating sample with $\omega_r/2\pi = 14.3$ kHz. The maximal splittings in Hz of the spectral bands of the CH_2 protons, H_3 and H_4, (filled squares) and of the CH proton, H_2 (filled circles) were measured as a function of a scale factor $0 < s_D < 1$. This scale factor was introduced to reduce all dipolar interactions in the calculation by replacing ω_{ab} by $s_D\omega_{ab}$. The results of these measurements for an arbitrary orientation of the model compound in the rotor are shown in (c-d). The simulations were performed at ^{1}H Larmor frequencies of **c** 300 MHz, **d** 600 MHz and **e** 800 MHz, with $\omega_1/2\pi = 81.6$ kHz. Lines with slopes 3 and 2 (dotted lines) are added to the plot to demonstrate the power dependence of the bandwidths on the dipolar scaling. At high fields the bandwidths of the $H_{3,4}$ protons, as well as the H_2 proton, show a slope close to 2, indicating a square dependence as in Eq. 97, and thus corresponding to the first-order broadening terms in the effective Hamiltonian

$$\mathcal{H}_{DD}^{(1)} \propto s_D\omega_{ab}s_D\omega_{bc} = s_D^2\omega_{ab}\omega_{bc} \qquad (97)$$

The second-order terms of the effective Hamiltonian are proportional to the s_D parameter to the third power, and in general, an nth order correction is proportional to s_D^{n+1}. The correction terms shift eigenvalues and hence the spectral positions of the observed lines composing the spectrum. Consequently, linewidths measured in the single crystal spectra can indicate which correction order is dominant. When the linewidth values as a function of the scaling parameter are plotted on a logarithmic scale, the slope of the line indicates which correction term is dominantly influencing the linewidth. These plots are shown in Fig. 19c–e. From the Figure it is evident that the main contribution to the linewidth of the CH_2 protons is determined by the first-order correction terms. The linewidths of other protons, more weakly coupled than in the CH_2 group and in the CH group adjacent to the CH_2, show slightly different dependences (not shown here). Overall it can be concluded from these simulations that, in the

case of PMLG at high fields, the first-order corrections have a strong influence on the linewidths of strongly coupled protons.

For a fixed spinning frequency and a characteristic RF frequency there are 100 parameters

$$D_{n,m,m'}^{DD}(\omega_r,\omega_c) = \sum_k \frac{d_{mk}^{(2)}d_{m'-k}^{(2)}}{n\omega_r + k\omega_c} \tag{98}$$

for $n = \pm 1, \pm 2$ and $m,m' = -2,..,2..$ These parameters determine the first-order contributions to the linewidths and provide an indication of the differences between the different decoupling schemes. A simple observation reveals that for symmetric Hamiltonians there are only 30 different $\left|D_{n,m,m'}^{DD}\right|$ values, which correspond to $n = 1,2$ and $m \geq m'$. For slow spinning cases, $n\omega_r + k\omega_c \simeq k\omega_c$, and when $d_{m0}^{(2)} = 0$ these parameters approach zero.

In the following we present a comparative study of the decoupling efficiency of three groups of schemes, {WHH4,MREV8,BR24}, {BLEW12,FSLG, DUMBO} and {PMLGn, wPMLGn}.

The fact that the first-order terms of the effective Hamiltonian are non-zero makes the discussion about pulse sequences that improve higher-order terms not always necessary. Of course, for lines with negligible first-order broadenings these higher-order effects are crucial and should be investigated. However, we will restrict ourselves to the first-order effects at high spinning rates. When $\omega_c >> \omega_r$, and the D-parameters approach zero, higher-order parameters must also be considered, as for the non-spinning case.

The first-order CSA correction can be defined similarly for Eq. 95, and it can be verified that this term is zero.

D parameters for the DD×CSA first-order corrections can also be derived and they can easily be calculated for the different pulse schemes:

$$D_{n,m,m'}^{DD \times CSA}(\omega_r,\omega_c) = \sum_k \frac{d_{mk}^{(1)}d_{m'-k}^{(2)}}{n\omega_r + k\omega_c} \tag{99}$$

Although these parameters are not zero we will restrict our discussion to the DD contributions only, because we are mainly interested in the high spinning frequency regime where the DD×CSA contributions are small.

Before discussing the different decoupling pulse sequences, we should comment on the two following aspects. Let us first consider the zero-order effective Hamiltonian. Because $\tilde{\mathcal{H}}_{eff}^{(0)}$ is solely determined by the scaled isotropic chemical shifts of the protons, the terms $-\Delta\omega_a \sum d_{m0}^{(1)}T_m^{(1)}$ determine the basic spectral resolution of the spectra. The scale factor for each pulse cycle differs and therefore similar absolute line-broadening of the lines will have a different appearance when plotted on a corrected chemical shift scale. Furthermore, because of the strong dependence of the $d_{m0}^{(1)}$ terms on the amplitudes of the RF irradiation, small inhomogeneities in the sample coil will result in inhomogeneous line-broadening that can not be corrected easily. For example, an RF intensity change

of about 10% in the case of FSLG will result in a change of about 8% in its scale factor, resulting in a line shift of 0.8 ppm of a line that is 10 ppm off-resonance. Similar efforts that improve or correct the decoupling sequences to higher-orders in the case of non-spinning samples can be inadequate when inhomogeneous broadening caused by RF imperfections determine part of the linewidths. Recently, Emsley et al. have discussed the effects of B_1 inhomogeneities in RF coils in the context of homonuclear dipolar decoupling [106].

The other aspect is the presence of the tilt angle θ of the effective field direction determined by $\mathcal{H}_{eff}^{(0)}$. It would have been convenient if θ would have been zero. However, in general, this is not the case, except for the TREV and the MSHOT sequences. This angle requires insertion of compensating pulses in pulse sequences and can complicate phase cycling schemes when decoupling sequences are incorporated in 2D experiments. Lately efforts have been undertaken to eliminate the presence of this tilt angle in the case of wPMLG5 [107].

7
A Comparative Study

7.1
The MSHOT3 Sequence

We here analyse the MSHOT scheme shown in Fig. 5. Using the fact that odd- and even-order average Hamiltonian terms transform as first- and second-rank irreducible tensor elements, $T_m^{(l)}$, using the z-rotational properties of these tensor elements, and using the fact that the different terms of the average Hamiltonian of a composite pulse sequence are the sum of the corresponding terms of the composing pulse units, it was shown that this sequence eliminates the $m \neq 0$ parts of the fourth-order dipolar average Hamiltonian [44, 45, 47]. This result holds for spin pairs in static cases. Effects of pulse lengths, pulse imperfections and RF inhomogeneities were also considered for this sequence. In practice, together with MAS, it was shown that MSHOT3 has the features of BR24, is robust to RF imperfections, and that it can be applied at higher spinning frequencies, 2–4 kHz.

Here we will restrict ourselves to discussing the first-order effective Hamiltonian of MSHOT3, and try to estimate changes in its D-parameters. The time dependent part of the interaction Hamiltonian that is induced by the RF pulses determines the values of their $d_{mk}^{(l)}$ coefficients. If each RF unit of length $\tau_c/3 = 2\pi/3\omega_c$ has a dipolar Hamiltonian with terms proportional to

$$\omega_{ab} \sum_k \delta_{m,k}^{(2)} e^{i3k\omega_c t} T_{m,ab}^{(2)} \tag{100}$$

then the three units together exhibit terms proportional to

$$\omega_{ab} \sum_k d_{mk}^{(2)} e^{ik\omega_c t} T_{m,ab}^{(2)} = \omega_{ab} \sum_{k'} \delta_{mk'}^{(2)} T_{m,ab}^{(2)} e^{ik'3\omega_c t} F(m,3) \tag{101}$$

where the time dependent function $F(m,3)$ has three consecutive values, 1, $\exp(i2\pi m/3)$, and $\exp(i4\pi m/3)$. The Fourier expansion of this function (see Appendix 2) has the form

$$F(m,3) = \sum_{k''} \varepsilon_{k''} e^{ik''\omega_c t} \tag{102}$$

where $k'' = k''' - m$. Inserting this series in Eq. 101 the non-zero $d_{mk}^{(2)}$-coefficients of MSHOT3 have values $k = 3(k'+k''') - m$, *i.e.* when $k = .. -m, -6-m, -3-m, m, 3-m, 6-m...$ Insertion of these non-zero coefficients in the expression for the first-order D-parameter results in non-zero contributions to D only when d_{mk} and $d_{m'-k}$ are simultaneously non-zero. This will happen when $m' = m \pm 3k$ and k is an integer. For all other combinations $D_{n,m,m'}^{DD}(\omega_r, \omega_c) = 0$. The non-zero parameters will be of the same order of magnitude as the $D-$ parameters of a sequence with three identical magic-echo units. Thus, in those instances when the first-order broadening is significant, we do not expect much line narrowing when going from TREV4 to MSHOT3. This is shown in Fig. 20 where the $D-$parameters of a MSHOT3 sequence are compared with the parameters of three identical units of TREV4. The experimental parameters of the pulse sequences are given in the figure caption. An RF irradiation field of 100 kHz is considered at two spinning frequencies, 1.559 kHz with $\omega_c = 19\omega_r$ and 8.465 kHz with $\omega_c = 3.5\omega_r$ (ω_c corresponds here to the characteristic frequency of a single TREV4 unit). The m and m' assignments of the parameters are not explicitly given in the figure, but the maximum values are obtained for $m = m' = 0$. The improvement at low spinning frequencies is a result of the presence of $n\omega_r$ in the denominator of Eq. 98. The fact that, for the pulse parameters chosen for these calculations, the zero-order $d_{m0}^{(2)}$'s are not zero does not disturb the evaluation of the first-order parameters, but at low spinning frequencies the requirement for the use of the perturbation expansion in Eqs. 48a and 48b will no longer be fulfilled, and hence, the first-order parameter D is not a good estimate for the actual dipolar decoupling performance. It is expected that at low spinning frequencies ($\omega_r << \omega_c$) the quasi-static limit is approached and non-zero $d_{m0}^{(2)}$ values will lead to significant line-broadening, similar to the static case.

7.2
WHH4 and Extensions

The WHH4 decoupling sequence with finite pulse lengths has non-zero $d_{m0}^{(2)}$ coefficients that can become too large to allow the use of the van Vleck expansion at low spinning frequencies. This is overcome by the MREV8 sequence and it is justified to evaluate the first-order D-parameters for high as well as for low ω_r. In Fig. 20 $D_{n,m,m'}^{DD}(\omega_r, \omega_c)$ parameters of three sequential units of MREV8 and of BR24 are shown for RF pulses with an intensity of 147 kHz and at spinning frequencies 19.048 kHz and 2.222 kHz. These frequencies correspond to $\omega_c = (3.5/6)\omega_r$ and $\omega_c = (30/6)\omega_r$, respectively, where ω_c corresponds to the characteristic RF frequency of BR24, which is six times larger than that of
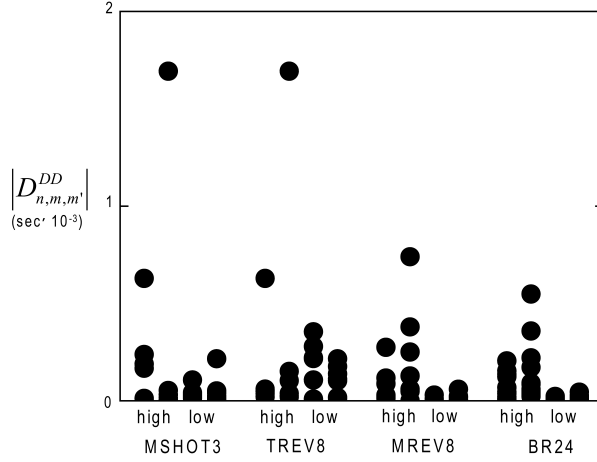
Fig. 20 The absolute values of the first-order $D^{DD}_{n,m,m'}$ parameters, defined in Eq. 98, for the MSHOT3, TREV8, MREV8, and BR24 sequences at high and low spinning frequencies. Of the four columns shown for each pulse sequence, the two at the left correspond to the $n = 1$ (left) and $n = 2$ (right) values at high spinning frequencies and the two at the right to low spinning frequencies. The parameters in the calculations for the MSHOT3 and TREV8 sequences were: $\omega_1/2\pi = 100\,\mathrm{kHz}$, the lengths of the $90°$ pulses were $\tau_p = 2.5\,\mu s$, and the interpulse delay, defined in Fig. 5, $\tau = 7/4\tau_p = 4.375\,\mu s$. Hence, the length of a single TREV4 unit was $\tau_c = 33.75\,\mu s$ ($\omega_c = 29.63\,\mathrm{kHz}$). The total length of the TREV8 sequence was therefore $\tau_c = 67.5\,\mu s$ ($\omega_c = 14.81\,\mathrm{kHz}$) and of the MSHOT3 was $\tau_c = 101.25\,\mu s$ ($\omega_c = 9.88\,\mathrm{kHz}$). The high spinning frequency was chosen at $8.465\,\mathrm{kHz}$ with $\omega_c = 3.5\omega_r$ and the low spinning frequency at $1.559\,\mathrm{kHz}$ with $\omega_c = 19\omega_r$ (with ω_c being the characteristic frequency of a single TREV4 unit). The MREV8 and BR24 sequence parameters were: $\omega_1/2\pi = 147\,\mathrm{kHz}$, the lengths of the $90°$ degree pulses $\tau_p = 1.7\,\mu s$, and the interpulse delay, as defined in Fig. 1 $\tau_w = \tau - \tau_p = 0.8\,\mu s$. Hence, the length of the MREV8 unit was $\tau_c = 30\,\mu s$ ($\omega_c = 33.33\,\mathrm{kHz}$) and of the BR24 unit was $\tau_c = 90\,\mu s$ ($\omega_c = 11.11\,\mathrm{kHz}$). The high spinning frequency was chosen as $19.048\,\mathrm{kHz}$ and the low spinning frequency as $2.222\,\mathrm{kHz}$. These frequencies correspond to $\omega_c = (3.5/6)\omega_r$ and $\omega_c = (30/6)\omega_r$, respectively, where ω_c corresponds to the characteristic RF frequency of BR24. The $D^{DD}_{n,m,m'}$ parameters obey $\left|D^{DD}_{n,m,m'}\right| = \left|D^{DD}_{-n,m',m}\right|$, and, hence, only values for $n = 1$ (left) and 2 (right) are shown

WHH4. Additional parameters of the sequences are given in the figure caption. The results of Fig. 20 show again the decrease of the D-parameters for decreasing spinning frequencies, and the fact that at high spinning rates the first-order parameters are significantly different from zero.

MREV8, the first extension of the basic WHH4 unit, consists of two consecutive units of four pulses that are not correlated via a simple z-rotation. It is therefore not possible to easily correlate the $d^{(2)}_{mk}$'s of MREV8 with those of WHH4. As a result almost all $D^{DD}_{n,m,m'}(\omega_r,\omega_c)$ parameters are different from zero and are about the same magnitude as those for WHH4. A similar evaluation of the parameters of the BR24 sequence shows that again the $D^{DD}_{n,m,m'}(\omega_r,\omega_c)$'s stay significantly different from zero at high-spinning speeds.

The source of the dipolar line-broadening for small ω_r values is of course determined by the higher-order contributions, as well as by the $DD\times$CSA contributions. Just as in the case of MSHOT3, the slow spinning proton spectra obtained with BR24 benefit from the (non-spinning) eliminations of higher orders. However, at high sample spinning even the original WHH4 sequence can result in spectra that are comparable with, or even better than, the BR24 spectra.

7.3
Performance Efficiency at High Spinning Speeds

Now we present a comparative study of the performance of a set of decoupling techniques at relatively high spinning frequencies. To do so we evaluated proton spectra of the model molecule, shown in Fig. 19a, containing five protons. The chemical shifts of these protons were chosen as shown in Table 4 and the coordinates of the protons in an orthogonal molecular frame are also tabulated. For all sequences a spinning frequency was chosen to satisfy $\omega_c = 3.5\omega_r$, except for MREV8 and BR24. In these two cases ω_r and ω_c were chosen according to their corresponding WHH4 sequence. A summary of the simulation parameters for the spectra shown in Fig. 22 are given below. The phases and number of pulses are defined according to Fig. 1, τ_p is the pulse-width and τ is the interpulse delay.

- WHH4 [$\tau_p = 1.7\,\mu s$, $\tau = 0.8\,\mu s$, $2\tau = 2.5\,\mu s$, $\omega_r/2\pi = 19.048\,kHz$, $\omega_c/2\pi = 66.66\,kHz$], MREV8 [$\tau_p = 1.7\,\mu s$, $\tau = 0.8\,\mu s$, $2\tau = 2.5\,\mu s$, $\omega_r/2\pi = 19.048\,kHz$, $\omega_c/2\pi = 33.33\,kHz$], BR24 [$\tau_p = 1.7\,\mu s$, $\tau = 0.8\,\mu s$, $2\tau = 2.5\,\mu s$, $\omega_r/2\pi = 19.048\,kHz$, $\omega_c/2\pi = 11.11\,kHz$], BLEW12 [$\tau_p = 2.5\,\mu s$, no detection windows, $\omega_r/2\pi = 9.52\,kHz$, $\omega_c/2\pi = 33.33\,kHz$], DUMBO [64 pulses with $\tau_p = 0.467\,\mu s$, no detection windows, $\omega_r/2\pi = 9.52\,kHz$, $\omega_c/2\pi = 33.33\,kHz$]
- FSLG [$\Delta\omega = \pm 70.71\,kHz$, $\tau_{LG} = 16.33\,\mu s$, no detection windows, $\omega_r/2\pi = 17.50\,kHz$, $\omega_c/2\pi = 61.24\,kHz$], PMLG9 [18 pulses with $\tau_p = 0.91\,\mu s$, no detection windows, $\omega_r/2\pi = 17.50\,kHz$, $\omega_c/2\pi = 61.24\,kHz$], PMLG3 [6 pulses with $\tau_p = 2.92\,\mu s$, no detection windows, $\omega_r/2\pi = 16.30\,kHz$, $\omega_c/2\pi = 57.05\,kHz$], wPMLG5 [10 pulses with $\tau_p = 1.56\,\mu s$, detection window $\tau = 3.12\,\mu s$, $\omega_r/2\pi = 15.25\,kHz$, $\omega_c/2\pi = 53.39\,kHz$]

Table 4. The proton coordinates in an arbitrary molecular reference frame and chemical shift values for the model compound shown in Fig. 19a

Protons	$x(\mathring{A})$	$y(\mathring{A})$	$z(\mathring{A})$	$\Delta\omega/2\pi\ (ppm)$	$\omega_a/2\pi\ (ppm)$	η	α	β	γ
$H^{(1)}$	-4.58	12.57	7.26	8.3	-10.4	0.19	$0°$	$20°$	$50°$
$H^{(2)}$	-2.26	11.71	6.08	4.6	-2	0.9	$30°$	$45°$	$140°$
$H^{(3)}$	-4.42	9.86	6.73	3.1	-4.5	0.17	$35°$	$80°$	$34°$
$H^{(4)}$	-3.24	9.47	5.93	3.1	-4.5	0.17	$50°$	$70°$	$120°$
$H^{(5)}$	-3.81	7.87	8.31	10.1	-9	0.19	$20°$	$60°$	$80°$
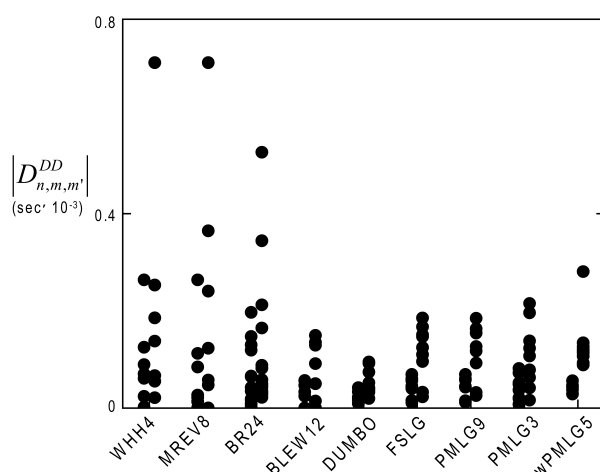
Fig. 21 The absolute values of the first-order $D^{DD}_{n,m,m'}$ parameters, Eq. 98, for the WHH4, MREV8, BR24, BLEW12, DUMBO, FSLG, PMLG9, PMLG3, and wPMLG5 sequences for $n = 1$ (left) and $n = 2$ (right) at high spinning frequencies. The parameters used for the simulations, along with the spinning frequencies, are given in Section 7

In Fig. 21 the first order $D^{DD}_{n,m,m'}(\omega_r,\omega_c)$ parameters are shown for all sequences. It is clear that the DUMBO scheme exhibits the lowest first-order parameters. In all cases, the largest parameters are $D_{n,0,0}$. The significance of this parameter lies in the fact that its corresponding spin operator $[T^{(2)}_{m,ab}, T^{(2)}_{0,bc}]$ is in general not zero. We did not make any effort to evaluate similar parameters for the second-order contributions from Eq. 92. Furthermore, we should mention that all calculations assumed RF pulses with no phase distortions. In actual experiments instabilities occur and the appearances of these parameters can govern part of the observed linewidths in the proton spectra.

The simulated spectra in Fig. 22 are only examples and should be considered as such. However, they demonstrate some of the general features of the sequences. In Fig. 22 the spectra obtained with WHH4, MREV8 and BR24 at the same spinning frequency are shown. Despite the relatively broad CH_2 proton line in the WHH4 spectrum, its overall result is not much worse than that of MREV8 and BR24. This is perhaps not surprising when we compare their first-order parameters. Excellent line narrowing of the CH_2 line is obtained in Fig. 22 for the case of BLEW12 and DUMBO. This is in qualitative agreement with their relatively small first-order parameters. The results of the PMLGn sequences are interesting as they do not differ significantly mutually and with respect to the FSLG result, despite the fact that $n = 3,5,9$ and despite the presence of the detection window in wPMLG-5.

Because we chose the simulations around the condition $\omega_c = 3.5\omega_r$ and restricted ourselves to 100 kHz RF power, the highest spinning frequencies were around 17 kHz for the PMLG series. At higher spinning rates ω_c/ω_r can be de-
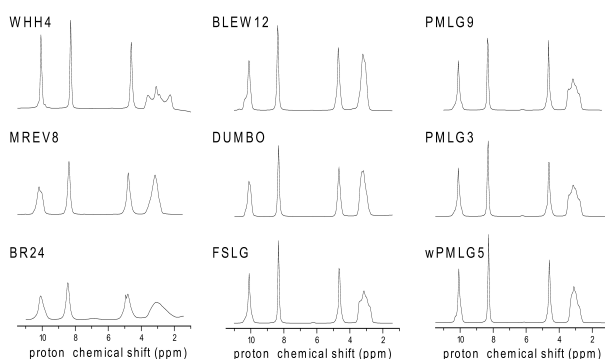
Fig. 22 Simulated ^{1}H spectra of the five-proton model system (shown in Fig. 19a and with coordinates as in Table 4) obtained with the decoupling schemes as indicated in the figure and at an external magnetic field of 14.1 T. The parameters of the sequences used in the simulations are summarised in Section 7

creased as long as the $\omega_c < 3\omega_r$ condition is avoided. Overall, the differences in decoupling performance are not very large and the choice of technique should be determined by the quality of pulse performance, stability, and the B_0 and B_1 homogeneities of the spectrometer. In case of direct signal detection, the detection windows should be made as short as possible and their presence should be partially compensated by a modification of the RF intensity. Each decoupling scheme has a different off-resonance response profile and RF inhomogeneity compensation. It is for the experimentalist to decide which sequence fits best for the measurements.

Finally we should mention the symmetry based decoupling schemes with $\omega_c < \omega_r$. In particular, for the short C- and R-sequences, experiments at very high spinning frequencies can be performed. Accurate setting of the experimental parameters are necessary for these experiments, however spinning frequencies of about 20 kHz can be reached for RF intensities no higher than 150 kHz. Simulated spectrum for $R18_2^9$ decoupling experiment on our model compound is shown in Fig. 23, again for 100 kHz of RF intensity. The resolution obtained is comparable to that obtained with other techniques.

8
Conclusions

We have presented here an analysis of several homonuclear dipolar decoupling multipulse schemes based on bimodal Floquet theory. A careful implementation of any of these schemes leads to considerable ^{1}H line narrowing and hence to resolved ^{1}H spectral lines. Sequences like PMLG and DUMBO are preferred due to the relative ease in their implementation together with their short cycle times, making them adaptable at high MAS rates. RF inhomogeneity is found to limit the attainable resolution, together with the contribution of higher-order terms
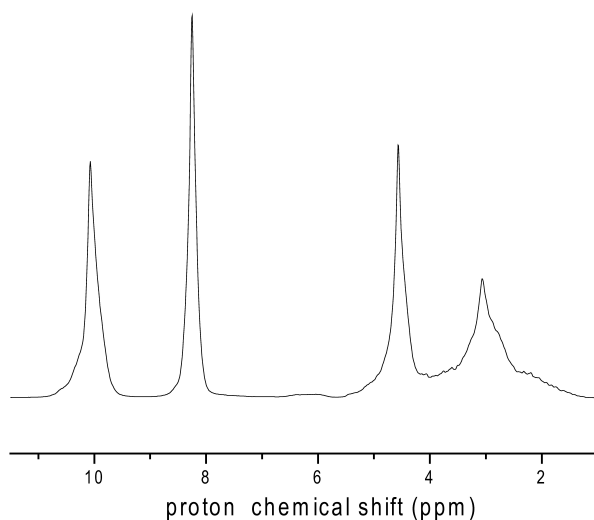
Fig. 23 Simulated $R18_2^9$ ^{1}H spectrum of the model spin system (shown in Fig. 19a with coordinates as in Table 4). The $180°$ pulse pairs were replaced by the composite pulse unit $\{90_{45}^o 90_{135}^o 90_{45}^o 90_{-45}^o 90_{-135}^o 90_{-45}^o\} \equiv 180_{90}^o 180_{-90}^o$. $\omega_1/2\pi$ was $100\,\text{kHz}$ and $\omega_r/2\pi$ was $14.81\,\text{kHz}$

under MAS conditions. Overcoming these remain the current challenges in this field. It is expected that an estimate of such terms following the theory presented here, and further numerical design, may aid in improving homonuclear dipolar decoupling pulse sequence performance.

Appendix 1

In this Appendix the expressions for the terms of the interaction Hamiltonian of a homonuclear spin system in the on-resonance rotating frame are given.

The chemical shift interaction Hamiltonian has the form:

$$\mathcal{H}_{ISO} + \mathcal{H}_{CSA}(t) = \sum_{a=1}^{N} \left\{ -\Delta\omega_a I_{za} + \sum_{n=-2}^{2} -\omega_a g_n(\Omega_a, \eta_a) e^{in\omega_r t} I_{za} \right\} \quad (A1)$$

where $\Delta\omega_a$ is the isotropic chemical shift, ω_a is the CSA frequency parameter, and η_a is the CSA asymmetry parameter. The geometric parameters g_n are functions of Euler angles $\Omega_a \equiv (\alpha_a, \beta_a, \gamma_a)$, that define the transformation of the initial principal axis systems of the CSA tensors to the rotor frame, and are defined in the following way with $m = 1,2$:

$$g_n(\Omega_a; \eta_a) = g^*_{-n}(\Omega_a; \eta_a) = \frac{1}{2}(g_{cn} - ig_{sn})e^{in\gamma} = |g_n| e^{i\xi_n} e^{in\gamma} \tag{A2}$$

with

$$g_{c1} = \frac{\sqrt{2}}{4}\sin 2\beta + \frac{\eta\sqrt{2}}{12}\cos 2\alpha \sin 2\beta \tag{A3a}$$

$$g_{s1} = -\frac{\eta\sqrt{2}}{6}\sin 2\alpha \sin \beta \tag{A3b}$$

$$g_{c2} = \frac{1}{2}\sin^2\beta - \frac{\eta}{6}\cos 2\alpha(\cos^2\beta + 1) \tag{A3c}$$

$$g_{s2} = \frac{\eta}{3}\sin 2\alpha \tag{A3d}$$

and

$$|g_n| = (g_{cn}^2 + g_{sn}^2)^{1/2} \tag{A4a}$$

$$\sin \xi_n = -g_{sn}/2\,|g_n| \quad ; \quad \cos \xi_n = g_{cn}/2\,|g_n| \tag{A4b}$$

where angle θ_n defines the magic-angle between the external magnetic field and the rotor axis.

The proton-proton dipolar interaction term is [89]

$$\mathcal{H}_{DD}(t) = \sum_{a<b=1}^{N} \sum_{n=-2}^{2} \omega_{ab} G_{n,ab}(\Omega_{ab})e^{in\omega_r t}(3I_{za}I_{zb} - \bar{I}_a \cdot \bar{I}_b) \tag{A5}$$

where ω_{ab} is the dipolar coupling constant, given by

$$\omega_{ab} = \frac{\mu_0}{4\pi}\frac{\gamma^2\hbar}{r_{ab}^3} \tag{A6}$$

where r_{ab} is the vector connecting the two interacting nuclei and γ is the proton gyromagnetic ratio.

$$G_n(\Omega_{ab}) = G^*_{-n}(\Omega_{ab}) = \frac{1}{2}G_{|n|}e^{in\gamma} \tag{A7}$$

with

$$G_{|1|,ab} = \frac{\sqrt{2}}{4}\sin 2\beta_{ab} \tag{A8a}$$

$$G_{|2|,ab} = -\frac{1}{2}\sin^2\beta_{ab} \tag{A8b}$$

and $\Omega_{ab} = (0, \beta_{ab}, \gamma_{ab})$ the Euler angles of of the dipolar tensor with respect to the sample rotor at time $t = 0$.

The Hamiltonian in Eq. A1 can be expressed in terms of the irreducible tensor operators (ITO), defined as:

$$T^1_{0,a} = I_{z,a} \tag{A9a}$$

$$T^1_{1,a} = -\frac{1}{\sqrt{2}}(I_{x,a} + iI_{y,a}) \tag{A9b}$$

$$T^1_{-1,a} = \frac{1}{\sqrt{2}}(I_{x,a} - iI_{y,a}) \tag{A9c}$$

$$T^2_{0,ab} = \frac{1}{\sqrt{6}}(3I_{z,a}I_{z,b} - \bar{I}_a \cdot \bar{I}_b) \tag{A9d}$$

$$T^2_{\pm 1,ab} = (T^1_{0,a}T^1_{\pm 1,b} + T^1_{\pm 1,a}T^1_{0,b}) \tag{A9e}$$

$$T^2_{\pm 2,ab} = T^1_{\pm 1,a}T^1_{\pm 1,b} \tag{A9f}$$

Using the ITO's the chemical shift Hamiltonian at high field becomes

$$\mathcal{H}_{ISO} + \mathcal{H}_{CSA}(t) = \sum_{a=1}^{N}\left\{ -\Delta\omega_a + \sum_{n=-2}^{2} -\omega_a g_{n,a}(\Omega_a,\eta_a)e^{in\omega_r t}\right\} T^1_{0,a} \tag{A10}$$

and the dipole-dipole interaction Hamiltonian

$$\mathcal{H}_{DD}(t) = \sqrt{6}\sum_{a<b=1}^{N}\sum_{n=-2}^{2} \omega_{ab}G_{n,ab}(\Omega_{ab})e^{in\omega_r t}T^2_{0,ab} \tag{A11}$$

Appendix 2

In this Appendix the k values of the non-zero Fourier series $d^{(l)}_{mk}$ coefficients of $T^{(l)}_m$ in the RF interaction frame for the CN^χ_κ and RN^χ_κ sequences are derived.

CN^χ_κ-Sequences

To evaluate the $d^{(l)}_{mk}$-coefficients of the CN^χ_κ RF sequence we must transform the $T^{(1,2)}_0$ operators in the normal rotating frame ((1) for the CSA interaction and (2) for the dipolar interaction), to the RF interaction frame and Fourier expand the results. For $0 < t \leq \tau_c$ and $\omega_c = 2\pi/\tau_c$ we can write

$$T^{(l)}_0(t) = U^{-1}_{RF}(t)T^{(l)}_0 U_{RF}(t) = \sum_m \left[\sum_k d^{(l)}_{mk}e^{ik\omega_c t}T^{(l)}_m \right] \tag{A12}$$

The derivation of the values for k of the non-zero Fourier coefficients can be accomplished by transforming each "2π" pulse separately, taking into account the overall phase differences between the N pulses. Assuming that the Fourier expansion of a single "2π" unit is given by

$$\sum_m \sum_{k'} \delta^{(l)}_{mk'}e^{ik'N\omega_c t}T^{(l)}_m, \tag{A13}$$

the $q + 1$-th "2π" pulse, with overall relative phase $2\pi\chi q/N$, during the time interval $q\tau_c/N < t < (q+1)\tau_c/N$ will obey

$$T_0^{(l)}(t) = \sum_m \left[\sum_{k'} \delta_{mk'}^{(l)} e^{ik'N\omega_c t} T_m^{(l)} \right] e^{i2\pi q m\chi/N} \tag{A14}$$

The overall time dependence can then be written as $(0 < t \leq \tau_c)$

$$T_0^l(t) = \sum_m \left[\sum_{k'} \delta_{mk'}^l e^{ik'N\omega_c t} T_m^l \right] F_C(m\chi, N) \tag{A15}$$

where the time-dependent function $F_C(m\chi, N)$ is consecutively equal to $e^{i2\pi(m\chi/N)q}$ during the time intervals $q\tau_c/N < t < (1+q)\tau_c/N$ with $q = 0, 1, \ldots, N-1$. Fourier transformation of this function can be evaluated straightforwardly and results in

$$F_C(m\chi, N) = \sum_{k''} \varepsilon_{k''} e^{ik''\omega_c t} \tag{A16}$$

with

$$\varepsilon_{k''} = \left\{ \int_0^{\tau_c/N} e^{-ik''\omega_c t} dt \right\} \sum_{q=0}^{N-1} e^{i2\pi q \left\{ \frac{(m\chi+k'')}{N} \right\}} \tag{A17}$$

It is evident that $\varepsilon_{k''}$ will be zero, unless $(m\chi + k'')/N$ is any integer k'''; thus

$$k'' = k'''N - m\chi. \tag{A18}$$

Inserting Eq. A16 in A15 we get for $0 < t \leq \tau_c$

$$T_0^{(l)}(t) = \sum_m \sum_{k',k''} \delta_{mk'}^l \varepsilon_{k''} \exp^{i(k'N+k'')\omega_c t} T_m^{(l)} \tag{A19}$$

Comparing this results with Eq. A12 reveals that the k's of the non-zero $d_{mk}^{(l)}$ coefficients get the values

$$k = k'N + k'' = (k' + k''')N - m\chi \tag{A20}$$

Replacing $(k' + k''')$ by k' which can take any integer value, the result for k values of the non-zero $d_{mk}^{(l)}$ coefficients become

$$k = k'N - m\chi \tag{A21}$$

For zero-order decoupling selection rules these k values should not be equal to $-n\kappa$, resulting in the decoupling condition

$$-n\kappa \neq k'N - m\chi \tag{A22}$$

which is the same as Levitt's symmetry condition.

To evaluate the actual values of the $d_{mk}^{(l)}$ coefficients requires calculation of the expression

$$d_{mk}^{(l)} = \frac{\omega_c}{2\pi} \sum_q e^{i2\pi \frac{m\chi}{N} q} \int_{((q-1)/N)\tau_c}^{(q/N)\tau_c} \delta_{mk'}^{(l)} e^{i(k'N-k)\omega_c t} dt \tag{A23}$$

In order to estimate the isotropic chemical shift scale factor we must calculate the coefficients $d_{m0}^{(1)}$. When $k = 0$, the above expression becomes for $l = 1$ simply

$$d_{m0}^{(1)} = \frac{1}{N}\left\{\sum_q e^{i2\pi\frac{m\chi}{N}q}\right\}\delta_{m0}^{(1)} \tag{A24}$$

and only when $m\chi = k'''N$ for all integers k''' the coefficients $d_{m0}^{(1)}$ can become different from zero, as long as $\delta_{m0}^{(1)} \neq 0$. The values of the coefficients $\delta_{mk'}^{(1)}$ for the simple basic C-element of 2π pulse units of constant amplitude $\omega_1 = N\omega_c$ can be evaluated using the Wigner matrix elements $D_{m0}^{(1)}$:

$$\begin{aligned}
T_0^{(1)}(t) &= \sum_m D_{m0}^{(1)}(\frac{\pi}{2},\omega_1 t, -\frac{\pi}{2})T_m^{(1)} \\
&= \cos\omega_1 t\, T_0^{(1)} - \frac{1}{\sqrt{2}}i\sin\omega_1 t(T_1^{(1)} - T_{-1}^{(1)})
\end{aligned} \tag{A25}$$

with the result that the average coefficients become

$$\delta_{00}^{(1)} = \frac{N\omega_c}{2\pi}\int_0^{2\pi/N\omega_c}\cos N\omega_c t\, dt = 0 \tag{A26a}$$

$$\delta_{\pm10}^{(1)} = \mp i\frac{N\omega_c}{2\pi}\frac{1}{\sqrt{2}}\int_0^{2\pi/N\omega_c}\sin N\omega_c t\, dt = 0 \tag{A26b}$$

and thus the $d_{m0}^{(l)}$ coefficients are zero. Hence, the scale factor for the CN_κ^χ sequences meant for isotropic chemical shift selection with the C-element as 2π pulse is zero.

RN_κ^χ-Sequences

In this section the k values of the non-zero $d_{mk}^{(l)}$−coefficients of the RN_κ^χ sequence are derived. Like the C-sequence the time dependence of the transformed $T_0^{(l)}$ operators in the RF interaction frame during a whole RN_κ^χ sequence can be Fourier expanded as

$$T_0^{(l)}(t) = U_{RF}^{-1}(t)T_0^{(l)}U_{RF}(t) = \sum_m\left[\sum_k d_{mk}^{(l)}e^{ik\omega_c t}T_m^{(l)}\right] \tag{A27}$$

When a "π" pulse segment with an overall phase of $\varphi = 0$ applied during a time interval $0 < t < \tau_c/N$ is represented in the RF interaction frame by the transformation

$$T_0^{(l)}(t;0) = \sum_m\left[\sum_{k'}\delta_{mk'}^{(l)}e^{ik'N\omega_c t}T_m^{(l)}\right] \tag{A28}$$

then the same "π" pulse segment with an overall phase of $\varphi = \pi\chi/N$ during the same interval results in

$$T_0^{(l)}(t;\varphi) = R_z(\varphi)\left\{ U_{RF}^{-1}(t;0)T_0^l U_{RF}(t;0) \right\} R_z(-\varphi) \tag{A29a}$$

$$= \sum_m \sum_{k'} \delta_{mk'}^l e^{ik'N\omega_c t} T_m^l e^{im\varphi}. \tag{A29b}$$

If at the end of this pulse the RF has performed a full π rotation around an axis in the xy-plane, we get

$$T_0^{(l)}(\tau_c/N;\varphi) = \mp T_0^{(l)} \tag{A30}$$

where the $-$ sign belongs to $T_m^{(1)}$ and the $+$ sign to $T_m^{(2)}$. This creates a distinction between the DD and the CSA terms in the Hamiltonian that are proportional to $T_m^{(1)}$ and $T_m^{(2)}$, respectively.

During the second segment $\tau_c/N < t < 2\tau_c/N$ the RF irradiation is defined by an inversion of all the irradiation components around the x-direction, $R_x(\pi)$, and has an overall phase of $-\varphi$. Assuming that the basic "π" pulse in Eq. A28 performs a rotation around the x-axis in the rotating frame, $U_{RF}(\tau_c/N;0) = U_x(\pi)$ then we get for $\tau_c/N < t < 2\tau_c/N$

$$\begin{aligned}
T_0^{(l)}(t;-\varphi) &= R_z(\varphi)U_x(\pi)R_z(-\varphi)\{ R_z(-\varphi)R_x(\pi)U_{RF}(t,0)R_x(-\pi) \\
&\quad T_0^{(l)}R_x(\pi)U_{RF}^{-1}(t;0)R_x(\pi)R_z(\varphi)\}R_z(\varphi)U_x(-\pi)R_z(-\varphi) \\
&= R_z(3\varphi)U_{RF}(t;0)(\mp)T_0^{(l)}U_{RF}^{-1}(t;0)R(-3\varphi) \\
&= (\mp)\sum_{k'} \delta_{mk'}^{(l)} e^{ik'N\omega_c t}T_m^{(l)}e^{i3m\varphi} \tag{A31a}
\end{aligned}$$

At the end of this segment the $T_0^{(l)}$ operators for $l = 1,2$ return to themselves. This will repeat itself each time after two additional segments. Hence, during each single segment $q,(q = 0,1,\dots,N-1)$, during the time interval $q\tau_c/N < t \le (q+1)\tau_c/N$, the $T_0^{(l)}$ operators in the RF interaction representation become:

$$\text{even } q : \qquad T_0^{(l)}(t) = \sum_m \delta_m^{(l)}(t)T_m^{(l)}e^{i(1+2q)m\pi\chi/N} \tag{A32a}$$

$$\text{odd } q : \qquad T_0^{(l)}(t) = (\mp)\sum_m \delta_m^{(l)}(t)T_m^{(l)}e^{i(1+2q)m\pi\chi/N} \tag{A32b}$$

again with the $-$ sign for the $T_m^{(1)}$ and the $+$ sign for the $T_m^{(2)}$ terms.

The overall time dependence of $T_0^{(l)}(t)$ during $0 < t \le \tau_c$ in the RF interaction representation results in a product of two functions; an odd function for $T_0^{(1)}(t)$ and an even function for $T_0^{(2)}(t)$ times a function $F_R(m\chi,N)$. This function takes on sequentially N values $\exp(ilq\pi + (2q+1)m\pi\chi/N)$ each for a duration of τ_c/N with $q = 0,1,\dots,N-1$:

$$T_0^l(t) = \left[\sum_{k'} \delta_{mk'}^l e^{ik'N\omega_c t}T_m^l \right] F_R(m\chi,N) \tag{A33}$$

Calculation of the Fourier expansion of $F_R(m\chi,N)$, in analogy with the expansion of $F_C(m\chi,N)$, leads to the following $\varepsilon_{k''}$ coefficients:

$$\varepsilon_{k''} = \left\{ \int_0^{T_c/N} e^{-ik''\omega_c t} \right\} e^{i\pi(m\chi/N)} \sum_{q=0}^{N-1} \exp^{iq2\pi\left\{ \frac{l}{2} + \frac{m\chi + k''}{N} \right\}} \tag{A34}$$

From this expression it is evident that $\varepsilon_{k''}$ is zero unless the expression $l/2 + (m\chi + k'')/N$ is an integer k''':

$$k'' = N(k''' - l/2) - m\chi \tag{A35}$$

Thus finally we get for $T_0^{(l)}(t)$ during $0 < t \le \tau_c$ in

$$T_0^l(t) = \sum_{k',k''} \delta_{mk'}^l \varepsilon_{k''} \exp\{i(k'N + k'')\omega_c t\} T_m^l \tag{A36}$$

and with Eq. A27 the non-zero coefficients $d_{mk}^{(l)}$ have k values

$$k = k'N + k'' = (2k' + 2k''' - l)N/2 - m\chi \tag{A37}$$

Replacing $2k' + 2k''' - l$ by k', which is an integer of the same parity as rank l, we get the k values of the non-zero $d_{mk}^{(l)}$ coefficients:

$$k = k'N/2 - m\chi \tag{A38}$$

For zero-order decoupling selection rules these k values should not be equal to $-n\kappa$ and we obtain the selection rules as

$$-n\kappa \ne k'N/2 - m\chi \tag{A39}$$

with k' an integer with the same parity as the spin rank, which is the same as derived by Levitt [77,87].

The derivation of the scale factor of the R-sequences is similar to that of the C-sequences. The d-coefficients can be evaluated using the expression:

$$d_{mk}^{(l)} = \frac{\omega_c}{2\pi} \sum_q e^{i\pi\left\{ ql + \frac{m\chi}{N}(2q+1) \right\}} \int_{(q-1)/N\tau_c}^{(q/N)\tau_c} \delta_{mk'}^{(l)} e^{i(k'N-k)\omega_c t} dt \tag{A40}$$

and for $k = 0$ and $l = 1$

$$d_{m0}^{(1)} = \frac{1}{N} \left\{ e^{i\pi\frac{m\chi}{N}} \sum_q e^{i2\pi q\left\{ \frac{1}{2} + \frac{m\chi}{N} \right\}} \right\} \delta_{m0}^{(1)} \tag{A41}$$

The sum is different from zero when $m\chi = (k''' - \frac{1}{2})N$ for all integers k'''. As can be seen in Section 5.2 for all symmetry allowed terms $\chi = \frac{N}{2}$, and as a result $m = (2k''' - 1)$, i.e. $m = \pm 1$ only. Thus $d_{\pm 10}^{(1)} = e^{\pm i\pi/2} \delta_{\pm 10}^{(1)}$ and because for the π-pulse the coefficients $\delta_{\pm 1}^{(1)} \ne 0$, the scale factor is not zero and is also independent of N (i.e. independent of the choice of RN_κ^χ), and the tilt angle $\theta = 90°$.

References

1. Mackenzie KJD, Smith ME (2001) Multinuclear Solid-State Nuclear Magnetic Resonance of Inorganic Materials (Pergamon Material Science) Pergamon Press, Oxford, 2002
2. Schmidt-Rohr K, Spiess HW (1994) Multidimensional Solid-State NMR and Polymers, Academic Press, London
3. Castellani F, Van Rossum B, Diehl A, Schubert M, Rehbein K, Oschkinat H (2002) Nature 420:98
4. Tycko R (2003) Prog NMR Spectroscopy 42:53
5. Duer M (2002) Introduction to Solid-State NMR Spectroscopy: Principles and Applicatons, Blackwell Science, UK
6. Andrew ER, Bradbury A, Eades RG (1958) Nature 182:1659
7. Lowe IJ (1959) Phys Rev Lett 2:285
8. Royden V (1954) Phys Rev 96:543
9. Bloom AL, Shoolerly JN (1955) Phys Rev 97:1261
10. Mehring M, Pines A, Rhim W-K, Waugh JS (1971) J Chem Phys 54:3239
11. Hartmann SR, Hahn EL (1962) Phys Rev 128:2042
12. Lurie FM, Slichter CP (1964) Phys Rev A133:1108
13. Pines A, Gibby MG, Waugh JS (1973) J Chem Phys 59:569
14. Mehring M (1976) High Resolution NMR Spectroscopy in Solids, Springer-Verlag, Germany
15. Samoson A, Lippmaa E, Pines A (1988) Mol Phys 65:1013
16. Llor A, Virlet J (1988) Chem Phys Lett 152:248
17. Chmelka BF, Müller KT, Pines A, Stebbins J, Wu Y, Zwanziger JW (1989) Nature 339:42
18. Frydman L, Harwood JS (1995) J Am Chem Soc 117:5367
19. Gan Z (2000) J Am Chem Soc 122:3242
20. Gerstein BC, Dybowski CR (1985) Transient techniques in NMR of Solids, Academic Press, Orlando, Florida
21. Slichter CP (1983) Principles of Magnetic Resonance, Springer-Verlag, Berlin
22. Ernst RR, Bodenhausen G, Wokaun A (1994) Principles of Nuclear Magnetic Resonance in One and Two Dimensions, Clarendon Press, Oxford
23. Maricq MM, Waugh JS (1979) J Chem Phys 70:3300
24. Lee M, Goldburg WI (1965) Phys Rev 140:1261
25. Waugh JS, Huber LM, Haeberlen U (1968) Phys Rev Lett 20:180
26. Haeberlen U (1976) High Resolution NMR in Solids- Selective Averaging, Supplement 1 Adv Magn Reson, Academic Press, New York
27. Mansfield P (1971) J Phys C4:1444
28. Rhim WK, Pines A, Waugh JS (1971) J Chem Phys B3:684
29. Mehring M, Waugh JS (1972) Phys Rev B5:3459
30. Rhim WK, Elleman EE, Vaughan RW (1973) J Chem Phys 59:3740
31. Gerstein BC, Clor C, Pembleton RG, Wilson RC (1977) J Phys Chem 81:565
32. Burum DP, Rhim WK (1979) J Chem Phys 71:944
33. Burum DP, Rhim WK (1979) J Chem Phys 70:3553
34. Burum DP, Linder M, Ernst RR (1981) J Magn Reson 44:173
35. Takegoshi K, McDowell CA (1985) Chem Phys Lett 116:100
36. Bronnimann CE, Hawkings BL, Zhang M, Maciel GE (1988) Anal Chem 60:1743
37. Bielecki A, Kolbert AC, Levitt MH (1989) Chem Phys Lett 155:41
38. Bielecki A, Kolbert AC, De Groot HJM, Griffin RG, Levitt MH (1990) Adv Magn Reson 14:111
39. Cory DG (1991) J Magn Reson 94:526
40. Buszko ML, Bronnimann CE, Maciel GE (1993) J Magn Reson A103:183

41. Levitt MH, Bielecki A, Kolbert AC, Ruben DJ (1993) Solid State NMR 2:151
42. Demco DE, Hafner S, Spiess HW (1995) J Magn Reson A116:36
43. Hafner S, Spiess HW (1996) J Magn Reson A121:160
44. Hohwy M, Nielsen NC (1997) J Chem Phys 106:7571
45. Hohwy M, Bower PV, Jakobsen HJ, Nielsen NC (1997) Chem Phys Lett 273:297
46. Hafner S, Spiess HW (1997) Solid State NMR 8:17
47. Hohwy M, Nielsen NC (1998) J Chem Phys 109:3780
48. Vinogradov E, Madhu PK, Vega S (1999) Chem Phys Lett 314:443
49. Vinogradov E, Madhu PK, Vega S (2000) Chem Phys Lett 329:207
50. Sakellariou D, Leasge A, Hodgkinson P, Emsley L (2000) Chem Phys Lett 319:253
51. Filip C, Hafner S (2000) J Magn Reson 147:250
52. Vinogradov E, Madhu PK, Vega S (2001) J Chem Phys 115:8983
53. Madhu PK, Zhao X, Levitt MH (2001) Chem Phys Lett 346:142
54. Vinogradov E, Madhu PK, Vega S (2002) Chem Phys Lett 354:193
55. Hafner S, Demco DE (2002) Solid State Nucl Magn Reson 22:247
56. Van Rossum B-J, Foerster H, De Groot HJM (1997) J Magn Reson 124:516
57. Lesage A, Sakellariou D, Steuernagel S, Emsley L (1998) J Am ChemSoc 120:13194
58. Lesage A, Charmont P, Steuernagel S, Emsley L (2000) J Am Chem Soc 122:9739
59. Van Rossum B-J, De Groot CP, Ladizhansky V, Vega S, De Groot HJM (2000) J Am Chem Soc 122:3456
60. Sakellariou D, Lesage A, Emsley L (2001) J Am Chem Soc 123:5604
61. Van Rossum B-J, Castellani F, Rehbein K, Pauli J, Oschkinat H (2001) Chem Bio Chem 2:906
62. Massiot D, Alonso B, Fayon F, Fredoueil F, Bujoli B (2001) Solid State Sciences 3:11
63. Yao XL, Schmidt-Rohr K, Hong M (2001) J Magn Reson 149:139
64. Creemers AFL, Kiihne S, Bovee-Geurts PHM, De Grip WJ, Lugtenburg J, De Groot HJM (2002) Proc Natl Acad Sci 99:9101
65. Riou D, Fayon F, Massiot D (2002) Chem Mater 14:2416
66. Alonso B, Klur I, Massiot D (2002) Chem Comm 8:804
67. Yamauchi K, Kuroki S, Ando I (2002) J Mol Struct 9:602
68. Chevelkov V, Van Rossum BJ, Castellani F, Rehbein K, Diehl A, Howhy M, Steuernagel S, Engelke F, Oschkinat H, Reif B (2003) J Am Chem Soc 125:7788
69. Haeberlen U, Waugh JS (1968) Phys Rev 175:453
70. Maciel GE, Bronnimann CE, Hawkins BL (1990) Adv Mag and Opt Reson 14:125
71. Burum DP (1990) Conc in Mag Reson 2:213
72. Samoson A, Tuherm T, Gan Z (2001) Solid State Nucl Magn Reson 20:130
73. Schnell I, Spiess HW (2001) J Magn Reson 151:153
74. Goward GR, Schnell I, Brown SP, Spiess HW (2001) Magn Reson Chem 39:S5
75. Goward GR, Schuster MFH, Sebastiani D, Schnell I, Spiess HW (2002) J Phys Chem B106:9322
76. Pawsey S, McCormic M, De Paul S, Graf R, Lee YS, Reven L, Spiess HW (2003) J Am Chem Soc 125:4174
77. Levitt MH (2002) Encyclopaedia of Nuclear Magnetic Resonance, 9:165, Wiley, UK
78. Powles IG, Mansfield P (1962) Phys Lett 2:58
79. Powles IG, Strange IH (1963) Proc Phys Soc London 82:6
80. Hausser R, Siegle G (1965) Phys Lett 19:356
81. Siegle G (1966) Z Naturforsch A21:1722
82. Lesage A, Sakellariou D, Hediger S, Elèna B, Charmont P, Steuernagel S, Emsley L (2003) J Magn Reson 163:105
83. Prigl R, Haeberlen U (1996) Adv Mag and Opt Reson 19:1
84. Hohwy M, Rasmussen JT, Bower PV, Jakobsen HJ, Nielsen NC (1998) J Magn Reson 133:374
85. Rasmussen JT, Hohwy M, Jakobsen HJ, Nielsen NC (1999) Chem Phys Lett 314:239

86. Edèn M, Levitt MH (1999) J Chem Phys 111:1511
87. Caravetta M, Edèn M, Zhao X, Brinkmann A, Levitt MH (2000) Chem Phys Lett 321:205
88. Brinkmann A, Levitt MH (2001) J Chem Phys 115:357
89. Bennet AE, Griffin RG, Vega S (1994) Recoupling of Homo- and Heteronuclear Dipolar Interactions in Rotating Solids in: NMR Basic Principles and Progress, Springer-Verlag, Berlin, Heidelberg
90. Floquet MG (1883) Ann Ec Norm Suppl 12:47
91. Vega S (1996) Encyclopaedia of Nuclear Magnetic Resonance, 3:2011, Wiley, UK
92. Ho TS, Chu SI, Tietz JV (1983) Chem Phys Lett 96:464
93. Chu SI (1999) Adv Chem Phys 73:739
94. Boender GJ, Vega S, De Groot HJM (1998) Mol Phys 95:921
95. Boender GJ, Vega S, De Groot HJM (2000) J Chem Phys 112:1096
96. Van Vleck JH (1929) Phys Rev 33:467
97. Shirley JH (1965) Phy Rev 138:B979
98. Goldman M, Grandinetti PJ, Llor A, Olejniczak Z, Sachleben JR, Zwanziger JW (1992) J Chem Phys 97:8947
99. Goldman M (1993) J Magn Reson A102:173
100. Maricq MM (1982) Phys Rev B25:6622
101. Maricq MM (1986) J Chem Phys 85:5167
102. Maricq MM (1986) J Chem Phys 86:5647
103. Llor A (1992) Chem Phys Let 199:383
104. Buishvili LL, Kobakhidze GV, Menabde MG (1983) Sov Phys JETP 56:347
105. Veshtort M, Griffin RG (unpublished)
106. Charmont P, Sakellariou D, Emsley L (2002) J Magn Reson 154:136
107. Bosman L, Madhu PK, Vega S, Vinogradov E (2004) J Magn Reson 169:39

High-Resolution Solid-State NMR Studies of Inclusion Complexes

Marek J. Potrzebowski (✉) · Slawomir Kazmierski

Polish Academy of Sciences, Department of Structural Studies and NMR Laboratory, Centre of Molecular and Macromolecular Studies, Sienkiewicza 112 90-363 Lodz, Poland
marekpot@bilbo.cbmm.lodz.pl

Abstract New applications of 1D and 2D solid state (SS) NMR spectroscopy in structural studies of inclusion complexes (ICs) formed by organic host lattices (cyclodextrins, calixarenes, cyclophosphazenes, and fullerenes) are described. Each section of the review gives short characteristics of host molecules and recent applications of SS NMR. Less common systems, which are interesting as models for SS NMR studies, (bis[6-O,6-O′-(1,2;3,4-diiso-propylidene-α-D-galactopyranosyl) thiophosphoryl] disulfide (DGTD) and 1,2-dichloro-ethane/tris(5-acetyl-3-thienyl) methane (TATM)), are also discussed.

Keywords CP/MAS · Host-guest chemistry · Molecular motion · Calixarenes · Cyclodextrins · Cyclophosphazenes · Fullerenes · Solid-state NMR

1
Introduction

One of the most important challenges before modern chemistry is to understand the nature of processes responsible for the formation of complex multicomponent structures. Such assemblies are synthesized with the intention of obtaining products with desired properties and potentially being used as "molecular machines" [1]. There are several classes of compounds which can form multi-component structures [2], and inclusion complexes (ICs) are one of the most important. Synthetic procedures and structural studies of inclusion compounds have been exhaustively discussed and described in several textbooks [3]. The nature of host-guest interactions, the spatial arrangement of components, and the character of inter-molecular contacts have been analyzed different techniques in the liquid and solid phase [4].

Solid State (SS) NMR is a spectroscopic technique which can answer most of these questions for any solids; crystalline, polycrystalline, amorphous phases, glasses, etc. Thus the growing popularity of NMR spectroscopy as a tool for structural elucidation of different solid supramolecular assemblies is fully understandable. Ripmeester and Ratcliffe reviewed the literature on applications of solid state NMR in supramolecular chemistry up to 1996 [5] where a short introduction to the theoretical background, experimental NMR techniques, and examples of problems which can be resolved by NMR, are presented.

In this chapter, we would like to present recent achievements of high-resolution solid-state NMR in the field of structural studies of inclusion complexes. A similar subject was recently covered by Ripmeester and colleagues in a review published in the Encyclopedia of Nuclear Magnetic Resonance Spectroscopy [6]. However, as the authors stated "a great variety of both organic and inorganic hosts and guests are amenable to study by NMR spectroscopic techniques, but it is not possible to cover the field in a comprehensive manner as it has now so widely diversified". Although only two years have passed from the publication of Ripmeester et al., a similar problem occurred during the preparation of this article. This fact clearly proves how SS NMR has become a common and important diagnostic tool in structural studies of ICs.

The inclusion complexes are two-component assemblies consisting of host and guest molecules. Although NMR spectroscopy is a technique which permits the monitoring of both components in one experiment, in more advanced structural studies different methodological approaches are usually implemented. The most powerful method of exploring the structure and dynamics of guest molecules in a host lattice is ^{2}H NMR broad-line shape analysis. The current literature describing ^{2}H SS NMR of ICs is very extensive, and as it seems to us that low resolution ^{2}H NMR forms a separate topic, it will not be discussed here.

Narrowing the field of discussion further, we will only present here NMR studies of ICs formed by organic host molecules. Readers interested in inor-

ganic systems are referred to [5, 6] and to the paper of Klinowski [7]. This chapter is mostly limited to such important host species as cyclodextrins, calixarenes, and cyclophosphazenes; however, some less common systems, which we have found interesting, will be also discussed. The chapter is divided into sections, which presents short descriptions of the host molecule and recent applications of SS NMR.

2
Cyclodextrins and Other Carbohydrate Derivatives

2.1
Cyclodextrins

In the chemistry of inclusion compounds, there is no doubt that cyclodextrins (CDs) belong to the most important class of host molecules. The remarkable career of cyclodextrins in research and industrial applications is due to their ability to incorporate selectively many organic/inorganic molecules, ions and even radicals. CDs have found numerous applications in many areas, especially in the pharmaceutical, agrochemical, food and tobacco industries, as well as in cosmetics and toiletry [8].

Natural cyclodextrins (CD), obtained by the enzymatic degradation of starch, are macrocyclic oligosaccharides consisting of at least 6, 7 or 8 glucopyranoside rings joined by α-1,4-glycosidic linkages [9] and are named as α- (**1**), β- (**2**) and γ-CD (**3**) (see Scheme 1). Most CDs are composed of glucopyranose units in $^4C_1$ conformation as shown in Scheme 1. However, it is possible to synthesize cyclodextrins with $^1C_4$ or *skew* sugar ring conformation or composed of other than glucose units [10].

Naturally occurring cyclodextrins and their higher homologues are truncated cone-shape molecules with a hollow, tapered cavity 7.9 Å deep

| 1 | 2 | 3 |
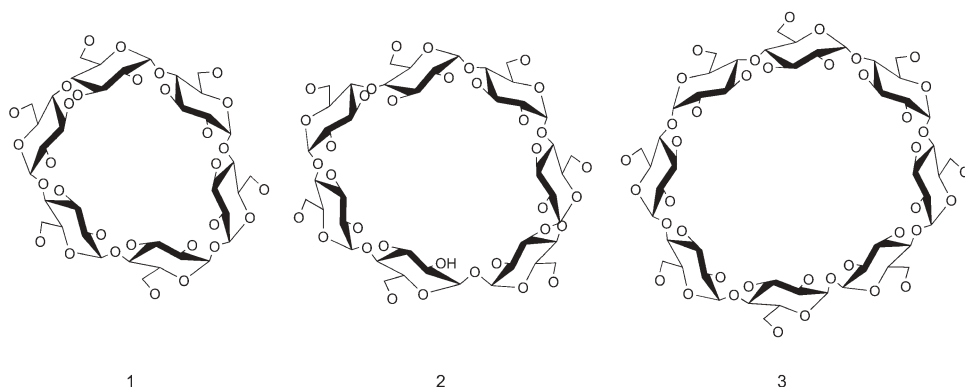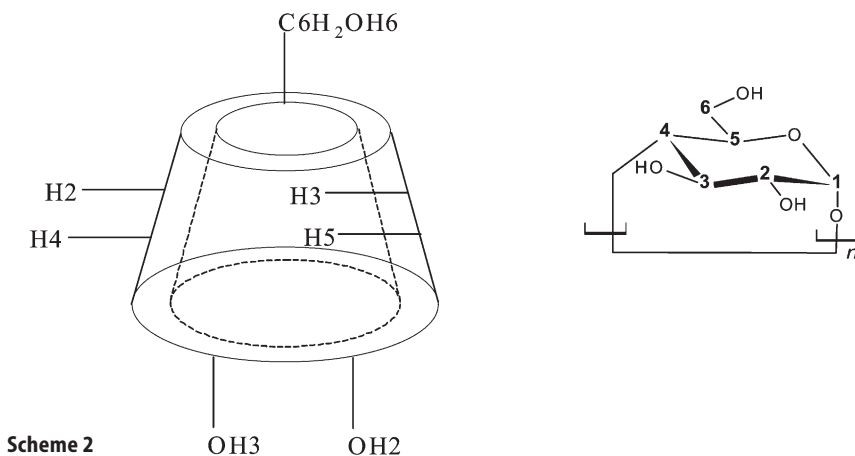
Scheme 1

Scheme 2

(Scheme 2). The top and bottom diameters of the cavity of the most widely used cyclodextrins are 4.7 and 5.3 Å for α-cyclodextrin, 6.0 and 6.5 Å for β-cyclodextrin and 7.5 and 8.3 Å for γ-cyclodextrin [11]. The open top of the cone is encircled by primary hydroxyl groups at C6, and the bottom is encircled by secondary hydroxyl groups at the C2 and C3 positions of the glucopyranose residues. The interior of the cone is lined with hydrogen atoms located at the C3 and C5 positions of the sugar ring [12] (Scheme 2).

The mechanism of host-guest interactions and mode of binding of CD complexes has been exhaustively investigated and discussed in a number of reviews [11, 13, 14]. Different experimental techniques, in the liquid and solid state, have been used for the investigation of CD ICs. Among them, NMR spectroscopy is an invaluable tool. Schneider and coworkers reviewed the literature describing the application of NMR in structural studies of CD inclusion compounds to 1998 [15]. The short final part of their paper presents the achievements of high-resolution solid state NMR. Ripmeester and Ratcliffe discussed the more advanced applications of SS NMR, in particular for small guest species [16].

At the beginning of last decade of the twentieth century, it was observed that cyclodextrins can include in their narrow channels not only small molecules, but are able to complex large molecular guests such as polymers. In 1990, Harada and Kamachi [17] described the formation of inclusions between CD and low molecular weight hydrophilic polymers. Later, a number of papers have been published about inclusion complexes of cyclodextrins with hydrophilic and hydrophobic polymers. The considerable majority of papers published in the last three years concentrate on polymer molecules as guest species in cyclodextrin ICs. Inclusion compounds formed between CDs and low molecular weight guests can have either channel or cage structures. Figure 1 shows the crystal type structures of crystalline CD inclusion complexes [18].

In channel structure ICs, the cyclodextrin rings are stacked on top of each other to produce cylindrical central cavities. In cage structures, the cavity of
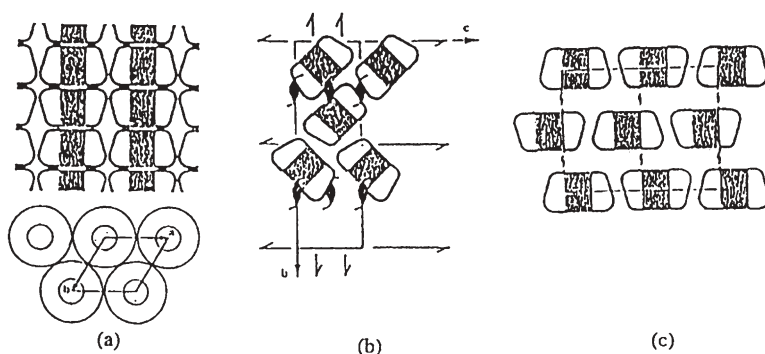
Fig. 1a–c Schematic representation of: **a** channel type; **b** cage herringbone type; **c** cage brick type, crystal structures formed by crystalline cyclodextrin inclusion complexes. (Adopted from [18] with permission)

one CD molecule is closed on both sides by adjacent molecules. Because of the long chain nature of polymers, normally the crystal structure of polymer-CD-IC is the channel type, which provides the opportunity to study the behavior of a single chain squeezed inside a cyclodextrin channel.

Tonelli and coworkers [18] prepared two inclusion complexes of the α- and γ-cyclodextrin with poly(ε-caprolactone) (PCL) and polyethylene oxide (PEO): PCL-PEO-PCL-α-cyclodextrin and PCL-PEO-PCL-γ-cyclodextrin. The channel structures of both the triblock inclusion complexes obtained were characterized by several methods (TGA, DSC, X-ray diffraction, FTIR and Solid State NMR spectroscopy).

The ^{13}C CP/MAS spectrum of α-cyclodextrin showed multiple resonances for each carbon type of α-CD, while in the spectrum of the triblock-α-CD-IC, each glucose carbon is observed as a single peak (Fig. 2). This indicates that for the latter case, α-cyclodextrin adopts a symmetrical conformation with each glucose unit in a similar environment. The X-ray studies of the single crystals showed that α-CD adopts a less symmetrical conformation when it does not include a guest in the cavity and a symmetrical conformation when a guest is present. The ^{13}C CP/MAS spectra of pure α-cyclodextrin and triblock-α-CD-IC are consistent with the X-ray data. Similar methodology was used to investigate the triblock copolymer PCL-PEO-PCL inclusion complex with γ-cyclodextrin (PCL-PEO-PCL-γ-cyclodextrin).

To get a better insight into the dynamics of prepared ICs, more advanced NMR experiments were carried out [19]. Distinctive cross-polarization parameters were observed for guest polymer and host α-cyclodextrin in the inclusion complex. For α-CD, as expected from the relatively rigid molecule, the intensity quickly rises to a maximum, and then quickly decays. The behaviour is quite different for the PCL-PEO-PCL block copolymer, which has a slow rise in intensity followed by a slower decay. Maximum intensity was observed at 1 ms and 0.5 ms CP-time for PCL-PEO-PCL and α-CD. To evaluate the domain size
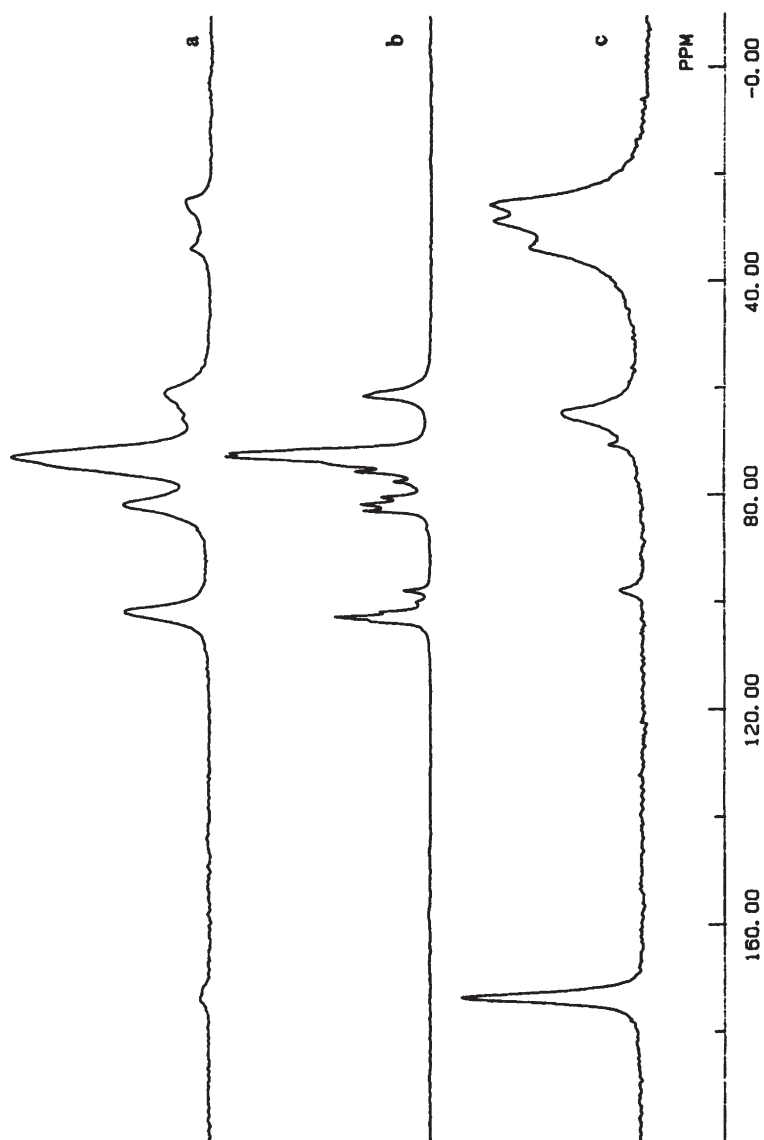
Fig. 2a–c CP/MAS/DD ¹³C NMR spectra of: **a** PCL-PEO-PCL-αCD-IC; **b** γ-cyclodextrin; **c** PCL-PEO-PCL. (Adopted from [18] with permission)

of the complexes, proton T_1 and $T_{1\rho}$ measurements were undertaken. Assuming a diffusion coefficient of ca. 10^{-12} cm^2 s^{-1}, the spin diffusion of the triblock copolymer inside the narrow α-CD channels with ^{1}H T_1 of 1.86 s is about 344 Å. Therefore the identical proton T_1 observed for the polymer guest and α-CD in the complex shows that the complex is homogenous on the length scale of 344 Å.

For PCL-PEO-PCL-γ-cyclodextrin, the measured ^{1}H T_1 value is shorter, so the length scale of spin diffusion in the γ-CD/PCL-PEO-PCL complex is smaller than that in the α-CD/PCL-PEO-PCL. The PCL-PEO-PCL has a long proton $T_{1\rho}$ (35.6 ms) while for the α-CD it is much shorter (4.9 ms). The identical values measured for both PCL-PEO-PCL and α-CD in the complex demonstrate that the protons of included PCL blocks are in close homogeneous contact with the cyclodextrin protons. Similar behavior was observed for the PCL-PEO-PCL-γ-CD-IC, which is due to the accommodation of two side-by-side polymer chains in larger γ-CD channels. These data were fully confirmed by a 2D heteronuclear correlation experiment run with BLEW-12/BB-12 decoupling for suppressing homonuclear dipolar interactions and WIM-24 sequence for magnetization transfer. This experiment is more powerful and straightforward than proton $T_{1\rho}$ measurement.

Spin-lattice relaxation times $T_1(^{13}\text{C})$ to evaluate high frequency motions (MHz scale) and proton line shape, with 2D WIM/WISE to explore the low frequency motions (kHz), of PCL-PEO-PCL-CDs-IC materials were investigated. $T_1(^{13}\text{C})$ values observed both for copolymer and CD engaged in the formation of ICs were much smaller compared to T_1s measured for "free state" molecules. This shows that the complexes experience faster molecular motions in the megahertz regime than copolymer in bulk and CD in the cage structure (H$_2$O-CD). From the analysis of the linewidth observed in the proton dimension in 2D WIM/WISE (Fig. 3) experiments for PCL-PEO-PCL-αCD, it is apparent that the included polymer chains show much more mobility than α-CD in the kilohertz regime. However, the dynamics are not identical for all methylene carbons of guest chains in the complex. For PCL-PEO-PCL-γCD broader lines are observed, showing that the polymer chains are more restricted in γ-CD than in α-CD inclusion complexes but are more mobile than in bulk triblock copolymer or CD solid. Very likely, there are pairs of side-by-side parallel chains inside the γ-CD channel instead of the single polymer chains inside the narrower α-CD channels.

^{13}C CP/MAS spectroscopy is a convenient preliminary tool proving the formation of the IC [20, 21]. Using this simple technique, it was possible to confirm the formation of CD inclusion complexes with many different copolymer compounds, e.g. PPO-PEO-PPO [22], PEO-poly[(R)-3-hydroxybutyrate]-PEO [23], PCL-PPG-PCL [24], as well as ferrocene derivatives [25] as guest molecules. Recently, ^{13}C and ^{29}Si CP/MAS solid state NMR spectra were used for characterization of the inclusion complex of polysilsesquioxane with β-cyclodextrin [26]. Saalwächter reported using ^{1}H Fast-MAS solid state NMR techniques for elucidating the dynamics of the poly(dimethylsiloxane) (PDMS) in-
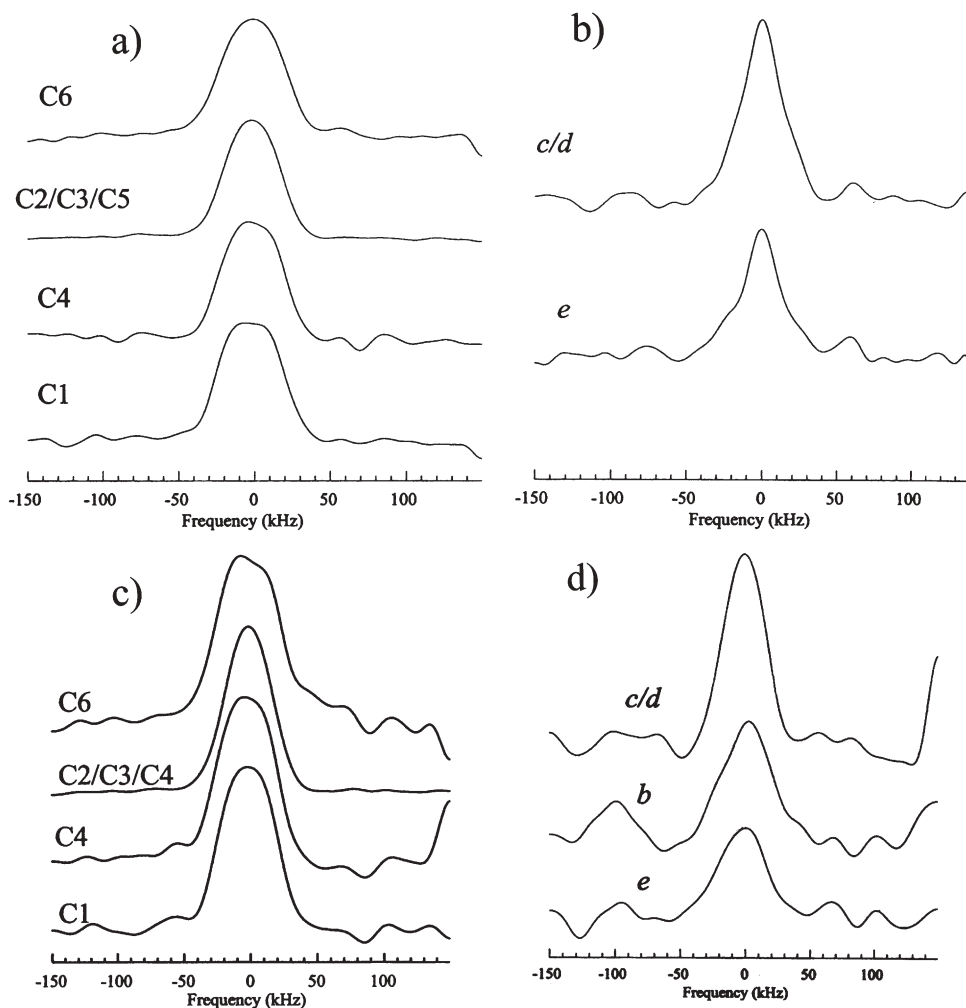
Fig. 3a–d Cross-sections through the 2D WIM/WISE spectrum for the PCL-PEO-PCL-CD inclusion complexes at the frequency of: **a** α-CD carbons of the PCL-PEO-PCL-αCD; **b** PCL-PEO-PCL of the PCL-PEO-PCL-αCD; **c** γ-CD carbons of the PCL-PEO-PCL-γCD; **d** PCL-PEO-PCL of the PCL-PEO-PCL-γCD. (Adopted from [19] with permission)

clusion complex with γ-cyclodextrin [27]. In well-resolved MAS spectra, the separation of signals from the host and the polymer is straightforward, and it was possible to measure residual homonuclear (^{1}H-^{1}H) and heteronuclear (^{1}H-^{13}C) dipolar couplings associated with the polymer. A simple ^{1}H spectrum provides preliminary insight into the dynamic states of the host and guest. Even at 30 kHz MAS and a ^{1}H Larmor frequency of 500 MHz, the resonances of the individual protons in the glucopyranose rings are not resolved and form a
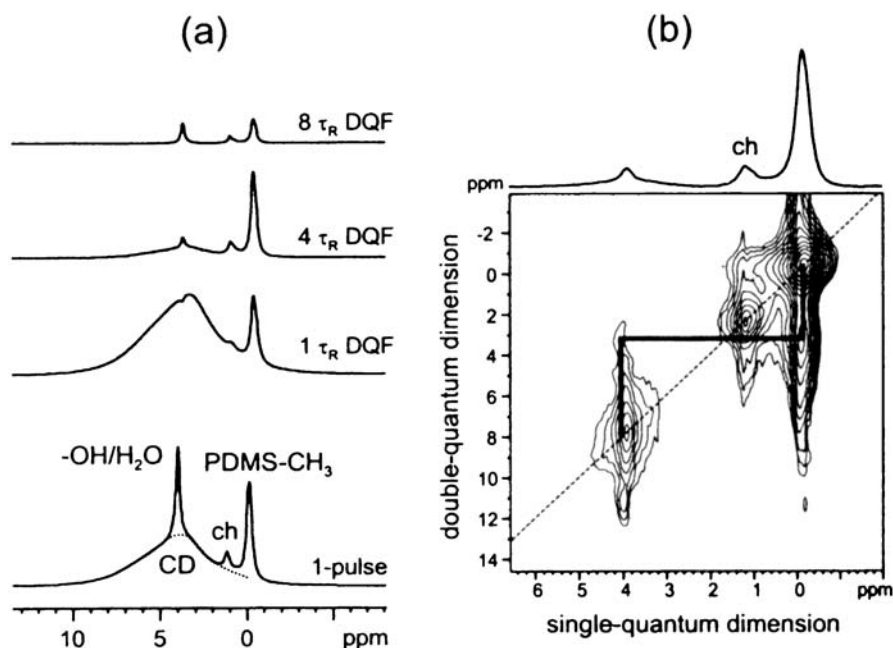
Fig. 4a,b ^{1}H MAS spectra of PDMS-γCD inclusion complex ($\omega_R/2\pi$=30 kHz): **a** comparison of the regular one pulse spectrum with a series of double quantum filtered spectra recorded with increasing recoupling time; **b** 2D DQ correlation spectrum with selected slice. The *grey bar* identifies the cross peak corresponding to the guest-host dipolar proximity; "ch" identifies the signal from the cyclohexane impurity. (Adopted from [27] with permission)

broad line extending from 1 to 8 ppm (Fig. 4a). This effect indicates an essentially rigid ^{1}H environment for these signals. In contrast, signals from the OH/H$_2$O hydrogen bonding region and the guest molecules are much sharper, because of molecular motion, faster than hundreds of kHz, by which ^{1}H dipolar couplings are partly averaged.

This is confirmed by comparing 1D double-quantum filtered experiments with increasing recoupling times. Extension of this to 2D SQ/DQ correlation identifies the nature of the dipolar coupled pair, since the coupling partner of the directly detected spin can be identified in the indirect dimension, where the chemical shift is the sum of the shift of the two protons involved. This spectrum (Fig. 4b) exhibits intense and well-resolved cross peaks between CD and PDMS. The dipolar coupling constant between the guest and host must therefore be of the order of, or exceed, a few hundred Hz, proving that whatever fast motion the polymer chain performs, it must be a local one.

Quantitative analysis of PDMS chain dynamics was derived from both the REPT-HDOR experiment and analysis of the 1D signal intensity as a function of recoupling time. The conclusion is that PDMS seem to exist in a highly symmetric conformation, with all methyl groups experiencing the same local en-

Scheme 3
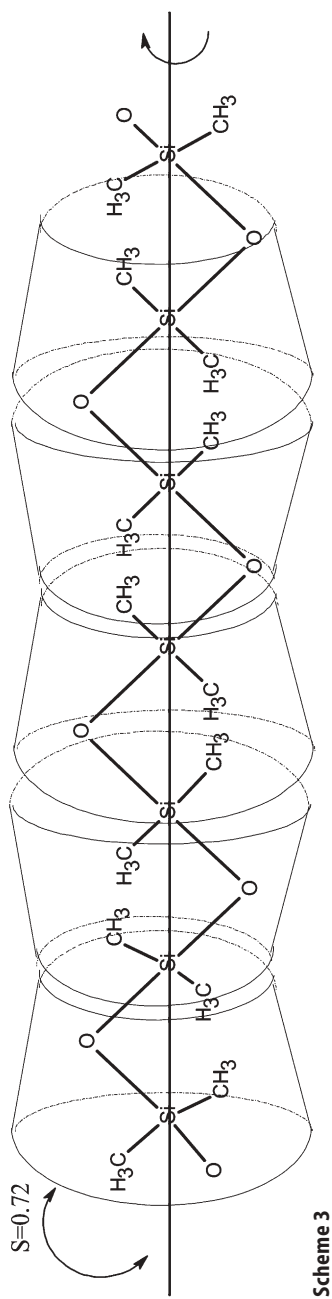
vironment and the same kind of motion. Additional information was derived from analysis of the sideband system in 1D homonuclear DQ spectra. From analysis of the results of all derived NMR experiments, it is apparent that the PDMS chain in γ-CD most likely performs rotational motions about the polymer backbone or segmental fluctuations in the MHz regime. Methyl groups exist in the same motional state, which is characterized by a tilt angle of about 73° between the Si-C bond and the rotational axis or, more generally, by the order parameter of Sb=0.72. On this basis the proposed structure of the PDMS-γCD inclusion complex is shown in Scheme 3.

It is apparent from the papers cited that ^{1}H Fast MAS solid state NMR spectroscopy is a powerful method for obtaining information about the structure and dynamic properties of inclusion complexes. The recent promising NMR technique, applicable to a wide range of samples with restricted motions and limited solubility, is high-resolution magic-angle spinning (HRMAS) spectroscopy. The combination of spinning the sample at the magic angle with HRMAS probes permits recording liquid-like spectra for the ^{1}H nucleus. With this methodology, classical 2D liquid-phase NMR experiments, such as COSY, TOCSY, HSQC and HMBC, can be used to search solid (semi-solid) samples.

Crini et al. used HRMAS NMR spectroscopy for exploring inclusion complexes of β-cyclodextrin with textile dye [28]. The authors performed a series of 2D solid-state experiments (NOESY, TOCSY and HSQC) to establish the structure of the IC under investigation. An important contribution was achieved through the HOHAHA experiment. The results showed that, through this new NMR technique, it is possible to characterize cross-linked materials with limited mobility.

Although most of the recent papers describing inclusion complexes of cyclodextrins concentrate on the polymer molecules as the guest species, it should be stressed that CD ICs with smaller molecules still remain attractive models. Crini et al. characterized the dynamical properties of the β-CD complex with epichlorohydrin [29]. The β-cyclodextrin-coumarin inclusion complex was described by Brett et al. [30], and Garbow and coworkers [31] investigated aspartame and neotame as the guest molecules in β-CD complexes. Recently, Ripmeester and coworkers [32] reported using solid state NMR spectroscopy for investigating the inclusion complex of β-cyclodextrin with (Z)-tetradec-7-en-1-al.

2.2
Thiophosphoryl Carbohydrate Derivatives

Carbohydrate derivatives employed as host molecules often posses in their molecular structure other NMR active nuclei than carbon-13, which offer additional probes to investigate subtle structural effects. In particular, phosphorus-31 is an attractive nucleus owing to 100% abundance and high sensitivity. As reported by Potrzebowski and coworkers, bis[6-*O*,6-*O*′-(1,2;3,4-diisopropylidene-α-D-galactopyranosyl) thiophosphoryl] disulfide (DGTD) shown in
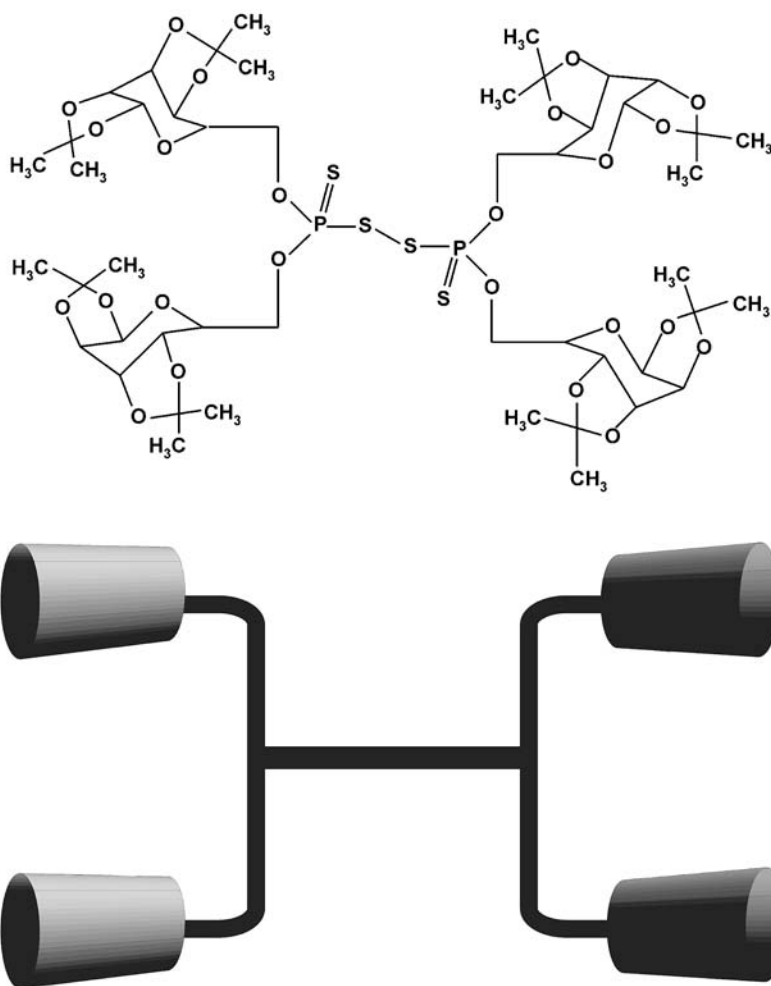
Scheme 4

Scheme 4 is a compound which shows a strong tendency to form inclusion complexes [33–35].

The DGTD belongs to a group of "wheel and axle host" molecules. Compared to the classical representative of this group (linear acetylenic spacer coupled with bulky end groups), DGTD can be called a "four wheeled system" where guest molecules can be included in the space between the front wheels (and/or rear wheels).

The crystal and molecular structure of eight different complexes was established by X-ray analysis, indicating three types of disulfide arrangements in the crystal lattice. All crystals are built up from DGTD molecules packed along the twofold symmetry axes and solvent molecules located around the twofold
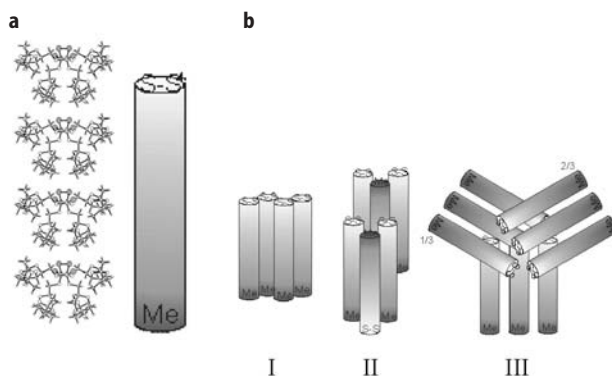
Fig. 5a, b **a** Packing of host molecules DGTD within the column, and a symbolic description. **b** Types of molecular column orientation of DGTD observed in its inclusion complexes: **I** – parallel columns in space group C2, **II** – antiparallel columns in space group P2$_1$ and P2$_1$2$_1$2$_1$, **III** – columns rotated by 120° in space group P3$_2$. (Adopted from [33] with permission)

screw axes. The guest molecules are locked in channels in which isopropylidene methyl groups of DGTD are directed to the inside of channels, causing steric hindrance. The dimension of a channel is about 8×13 Å, but the distance between methyl groups lying on the opposite walls of the channel is ~6 Å. Therefore these groups are the main factor promoting the inclusion of guest molecules, even when no strong host⋯guest hydrogen bonds are formed.

The common feature observed in each of the crystals is the presence of molecular columns formed by the host (Fig. 5a): molecules aggregate in the 'head-to-tail' mode, i.e. the disulfide bridge contact methyl groups from the opposite side of the DGTD, and they are repeated by translation along the column.

Different relative orientations of the columns in the three-dimensional crystal lattices depend on crystal symmetry. So far, three types of column packing have been observed (Fig. 5b):

1. Columns are parallel in the space group C2
2. Columns are antiparallel, rotated by 180° in the space groups P2$_1$ and P2$_1$2$_1$2$_1$
3. Columns are rotated by 120° in the space group P3$_2$

^{31}P CP/MAS is a tool which permits the recognition of different crystallographic forms of ICs (Fig. 6). The guest molecules occupy free volumes between columns and/or are encapsulated in the cavity formed by the sugar derivatives.

The role of weak intermolecular interactions in the formation of inclusion complexes is one of the most challenging questions. From the analysis of chemical shift tensor (CST) parameters, conclusions regarding strong and weak hydrogen bonding can be drawn. In particular, weak hydrogen bonds have recently attracted much attention as important structural elements of complex architecture [36]. In all structures of DGTD complexes, intermolecular C-H⋯S=P contacts were observed (see [33] for details).
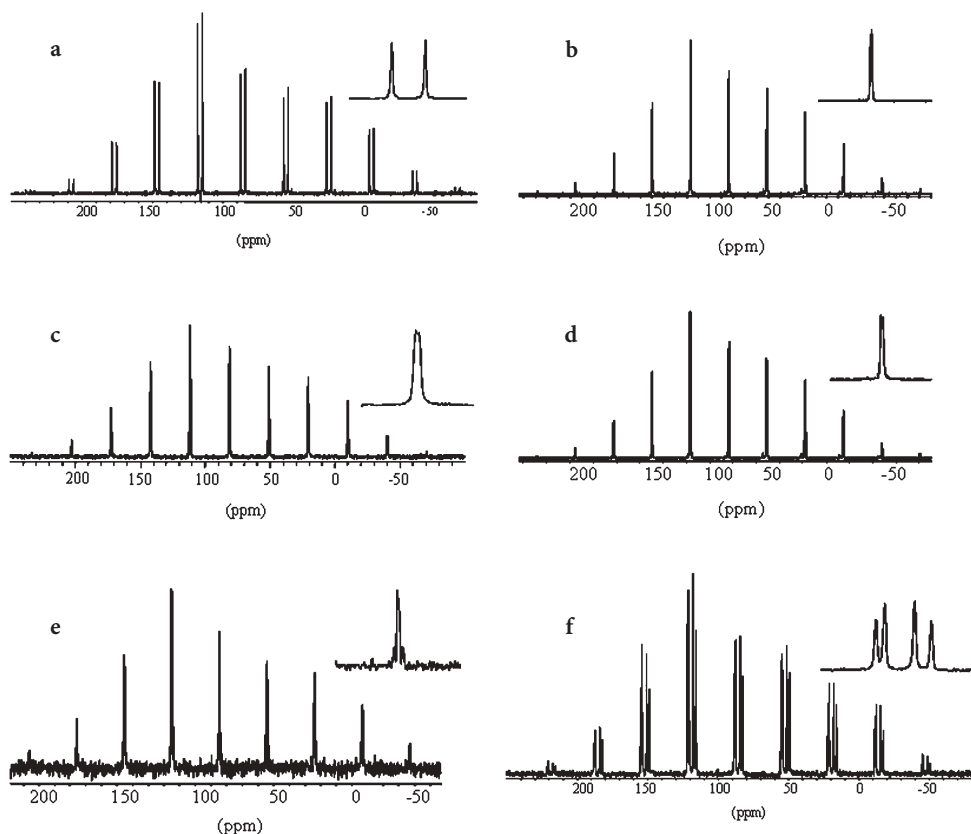
Fig. 6 125.49 MHz, ^{31}P CP/MAS experimental spectra of DGTD modifications crystallised from: **a** methanol; **b** n-propanol; **c** 2-propanol; **d** n-butanol; **e** isopropyl ether; **f** methylocyclohexane

The principal values, δ_{11}, δ_{22}, δ_{33}, of the ^{31}P chemical shift tensor were obtained for each form by ^{31}P CP/MAS NMR experiments. The orientation of the principal axes with respect to the molecular frame was investigated by ^{31}P CP/single-crystal NMR for the complex with propan-2-ol. The principal axis 1 of both chemically equivalent phosphorus atoms is nearly parallel to the P-S bond and the principal axis 3 is very close to the P=S bond. The comparison of experimental ^{31}P δ_{ii} parameters with theoretical data calculated by the DFT GIAO approach provided complementary information about the most sensitive NMR parameters, which best characterize the nature of the C-H···S contacts.

In theoretical work, the molecular complex was built (Scheme 5) with the methane guest molecule in close proximity to one of the thiono-sulfurs of the model compound and the P1=S···H-C unit was aligned in the plane of the S=P1-S bonds. The distance, d, between the sulfur and the carbon in the P1=S···H-C fragment was varied in the range 2.4–4.1 Å. Several DFT GIAO calculations

a)

d

z
y x

b)

d

z
y   x
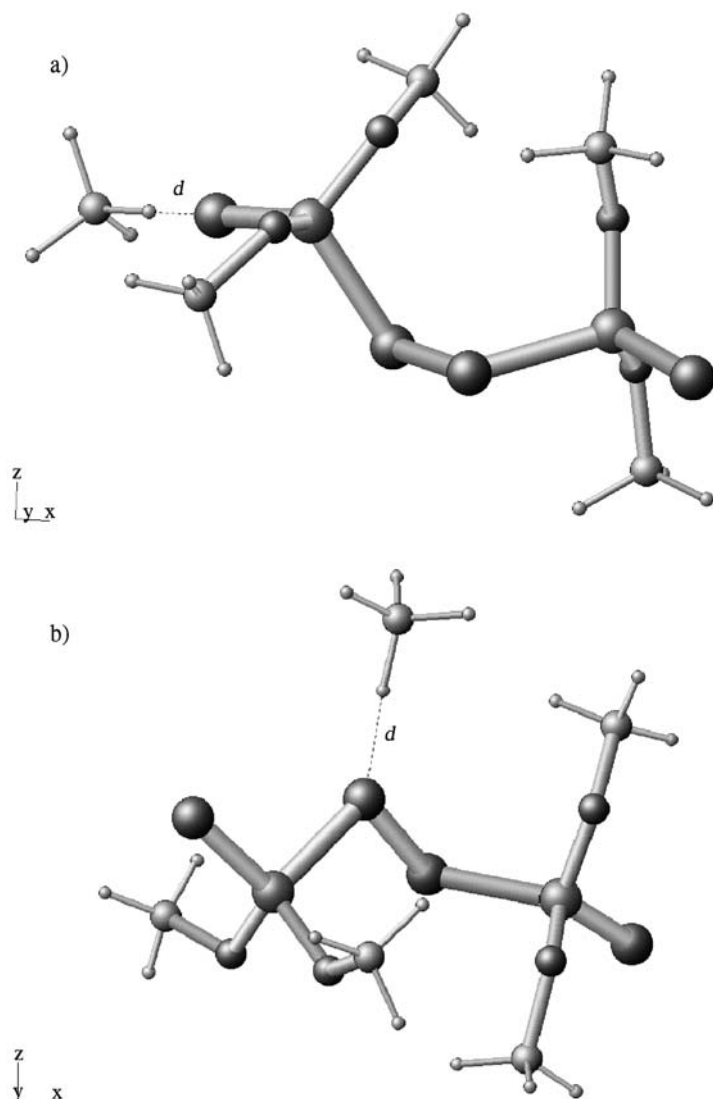
Scheme 5

were carried out with constant increments of d equal to 0.1 Å. When d is equal to 4.0 Å, the shielding parameters for both centers P1 and P2 are the same as in the isolated molecule.

The calculated isotropic ^{31}P resonances of P1 and P2 are separated by 2.2 ppm. It was found that with decreasing d a change of the P1 takes place, while these values for P2 remain practically constant. It is interesting to note that the changes of σ_{11}, and σ_{22}, on the one hand and σ_{33} on the other hand go in opposite directions, with increasing σ_{11} and σ_{22} a decrease of σ_{33} is observed.
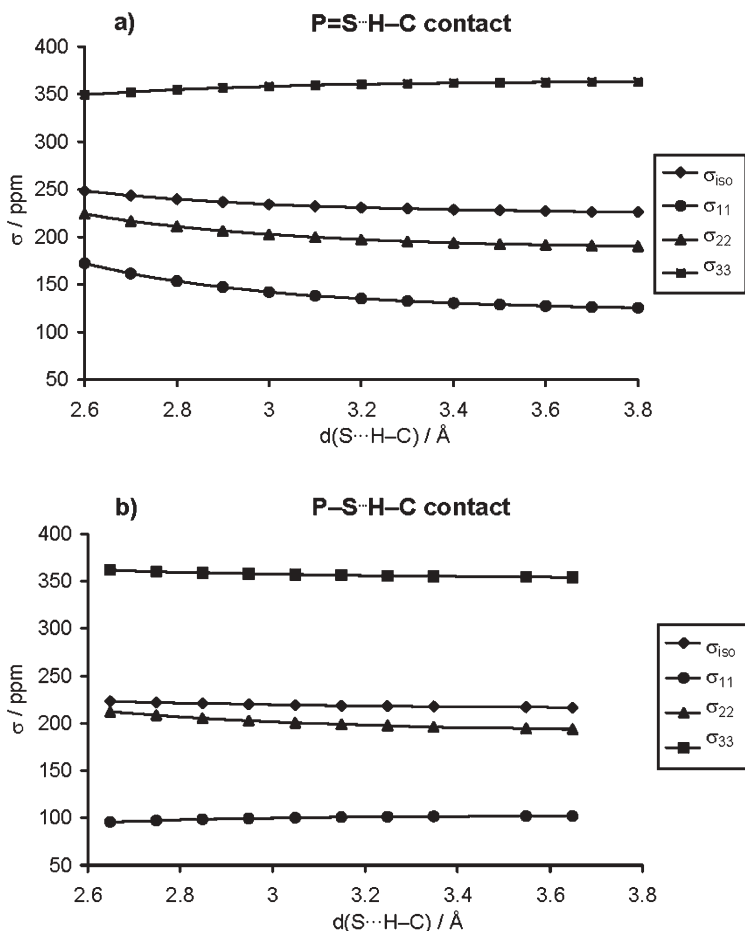
Fig. 7a, b The relationship between the distance d between the sulfur and the carbon in the P=S··H-C and the P-S··H-C units and the values of the principal elements of the ^{31}P nuclear magnetic shielding tensors calculated by the DFT GIAO method

When d is in the range 3.2–3.8 Å (the region of interest) the changes of σ_{11} and σ_{33} amount to a few ppm (Fig. 7).

The influence of P1-S··H-C forces on ^{31}P NMR shielding parameters considering thiolo sulfur was discussed earlier. Analysis of the data proved that the influence of this type of interaction on ^{31}P NMR shielding is much smaller compared to the analogous thiono S··CH$_4$ contacts. It was concluded that the most sensitive parameter, which characterizes the C-H··S weak contacts, is span Ω parameter defined as σ_{33}–σ_{11}.

The presence of solvent in the crystal lattice can lead to very complex patterns, and interpretation of solid state spectra became ambiguous. Such problems were met during the synthesis of bis[6-O,6-O'-(1,2:3,4-diisopropylidene-
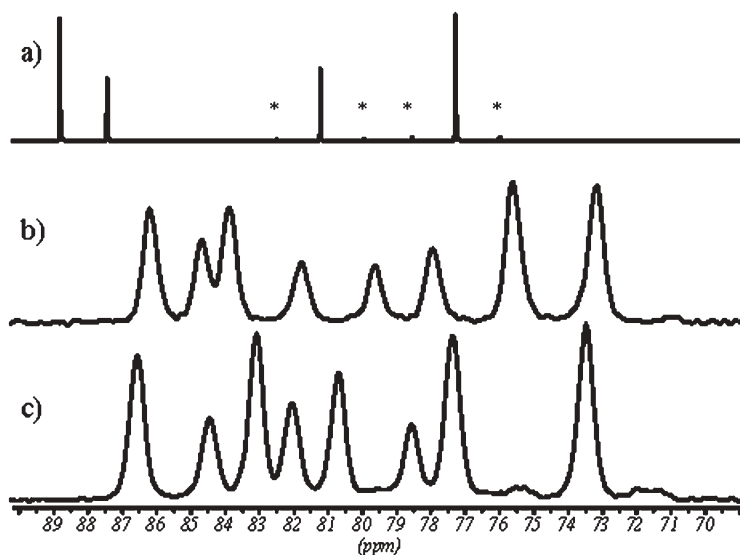
Fig. 8a–c Spectra of a crystal containing three isostructural components: bis[6-*O*,6-*O*′-(1,2:3,4-diisopropylidene-α-D-galactopyranosylthiophosphoryl]disulfide, bis[6-*O*,6-*O*′-(1,2:3,4-diisopropylidene-α-D-galactopyranosylthiophosphoryl]diselenide and bis[6-*O*,6-*O*′-(1,2:3,4-diisopropylidene-α-D-galactopyranosylthiophosphoryl]seleno-sulfide, in 1:1:1 ratio: **a** 202.40 MHz ^{31}P spectrum of crystal dissolved in CDCl₃. *Asterisks* denote the satellites corresponding to [31]P-[77]Se *J* coupling; **b** 121.49 MHz ^{31}P CP/MAS spectrum of a single crystal held in silica gel and spun at 10 kHz; **c** 121.49 MHz ^{31}P CP/MAS spectrum of a single crystal heated to 390 K

α-D-galactopyranosyl) thiophosphoryl] seleno-sulfide [37]. The preparation of mixed seleno-sulfides with high yield is still a challenge for synthetic chemistry and often mixtures of products are obtained. It was found that systems which consist of isostructural dichalcogenides in a crystal lattice have a great ability to form inclusion complexes. The assignment of host molecules in the liquid phase was based upon ^{31}P NMR spectral characteristics (Fig. 8a), the values of direct phosphorus 31-selenium 77 spin-spin coupling constants. It was found that the ^{31}P CP/MAS spectrum was much more complex. Moreover, during the solvent migration at higher temperature, a change of phase organization was observed (Fig. 8).

The assignment of spectrum and connectivity between individual phosphorus sites was done by the 2D approach. Figure 9 displays the 2D spin exchange spectrum of a crystal containing solvent in the lattice with mixing equal to 1 s. The relatively long mixing time reflects P···P distances larger than 4.2 Å. The solid state NMR data are considered as a tool to assign the solvent localization in the crystal lattice and give important hints facilitating the choice of the best X-ray refinement.
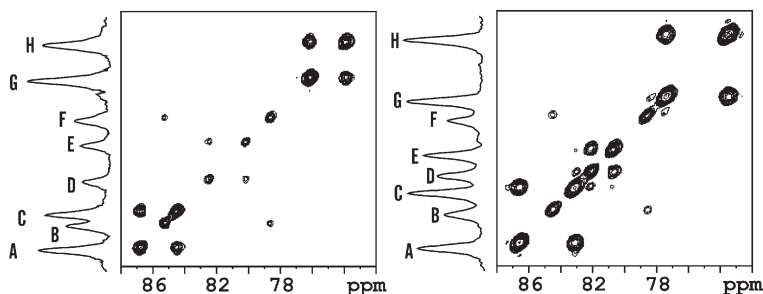
Fig. 9a, b ^{31}P 2D spin-exchange MAS spectra of the crystal (see Fig. 8 for description) obtained with a mixing time of 1 s at 10 kHz: **a** crystal at ambient temperature; **b** crystal heated to 390 K

3
Calixarenes

Calixarenes are macrocyclic molecules synthesized with high yield by condensation of appropriate arenes and aldehyde derivatives. Calix means 'bowl' in Latin and Greek, and this phrase reflects the shape of the tetramer, which usually adopts a bowl or beaker-like conformation. Gutsche first introduced the name 'calixarene' for this class of compounds [38]. Several authors have exhaustively reviewed the chemistry and synthetic procedures, which lead to different structural modifications of calixarenes [39–42]. In general, three types of calixarenes derivatives are known: first, metacyclophanes (type I); second, those obtained by condensation of formaldehyde with phenol (type II), and third, those obtained by reaction with resorcinol (type III) (Scheme 6). The latter modifications are also called 'resorcarenes' to distinguish calixarenes of type III from those of type II.

The index n describes the number of repeating units of calix[n]arenes. Recently various means have been used, by which not only calix[4]arenes, but also calix[6]arenes and calix[8]arenes were synthesized [43]. Much attention has been focused to calixarenes of type II, because of their conformational flexibility and the possibility of obtaining different chemical modifications. In the case of calix[n]arenes, the different relative orientations of phenyl and hydroxyl

Scheme 6

cone   partial cone   1,3-alternate   1,2-alternate
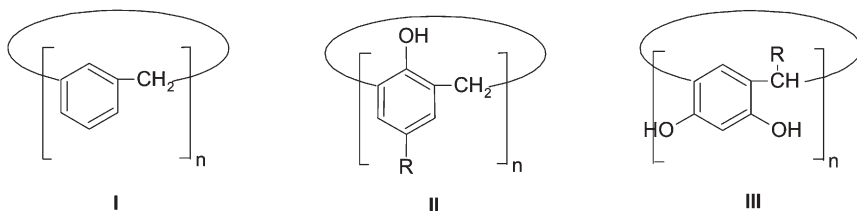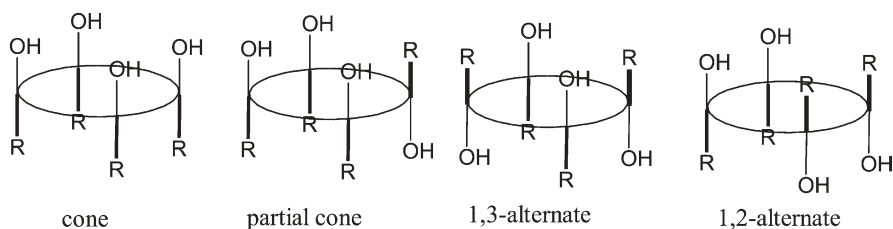
Scheme 7

groups can be considered. The notation introduced by Gutsche, 'cone', 'partial cone', '1,3-alternate' and '1,2-alternate' is still in use (see Scheme 7) and precisely describes the geometry of calix[4]arenes. Calixarenes have attracted much attention as models in the search for mechanisms of molecular recognition, as metal binding agents and as host molecules with unusual complexing properties.

In the family of calix[n]arenes, the best characterized compound is *p-tert*-butylcalix[4]arene. A variety of remarkable arrangements has been described in the crystalline state. Leon and coworkers, from theoretical calculations and statistical analyses, have recently searched most of the known host-guest complexes to see the effect of guest inclusion on crystal packing [44]. Structures of *p-tert*-butylcalix[4]arene and its derivatives corresponding to 'molecule-within-molecule', where the guest is inside the cavity (*endo* complex), as well as 'guest-free' structures or *exo* complexes, retrieved from the Cambridge Structural Database (CSD), were considered. It was concluded that these species may be classified into five groups: 1) guest-free and *exo* complexes, 2) 1:1 and 2:1 host-guest complexes, 3) hydrogen-bonded structures with amine guests, 4) self-inclusion structures and 5) 1:1 host-guest clay mimic structures. The structural motifs of *p-tert*-butylcalix[4]arene with guests and guest-free systems are shown in Fig. 10. Each motif can be recognized and distinguished by solid state NMR. The complexes of group 3 (see Fig. 10d) are of particular interest. Many amines with *p-tert*-butylcalix[4]arene gave standard 1:1 complexes [45]. The case of *n*-butyl amine guests is more complicated, and the formation of three pseudopolymorphic structures was recently reported by Udachin et al. [46].

In the 3:1 complex three molecules of *n*-butylamine are in the asymmetric unit. One molecule acts as guest and is deep inside the cavity. Two other molecules of guest are outside the cavity and are connected by hydrogen bonds to the molecule inside the cage, forming a "T" shape fragment of three molecules. In the 1:1 guest-host species, the amine molecule lies along the calixarene axis and is disordered over four sites, consistent with the symmetry of the host. In such complex, there is no interaction between guest and host other than non-specific short-range interactions. Finally, the third form is the 1:2 guest-host complex, where the guest is encapsulated between two molecules of host (Fig. 11).
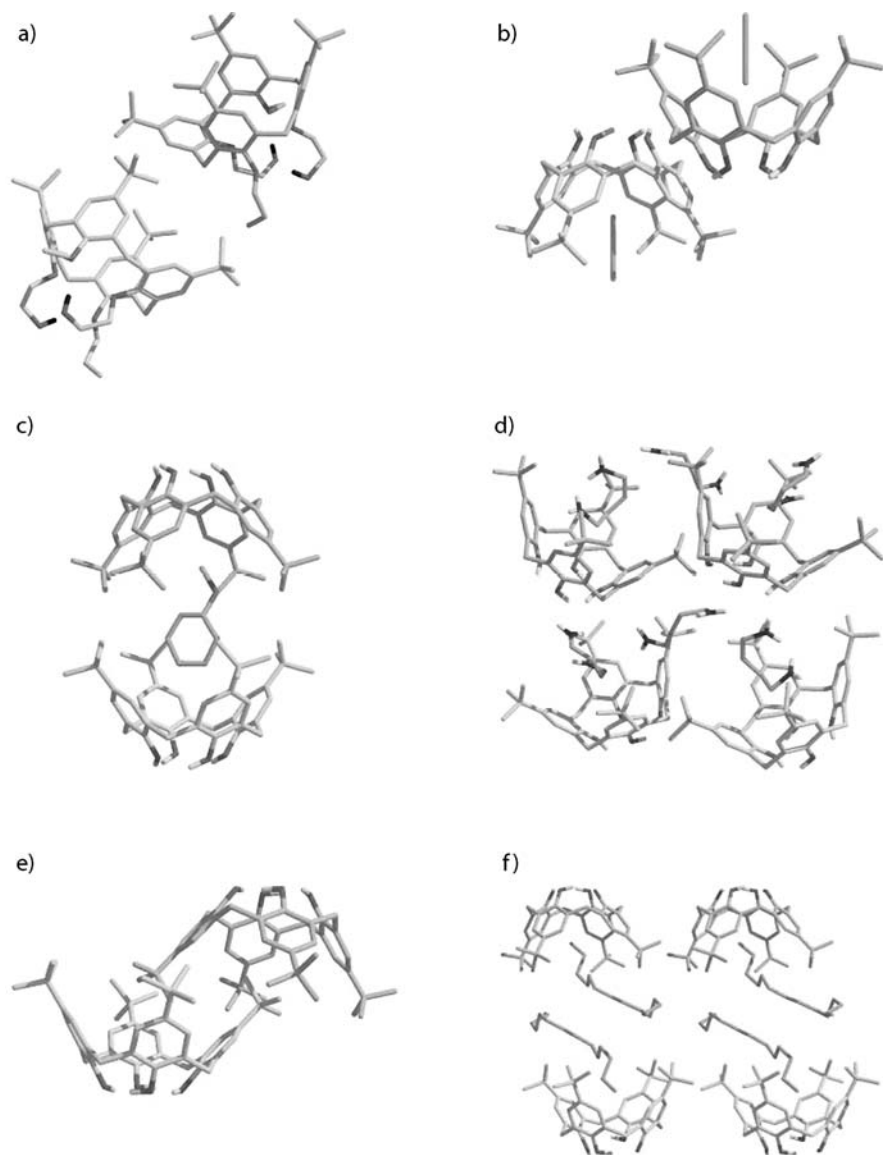
Fig. 10a–f Examples of the structural motifs of *p-tert*-butylcalix[4]arene derivatives: **a** guest-free structure; **b** 1:1 complex; **c** 2:1 host-guest complex; **d** hydrogen-bonded structure with an amine guest; **e** self-inclusion structure; **f** 1:1 host-guest clay mimic structure. (Adopted from [44] with permission)
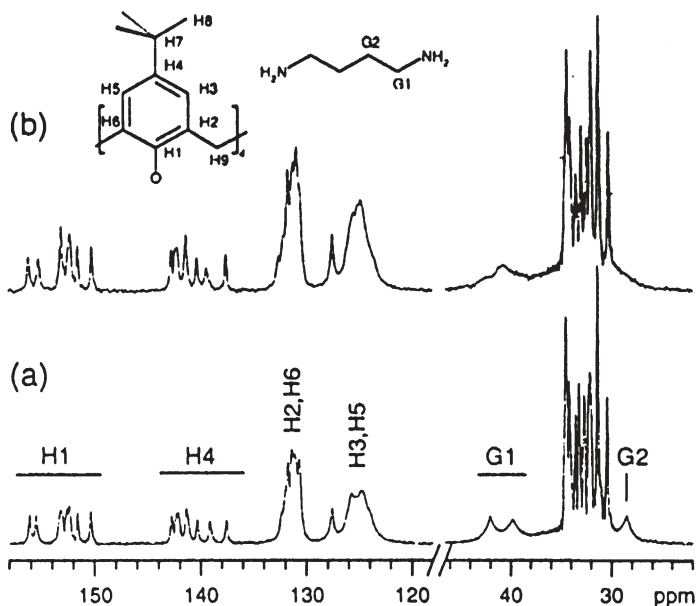
Fig. 11a, b Partial 75.48 MHz ^{13}C-{^{1}H} CP-MAS spectra: **a** *p-tert*-butylcalix[4]arene; **b** *p-tert*-butylcalix[4]arene after stirring in *n*-hexane. The aromatic host carbons are assigned; the aliphatic host carbons (H7, H8, H9) occur in the δ 27–36 region. For experimental details see [45]. (Adopted from [45] by permission of The Royal Society of Chemistry)

^{13}C CP/MAS experiment is an invaluable tool in the search for the subtle structural effects of pseudopolymorphs, and at least two goals are achieved in this experiment. First, the presence and amount of the guest in the host lattice is established, and second, the relative orientations of the guest with respect to the molecular frame of the host is recognized.

p-tert-Butylcalix[4]arenes form many 1:1 complexes with small organic molecules such as DMSO, nitrobenzene and cyclohexane [47]. Klinowski and coworkers have recently reported a new complex with acetone inside the cavity [48]. Among other analytical techniques, the ^{13}C CP/MAS experiment was found to be a source of useful information about the structure of the host and the dynamics of the guest. Despite the variety of possible conformations, most alkylcalix[4]arenes prefer the 4-fold symmetric cone conformation (see above) in the solid state. Such symmetry is preserved for many complexes when the guest molecular and the host symmetry axes are collinear. The distortion of the host cavity is expected to occur when the guest molecule presents asymmetry in shape and/or in electronic charge density. According to ^{13}C CP/MAS NMR data for complexes with acetone, the host is most likely to be in cone conformation and the guest molecule is contained inside the basket with a certain freedom of motion. The symmetry imposed by the space group suggests that the guest molecule is dynamically disordered about the fourfold axis of the calix.

a)   b)
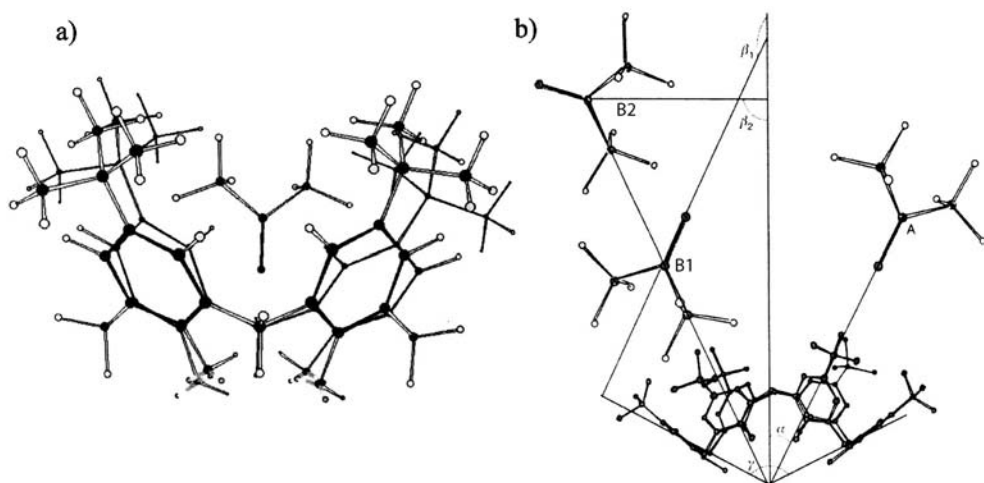
Fig. 12a, b **a** The structure of C4-acetone. **b** Possible orientation of the acetone molecule with respect to C6 in pinched cone conformation. Γ is ca. 120° and is equally divided into four angles of 30°. The angles between the twofold axes of calixarene and the CD_3 vector averaged about the twofold axis of acetone are α, β_1 and β_2 for the A, B_1 and B_2 orientations. (Adopted from [48] by permission of the PCCP Owner Societies)

The comparative analysis of complexes of *p-tert*-butylcalix[4]arene with *p-tert*-butylcalix[6]arene containing, for both compounds, acetone molecules in the cavity, is a source of significant information about the nature of the complex in terms of the size of the calix.

Figure 12 presents possible orientations of acetone in C4 and C6 complexes and Fig. 13 the corresponding ^{13}C CP/MAS spectra.
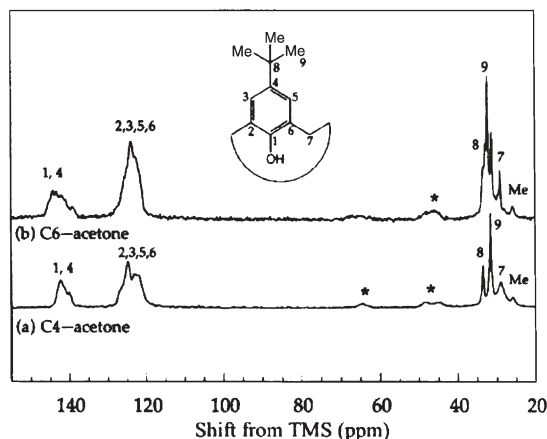
Fig. 13a, b ^{13}C CP/MAS spectra of: **a** C4-acetone; **b** C6-acetone. MAS at 6 kHz, 512 scans, 6 ms contact time and 5 s relaxation delays. *Asterisks* indicate spinning sidebands. (Adopted from [48] by permission of the PCCP Owner Societies)

The hydrogen bonding and steric hindrance of the *tert*-butyl groups favor the formation of cone-like conformations for both calixarenes. The hydrogen bonding network is stronger in *p-tert*-butylcalix[4]arene, so that even strongly hydrogen-bonding guests do not interfere with the conformation of the calix. In C4, the oxygen atoms are disposed in a circular manner, so that all contribute equally to the hydrogen bonding network. In the typical pinched-cone conformation of C6, the oxygen atoms form a boat in which two symmetrical networks of three oxygen atoms each can be identified. The cross-polarization parameters for both complexes revealed that the values of T_{CP} for all peaks are similar with the exception of $CH_2(7)$, which appears to be much more mobile in C6-acetone than in C4-acetone. $T_{1\rho H}$ is much longer for the carbon atoms in C6-acetone, suggesting that in the larger calixarene the host is more mobile.

The comparison of the isotropic chemical shifts of selected nuclei for the free host or guest molecules with the host-guest complexes are well understood, and conclusions regarding the three dimensional arrangement of the assembly can be drawn. The complexation-induced shifts (CIS) effect, related to strong and weak hydrogen bonding, aromatic-aromatic interactions, electrostatic interactions etc., is usually used only for qualitative description of the geometry of inclusion complexes. More reliable prediction is obtained when experimental NMR results are supported by theoretical calculations. Schatz and coworkers recently reported an interesting correlation between the geometry of *p-tert*-butylcalix[4]arene with carbon disulfide in the cavity and experimental vs GIAO-DFT calculated chemical shift [49] (see Fig. 14 and Table 1).

The complex was characterized by thermogravimetric analysis (TGA) and solid state NMR. Low temperature X-ray crystal structure analysis of the compound indicated the inclusion of CS_2 in the calixarene cavity to be highly symmetrically oriented directly on the C_4 axis of the host. The ^{13}C CP/MAS experiment showed significant complexation-induced chemical shift (CIS=
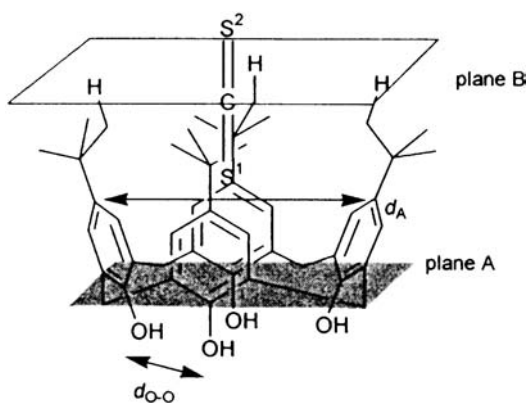
Fig. 14 Structure of the complex of *p-tert*-butylcalix[4]arene with carbon disulfide in the cavity. (Adopted from [49] by permission of The Royal Society of Chemistry)

Table 1 Comparison between calculated structural parameters and crystal structure

Method	SYBYL	MM+	RHFG/6-31G(d)	Crystal structure
d_A/Å	7.35, 8.17	7.95	8.48	8.34
$d_{o\text{-}o}$/Å	2.79, 2.86	2.80	2.73	2.69
$d_{S2\text{-}c}$/Å	1.58	1.62	1.55	1.55
a^a/Å	55, 75	61	54	56.5
I^b(%)	100	88	57	92

[a] a is defined as the angle between a phenyl ring and plane A (plane of the methylene bridges).
[b] The inclusion I is defined as: $I=[(d_{S1\text{-}S2}-d_{S2\text{-}planeB})/d_{S1\text{-}S}]\times100\%$. Plane B represents the top of the calix[4]arene cavity (see Fig. 14 for details).

–2.2 ppm) compared to solution data (Table 2). Several approaches were employed to optimize the geometry of the complex, including SYBYL and MM+ force fields, semi-empirical PM3 and ab initio Hartree-Fock procedure.

The ^{13}C NMR chemical shift of the guest molecule was calculated using the GIAO-DFT method with B3LYP/6-311G(d,p) and compared to the chemical shift of carbon disulfide calculated at the same level. It was found that on the simple model, shift difference is in good agreement with the experimentally determined complex-induced shift.

This approach was also used in the structural analysis of more complicated host-guest complexes with toluene, THF and acetone in the cavity of *p-tert*-butylcalix[4]arene [50]. As in the previous case, the geometry of the complexes was optimized and different spatial arrangements of guest vs host molecule were considered. The *p-tert*-butylcalix[4]arene-toluene inclusion compound is a special case in terms of guest dynamics and orientation in the cavity. The toluene is inserted methyl group first into the calix along the fourfold axis and satisfies the high symmetry requirements by showing twofold disorder. However, a minute contribution of the upside down orientation in the calix cannot be excluded. At ambient temperature, the NMR signal of the quaternary carbon of toluene is observed as a single line. At 115 K the signal splits into at least seven components with slightly different chemical shifts and of different in-

Table 2 Comparison between calculated and experimentally obtained chemical shift data

	δ_C		
	Complex	Free guest	CIS^a (ppm)
δ_{exp}	190.1	192.3	–2.2
$\delta_{calc}{}^b$	204.4	205.5	–1.1

[a] CIS=complex-induced chemical shift=$\Delta\delta=\delta$(complex)-δ (free guest).
[b] GIAO-DFT calculated chemical shift [B3LYP/6–311G(d,p)//RHF/6–31G(d)] referenced to TMS calculated on the same level.
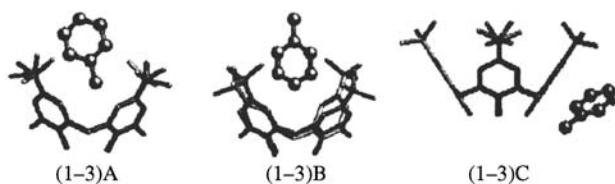
Fig. 15 MMFF optimized structures of *p-tert*-butylcalix[4]arene complexes with toluene. (Adopted from [50] by permission of The Royal Society of Chemistry)

tensities. This result proves that isotropic chemical shift is sensitive probe of the orientation of the guest inside the cavity [51].

The challenging question is whether such subtle changes can be correlated with the theoretical approach. Backes et al. have considered different geometries of *p-tert*-butylcalix[4]arene-toluene, with the CH_3 group pointing inside the cavity, the CH_3 group pointing outside the cavity and with toluene molecule outside the cavity (Fig. 15) [50]. DFT GIAO calculations clearly prove the sensitivity of this theoretical approach. As is shown, only the first geometry of the host-guest complex corresponds well to the CIS effect (Table 3). Thus, it can be concluded that this approach is a fast and convenient tool for the identification of possible spatial arrangements of supramolecular assemblies.

One of the important applications of butylcalix[4]arenes arises from their ability to trap alkali metal ions. In particular, Cs^+-calixarene complexes have received much attention because of the need to remove the ^{137}Cs radionucleotide from nuclear wastes. Benevelli et al. have used one-pulse solid state NMR experiments to directly observe [7]Li, [23]Na and [133]Cs ions in the host cavity [52]. More advanced experiments, which allow the investigation of metal lattice interactions were also reported. Rotational-echo double resonance (REDOR) NMR is a useful tool for obtaining structural details of butylcalix[4]arene [53]. Gullion and coworkers used [13]C-[133]Cs REDOR to determine the position of the cesium cation in complex [54]. The pulse sequence employed and the corresponding spectra are shown in Fig. 16.

Table 3 GIAO-DFT calculated and experimentally derived CISa of toluene in *p-tert*-butylcalix[4]arene-toluene complex (1–3) (see Fig. 15)

	$\triangle\delta_C$[a]			
Geometry	(1–3)A	(1–3)B	(1–3)C	Exp
E_{rel}[b]	0.0	0.2	5.1	–
P-CH_3[c]	–3.65	–0.34	–0.02	–6.2
	–4.41	–0.07	–0.57	

[a] $\triangle\delta C$ denotes upfield shift of the ^{13}C NMR signal of the observed carbon atom.
[b] Potential energy (kcal mol^{-1}) obtained from the force field (MMFF) optimization.
[c] First line GIAO-DFT (B3LYP/6-3-21G//MMFF, second line (italics) GIAO-DFT (B3LYP/6-3-31G(d)//MMFF.
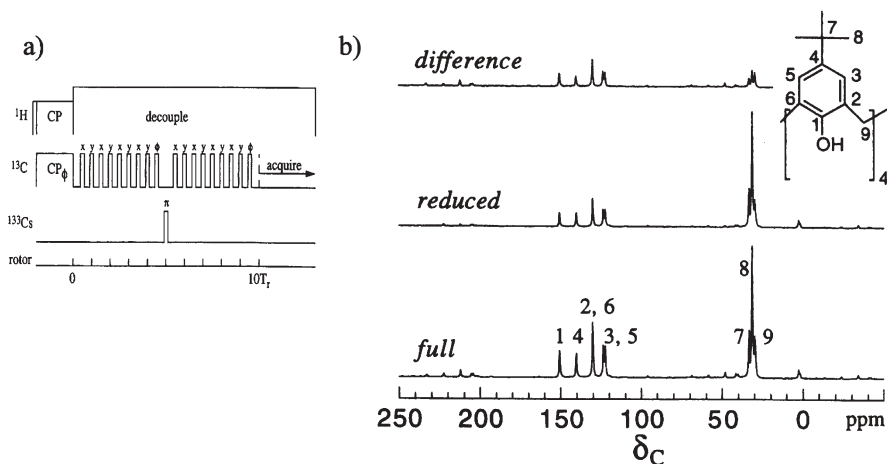
Fig. 16 a ^{13}C observed REDOR experiment shown with a dipolar evolution period of ten rotor cycles. **b** ^{13}C-^{133}Cs REDOR results for a dipolar evolution period lasting ten rotor cycles. The ^{13}C resonances are labeled according to the numbering of the structure shown in the insert. (Adopted from [54] with permission)

Under magic angle spinning, ^{13}C transverse magnetization dephases under ^{13}C-^{133}Cs dipolar coupling during the first half of the rotor period and is then refocused during the second half. The difference between the ^{13}C intensity at the end of the rotor period and between the experiment where no pulses are applied to the ^{133}Cs spin, and the ^{13}C intensity in the experiment where 180° pulses are applied to the ^{133}Cs, depends quantitatively on the dipolar coupling strength, expressed by equation $D=\mu_0\gamma_{Cs}\gamma_C\hbar/4\pi r^3$. The extent of ^{13}C spin dephasing resulting from incomplete refocusing of the rotational echoes is monitored as a function of the number of rotor periods for which dephasing is allowed to occur. Figure 17 presents normalized dipolar dephasing for the ^{13}C-^{133}Cs REDOR experiment as a function of the dimensionless parameter λ. The parameter λ is equal to the product of the dipolar evolution time and the dipolar coupling. From comparative analysis of the distances taken from X-ray diffraction and the REDOR experiment (see Fig. 17), it is apparent that this NMR technique provides geometrical parameters with satisfying accuracy (see Table 4).

Table 4 Cesium-carbon dipolar couplings and distances

Carbon	D(Hz)	r_{REDOR}(Å)	r_{model}(Å)	r_{X-ray}(Å)
C1	75	3.75	3.75	3.546
C2 and C6	70	3.84	3.84	3.689
C3 and C5	60	4.04	4.02	3.951
C4	55	4.16	4.13	4.122
C7	29	5.14	5.08	5.145
C9	43	4.51	4.48	4.310
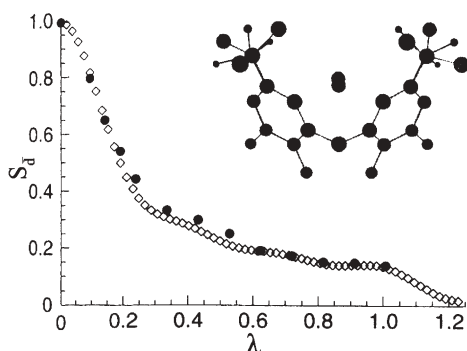
Fig. 17 Normalized dipolar dephasing for the ^{13}C-^{133}Cs REDOR experiment as a function of the dimensionless parameter λ. The *diamonds* are the universal dipolar dephasing curve for an S=1/2, I=7/2 spin system. The *closed circles* are the experimental results for the C1 carbon plotted with dipolar coupling of 75 Hz. The *insert* shows the structural relationship between the calixarene molecule and the cesium cation. The *light and dark colored atoms* in the centre of the structure represent the cesium positions determined by the REDOR experiment and the previous X-ray diffraction work, respectively. (Adopted from [54] with permission)

Resorcinarenes, macromolecules of type III, are an interesting class of compounds through their prospective applications as molecular devices for molecular recognition, HPLC experiments, ion transport across membranes, etc. Much attention has recently been paid to solid state NMR studies of the tetra(C-undecyl)calix[4]resorcinarene host obtained from resorcinol and lauryl aldehyde (Scheme 8) [55, 56].
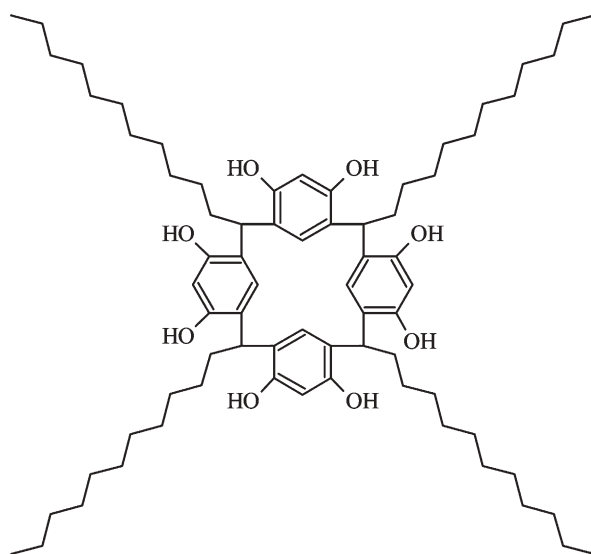
Scheme 8

Structural studies of two complexes with dimethylformamide (DMF) and dimethylacetamide (DMA) were reported. In the former, three types of solvent molecules are embedded in the crystal lattice: first, disordered isolated molecules located just above the cavities formed by the resorcinol units; second, clusters of four DMF molecules located between the calixarene layers; and third, single DMF molecules located inside the layers close to the alkyl chains. The challenge for solid state NMR is to recognize and locate guest molecules in the lattice. [13]C CP/MAS, dipolar dephasing and variable contact-time experiments were used in structure assignment. Although methyl and aldehyde signals of DMF can be identified (see Fig. 18), the resolution of the spectra is not sufficient to answer the question precisely.

Analysis of CP kinetics and the parameters obtained are a source of important information about host-guest interactions. From the classic **I-S** model of cross polarization, it was found that the values of $T_{1\rho H}$ relaxation times for guest and host molecules are considerably different. This suggests that DMF carbons cross-polarize from the DMF protons, not from the remote protons, of calixarene. Moreover, such a result proves that the DMF is located outside the calices and between the calixarene molecules. The simple **I-S** model is not sufficient to describe the cross-polarization of the complex of tetra (C-undecyl)calix[4]resorcinarene with DMA. The best fit of experimental data was seen when the more advanced I-I*-S model of cross polarization was adopted [57]. Analysis of CP kinetic parameters provides important information on molecular mobility (Fig. 19, Table 5).
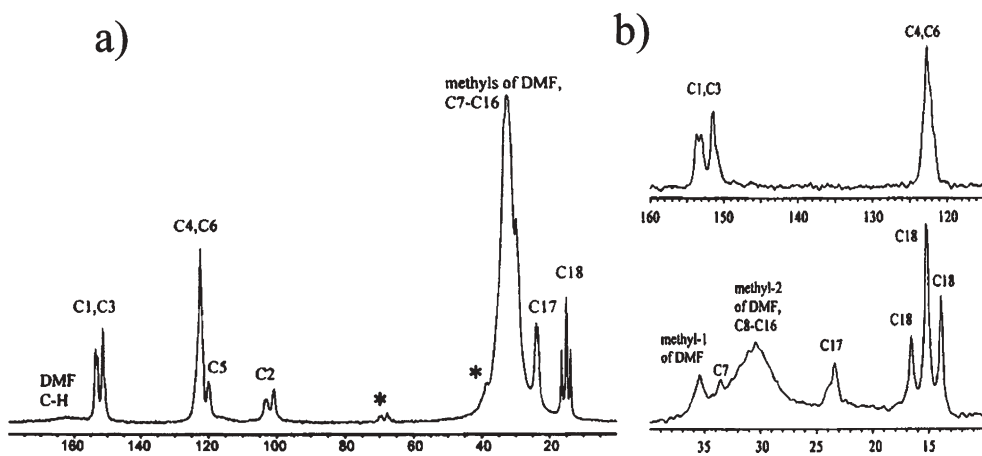
Fig. 18a, b Spectra of the CAV11/DMF crystals: **a** [13]C CP/MAS spectrum recorded with 4 ms contact time. *Asterisks* denote spinning sidebands; **b** dipolar-dephased ^{13}C CP/MAS spectrum. Peaks C2 and C5 are absent from the spectrum while C7 and CH$_2$ peaks are still visible, probably due to segmental mobility of the aliphatic chains. (Adopted from [55] with permission)
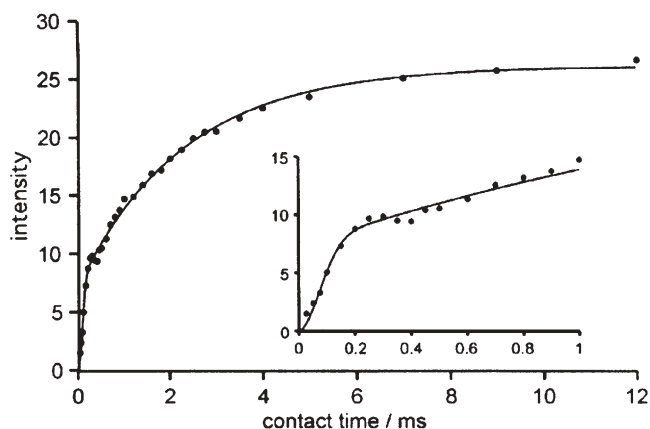
Fig. 19 Example of fitting CP kinetic data for the methyl peak of CAV11/DMA at 14.6 ppm. Fitting parameters are given in Table 5. (Adopted from [56] by permission of the PCCP Owner Societies)

Table 5 Selected CP kinetic parameters for DMA (first five rows) and CAV11 (last row) for the CAV/DMA complex. $T_{1\rho H}$ was infinitely long or very long but determined with insufficient precision. The peak positions are in ppm, the time constants T_{df} and T_2 are in ms

Peak	T_{df}	T_2	λ
174.9 (CO)	1.5±0.2	0.10±0.01	0.68±0.03
173.1 (CO)	1.7±0.2	0.13±0.02	0.68±0.03
38.5 (CH_3)	1.2±0.3	0.041±0.003	0.45±0.02
37.4 (CH_3)	1.2±0.2	0.031±0.003	0.48±0.02
19.9 (CH_3)	1.4±0.2	0.050±0.003	0.60±0.02
14.6 (CH_3)	2.3±0.1	0.077±0.005	0.720±0.008

For the methyl groups of the host molecule, proton spin diffusion and cross-polarization are slower compared to the methyl groups of DMA. Moreover, for the methyl groups of resorcinarene, the value of T_{df} is larger than that found for the carbonyl peak and the T_2 comes close to that of unprotonated carbonyl carbon. All parameters indicate that in the host molecule ^1H-^1H and ^1H-^{13}C dipolar interactions are weaker than in DMA. The DMA molecules appear to be trapped between the layers of resorcinarene and are kept quite rigid by intermolecular forces.

4
Cyclophosphazenes

The chemistry of cyclic phosphazenes has a long history, going back to the nineteenth century [58]. In 1895 Stokes suggested a cyclic structure for

compounds obtained by the reaction of ammonia and phosphorus pentachloride [59]. Cyclophosphazenes (CPz) are characterized by a repeating unit $-[N=PR_2-]_n-$, where n varies from 3 to 40 units. A number of synthetic modifications are known so far, and several reviews of the chemistry of this class of compounds are available [60–64]. The attractiveness of phosphazenes is due to their wide range of applications in fields such as medicine, flame retardancy and microlithography. It is also well known that cyclophosphazenes show a strong tendency to form inclusion complexes. Their selectivity with respect to some guests makes them good materials for separation agents.

A number of analytical techniques have been used for determining the structure of ICs of CPz. Although X-ray diffraction still has a pre-eminent role in structural studies of cyclophosphazene ICs, a few applications of solid state NMR have appeared recently. Sozzani and coworkers reported ^{13}C and ^{31}P CP/MAS studies of two organic derivatives, tris(*o*-phenylene-dioxy)cyclotriphosphazene (TPP) and tris(2,3-naphthalenedioxy)cyclotri-phosphazene (TNP) (Scheme 9) [65, 66].

TPP   TNP
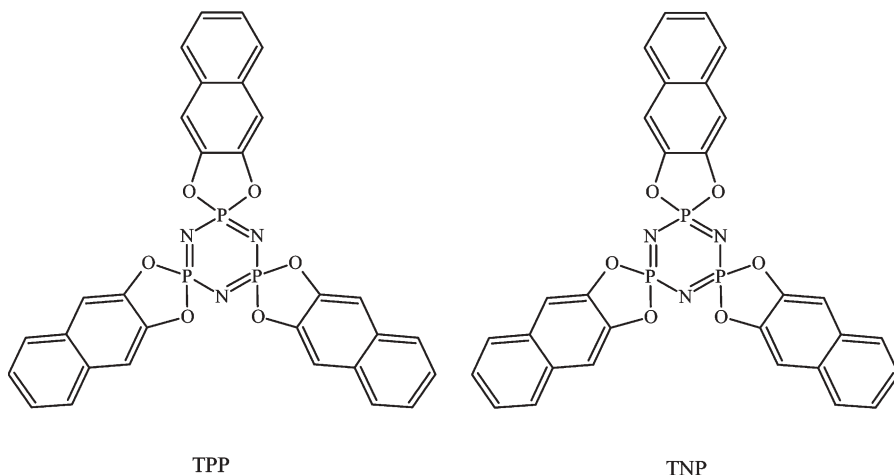
Scheme 9

Solid state NMR was used to recognize guest-free TNP matrix and ICs with guests, e.g. benzene, tetrahydrofuran and *p*-xylene. Carbon relaxation times were used to study the motion mechanism of the guests. ^{31}P CP/MAS spectra were particularly informative about the symmetry of the phosphazene ring. Figure 20 presents ^{13}C MAS spectra of TNP ICs with benzene and THF guests in the matrix.

Different approaches were used to distinguish between the signals of guest and host molecules. In single-pulse experiments (SPEs), with a relatively short delay of 8–10 s, only solvent ^{13}C resonances were monitored (Fig. 20a, and top trace Fig. 20c,). This so-called T_1 discrimination experiment takes advantage of the significant distinction of the spin-lattice relaxation times of the mobile
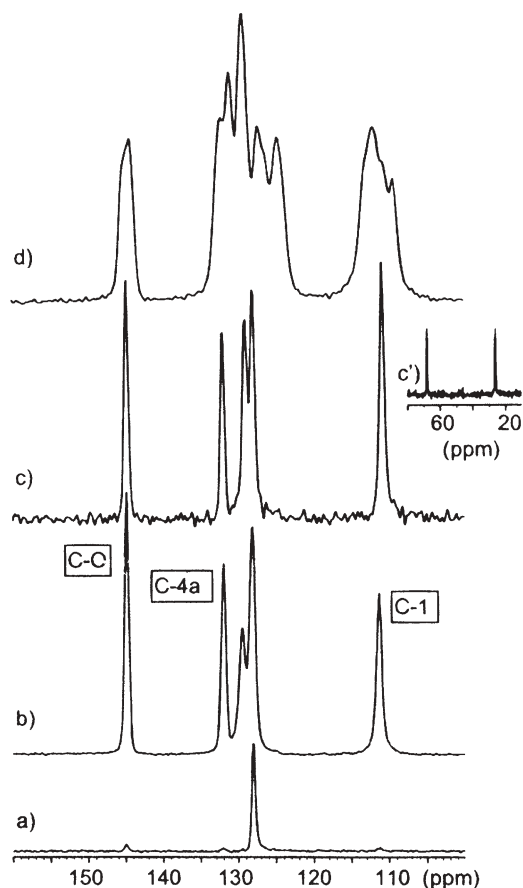
Fig. 20a–d ^{13}C MAS NMR spectra of TNP/benzene IC, spinning speed of 5530 Hz: **a** single pulse sequence (SPE) with delay of 10 s; **b** cross-polarization sequence with contact time 8 ms. ^{13}C MAS NMR spectra of TNP/THF IC, spinning speed 4000 Hz; **c** cross-polarization sequence with contact time 3 ms; **d** ^{13}C CP/MAS NMR spectra of TNP after thermal treatment with contact time 1 ms. (Adopted from [65] with permission)

(guest) and rigid (host) parts of ICs. It is worth noting that in SPE, with an extremely long recycle delay, it would be possible to observe all the signals of the ICs. In the ^{13}C CP/MAS experiment, where the relaxation time of the proton is a crucial parameter, a delay of a few seconds is usually sufficient to record all signals. From analysis of Fig. 20, it is apparent that the symmetry of the TNP host matrix of the complex with benzene (Fig. 20b) and tetrahydrofuran (Fig. 20c) is the same. Removing the guest molecule from the TNP changes the symmetry of the crystals, from the highly symmetrical hexagonal crystalline phase to the lower symmetry guest free cell. This is immediately recognized by ^{13}C CP/MAS (Fig. 20d) and ^{31}P CP/MAS (Fig. 21) experiments. It is worth noting that the inclusion complex of TNP crystallized from *p*-xylene forms a cage
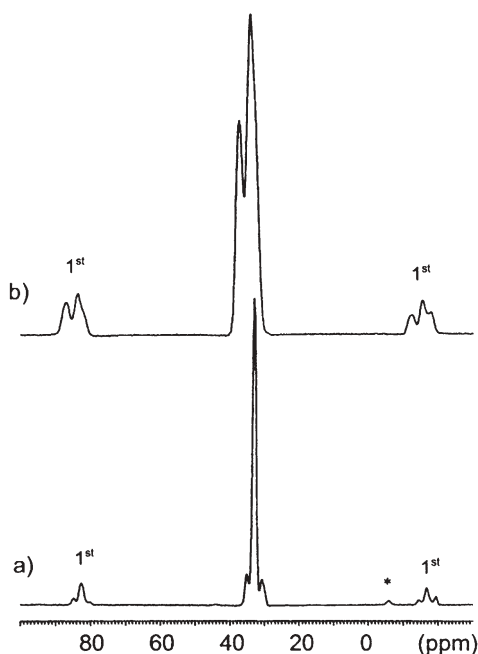
Fig. 21a, b ^{31}P CP/MAS spectra of: **a** TNP/benzene IC; **b** monoclinic TNP; contact time 2 ms, spinning speed 6000 Hz, recycle delay 10 s. (Adopted from [65] with permission)

type structure, which is represented by the more complex ^{13}C NMR pattern displayed in Fig. 22.

Valuable results were obtained while investigating the dynamic behavior of cyclophosphazene ICs. ^{13}C spin lattice relaxation time is a diagnostic tool, which characterizes the molecular motion of the guest inside the cavity, as well as the rigidity of matrix. The values of ^{13}C T_1 of benzene in the TPP and TNP matrices are different (24 s and 12 s respectively). This suggests that, in TPP IC with channel-type structure and channel diameter of 10Å, the guest molecules undergo faster molecular motion in comparison with those in TNP. The relaxation times of the TNP host indicate that the structure of TNP/benzene IC is less rigid than that of the TPP/benzene adduct (Fig. 23). Finally, the relaxation times for hexagonal crystals of guest-free TPP are of the order of 200 s, except for the C-1 carbon atom where a value of 1000 s is measured.

The crystal structures of organic clathrates, which are stabilized by van der Waals forces and contain sorbed molecules, generally collapse, when the guest molecules are removed, to a more stable crystal packing. The TPP IC is one of the rare exceptions, which proves that a guest-free structure can exist. The empty channel-like structure can be obtained from hexagonal TPP/benzene IC by mild evacuation of the volatile guest. The strategy for obtaining the unusual polymorph of TPP was based on a careful study of the solid-solid transforma-
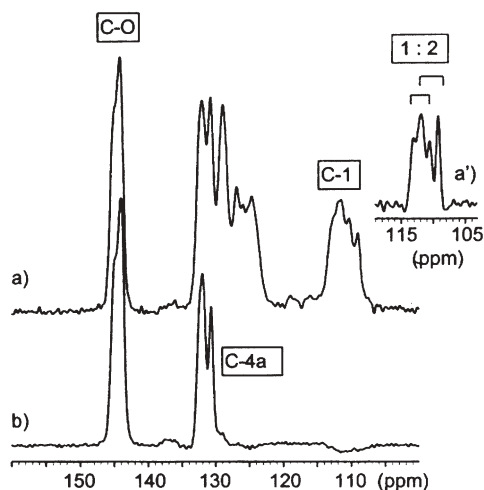
Fig. 22 **a** ^{13}C CP/MAS NMR spectra contact time 8 ms, spinning rate 5550 Hz the guest-free TNP, sample after *o*-xylene crystallization. **b** Protonated carbon suppression pulse sequence with a delay of 50 µs. **a′** C-1 signals obtained by applying resolution enhancement: line broadening =−40 Hz and Gaussian broadening=50%. (Adopted from [65] with permission)

tion of the IC. As in previous cases, solid state NMR spectroscopy was used as a tool to monitor changes in the phase transition and symmetry of the host matrix. As reported by Sozzani et al., such a guest-free cell is able to absorb gases. This was confirmed by ^{129}Xe NMR spectroscopy [67]. Figure 24 shows the ^{129}Xe NMR spectra of laser-polarized xenon following diffusion into porous crystalline material for several xenon/helium gas mixtures. The high sensitivity of the technique permits detection of xenon concentrations as low as 1% in helium. Line shape analysis of the xenon signals provides important information about xenon-wall and xenon-xenon interactions. Hence, it can be concluded that the ^{129}Xe anisotropic signals show squeezing of the atoms into the crystal nanochannels.

Muller and coworkers have recently reported the molecular behavior of 1,3,5-trioxane in a cyclophosphazene inclusion compound using H-2 NMR [68]. The experimental data were obtained by variable-temperature line shape analysis, spin-spin and spin-lattice relaxation time measurements and by 2D exchange between 30 and 370 K. At room temperature, highly mobile trioxane guests were observed. They undergo various overall and conformational motions which give rise to substantial orientational disorder within the hexagonal cyclophosphazene channels.
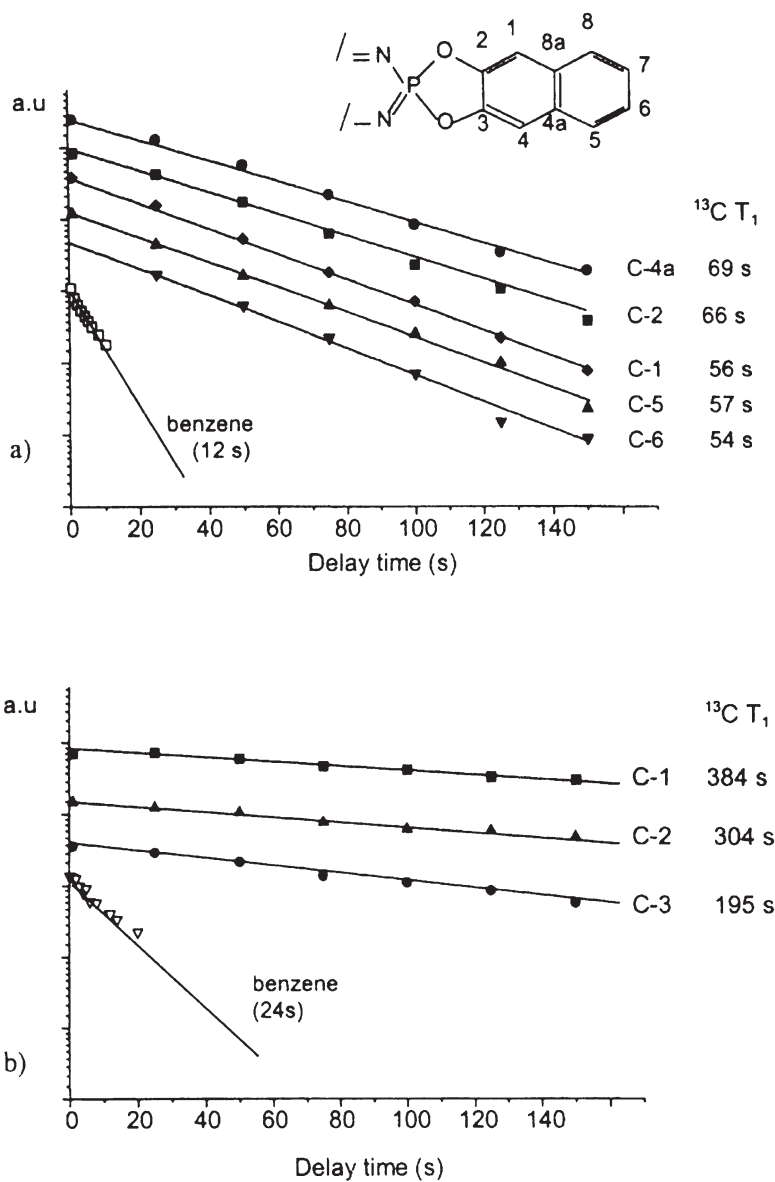
Fig. 23a, b Semilogarithmic plot of the ^{13}C T_1 relaxation times: **a** TNP/benzene IC; **b** TPP/benzene IC. (Adopted from [66] with permission)
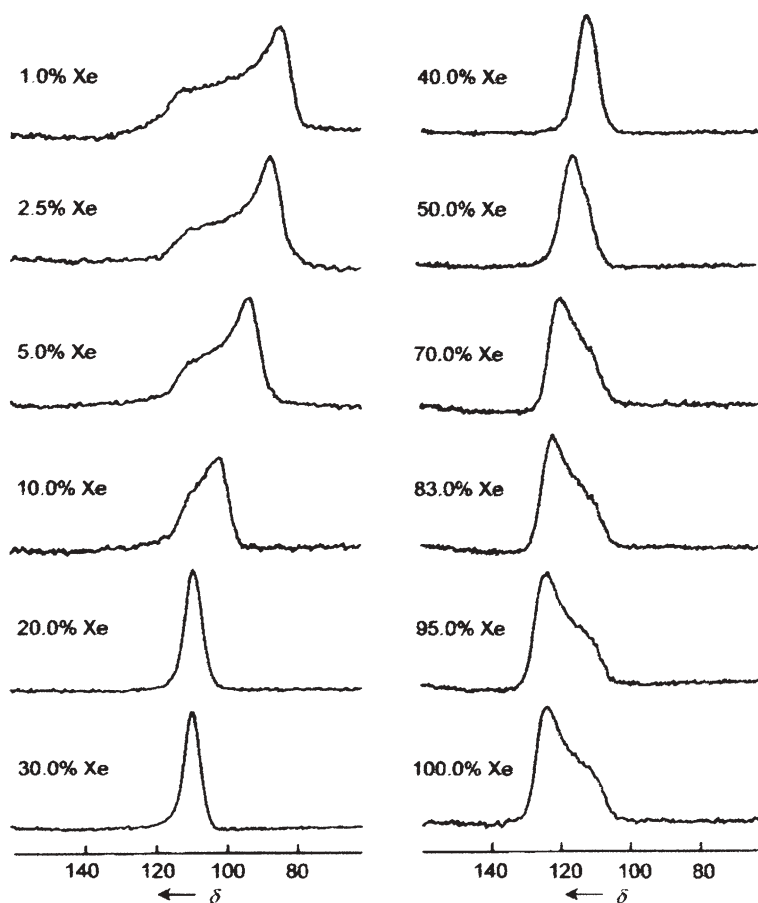
Fig. 24 Continuous-flow laser-polarized ^{129}Xe NMR spectra of Xe/He mixtures flowing in the TPP pseudohexagonal phase at atmospheric pressure and room temperature. The time for diffusion of the optically polarized xenon into the TPP channels was set by the recycle delay to 200 ms. The components of the CSA tensors (δ_{11}, δ_{22} and δ_{33}) were calculated by a numerical fitting procedure. (Adopted from [67] with permission)

5
Fullerenes

The fullerenes, discovered in 1985, represent a truly pure molecular form of carbon. In the beginning, there was no proof of the existence this material except for mass spectra. Final proof came in 1990, with the isolation of macroscopic amounts of C_{60}, which permitted the recording of the ^{13}C spectrum. Since of the carbon atoms in C_{60} are equivalent, a single line at δ 143 ppm was observed [69].
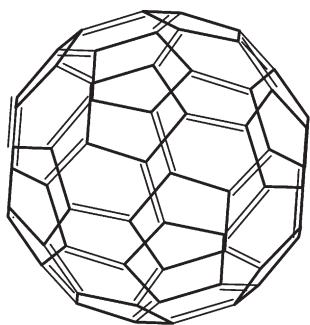
Scheme 10   C$_{60}$ "buckyball"

Fullerenes, especially buckminsterfullerene (C$_{60}$, "buckyball") (see Scheme 10) and C$_{70}$, have received much attention from many areas of chemistry. In the field of ICs, they have made appearances as both hosts and guests. As hosts, they exhibit intercalation behavior somewhat analogous to graphite, and can also include such species as hydrogen, oxygen [70], methane [71], rare gases [72] and carbon monoxide [73]. For these reasons, the fullerenes are of interest for solid state gas storage. As guests, the fullerenes represent a large, electron-deficient template capable of forming a variety of charge transfer compounds with electron donors. Among the macromolecular hosts are cyclodextrins, dendrimers, porphyrins and calixarenes [74]. Most of these complexes were characterized by means of techniques other than solid state NMR, but in the last five years, a few papers using NMR techniques in the solid phase for the description of fullerene inclusion complexes were published.

Klinowski and coworkers were the first to undertake a study of intercalates of water (D$_2$O) and fullerene C$_{60}$ by of high resolution ^{2}H Solid State NMR [75]. The authors confirmed that the C$_{60}$/D$_2$O intercalate presents a dynamical system and equilibrates in a matter of hours to the 17-day stable form. ^{13}C MAS spectra of the C$_{60}$/D$_2$O intercalate do not show a single resonance at 144.0 ppm, as for pure fullerene, because of the intercalated gases, and possibly perdeuterated water, both affecting the ^{13}C chemical shift. The room temperature ^{2}H MAS NMR spectrum of the equilibrated material reveals that the D$_2$O molecules are in two different magnetic environments, corresponding to two lines at –0.1 and –3.9 ppm (see Fig. 25a), characterized by totally different T$_1$ relaxation times, 0.37 and 9.4 s.

When the measurement temperature is decreased, the peak at –3.9 ppm survives below –100 °C. Initially, the –0.1 peak remains at –100 °C, but when the sample is heated to –50 °C, the intensity of the resonance is significantly reduced, even if the temperature is returned to –100 °C. Heating the sample to 210 °C in a sealed rotor has no influence on the spectrum; all peaks are unchanged. At 210 °C the signal at –0.1 ppm suddenly disappears and a new resonance at –4.5 ppm appears (see Fig. 25b).

a)

b)
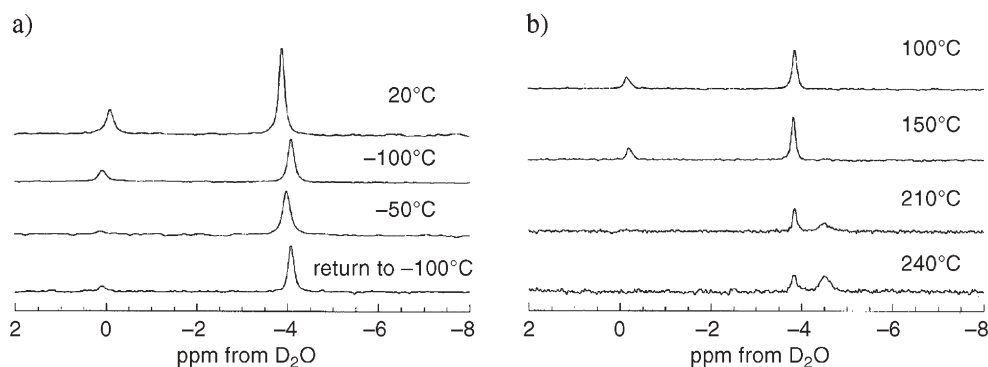
Fig. 25a, b   **a** Low temperature ^2H MAS NMR spectra of the C_{60}/D_2O intercalate. **b** High temperature ^2H MAS NMR spectra of the C_{60}/D_2O intercalate. (Adopted from [75] with permission)

The chemical shift of the ^2H line at –0.1 ppm indicates a hydrogen-bonded water cluster, while the peak at –3.9 ppm results from monomers or small multimers. The authors suggested that the monomolecular species are in one of two sites, an octahedral void or a small vacancy left by a missing fullerene cage. The remaining signal at –0.1 ppm comes from large water clusters. Support for this conclusion comes from four observations:

- The line broadens on freezing (as in ice)
- It is possible to supercool the species responsible by slowly decreasing the temperature
- On heating, the line persists up to 200 °C and then gives way to a line at –4.5 ppm
- The relaxation time of the species responsible is very similar to that of liquid water

Solvent molecules trapped inside the fullerene cage are in quite a restricted space and usually their motional behaviour is different from that in the "free state". Tekely et al. [76], presented the first experimental evidence of the highly anisotropic motion of benzene molecules in the C_{60} $4H_2O$ solvate. To gain insight into the structural and motional features of the solvate, different 1D and 2D NMR experiments were carried out. The standard proton decoupled ^{13}C cross-polarization static spectrum of the $C_{60} \cdot 4H_2O$ solvate at 294 K shows a relatively narrow line at 143.7 ppm, assigned to the C_{60}, and a broad pattern, with a width of about 170 ppm, assigned to the benzene fraction (see Fig. 26). The broad line visualizes the dramatic motional restriction of the solvent molecules lying within the channels separating the columns of fullerene molecules.

The absence of rapid isotropic motion of the benzene molecules allows efficient transfer of proton magnetization, not only to the directly bonded benzene carbons, but also to the C_{60} carbons. For this reason, the ^{13}C CP/MAS spectrum consists of a single narrow line at 143.7 ppm surrounded by a set of spinning sidebands (Fig. 27).

a)

×18

PPM   150.0   100.0   50.00   0.00

PPM   100.0   0.0

b)

PPM   150.0   100.0   50.00   0.00
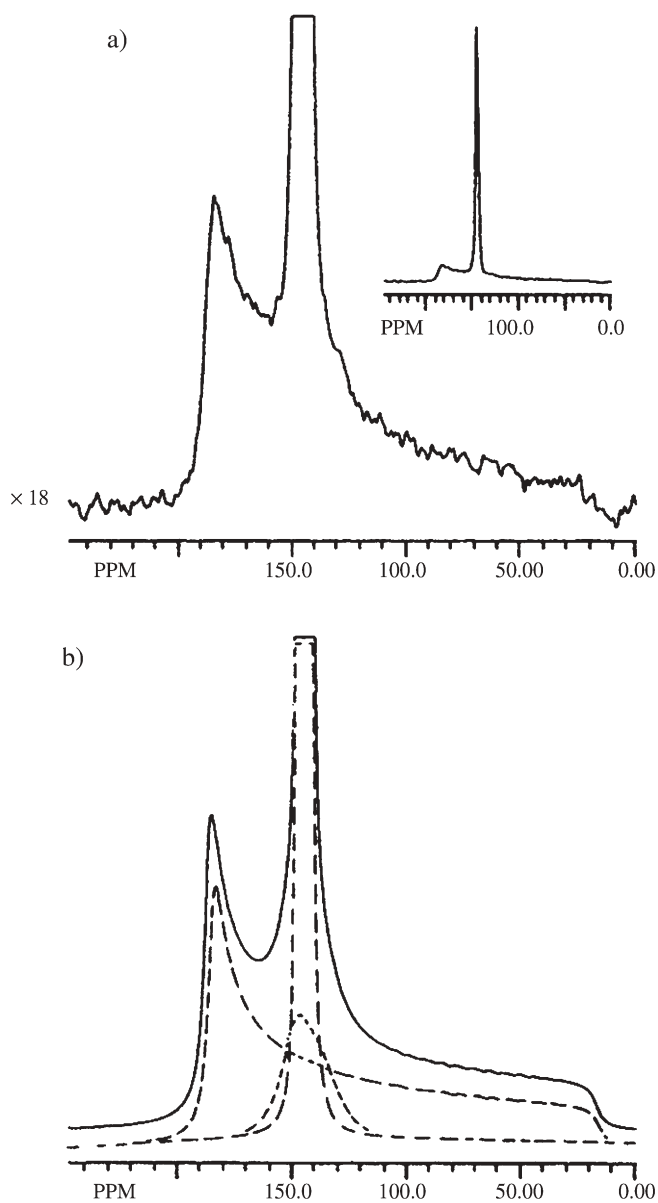
Fig. 26a, b **a** Experimental static proton decoupled ^{13}C spectra of $C_{60} \cdot 4H_2O$. **b** Calculated static proton decoupled ^{13}C spectra of $C_{60} \cdot 4H_2O$. Cross-polarization contact time (CT) was 10 ms, number of scans (NS) 1000, repetition time (D1) 18 s, line broadening (LB) 100 Hz. Spectra were simulated with line width ($1/T_2$) of 100 and 3300 s^{-1} for the narrow and broad C_{60} components and at 1000 s^{-1} for benzene component. (Adopted from [76] with permission)
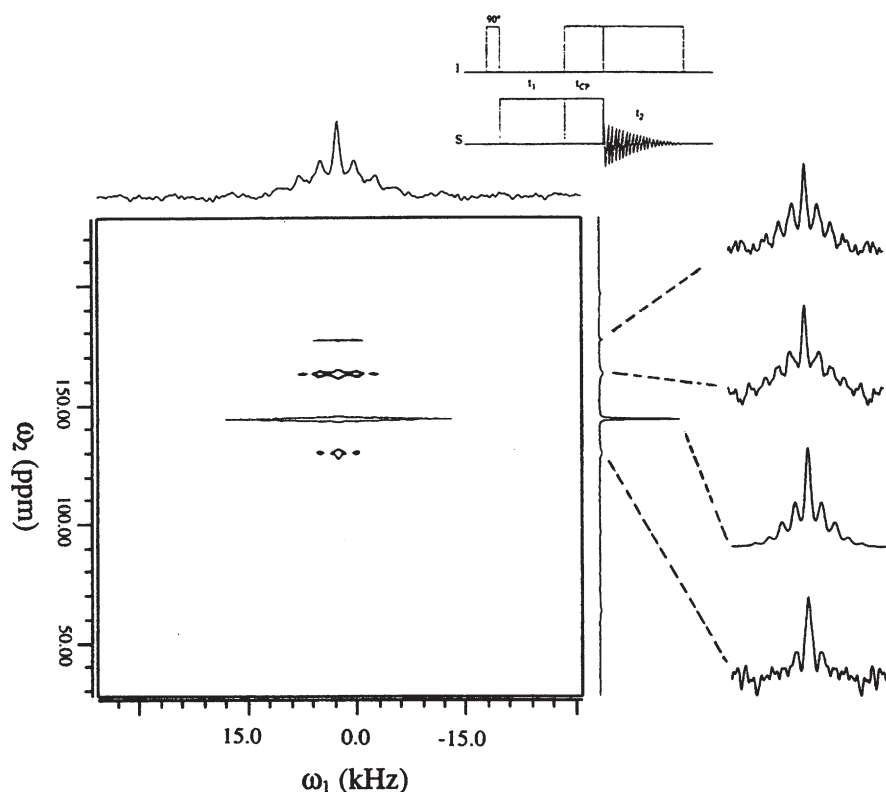
Fig. 27 Dipolar/chemical shift correlated spectrum of $C_{60} \cdot 4H_2O$ obtained by the pulse sequence shown at *the top of the figure*. Dipolar cross-sections are shown for the isotropic ^{13}C peak of benzene and C_{60} as well as for their respective spinning sidebands; 128 increments of 15 μs were used in t_1, contact time was 5 ms and ν_r=2.5 kHz. (Adopted from [76] with permission)

A 2D dipolar/chemical shift correlated experiment gave insight into the residual dipolar interactions in the presence of the highly anisotropic rotation of the benzene molecules. Comparison of the isotropic C_{60} lines under magic angle spinning obtained with and without cross-polarization (Fig. 28) is another source of information. Under CP, a single line is obtained, whereas a complex shape line is observed in the standard one pulse experiment. Under cross-polarization, only part of the C_{60} molecules can 'feel' the spatial proximity of the benzene molecules on the time scale of the few milliseconds used for polarization transfer. The complex shape of the line obtained without cross-polarization comes from the presence of three distinct components with slightly different isotropic chemical shifts. This proves the existence of magnetically non-equivalent positions or sites of the C_{60} molecules. This conclusion was confirmed by line-shape analysis and by simulating the standard one-pulse ^{13}C spectrum recorded under slow magic angle spinning.
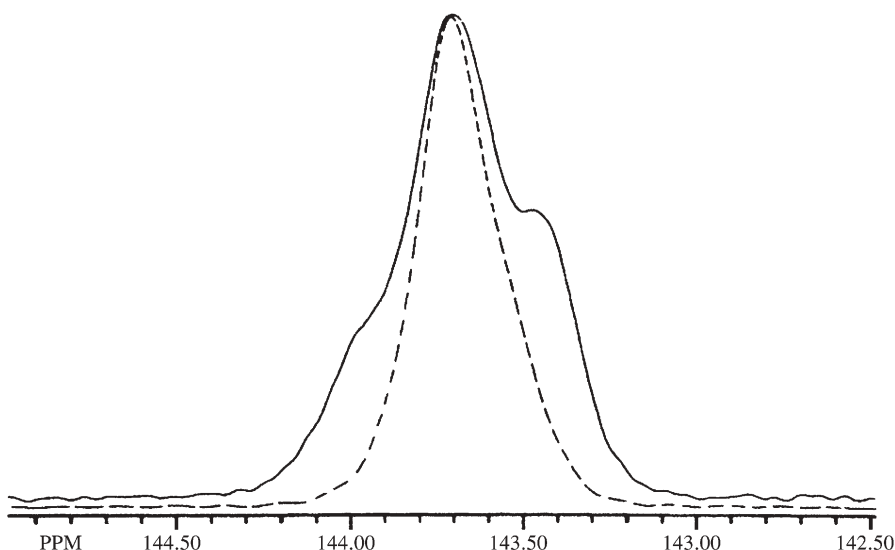
Fig. 28 ^{13}C line shape of C$_{60}$ in C$_{60}$ · 4H$_2$O recorded under one pulse (*solid line*) and after cross-polarization (CP) (*dashed line*). CP contact time 5 ms, ν_r=2.5 kHz, D1=140 s and 18 s, NS=500 and 2800. (Adopted from [76] with permission)

Buvari-Barcza and co-workers [77] showed, by comparing several complexing agents, that γ-CD is the best host for solubilising C$_{60}$ fullerene in a water environment. The interaction of C$_{60}$ and γ-CD forms a C$_{60}$-(γ-CD)$_2$ inclusion complex. The analytical data and solid state NMR indicated that the essentially 1:2 complex exists as two different forms. In the violet colored form, unhydrated C$_{60}$ is included, while in the brownish one, C$_{60}$ is also hydrated. The inner diameter of the γ-cyclodextrin is only 0.95 nm while the diameter of C$_{60}$ is estimated to be 1.0 nm. Because of this dimensional difference, complete inclusion is inconceivable, but the secondary hydroxyls of the γ-CD rims can be connected by hydrogen bonds and possibly mediated by water molecules (Fig. 29).

The results of ^{13}C solid state NMR experiments on dehydrated and hydrated C$_{60}$-(γ-CD)$_2$ complexes prove, not only the general formation of [C$_{60}$-(γ-CD)$_2$]·(H$_2$O)$_x$ species, but also the hydration of C$_{60}$ itself, since the data measured for different carbon atoms of C$_{60}$ are definitely non-equivalent in the two cases. In the violet [C$_{60}$-(γ-CD)$_2$]·(H$_2$O)$_x$ species, the water molecules seem to be connected only to the γ-CD domain of the supramolecule, while in the hydrated brown complex, the included fullerene is also hydrated [C$_{60}$·(H$_2$O)$_y$(γ-CD)$_2$]·(H$_2$O)$_z$].

This conclusion was reached by measuring the relaxation times. Both, T$_{CH}$ and T$_{1\rho H}$ values are increased for the [C$_{60}$·(H$_2$O)$_y$(γ-CD)$_2$]·(H$_2$O)$_z$] complex, indicating that the flexibility of this complex is enhanced. Examining Fig. 29,
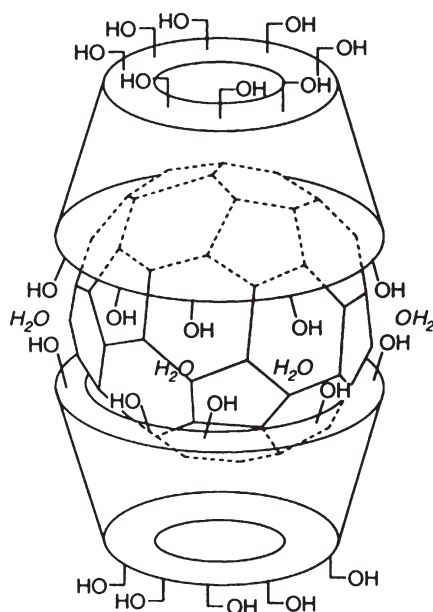
Fig. 29 The hydrated C_{60}-$(\gamma$-CD$)_2$ complex showing the hydration of the host and guest molecules. (Adopted from [77] by permission of The Royal Society of Chemistry)

which represents the correct relative sizes, the water molecules hydrating the fullerene can find space between the two γ-CDs. Since the ^{13}C NMR spectra are also different depending on the presence of C_{60} or $C_{60} \cdot (H_2O)_x$, the properties of these guests (and their inclusion complexes) must also be different. These differences were confirmed by UV-VIS spectra and the conclusions were in agreement with those proposed earlier by Tseng at al. [78].

Another molecule which can acts as host in C_{60} fullerene inclusion complexes is 1,8,15,22-tetraphenyl[14]metacyclophan-4,11,18,25-tetramethyl-3,5,10,12,17,19,24,26-octol. As shown by Garcia et al. [79], this macrocycle can guest one or two fullerene molecules in its structure. By ^{13}C CPMAS data analysis, and with the help of FTIR spectroscopy, π-π, σ-π and n-π interactions were observed.

C_{60} and C_{70} fullerenes are able to form complexes with resorcinarene [80]. In this case, the host molecule can guest only one fullerene molecule in its inclusion complex structure. The π-π, CH-π and n-π interactions were observed by ^{13}C CPMAS and FTIR analysis data. Chattopadyay and coworkers [81] investigated the ability of C_{60} and C_{70} fullerenes to form ICs with a series of crown ethers. They showed that fullerenes can form 1:1 molecular complexes with crown ethers, but two of them, dibenzeno-24-crown-8 and dibenzeno-30-crown-10, are able to form complexes only with C_{60} fullerene, not with C_{70}.

Although most published papers concern fullerenes inclusion complexes with organic molecules, fullerenes can also bind inorganic compounds. This

problem, however, is beyond the scope of this review and readers interested in this subject are referred to the original literature. It is worth mentioning that, very recently, Panich et al. [82] published ^{19}F solid state NMR studies of fullerenes doped with AsF_6 and SbF_6 species. Inclusion complexes of fullerene with a ferrocene derivative [83] and CO_2 [84] were characterized by solid state NMR.

6
1,2-Dichloroethane/tris(5-Acetyl-3-Thienyl) Methane (TATM)

Reviewing interesting systems which form inclusion compounds and are investigated by high resolution solid state NMR, in this section we present complexes of 1,2-dichloroethane/tris(5-acetyl-3-thienyl) methane (TATM). TATM (Scheme 11) is a conformationally flexible tripoidal host molecule [85].
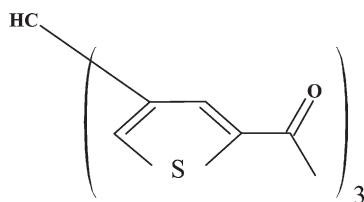
Scheme 11

This molecule forms inclusion compounds with a wide variety of organic compounds. Bin Din and Meth-Cohn reported melting points for TATM ICs with 39 different guests, the majority of which were of 2:1 host : guest ratio [86]. X-ray crystallography of single crystals, as in many cases, was the source of invaluable structural information. Most known TATM complexes, crystallize in the triclinic P-1 space group, although monoclinic systems with the $P2_1/c$ space group were also reported. In the field of solid state NMR studies of TATM ICs, an important recent contribution comes from Ripmeester's Laboratory [87, 88]. Searching the ICs with 1,2-dichloroethane, Sidhu et al. found that this guest crystallizes both as triclinic P-1 as well monoclinic $P2_1/c$. This is a rare case of inclusion complex polymorphism. The molecular packing of the triclinic form is shown in Fig. 30.

The difference between monoclinic and triclinic forms arises from the layering of ribbons in adjacent sheets (within one layer, the two forms are almost isostructural). In the triclinic form, the adjacent sheets are related by a unit cell translation, and the ribbons in adjacent sheets run parallel to one another. In the monoclinic form, the adjacent sheets are related by a c glide, and ribbons in adjacent sheets run in perpendicular directions. Although this distinction is very subtle, careful analysis of ^{13}C CP/MAS spectra allows these differences to be recognized.

Figure 31 presents spectra of pure triclinic (A) and of a mixture of triclinic and monoclinic systems. The multiplicity of the TATM signals proves that one
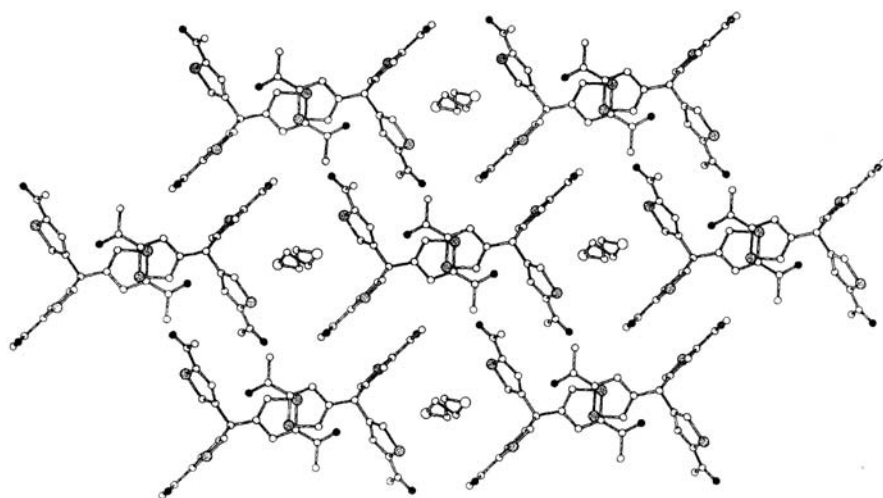
Fig. 30 A packing diagram illustrating three ribbons in one sheet of the triclinic form of 1,2-dichloroethane/TATM at –100 °C. (Adopted from [87] with permission)
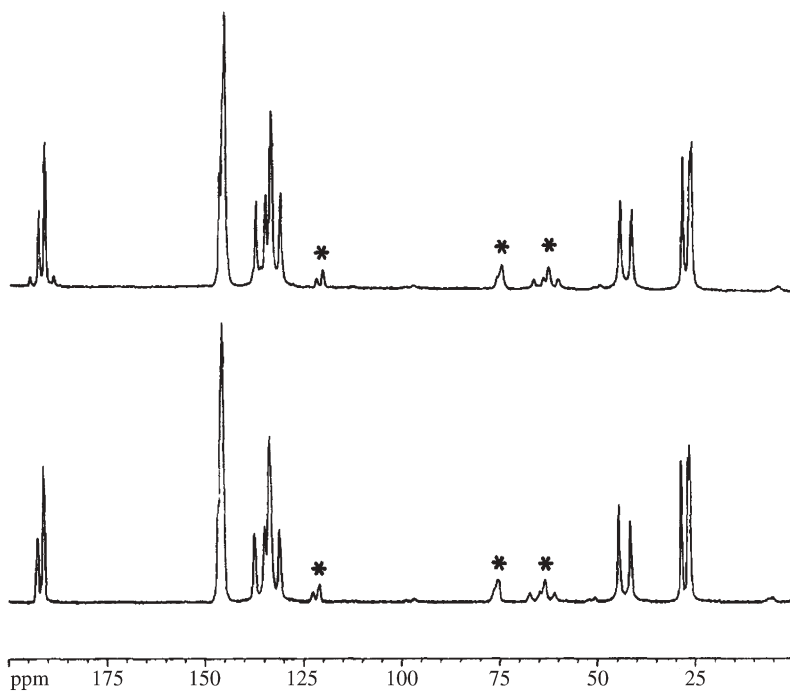
Fig. 31 ^{13}C CP/MAS spectra of 1,2-dichloroethane/TATM samples. (Adopted from [87] with permission)
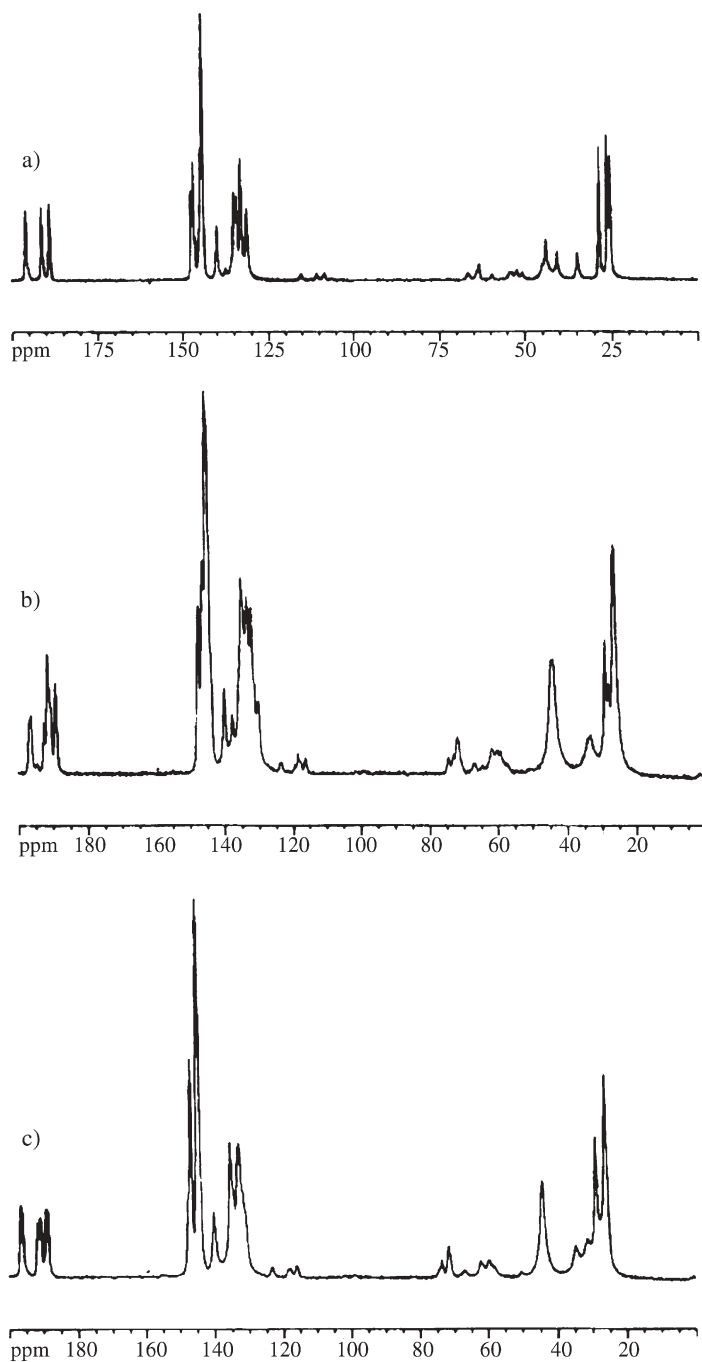
Fig. 32a–c ^{13}C CP/MAS spectra of TATM inclusion compounds with three different *n*-dichloroalkane guests: **a** 1,3-dichloropropane-TATM; **b** 1,5-dichloropentane-TATM; **c** 1,9-dichlorononane-TATM. (Adopted from [88] with permission)

molecule of the host is an independent part of the asymmetric unit. At first glance, there is no difference between spectrum A and B. However, the small intensity peaks in the carbonyl region correspond to the monoclinic phase. There is also a weak signal visible at 136 ppm, partially hidden under the main signal from the TATM tertiary thienyl signal. The small amount of the monoclinic form in the mixture was confirmed by powder X-ray diffraction studies. In this work, advanced NMR studies of guest dynamics and their conformational equilibrium are discussed.

Extending studies of TATM complexes with dichloroalkene homologues, Sidhu and Ripmeester investigated a number of assemblies with $Cl(CH_2)_nCl$ guest molecules, where n is in the range of 1 to 10 [88]. It was found that the smallest guests (n=1–4) form 2:1 host: guest complexes, intermediate size guests (n=5, 6) form 3:1 compounds, while the largest guests (n=8–10) form 4:1 TATM inclusion complexes. The challenge for solid state NMR is recognizing the host:guest ratio and the symmetry of the crystal lattice. The ^{13}C CP/MAS spectra of three selected TATM inclusion complexes are shown in Fig. 32. The guests are 1,3-dichloropropane (Fig. 32a), 1,5-dichloropentane (Fig. 32b) and 1,9-dichlorononane (Fig. 32c). For 1,3-dichloropropane-TATM, the multiplicity of the host carbonyl signal at 190 ppm is three, as is the multiplicity of the host methyl signal at 26 ppm. This implies that there is one TATM molecule in the asymmetric unit. Since the stoichiometric host:guest ratio for this complex is 2:1, it can be assumed that there are two host molecules and one guest molecule in the unit cell. It is very likely that two host molecules are related by symmetry. For 1,5-dichloropentane-TATM the multiplicity of the host carbonyl signal at 190 ppm as the methyl signal at 26 ppm is nine for each group. Therefore, this splitting pattern suggests that there are three host molecules in the asymmetric unit of the inclusion complex.

Finally, the ^{13}C CP/MAS spectrum of inclusion compounds with 1,9-dichlorononane is shown in Fig. 32c. In this case, the multiplicity of the host carbonyl signal at 190 ppm is six, and the host methyl signal at 26 ppm is also split into six signals. The splitting pattern suggests that there are two host molecules in the asymmetric unit. These results clearly prove that examination of high-resolution solid state NMR spectra can give information about the contents of the asymmetric unit and has potential for the analysis of polycrystalline solids.

7
Other Organic Host Lattices

There are of course more organic compounds which can be used as host molecules in the formation of inclusion complexes. For most of them, e.g. urea and thiourea, crown ethers, cholic acid, hydroquinone, tri-*o*-thymotides and Dianin's compound, the literature describing SS NMR applications in structural

studies of ICs was reviewed to 1996. In recent years, for some of the compounds under discussion, interesting SS NMR works have been published.

4-*p*-Hydroxy-2,4,4-trimethylchroman (Dianin's compound) forms a lattice, which consist of six molecules connected in such a way that the phenolic oxygen atoms form a regular hydrogen bonded six-membered ring with alternate host molecules pointing to the host lattice. There is a single molecule in the asymmetric unit, and thus the ^{13}C CP/MAS spectrum consists of 18 lines. The guest molecule can break the local symmetry or even the lattice symmetry. The latter case is most likely to occur where a relatively tightly held molecule of lower symmetry serves as guest. For this reason, much attention has been paid to the IC of Dianin's compound with *p*-xylene. Zaborowski et al. used solid state NMR and molecular modeling to refine the structure and dynamics [89]. Calculations revealed six different possible orientations of the molecules in the cage. These correspond to two types of guest, not related by any symmetry, each consisting of three C-3 symmetry related sites. The two types induce significant distortions to the local structure of the host crystal cage. [13]C CP/MAS confirmed that the methyl groups of the host, in the middle of cage, are influenced strongly by inclusion of the *p*-xylene molecules. These results were questioned by Enright et al., who, by single-crystal X-ray diffraction and ^{13}C solid state NMR, concluded that there is a single (symmetry disordered) guest site without any significant distortion of the host framework [90].

A single ^{13}C label at the methyl group of *p*-xylene was used to establish [13]C···[13]C distances between guest molecules and hosts with naturally abundant ^{13}C, using the 2D RFDR approach [91]. Other Dianin ICs, with *n*-hexane and *n*-pentanol guest molecules, have been reported [92]. Eckhardt and coworkers investigated Dianin clathrates containing two ethanol molecules and a heptanol, [93] as well as 1,6 hexanediol, 1,5 pentenediol and 1-heptanol [94].

In the last few years, considerable attention has been paid to thiourea ICs, mainly investigating the dynamics of different guest molecules [95]. Sidhu et al. explored the molecular motion of the 4-alkyl-*tert*-butylbenzene/thiourea complex, using ^{2}H and ^{13}C CP/MAS NMR [96]. The bromocyclohexane/thiourea inclusion compound was investigated by Ternieden and Muller [97]. ^{19}F solid state NMR and the two-dimensional EXSY method were used to study ring inversion of flurocyclohexane in a thiourea host lattice [98]. The phase transition of thiourea complexes with cycloheptane, cyclooctane and cyclooctanone was investigated by variable temperature single-crystal X-ray diffraction and solid state NMR [99]. Urea was found to form inclusion compounds with many polymers. Some of the polymer-urea complexes crystallize in hexagonal or trigonal form with 5.0 Å diameter channels, while others crystallize in "expanded tetragonal" forms with larger channel diameter. Details of SS NMR studies of the structure and dynamics of polymer-urea ICs were recently reviewed by Tonelli and coworkers [100].

8
Concluding Remarks

In this chapter we have presented recent applications of high-resolution SS NMR in structural studies of inclusion compounds. In most papers reviewed, the well known CP/MAS sequence is used as a preliminary test of the structure of a complex. With rapid, recent progress in software and hardware technologies, the possibilities of NMR spectroscopy have been greatly extended. Today, 2D SS NMR spectroscopy, Fast MAS and HR MAS experiments have become the routine approach to investigation of ICs. In the work reviewed, attention is mostly paid to the 'host-story', although it is apparent that guest molecules always manifest their presence in the host lattice, but not always in a direct way.

In many cases, solid-state spectra are similar to those recorded in the liquid phase, but usually contain a wider range of information than is available in liquid NMR spectroscopy. The solid state represents the best environment for the investigation of intermolecular host-guest interactions. Analysis of the tensorial nature of the chemical shifts of the active bonding centers of host and/or guest provides subtle structural information. Strategies based on dipolar recoupling indicate a number of ways in which dipolar coupling constants can be measured, to yield direct data on internuclear distances. This approach, combined with advanced theoretical calculations, traces new trends in structural studies of inclusion complexes in the solid state.

References

1. Stoddart JF (2001) Acc Chem Res 34:410 and other papers published in this special issue
2. Lehn J-M (1995) Supramolecular chemistry, concepts and perspectives. VCH, Weinheim
3. Steed JW, Atwood JL (eds) (2000) Supramolecular chemistry. Wiley, Chichester New York Weinheim Brisbane Singapore Toronto
4. Davies JED, Ripmeester JA (1996) Physical methods in supramolecular chemistry. In: Davies JED, Ripmeester JA (eds) Comprehensive supramolecular chemistry, vol 8. Elsevier Science, New York
5. Ripmeester JA, Ratcliffe CI (1996) Physical methods in supramolecular chemistry. In: Davies JED, Ripmeester JA (eds) Comprehensive supramolecular chemistry. Elsevier Science Ltd, New York, p 323
6. Ripmeester JA, Ratcliffe CI, Brouver EB (2002) Inclusion compounds. In: Grant DM, Harris RK (eds) Encyclopedia of nuclear magnetic resonance, vol 9. Wiley, Chichester, p 558
7. Klinowski J (2002) In: Duer MJ (ed) Solid state NMR spectroscopy principles and applications. Blackwell Science, Oxford, London Edinburgh, p 437
8. Szejtli J (1998) In: Cyclodextrin technology. Kluwer Academic Publishers, Dordrecht
9. a) Szejtli J (1998) Chem Rev 98:1743; b) Seanger W (1980) Angew Chem Int Ed Engl 19:344
10. a) Gadelle A, Defaye J (1991) Angew Chem Int Ed Engl 30:78; b) Caira MR, Griffith VJ, Nassimbeni LR, van Oudtshoorn B (1994) J Chem Soc Perkin Trans 2 2071; c) Nogami Y, Nasu K, Koga T, Ohta K, Fujita K, Immel S, Linder HJ, Schmitt GE, Lichtenthaler FW (1997) Angew Chem Int Ed Engl 36:1899

11. Rekharsky MV, Inoue Y (1998) Chem Rev 98:1875 and literature cited therein
12. Philp D, Stoddart JF (1996) Angew Chem Int Ed Engl 35:1154
13. See references 3, 8–11 and 17–22 in Rekharsky MV, Inoue Y (1998) Chem Rev 98: 1875
14. Dodziuk H (2002) J Mol Struct 614:33
15. Schneider H-J, Hacket F, Rüdiger V, Ikeda H (1998) Chem Rev 98:1755
16. Ripmeester JA, Ratcliff CI (1996) Comprehensive supramolecular chemistry, vol 8
17. Harada A, Kamachi M (1990) Macromolecules 23:2821
18. Lu J, Shin ID, Nojima S, Tonelli AE (2000) Polymer 41:5871
19. Lu J, Mirau PA, Shin ID, Nojima S, Tonelli AE (2002) Macromol Chem Phys 203:71
20. a) Michishita T, Okada M, Harada A (2001) Macromol Rapid Commun 22:784; b) Probeni FE, Edeki EM, Shin ID, Tonelli AE (2001) Polymer 42:6907
21. a) Shuai X, Porbeni FE, Wei M, Bullions T, Tonelli AE (2002) Macromolecules 35:3126; b) Wulff M, Aldén M, Tegenfeldt J (2002) Bioconjugate Chem 13:240
22. Li J, Ni X, Zhou Z, Leong KW (2003) J Am Chem Soc 125:1788
23. Li X, Li J, Leong KW (2003) Macromolecules 36:1209
24. Shuai X, Porbeni FE, Wei M, Bullions T, Tonelli (2002) Macromolecules 35:2401
25. Cunha-Silvia L, Gonçalves IS, Pillinge M, Xue W-M, Rocha J, Teixeira-Dias JJC, Kühn FE (2002) J Organometalic Chem 656:281
26. Lambert JB, Liu C, Boyne MT, Zhang AP, Yin Y (2003) Chem Mater 15:131
27. Saalwächter K (2002) Macromol Rapid Commun 23:286
28. Crini G, Bourdonneau M, Martel B, Piotto M, Morcellet M, Richter T, Vebrel J, Torri G, Morin N (2000) J Appl Polym Sci 75:1288
29. Crini G, Cosentino C, Bertini S, Naggi A, Torri G, Vecchi C, Janusz L, Morcellet M (1998) Carbohydr Res 308:37
30. Brett TJ, Alexander JM, Clark JL, Ross CR, Harbison GS, Stezowski JJ (1999) Chem Commun 14:1275
31. Garbow JR, Likos JJ, Schroeder SA (2001) J Agric Food Chem 49:2053
32. Yannakopoulou Y, Ripmeester JA, Mavridis IM (2002) J Chem Soc Perkin Trans 2 1639
33. Potrzebowski MJ, Grossman G, Ganicz K, Olejniczak S, Ciesielski W, Koziol AE, Wawrzycka I, Bujacz G, Haeberlen U, Schmitt H (2002) Chem Eur J 8:2691
34. Potrzebowski MJ, Blaszczyk J, Wieczorek MW (1995) J Org Chem 60:2549
35. Potrzebowski MJ, Ganicz K, Skowronska A, Wieczorek MW, Blaszczyk J, Majzner W (1999) J Chem Soc Perkin Trans 2:2163
36. Steiner T (2002) Angew Chem Int Ed Engl 41:48 and references cited therein
37. Potrzebowski MJ, Helinski J, Ciesielski W (2002) Chem Commun 1582
38. Gutsche CD (1989) Calixarenes In: Stoddart JF (ed) Monograph in supramolecular chemistry. Royal Society of Chemistry, Cambridge
39. Gutsche CD (1998) Calixarenes revisited. In: Monograph in supramolecular chemistry. Royal Society of Chemistry, Cambridge
40. Morohashi N, Iki N, Miyano S (2002) J Synth Org Chem Jpn 60:550
41. Menon SK, Gidwani MS, Agarwal YK (2003) Rev Anal Chem 21:35
42. Böhmer V (1995) Angew Chem Int Ed Engl 34:713
43. Ikeda A, Shinkai S (1997) Chem Rev 97:1713
44. León S, Leigh DA, Zerbett F (2002) Chem Eur J 21:8
45. Brouwer EB, Udachin KA, Enright GD, Ripmeester JA (2000) Chem Commun 1905
46. Udachin KA, Enright GD, Brown PO, Ripmeester JA (2000) Chem Commun 2161
47. a) Furphy BM, Harrowfield JM, Ogden MI, Skelton BW, White AH, Wilner FR (1989) J Chem Soc Dalton Trans 2217; b) Brouver EB, Enright GD, Ripmeester JA (1996) Supramol Chem 7:7; c) Brouver EB, Enright GD, Ripmeester JA (1996) Supramol Chem 7:143

48. Benevelli F, Kolodziejski W, Wozniak K, Klinowski J (2001) Phys Chem Chem Phys 3:1762
49. Schatz J, Backes AC, Siehl H-U (2000) J Chem Perkin Trans 2 609
50. Backes AC, Schatz J, Siehl H-U (2000) J Chem Perkin Trans 2 484
51. Brouwer EB, Enright GD, Ratcliffe CL, Ripmeester JA (1996) Supramol Chem 7:79
52. Benevelli F, Kolodziejski W, Wozniak K, Klinowski J (2001) Chem Phys Lett 308:65
53. Brouwer EB, Gougeon RDM, Hirschinger J, Udachin KA, Harris RK, Ripmeeser JA (1999) Phys Chem Chem Phys 1:4043
54. Hughes E, Jordan J, Gullion T (2001) J Phys Chem B 105:5887
55. Pietraszkiewicz M, Pietraszkiewicz O, Kolodziejski W, Wozniak K, Feeder F, Benevelli F, Klinowski J (2000) J Phys Chem B 104:1921
56. Kuzmicz R, Dobrzycki L, Wozniak K, Benevelli F, Kolodziejski W, Klinowski J (2002) Phys Chem Chem Phys 4:2387
57. Kolodziejski W, Klinowski J (2002) Chem Rev 102:613
58. Liebig J (1834) Ann Chem 11:139
59. Stokes HN (1895) Chem Ber 28:437
60. Allcock HR (1972) Phosphorus-nitrogen compounds. Academic Press, New York
61. Allen CW (1991) Chem Rev 91:119
62. Chandrasekhar V, Justin-Thomas KR (1993) Struct Bond 81:43
63. Allen CW (1994) Phosphorus-31 NMR spectral properties in compound characterization and structural analysis. Quinn LD, Verkade JG (eds). VCH, New York, Weinheim, Cambridge, p 103
64. Chandrasekhar V, Krishnan V (2002) Adv Inorg Chem 53:159
65. Comotti A, Gallazzi MC, Simonutti R, Sozzani P (1998) Chem Mater 10:3589
66. Comotti A, Simonutti R, Stramare S, Sozzani P (1999) Nanotechnology 10:70
67. Sozzani P, Comotti A, Simonutti R, Meersmann T, Logan JW, Pines A (2000) Angew Chem Int Ed 39:2695
68. Liebelt A, Detken A, Muller K (2002) J Phys Chem B 106:7781
69. Kroto HW (1992) Angew Chem Int Ed Engl 31:111
70. Assink RA, Schirber JE, Loy DA, Morosin B, Carlson GA (1992) J Mater Res 7:2136
71. Carlson GA, Assink RA, Dunn RG, Massin TM, Schirber JE (1997) Phys Rev B 56:13611
72. Kwei GH, Jorgensen JD, Schirber JE, Morosin B (1997) Fullerene Sci Technol 5:243
73. Holleman I, von Helden G, Olthof EHT, van Bentum PJM, Engeln R, Nachtegaal GH, Kentgens APM, Meier BH, van der Avoird A, Meijer G (1997) Phys Rev Lett 79:1138
74. See refs 3–14 in Wang J, Bodegi GB, Watson WH, Gutsche CD (2000) J Org Chem 65:8260
75. Collins C, Kolodziejski W, Foulkes J, Klinowski J (1998) Chem Phys Lett 289:338
76. Tekely P, Palmas P, Mutzenhardt P, Masin F, Grell A-S, Mesami I, Gelbcke M (1998) Solid State Commun 106:391
77. Buvari-Barcza Á, Rohonczy J, Rozlosnik N, Gilányi T, Szabó B, Lovas G, Braun T, Samu J, Barcza L (2001) J Chem Soc Perkin Trans 2 191
78. Tseng WY, Chen YH, Khairullin II, Cheng SF, Hwang LP (1997) Solid State NMR 8:219
79. Garcia MM, Uribe MIC, Palcios EB, Ochoa FL, Toscano A, Cogordan JA, Rios S, Cruz-Almanaza R (1999) Tetrahedron 55:6019
80. Garcia MM, Cabanas RT, Ochoa FL, Toscano A, Cruz-Almanaza R (2000) Fullerene Sci Technol 8:475
81. Bhattacharya S, Sharma A, Nayak SK, Chattopadyay S, Mukherjee AK (2003) J Phys Chem B 107:4213
82. Panich AM, Veith HM, Ummat PK, Datars WR (2003) Physica B Condensed Matter 327:102
83. Arrias A, Diana E, Gobetto R, Milanesio M, Vitrebo D, Stanghellini PL (2003) Eur J Inorg Chem 6:1186

84. Field CN, Hamley PA, Webster JM, Gregory DH, Titman JJ, Poliakoff M (2000) J Am Chem Soc 122:2480
85. Yakubov AP, Sudarushkin YK, Balenkii LI, Goldfarb YL (1973) J Org Chem (USSR) 9:1549
86. Bin Din L, Meth-Cohn O (1977) J Chem Soc Chem Commun 21:741
87. Sidhu PS, Enright GD, Ripmeester JA (2002) J Phys Chem B 106:8569
88. Sidhu PS, Ripmeester JA (2003) Supramol Chem 15:433
89. Zaborowski E, Vega S, Speier P, Zimmermann H, Haeberlen U (1997) Mol Phys 91:1083
90. Enright GD, Ratcliffe CI, Ripmeester JA (1999) Mol Phys 97:1193
91. Zaborowski E, Zimmermann H, Vega S (1999) J Magn Reson 136:47
92. Zaborowski E, Zimmermann H, Vega S (1998) J Am Chem Soc 120:8113
93. Sandstedt CA, Michalski D, Eckhardt CJ (2000) J Chem Phys 112:7606
94. Selbo JG, Desper JM, Eckhardt CJ (2003) J Incl Phenom Macrocyc Chem 45:73
95. Harris KDM (1996) J Mol Struct 374:241
96. Sidhu PS, Penner GH, Jeffrey KR, Zhao BY, Wang ZL, Goh IU (1997) J Phys Chem B 101:9087
97. Ternieden S, Muller K (1998) J Incl Phenom Molec Recogn Chem 30:289
98. Harris RK, Nordon A, Harris KDM (1999) Magn Reson Chem 37:15
99. Maris T, Henson MJ, Heyes SJ, Prout K (2001) Chem Mater 13:2483
100. Lu J, Mirau PA, Tonelli AE (2002) Prog Polym Sci 27:357

Progress in Multiple-Quantum Magic-Angle Spinning NMR Spectroscopy

João Rocha[1] (✉)· Cláudia M. Morais[2] · Christian Fernandez[2]

[1] University of Aveiro, Department of Chemistry, CICECO, 3810-193 Aveiro, Portugal
   Rocha@dq.ua.pt

[2] ENSICAEN and Université de Caen-Basse, Normandie,
   Laboratoire Catalyse et Spectrochimie (CNRS UMR 6506), 14050 Caen, France

Abstract Recent advances in nuclear magnetic resonance spectroscopy of quadrupolar ($I>1/2$) nuclei with half-integer spins in solids have been reviewed. The advent of multiple-quantum (MQ) magic-angle spinning (MAS) spectroscopy gave new momentum to the study of quadrupolar nuclei in materials of academic and industrial interest such as min-

erals, ceramics and glasses, microporous and mesoporous solids and biological materials. It is now possible to record high-resolution solid-state NMR spectra of a range of important nuclei, namely [11]B, [17]O, [23]Na, [27]Al, [71]Ga, [91]Nb. Since its introduction in 1995 MQMAS NMR has evolved considerably and, at present, a range of very useful related techniques are available and have been reviewed, in particular satellite transition (ST) MAS, Inverse-STMAS NMR, fast amplitude modulation, and techniques based on the dipolar interactions between quadrupolar and spin-1/2 nuclei, such as cross-polarization MQMAS and MQ heteronuclear correlation spectroscopy (HETCOR) and the recently introduced *J*-coupling based experiments (such as *J*-HMQC).

Keywords   Solid state NMR · Quadrupolar nuclei · MQMAS · STMAS · HETCOR

1
Introduction

Several NMR-active nuclei are available to study solids. Some of these are $I=1/2$ nuclei with a low natural abundance (e.g. [29]Si) or they may be ca. 100% abundant (e.g. [1]H). Over 70% of all NMR active nuclei are quadrupolar, with integer (e.g. [2]H, $I=1$) or half-integer (e.g. [27]Al, $I=5/2$) spin. Normally, NMR spectra cannot be recorded in the same manner for solids as for liquids. This is because, in the solid state, one has to consider a number of anisotropic interactions, which can be overlooked for solutions, as the random molecular tumbling averages the NMR interactions to isotropic values. These interactions broaden the NMR spectral lines of solids considerably. For $I=1/2$ nuclei several methods are well established for eliminating or reducing significantly the effects of the broadening interactions, affording high-resolution solid-state NMR spectra. In contrast, narrowing the spectral lines of half-integer quadrupolar nuclei is a particularly challenging task and has attracted the efforts of NMR spectroscopists in the last 15 years or so. The introduction in 1995 of Multiple-Quantum (MQ) Magic-Angle Spinning (MAS) NMR spectroscopy prompted a revolution in this field. It is now possible to record high-resolution NMR spectra of half-integer quadrupolar nuclei in solids. MQMAS NMR has evolved and many new techniques have been proposed for improving efficiency and the extraction of information of chemical interest.

In this review, we shall introduce some basic concepts about solid-state NMR of half-integer quadrupolar nuclei and discuss the most useful and promising methods presently available to study them. These include older methods, such as Double Rotation (DOR) and Dynamic Angle Spinning (DAS), and novel techniques including MQMAS, Quadrupolar Phase Adjusted Spinning Sidebands QPASS, Satellite Transition (ST) MAS and Inverse-STMAS NMR, and Fast Amplitude Modulation (FAM). We also discuss several techniques based on dipolar interactions between quadrupolar and spin-1/2 nuclei, such as Cross-Polarization (CP) MQMAS, MQ Heteronuclear Correlation Spectroscopy

(HETCOR), MQ REDOR (Rotational Echo Double Resonance), TRAPDOR (TRAnsfer of Populations in DOuble Resonance) and REAPDOR (Rotational Echo Adiabatic Passage Double Resonance), and the recently introduced *J*-coupling based experiments. A few other excellent reviews on MQMAS NMR have been recently published and complement the present review [1, 2].

2
Quadrupolar Nuclei: Basic Ideas

2.1
Quadrupolar Hamiltonian

In addition to the interactions which broaden the solid-state NMR resonances of spin-1/2 nuclei, the electric quadrupole interaction considerably decreases the resolution of the spectra of quadrupolar nuclei (spin $I>1/2$). These nuclei have a non-spherically symmetrical distribution of nuclear charge and possess an electric quadrupole moment, which interacts strongly with any electric field gradient, created by the surrounding electron cloud, at the site of the nucleus. In the tensorial Cartesian form the quadrupolar Hamiltonian is

$$\hat{H}^Q = \frac{eQ}{2I(2I-1)} \, \hat{I} \cdot \bar{\bar{V}} \cdot I \tag{1}$$

where $\bar{\bar{V}}$ is the symmetric and traceless electric field gradient (EFG) tensor. The quadrupole coupling constant, C_Q, and the asymmetry parameter, η_Q, are defined from the principal values of the EFG tensor ($V_{xx}, V_{yy}, V_{zz}=eq$) as follows:

$$C_Q = e^2qQ/\hbar \quad \text{and} \quad \eta_Q = (V_{yy} - V_{xx})/V_{zz} \tag{2}$$

where Q is the quadrupole moment of the nucleus. The quadrupole coupling constant, here in units of rad·s^{-1}, is frequently given in Hz ($C_Q=e^2qQ/\hbar$) and, in general, is of the order of MHz. In the spherical representation, the quadrupolar Hamiltonian in the laboratory (LAB) frame is [3]

$$\hat{\mathcal{H}}^Q = \frac{eQ}{2I(2I-1)} \sum_{k=-2}^{+2} (-1)^k \, A_{2,-k}^{Q,LAB} \, T_{2,k}^Q \tag{3}$$

$A_{2,-k}^{Q,LAB}$ are written in terms of $A_{2,-k}^{Q,PAS}$ using the proper Wigner rotation matrix elements:

$$A_{2,-k}^{Q,LAB} = \sum_{n=-2}^{2} D_{n,k}^2 \, (\alpha, \beta, \gamma) \, A_{2,k}^{Q,PAS} \tag{4}$$

where α, β and γ are the Euler angles defining the orientation of the principal axis system (PAS) of the EFG tensor in the laboratory frame and $A_{2,k}^{Q,PAS}$ are given by:

$$A_{2,0}^{Q,PAS} = \sqrt{\frac{3}{2}}\, eq$$

$$A_{2,\pm 1}^{Q,PAS} = 0$$

$$A_{2,\pm 2}^{Q,PAS} = \frac{1}{2}\, eq\eta_Q$$

$T_{2,k}^Q$ are the irreducible spherical tensor operators for the quadrupole interaction given by

$$T_{2,0}^Q = \frac{1}{\sqrt{6}}\,(3\hat{I}_z^2 - \hat{I}^2)$$

$$T_{2,\pm 1}^Q = \mp\frac{1}{2}\,(\hat{I}_z\hat{I}_{\mp} - \hat{I}_{\mp}\hat{I}_z)$$

$$T_{2,\pm 2}^Q = \frac{1}{2}\,\hat{I}_{\pm}^2$$

When the Zeeman interaction is dominant, the contribution of the quadrupole Hamiltonian to the energy of the spin states may be calculated using perturbation theory. Corrections up to second order are generally needed, causing an energy splitting of less than one tenth of the Zeeman splitting. In the following, we discuss separately the first- and second-order energy corrections to the Zeeman levels, caused by the quadrupole coupling of half-integer quadrupolar nuclei.

In the laboratory frame, the first-order secular quadrupolar Hamiltonian (term with k=0 in Eq. 3 is

$$\hat{\mathcal{H}}^{Q(I)} = \frac{e^2qQ}{2I(2I-1)}\, T_{2,0}^Q \left[\sqrt{\frac{3}{2}}\, D_{0,0}^2 + \frac{1}{2}\,\eta_Q\,(D_{2,0}^2 + D_{-2,0}^2) \right] \tag{5}$$

where the elements of the Wigner rotation matrix $D_{K,0}^2$ may be expressed in terms of the orientation of the principal axis system in the laboratory frame. The Hamiltonian becomes

$$\hat{\mathcal{H}}^{Q(I)} = \hbar\frac{\omega_Q}{12}\,(3\cos^2\beta - 1 + \eta_Q \sin^2\beta \cos 2\alpha)\,(3\hat{I}_z^2 - \hat{I}^2) \tag{6}$$

In Eq. (6) ω_Q is the quadrupolar frequency (in units of rad·s^{-1}):

$$\omega_Q = 2\pi\nu_Q = \frac{3C_Q}{[2I(2I-1)]} \tag{7}$$

Because it simplifies equations, the use of ω_Q (or ν_Q, in Hz) is often preferred over C_Q. Moreover, the quadrupolar frequency describes well the actual

strength of the quadrupolar interaction. The energy correction due to first-order quadrupole interaction is, therefore

$$E_m^{Q(l)} = \hbar \frac{\omega_Q}{12} (3\cos^2\beta - 1 + \eta_Q \sin^2\beta \cos 2\alpha)(3m^2 - I(I+1)) \qquad (8)$$

and the correction to the transition frequency between two levels m and m' is

$$\omega_{m,m'}^{Q(l)} = \frac{\omega_Q}{2} (3\cos^2\beta - 1 + \eta_Q \sin^2\beta \cos 2\alpha)(m'^2 - m^2) \qquad (9)$$

An important conclusion drawn from this equation is that the first-order quadrupolar interaction has no effect on symmetric transitions, namely on the single-quantum central transition ($m=1/2 \leftrightarrow m'=-1/2$) and multiple-quantum transitions ($m=3/2 \leftrightarrow m'=-3/2$, ($m=5/2 \leftrightarrow m'=-5/2$,...). The first-order quadrupolar interaction affects the satellite transitions, $m=\pm 1/2 \leftrightarrow m'=\pm 3/2$... (Fig. 1).

The second-order quadrupolar Hamiltonian in the laboratory frame (terms with $k=\pm 1$ and $k=\pm 2$ in Eq. (3) is

$$\hat{\mathcal{H}}^{Q(2)} = -\hbar \frac{\omega_Q^2}{32\omega_0} \hat{I}_z [(4\hat{I}^2 - 8\hat{I}_z^2 - 1)|f_1|^2 + (2\hat{I}^2 - 2\hat{I}_z^2 - 1)|f_2|^2] \qquad (10)$$

where $f_k = \sqrt{\dfrac{3}{2}} D_{0,k}^2 + \dfrac{1}{2} \eta_Q (D_{2,k}^2 + D_{-2,k}^2)$. This corresponds to the energy correction [3].

$$E^{Q(2)} = \hbar \frac{\omega_Q^2}{32\omega_0} m [(4I(I+1) - 8m^2 - 1)|f_1|^2 + (2I(I+1) - 2m^2 - 1)|f_2|^2] \qquad (11)$$
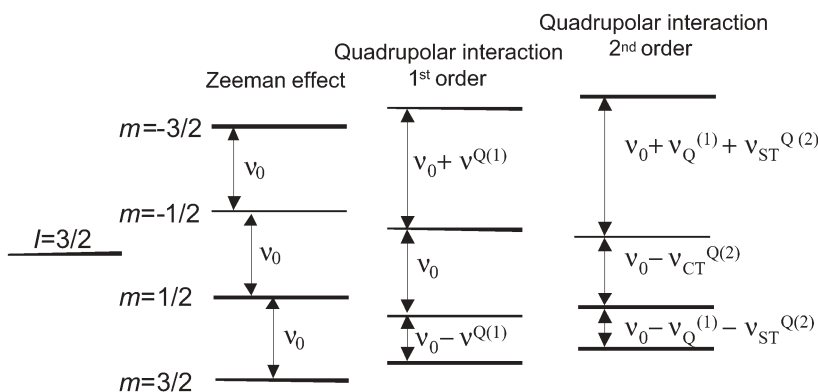
Fig. 1 Energy diagram for a spin–3/2 nucleus

The frequency splitting due to the second-order quadrupolar interaction may be obtained from this equation for consecutive ($m'=m+1$) or anti-symmetric ($m'=-m$) transitions [4]:

$$\omega^{Q(2)}_{m,m+1} = \frac{\omega^2_Q}{18\omega_Q}\left[\begin{array}{l}(4I(I+1)-24m(m+1)-9)|f_1|^2\\ \qquad\qquad\qquad +(2I(I+1)-6m(m+1)-3|f_2|^2\end{array}\right] \qquad (12)$$

$$\omega^{Q(2)}_{m,-m} = \frac{\omega^2_Q}{18\omega_Q}\, m\,[(4I(I+1)-8m^2-1)|f_1|^2 + (2I(I+1)-2m^2-1)|f_2|^2] \qquad (13)$$

In particular, for the central transition the frequency splitting is

$$\omega^{Q(I)}_{-1/2,1/2} = \frac{\omega^2_Q}{9\omega_Q}\left(I(I+1)-\frac{3}{4}\right)\left[|f_1|^2+\frac{|f_1|^2}{2}\right] \qquad (14)$$

which, for $\eta_Q=0$, reduces to

$$\omega^{Q(I)}_{-1/2,1/2} = \frac{\omega^2_Q}{16\omega_Q}\left(I(I+1)-\frac{3}{4}\right)(1-\cos^2\beta)(9\cos^2\beta-1) \qquad (15)$$

The $|f_k|^2$ terms in the above equations contain products of the Wigner matrix elements and thus may be expressed as a linear arrangement (up to the fourth order) of Wigner matrices [5]. The frequency splitting due to the second-order quadrupolar interaction may be written as a sum of three terms:

$$\omega^{Q(2)}_{m,m'} = \frac{\omega^2_Q}{9\omega_Q}\sum_{k=0,2,4}\sum_{n=-k}^{k} A^{2k}(I,m,m')\, B^{2k}_{2n}(\eta_Q)\, D^{2k}_{2n,0}(\alpha,\beta,\gamma) \qquad (16)$$

where $D^{2k}_{2n,0}(\alpha,\beta,\gamma)$ are the Wigner matrices giving the orientation dependence, and the functions $A^{2k}(I,m)$ and $B^{2k}_{2n}(\eta_Q)$ may be deduced from Eqs. (15) and (16), respectively, for consecutive and symmetrical transitions [5].

Equation (16) is very important because it uncovers two central ideas. First, the second-order frequency splitting depends inversely on the Larmor frequency, thus the importance of this term diminishes with increasing external magnetic field strength. Second, the k=0 term has no orientation dependence ($D^0_{0,0}=1$) or, in other words, it is an isotropic term. This means that the isotropic shift observed in the NMR spectrum of a quadrupolar nucleus has, in addition to the usual isotropic chemical shift, a contribution from the quadrupole coupling, which is given by

$$\omega^{Q(2)}_{m,m+1} = \frac{\omega^2_Q}{30\omega_Q}\left(1+\frac{\eta^2_Q}{3}\right)[I(I+1)-3-9m(m-1)] \qquad (17)$$

2.2
Effect of rf Pulses on Quadrupolar Nuclei

In general, the interaction of a nucleus with the rf field is much larger than the internal interactions which may thus be neglected. This means that each nuclear spin behaves as an isolated spin system. However, the first-order quadrupolar interaction is often larger than the interaction of the nuclei with the rf field and can not be neglected during the pulse. For quadrupolar nuclei, during the pulse, one must include in the Hamiltonian the term corresponding to the first- (and sometimes the second-) order quadrupolar interaction, in addition to the Zeeman and the rf terms [6–9].

Applying the rf pulse at a frequency ω_{rf} near the Larmor frequency, only the central transition, which is unaffected by the first-order quadrupolar interaction, is effectively irradiated. The satellite transitions, which are moved away from the Larmor frequency by $\omega^{Q(1)}$ due to the first-order quadrupolar interaction, are well off-resonance. Thus, in general, an additional term accounting for this offset must be considered. In the rotating frame, the Hamiltonian during the pulse is

$$\hat{\mathcal{H}}^{pulse} = \hat{\mathcal{H}}^{rf} + \hat{\mathcal{H}}^{offset} + \hat{\mathcal{H}}^{Q(1)} \tag{18}$$

where $\hat{\mathcal{H}}^{rf}(t) = \hbar\omega_1 (\hat{I}_x\cos\varphi_p + \hat{I}_x\sin\varphi_p)$ (ω_1 and φ_p are, respectively, the rf pulse field amplitude and phase), $\hat{\mathcal{H}}^{offset} = (\omega_1 - \omega_1)\hat{I}_x$ and

$$\hat{\mathcal{H}}^{Q(1)} = \hbar\omega'_Q [3\hat{I}_z^2 - \hat{I}^2], \text{ with } \omega'_Q = \frac{\omega_Q}{12} (3\cos^2\beta - 1 + \eta_Q \sin^2\beta \cos2\alpha) \tag{19}$$

In order to determine the effects of rf pulses on quadrupolar nuclei, this Hamiltonian is used to calculate the density matrix describing the spin system at a time τ after the beginning of the pulse. Such calculation is complex, time consuming and, in some cases, no analytical solution is available. Thus, in general, numerical calculations are performed. The central-transition signal intensity of spin $I=3/2$ and $5/2$ nuclei as a function of the pulse flip angle, for different values of ω_Q/ω_1, is shown in Fig. 2 (numerical calculations were performed with programme PULSAR [10]). Satellite transitions display similar behaviour but with different signal amplitudes and frequencies.

Under rf irradiation, the general behaviour of quadrupolar nuclei may be summarised by considering the following three cases:

1. If $\omega_1 >> \omega_Q$, all transitions are effectively on resonance, and the offset and quadrupole terms need not be considered (non-selective excitation). This is similar to an isolated spin-1/2 nucleus: the evolution of each transition as a function of τ is sinusoidal, with frequency ω_1.
2. If $\omega_Q >> \omega_1$, selective excitation of the on-resonance transition occurs. No irradiation of the other transitions is assumed so that only the on-resonance transition (m, $m+1$) is considered, as if these were the only two spin levels
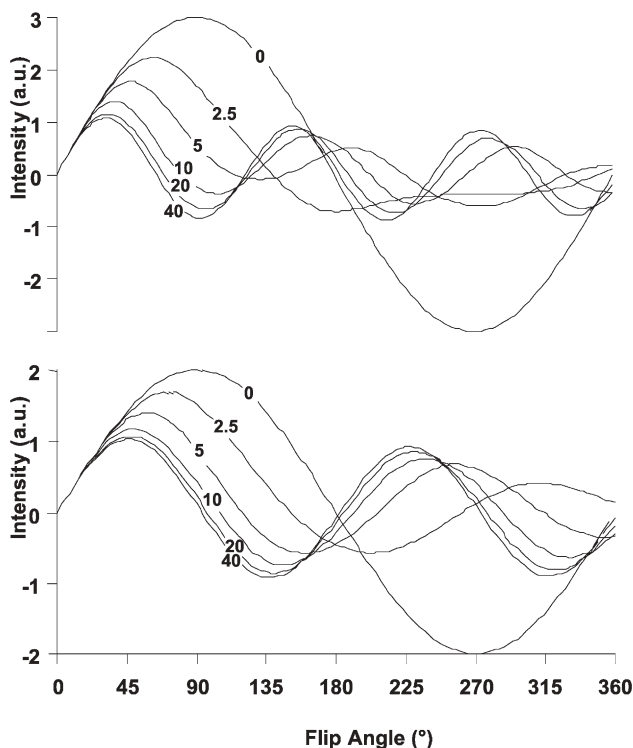
Fig. 2 Signal intensity of the central transition of spins $I=3/2$ (*bottom*) and $I=5/2$ (*top*) under rf irradiation for different values of ω_Q/ω_1

present. The corresponding fictitious spin operator is used to calculate its evolution as a function of the flip angle [11, 12]. It may be shown that this evolution is sinusoidal, with frequency $\sqrt{[I(I+1) - m(m+1)]}\,\omega_1$ [6, 8, 9]. In particular, for the central transition ($m=-1/2$) the pulse length corresponding to the maximum signal intensity ('solid' or selective $\pi/2$-pulse) is shorter than the non-selective pulse length (non-selective $\pi/2$-pulse):

$$\left(\frac{\pi}{2}\right)_s = \frac{1}{(I+1/2)}\left(\frac{\eta}{2}\right)_{ns} \tag{20}$$

3. If $\omega_Q \approx \omega_1$, the degree of excitation depends on ω_1, ω_Q and on the molecular orientation in the applied field. In a powdered sample, nuclei in equivalent sites but different crystallites may be excited differently, resulting in distorted powder patterns and in intensities that are not proportional to the number of nuclear spins corresponding to the different sites. The evolution of the system is not periodic and in this case it is possible to excite multiple-quantum coherences with a single pulse. The rf excitation becomes less de-

pendent on ω_Q as the length of the pulse decreases and its amplitude increases. It has been shown that hard pulses shorter than $\pi_I/[2(2I+1)]$, provide nearly homogeneous excitation of all the quadrupolar nuclei in a powder sample and, hence, they are normally used.

2.3
Magic-Angle Spinning

The Magic-Angle Spinning (MAS) technique consists of rotating a sample around an axis inclined at an angle $\chi_m=54.74°$ with respect to the external magnetic field. It is used routinely in the majority of solid-state NMR experiments to remove chemical shift anisotropy and heteronuclear dipolar-coupling effects. MAS also narrows the spectral lines of quadrupolar nuclei and at, very high spinning speeds, may average out the (e.g. ^1H-^1H) homonuclear dipolar coupling.

Under MAS conditions, the description of a spin interaction in the laboratory frame requires two consecutive frame transformations. First, the $A^{\lambda}_{L,k}$ components of the spherical tensors giving the orientation dependence of the interaction are transformed from the principal axis system of the interaction into the rotor frame with the appropriate Wigner matrix $D(\alpha^{\gamma}_r, \beta^{\gamma}_r, \gamma^{\gamma}_r)$, where the angles $(\alpha^{\gamma}_r, \beta^{\gamma}_r, \gamma^{\gamma}_r)$ describe the relative orientation of the rotor axis in the interaction PAS. Only then the transformation into the laboratory frame is performed using the Wigner matrix $D(\omega_r t, \chi_m, 0)$, where $\omega_r t$ is the phase angle experienced by the rotor while spinning at a frequency ω_r, and χ_m is the angle of the rotor axis with respect to the static field:

$$PAS \xrightarrow{D(\alpha^{\gamma}_r, \beta^{\gamma}_r, \gamma^{\gamma}_r)} \text{rotor frame} \xrightarrow{D(\omega_r t, \chi_m, 0)} \text{laboratory frame}$$

Therefore, the $A^{\lambda, LAB}_{L, k}$ components become

$$A^{\lambda, LAB}_{L, k} (t) = \sum_{k'=-L}^{L} D^L_{k',k} (\omega_r, t, \chi, 0) \sum_{p=-L}^{L} D^L_{p,k'} (\alpha^{\gamma}_r, \beta^{\gamma}_r) A^{\lambda, PAS}_{L, p} \qquad (21)$$

In the fast spinning limit, the time-dependent terms ($k' \neq 0$) of Eq. (21) are averaged to zero at the end of each rotation cycle and the $A^{\lambda, LAB}_{L, k}$ components may then be written as

$$A^{\lambda, LAB}_{L, k} = d^L_{0, k}(\chi) \sum_{p=-L}^{L} D^L_{p,k'} (\alpha^{\gamma}, \beta^{\gamma}) A^{\lambda, PAS}_{L, p} \qquad (22)$$

where $d^L_{0,k}(\chi)$ are the elements of the reduced Wigner matrices.

It may be shown that in these conditions the transition frequency between levels m and m' may be written as a sum of Legendre polynomials with ranks 0, 2 and 4, taking the following general form

$$\omega^\lambda_{m,m'} = X_0 P_0(\cos\chi) + X_2(\alpha^Y_r, \beta^Y_r)\, P_2(\cos\chi) + X_4(\alpha^Y_r, \beta^Y_r)\, P_4(\cos\chi) \tag{23}$$

where the X_L coefficients are functions specific of each interaction that depend (except for $L=0$) on the orientation of the crystallites in the rotor frame, and $P_L(\cos\chi)$ are the rank L Legendre polynomials:

$$
\begin{aligned}
P_0(\cos\chi) &= 1 \\
P_2(\cos\chi) &= \frac{1}{2}\,(3\cos^2\chi - 1) \\
P_4(\cos\chi) &= \frac{1}{8}\,(35\cos^4\chi - 30\cos^2\chi + 3)
\end{aligned}
\tag{24}
$$

For first-order interactions (dipole-dipole coupling, chemical shift anisotropy, first-order quadrupolar interaction) the expansion in Eq. (23) contains only the zero- and second-rank terms. As shown in Fig. 3, the Legendre polynomial of rank 2 is zero at the magic angle ($P_2(\cos\chi_m)=0$ for $\chi_m=54.74°$). Therefore, under MAS, and provided that the spinning rate is larger than the anisotropic linewidth, the anisotropic terms of the first-order interactions are averaged to zero and isotropic spectra are obtained.

For the second-order quadrupolar interaction the fourth-rank term must be considered. As can easily be concluded from Fig. 3, there are no common roots for the $P_2(\cos\chi)$ and $P_4(\cos\chi)$ Legendre polynomials. Spinning at the magic angle $\chi_m=54.74°$ will zero the $P_2(\cos\chi)$ term but will always leave behind the anisotropic contribution from the $P_4(\cos\chi)$ term, which has roots 30.56° and
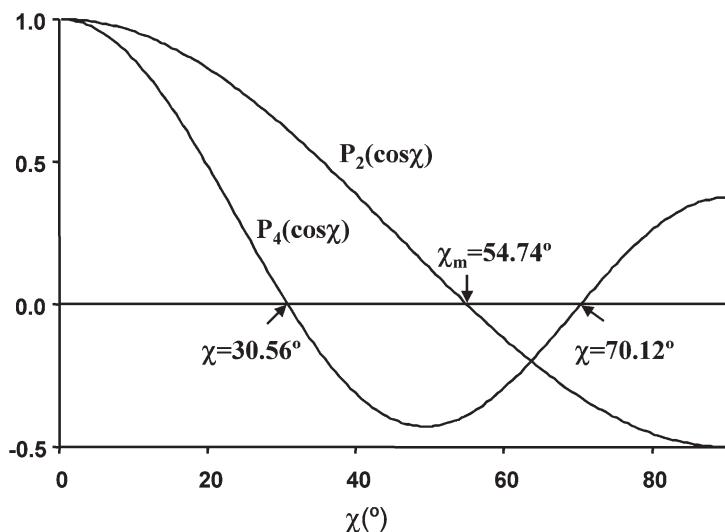
Fig. 3 Legendre polynomials as a function of χ, the angle between the rotor axis and the applied magnetic field

70.12°. Therefore, an anisotropic powder pattern (sharper than the static sample pattern by a factor ca. 3) remains, even under conditions of very rapid MAS.

3
The Multiple-Quantum MAS Experiment

Because no value of χ satisfies simultaneously the condition $P_2(cos\chi)=P_4(cos\chi)=0$ it is not possible to obtain high-resolution spectra of quadrupolar nuclei in a standard single-pulse experiment using a fixed rotation axis. In consequence, line-narrowing methods must accomplish more complex manipulations of the spatial or spin parts of the Hamiltonian. The two experimental approaches which achieved, for the first time, complete removal of the anisotropic part of the second-order quadrupole interaction, providing isotropic spectra of half-integer quadrupole nuclei, were double rotation (DOR) [13] and dynamic angle spinning (DAS) [14, 15]. In the one-dimensional DOR technique, the sample is spun about two axes simultaneously, one inclined at the magic angle (54.74°) with respect to the external magnetic field, the other at either 30.56° or 70.12° to the first angle. In the two-dimensional dynamic angle spinning (DAS) experiment the sample is spun sequentially about two different angles (e.g. 37.38° and 79.19°) to the external magnetic field for equal periods of time, with the magnetisation stored by a z-filter pulse sequence during the angle-switching period. DOR and DAS require dedicated NMR probes and their implementation still poses technical problems. In DAS much of the NMR signal may be lost in the angle-switching period when the sample longitudinal relaxation is fast (<150 ms, as is often the case for quadrupole nuclei). This technique is also limited in strongly dipolar-coupled systems, where spin exchange due to dipolar interactions, which cannot be eliminated during the relatively long flipping time of the rotor axis, has to be sufficiently small.

In 1995 Frydman and Harwood proposed a revolutionary new two-dimensional NMR technique known as Multiple-Quantum Magic-Angle Spinning (MQMAS) [16]. In this experiment, narrowing of the central transition is achieved by correlation of the phase evolutions of the symmetric multiple-quantum (MQ) and single-quantum (1Q) transitions under MAS. It only requires a conventional MAS NMR probe and its practical implementation is relatively straightforward. The experiment has become quite widespread and has enabled new applications to a variety of nuclei possessing different spin quantum numbers and coupling environments such as ^{23}Na, ^{27}Al, ^{87}Rb, ^{17}O and ^{93}Nb.

3.1
Principle

MQMAS is a two-dimensional solid-state NMR experiment, which affords high-resolution central transition spectra of half-integer quadrupolar nuclei by using both spin and spatial manipulations of the broadening interactions. MAS

performs the spatial averaging and removes the chemical shift anisotropy, the heteronuclear dipolar interactions and the second-rank elements of the first- and second-order quadrupolar interactions. The rf pulses are used to manipulate the spin part and average out the fourth-rank elements of the second-order quadrupolar Hamiltonian.

For symmetric transitions ($p/2 \rightarrow -p/2$, $p=2m$) the static evolution phase can be written as [1b]

$$\phi^{static}_{p/2,-p/2} = \{p[\nu_0\Delta\delta + m_s J + F(\alpha,\beta)]\} + \sum_{k=0,2,4} A^Q_k(\alpha,\beta,\eta Q) \, C_k(I,p)\}t \qquad (25)$$

where $\Delta\delta$ is the resonance offset (in ppm), J the scalar coupling between spin I and spin S with magnetic quantum number m_s, $F(\alpha,\beta)$ accounts for chemical shift and J-coupling anisotropies and heteronuclear dipolar couplings, and the angles α and β describe the direction of the laboratory frame in the PAS of the EFG tensor. $C_k(I,m)$ are zero-, second- and fourth-rank spin coefficients depending on the spin and magnetic quantum numbers:

$$\begin{aligned} C_0(I,m) &= 2m\,[I(I+1) - 3m^2) \\ C_2(I,m) &= 2m\,[8I(I+1) - 12m^2 - 3) \\ C_4(I,m) &= 2m\,[18I(I+1) - 34m^2 - 5) \end{aligned} \qquad (26)$$

Under fast MAS [$P_2(\cos\chi_m)=0$] and neglecting the scalar coupling term, the evolution phase of a symmetric coherence reduces to

$$\phi^{static}_{p/2,-p/2} = \{p[\nu_0\Delta\delta) + A^Q_0(\eta_Q)\,C_0(I,p) + A^Q_4(\alpha_R,\beta_R,\eta_Q)\,C_4(I,p)\,P_4(\cos\chi_m)\}\,t \qquad (27)$$

where the polar angles α_R and β_R describe the orientation of the rotor axis with respect to the PAS of the EFG tensor. The remaining anisotropic broadening arises from the last term, which is scaled with respect to the static case but not completely eliminated by MAS. In order to obtain an isotropic spectrum, this term should be averaged to zero. In the two-dimensional MQ MAS experiment, this is done by manipulating the spin coherences so that

$$C_4(I,p)\,t_1 + C_0(I,p)\,t_2 = 8 \qquad (28)$$

where p_1 and p_2 are the order of the coherences evolving, respectively, during t_1 and t_2.

With $p_2=-1$ (the coherence evolving during t_2 is the observable single-quantum coherence) the anisotropic second-order quadrupolar broadening is averaged out when the ratio of the times t_1 and t_2 spent on quantum levels pQ and $-1Q$, respectively, fulfils the condition

$$t_2 = -\frac{C_4(I,p)}{C_4(I,-1)}\,t_1 = p\,\frac{36I(I+1) - 17p^2 - 10}{36I(I+1) - 27}\,t_1 = R(I,p)\,t_1 \qquad (29)$$

Table 1 Numerical values of the ratio $|R(I, p)|$

$|p|$	3	5	7	9
$I=3/2$	7/9			
$I=5/2$	19/12	25/12		
$I=7/2$	101/45	11/9	161/45	
$I=9/2$	91/36	95/36	7/18	31/6

Since Eq. (29) is orientation independent, all crystallites are refocused at the same time $t_{2e}=R(I,p)t_1$, giving rise to an isotropic echo. After a double Fourier transform in t_2 and t_1, the NMR resonances appear along the anisotropic axis A with direction $\nu_1=R(I,p)\nu_2$, where ν_2 and ν_1 are the single- and multiple-quantum dimensions frequencies, respectively. The projection of the spectrum onto an axis perpendicular to A yields an isotropic, highly resolved, spectrum.

As the sign of $C_4(I,p)$ is reversed when changing the sign of p (Eqs. 26 and 29), it is always possible to obtain a positive ratio $R(I,p)$, which corresponds to a detectable echo at a positive acquisition time t_{2e}. A signal arising from a negative value of $R(I,p)$ is called an antiecho and it refocus at negative values of the acquisition time. Numerical values of the ratio $R(I,p)$ are given in Table 1 for relevant I and p values [17].

In principle, any coherence order can be used, keeping in mind that the detection must be performed on the single-quantum coherences. Recently, Jerschow et al. showed that, for half-integer quadrupolar nuclei with spin $I>3/2$, higher-order coherences may be correlated with each other provided an additional detection pulse is employed at the end of the sequence [18]. While experiments correlating MQ and SQ coherences are named MQMAS, techniques correlating different multiple-quantum coherences are named MQ/NQMAS, where M and N are the coherence orders evolving during t_1 and t_2, respectively. The values of the ratio $R(I,p)$ for the MQ/NQ MAS experiments can be easily obtained using the $C_4(I,m)$ coefficients given in Eq. (26).

3.2
Acquisition Schemes

In the first MQMAS pulse sequence proposed by Frydman and Harwood, excitation of the multiple-quantum coherences was accomplished using two pulses separated by a time delay of the order of the quadrupolar splitting [14]. Based on the work of Vega and Naor [19], several authors [20–23] suggested excitation of multiple-quantum coherences with a single pulse. The resulting MQMAS sequence, shown in Fig. 4 for $I=3/2$, consists of two short and powerful radio-frequency pulses separated by a delay t_1, which is incremented. The first pulse excites all possible MQ coherences, and the desired symmetric MQ coherence with the quantum level pQ is chosen by appropriate phase cycling. After evolving during time t_1, the selected symmetric MQ coherence is converted,
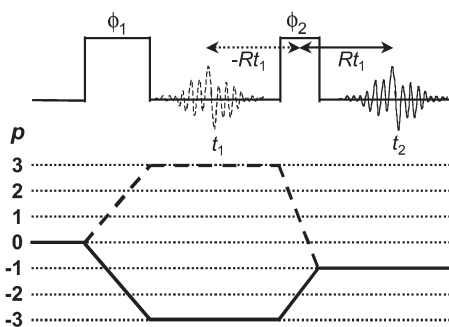
Fig. 4 Schematic diagram of the two-pulse 3QMAS NMR experiment (*top*) and coherence pathways (*bottom*). Isotropic echoes form at time $t_2=R(I,p)t_1$. ϕ_1 and ϕ_2 are the phases of the first and second pulses

by the second pulse, into single-quantum coherence and observed during the acquisition time t_2. The flip angles of the first and second pulse must be optimised to yield the highest signal amplitude. The result depends on the nuclear spin I, Larmor frequency, chosen coherence order (pQ) and ratio between the amplitude of the rf field and the quadrupolar frequency.

As stated before, the sign of the ratio $R(I,p)$ determines the sign of the triple-quantum level necessary to refocus the second-order broadening and form an isotropic echo. For spin $I=3/2$ nuclei the echo pathway corresponds to the correlation of $p=-3$ and $p=-1$ coherences (solid line in Fig. 4) whereas for spins $I=5/2, 7/2, 9/2$ the echo pathway corresponds to the correlation of $p=3$ and $p=-1$ coherences (dashed line in Fig. 4). For the antiecho pathway, for which the anisotropic broadening is refocused at negative values of the acquisition time t_2, the assignments are reversed.

If the phase cycling used selects only one coherence transfer pathway, a two-dimensional spectrum with "phase-twist" lineshapes is obtained. However, the experiment can be easily modified to ensure that pure absorption (pure phase) lineshapes are obtained. The most commonly used modified acquisition schemes that allow pure-phase MQMAS spectra to be obtained include amplitude-modulated experiments, with hyper-complex (States) acquisition, and phase-modulated experiments, with delayed acquisition such as shifted echo or antiecho and split-t_1 methods.

3.2.1
Amplitude-Modulated Experiments

In this type of experiment, the echo and antiecho are linearly combined with the same amplitude to yield an amplitude-modulated signal in t_1. Pure absorption lineshapes may then be obtained in the frequency domain spectrum after a two-dimensional Fourier transform is performed. The disadvantage of this method is that it is not possible to discriminate the sign of the MQ coher-

ences evolving in t_1. Sign discrimination can be restored using the States (or TPPI) method, which involves performing two consecutive experiments, phase shifting the first pulse by 90°/p, where p is the order of the coherence evolving during t_1.

3.2.1.1
Two-Pulse Experiments

An important shortcoming of the two-pulse methods is the difficulty of balancing the echo and antiecho amplitudes to obtain undistorted two-dimensional lineshapes, especially for nuclei with spin larger than 3/2. The two coherence-transfer pathways being different, it has been shown that their amplitude depends on the quadrupole coupling and the orientation of the crystallites. In a powder, it is nearly impossible to reach a perfect equalisation of these amplitudes.

3.2.1.2
Z-Filter Experiments

To overcome these difficulties, the z-filter experiment was adapted to MQMAS by Amoureux et al. [24]. In this three-pulse scheme the two hard pulses (excitation of the MQ coherences and conversion into 0Q coherence) are followed by a short delay during which the magnetisation is stored along the z-axis as zero-quantum coherences and then transferred into observable 1Q coherences using a selective π/2 pulse (Fig. 5a). The symmetrisation of the echo and antiecho pathways during the two hard pulses (p=0→±3→0) forces an equal intensity of the echo and antiecho signals, leading to amplitude-modulated FIDs and, thus, to pure absorption spectra. This is a robust method, easy to optimise.

3.2.2
Phase-Modulated Experiments

3.2.2.1
Shifted-Echo or Antiecho Methods

These methods use the properties of evenness and oddness of the time-domain signals and their Fourier transforms to eliminate the dispersive components from the two-dimensional NMR spectrum. In the MQMAS shifted-echo experiment a refocusing π pulse is introduced at the end of the pulse sequence, in order to delay the formation of the echo (or antiecho) in the t_2 domain by a time τ. The corresponding pulse sequence and coherence transfer pathway diagram are shown in Fig. 5b. The delay τ must be long enough to avoid truncation of the signal at any t_1 value (whole-echo acquisition). Even though the time-domain signal is phase-modulated, as in the original experiment proposed by Frydman and Harwood, a complex two-dimensional Fourier transform leads
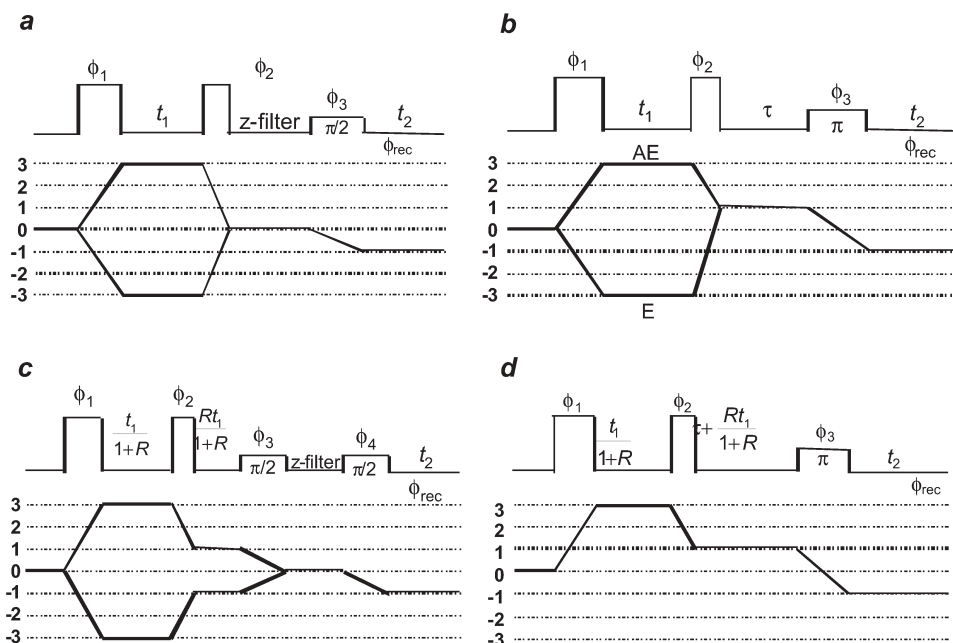
Fig. 5a–d Pulse sequences and coherence transfer pathways for 3QMAS NMR experiments: **a** amplitude-modulated z-filter acquisition scheme; **b** phase-modulated shifted-echo experiment for spin $I=3/2$; E and AE represent the echo and antiecho pathways. Split-t_1: **c** z-filter; **d** shifted-echo acquisition schemes for spin $I=3/2$. ϕ_n represents the phase of pulse n

to a pure-phase spectrum, provided relaxation effects are negligible. Experimentally, since the echo forms at $t_{2e}=\tau$, rather than $t_{2e}=0$, when $t_1=0$, a first-order phase correction must be applied in the F_2 dimension. Whole-echo acquisition was adapted to MQMAS by Massiot et al. [25]. The experiment can also be performed with the combination of the shifted-echo and shifted-antiecho experiments in order to increase the signal-to-noise ratio. An amplitude-modulated signal is obtained when the shifted echo and antiecho amplitudes are equal. However, because of the properties of whole echoes, a hypercomplex two-dimensional Fourier transform still affords pure absorption lineshapes, even when the contributions of the two pathways are not equal.

3.2.2.2
Split-t_1 Experiments

As stated above, the second-order broadened ridges appear in the two-dimensional MQMAS spectrum along the anisotropic axis A with direction $v_1=R(I,p)v_2$. Therefore, the projection of the two-dimensional spectrum onto the v_1 axis (F_1) does not yield an isotropic spectrum. In order to obtain a two-dimensional spectrum with an isotropic projection a shearing operation has to

be performed. An interesting alternative experiment, which avoids the need for using this shearing transformation, is the MQMAS split-t_1 method introduced by Brown et al. [26], which splits t_1 into 1Q and MQ evolution periods in the proportion $R(I,p)$, refocusing the second-order anisotropic broadening at the end of the t_1 period. After a two-dimensional Fourier transform the anisotropic axis A appears parallel to the ν_2 axis (F_2). This method may be combined with the z-filter or shifted-echo (whole-echo) schemes shown Fig. 5c,d, respectively, for 3Q MAS experiments on spin–3/2 nuclei [27]. These schemes may be easily extended to spins 5/2, 7/2 and 9/2 [28]. The four-pulse z-filter split-t_1 experiment is less efficient than the three-pulse shifted-echo split-t_1 experiment. Indeed, the latter is probably the most efficient MQMAS scheme for spin–3/2 nuclei, in which the loss of magnetisation due to T_2 effects is minor.

3.3
Analysis of MQMAS NMR Spectra

A major advantage of MQAS is that it allows separation and measurement of the isotropic chemical shifts and quadrupolar-induced shifts by recording and analysing a single two-dimensional spectrum. Determination of quadrupole parameters and relative site populations are also possible, even for disordered and amorphous materials. In the present section we address these problems.

3.3.1
Sheared and Unsheared Spectra

Figure 6b shows the *unsheared* 3Q MAS NMR spectrum of zeolite scolecite (which contains two non-equivalent four-coordinated Al sites) acquired with the three-pulse z-filter sequence.

To assist the analysis of the spectrum, this figure also depicts the chemical shift (CS) axis, the anisotropic (A) axis and the quadrupolar-induced shift (QIS) axis. The slope of the CS axis is –p and 1, when scales are in Hz or in ppm, respectively. Axis A is defined by the orientation of the anisotropic ridges in the spectrum and has slope $R(I,p)$. The centre of gravity of a given resonance is shifted from the CS axis, in both dimensions, by the QIS. This shift occurs in the direction of the QIS axis, which has a slope ξ given by [17]

$$\xi(I,p) = -p\,\frac{4I(I+1) - 3p^2}{4I(I+1) - 3} \tag{30}$$

Because for a given (I,p) pair the induced quadrupolar shifts have a unique sign, all observed signals (except the spinning sidebands) appear on the same side of the CS axis. Using the values of R and ξ, which are given for all I and p values in Tables 1 and 2 [29], it is possible to estimate directly from the MQMAS spectrum the isotropic Chemical Shift δ_{CS} and the second-order quadrupolar effect parameter (SOQE) of the NMR peaks.

Table 2 Numerical values of ξ factors used in MQMAS spectral analysis

$|p|$	3	5	7	9
$I=3/2$	−3			
$I=5/2$	3/4	25/4		
$I=7/2$	9/5	−1	−49/5	
$I=9/2$	9/4	5/4	−5/2	−15/2

However, a practical inconvenience of the *unsheared* MQMAS NMR spectrum is that its projection onto F_1 is not isotropic. This is clearly shown in Fig. 6b where the F_1 projection does not resolve the two ^{27}Al NMR scolecite resonances. Hence, it is convenient to perform a shearing transformation on the MQMAS spectrum, which consists of the application of a linear phase correction in the mixed (t_1,ν_2) domain. This procedure makes the A axis parallel to F_2 and thus theprojection onto the newly defined δ_{iso} axis (F_{iso}) of the *sheared* spectrum is isotropic and highly resolved, as shown in Fig. 6c, while the F_2 projection provides the corresponding pQ-filtered MAS spectrum (which is essentially the 'conventional' (1Q) MAS NMR spectrum). The ppm scale in the F_{iso}
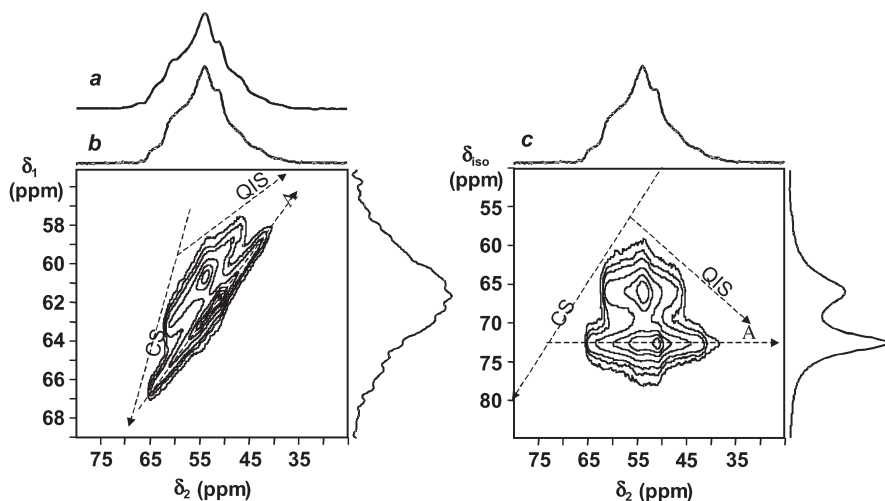
Fig. 6a–c ^{27}Al: **a** single-quantum; **b** unsheared; **c** sheared z-filter 3Q MAS spectra of zeolite scolecite recorded at 9.4 T. 'A', 'CS' and 'QIS' depict the anisotropic axis, chemical shift axis and quadrupolar-induced shift axis. Scolecite gives ^{27}Al NMR resonances S1 and S2 with: δ_{CS}=61.7 and 65.6 ppm, C_Q=3.25 and 4.33 MHz, η=0.80 and 0.70. The lengths of the first and second hard pulses were 3.6 μs and 1.1 μs (B_1=100 kHz). The soft pulse (B_1=5 kHz) length was 16 μs; 150 data points (96 transients per point) were acquired in the t_1 dimension in increments of $(1/\nu_r)$=80 μs. The ppm scale referenced to ν_0 in the F_2 domain and to 1.42 ν_0 and $p\nu_0$ for the sheared and the unsheared spectrum in the F_1 domain (reference aqueous Al(NO$_3$)$_3$)

dimension is now referred to R(I,p)–|p|ν_0. The isotropic chemical shift is now given by

$$\delta_{CS} \, (\text{ppm}) = \frac{10}{27} \, \delta_{G2} + \frac{17}{27} \, \delta_{iso} \tag{31}$$

where δ_{G2} and δ_{iso} are the centres of gravity of the resonance along F_2 and F_1. SOQE is given by

$$\text{SOQE}^2 = \frac{\delta_{G2} - \delta_{CS}}{k} \tag{32}$$

where

$$k = \frac{3}{10} \frac{4I(I+1) - 3}{[4I(2I-1) \, \nu_0]^2} \times 10^6 \tag{33}$$

Cross-sections of the different resonances taken along F_2 may be used to determine C_Q and η_Q.

As another example, Fig. 7 shows the ^{27}Al MAS and the sheared 3Q MAS NMR spectrum of microporous aluminophosphate AlPO-40. The MAS NMR spectrum displays two broad peaks ranging from ca. 45 to 25 ppm and from 25 to –10 ppm, showing several singularities. The resolution of the 3Q MAS NMR spectrum F_{iso} projection is amazing, exhibiting at least 12 peaks (although the full two-dimensional spectrum reveals the presence of 18 resonances). The quadrupole coupling parameters and the isotropic chemical shift of individual resonances may be obtained by simulating the cross-sections taken through each peak and parallel to F_2. Three examples are depicted in Fig. 7. Consider cross-section B taken at 29 ppm F_{iso}. While along F_2 this peak spans some 35 ppm, along F_{iso} its Full-Width-at-Half-Maximum (FWHM) is only ca. 3 ppm. This is because the resonance corresponds to an Al site with a relatively large quadrupolar-coupling constant, revealed by simulation to be 4.9 MHz (η=0.50). Cross-section A is narrower along F_2, corresponding to a smaller C_Q of 1.6 MHz (η=0.90).

3.3.2
Higher-Order MQMAS Experiments

Several authors have reported an enhancement of spectral resolution with the increase of the MQ coherence evolving during t_1 [30–32]. However, the excitation of higher-order coherences for $I>3/2$ spins is more difficult than the 3Q excitation and, therefore, higher-order MQMAS experiments suffer from low sensitivity. Moreover, it has been noticed that this enhancement in resolution is not uniform among different spin systems. Recent investigations have attributed these effects to the interplay between homogeneous and inhomogeneous con-
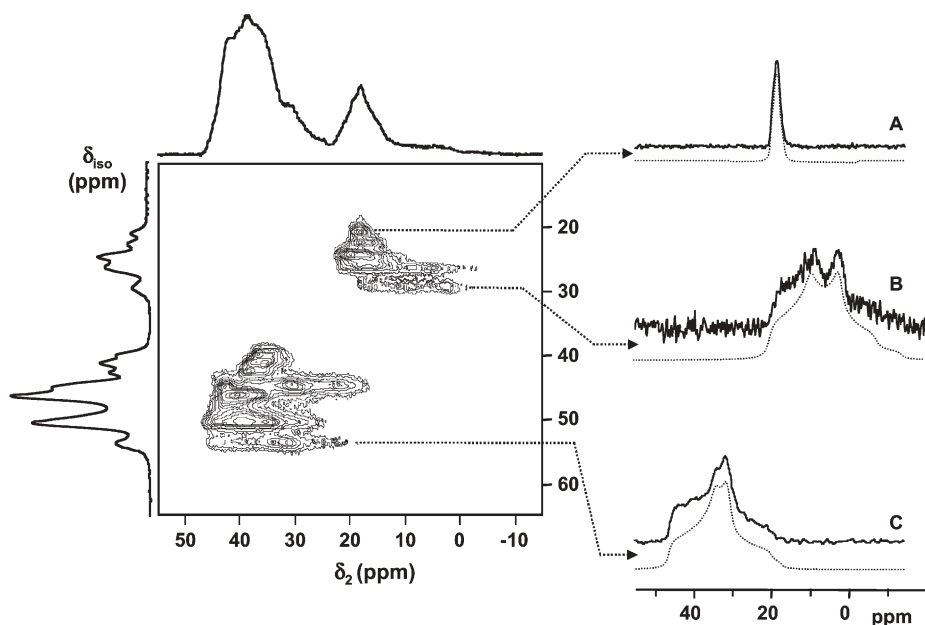
Fig. 7 Sheared ^{27}Al 3QMAS NMR spectrum of microporous aluminophosphate AlPO-40 recorded at 9.4 T. The lengths of the first and second hard pulses were 2.5 μs and 0.8 μs, (B_1=100 kHz). The soft pulse (B_1=10 kHz) length was 9 μs. 200 data points (240 transients per point) were acquired in the t_1 dimension in increments of $(1/v_r)$=80 μs. The recycle delay was 1.5 s. The ppm scale is referenced to v_0 in the F_2 domain and to 1.42 v_0 in the F_1 domain (reference aqueous Al(NO$_3$)$_3$). Experimental (*solid lines*) and simulated (*dashed lines*) cross-sections taken parallel to the F_2 axis for three selected resonances (A, B, C) are given on the right of the 2D spectrum. The following parameters were obtained from the simulations: cross-sections A (δ_{CS}=19.7 ppm, C_Q=1.6 MHz, η=0.60); B (δ_{CS}=20.7 ppm, C_Q=4.9 MHz, η=0.50); C (δ_{CS}=46.2 ppm, C_Q=4.3 MHz, η=0.80)

tributions to the isotropic linewidth [30, 31]. Inhomogeneous contributions, due to inhomogeneity of the static magnetic field, changes in magnetic susceptibility, heteronuclear dipolar coupling and second-order quadrupolar-dipolar couplings, scale in the same way as the dispersion of isotropic shifts vs *p*. However, the homogeneous contributions are not expected to increase with *p*, which should lead to the observed effect. Therefore, for well-crystallised samples with a strong homogeneous contribution to the linebroadening, considerable enhancement of the isotropic resolution should be observed in higher-order MQMAS experiments. As an example, Fig. 8 shows the 5QMAS spectrum of zeolite scolecite and compares the isotropic projections of the 3Q and 5Q MAS spectra. Clearly, the latter is better resolved and thus, despite lower signal intensity, it may be useful to record 5Q (or higher order MQ) MAS spectra. With amorphous samples, where the distribution of isotropic shifts dominates the spectra, this enhancement is less evident and the more sensitive 3QMAS experiment is recommended.
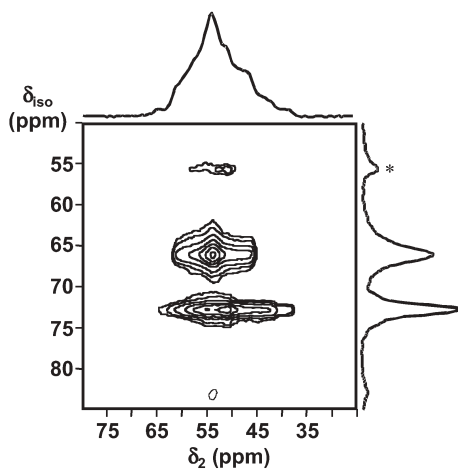
Fig. 8 a ^{27}Al z-filter 5QMAS NMR spectra of scolecite recorded at 9.4 T. The lengths of the first and second hard pulses were 4.1 μs and 1.05 μs (B_1=220 kHz). The soft pulse (B_1=5 kHz) length was 16 μs; 100 data points (880 transients per point) were acquired in the t_1 dimension in increments of ($1/4\nu_r$)=20 μs. The recycle delay was 1 s. The ppm scale is referenced to ν_0 in the F_2 domain and to 7.08 ν_0 in the F_1 domain (reference aqueous Al(NO$_3$)$_3$). **b** The isotropic projections of the 3Q spectra; **c** The isotropic projections of the 5Q MAS spectra. The *asterisk* depict spinning sideband

3.3.3
Distribution of Parameters: Amorphous and Disordered Materials

Although for highly crystalline solids, such as scolecite and AlPO-40, the MQ-MAS NMR resonances are, in general, very narrow along F_1, this is not the case for disordered or amorphous materials. Indeed, in the latter materials, distributions of bond angles and bond lengths are present, resulting in distributions of isotropic chemical shifts and quadrupole parameters, which may considerably broaden the lines along axes CS and QIS. The relatively poor resolution of the MQMAS NMR spectra of glasses and other amorphous materials is, therefore, not due to a limitation of the technique but is intrinsic to the material.

Figure 9 shows the schematic representations of Gaussian distributions of δ_{cs} and second-order quadrupolar effect parameters (SOQEs). A Gaussian distribution of chemical shifts results in Gaussian broadening along the isotropic and anisotropic dimensions. However, in the case of a Gaussian distribution of SOQEs, an asymmetrical broadening occurs because the intensities and widths of the individual spectra depend on the quadrupolar parameters. In most real cases the distributions of δ_{cs} and P_Q occur simultaneously, complicating the spectral analysis. Nevertheless, these distributions can be easily separated because the directions of the CS and QIS axes differ by approximately 75°.

Numerical analysis of MQMAS spectra permits the determination of the isotropic chemical shift and quadrupolar parameter distribution. The simula-

tion programme MASAI, which assumes that chemical shift and quadrupolar parameter distributions are independent, is able to perform this analysis [33]. It is further assumed that δ_{CS} is described by a Gaussian distribution:

$$\Pi_{CS}(\delta_{CS}) = \frac{1}{\sqrt{2\pi}\sigma_{CS}} \exp\left[-\frac{(\delta_{CS} - \langle\delta_{CS}\rangle)^2}{2\sigma_{CS}^2} \right] \tag{34}$$

where σ_{CS} is the variance of the chemical shift distribution around its average value $\langle\delta_{CS}\rangle$. The C_Q and η_Q distributions may be considered using Gaussian distributions or the more convenient two-dimensional probability uncorrelated Czjzek function, which depends on a single parameter σ_Q [34]:

$$\Pi_{CS}(C_Q, \eta_Q) = \frac{C_Q^4 \eta_Q}{\sqrt{2\pi}\sigma_{CS}^5} \left[1 - \frac{\eta_Q^9}{9} \right] \exp\left[-\frac{C_Q^2\left(1 + \frac{\eta_Q^2}{3}\right)}{2\sigma_{CS}^2} \right] \tag{35}$$

The three parameters (σ_{CS}, $\langle\delta_{CS}\rangle$, σ_Q) that describe the chemical shift and quadrupolar distributions are obtained by simulation of the experimental spectrum, which is described by a sum of individual two-dimensional spectra over all possible combinations of chemical shifts and quadrupolar parameters as follows:

$$S_e(\delta_{iso}, \delta_2) = \int_{-\infty}^{+\infty} \int_0^{+\infty} \int_0^1 S_c(\delta_{iso}, \delta_2, \delta_{CS}, C_Q, \eta_Q)\, \Pi(C_Q, \eta_Q) \cdot \tag{36}$$
$$\Pi(\delta_{CS}) \cdot d\delta_{CS} dC_Q d\eta_Q$$

where S_c is the calculated MQMAS spectrum corresponding to a single set of lineshape parameters. The probability function is then obtained by an iterative fit using a linear least square procedure to minimise the deviation between experimental and simulated spectra. One example of such spectral simulations is given in Fig. 9c.

3.3.4
Quantification

An outstanding problem in MQMAS NMR spectroscopy is the quantification of the different resonances present. In general, the intensity (area) of resonances is not representative of the actual concentrations of the chemical species because the excitation (and conversion) of multiple-quantum coherences is strongly dependent on the NMR quadrupole frequency, pulse lengths and rf field amplitude. The most accurate way to overcome this limitation consists of the simultaneous simulation of the quantitative single-quantum and the full two-dimensional MQ MAS NMR spectra using a program [33] that takes into account the efficiency of the MQMAS experiment as a function of the quadrupolar parameters (including distribution of quadrupole coupling pa-
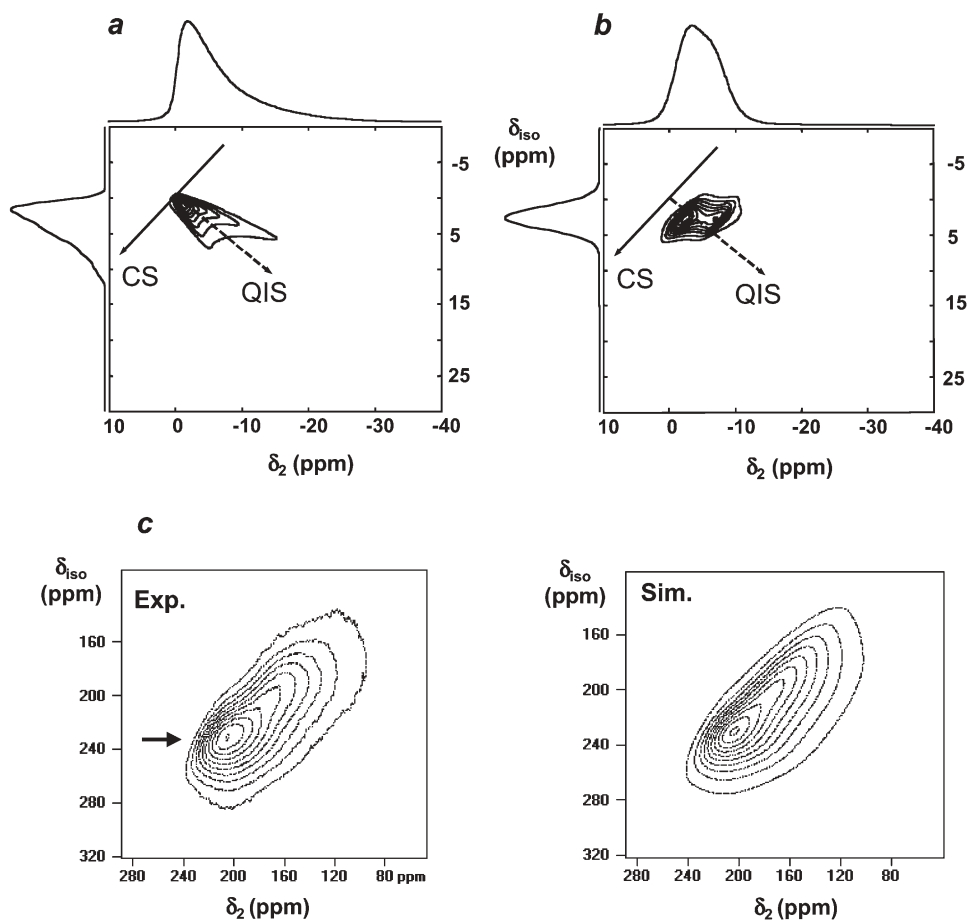
Fig. 9a–c Schematic representation of a Gaussian distribution of: **a** chemical shifts; **b** quadrupolar parameters; **c** experimental and simulated triple-quantum ^{93}Nb MAS NMR spectrum (9.4 T) of mixed lead and tin niobates, $Sn_{0.06}(II)Pb_{1.18}Nb_{1.66}Sn(IV)_{0.34}O_{6.07}$, revealing sites S1 and S2 on a 2:1 population ratio. Site 1 (Site2): δ_{CS}=221 (193) ppm, σ_{CS}=10.0 (30) ppm, C_Q=14.4 (17.8) MHz σ_{CS}=7.5 (9.3) MHz, asymmetry parameter η has been set to 0.65

rameters and isotropic chemical shifts, if present, see Fig. 9c). This is not, however, a trivial procedure and cannot be done routinely.

When a small number (say 2–4) of resonances are present in the MQMAS NMR spectrum and there is no (or little) distribution of parameters, it is possible to calculate the peak intensities in a simpler way. First, the (average) quadrupole parameters and isotropic chemical shift of each resonance are obtained by simulation of the F_2 cross-sections of the MQMAS spectrum. Then, these parameters are used to simulate the quantitative MAS NMR spectrum. This is a relatively straightforward procedure (particularly when the spectrum is partially resolved or displays singularities), which can be performed with
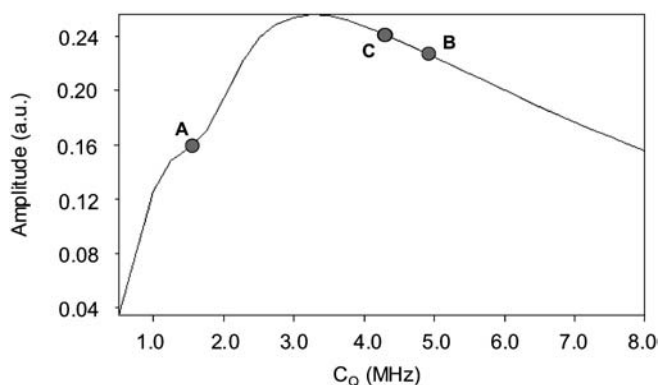
Fig. 10 Calculated efficiency of the z-filter MQMAS experiment as a function of the quadrupole coupling constant. Numerical calculations were performed using program PULSAR with the experimental conditions used to record the 3QMAS NMR spectrum of AlPO-40. Letters A–C refer to the cross-sections in Fig. 7

available (free) software. However, when a large number of resonances overlap, it may not be possible to calculate the relative intensities using this strategy. In this case, quantitative information may still be obtained from the MQMAS spectrum by calculating the efficiency of the MQMAS experiment as a function of the quadrupolar parameters previously obtained by simulation of the MQMAS spectrum F_2 cross sections. This can be done with programs PULSAR [35], GAMMA [36] or SIMPSON [37].

As an example of the latter strategy, consider again the AlPO-40 sites giving the A-C cross-sections in Fig. 7. With the quadrupole coupling parameters extracted from the cross-section simulations and taking into account the experimental conditions (described in the caption of Fig. 7) it is possible to calculate the efficiency of the 3QMAS experiment for the three Al sites and obtain the correct relative intensities (Fig. 10).

3.4
MQMAS Related Experiments

3.4.1
STMAS

MQMAS is a very robust technique widely used at present. However, in spite of considerable efforts in optimising the pulse sequence, MQMAS remains non-quantitative and suffers from low sensitivity, particularly when large quadrupole coupling constants are present. This is because coherences must be transferred between the observable and unobservable parts of the density matrix. Recently, Gan proposed an ingenious new technique, known as satellite transition (ST) MAS NMR, which affords nearly quantitative spectra (at least for a

large range of quadrupole coupling constants) [38, 39]. In this experiment, single-quantum satellite transitions (ST, $m=\pm1/2\leftrightarrow m=\pm3/2, m=\pm3/2\leftrightarrow m=\pm5/2$, etc.), rather than the symmetric multiple-quantum transitions (as in MQMAS), are correlated with the central transition (CT, $m=-1/2\leftrightarrow m=+1/2$) in a two-dimensional experiment performed under MAS. CT is inherently free from first-order quadrupolar broadening, while a combination of MAS and rotor-synchronised acquisition removes ST first-order broadening. Under MAS, the residual CT and ST second-order quadrupolar broadenings differ by a scale factor only and thus it is possible to refocus the second-order broadenings in a two-dimensional correlation experiment. The creation of isotropic echoes occurs, therefore, in a way similar to the MQMAS experiment, although with much higher efficiency because coherence transfers occur only in the 1Q levels.

3.4.1.1
Principle of STMAS

In the rotating frame, under fast MAS, the first-order and the second-rank second-order quadrupolar effects are averaged to zero. The evolution phase of single-quantum transitions, $m=\pm(n-1/2)\leftrightarrow m=\pm(n+1/2)$ ($n=0$ corresponds to the central transition (CT), $n=1$ to the inner satellite transition (ST$_1$), etc.) may then be written as [28]

$$\phi_n^{MAS} = \nu_0\Delta\delta + A_0^Q(\eta_0)\, C_0(I,n) + A_4^Q(\alpha_R, \beta_R, \eta_Q)\, C_4(I,n)\, P_4(\cos\chi_m) \tag{37}$$

where the polar angles α_R and β_R describe the orientation of the rotor axis with respect to the PAS of the quadrupolar interaction, $\Delta\delta$ represents the resonance offset (in ppm), χ_m is the magic angle and the functions A_L^Q and $C_L(I,n)$ have been given in [39]. Therefore, the correlation between ST (during t_1) and CT (during t_2) leads to an isotropic echo at

$$t_{2e} = \left|\frac{C_4(I,n)}{C_4(I,0)}\right| t_1 = \left|R^4(I,n)\right| t_1 \tag{38}$$

Numerical values of the ratios $R^4(I,n)$ are given in Table 3 for relevant I and n values. The coherence transfer pathway required for observing the echo is

Table 3 Numerical values of the ratio $R^4(I,n)$

	$n=1$	$n=2$	$n=3$	$n=4$
$I=3/2$	−8/9			
$I=5/2$	7/24	−11/6		
$I=7/2$	28/45	−23/45	−12/5	
$I=9/2$	55/72	1/18	−9/8	−25/9

($p=0\rightarrow-1\rightarrow-1$) or ($p=0\rightarrow+1\rightarrow-1$), for negative and positive values of the ratio $R^4(I,n)$, respectively. After a double Fourier transform in t_2 and t_1 each $ST_n\rightarrow CT$ narrow resonance ridge appears along the direction $v_1=|R_4(I,n)|v_2$ in the two-dimensional STMAS spectrum.

3.4.1.2
Experimental Considerations

Figure 11a shows the pulse sequence and coherence transfer pathways for two versions of the phase modulated two-pulse sequence proposed by Gan [38]. Phase cycling may be used to select the $p=+1$ (dashed line) or the $p=-1$ (solid line) pathways during the t_1 evolution period. The coherence transfer pathway ($0\rightarrow-1\rightarrow-1$) generates echoes for positive $R^4(I,n)$ values while the pathway ($0\rightarrow+1\rightarrow-1$) originates echoes for positive $R^4(I,n)$ values. The selection of only one coherence transfer pathway yields two-dimensional spectra with "phase-twist" lineshapes. In analogy with MQMAS, the phase problems can be overcome using the three pulse z-filter (Fig. 11b) or shifted-echo acquisition schemes (Fig. 11c). In the z-filter experiment the two hard pulses are followed by a short delay during which the magnetisation is stored along the z-axis as zero-quantum coherence and then transferred into observable single-quantum coherence using a selective $\pi/2$ pulse. The symmetrisation of echo and antiecho pathways during the two hard pulses ($p=0\rightarrow\pm1\rightarrow0$) forces an equal intensity of the echo and antiecho signals, leading to amplitude-modulated FIDs and thus to pure absorption spectra. In the shifted-echo experiment a refocusing π pulse is introduced at the end of the pulse sequence, in order to delay the for-
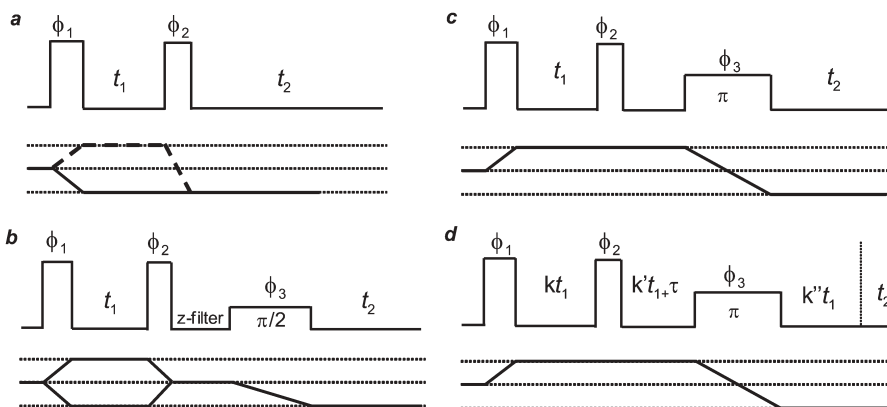
Fig. 11a–d Pulse sequences and coherence transfer pathways for the 2D STMAS experiment: **a** two-pulse sequence as described by Gan; **b** amplitude modulated z-filter acquisition scheme; **c** phase-modulated shifted-echo experiment; **d** split-t_1 shifted-echo experiment. The values of k, k' and k" are chosen to refocus the second-order quadrupolar broadening at the end of the t_1 period

mation of the echo and antiecho in the t_2 domain by a time τ. As t_1 increases, the echo signals move forward in t_2 while the antiecho signals move backward. If the interval τ is long enough, the antiecho signals will not be truncated, even when t_1 reaches its maximum length, and pure absorption lineshapes will be obtained in both cases.

In the three acquisition schemes described so far the spectra obtained have to be sheared so that the relevant $ST_n \rightarrow CT$ ridge appears parallel to F_2. The amount of shearing is determined by the fourth-rank expansion coefficients between ST and CT given in Table 3. An alternative, which does not require shearing, is the split-t_1 version of the experiment. The pulse sequence corresponding to the phase-modulated shifted-echo split-t_1 experiment is shown in Fig. 11d. In this experiment, the second-order anisotropic broadening is refocused at the end of the t_1 evolution period by splitting it into two parts and setting the ratio of their durations equal to the relevant STMAS ratio ($R^4(I,n)$). The positioning of the second part of the evolution period, before or after the final pulse, depends on the sign of the STMAS ratio. For $ST_n \rightarrow CT$ correlation with negative $R^4(I,n)$, such as $ST_1 \rightarrow CT$ for $I=3/2$ nuclei, the second part of the t_1 evolution period is placed before the final pulse ($k''=0$). For positive $R^4(I,n)$, such as $ST_1 \rightarrow CT$ for $I>5/2$ nuclei, the second part of the t_1 evolution period occurs after the final pulse ($k'=0$).

In addition to the desired $ST_n \rightarrow CT$ echo, other echoes form during t_2 in STMAS experiments: $CT \rightarrow CT$ and $ST_n \rightarrow ST_n$ echoes, corresponding to diagonal ridges, and $ST_n \leftrightarrow CT$, $ST_n \leftrightarrow ST_{p \neq n}$ and $ST_{p \neq n} \leftrightarrow CT$ echoes, appearing along the directions $v_1 = |R_4(l,n)| v_2$ [40]. These echoes cannot be cancelled out by phase cycling because they correspond (as the targeted correlation echo) to coherences of the same quantum level during t_1. However, after transfer optimisation (pulse lengths and rf field amplitude) the only peaks that survive are those corresponding to the CT during t_2, i.e. $CT \rightarrow CT$, $ST_n \rightarrow CT$ and $ST_{p \neq n} \rightarrow CT$. In practice, the intensities of the last peaks are often too low to be observed and hence the remaining unwanted peak is the diagonal $CT \rightarrow CT$ correlation signal.

To simplify the interpretation of STMAS spectra, it is desirable to remove the $CT \rightarrow CT$ correlation signal, particularly when studying nuclei subjected to distribution of local environments or weak quadrupole interactions. Several methods are available to remove the $CT \rightarrow CT$ peak. In the first method, the CT transition is presaturated by a soft pulse, prior to the STMAS sequence (Fig. 12a) [38]. A sequence consisting of a selective soft pulse followed by a delay and a short excitation pulse may be used for optimising the presaturation pulse. Unfortunately, this simple method only works when all species present in the sample have very similar transverse relaxation times and quadrupole coupling constants.

Another method for suppressing the $CT \rightarrow CT$ peak takes advantage of the sharp ST signals. By slightly shifting the evolution time t_1, keeping the same increment, the mixing pulse acts on the dephased ST amplitude while the CT signal remains essentially unchanged. Therefore, by subtracting two consecutive acquisitions, one synchronised (t_1) and the other non-synchronised ($t_1 + \delta$), for
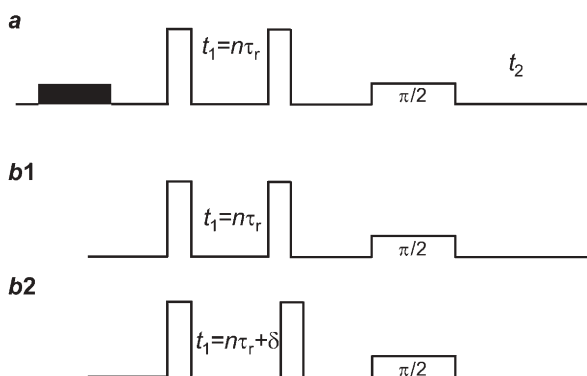
Fig. 12a, b STMAS pulse sequences that suppress CT→CT diagonal peaks using: **a** a soft pre-saturation pulse; **b** the subtraction method. In b the receiver phase is alternated between synchronised (b1) and non-synchronised (b2) for subtraction of the CT→CT signal

each increment value (t_1), a STMAS spectrum free from the diagonal CT→CT is obtained [41]. Using this approach, the CT→CT peaks are easily eliminated but the signal-to-noise (S/N) ratio is reduced by a factor of $\sqrt{2}$ and the experimental time is doubled.

To obtain a high-resolution spectrum free from the unwanted CT→CT peak, the third method proposed uses half-rotor synchronisation, instead of full-rotor period synchronisation, during t_1 [40]. The increment in t_1 (or kt_1 for split-t_1 experiments) is set to half the rotor period, thereby doubling the isotropic spectral width ($F_1 = 2\nu_r$, where ν_r is the MAS rate). This means that two sets of ST_n→CT resonances will be observed, a centreband and a spinning sideband. In principle, the latter will be well resolved from the CT→CT diagonal peaks, which in general do not display any sidebands in F_1. Compared with a full-rotor synchronisation, the S/N ratio is reduced by a factor of two and the experimental time is doubled. As an example, Fig. 13a shows the STMAS spectrum of zeolite scolecite.

Finally, the very recently proposed double-quantum (DQ) and double-quantum filtered (DFQ) STMAS experiments [42] allow filtering out diagonal (and outer satellite transitions) peaks of STMAS spectra with no loss on sensitivity. The experiments efficiently convert inner ST coherences from single to double-quantum with a central-selective transition π pulse. The conversion allows the selection of double-quantum transfer pathways with phase cycling, filtering out the unwanted peaks.

3.4.2
I-STMAS

As a complement to MQMAS and STMAS experiments, a new two-dimensional method has been recently proposed to obtain high-resolution NMR spectra of
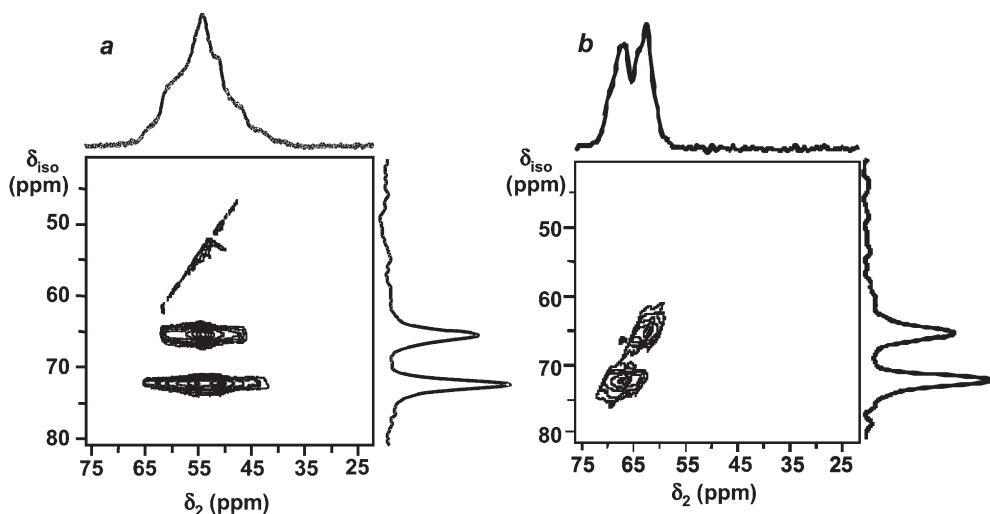
Fig. 13a, b Sheared ^{27}Al: **a** STMAS; **b** I-STMAS spectra of zeolite scolecite recorded at 9.4 T with a MAS rate of 12.5 kHz, using soft (5 kHz) and hard (50 kHz) pulses. Reprinted with permission from [43] Amoureux JP et al. (2003) Solid State Nucl Magn Reson 23:213. Copyright (2003) Elsevier Science (USA)

half-integer quadrupolar nuclei [43]. Like STMAS, the so-called Inverse-STMAS (I-STMAS) correlates second-order quadrupole dephasing occurring on the central transition (CT) and satellite transition (ST) coherences but does it in a reverse manner: CT evolves during the t_1 period while the STs are detected during t_2. Although STMAS and I-STMAS are symmetric, there are some interesting and useful differences between the two methods. For example, it is possible to over-sample and process the data to suppress the CT→CT correlation resonance during the acquisition. Figure 13b shows the I-STMAS spectrum of zeolite scolecite.

Figure 14 shows the basic I-STMAS pulse-sequence, which produces an amplitude-modulated signal acquired using the hypercomplex method and leads, after a two-dimensional Fourier transform, to a pure-absorption spectrum. I-STMAS uses three pulses: the first two are soft selective 90° pulses and transfer the |±1/2> Zeeman state populations to the CT coherences. After t_1 evolution, CT coherences are transferred back to the original |±1/2> states by the second 90° selective pulse. The third hard-pulse transfers the signal to the inner STs, which are observed during t_2. The selected pathway is thus 0Q→±1Q[CT]→0Q→−1Q [STs]. The delay between the last two pulses introduces a short period where the coherences are along the z-axis. This period plays the same role as in the z-filter MQMAS and STMAS experiments, allowing equalisation of the echo and anti-echo signal amplitudes. The CT→CT is observed at time $t_{2e}=t_1$, while the desired echo (CT→ST) appears at $t_{2e}=R^4(I,n)$ t_1 (the $R^4(I,n)$ ratio in I-STMAS corresponds to the inverse of the STMAS ratio given in Table 3).
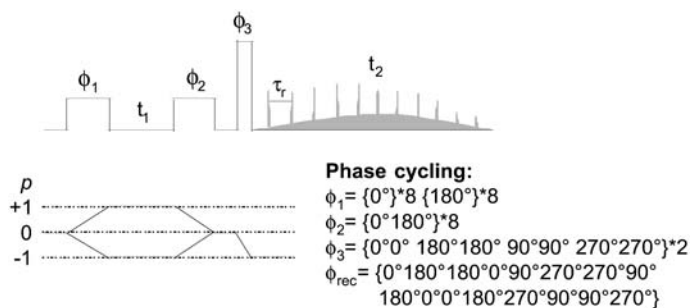
Fig. 14 Pulse sequence (*top*), coherence pathway and phases of the z-filter I-STMAS experiment. The acquisition of the hypercomplex data is performed with the States mode

The main limitation of the STMAS and I-STMAS experiments lies in the fact that they are technically demanding, requiring very accurate magic-angle setting (0.005°) and stable sample spinning (1–2 Hz) to average out the large ST first-order quadrupole interactions. A version of the STMAS experiment that Self-Compensates for Magic-Angle mis-sets (SCAM-STMAS) of up to 1° was recently proposed [44]. However, the sensitivity of this experiment is decreased when compared with standard STMAS. The latter and I-STMAS have other important drawbacks restricting their application. First, the spectral width along F_1 (STMAS) or F_2 (I-STMAS) is limited by the spinning rate. Second, both methods are very sensitive to any molecular motion, which leads to short transverse relaxation times and, consequently, to a large signal decrease and to degradation of isotropic resolution [45].

3.5
Sensitivity Enhancements in MQMAS

The MQMAS experiment is inefficient for studying resonances with large quadrupole coupling constants, even when using the largest radio-frequency (B_1) fields available (ca. 250 kHz). In extreme cases (low B_1 and large quadrupole couplings), the peak intensity may be so low that the resonance remains buried in the noise and is not detected.

The first attempts to enhance the MQMAS efficiency by rf pulse manipulation were reported by Ding and McDowell [46] and by Marinelli et al. [47]. These authors showed that 3Q excitation in spin–3/2 systems could be improved by using shaped or composite pulses instead of CW irradiation. However, the intensity gains (up to 30%, under relatively slow spinning conditions) achieved were only moderate. As shown in Fig. 15, the low efficiency of the conversion of MQ to 1Q coherences explains the poor signal-to-noise ratio of the MQMAS spectra. In order to deal with this problem, several modifications of the MQMAS NMR experiment have been reported, and they extend to larger values the range of observable quadrupole couplings.
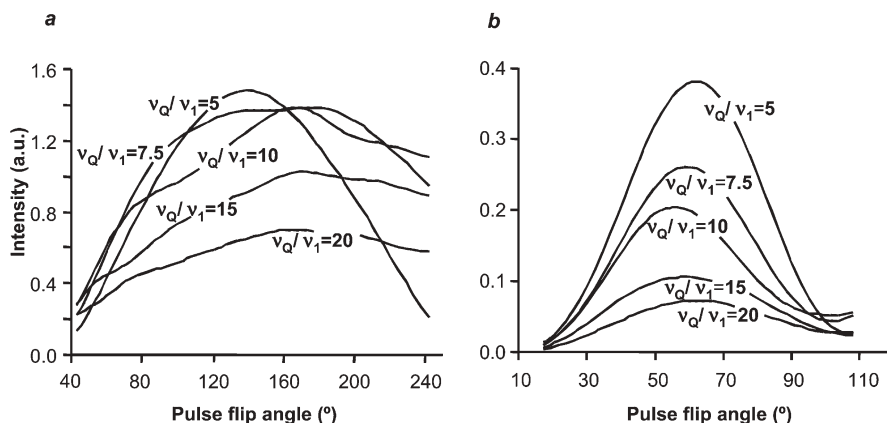
Fig. 15a, b Plot of the intensity corresponding to: **a** 3Q excitation; **b** 3Q to SQ conversion in a 3QMAS experiment, as a function of the flip angle and for several values of the v_Q/v_{rf} ratio. The curves were obtained using programme PULSAR [35]. Intensities are normalised to the intensity of the signal obtained in a conventional MAS experiment using selective excitation of the central transition by a $\pi/2$ pulse

A significant step towards enhancing MQMAS efficiency was the introduction of the RIACT-II scheme by Wu et al. [48]. This technique employs Rotation-Induced Adiabatic Coherence Transfer between 3Q and 1Q coherences in spin–3/2 systems, under MAS [49]. The excitation consists of a selective 90° pulse, immediately followed by a long (1/4 of the rotor period) hard pulse. In the conversion step, a long hard pulse of the same duration is used. Although more quantitative than conventional MQMAS, RIACT spectra present distorted lineshapes along the MAS dimension and the position of the rf offset substantially affects its efficiency [50]. Caldarelli and Ziarelli showed that this approach can be used to excite selectively certain sites according to their quadrupolar constants while minimising the intensity of others and thus it may be used as a spectral editing technique [51].

Two other successful modifications of the MQMAS NMR experiment that achieve significant signal enhancement are the DFS (Double Frequency Sweeps) and the FAM (Fast Amplitude Modulation) methods introduced, respectively, by Kentgens et al. [52] and Madhu et al. [53]. DFS and FAM use modulated, instead of continuous wave (CW), pulses for the conversion of MQ to 1Q coherences. They rely on the selective irradiation of the satellite transitions, following the idea introduced by Vega and Naor [54] for the 3Q to 1Q conversion in single crystals containing spin–3/2 nuclei. Although both approaches are based on similar physical principles their practical implementation is quite different. DFS sweeps the rf-carrier frequency over the entire satellite spectrum, while FAM corresponds to irradiation at two distinct frequencies, ideally on the singularities of the satellite powder pattern (Fig. 16). Like RIACT, FAM (referred to as FAM-I) and DFS methods (initially introduced for spin–3/2-nuclei) use
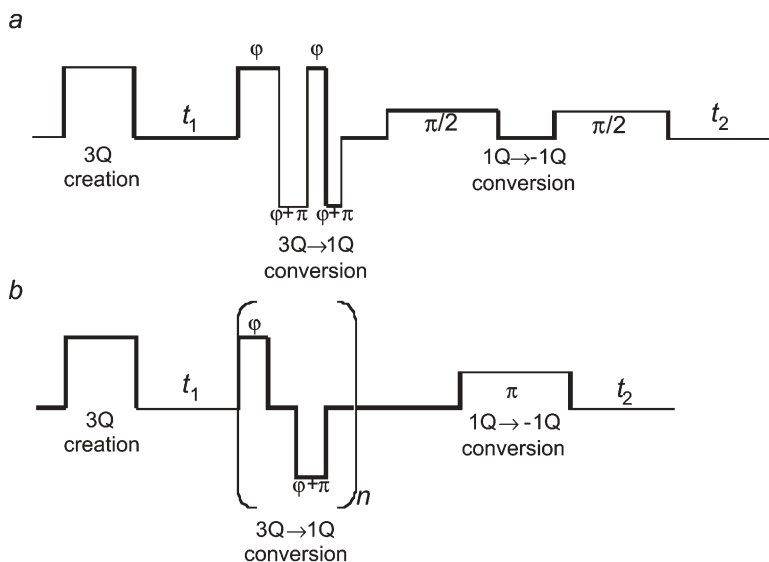
Fig. 16 **a** z-filter FAM-II MQMAS pulse sequences. **b** Shifted-echo FAM-I MQMAS pulse sequences. For $I=5/2$, $7/2$ and $9/2$ nuclei the echo coherence transfer pathway is $p=0\rightarrow3\rightarrow-1$, while the antiecho coherence transfer pathway is $p=0\rightarrow-3\rightarrow-1$, where p is the coherence order. For $I=3/2$ nuclei these assignments are reversed

adiabatic energy level anti-crossings, in order to convert efficiently the 3Q into 1Q coherences [55, 56]. The major advantage they present over RIACT is the improved lineshapes along the anisotropic dimension.

Using fast amplitude modulation pulses it is possible to redistribute the population of the spin energy levels. This is the Rotor Assisted Population Transfer (RAPT) method introduced by Yao et al. [57]. It has been shown that enhancement by a factor of 1.5–2 is achieved in a MAS experiment of spin–3/2 nuclei when RAPT is applied before the excitation pulse. It is also possible to combine RAPT with MQMAS in an experiment which uses single-quantum coherences for the excitation of multiple-quantum coherences. Madhu and Levitt [58] have shown that a combination of RAPT and RIACT-FAM gives the best performance for MQMAS experiments of spin-3/2 systems.

Although Vosegaard et al. [59] reported sensitivity enhancements of 3Q MAS and 5Q MAS spectra of $I=5/2$ nuclei using FAM-I pulses, this approach is not well suited to these spin systems. To improve 3Q MAS spectra of spin-5/2 nuclei Goldbourt et al. [60] introduced FAM-II pulses, which are built from a set of equal intensity segments with alternating positive and negative phases (φ, $\varphi+\pi$) (Fig. 16). The success of FAM-II pulses depends on the quadrupolar frequency parameters of the sample and on the length and intensity of the segments of the pulse, both determined numerically or experimentally. In contrast with FAM-I, FAM-II pulses do not contain zero intensity delays (except the very short delays related to instrumental limitations) and the lengths of the seg-

ments are different. The MQ to SQ coherence transfer mechanism during FAM-II pulses is not thought to be adiabatic, rather it is a cumulative direct process.

Recently, we [61] have proposed a FAM-II approach slightly different from the approach of Goldbourt et al. In the FAM-II experiment introduced by these workers the lengths of the segments of the modulated pulse are optimised by sequential maximisation of the echo signal, switching the phase ($\varphi \rightarrow \varphi + \pi$) when a maximum of the curve is reached. However, we have found that the efficiency of the conversion can be improved as follows: The length of the first segment of the FAM pulse is determined by the intersection point of the echo (–3Q→–1Q coherence transfer for I=3/2 nuclei) and antiecho (3Q to –1Q coherence transfer for I=3/2 nuclei) curves. Furthermore, the lengths of the other segments do not correspond to the maximum intensity of the –3Q→–1Q coherence transfer curve, but rather to a point after the maximum. The phase is switched ($\varphi \rightarrow \varphi + \pi$) between each segment and the procedure is repeated until no enhancement is obtained by the addition of a segment.

Figure 17 shows ^{27}Al z-filter 3Q MAS NMR spectra of the mineral andalusite, recorded with CW and FAM-II pulses with (0→±3→±1→0→–1) transfer pathway. A comparison of the F_1 projections of these spectra (Fig. 17c) reveals that FAM-II enhances the octahedral ^{27}Al signal (C_Q ca. 15.3 MHz) by a factor of ca. 1.9. However, the relative intensities of the two (penta-coordinatedandoctahedral) FAM-II peaksare in a 2:1 ratio and thus the correct 1:1 ratio is still not obtained. Numerical simulations (Fig. 17d) confirm that our method performs better than the other two methods. For the octahedral ^{27}Al peak, an intensity gain of ca. 17% over the method of Goldbourt et al. is calculated. Because the lengths of the segments become very short (≤0.30 μs), a short phase switching delay has been introduced between each FAM segment. This causes an intensity loss relative to an ideal experiment with instantaneous phase switching. However, experimentally it results in significant improvement because the segments that constitute the FAM-II pulse are better defined. It was only by introducing such a delay, of the order of the actual phase switching time, that we could see improvements in the performance of the FAM-II method when adding very short segments to the FAM pulse.

As another example, consider the ^{45}Sc z-filter 3Q MAS NMR CW and FAM-II spectra of Sc$_2$O$_3$ (Fig. 18). A comparison of the F_2 cross sections of these spectra reveals that FAM-II enhances the signal intensity of the ^{45}Sc site with larger quadrupole coupling constant by a factor of ca. 3. However, although the populations of the two scandium environments are in a 3:1 ratio FAM-II yields a 5:1 ratio and thus the broad ^{45}Sc NMR resonance is misrepresented. Numerical simulations (Fig. 18c) show that for quadrupolar coupling constants in the range 6–30 MHz our optimisation method performs better than the method proposed by Goldbourt et al. For the broad (C_Q=23.3 MHz) Sc$_2$O$_3$ site the calculated signal intensity increases by a factor of 3, relative to MQ z-filter conversion, and ca. 20% relative to the Goldbourt et al. method.

Another approach to obtain sensitivity enhancement in MQMAS experiments of spin–3/2 systems was suggested by Vosegaard et al. [62]. The proposed
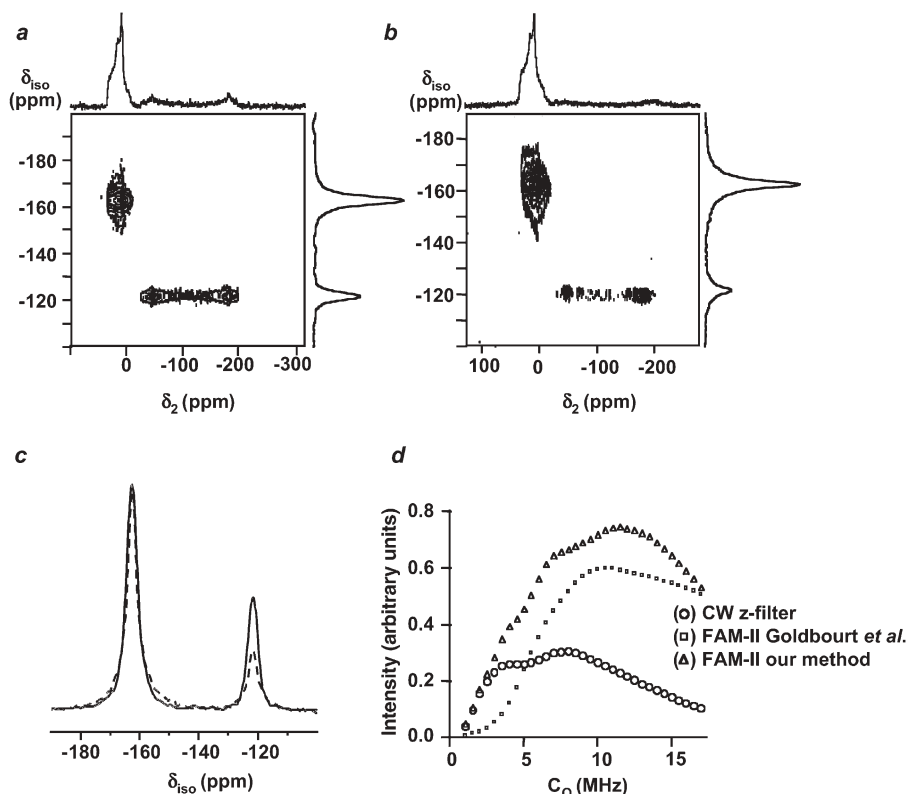
Fig. 17a–d ^{27}Al: **a** FAM-II NMR spectra of andalusite. **b** CW 3QMAS NMR spectra of andalusite. Both spectra were obtained with a 31 kHz spinning rate and 1 s recycle delay. The length of the first hard pulse (B_1=250 kHz) was 1.4 μs. The length of the CW conversion pulse was 0.6 μs. The FAM-II conversion pulse was composed of six segments with lengths 0.70, 0.45, 0.30, 0.25, 0.20 and 0.15 μs. The soft pulse (B_1=8 kHz) length was 10 μs. 200 data points (1920 transients per point) were acquired in the t_1 dimension in increments of ($1/\tau_r$)μs. The ppm scale of the sheared spectra was referenced to ν_0 frequency in the F_2 domain and to 1.42 δ_0 in the F_1 domain (reference aqueous Al(NO$_3$)$_3$). **c** Isotropic δ_{iso} projections. **d** Simulated intensity of the MQ to SQ conversion as a function of the quadrupole coupling constant for CW z-filter irradiation, Goldbourt et al. FAM-II and the FAM-II method proposed by us. The pulse lengths used correspond to the maximum intensity transfer obtained for each method with a quadrupole coupling constant of 15.3 MHz. Reprinted with permission from [61], Morais CM et al. (2003) Magn Reson Chem 41:679–688. Copyright (2003) Wiley

experiment called FASTER (FAst Spinning gives Transfer Enhancement at Rotary Resonance) exploits a rotary resonance between the rf field amplitude (ν_1) and the spinning rate (ν_r) at high spinning rates and low rf field amplitudes. 3Q excitation efficiency is enhanced when ν_r and ν_1 are between adjacent rotary resonance conditions ($\nu_1=n\nu_r/2$) and the 3Q to 1Q conversion is slightly enhanced when $\nu_1=n\nu_r$. Like RIACT, FASTER MQMAS spectra present distorted
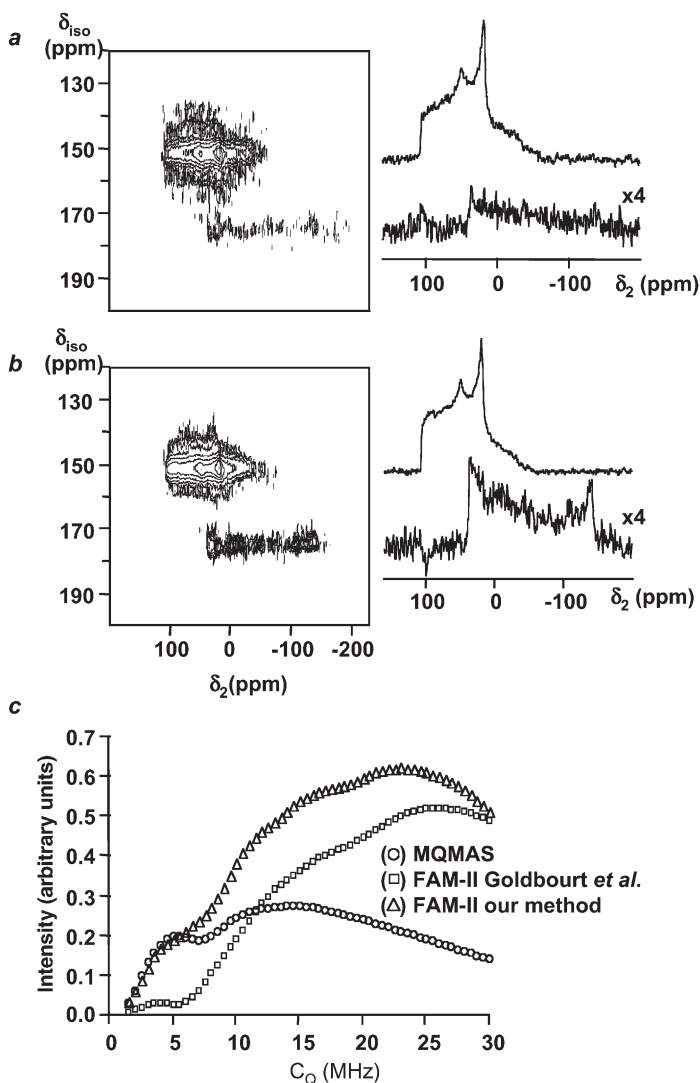
Fig. 18a–c ^{45}Sc: **a** CW NMR spectra; **b** FAM-II 3QMAS NMR spectra of Sc_2O_3, depicting F_2 cross-sections of the two resonances present, recorded with a 28 kHz spinning rate and 1 s recycle delay. The length of the first hard pulse (B_1=250 kHz) was 1.4 µs. The length of the CW conversion pulse was 0.45 µs. The FAM-II conversion pulse was composed of four segments with lengths 0.6, 0.4, 0.2, and 0.15 µs. The soft pulse length was 8 µs (B_1=8 kHz). A short phase-switching delay was inserted between each FAM-II segment. 128 data points (1344 transients per point) were acquired in the t_1 dimension in increments of ($1/\tau_r$) µs. The ppm scale of the sheared spectra was referenced to ν_0 frequency in the F_2 domain and to 0.76 ν_0 in the δ_{iso} domain (reference $ScCl_3$ solution). **c** Simulated intensity of the MQ to SQ conversion as a function of the quadrupole coupling constant for CW z-filter irradiation, Goldbourt et al. FAM-II and the FAM-II method we proposed. The pulse lengths used correspond to the maximum intensity transfer obtained for each method with a quadrupole coupling of 23.3 MHz. Reprinted with permission from [61], Morais CM et al. (2003) Magn Reson Chem 41:679–688. Copyright (2003) Wiley

lineshapes along the anisotropic dimension. However, this phenomenon may be used on very high-field narrow-bore spectrometers (small rotors and thus large v_r) when using triple resonance probes (weak rf fields).

Additional gain in the signal-to-noise ratio can also be obtained by synchronous detection [63] or by acquiring multiple echoes during the free precession period of the observable single-quantum coherence (MQ-QCPMG-MAS experiment proposed by Vosegaard et al. [64]).

When the quadrupolar couplings are so large that, at normal field strengths and spinning rates, the MAS spectrum is complicated by the overlap of the numerous spinning sidebands, it becomes impossible to record MQMAS spectra. Massiot et al. [65] showed that in such cases the spinning sidebands can be separated by order in a two-dimensional experiment from which it is possible to obtain an infinite spinning rate (spinning sideband free) MAS spectrum. The proposed experiment called QPASS (Quadrupolar Phase Adjusted Spinning Sidebands) provides MAS spectra with enhanced resolution enabling the extraction of quadrupolar parameters and isotropic chemical shifts. The method has been applied to several materials containing ^{71}Ga [66].

4
Double-Resonance Experiments

The development of high-resolution solid-state NMR methods for the study of half-integer quadrupolar spins raised the possibility of measuring their interactions with the neighbouring nuclei under isotropic resolution. Using double-resonance techniques in tandem with MQMAS NMR permits spectral editing, providing a means of simplifying the NMR spectra and assisting the attribution of the NMR resonances. In addition, it offers a simple method for measuring the dipolar interactions between the observed nuclei and their neighbours, permitting the direct estimation of interatomic distances. Double-resonance dipolar-based experiments, including single- and multiple-quantum cross-polarization (CP) MQMAS [67, 68], heteronuclear correlation (HETCOR) MQMAS [69] and Rotational Echo Double Resonance (REDOR) based methods [70, 71], together with J- coupling based experiments [72], are now described.

4.1
Cross-Polarization of Half-Integer Quadrupolar Nuclei

Cross-polarization between spin I=1/2 and S=1/2 systems is a relatively simple and well-understood process. For a static sample, under on-resonance conditions, there is a unique "Hartmann-Hahn matching condition"[73] at which polarization is transferred between the two sets of nuclei, given by

$$v_{1I} = v_{1S} \tag{39}$$

where $v_{1I}=-\gamma_I B_{1I}$ and $v_{1S}=-\gamma_S B_{1S}$ are the strengths (or the nutation rates) of the rf fields, B_{1I} and B_{1S}, applied to the I and S nuclei during the spin-locking period. MAS introduces a modulation of the dipolar interaction between spins I and S and, as result, modifies the Hartmann-Hahn matching condition. Under fast MAS, the optimum transfer occurs at the modified Hartmann-Hahn condition [74]:

$$v_{1I} = v_{1S} \pm nv_R \tag{40}$$

where v_R is the spinning frequency and n is an integer (usually n=1 or 2).

When S is a quadrupolar nucleus the polarization matching conditions are more complex. The reason for this can be seen by considering the rotating frame Hamiltonians of the individual I and S nuclei during the application of an on-resonance x-pulse:

$$\hat{\mathcal{H}}_1 = v_{1I}I_x \tag{41}$$

and

$$\hat{\mathcal{H}}_S = v_{1S}S_x + v'_Q\,[3S_z^2 - S^2] \;\; \text{with} \;\; v'_Q = \frac{v_Q}{12}\,(3\cos^2\beta - 1 + \eta\sin^2\beta\,\cos2\alpha) \tag{42}$$

where v_Q is the quadrupolar frequency and the angles α and β describe the orientation of the PAS of the quadrupole tensor in the laboratory frame. In Eq. (41) the quadrupolar interaction perturbs the eigenstates of $v_{1S}S_x$ with the result that, instead of a single nutation rate v_{1S}, there are now several S-spin nutation rates $v_{r,s}$ that can be matched to the I-spin nutation rate v_{1I}, all of which are functions of both v_{1S} and v'_Q (r and s are two of the 2S+1 eigenstates of the spin-locking Hamiltonian of the quadrupolar spin S). However, matching the I-spin nutation rate v_{1I} to one of the S (2S+1) nutation rates $v_{r,s}$ of spin S does not necessarily result in cross-polarization. A further condition is that there must be a matrix element in the IS dipolar Hamiltonian expressed in the eigenbasis of $\hat{\mathcal{H}}_I$ and $\hat{\mathcal{H}}_S$ connecting the S-spin transition (r,s) with the I-spin transition. For a spin S=3/2, it may be shown that this dipolar Hamiltonian is

$$\hat{\mathcal{H}}_{IS}^D = - d_{IS}I_x(C_{1,2}S_x^{1,2} + C_{1,4}S_x^{1,4} + C_{2,3}S_x^{2,3} + C_{3,4}S_x^{3,4}) \tag{43}$$

where $S_q^{r,s}$ ($q = x, y, z$) is a fictitious spin operator for the (r,s) transition and the four non-zero coefficients $C_{r,s}$ are given in [74].

In general, in the eigenbasis of the on-resonance I and S spin-locking Hamiltonians, only $(S+1/2)^2$ transitions have matrix elements in the IS dipolar coupling Hamiltonian linking them to spin I. Thus, only $(S+1/2)^2$ transitions are available for cross-polarization and these correspond to the transitions in the eigenbasis of H_S that have s-r equal to an odd integer [74]. Therefore, in a static sample, the Hartmann-Hahn matching condition for on-resonance cross-polarization from a spin I=1/2 nucleus to an half-integer spin S>1/2 nucleus is

$$v_{1I} = v_{r,s} \tag{44}$$

where $\nu_{r,s}$ is one of the $(S+1/2)^2$ allowed S-spin nutation rates. It is important to note that this transition cannot, in general, be classified as a single- or triple-quantum coherence because it is a transition in the spin-locking eigenbasis and not in the normal rotating frame [75]. At the end of the spin-locking period, when it is useful to view the system in the normal rotating frame again, this spin-locking transition is mixed by coordinate transformation into all possible S-spin population and coherence orders. The single-quantum satellite transitions are not observed and central-transition and multiple-quantum cross-polarization are not distinct processes.

In the case $\nu'_Q \gg \nu_{1S}$ (selective excitation of the on-resonance transition), it has been shown that the on resonance spin-locking eigenbasis of the S spin has a much closer relationship with the normal rotating frame, and now only the $(S+1/2)$ transitions are linked to the I-spin by the IS dipolar Hamiltonian and available for cross-polarization. For a spin–3/2, for example, the matching condition $\nu_{1I}=\nu_{1,2}$ results in selective single-quantum CP to the central transition of $S=3/2$, while $\nu_{1I}=\nu_{3,4}$ yields pure triple-quantum CP, with ν_{1I} and ν'_Q positive [75, 76]. In this limit, single- and multiple-quantum CP are distinct processes, occurring at the following on-resonance matching conditions:

$$\nu_{1I} = (S + 1/2) \, \nu_{1S} \tag{45}$$

$$\nu_{1I} = \frac{k\nu_{1S}^3}{(\nu'_Q)^2} \tag{46}$$

with $k=3/8$ for spin $S=3/2$ [76, 77] and 1.5 for spin $S=5/2$ [75]. Clearly, this implies a very low value (few kHz) for ν_{1I}, particularly for spin–3/2 nuclei, which in most cases is insufficient for spin–1/2 spin-locking. This is why the theoretical assessments of the potential of the multiple-quantum CP have tended to be pessimistic. In contrast, Ashbrook and Wimperis [75] have recently shown that in the experimentally more appropriate case $\nu'_Q \approx \nu_{1S}$, some of the $(S+1/2)^2$ spin-locking transitions mix strongly into multiple-quantum coherences and a few have nutation rates larger than ν_{1S}. As a result, it is not difficult to match ν_{1S} and the nutation rates of three and five-quantum coherences in half-integer quadrupolar nuclei.

MAS leads to further complications in a quadrupolar spin system because it not only renders the IS dipolar interaction time dependent, but it also modulates the quadrupolar interaction and, hence, the S-spin nutation rates. This increases the complexity of the cross-polarization experiment [78–80]. For static samples, single- and multiple-quantum quadrupolar nutation spectra may be used to measure the $(S+1/2)^2$ nutation rates available for matching in the single- or multiple-quantum cross-polarization experiment [75]. Therefore, nutation spectra can be used to determine independently the optimum matching conditions for performing single and multiple-quantum cross-polarization in static samples. Under MAS it is still possible to record single- and multiple-quantum nutation spectra and, when the spinning rate is low, it has been shown that these do not differ greatly from static nutation spectra [81].

Although the CP matching conditions are approximately the same for static and slowly spinning samples, the intensity of the CPMAS signal depends crucially upon the extent to which spin locking of the S-spin transitions can be maintained in the presence of the rotor-driven modulation of the quadrupolar Hamiltonian [79, 80, 82]. This applies to single- and multiple-quantum transitions because, as noted above, in general the two processes originate from the same S-spin transition in the spin-locking eigenbasis.

The spin-locking efficiency under MAS depends on the amplitude and frequency of the spin-locking rf field, MAS frequency and magnitude of the quadrupolar interaction. Vega [80] introduced the adiabatic-passage parameter

$$\alpha = \frac{v_{1S}^2}{v_Q v_r} \tag{47}$$

to indicate whether the rotor-driven modulation of the eigenvalues of the quadrupolar spin-locking Hamiltonian occurs adiabatically ($\alpha \gg 1$) or suddenly ($\alpha \ll 1$). In both regimes spin-locking is possible, while in intermediate regime, $\alpha \sim 1$, spin locking is not maintained and the CP efficiency decreases.

The optimum matching conditions for single- and multiple-quantum CP to quadrupolar nuclei depend on a large number of variables, particularly under MAS, with the relative efficiencies of the two processes often being very similar. However, CP is, in general, performed in the weak field limit, i.e. with a quadrupolar spin rf field strength v_{1S} much smaller than the quadrupolar interaction v'_Q. In these conditions, single-quantum CP will be more efficient than CP directly to multiple-quantum coherences. This is because single-quantum Hartmann-Hahn matching may be achieved for most powder crystallites at the condition $v_{1I} = (S+1/2)v_{1S} \pm n v_R$. The corresponding multiple-quantum matching conditions are functions of the quadrupolar interaction and thus vary from crystallite to crystallite, preventing uniform CP across the powder lineshape. In this limit, it is preferable to perform single- rather than multiple-quantum CP.

4.2
Cross-Polarization MQMAS

Pruski et al. [83] and Fernandez et al. [84] showed that it is possible to introduce CP into the MQMAS experiment, allowing editing of the high-resolution spectra of quadrupolar nuclei, based upon the distances to an abundant spin–1/2 nucleus (e.g. ^1H or ^{19}F). CP-MQMAS, is thus a powerful method of simplifying spectra, helping with the attribution of resonances. The experiment begins with a conventional CP step employing a very low rf field on the quadrupolar spin channel, during which the magnetisation is transferred from the spin $I=1/2$ nucleus to the single-quantum (SQ) coherences of spin S (quadrupolar nucleus). The resulting SQ coherences are then converted back

to a population difference across the quadrupolar eigenstates, $m_s=\pm 1/2$, by a selective 90° pulse. After a short delay, a standard z-filter MQMAS experiment is performed. While, in a conventional MQMAS experiment, triple-quantum (TQ) coherences are excited by a single pulse, which acts on the equilibrium population difference across the Zeeman levels $m_s=\pm 3/2$, in the CP-MQMAS experiment TQ coherences are created from a population difference across the central transition. This is expected to be a very inefficient process unless $\nu_Q \approx \nu_{1S}$. Therefore, in addition to the large number of coherence transfer steps involved, this CP-MQMAS experiment is expected to have poor sensitivity. High rf fields may be required to achieve an acceptable sensitivity.

Ashbrook et al. proposed an alternative route for combining CP with MQMAS [85, 86]. In this method, S-spin multiple-quantum (MQ) coherences are created directly by CP from the I spin and then correlated with SQ coherences in a two-dimensional MQMAS experiment. This seems the simplest and most direct method of using CP to excite MQ coherences at the beginning of an MQMAS experiment. It should be noted that although the theoretical possibility of performing MQCP had been mentioned before by a number of authors, and experimentally demonstrated on a single crystal [75], Ashbrook et al. [85, 86] were the first to show that it is experimentally viable on powdered samples under MAS conditions. This more efficient and direct approach was also demonstrated by Lim and Grey[87] and by Rovnyak et al. [88].

Recently, Asbrook and Wimperis[89] proposed a novel approach for combining SQ cross-polarization and MQMAS: the SQ coherences created in the CP step are transferred directly to 3Q coherences, rather than via a population state. This results in a pulse sequence with a minimum number of coherence-transfer steps. Two types of experiments have been proposed, using either a z-filter or a reversed split-t_1, where pure-phase lineshapes are recorded via acquisition of the whole-echo. In addition, the authors showed that the sensitivity of both experiments is considerably improved by incorporating FAM pulses in the SQ to MQ excitation step.

As an example of the usefulness of combining CP and MQMAS, consider the 3QMAS and ^{1}H→^{27}Al 3QCP 3QMAS NMR spectra of partially decomposed calcined kaolinite (Fig. 19). Because the remaining parent (non-decomposed) kaolinite is much richer than metakaolinite in hydroxyl groups, the ^{1}H→^{27}Al FAM-II 3QCP 3QMAS NMR spectrum displays only the hexacoordinated Al resonance given by the former or, in other words, the metakaolinite peaks are filtered out of the spectrum. The ^{1}H→^{27}Al 3QCP MAS NMR spectrum was acquired using a FAM-II shifted-echo version of the MQCP MQMAS proposed by Ashbrook et al. (Fig. 20), which was found to be the most efficient version of the experiment.

Because of the complex spin-dynamics of the CP transfer involving quadrupolar nuclei, CP-based methods may not be quantitative. An alternative approach to CP spectral editing, introduced by Fernandez et al. [70], combines MQMAS with (quadrupolar spin)-observe (spin 1/2)-dephase Rotational Echo Double Resonance (REDOR) [90]. The method relies on reintroducing the het-
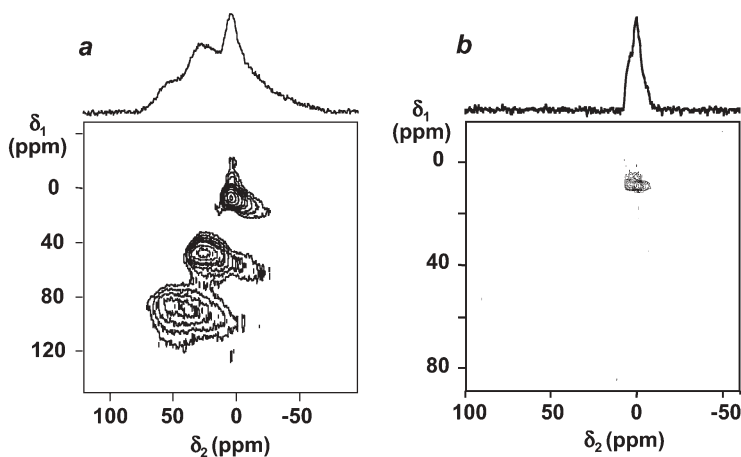
Fig. 19a, b ^{27}Al: **a** FAM-II 3QMAS spectra; **b** ^{1}H→^{27}Al FAM-II 3QCP spectra of kaolinite cal-cined at 500 °C for 1 h, recorded at 9.4 T with a 15 kHz spinning rate and a 1 s recycle delay. The ^{1}H→^{27}Al MQCP MAS NMR spectrum was recorded with a 2.75 μs ^{1}H π/2 pulse (B_1=90 kHz). During the 2 ms contact time, ^{1}H and ^{27}Al B_1 fields of, respectively, 65 and 80 kHz, were used. The FAM-II conversion pulse was composed of four segments with lengths 0.85, 0.6, 0.35, and 0.2 μs. The length of the π pulse was 11 μs (B_1=15 kHz); 70 data points (960 transients per point) were acquired in the t_1 dimension in increments of 20 μs. The ppm scale of the sheared spectra was referenced to v_0 frequency in the v_2 domain and to 1.42 v_0 in the δ_{iso} domain. Reprinted with permission from [61], Morais CM et al. (2003) Magn Reson Chem 41:679–688. Copyright (2003) Wiley
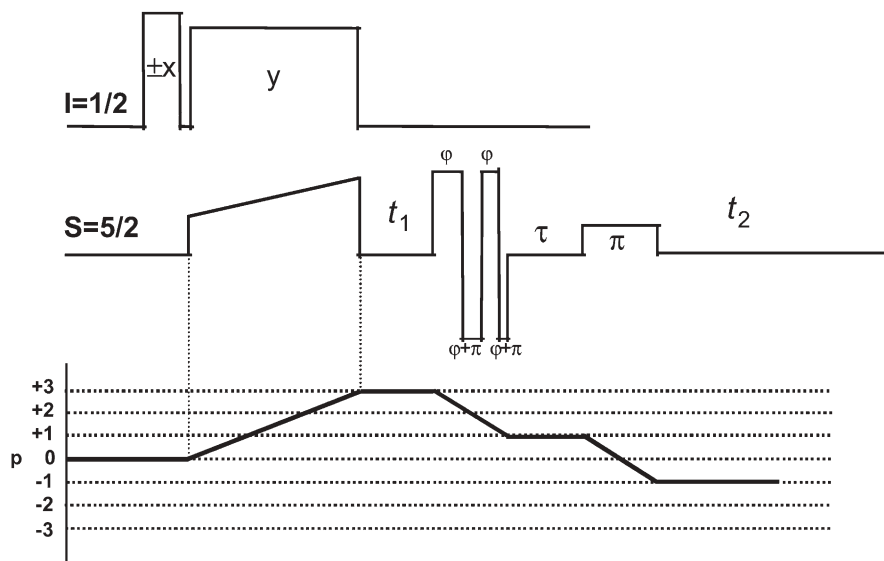
Fig. 20 Pulse sequence and coherence transfer pathway for ^{1}H→^{27}Al FAM-II 3QCP shifted-echo experiment

eronuclear dipolar dephasing between spins using rotor-synchronised rf (π) pulses, which are applied during the 1Q evolution (MQ-t_2-REDOR) of an MQ-MAS experiment. Under MAS, the heteronuclear dipolar coupling is usually averaged out in the course of a rotation period. Indeed, any transverse spin magnetisation that dephases under the dipolar interaction during the first half-rotor period is refocused during the second half. Applying a π pulse in the middle of a rotor period inverts the dipolar dephasing, thus preventing the total refocusing of magnetisation. Combining this idea with a Hahn-echo leads to the REDOR experiment, where the π pulses are applied at each half rotor-period, producing a controlled decay of the echo amplitude. Monitoring this amplitude as a function of the number of rotor periods, N, provides a direct way of determining the dipolar coupling and, hence, the distance between the coupled spins. This technique allows the measurement of distances between quadrupolar and spin–1/2 nuclei. Pruski et al. [71] showed that the application of REDOR recoupling pulses during 3Q, rather than 1Q, evolution (MQ-t_1-REDOR) enhances the dipolar interaction by a factor of three and thus has potential for improving sensitivity in weakly-coupled spins. Moreover, in contrast with CP, REDOR may be easily combined with the high-resolution technique STMAS (Fig. 21) [91].

4.3
Heteronuclear Correlation MQMAS Spectroscopy

Heteronuclear-correlation (HETCOR) MQMAS NMR is a very useful method for studying the connectivity between spin–1/2 and quadrupolar nuclei under high-resolution conditions. It was first demonstrated for a spin–3/2 nucleus by Wang et al. with a spectrum of $Na_3P_3O_9$ correlating the ^{23}Na and ^{31}P ($I=1/2$) isotropic resonances [69]. Several schemes have been proposed to obtain similar spectra for spin-5/2 nuclei [92–94]. However, we have recently demonstrated that these schemes result in distorted spectra and that an extension of the original scheme proposed by Wang et al. should be used instead[95].

The solid-state HETCOR NMR spectra are easily obtained under MAS conditions using CP for mixing (Fig. 22) [96]. Such CPMAS-based HETCOR experiments between quadrupolar and spin–1/2 nuclei have been extensively used by Fyfe and coworkers [97, 98]. The two-dimensional spectra obtained reveal nuclear connectivities but, owing to incomplete averaging of the quadrupolar interaction under MAS, lack high-resolution in the quadrupolar-nucleus dimension. Using DAS to achieve high-resolution in this dimension, Jarvie et al. obtained the first high-resolution solid-state correlation spectrum (of $Na_3P_3O_9$)between quadrupolar (^{23}Na, $I=3/2$) and spin–1/2 (^{31}P) nuclei [99].

MQMAS/HETCOR experiments involving spin-5/2 nuclei have been reported by Chan [93] and more recently by Mali et al. [94] who obtained, respectively, an $^{27}Al \rightarrow {}^{11}B$ MQHETCOR spectrum of magnesium aluminoborate and $^{27}Al \rightarrow {}^{31}P$ MQHETCOR spectra of aluminophosphate molecular sieves. The authors of both reports used the z-filter sequence to convert both triple-quan-
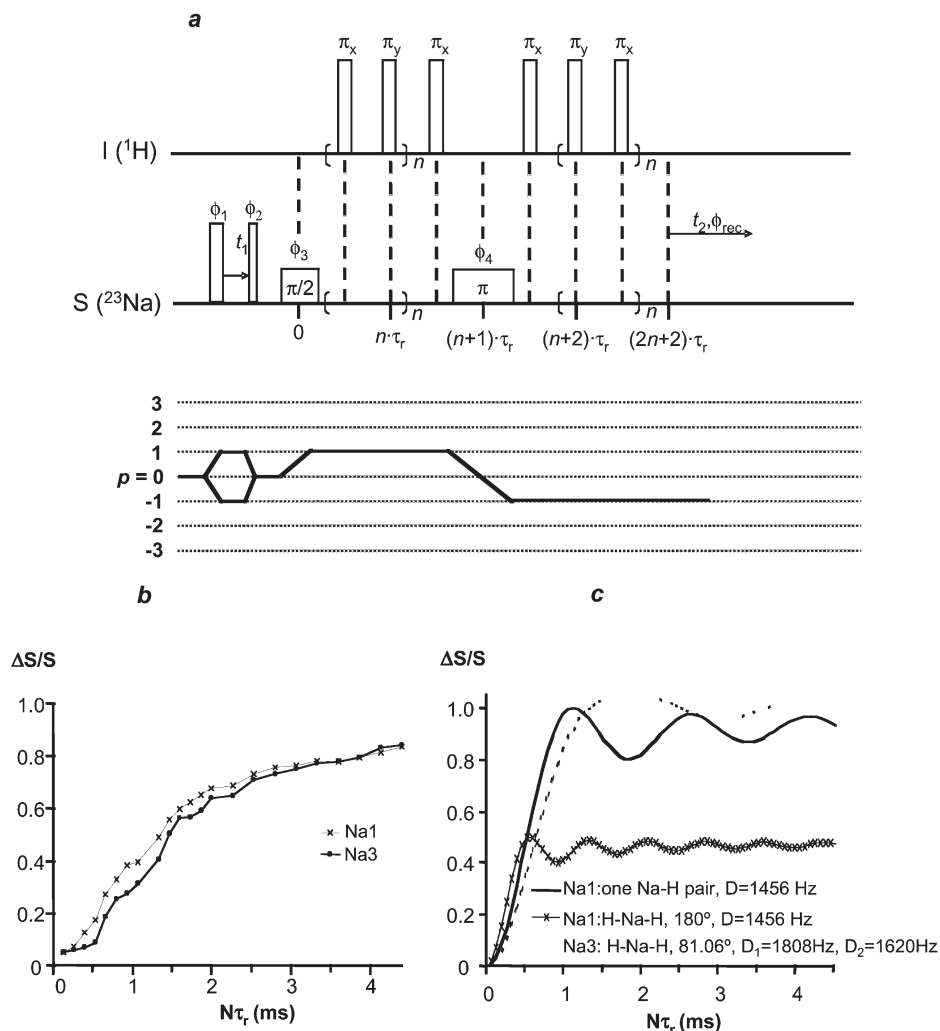
Fig. 21a–c **a** Pulse sequence and coherence transfer pathway of the $^1H \rightarrow {}^{23}Na$ STMAS REDOR experiment (n is an integer number and τ_r is the rotor period). **b** Experimental curves for anhydrous di-sodium hydrogen phosphate (Na_2HPO_4). **c** Calculated STMAS REDOR curves for anhydrous di-sodium hydrogen phosphate (Na_2HPO_4). Two of the three sodium sites (Na1 and Na2) in Na_2HPO_4 have a slightly distorted octahedral coordination (C_{Q1}=2.13 MHz, η_{Q1}=0.69, δ_{CS1}=5.52 ppm; C_{Q2}=1.37 MHz, η_{Q2}=0.21, δ_{CS2}=6.20) while Na3 has a strongly distorted tetrahedral coordination (C_{Q3}=3.70 MHz, η_{Q3}=0.27, δ_{CS3}=7.24 ppm). According to the crystal structure, each Na atom has only 2 H atoms in close proximity, the other H neighbours being much further away (>4.2Å). Na1 and Na2 are just in the centre of their two nearest H atoms, with Na1-H and Na2-H equal to 2.79Å (D=1456 Hz) and 2.70Å (D=1607 Hz), respectively, and Na3-H1=2.596Å (D_1=1808 Hz), Na3-H2=2.693Å (D_2=1620 Hz), (H1-Na3-H2)=81.06° (D is the dipolar coupling constant). However, the experimental STMAS REDOR curves obtained for Na1 and Na3 (b) are similar and do not agree with the STMAS REDOR curves calculated from the crystallographic data, most probably due to spin diffusion
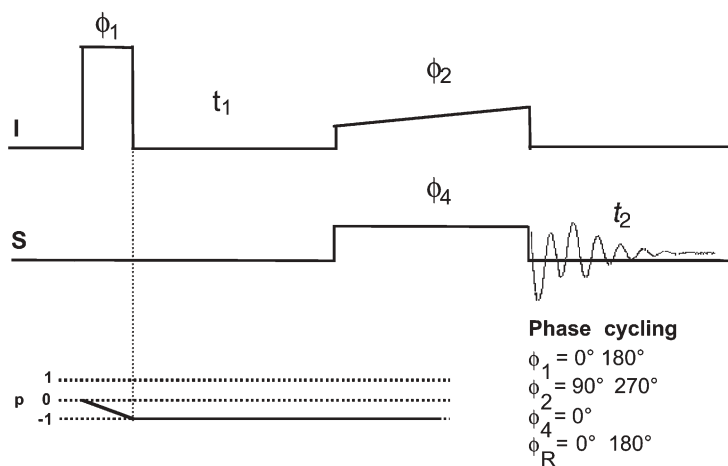
Fig. 22 Pulse sequence, coherence transfer pathway and phase-cycling for standard HET-COR experiment

tum coherences (±3Q) into single-quantum coherence (–1Q). In the case of a simple MQMAS experiment, the z-filter scheme allows for simultaneous acquisition of the echo and antiecho signals with equal intensity, which leads to cosine modulated FIDs and thus to pure absorption phase spectra. However, we have shown [95] that the z-filter approach cannot be used in MQHETCOR NMR experiments as proposed by Chan [93] and Mali et al. [94]. One possibility is to eliminate the antiecho pathway from their z-filter pulse sequence (recording just the echo signal). A better alternative is to adapt to spin-5/2 nuclei the scheme proposed by Wang et al. for spin–3/2 nuclei. The schematic diagrams of 3Q and 5QHETCOR experiments for I=5/2 nuclei (^{27}Al) using this approach are given in Figs. 23 and 24. The excitation of MQ coherences and their conversion into –1Q coherences is achieved by applying a pair of strong rf pulses at the I spin Larmor frequency. During the MQ and –1Q evolution periods, the I spins evolve under the effect of the internal Hamiltonian which primarily includes the second-order quadrupolar term. Only the isotropic echo, forming at time kt_1 after the second pulse (k=19/12 or 25/12, for 3Q or 5Q schemes, respectively) is then spin-locked to be used as a source of polarization for spin–1/2 (^{31}P) nuclei.

For the 3Q experiment, the echo pathway $0 \rightarrow +3(t_1) \rightarrow -1(kt_1)$–CP is selected by phase-cycling a series of 24 scans. The phase ϕ_1 of the first pulse is then shifted by 60° for the additional 24 scans, in order to achieve the spin temperature inversion, as it results in a 3×60°=180° shift of the coherence prior to the CP transfer. The same principle is applied to the selection of the $0 \rightarrow -5(t_1) \rightarrow -1(kt_1)$–CP pathway in the 5QHETCOR experiment. In this case, the phase ϕ_1 in a series of 40 scans is shifted by 36° to achieve the spin temperature inversion. It should be noted that the phases applied to the CP pulse on the I (^{27}Al) channel follow those of the I spin coherence at time kt_1. This procedure

Phase cycling

ϕ_1 = {0° 60° 120° 180° 240° 300°}*4
      {60° 120° 180° 240° 300° 0°}*4
ϕ_2 = {0°}*6 {180°}*6 {90°}*6 {270°}*6
ϕ_3 = 90° 270°
ϕ_4 = 0°
ϕ_R = {0°}*24 {180°}*24
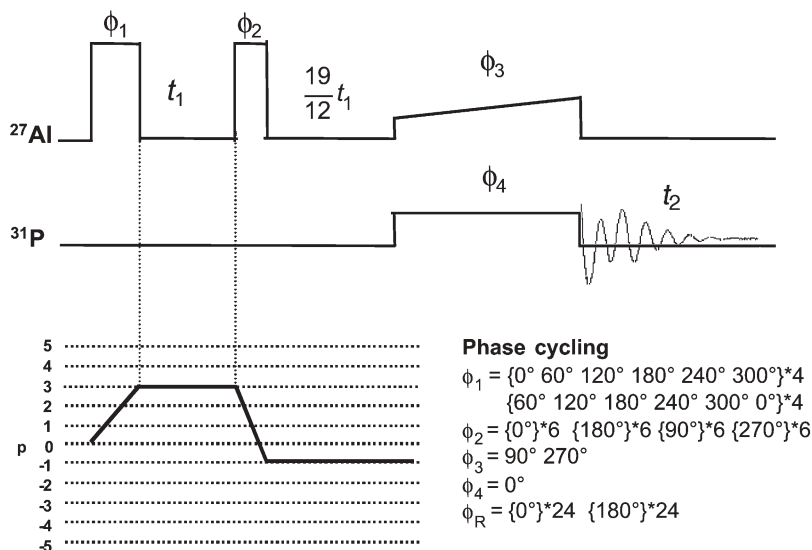
Fig. 23   Pulse sequence, coherence transfer pathway and phase cycling for 3Q HETCOR experiment of spin I=5/2 nuclei

Phase cycling

ϕ_1 = {0° 36° 72° 108° 144° 180° 216° 252° 288° 324°}*4
      {36° 72° 108° 144° 180° 216° 252° 288° 324° 0°}*4
ϕ_2 = {0°}*10 {180°}*10 {90°}*10 {270°}*10
ϕ_3 = 90° 270°
ϕ_4 = 0°
ϕ_R = {0°}*40 {180°}*40
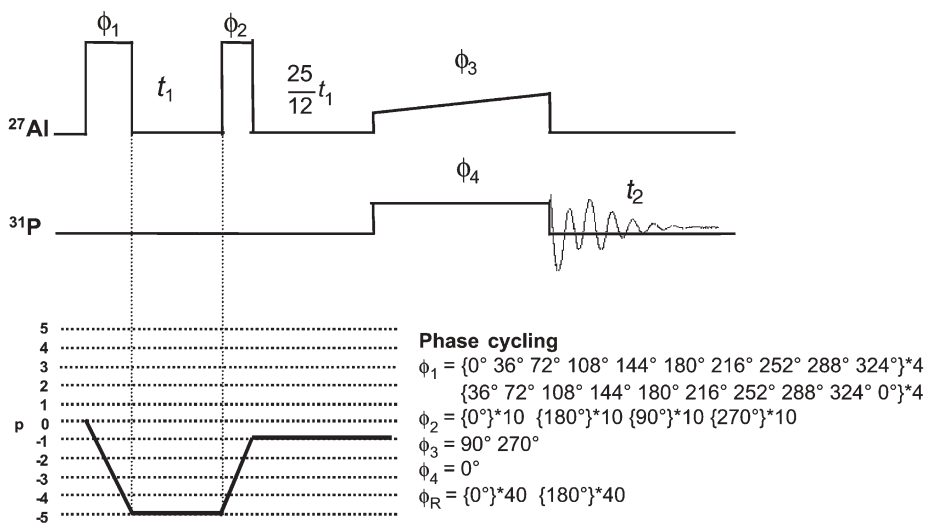
Fig. 24   Pulse sequence, coherence transfer pathway and phase cycling for 5Q HETCOR experiment of spin I=5/2 nuclei

results in the selection of the "real" component of the magnetisation, leading to a pure cosine evolution in t_1. Phase sensitive detection is accomplished using the hypercomplex method, which involves acquisition of a second set of data corresponding to the sine ("imaginary") part of the t_1 evolution. This is done by shifting the phase of the CP pulse by 90° or equivalently, the phase ϕ_1 by 90°/p, where p=3 or 5 for 3Q and 5QHETCOR experiments.

Delevoye et al. showed that low-power ^{27}Al decoupling may be used to remove residual J-coupling interactions between ^{31}P and ^{27}Al in some aluminophosphates [100]. Used in tandem with ^{1}H high-power decoupling, ^{27}Al decoupling greatly improves the resolution of ^{31}P MAS and ^{31}P→^{27}Al MQ HETCOR spectra. Figure 25 shows the ^{31}P→^{27}Al 3Q HETCOR spectrum of microporous aluminophosphate AlPO$_4$-14 [100]. No connectivity is observed for hexacoordinated Al(4) and P(1), tetracoordinated Al(3) and P(2), and tetracoordinated Al(2) and P(3). Pentacoordinated Al(1) exhibits connectivity between all four P sites. These results are in accordance with crystallographic evidence.

As another example, the ^{27}Al decoupled ^{27}Al→^{31}P 3QHETCOR spectrum (four-coordinated Al region only) of AlPO$_4$-40 acquired at 9.4 T is shown in Fig. 26 [101]. In spite of the high resolution, in both dimensions, of the decou-
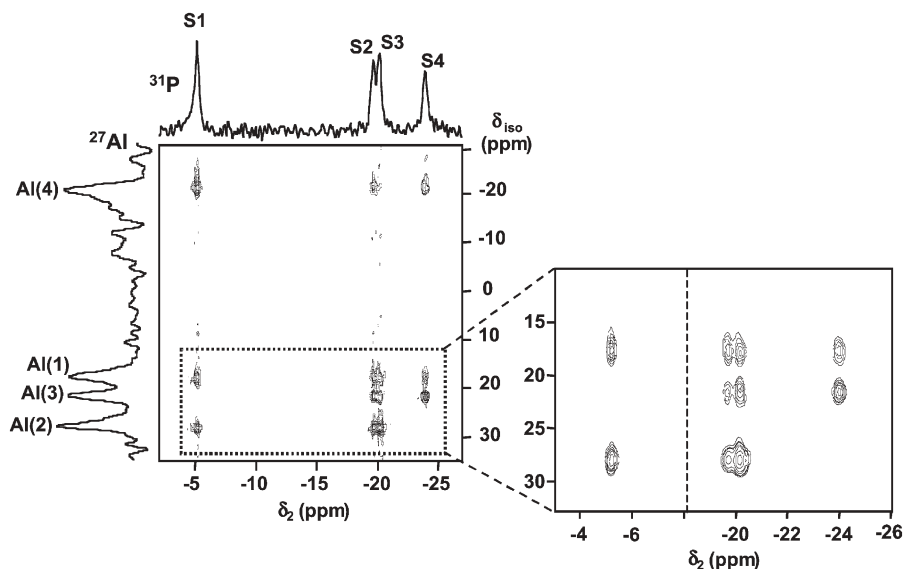
Fig. 25 ^{27}Al→^{31}P 3QHETCOR MAS spectrum of AlPO$_4$-14 with double-resonance ^{1}H/^{27}Al decoupling. Triple-quantum excitation and conversion were achieved with two pulses with lengths of 5.8 µs and 2.1 µs (B_1=100 kHz). The cross-polarization part of the sequence was carried out with ^{31}P and ^{27}Al B_1 fields of 29 and 6 kHz and a contact time of 1.5 ms. Decoupling B_1 fields were set to 90 kHz and 12 kHz for ^{1}H and ^{27}Al. The spectrum was acquired with 768 transients. The recycling delay was set to 1 s and the MAS rate was 10 kHz
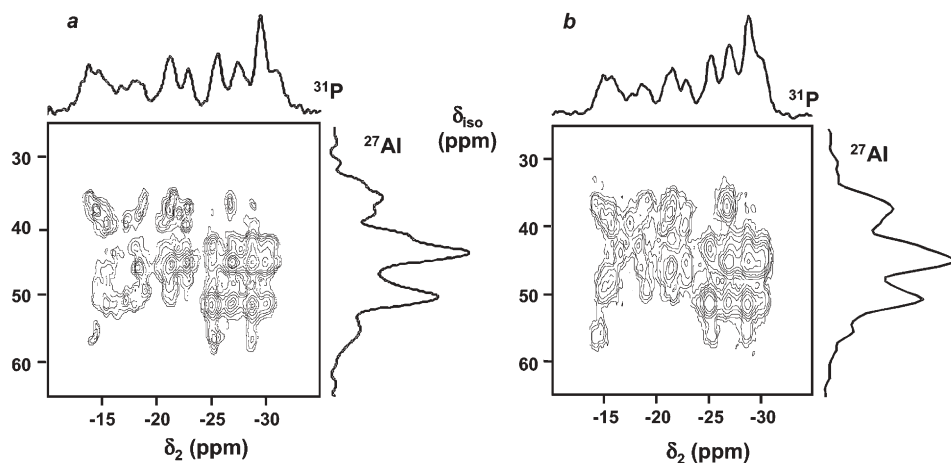
Fig. 26a, b Four-coordinated Al region of the: **a** $^{27}Al\rightarrow^{31}P$ 3QHETCOR; **b** MQ-*J*-HETCOR {^{31}P}^{27}Al spectra of AlPO$_4$-40 recorded with ^{27}Al decoupling during the acquisition. For the former spectrum 3Q excitation and conversion were achieved with two pulses with lengths of 3.8 µs and 1.8 µs (ν_1=120 kHz). Efficient CP was achieved with ^{31}P and ^{27}Al B_1 fields of 31 and 3 kHz and a contact time of 2.5 ms. 80 points (1056 transients per point) were acquired in the t_1 dimension in increments of $1/\nu_r$=100 µs. The recycling delay was set to 1 s and the MAS rate was 10 kHz. For the MQ-*J*-HETCOR spectrum 3Q excitation and conversion were achieved using two pulses with lengths of 4.0 µs and 1.8 µs (ν_1=100 kHz). The lengths of the 90° pulses were 8.5 µs and 18 µs for ^{31}P and ^{27}Al; 100 points (384 transients per point) were acquired in the t_1 dimension in increments of $1/\nu_r$=71.4 µs. The recycling delay was set to 1 s and the MAS rate was 14 kHz

pled 3QHETCOR spectrum, the interpretation of Al-O-P AlPO$_4$-40 connectivities is not straightforward due to the large number of lines present and to the overlap of some of these lines.

4.4
J-Coupling Based Experiments

Indirect spin-spin coupling constants, *J*, provide detailed information on the chemical bonding and molecular structure in liquids and solids. Typical isotropic values of spin-spin coupling constants between light nuclei and across oxygen bonds range across a few tens of Hertz. Weak unresolved *J*-couplings of ca. 20 Hz or less, involving quadrupolar nuclei, may be used to promote magnetisation transfer in INEPT-based sequences [102–104]. Recently, Massiot et al., have shown that (given sufficiently long coherence life times) it is possible to measure accurately *J*-couplings involving quadrupolar nuclei (^{27}Al) bonded to I=1/2 nuclei (^{31}P), using *J*-Resolved experiments [72]. Under MAS it is possible to measure the spin-echo decay time, T_2' of the selectively irradiated ^{27}Al central transition (pulse sequence π/2-τ-π-τ-acquisition), which corresponds to a non-refocusable line-width (due to isotropic chemical shifts, second-order
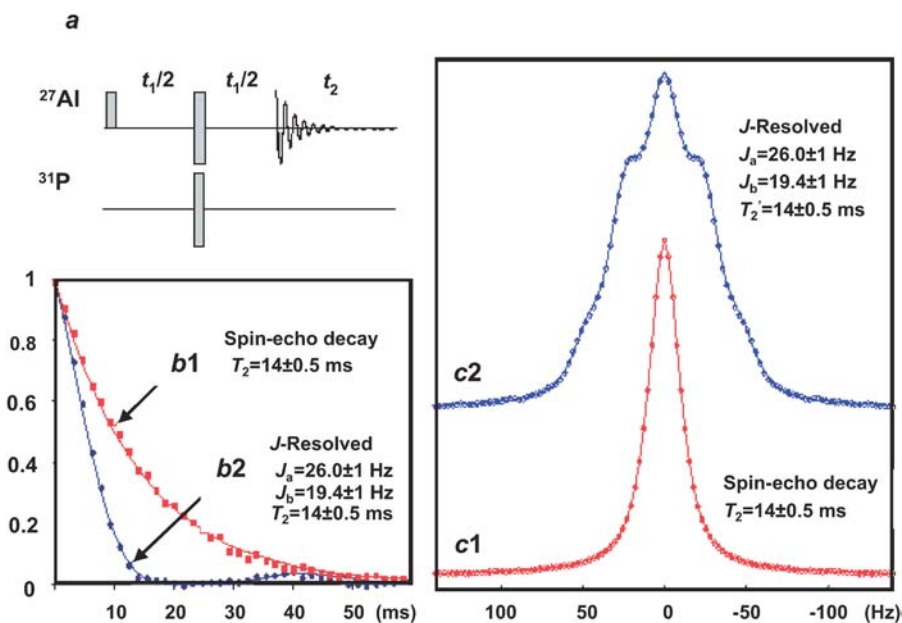
Fig. 27a–c $\{^{31}P\}^{27}Al$ *J*-Resolved experiment on $AlPO_4$ berlinite, acquired with υ_r=13 kHz: **a** pulse sequence; **b1, c1** time and frequency domains of the ^{27}Al spin-echo spectra (no ^{31}P pulse); **b2, c2** time and frequency domains of the $\{^{31}P\}^{27}Al$ *J*-Resolved spectra (*symbols*) with their modelling (*continuous line*). Reprinted with permission from [72], Massiot D et al. (2003) J Mag Reson 164:160–164. Copyright (2003) Elsevier Science

quadrupolar shifts and scalar couplings). The spin-echo decay of aluminophosphate berlinite exhibits a single exponential behaviour in time, (Fig. 27b1) while its Fourier transform (Fig. 27c1) may be modelled with a Lorentzian line, in the frequency domain, leading to a T_2' of ca. 14.1 ms [72]. The application of a π pulse on the ^{31}P channel simultaneously with the ^{27}Al pulse (Fig. 27a) introduces a modulation of the signal obtained by heteronuclear Al-O-P *J*-coupling, which can be modelled as

$$S(\tau) = \prod_n \cos(2\pi J_n \tau) \exp(-2\tau/T_2') \tag{48}$$

where n are the different coupled nuclei with their coupling J_n and T_2' corresponding to the non-refocusable linewidth under this experiment. A good fitting for the time and frequency domain data of berlinite is obtained by considering a model which comprises two different *J*-couplings J_a=$J_{Al-Oa-P}$=26.0 Hz (n=2), J_b=$J_{Al-Ob-P}$=19.5 Hz (n=2), and T_2' ca. 14.1 ms (Fig. 27b2,c2).

Massiot et al. have also shown that the Al-O-P *J*-coupling may be used to generate a *J*-HMQC heteronuclear correlation experiment (Fig. 28) [72]. *J*-HMQC directly derives from the *J*-resolved experiment, by splitting the ^{31}P π
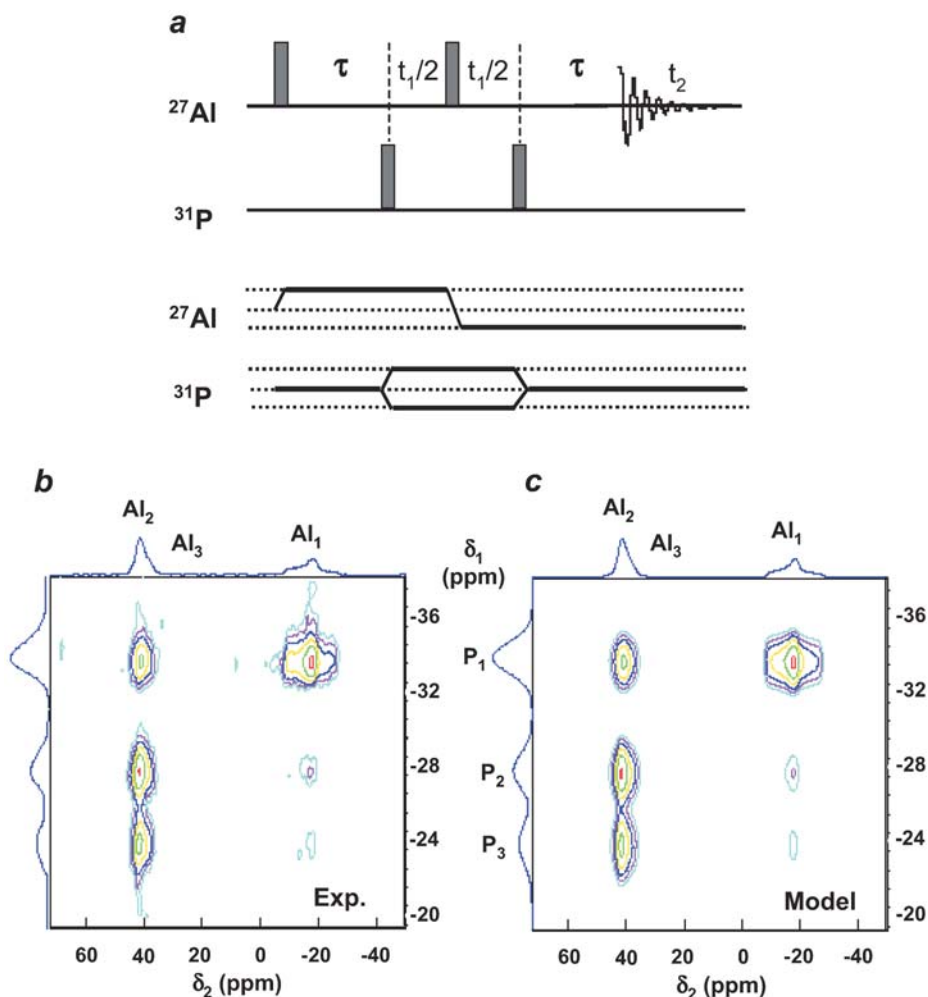
Fig. 28 **a** *J*-HMQC pulse sequence and coherence transfer pathways. **b** Experimental MAS *J*-HMQC {^{31}P}^{27}Al spectrum. **c** Simulated MAS *J*-HMQC {^{31}P}^{27}Al spectrum of microporous aluminophosphate VPI-5. See [70] for details. Reprinted with permission from [72], Massiot D et al. (2003) J Mag Reson 164:160–164. Copyright (2003) Elsevier Science

pulse into two $\pi/2$ pulses placed on both parts of the central ^{27}Al π pulse and separated by an incremented $T_1/2$ evolution encoding the indirect dimension of the two-dimensional spectrum (Fig. 28a). The phase cycling builds up the difference signal arising from double-quantum heteronuclear coherence, which evolves under ^{31}P isotropic chemical shift during T_1. As an example, consider the *J*-HMQC spectrum of microporous aluminophosphate VPI-5, shown in Fig. 28b,c [72]. The intensity of cross-peaks in this spectrum depends on T_2' of the three different and individual Al-O-P *J*-couplings. In the spectrum of VPI-
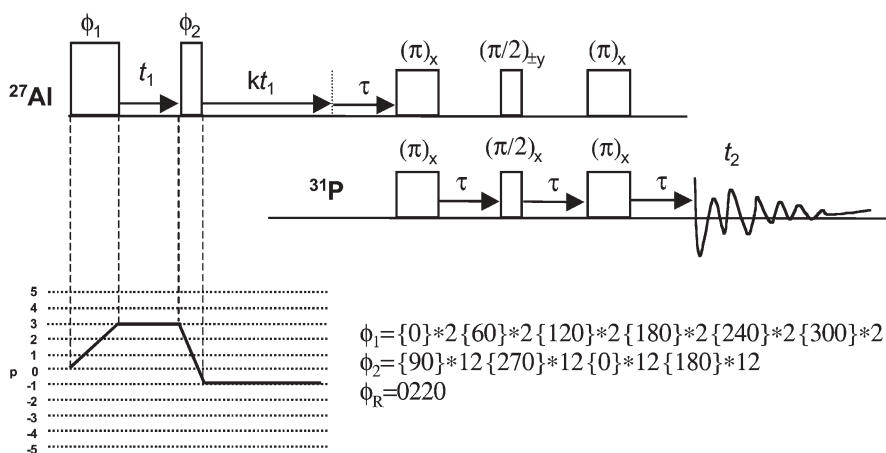
Fig. 29 Pulse sequence used to record the MQ-*J*-HETCOR {^{31}P}^{27}Al spectrum of AlPO$_4$-40 shown in Fig. 26b

5, tetrahedral Al$_2$ and Al$_3$ resonances overlap and both are well separated from the octahedral Al$_1$ resonance. Signals of sites Al$_2$ and Al$_1$ are minimised and maximised because they display the shorter and longer T_2' values. Examination of the HMQC build up curves yields J_{Al1-P1}~23 Hz, J_{Al1-P2}~J_{Al1-P3}~14 Hz. Because the P$_1$ sites have Al$_1$-O-P$_1$ angles of 150–169°, while the P$_2$ and P$_3$ sites have almost equal Al$_1$-O-P$_{2,3}$ angles, *J*-coupling may be very sensitive to the Al-O-P bond angle for octahedral Al sites. In addition, the large range of *J*-coupling values may allow spectral edition based on chemical bond [72].

Recently, the combination of *J*-based correlation methods (INEPT) with MQMAS (MQ-*J*-HETCOR experiment) was accomplished (Figs. 26b and 29) [105]. Unlike MQ-HETCOR, which is based on the spatial proximity of nuclei probed by the dipolar interaction, MQ-*J*-HETCOR maps the chemical bonding between the quadrupolar nuclei and the coupled spin under high-resolution conditions. This technique does not require the spin-locking of quadrupolar nuclei as is the case with CP-based HETCOR experiments. The short T_2 in solids may prevent the observation of relatively small *J*-couplings.

Trebosc et al. introduced a frequency-selective (FS) REDOR approach to a multi-spin system SI_n, where S is a quadrupolar nucleus. FS-REDOR may be used for accurate trough-space distance measurements in spin pairs that involve quadrupolar nuclei [106]. The experiment reveals heteronuclear dipolar and scalar couplings, which can be reintroduced selectively, site after site. Importantly, FS-REDOR may also be used under high-resolution provided by MQ-MAS, STMAS or I-STMAS.

5
Conclusion and Outlook

Multiple-Quantum Magic-Angle Spinning NMR is a powerful tool to study half-integer quadrupolar nuclei. It is capable of resolving inequivalent crystallographic and chemical sites in solids, separating isotropic chemical from isotropic quadrupolar shifts, and determining the quadrupolar coupling parameters e^2Qq/h and η_Q of individual local sites. MQMAS prompted a revolution in the dormant field of MQ quadrupolar NMR is solids. Despite its success and the recent advances, MQMAS continues to evolve and NMR spectroscopists and practitioners still face many challenges. Some of these are of a technical nature and involve issues such as employing MQMAS data for quantifying the abundance of chemical sites and improving the signal-to-noise ratio of the experiment, for example when it comes to observing low-γ nuclei, characterising systems affected by large chemical shielding, or unlocking the potential of 5Q and 7Q MAS spectroscopies towards improving spectral resolution [1a]. Other important problems to be addressed include the attribution of resonances to individual sites and the simplification of spectra and thus the use of double-resonance techniques in tandem with MQMAS NMR will play an increasingly important role in the near future. These techniques also offer the possibility of measuring dipolar interactions between the observed nuclei and their neighbours, permitting the direct estimation of interatomic distances. Clearly, it is necessary to develop further homo- and heteronuclear recoupling techniques on quadrupolar nuclei, and to make these recoupling protocols integral parts of MQMAS methodology [1a]. It is also anticipated that *J*-coupling based experiments will deserve much attention in the near future.

References

1. a) Frydman L (2002) Fundamentals of multiple-quantum magic-angle spinning NMR on half-integer quadrupolar nuclei. In: Grant DM, Harris, RK (eds) Encyclopedia of nuclear magnetic resonance. Wiley, Chichester, vol 9, p 262; b) Amoureux JP, Pruski M (2002) Advances in MQMAS. In: Grant DM, Harris, RK (eds) Encyclopedia of nuclear magnetic resonance. Wiley, Chichester, vol 9, p 226
2. Goldbourt A, Madhu PK (2002) Monatshfte Chem 133:1497
3. Engelhardt G, Michel D (1987) High resolution solid-state NMR of silicates and zeolites. Wiley, Chichester, New York
4. Freude D (2000) Quadrupolar nuclei in solid-state nuclear magnetic resonance. In: Meyers RA (ed) Encyclopedia of analytical chemistry. Wiley, Chichester, p 12188
5. Amoureux JP (1993) Solid State Nucl Magn Reson 2:83
6. Duer MJ (2002) (ed) Solid-state NMR spectroscopy. Principles and applications, Blackwell Science, Oxford
7. Samoson A, Lippmaa E (1983) Chem Phys Lett 100:205
8. Fenzke D, Freude D, Fröhlich T, Haase J (1984) Chem Phys Lett 111:171
9. Man PP, Klinowski J, Trokiner A, Zanni H, Papon P (1988) Chem Phys Lett 191:43
10. Amoureux JP, Fernandez C, Dumazy Y (1995) J Chim Phys 2:1939

11. Vega S, Pines A (1977) J Chem Phys 66:5624
12. Vega S (1977) J Chem Phys 68:5518
13. Samoson A, Lipmaa E, Pines A (1988) Mol Phys 65:1013
14. Chmelka BF, Mueller KT, Pines A, Stebbins J, Wu Y, Zwanziger JW (1989) Nature 339:42
15. Llor A, Virlet J (1988) Chem Phys Lett 152:248
16. Frydman L, Harwood JS (1995) J Am Chem Soc 117:5367
17. Amoureux JP, Fernandez C (1998) Solid State Nucl Magn Reson 10:211
18. Jerschow A, Logan JW, Pines A (2001) J Magn Reson 149:268
19. Vega S, Naor Y (1981) J Chem Phys 75:75
20. Fernandez C, Amoureux JP (1995) Chem Phys Lett 242:449
21. Medek A, Harwood JS, Frydman L (1995) J Am Chem Soc 117:12779
22. Wu G, Rovnyak D, Sun BQ, Griffin RG (1996) Chem Phys Lett 249:210
23. Massiot D, Touzo B, Trumeau D, Coutures JP, Virlet J, Florian P, Grandinetti P (1996) Solid State Nucl Magn Reson 6:73
24. Amoureux JP, Fernandez C, Steuernagel S (1996) J Magn Reson A 123:116
25. Massiot D, Touzo B, Trumeau D, Coutures JP, Virlet J, Florian P, Grandinetti PJ (1996) Solid State Nucl Magn Reson 6:73
26. Brown SP, Heyes SJ, Wimperis S (1996) J Magn Reson A 119:280
27. Brown SP, Wimperis S (1997) J Magn Reson 128:42
28. Amoureux JP, Fernandez C (1998) Solid State Nucl Magn Reson 10:211
29. Massiot D, Fayon F, Capron M, King I, Le Calvé S, Alonso B, Durand JO, Bujoli B, Gan Z, Hoatson G (2002) Magn Reson Chem 40:70
30. Fernandez C, Amoureux JP, Chezeau JM, Delmotte L, Kessler H (1996) Microporous Mater 6:331
31. Wang SH, Xu Z, Baltisberger JH, Bull LM, Stebbins JF, Pines A (1997) Solid State Nucl Magn Reson 8:1
32. Pike KJ, Malde RP, Ashbrook SE, McManus J, Wimperis S (2000) Solid State Nucl Magn Reson 16:203
33. Quoineaud AA (2002) PhD thesis, Université de Caen
34. Czjzek G, Fink J, Gotz F, Schmidt H, Coey JMD, Rebouillat JP, Lienard A (1981) Phys Rev B 23:10356
35. Amoureux JP, Fernandez C, Dumazy Y (1995) J Chim Phys 2:1939
36. Smith SA, Levante TO, Meier BH, Ernst RR (1994) J Magn Reson A 106:75
37. Bak M, Rasmussen JT, Nielsen NC (2000) J Magn Reson 147:296
38. Gan Z (2000) J Am Chem Soc 122:3242
39. Gan Z (2001) J Chem Phys 114:10845
40. Pike KJ, Sharon SE, Wimperis S (2001) Chem Phys Lett 345:400
41. Huguenard C, Taulelle F, Gan Z (2002) J Magn Reson 156:131
42. Kwak HT, Gan Z (2003) J Magn Reson 164:369
43. Amoureux JP, Morais CM, Trebosc J, Rocha J, Fernandez C (2003) Solid State Nucl Magn Reson 23:213
44. Ashbrook SE, Wimperis S (2002) J Am Chem Soc 124:11602
45. Ashbrook SE, Antonijevic S, Berry AJ, Wimperis S (2002) Chem Phys Lett 364:634
46. Ding S, McDowell CA (1997) Chem Phys Lett 270:81
47. Marinelli L, Medek A, Frydman L (1998) J Magn Reson 132:88
48. Wu G, Rovnyak D, Griffin RG (1996) J Am Chem Soc 118:9326
49. Vega AJ (1992) J Magn Reson 96:50
50. Lim KH, Grey CP (1998) Solid State Nucl Magn Reson 13:101
51. Caldarelli S, Ziarelli F (2000) J Am Chem Soc 122:12015
52. Kentgens APM, Verhagen R (1999) Chem Phys Lett 300:435
53. Madhu PK, Goldbourt A, Frydman L, Vega S (1999) Chem Phys Lett 307:41

54. Vega S, Naor Y (1981) J Chem Phys 75:75
55. Madhu PK, Goldbourt A, Frydman L, Vega S (2000) Chem Phys Lett 112:2377
56. Schäfer H, Iuga D, Verhagen R, Kentgens APM (2000) J Chem Phys 114:3073
57. Yao Z, Kwak HT, Sakellariou D, Emsley L, Grandinetti PJ (2000) Chem Phys Lett 327:85
58. Madhu PK, Levitt MH (2000) J Magn Reson 155:150
59. Vosegaard T, Massiot D, Grandinetti PJ (2000) Chem Phys Lett 326:454
60. Goldbourt A, Madhu PK, Vega S (2000) Chem Phys Lett 320:448
61. Morais C, Lopes M, Fernandez C, Rocha J (2003) Magn Reson Chem 41:679
62. Vosegaard T, Florian P, Massiot D, Grandinetti PJ (2001) J Chem Phys 114:4618
63. Massiot D (1996) J Magn Reson A 122:240
64. Vosegaard T, Larsen FH, Jakobsen HJ, Ellis PD, Nielsen CN (1997) J Am Chem Soc 122:9055
65. Massiot D, Montouillout V, Fayon F, Florian P, Bessada C (1997) Chem Phys Lett 272:295.
66. Massiot D, Vosegaard T, Magneron N, Trumeau D, Montouillout V, Berthet P, Loiseau T, Bujoli B (1999) Solid State Nucl Magn Reson 15:159
67. Pruski M, Lang DP, Fernandez C, Amoureux JP (1997) Solid State Nucl Magn Reson 7:327
68. Ashbrook SE, Brown SE, Wimperis S (1998) Chem Phys Lett 288:509
69. Wang SH, De Paul SM, Bull LM (1997) J Magn Reson 125:364
70. Fernandez C, Lang DP, Amoureux JP, Pruski M (1998) J Am Chem Soc 120:2672
71. Pruski M, Baily A, Lang DP, Fernandez C, Amoureux JP (1999) Chem Phys Lett 307:35
72. Massiot D, Fayon F, Alonso B, Trebosc J, Amoureux J-P (2003) J Magn Reson 164:160
73. Hartmann SR, Hahn EL (1962) Phys Rev 128:2042
74. Stejskal EO, Schaefer J, Waugh JS (1977) J Magn Reson 28:105
75. Ashbrook SE, Wimperis S (2000) Mol Phys 98:1
76. Vega S (1981) Phys Rev A 23:3152
77. Wokaun A, Ernst RR (1977) J Chem Phys 67:1752
78. Müller L, Eckman R, Pines A (1980) Chem Phys Lett 76:149
79. Vega AJ (1992) J Magn Reson 96:50
80. Vega AJ (1992) Solid State Nucl Magn Reson 1:17
81. Ding S, McDowell CA (1995) J Magn Reson A 114:80
82. Sun W, Stephen JT, Potter LD, Wu Y (1995) J Magn Reson A 116:181
83. Pruski M, Lang DP, Fernandez C, Amoureux JP (1997) Solid State Nucl Magn Reson 7:327
84. Fernandez C, Delevoye L, Amoureux JP, Lang DP, Pruski M (1997) J Am Chem Soc 119:6858
85. Ashbrook SE, Brown SP, Wimperis S (1998) Chem Phys Lett 288:509
86. Ashbrook SE, Wimperis S (2000) J Magn Reson 147:238
87. Lim KH, Grey CP (1999) Chem Phys Lett 312:45
88. Rovnyak D, Baldus M, Griffin RG (2000) J Magn Reson 142:145
89. Ashbrook SE, Wimperis S (2001) Chem Phys Lett 340:500
90. Gullion T, Schaefer J (1990) J Magn Reson 81:379
91. Morais CM, Amoureux JP, Huguenard C, Fernandez C, Rocha J, Taullele F (2002) Book of abstracts, 16th European Experimental Nuclear Magnetic Resonance Conference, Prague, Czech Republic, PB45
92. Steuernagel S (1998) Solid State Nucl Magn Reson 11:197
93. Chan JCC (1999) J Magn Reson 140:487
94. Mali G, Amoureux JP, Kaucic V (2000) Phys Chem Chem Phys 2:5737
95. Fernandez C, Morais C, Pruski M (2001) Phys Chem Chem Phys 3:2552
96. Ernst RR, Bodenhausen G, Wokaun A (1997) Principles of nuclear magnetic resonance in one and two dimensions. Clarendon Press, Oxford

 97. Fyfe CA, Grodney H, Mueller KT, Wong-Moon KC, Markus T (1992) J Am Chem Soc 114:5876
 98. Fyfe CA, Mueller KT, Grodney H, Wong-Moon KC (1993) J Phys Chem 97:13484
 99. Jarvie TP, Wenslow RM, Mueller KT (1995) J Am Chem Soc 117:570
100. Delevoye L, Fernandez C, Morais CM, Montouillout C, Rocha J (2003) Solid State Nucl Magn Reson 21:61
101. Fernandez C, Morais C, Pruski M (2001) Solid State Nucl Magn Reson 21:61
102. Fyfe CA, Wong-Moon KC, Huang Y, Grondley H, (1995) J Am Chem Soc 117:10397
103. Fyfe CA, Meyer zu Altenschildesche KC, Wong-Moon KC, Grondley H, Chezeau JM (1997) Solid State Nucl Magn Reson 9:97
104. Kao H-M, Grey CP (1998) J Magn Reson 133:313
105. Massiot D, Fayon F, Alonso B, Montouillout V, Fernandez C, Morais C, Rocha J (2003) The 3rd Alpine Conference on Solid-State NMR, Chamonix Mont-Blanc
106. Trebosc J, Amoureux J-P, Wiench JW, Pruski M (2003) Chem Phys Lett 374:432

Dipolar Solid State NMR Approaches Towards Medium-Range Structure in Oxide Glasses

Hellmut Eckert (✉) · Stefan Elbers · Jan Dirk Epping · Michael Janssen ·
Martin Kalwei · Wenzel Strojek · Ulrike Voigt

Westfälische Wilhelms-Universität Münster, Institut für Physikalische Chemie,
Corrensstrasse 30, 48149 Münster, Germany
eckerth@uni-muenster.de

Abstract Modern solid state nuclear magnetic resonance presents new powerful opportunities for the elucidation of medium range order in glasses in the sub-nanometer region. In contrast to standard chemical shift spectroscopy, the strategy presented here is based on the precise measurement and quantitative analysis of internuclear magnetic dipole-dipole interactions, which can be related to distance information in a straightforward manner. The

review discusses the most commonly employed experimental techniques, producing dipolar coupling information in both homo- and heteronuclear spin systems. The approach is particularly powerful in combination with magic-angle sample spinning, producing site-resolved dipolar coupling information. We present new applications to oxide-based network glasses, permitting network connectivities and spatial cation distributions to be elucidated.

1
Introduction

Compared to crystalline solids, glasses present a much more formidable challenge to structure elucidation. Owing to the lack of long-range periodicity in the glassy state, diffraction techniques are fairly powerless, and structural concepts typically emerge from the joint interpretation of numerous complementary spectroscopic experiments. Because different techniques provide information with widely different inherent spatial resolution, it is useful to separate the structural description into different length scale domains. These domains include: (1) short-range order involving only the first atomic coordination spheres (distance region 0.15–0.3 nm), (2) second-nearest neighbour environments (0.3–0.5 nm), (3) nanostructure (0.5–3 nm), (4) mesostructure (3–500 nm) and, finally, (5) microstructure (>500 nm). While imaging techniques, such as electron microscopy, are particularly powerful for addressing structural issues in domains (4) and (5), methods such as nuclear magnetic resonance (NMR) spectroscopy and extended X-ray absorption fine structure (EXAFS) emphasize primarily local information at the atomic level. EXAFS can provide accurate bond distances and coordination numbers, and NMR spectra contain complementary information about site symmetries and coordination geometries, permitting the quantitative identification of specific types of coordination polyhedra. Unlike EXAFS, however, the utility of which is quickly diminished at longer distances, NMR spectroscopic information extends significantly beyond the first coordination sphere. For this reason NMR remains the most powerful approach for the study of structural issues on the 0.3 to 3 nm length scale (domains (2) and (3)), particularly in the sub-nanometer region, commonly dubbed 'medium-range structure'.

Figure 1a portrays the commonly accepted gross structural view of the oxide glasses subject to this review. Typically, a two- or three-dimensional network is established by *network former* species such as silica, boron oxide, or phosphorus pentoxide, containing the framework atoms in three- or fourfold coordination with oxygen. This network is transformed by the incorporation of group- I or II oxides, the so-called *network modifiers*, which rupture oxygen bridges and thereby impart negative charge to the framework. The sites for the
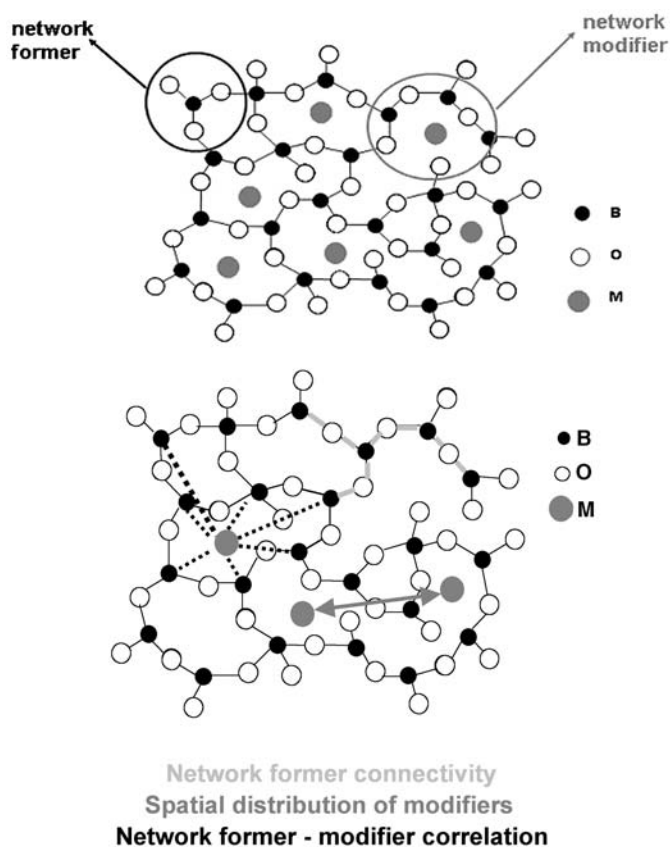
Fig. 1 Pictorial description of short- and medium-range structure in glasses (top and bottom)

charge-balancing alkaline or alkaline earth metal cations are created by this transformation. While the first coordination spheres of both the network formers and the network modifiers are dominated by oxygen, interesting structural issues arise on more extended coordination spheres, as summarized by Fig. 1b. These issues include (1) framework connectivity, (2) network former/network modifier distance correlations, and (3) the spatial distribution of the network modifier ions. Among the various types of internal interactions affecting NMR spectra, the magnetic dipole-dipole interactions are the most informative with regard to these questions, owing to their direct relation to inter-nuclear distance distributions. The research challenge thus consists of (1) selectively extracting reliable dipolar coupling information from the complex internal NMR Hamiltonian, and (2) translating this information into a structural description of the glasses in question. In the following review, we will illustrate the state of the art in the field, using specific examples from the literature as well as from recent work in our laboratory.

2
Theoretical Background and Methodology

2.1
The Solid State NMR Hamiltonian and its Simplification by Selective Averaging

In general, the internal solid state NMR Hamiltonian of a static sample can be written as

$$\mathscr{H}_{int} = \mathscr{H}_D + \mathscr{H}_J + \mathscr{H}_{CS} + \mathscr{H}_Q \qquad (1)$$

with

$$\mathscr{H}_D = \mathscr{H}_D\,(homo) + \mathscr{H}_D\,(hetero) \qquad (a)$$

$$\mathscr{H}_J = \mathscr{H}_J\,(homo,\,iso) + \mathscr{H}_J\,(hetero,\,iso) + \mathscr{H}_J\,(homo,\,aniso) \\ + \mathscr{H}_J\,(hetero,\,aniso) \qquad (b)$$

$$\mathscr{H}_{CS} = \mathscr{H}_{CS}\,(iso) + \mathscr{H}_{CS}\,(aniso) \qquad (c)$$

$$\mathscr{H}_Q = \mathscr{H}_Q^{(1)} + \mathscr{H}_Q^{(2)} \qquad (d)$$

comprising contributions from (Eq. 1a) homo- as well as heteronuclear dipole-dipole interactions, (Eq. 1b) isotropic and anisotropic indirect spin-spin interactions, (Eq. 1c) isotropic and anisotropic magnetic shielding ("chemical shifts"), and (Eq. 1d) nuclear electric quadrupolar interactions affecting the spectra to first- and second-order within the framework of perturbation theory.

In view of the complex Hamiltonian (Eq. 1) the analysis of a simple solid state NMR spectrum in terms of the individual interaction contributions is only possible in those rare cases where one interaction strongly dominates the others. For the more general case, special experimental strategies are required to simplify the Hamiltonian, by averaging out certain interactions in real space or spin space. Alternatively, multi-pulse schemes are often available which separate two selected interactions into two or three spectroscopic dimensions. Modern multidimensional pulsed NMR methodology has provided a plethora of such *selective averaging* experiments, greatly enhancing the informational content of spectra acquired in the solid state [1, 2]. The most popular averaging technique involves mechanical sample rotation about an axis inclined at 54.7° with respect to the external magnetic field direction. This manipulation averages out all the anisotropic interactions affecting static spectra in the first-order perturbation theory limit, resulting in the simplified MAS Hamiltonian

$$\mathscr{H}_{MAS} = \mathscr{H}_J\,(iso) + \mathscr{H}_{CS}\,(iso) + \mathscr{H}_Q^{(2)} \qquad (2)$$

In MAS-NMR spectra, only the isotropic chemical shielding and indirect interactions survive, and (for I>1/2 nuclei), the second-order nuclear electric

quadrupolar coupling is scaled down significantly, albeit not eliminated. For the structural elucidation of glasses, the MAS NMR approach has played an outstanding role for the past two decades, permitting the identification of bonding partners, coordination numbers and symmetries, as well as the quantification of resolvable sites, primarily on the basis of isotropic chemical shift measurements [3]. These studies have resulted in a considerable body of knowledge concerning the immediate nearest neighbour atomic environments in a large variety of oxide glasses.

2.2
Magnetic Dipole-Dipole Couplings in Multi-Spin Systems

Unfortunately, chemical shieldings are in general much less sensitive to configurational changes involving second- and third-nearest neighbor environments or even longer distance scales. Bonding and atomic distribution effects involving such higher coordination spheres can be addressed more specifically by measurements of magnetic dipole-dipole interactions. In the simplest case of an isolated two-spin system the homonuclear dipolar Hamiltonian takes the form

$$\mathcal{H}_d = \frac{\mu_0 \hbar}{4\pi} \frac{\gamma^2}{2r_{ij}^3} (3I_z^2 - I^2)(3\cos^2\theta - 1) \tag{3}$$

emphasizing the straightforward connection with internuclear distances r_{ij}. In this expression I and I_z are angular momentum operators representing the nuclear spin and its z-component, γ is the gyromagnetic ratio (a nuclear constant) and θ is the angle between the internuclear vector and the magnetic field direction. In glasses, however, the dipolar Hamiltonians are in general more complex, as they usually comprise multi-spin interactions. In these cases, the magnetic dipole-dipole couplings are most conveniently quantified in terms of the van-Vleck second moments [4, 5], which characterize the average mean square of the local field experienced by the observe-nuclei. due to the magnetic moments of surrounding spins. According to the van Vleck theory, these second moments relate to internuclear distance distributions via the formulae

$$M_2^{I-I} = \frac{3}{5}\left(\frac{\mu_0}{4\pi}\right)^2 \cdot \hbar^2\, \gamma_I^4 I(I+1) \cdot N_I^{-1} \sum_{i \neq j} r_{ij}^{-6} \tag{4a}$$

$$M_2^{I-S} = \frac{4}{15}\left(\frac{\mu_0}{4\pi}\right)^2 \cdot \hbar^2\, \gamma_I^2 \gamma_S^2 S(S+1) \cdot N_I^{-1} \sum_{s} r_{IS}^{-6} \tag{4b}$$

for homo- and heteronuclear dipolar couplings, where the summation extends over N observe spins considered. The different pre-factors shown in Eq. (4a,b) arise from the fact that the homonuclear dipole Hamiltonian contains an en-

ergy-conserving quantum mechanical contribution from spin exchange ("flip-flop"-transitions) which is absent in the heteronuclear case. We note further that in samples with inhomogeneously broadened lineshapes these "flip-flop" transitions will be absent from $\mathcal{H}_d$(homo) also, if the difference in the resonance frequencies of the interacting spins exceeds the magnitude of the dipolar coupling. In this case, the pre-factor 3/5 in Eq. (4a) must be replaced by 4/15 to account for the absence of spin exchange. For similar reasons the expression for $\mathcal{H}_d$(homo) must be modified if the resonance lines are subject to nuclear electric quadrupolar splittings. In this case, the appropriate van Vleck formula is given by

$$M_2 = F\,(I) \left(\frac{\mu_0}{4\pi}\right)^2 \gamma^4\,\hbar^2\,N_I^{-1} \sum_{i \neq j} \left\{\frac{3}{2}\left(\frac{1 - 3\cos^2\theta_{ij}}{r_{ij}^3}\right)\right\}^2 \tag{5}$$

where F(I) is a spin-dependent factor, which further depends on the homogeneity of the nuclear electric quadrupolar coupling within the sample [6].

3
Experimental Techniques

3.1
Static Spin Echo Decay Spectroscopy

To obtain the desired magnetic dipole-dipole coupling information, two principal strategies are available. Either the complex internal spin Hamiltonian (Eq. 1) in static samples is simplified by suitable averaging methods (*decoupling*), or the dipolar interaction is re-introduced into a simplified Hamiltonian (for example the MAS-Hamiltonian (Eq. 2)), using appropriate *recoupling* techniques. Nowadays the re-coupling approach is favoured, and all the techniques currently in use for measuring heteronuclear dipolar couplings in glasses belong to this family. For the recoupling of homonuclear interactions a wide variety of analogous techniques are available as well. However, so far their applications to glasses have remained at the qualitative level, e.g., for proving the existence of spatial proximity and/or bond connectivities. To date, the most reliable quantitative information in multi-spin systems comes from spin echo decay spectroscopy on static samples. The Hahn spin echo (see Fig. 2) eliminates all those interactions where the Hamiltonians scale linearly with the spin operator I_z, including chemical shielding and heteronuclear dipole-dipole interaction terms [7, 8]. As a result, a plot of normalized echo intensity I/I_0 as a function of evolution time $2t_1$ is only affected by homonuclear dipole-dipole interactions, which are bilinear in I_z. For a multi-spin system, a Gaussian decay is expected (and observed):

$$\frac{I(2t_1)}{I_0} \, ^2 \exp\left[-\frac{M_2^{I-I}}{2}(2t_1)^2\right] \tag{6}$$
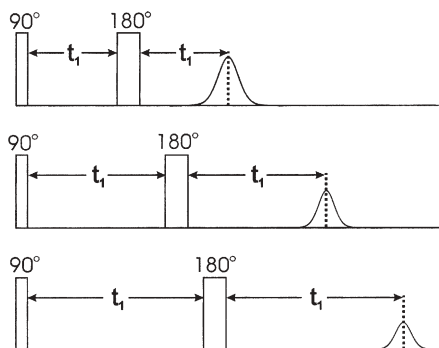
Fig. 2 Timing diagram of the spin echo decay spectroscopy method devised for the measurement of homonuclear dipole-dipole interactions

affording a reliable measurement of the homonuclear van Vleck second moment M_2^{I-I} [9, 10]. In principle, the experimental M_2 values also include a contribution from the indirect spin-spin couplings, as the spin echo sequence is unable to separate direct from indirect internuclear interactions. Fortunately, for most glasses, the indirect interactions are one to two orders of magnitude weaker than the direct dipole-dipole couplings and can therefore be safely neglected.

Serious complications arise, however, if the spins are subject to strong nuclear electric quadrupolar interactions, which tend to modify the echo amplitudes measured. In such cases, it is still possible to extract dipole-dipole coupling information from spin echo decay spectroscopy, if the π-pulses are applied entirely selectively to the central $|1/2\rangle \leftrightarrow |-1/2\rangle$ transition [6]. If the resonance frequencies between the coupled nuclei are sufficiently similar to allow for spin-exchange via the flip-flop mechanism, Eq. (5) turns into

$$M_2 = 0.9562 \left(\frac{\mu_0}{4\pi}\right)^2 \gamma^4 \hbar^2 N_I^{-1} \sum_{i \neq j} r_{ij}^{-6} \tag{7}$$

Experimental studies have shown that, in practice, the effect of second-order quadrupolar interactions can produce gross deviations from a Gaussian-type decay curve, reflecting the influence of higher moments on the time evolution behavior [11]. It has been shown, however, that dipolar information can still be obtained if the analysis is restricted to the initial curvature in the limit of short dipolar evolution times ($2t_1 < 200$ μs). The validity of this approach has been tested recently for homonuclear ^{23}Na-^{23}Na dipole-dipole interactions in crystalline solids, for which the M_2 values are readily calculable from the known crystal structures [11].

Figure 3 shows an excellent linear correlation between theory and experiment, confirming the validity of this procedure for sodium-containing materials.
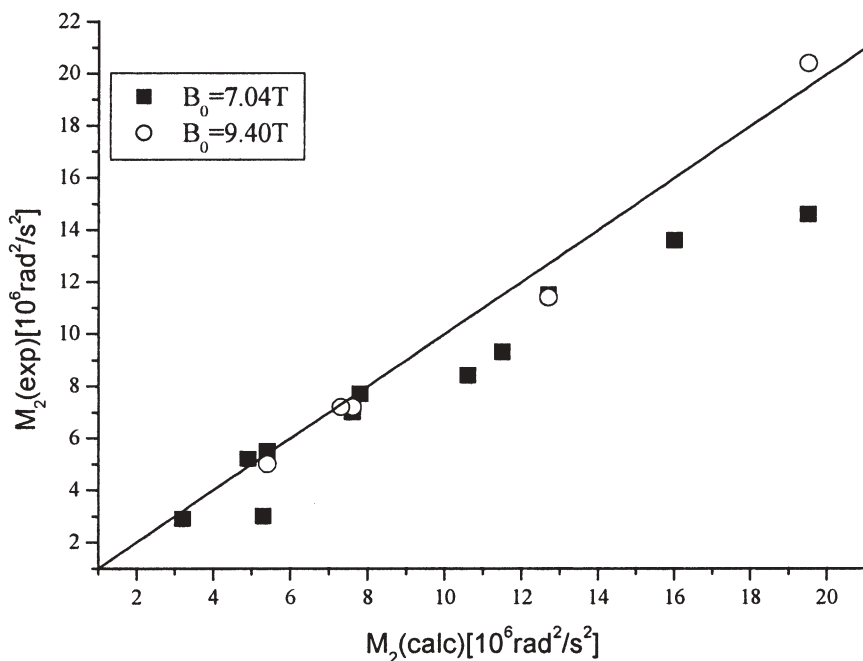
Fig. 3 Experimental and calculated M_2 values characterizing the ^{23}Na-^{23}Na magnetic dipolar interactions in crystalline sodium salts. *Squares*: data from [11] (7.04 T); *circles*: new data (9.4 T)

3.2
Spin Echo Double Resonance (SEDOR)

Static spin echo decay spectroscopy also forms the basis for the measurement of magnetic dipole-dipole interactions between two unlike nuclei I and S. While this interaction is refocused by the Hahn spin echo, it can be recoupled by applying a π-pulse to the S-spins during the dipolar evolution period [12]. This manipulation inverts the sign of the heterodipolar Hamiltonian, and thereby interferes with the ability of the Hahn spin echo technique to refocus this interaction. The corresponding pulse sequence, termed SEDOR (*spin echo double resonance*), shown in Fig. 4, compares the I-spin echo intensity as a function of dipolar evolution time (a) in the absence and (b) in the presence of the $\pi(S)$ pulses. Experiment (a) produces a decay $F(2t_1)/F_0$, which is dominated by homonuclear dipole-dipole interactions, while experiment (b) results in an accelerated decay, reflecting the contribution from the heteronuclear I-S dipole-dipole interaction, which is now re-introduced into the spin Hamiltonian. For multi-spin systems, a Gaussian decay is expected:

$$\frac{I(2t_1)}{I_0}^2 = \frac{F(2t)}{F_0} \cdot \exp - (2t_1^2 M_2^{Li-Na}) \tag{8}$$
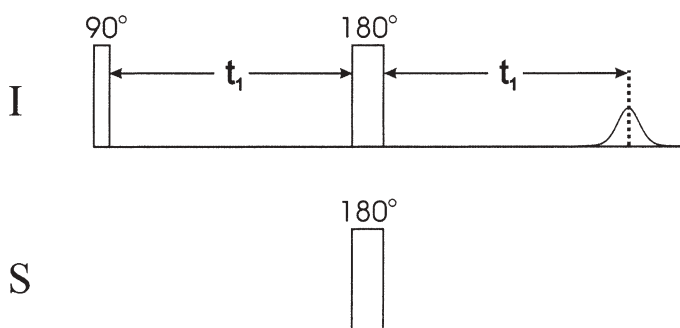
Fig. 4 Pulse sequence of spin echo double resonance (SEDOR) spectroscopy

the rate of which is given by the heteronuclear second moment M_{2d}(hetero). The quantitative reliability of SEDOR is compromised if the S-spins are subject to strong nuclear electric quadrupolar interactions. In such cases, the presence of first-order quadrupolar splittings generates large resonance offsets for the $|m|=3/2 \leftrightarrow |m|=1/2$ "satellite transitions", resulting in a spin population inversion that is incomplete [13]. An example is shown in Fig. 5 (left part), which compares the experimental ^{23}Na{^{7}Li}SEDOR result measured for the model compound LiNaSO$_4$ with the theoretical expectation (dotted curve). Clearly, the

$$\frac{I(2t_1)}{I(0)} = \left(\frac{F(2t_1)}{F(0)}\right)\left(1 - f\left[1 - \exp\frac{-M_2^{I-S}(2t_1)^2}{2}\right]\right)$$

^{7}Li: f = 0.75 ^{6}Li: f = 1.00
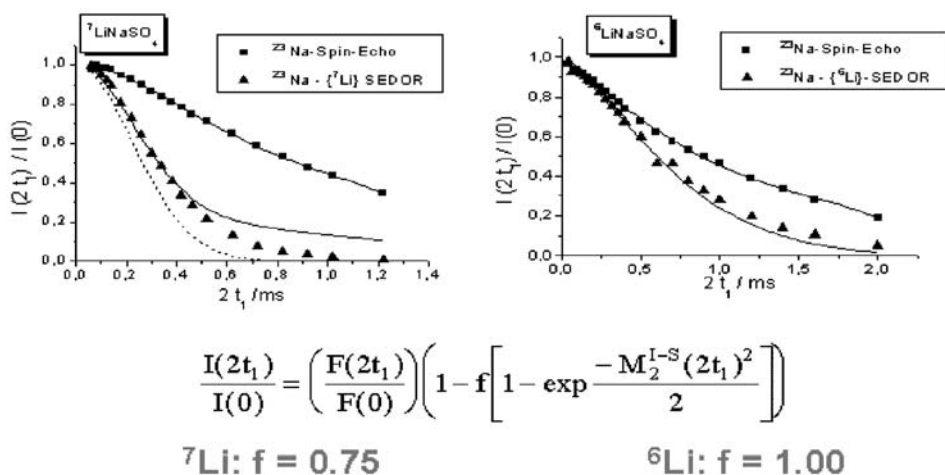
Fig. 5 ^{23}Na{^{7}Li} (*left side*) and ^{23}Na{^{6}Li} (*right side*) SEDOR results on the model compound LiNaSO$_4$. *Solid curves* show fits to the equation shown, where the inversion factor f takes into account the incomplete spin population inversion caused by strong quadrupolar splittings. The *dotted curve* shown on left is the theoretical prediction for f=1.00 in the ^{23}Na{^{7}Li} SEDOR experiment. Reproduced from [56]

experimental SEDOR curve is attenuated, resulting in an effective underestimation of the dipolar coupling. While it is possible to account for this systematic error by suitable calibration factors, a $^{23}Na\{^6Li\}$ SEDOR experiment on an isotopically enriched sample (Fig. 5, right part) is clearly preferable in this case. Owing to the small nuclear electric quadrupole moment of ^6Li, the quadrupolar splitting is very small, causing no systematic error in the corresponding SEDOR experiment.

3.3
Homonuclear Dipolar Recoupling Techniques

To re-introduce homonuclear dipole-dipole couplings into the MAS Hamiltonian, a whole family of two-dimensional NMR techniques has been developed [14], which are based on the fact that the dipole-dipole coupling between nuclei that are spatially close permits the build-up of *zero-quantum* (ZQ) or *double-quantum* (DQ) coherences. Zero-quantum coherences are the result of spin diffusion (nuclear flip-flop transitions) which can occur even under MAS conditions. The simplest experiment available to probe this effect is two-dimensional exchange spectroscopy (Fig. 6) [15]. Following excitation by a 90° pulse the spins are frequency labelled during the evolution time t_1. The subsequent 90° pulse terminates the evolution time and stores the magnetization along the magnetic field direction. During the subsequent mixing time, t_m, spin diffusion among spatially close nuclei is allowed to occur, and the corresponding frequency exchange picked up during the detection period, t_2, (following the final 90° pulse) manifests itself as a cross-peak in the corresponding two-dimensional correlation plot. The extent of spin diffusion during t_m can be enhanced by coherently applying trains of 180° pulses (*radio frequency driven recoupling* (RFDR), [16]).

Figure 7 illustrates the alternative DQ- approach [17–20]. During the preparation period, a DQ coherence involving two interacting nuclei resonating at frequencies ω_1 and ω_2 is generated using a suitable excitation scheme. This co-
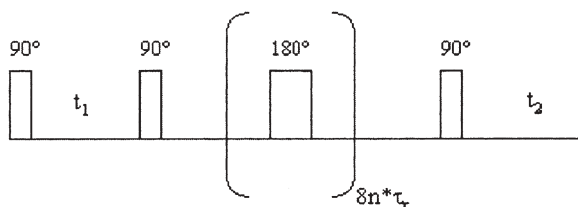
Fig. 6 The RFDR-sequence with two π/2-pulses sandwiching the t_1 evolution period. The mixing period is comprised of rotor-synchronized π-pulses. If these pulses are absent, the sequence is that for 2D-exchange spectroscopy. The third π/2-pulse produces transverse magnetisation
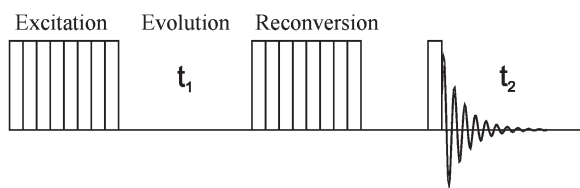
Fig. 7   General scheme of double-quantum NMR spectroscopy

herence oscillates with the sum frequency of the spins $\omega_1+\omega_2$ during the evolution period t_1. Subsequently, it is reconverted to observable single-quantum coherence by applying an analogous scheme as that used during the excitation period. The result is a 2-D plot, in which the single-quantum spectrum is correlated with the double quantum spectrum. Alternatively, double quantum coherences can be used for signal filtration in regular homonuclear 2-D correlation spectroscopy. During the past five years, a large family of excitation and reconversion schemes has been developed and suitable reviews are available [17–20]. In contrast to ZQ-methods, double quantum techniques are able to prove the existence of autocorrelations, resulting from dipole-dipole couplings between two nuclei with identical frequencies.

3.4
Rotational Echo Double Resonance (REDOR)

The *rotational echo double resonance* (REDOR) technique is essentially the MAS version of SEDOR, affording a site-resolved measurement of heteronuclear dipolar coupling information on rotating samples. Figure 8 shows two commonly used pulse sequences [21–24].

In both these variants the magnitude of a normalized difference signal $\Delta S/S_o=(S_o-S)/S_o$ is measured in the absence (intensity S_o) and the presence (intensity S) of the dipolar interactions. In the original version of REDOR [21], the signal of the observe-nuclei S is measured using a rotor-synchronized spin echo. Recoupling of the S-I interactions into the MAS Hamiltonian is accomplished by applying π-pulse trains during the middle of each rotor period, leading to a decrease in signal intensity of the observe-spins. By plotting $\Delta S/S_o$ as a function of dipolar evolution time, NT_r, (the duration of one rotor period multiplied by the number of rotor cycles) the internuclear dipole-dipole coupling constant D can be quantified. The normalized difference signal can be calculated using Average Hamiltonian Theory. For a powdered sample,

$$\frac{\Delta S}{S_0} = 1 - \frac{1}{4\pi} \int_0^{2\pi} d\alpha \int_0^{\pi} \sin\beta \, \cos(\Delta\Phi) \, d\beta \qquad (9)$$
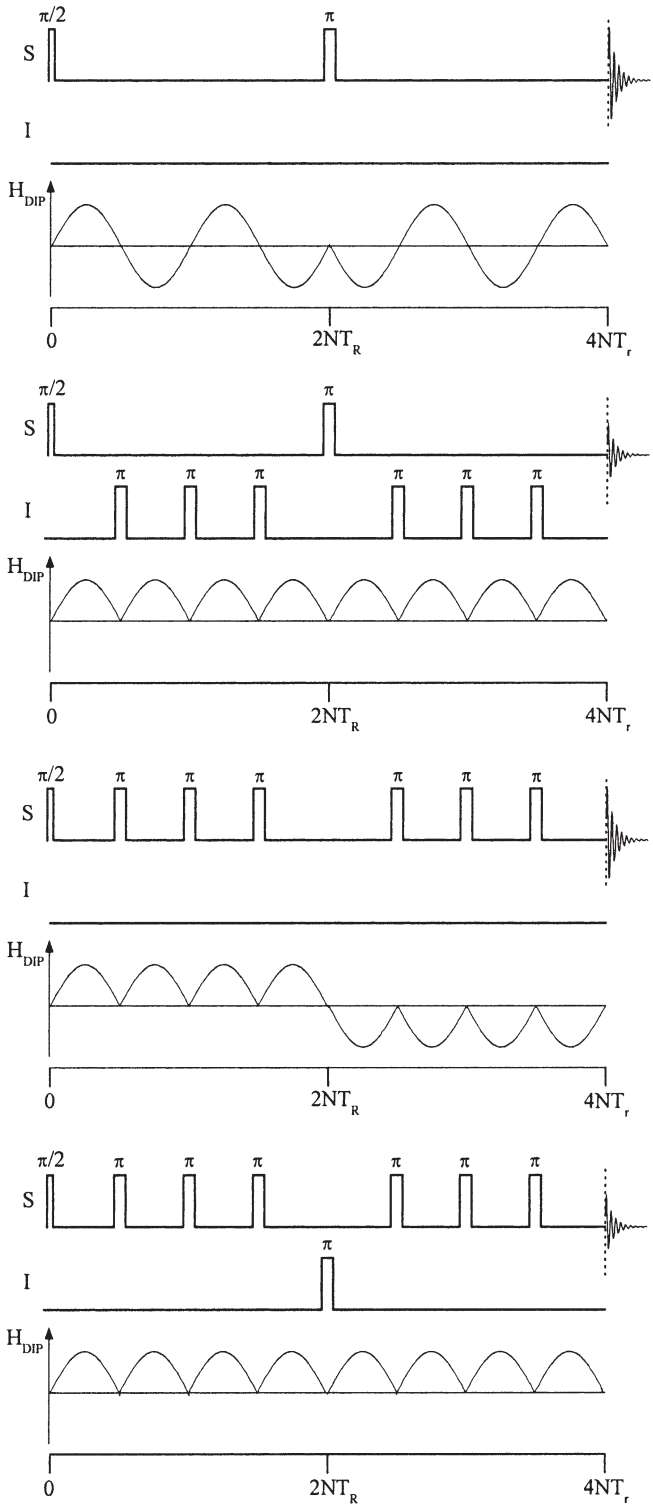
Fig. 8 Timing diagrams of two REDOR sequences: (a, *top*): sequence of Garbow and Gullion [21]; (b, *bottom*): sequence of Schaefer and Gullion [24], also known as REAPDOR. For each sequence the oscillatory behaviour of the dipolar Hamiltonian is illustrated. For further discussion see text

In this expression $\Delta\Phi$ is the dipolar de-phasing angle given by the product of the dipolar coupling frequency ω_D and the dipolar evolution time $N \cdot T_r$, (number of rotor cycles multiplied by the rotor period):

$$\Delta\Phi = 4\sqrt{2}NT_rD \sin\beta \cos\beta \sin\alpha \tag{10}$$

For two-spin systems, a useful analytical solution has been given by Mueller [25]:

$$\frac{\Delta S}{S_0} = 1 - [J_0 (\sqrt{2}\lambda_N)]^2 + 2 \sum_{k=1}^{\infty} \frac{1}{16k^2 - 1} [J_k (\sqrt{2}\lambda_N)]^2 \tag{11}$$

where the J_k are k-th order Bessel Functions of the first kind and $\lambda_N = NT_rD$. Application of this technique to structural studies of glasses faces a number of complications. First of all, the three-dimensional connectivities present in such inorganic networks, combined with the high natural abundances of the nuclear isotopes present, tend to produce multiple-spin interactions, affecting the REDOR curves in a way that is strongly dependent on the details of the local molecular architecture [26]. Unfortunately, in the case of disordered systems and glasses, the order and the geometry of the spin system are usually unknown, and the distance geometry may well be rather ill-defined due to a spread of internuclear distances and bond angles. Both these problems can be overcome by confining the REDOR data analysis to the initial curvature, where $\Delta S/S_o < 0.2$ [27, 28]. In this limit of short dipolar evolution times, the REDOR curve is found to be geometry-independent. For spin $-1/2$ systems a simple parabola,

$$\frac{\Delta S}{S_0} = \frac{4}{3\pi^2} (NT_r)^2 M_2^{I-S} \tag{12}$$

is an excellent approximation, yielding the van Vleck second moment from an analysis of the curvature.

3.5
REDOR Studies Involving Quadrupolar Nuclei

If quadrupolar nuclei are involved, a number of complications must be accounted for by appropriate procedures. In principle, one can distinguish four cases: (a) the standard case S=I=1/2 as discussed above; (b) S>1/2, I=1/2; (c) S=1/2, I>1/2; and (d) S>1/2, I>1/2. Cases (a) and (b) are handled well by the pulse sequence of Fig. 8a for either two- or multispin systems. Provided the length of the π(S) pulse is well-defined (in the limits either of entirely non-selective or entirely selective excitation of the central transition) any effect of nuclear electric quadrupolar coupling that is present in case (b) will have identical influence on the intensities S_o and S, resulting in overall cancellation.

For cases (c) and (d) one has to consider that the different possible Zeeman states m_I for the I- nuclei differ in the respective sizes of their z-components, and hence generate dipolar fields of different magnitudes at the observe spins [29, 30]. Therefore, the expression at Eq. (11) must be replaced by a superposition of 2I+1 individual de-phasing curves:

$$\frac{\Delta S}{S_0} = \frac{1}{2I + 1} \sum_{m=-I}^{I} \left(1 - [J_0\,(2\sqrt{2}|m|\lambda_N)]^2 + 2 \sum_{k=1}^{\infty} \frac{1}{16k^2 - 1}\,[J_k\,(2\sqrt{2}|m|\lambda_N)]^2 \right) \tag{13}$$

taking into account the fact that the dipolar field produced by the different Zeeman states scales with the magnitude of the orientational quantum number $|m_I|$. This expression remains valid, however, only in the limit of zero or very weak nuclear electric quadrupolar interactions (coupling constants C_q<50 kHz). For larger C_q-values, the anisotropic broadening of the $|1/2>\leftrightarrow|3/2>$ "satellite transitions" produces large resonance offsets, which reduce the efficiency of the π pulses to cause population inversion. The decisive parameter in this regard is the ratio ν_1/ν_q, where ν_1 is the nutation frequency of the I spins, which is governed by the amplitude of the rf pulses, and $\nu_q = \dfrac{3\,C_q}{2\,I\,(2I-1)}$ is the quadrupolar frequency. For sufficiently strong quadrupolar interactions, as ν_1/ν_q approaches zero the π pulses affect only the central $|1/2>\leftrightarrow|-1/2>$ coherences. In this limiting case only those S-spins that are coupled to I-nuclei in Zeeman states with $|m_I|$=1/2 are expected to yield a REDOR response.

Figure 9a summarizes the effect of the nuclear electric quadrupolar coupling constant on the REDOR curve for the S=1/2 {I=3/2} case, as calculated by the SIMPSON code [31] for the pulse sequence of Fig. 8a. Note that interpretable REDOR results are obtained only in the limit $C_q\rightarrow0$. For higher C_q-values, the simulations show greatly diminished REDOR effects, which turn out to be highly sensitive to experimental parameters and dependent on the specifics of the spin system considered. It is disappointing in particular, that in the limit of large C_q-values the REDOR effect is found to be much weaker than expected from the selective excitation limit. Furthermore, the curves are not universal

and depend on the magnitude of the dipole-dipole coupling constant. These results lead to the conclusion that the pulse sequence of Fig. 8a produces unreliable results if the non-observe I-spins are quadrupolar. We speculate that this unsatisfactory situation arises because the large number of π-pulses applied during the rotor cycle results in various unwanted side-effects, including adiabatic zero-crossings and the creation of multiple quantum coherences. It is therefore desirable to minimise the number of π-pulses applied to the I>1/2 spins. Thus the REDOR sequence of Fig. 8b is the method of choice. Figure 9b shows a typical set of S = 1/2{I=3/2} REDOR curves $\frac{\Delta S}{S_0}$ (λ) calculated via SIMPSON for systematic variation of the nuclear electric quadrupolar coupling constant C_q of the I-spins. Across the entire range of C_q-values, these REDOR curves calculated for dipolar coupling constants of different magnitudes (D=200 Hz, and D=600 Hz, open, and filled symbols) were found to be superimposable, indicating that they represent universal curves.

Figure 9b shows that for small C_q values, the two-component behavior, as predicted by Eq. (13), is readily apparent. With increasing magnitude of C_q, however, the REDOR response is successively attenuated, reflecting the fact that the spins in the outer $|\pm 3/2\rangle$ Zeeman states are less and less affected by the π(I) pulses. Note that the simulated curves approach the limiting cases (calculated via Eq. 13) of entirely non-selective irradiation of all the Zeeman states (upper dotted curve) and entirely selective irradiation of the $|1/2\rangle \leftrightarrow |-1/2\rangle$ coherence (lower solid curve) of the I-nuclei. Extending now the initial curvature analysis approach discussed above to Fig. 9b, the early parts of these REDOR curves can be approximated by a sum of parabolic functions:

$$\frac{\Delta S}{S_0} = \frac{1}{2I+1}\left(\sum_{m=-1}^{I} (2m)^2\right) \frac{1}{\pi^2 (I+1)I} (NT_r)^2 M_2^{I-S} \tag{14}$$

permitting determination of a dipolar second moment M_2^{I-S} from an analysis of the curvature. This approximation is valid for $\Delta S/S_0 < 0.2$. Equation (14) holds only for a nuclear electric quadrupolar coupling constant near zero. We can now introduce a phenomenological efficiency factor f_1 ($0 < f_1 < 1$) which takes into account the extent to which the dipolar coupling of S spins to I nuclei in their outer Zeeman states influences the REDOR curve, leading to

$$\frac{\Delta S}{S_0} = \frac{1}{15\pi^2} (2 + 18f_1) (NT_r)^2 M_2^{I-S} \tag{15}$$

The whole data analysis procedure can then be summarized as follows (see Fig. 10). Based on a nuclear electric quadrupolar coupling constant of the I spins known from experiment, a universal S{I}REDOR curve is computed via SIMPSON, at the precise conditions that were applied to obtain the experimental data. This simulation curve is fitted to a parabola, resulting in the appropriate f_1 value, which is then applicable to the analysis of the experimental
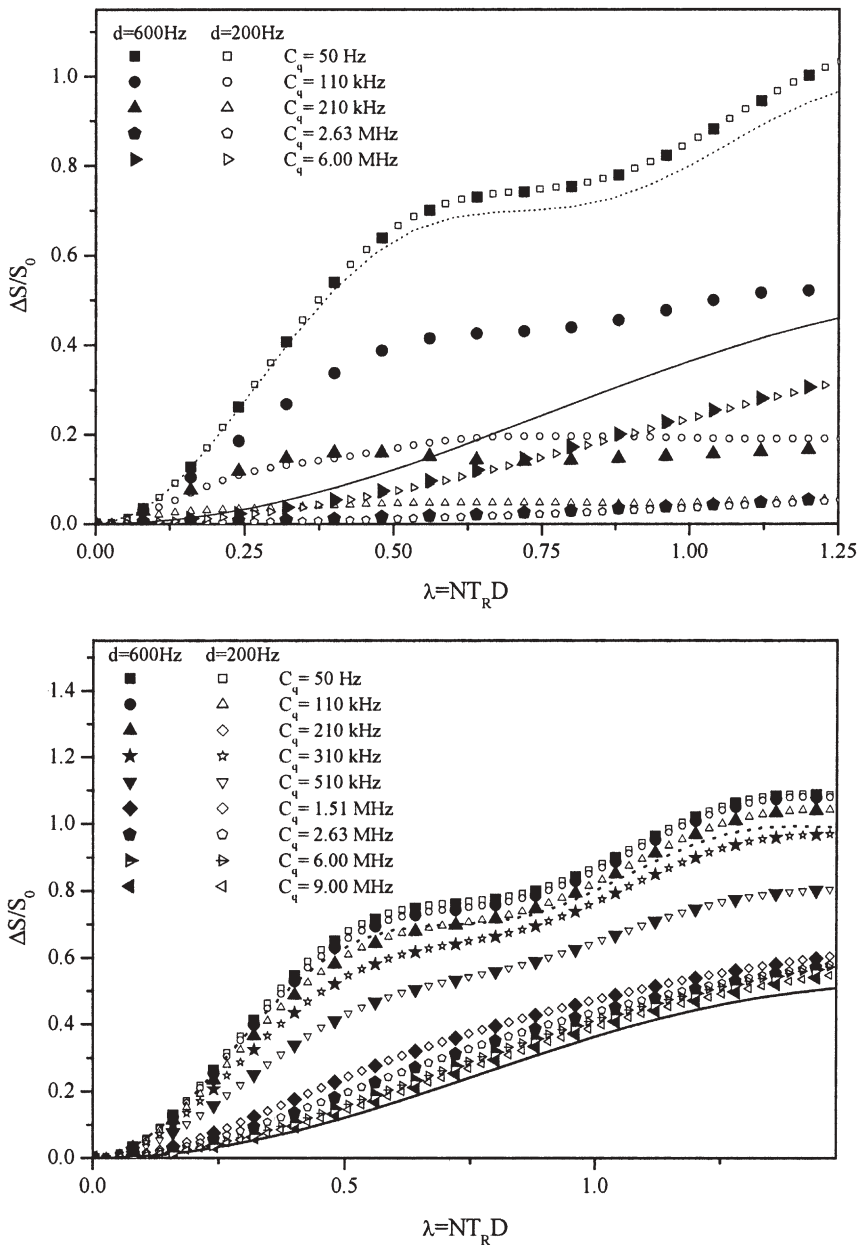
Fig. 9 Effect of the nuclear electric quadrupolar coupling constant on the universal REDOR curves of an S{I=3/2} two-spin system. Simulations assume $\nu_q^{(1)}=74$ kHz and $\nu_r=15$ kHz. *Open and closed symbols* represent results calculated for different magnitudes of the dipolar coupling constants. *Dotted curves* – theoretical behaviour predicted by Eq. (13). *Solid curves* – theoretical behaviour predicted by Eq. (13) in the limit of entirely selective excitation of the central coherence. *Top* – pulse sequence of Fig. 8a *bottom* – pulse sequence of Fig. 8b
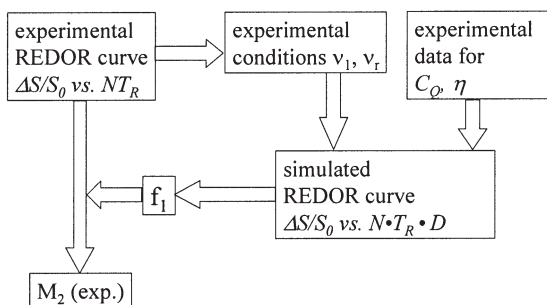
Fig. 10 Procedure for quantitative analysis of REDOR data on S{I>1/2} nuclei (see text)

data set. Using the f_1 value determined in this fashion, the experimental data set is fitted to Eq. (15), resulting in an experimental M_2^{I-S} value. This value can then be compared with a second moment calculation from the van Vleck formula for testing hypothetical structural scenarios.

Finally, a few words remain to be said about case (d) (S>1/2,I>1/2). At the present stage of knowledge, this case remains seemingly intractable for quantitative applications outside the non-selective excitation limit $\nu_1/\nu_q \gg 1$. The chief problem in applying pulse sequence at Fig. 8b) arises from the nuclear electric quadrupolar interactions affecting the S spins, which interfere with the ability of the π-pulse trains to refocus the transverse magnetization. In contrast, pulse sequence at Fig. 8a) is able to produce experimental REDOR curves, which are, however, difficult to interpret quantitatively. As a best-effort solution, one may resort to sample-to-sample comparisons on a relative basis and the use of empirical calibration procedures with closely related model compounds [32]. Alternatively, the SEDOR approach, which does not suffer from these restrictions, would be preferable.

3.6
Adiabatic Population Transfer Techniques

To overcome the specific problems arising from the fact that the nuclei involved in the dipolar analysis are also subject to nuclear electric quadrupolar interactions, alternative techniques such as TRAPDOR (*transfer of populations with double resonance*) [33, 34] and REAPDOR (*rotational echo adiabatic passage double resonance*) [35–37] have been designed. In both these techniques the I-spin flips needed for I-S dipolar recoupling are caused by adiabatic passages between the quadrupolar-perturbed Zeeman states of the I nuclei. They always occur when the quadrupolar splitting, which becomes time dependent owing to MAS, crosses through zero during the pulse. While both TRAPDOR and REAPDOR use simpler methods (continuous irradiation or application of single pulses) for I-spin state manipulation, the spin dynamics involved are still fairly complex. A valid data analysis then requires very detailed information

about interaction tensor components and mutual tensor orientations, which is usually not available in disordered materials. As a consequence, TRAPDOR and REAPDOR applications to glasses have to date remained at the qualitative level.

3.7
Cross-Polarization/Magic-Angle Spinning (CPMAS) Techniques

Cross-polarization (CP) uses the magnetic dipole-dipole couplings for the transfer of polarization between different spin systems [38]. Most of its applications have used this effect for the signal enhancement of rare nuclei (^{13}C, ^{15}N) via polarization transfer from protons. It is less-well known that CPMAS can also be a valuable technique for the quantitative measurement of heteronuclear dipole-dipole interactions. Figure 11 illustrates the experimental principle. Transverse abundant I-spin magnetization is created by a 90° pulse, and spin-locked in the rotating frame by applying a strong radiofrequency field along the direction of the magnetization in the rotating frame. This manipulation prepares the I spins into a state of very low spin temperature. At the same time, a second radio frequency field is applied to the dipolar-coupled rare S-spins. If the I- and S-precession frequencies in the rotating frame are equal, i.e., if the *Hartmann-Hahn matching condition* $\gamma_I B_{1I} = \gamma_S B_{1S}$ [39] applies, the I-spin system can relax towards thermal equilibrium by transferring some of its polarization to the S-spin system. This *cross-relaxation* pathway uses the exchange (*flip-flop*) term in the dipolar Hamiltonian and hence requires spatial proximity and a reasonable extent of rigidity on the NMR timescale. Thus, on a qualitative basis, the ability to obtain an S-signal via crosspolarization from an I-spin reservoir serves to prove the spatial proximity of both spin species. If the I-spin spectrum features several resolved signals, 2-D heteronuclear correlation spectra can be measured by preceding the Hartmann-Hahn contact period with an incremented evolution time, during which the I spins are labeled by their respective frequencies [40]. These HETCOR spectra can be immensely useful for establishing spatial proximities between different types of chemical species and for deriving connectivity maps. For characterizing the heteronuclear dipolar
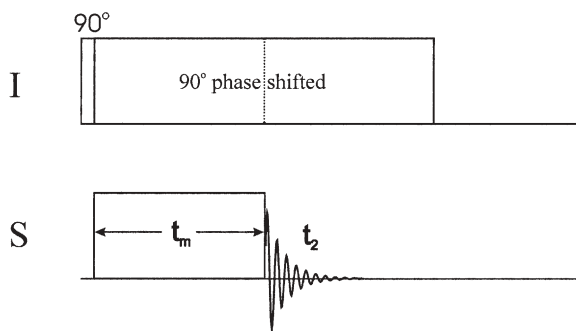
Fig. 11 Cross-polarization pulse sequence

couplings in more rigorously quantitative terms, the rates of magnetization transfer T_{IS}^{-1} need to be measured. These rates are governed by the second moments characterizing the strengths of both I-I and I-S interactions [38]:

$$T_{IS}^{-1} = C \cdot M_2^{I-S}/(M_2^{I-I})^{1/2} \qquad (16)$$

Thus, if M_2^{I-I} is known from separate experiments (spin echo decay spectroscopy, see above), M_2^{I-S} becomes accessible. Experimentally, the rate of this magnetization transfer is determined by measuring the CP signal intensity as a function of contact time. In reality, however, the kinetics of signal buildup are affected further by competing spin-lattice relaxation processes in the rotating frame, which are characterized by the corresponding relaxation times $T_{1\rho}(I)$ and $T_{1\rho}(S)$. In the commonly encountered situation, $T_{1\rho}(I) \ll T_{1\rho}(S)$ the S-spin signal intensity is given by [41, 42]:

$$S(t) = S_o \cdot \frac{e^{-t/T_{1\rho}(I)} - e^{-t/T_{IS}}}{1 - \dfrac{T_{IS}}{T_{1\rho}(I)}} \qquad (17)$$

Thus, by fitting CP buildup curves measured by determining S(t) as a function of the contact time, both time constants can be determined, and the quantity T_{IS}^{-1} can then be related to M_2^{I-S} via Eq. (16). The above description is valid only if both the I- and the S-nuclei are spin-1/2 species. If quadrupolar nuclei are involved it is still possible to exploit the qualitative aspects of the CP experiments, whereas the theoretical description of cross-relaxation rates becomes much more complicated [43]. To date, these complications have made it impossible to derive reliable quantitative information from such situations.

4
Applications to Structural Studies of Glasses

4.1
Cation Distributions in Single Alkali Glasses Studied by ^{23}Na Spin Echo Decay Spectroscopy

As illustrated by the model compound work summarized in Fig. 3, ^{23}Na spin echo decay spectroscopy is suitable in principle for elucidating the spatial distribution of sodium ions in solids [11, 44–47]. Meaningful results can be obtained provided that the measurement is carried out by selective excitation of the central $|1/2\rangle \leftrightarrow |-1/2\rangle$ transition, which needs to be ascertained by nutation NMR. Furthermore, sub-ambient temperatures may be required to suppress any potential influence of sodium dynamics. To date, promising applications have been published using ^{23}Na spin echo decay spectroscopy (I=3/2) on sodium-containing glasses, to address the vital issue of cation clustering. Fig-

ure 12 summarizes the M_2^{Na-Na} values as a function of number density in sodium silicate and borate glasses. Note in particular the strikingly different compositional dependences observed between these systems. While in the borate glasses a linear dependence of M_2 on sodium concentration is found, consistent with a statistical spatial distribution, for the silicate glass system a more or less constant value is observed at Na concentrations below 2×10^{28} m^{-3}. The latter behavior is most consistent with a large degree of cation clustering or even phase separation. The striking difference between silicate and borate glasses is also evident from complementary REDOR studies, to be discussed further below. At higher Na concentrations the curves for both systems seem to converge, suggesting similar ordering principles for the cations in these glasses. Sodium phosphate glasses appear to show intermediate behavior, suggesting that the alkali ion distribution is not entirely homogeneous in these systems [46].

At the present time it is unclear whether the spin echo decay spectroscopy approach successfully demonstrated for ^{23}Na is generally transferable to other alkali ion nuclei such as ^{7}Li and ^{133}Cs. The latter two isotopes have moderately small electric quadrupole moments causing first order quadrupolar splittings that are comparable to the radio frequency excitation window. As a result, the π-pulse length is ill-defined in many situations and the contribution of dipolar coupling of the observed spins to nuclei in the outer Zeeman levels is difficult to quantify. Nevertheless, some promising initial results on cesium borate
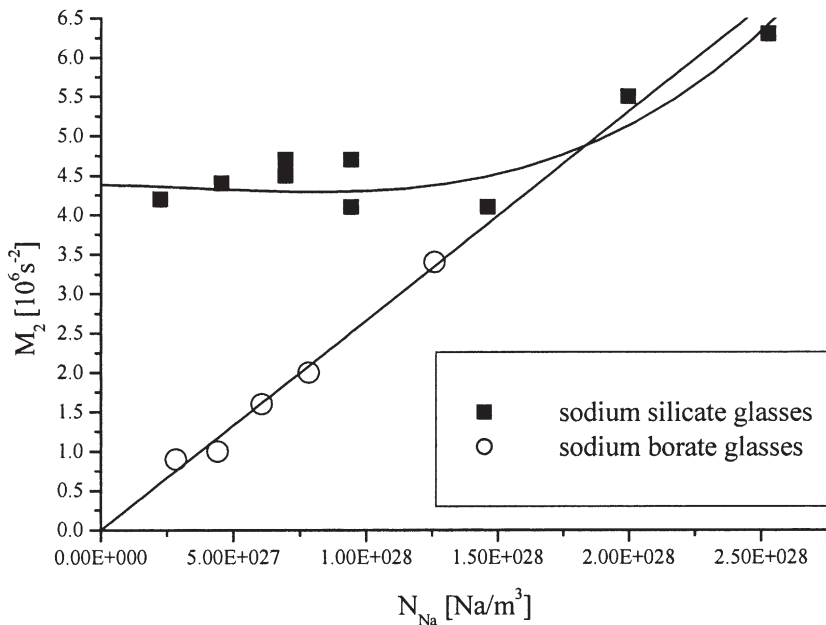
Fig. 12 Dependence of M_2^{Na-Na} on sodium atomic concentration in sodium silicate and sodium borate glasses. Data were taken at T=160 K [59]

glasses have been published, suggesting that the cesium ions are homogeneously distributed in these glasses [47]. However for further validation, additional model compound work and more extensive studies of different glass compositions are necessary.

4.2
Cation Distributions in Mixed-Alkali Glasses Studied by ^{23}Na Spin Echo and SEDOR Spectroscopies

A number of ^{23}Na spin echo and SEDOR studies have been conducted on glasses which contain more than one type of alkaline ion network modifier species, also termed *mixed-alkali glasses*. These studies have been triggered by the search for possible structural origins of the *mixed-alkali effect*, a nonlinear dependence of ionic conductivity as a function of cation composition [48, 49]. Previous explanations of this anomaly had invoked numerous ideas, ranging from preferred unlike-cation pairing [50] all the way to like-cation phase segregation [51, 52]. Again, these ideas can be tested on the basis of dipole-dipole coupling measurements between the nuclear magnetic moments of the relevant alkali elements involved. To this end ^{23}Na{^{6,7}Li} SEDOR studies have been carried out on numerous mixed lithium-sodium silicate [13, 52–54], thiogermanate [55], and alkali borate glass systems [56]. It is important to realize, however, that both the ^{23}Na spin echo decays and the ^{23}Na-{^{6,7}Li}SEDOR responses reflect the convolution of (1) the overall spatial cation distribution and (2) the distribution of Na and Li relative to each other. Thus, if information about the latter is desired, independent information (or correct assumptions) on the overall spatial cation distribution must be available. Based on a cation distribution deduced from molecular modelling, Yap and Elliott concluded from their SEDOR data that mixed lithium sodium disilicate glasses show a propensity of like-cation clustering [52]. In contrast, Gee and Eckert [13] assumed that the alkali ions in mixed Na-Li silicate glasses containing 40 mol% total alkaline oxide are homogeneously distributed, based on previous ^{23}Na spin echo decays measured on the binary sodium silicate system [11]. Their analysis of the SEDOR data led to the conclusion that the mutual Na/Li distribution in these glasses is essentially statistical [53, 54]. Analogous results were obtained in the glass systems 50(Na$_2$S-Li$_2$S)-50GeS$_2$, [53] and 30(Na$_2$O-M$_2$O)-70B$_2$O$_3$ (M=Li, K) [56]. In particular, for the latter systems both the ^{23}Na spin echo and the ^{23}Na{^{6,7}Li} SEDOR results were found to be in quantitative agreement with statistical alkali ion mixing within an otherwise homogeneous distribution of the entire cation inventory [56].

To probe the potential influence of cation size differences on the distribution, ^{23}Na{^{133}Cs} SEDOR experiments have also been conducted on mixed sodium cesium borate glasses containing 30 mol% alkali [57]. Being a nucleus (I=7/2) with a moderately small nuclear electric quadrupolar moment, the ^{133}Cs nucleus features similar spectroscopic characteristics as ^{7}Li. Usually sizeable first-order quadrupolar splittings reduce the inversion efficiency of the π-

pulses used in the SEDOR sequence. Thus, in the model compound pollucite, an inversion factor of 0.37 was determined by experiment [57]. Figure 13 shows typical results obtained on the glasses. Assuming that f=0.37 is transferable from the model compound measurement to the glass measurements, the ^{23}Na{^{133}Cs} SEDOR results also suggest the absence of like-cation segregation effects. This result implies that the size difference of the two cations does not affect the cation distribution in mixed alkali borate glasses. Furthermore, the linear dependence of M_2^{Na-Cs} on cation composition as indicated in Fig. 14 argues against like-cation segregation and is most compatible with a statistical distribution of the cations relative to each other [57].
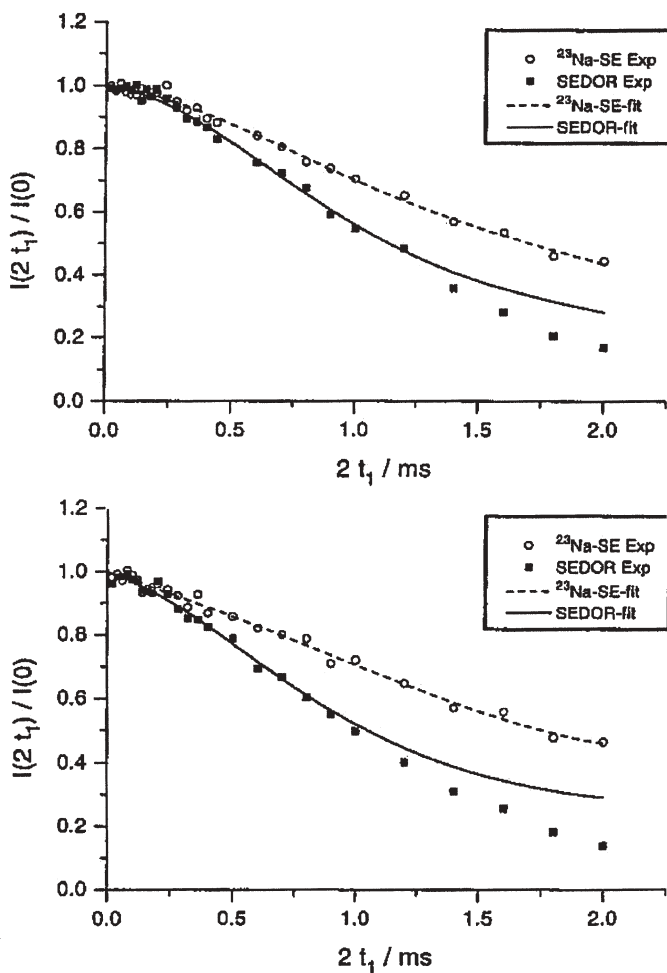
Fig. 13 ^{23}Na{^{133}Cs} SEDOR results on two mixed sodium caesium borate glasses with compositions 70B$_2$O$_3$-10Na$_2$O-20Cs$_2$O (*top*) and 70B$_2$O$_3$-5Na$_2$O-25Cs$_2$O (*bottom*) [57]
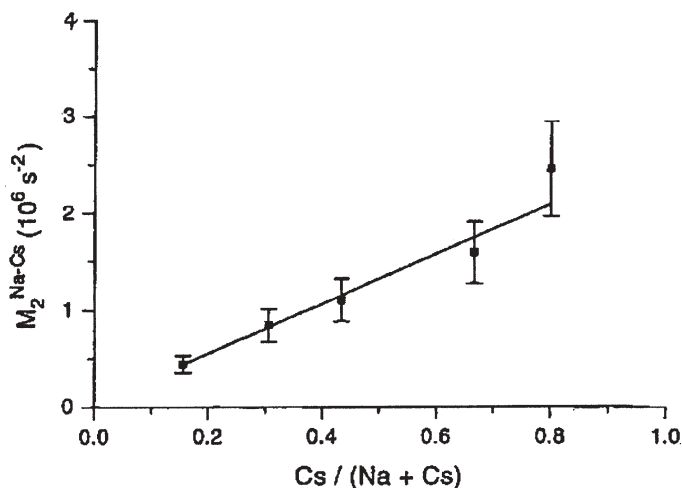
Fig. 14 Second moments M_2^{Na-Cs} describing the $^{23}Na\{^{133}Cs\}$ dipole-dipole interaction as a function of cation composition in mixed sodium caesium borate glasses of composition $70B_2O_3$-$30[(Cs_2O)_x(Na_2O)_{1-x}]$. The linear dependence of M_2 on the Cs/(Na+Cs) ratio is consistent with statistical cation mixing. Reproduced from [57]

4.3
Dipolar Recoupling Studies of Network Former-Network Modifier Correlations

An alternative approach to address the issue of cation clustering in glasses is to measure the magnetic dipole-dipole couplings between the nuclei associated with the network former ions and those nuclei associated with the network modifying ions. The rationale goes as follows: if the cations are clustered, the principle of local charge minimization demands that the charge-compensating anionic species are clustered as well [58]. In silicate glasses, these negative charges are associated with non-bridging oxygen species, which are bound to silicon, transforming the electrically neutral $Q^{(4)}$ units to partially depolymerized $Q^{(n)}$ units (n<4), having a negative charge of 4–n. Using ^{29}Si MAS NMR spectroscopy, these $Q^{(n)}$ sites can be reasonably well resolved on the basis of their different isotropic chemical shifts, so that their interactions with different alkali ion species can be studied by REDOR spectroscopy. As suggested by the diagram of Fig. 15, in case of cation clustering the anionic $Q^{(3)}$ units should interact more strongly with the alkali ions than the neutral $Q^{(4)}$ groups.

Figure 16 illustrates that this effect can indeed be observed in $^{29}Si\{^7Li\}$ REDOR data on lithium silicate glasses containing less than 20 mol% Li_2O. While the $Q^{(3)}$ units show a substantial REDOR effect, the signal of the $Q^{(4)}$ units is essentially unaffected by ^7Li irradiation, indicating that bridging oxygen atoms connecting between two $Q^{(4)}$ units make no contribution to the local Li environment. We conclude from these NMR results that the $Q^{(4)}$ species reside in spatial regions that are largely cation-depleted, consistent with the known ten-
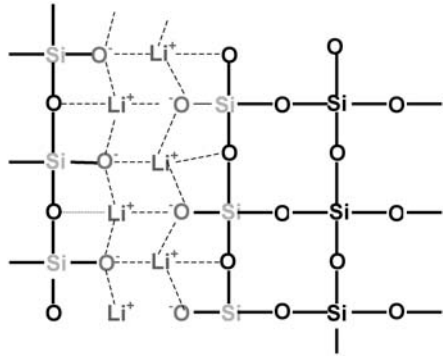
Fig. 15 Schematic illustrating lithium clustering in lithium silicate glasses
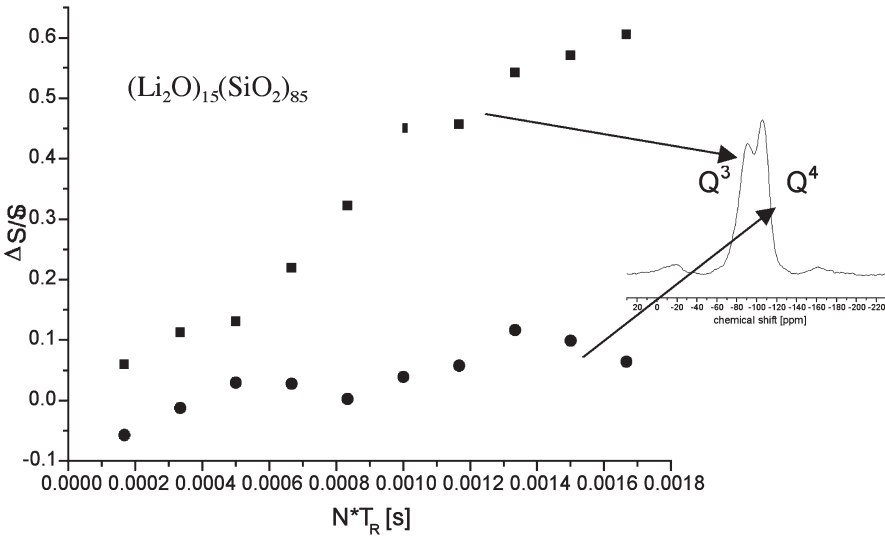
Fig. 16 Site-resolved ^{29}Si{^{7}Li}REDOR data $\left(\dfrac{\Delta S}{S_0} \text{ vs} \cdot \text{NTr/s}\right)$ on a lithium silicate glass, using the pulse sequence of Fig. 8b. Spin-lattice relaxation times were shortened by doping the glasses with 0.1 mol% MnO. The 180° pulse length for ^{7}Li was 11.9 µs and the rotor speed was 12 kHz [59]

dency of lithium silicate glasses to phase-separate. Figure 17 illustrates further that the $Q^{(3)}$ REDOR curves of lithium silicate glasses containing 5 to 15 mol% Li$_2$O are essentially superimposable. This result suggests that the regions in which the anionic $Q^{(3)}$ species and the Li$^+$ ions are mutually clustered are structurally rather similar in glasses with this concentration range [59]. Altogether, the different experiments shown in Figs. 12 and 15/16 both indicate that in alkali silicate glasses containing less than 20 mol% alkaline oxide, the cations are strongly clustered.
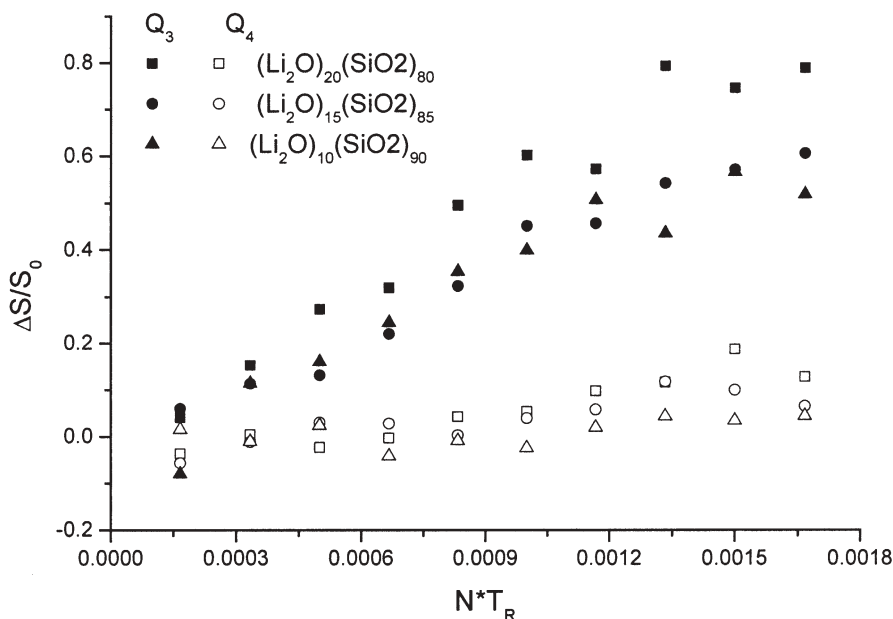
Fig. 17 Site-resolved ^{29}Si{^{7}Li}REDOR data $\left(\dfrac{\Delta S}{S_0} \text{ vs} \cdot \text{NTr/s}\right)$ on lithium silicate glasses with different Li/Si ratios. All the glasses were doped with 0.1 mol% MnO to shorten spin-lattice relaxation times. The 180° pulse length for ^{7}Li was 11.9 μs and the rotor speed was 12 kHz. Note the consistently large difference between the data relating to $Q^{(4)}$ units and the data relating to $Q^{(3)}$ units [59]

Analogous REDOR results on sodium borate glasses reveal a strikingly different picture. Unlike silicate glasses, the introduction of alkaline oxides into borate glasses does not create non-bridging oxygen species but rather converts the neutral trigonal planar $BO_{3/2}$ groups into anionic four-coordinate $BO_{4/2}^-$ species. The ^{11}B resonances of both structural units are nicely resolved by MAS, thereby facilitating site-resolved ^{11}B{^{23}Na} REDOR measurements [60]. Figure 18a shows a typical REDOR curve obtained in a glass with low Na concentration. Clearly, the extent of dephasing is rather similar for both types of boron structural units. In agreement with Fig. 12, this result argues strongly against cation clustering in sodium borate glasses. With increasing sodium content the M_2 values characterizing the ^{23}Na-^{11}B dipole-dipole interactions for the $BO_{3/2}$ groups increase linearly (Fig. 18b), consistent with a random distribution. In contrast, the $M_2(^{23}$Na-$^{11}BO_{4/2}^-)$ data approach a constant "baseline" value for low Na contents. This is expected in the case of isolated Na$^+$-$BO_{4/2}^-$ charge compensation pairs.

A situation intermediate between the two extreme cases discussed above is found in sodium phosphate glasses [61]. Figure 19 shows experimental REDOR curves for two samples containing 60% and 35% sodium oxide. Since the $Q^{(3)}$,
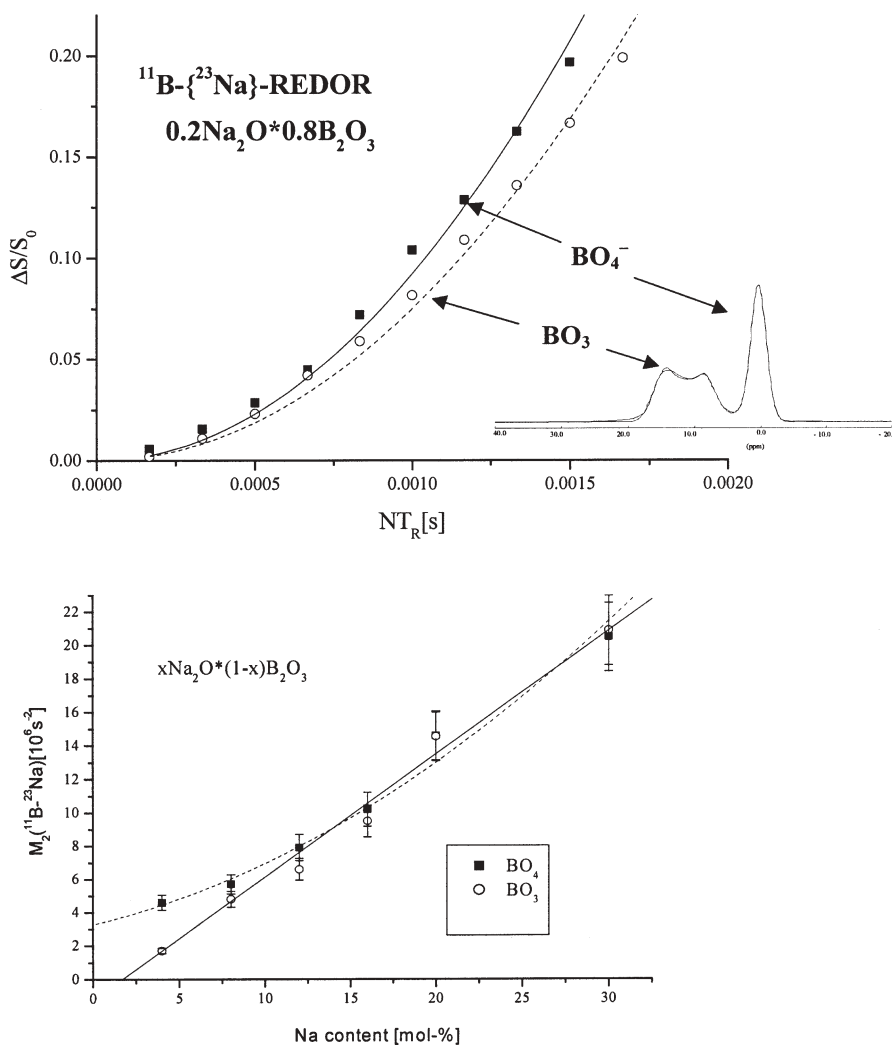
Fig. 18 ^{11}B{^{23}Na} REDOR results for sodium borate glasses recorded with the pulse sequence of Fig. 8a. The 180° solid pulse length on ^{23}Na was 8 μs and the rotor speed was 12 kHz. (a, *top*): site resolved REDOR data on trigonal and tetrahedral boron species. (b, *bottom*): site-selective M_2^{B-Na} values extracted from these data as a function of sodium oxide content [59]

$Q^{(2)}$, and $Q^{(1)}$ sites are well resolved by MAS-NMR, site-selective dipolar coupling information is available for the two different types of phosphate units. The magnitude of the ^{23}Na dipolar field present at the ^{31}P site increases with increasing number of non-bridging oxygen atoms. This behavior is similar to that observed in previous studies of silicate glasses [54]. Since the overall local charge requiring cationic compensation increases from zero to one to two in the sequence
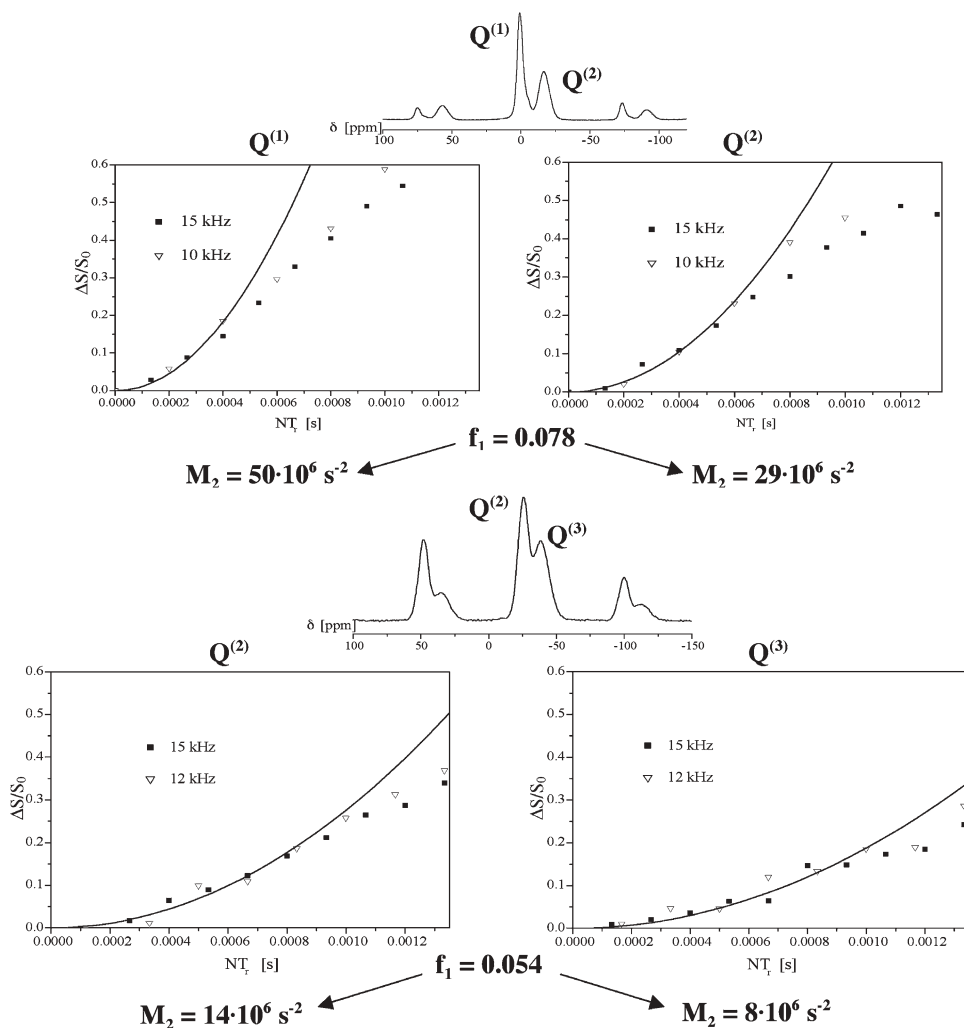
Fig. 19 Site resolved ^{31}P{^{23}Na} REDOR results on two sodium phosphate glasses using the sequence of Fig 8b. The 180° solid pulse length for ^{23}Na was 3.9 μs (*top*) and 5.5 μs (*bottom*). The REDOR curves were composed from measurements at two rotor frequencies (15 and 10 kHz, *top figure*, and 15 and 12 kHz, *bottom figure*)

$Q^{(3)} \rightarrow Q^{(2)} \rightarrow Q^{(1)}$ the observed experimental effect is not unexpected. For both the $Q^{(2)}$ and the $Q^{(1)}$ sites, the corresponding M_2^{P-Na} values measured in the glasses are similar to those obtained for the prototype crystalline model compounds $NaPO_3$ and $Na_4P_2O_7$. Still, the M_2 values measured for the $Q^{(2)}$ sites in the glasses also increase significantly with increasing sodium content in the glass. Furthermore, the neutral $Q^{(3)}$ site also displays dipolar coupling of significant strength to ^{23}Na nuclei, even though no charge compensation is needed for this

site. Both of these results are consistent with a statistical alkali ion distribution in the glass, rather than cation clustering or even phase separation.

The REDOR results discussed above reinforce previous conclusions proposed by Mueller and coworkers on the basis of $^{31}P\{^{23}Na\}$ CPMAS experiments [62]. Using variable contact time experiments these authors detected an interesting structural transition in the ultraphosphate region. The time constant T_{IS} measured for the $Q^{(2)}$ unit at very low sodium concentrations (Na/P=0.25) was found to be significantly longer than that measured in a glass with Na/P=0.78, suggesting a significant decrease in the average number of Na ions interacting with a $Q^{(2)}$ site. Similar observations have been made in $^{31}P\{^{7}Li\}$ REDOR studies of lithium phosphate glasses [63]. Figure 20 indicates that the $^{31}P\{^{7}Li\}$ REDOR curves of lithium phosphate glasses do not show a monotonic dependence on composition, but rather an abrupt decrease in interaction strength when the lithium oxide content is lowered from 30 to 20 mol%. Both of the above studies support the structural transformation illustrated in Fig. 20, previously proposed by Hoppe from diffraction data [64]. A structural reorganization of alkali phosphate glasses at alkali ion contents below 25 mol% had also been previously inferred from differential calorimetry data, which reveal T_g minima in this region [65]. As neither of the composition dependent one-dimensional NMR spectra show any indication of this reorganization, we can conclude that it does not affect short-range order, but rather concerns the network-former/network modifier correlations in the medium-range order regime.

4.4
Dipolar Recoupling Studies of Network Former Connectivities in Glasses

A number of homo- and heterodipolar recoupling techniques have been employed to probe spatial proximity of coordination polyhedra in a variety of oxide-based glasses. While the dipolar coupling information obtained by these methods is generally interpreted in terms of network former connectivities, this interpretation is not rigorous. In principle, dipolar recoupling can also occur by virtue of spatial proximity alone. On the other hand, since the internuclear distances arising from direct connectivity via shared oxygen atoms are significantly shorter compared to other through-space distances, the dipolar coupling associated with connectivity will dominate the response. Extensive work carried out on crystalline model compounds confirms that the translation of dipolar coupling into connectivity information is a reasonably good working assumption, as long as the analysis is confined to nearest or next-nearest neighbors [27, 28, 32]. Experimental studies focused on this topic can be grouped into (1) homodipolar recoupling analyses of $Q^{(n)}$ site connectivities in binary silicate and phosphate glasses, and (2) heterodipolar recoupling studies of site connectivities in mixed network former systems.
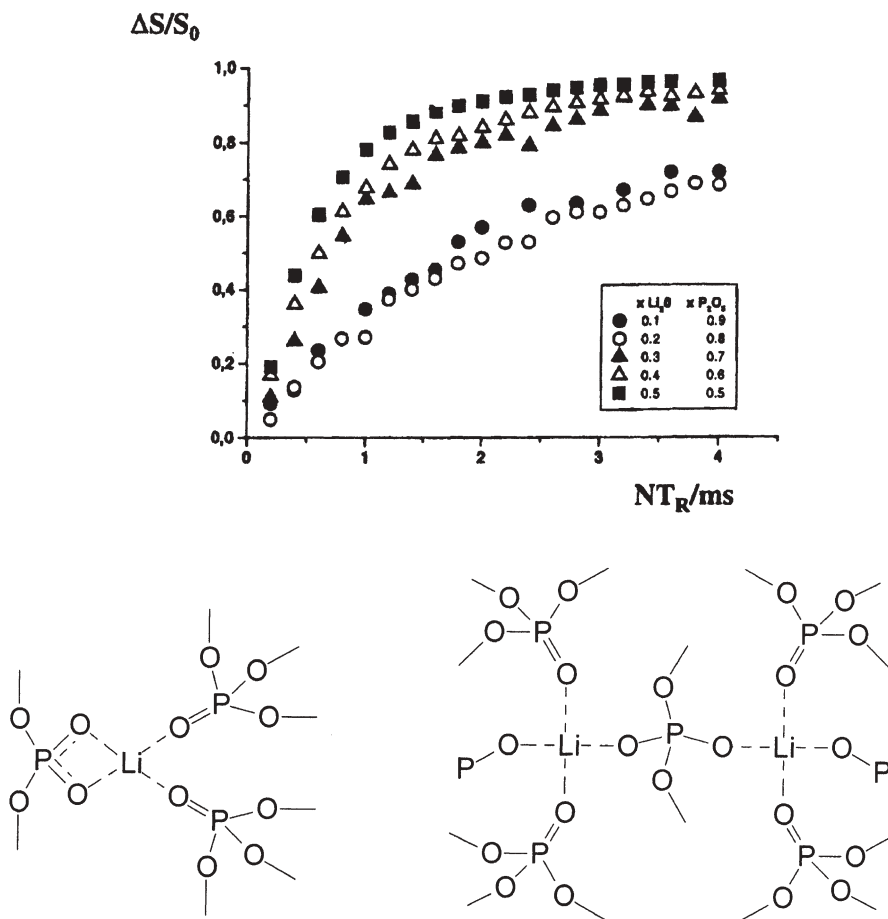
Fig. 20 $^{31}P\{^7Li\}$ REDOR curves of lithium phosphate glasses with composition $(Li_2O)_x(P_2O_5)_{1-x}$ ($0.1 \leq x \leq 0.5$). Data refer to the $Q^{(2)}$ phosphate units. These results favour a change in lithium local environment as illustrated in the bottom part of the figure. *Left*: coordination at Li_2O contents below 25 mol%. Each $Q^{(2)}$ phosphorus unit is coordinated by a single lithium ion. *Right*: coordination at Li_2O content above 25 mol%. Each $Q^{(2)}$ phosphorus unit is coordinated by two lithium ions [63]

4.4.1
$Q^{(n)}$ Connectivity Studies in Binary Glass Systems

NMR studies devoted to this issue exploit two-dimensional zero- or double quantum NMR methods to recouple homonuclear magnetic dipole-dipole interactions in MAS-spectra. The connectivity information then stems from the presence (or absence) of crosspeaks linking resolved resonances attributable to distinct $Q^{(n)}$ sites. To date, this type of analysis has been predominantly ap-

plied to spin-1/2 nuclei, specifically ^{29}Si and ^{31}P in binary silicate [66] and phosphate glasses [67–77]. Jäger and coworkers have used homonuclear 2D-double quantum NMR on ^{29}Si-enriched samples to explore the $Q^{(n)}$ connectivities in binary potassium silicate glasses [66]. From the 2D spectra they were able to show that the chemical shift of a given $Q^{(n)}$ unit is correlated with the number of bridging oxygen atoms present on the n adjacent silicate tetrahedra, which are specified by subscript symbols a,b,c,d. For example, a $Q^{(4)}$ site linked to four other $Q^{(4)}$ units (denoted by the symbol $Q^{(4)}_{4444}$) produces a different ^{29}Si chemical shift than (analogously defined) $Q^{(4)}_{4443}$, $Q^{(4)}_{4433}$ groups etc. Based on a detailed inspection of 2D- DQ NMR crosspeaks, the authors were able to specify approximate chemical shift ranges for the various $Q^{(4)}_{abcd}$, $Q^{(3)}_{abc}$, $Q^{(2)}_{a,b}$ units possible in silicate glasses. A detailed quantification of these units would be of great interest in order to explore whether the $Q^{(n)}$ site linking is simply random or whether there is any clustering tendency. Unfortunately, this task is rendered very difficult due to the excessive peak overlap present in the spectra.

An analogous approach has been applied to a number of binary and ternary phosphate glasses, resulting in very insightful qualitative and quantitative information [67–77]. First of all, the observation of crosspeaks in 2D-exchange, RFDR, as well as DQ-experiments unambiguously reveal the occurrence of $Q^{(1)}$-$Q^{(2)}$ and $Q^{(2)}$-$Q^{(3)}$ linkages.

The intensities of these crosspeaks strongly suggest that in binary lithium, sodium, silver, and lead phosphate glasses, the $Q^{(n)}$ units are linked in a more or less random fashion. A more detailed inspection of the double quantum crosspeaks as a function of composition indicates further that the ^{31}P chemical shift observed for a given $Q^{(n)}$ unit is correlated with the connectivity with adjacent $Q^{(n)}$ groups [75]. This has been most vividly illustrated by 2D spectra, signifying that the $Q^{(1)}$ endgroups involved in $Q^{(1)}$-$Q^{(1)}$ dimers have significantly different chemical shifts than those present in $Q^{(1)}$-$Q^{(2)}$-$Q^{(1)}$ trimers, which are again differentiable from the endgroups terminating longer phosphate chains. On this basis, chemical shift ranges can be specified for each type of $Q^{(n)}_{abc}$ unit (defined in the same way as discussed above for the silicates). Based on this information, Jäger and coworkers showed that the analysis can be extended to estimate average phosphate chain lengths from simple one-dimensional ^{31}P NMR spectra.

4.4.2
Connectivity Information in Multiple-Network Former Systems

At the qualitative level, NMR studies devoted to this issue exploit heteronuclear dipolar recoupling to correlate resolved MAS NMR signals of the nuclear species associated with different network formers. This information comes from the dephasing of the observe nuclei in REDOR, TRAPDOR, or REAPDOR experiments, or from one- or two-dimensional correlation spectroscopy involving coherence transfer via TEDOR (*transferred echo double resonance*) or

crosspolarization. More detailed quantitative information has been sought from a detailed analysis of REDOR dephasing, using the approach delineated earlier. The results obtained so far on the various systems are briefly summarized below.

4.4.2.1
Borosilicate Glasses

The pure network former system B_2O_3-SiO_2 was long thought to be completely phase separated. However, previous ^{17}O MQMAS-NMR data could be consistently interpreted in terms of the existence of B-O-Si linkages, suggesting some extent of miscibility [78]. This view was recently confirmed by high-resolution ^{11}B MQMAS NMR spectra which are able to differentiate between $BO_{3/2}$ groups linked to silicon and those linked only to other boron species [79]. Using MQ-MAS in combination with [29]Si{[11]B} REAPDOR, van Wüllen and Schwering estimated the extent of B/Si mixing and derived a conclusive structural model [79]. At low B_2O_3 contents the glass can be described in terms of $BO_{3/2}$ and $SiO_{4/2}$ groups, which are interlinked in a statistical fashion. However, for boron oxide contents exceeding the limiting composition of ca. 32mole %, the [29]Si{[11]B} REAPDOR curves show no further increase in the heteronuclear dipolar interaction. This result gives evidence of a phase separation effect, where the mixed phase remains at a fixed composition, corresponding to roughly equal proportions of $BO_{3/2}$ and $SiO_{4/2}$ units. Any boron oxide in excess of this composition is segregated into a pure B_2O_3 glass phase, producing a separate [11]B MAS signal and limiting the extent of [29]Si dephasing in the dipolar [11]B field. At the microscopic level, the extent to which silica and boron oxide can be interlinked is given by a maximum of two Si-O-B links per $Q^{(4)}$ unit. At present, no results are as yet available for the technologically interesting ternary alkali borosilicate glass systems.

Amorphous B/Si/N/C systems have generated considerable interest due to their extreme high- temperature stability. These materials are obtained via polycondensation reactions from molecular precursors in the presence of NH_3. Based on MAS NMR chemical shifts, it is known that all the boron atoms form trigonally planar $BN_{3/3}$ groups while silicon has a tetrahedral $SiN_{4/3}$ environment. Van Wüllen et al. have quantified the connectivities of these units in material with composition $B_3Si_3N_7$ on the basis of a comprehensive analysis of all the homo- and heteronuclear dipolar interactions involving the [29]Si and [11]B nuclei, using both [11]B and [29]Si dipolar spin echo decay (the latter on isotopically enriched samples), as well as [29]Si{[11]B}, [11]B{^{29}Si} REAPDOR and REDOR NMR [80] (Fig. 21). The results clearly indicate that the linking is non-statistical, and mixed Si-N-B connectivities are disfavored. Each silicon atom is surrounded by an average of 1.8 boron atoms in the second coordination sphere. In the related material $SiBCN_3$, the average extent of Si-N-B linking is further reduced to (on average) 1.2 boron atoms around silicon (see Fig. 22) and is replaced by some new Si-N-C links. [13]C{[11]B} REDOR data reveal that C-N-B links are present as
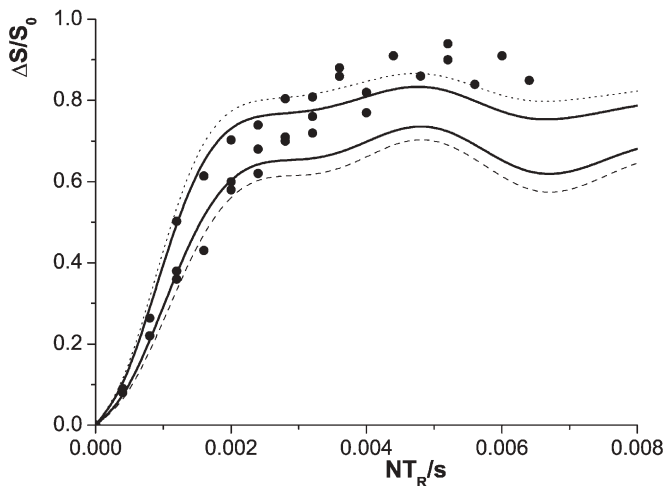
Fig. 21 $^{29}Si\{^{11}B\}$ REDOR results on $Si_3B_3N_7$ (*open circles*) and $SiBCN_3$ (*full circles*). *Solid curves* represent best fits to the respective experimental data sets (1.8 and 1.2 Si-N-B links). The *dashed curve* and *dotted curve* are calculated scenarios based on one and two Si-N-B links. Reproduced from [81]

well, but evidently only part of the carbon inventory is integrated into the framework [81].

4.4.2.2
Alumino- and Borophosphate Glasses

Network former connectivities have been explored in a variety of phosphate glasses containing aluminum or boron as a second network former component. A number of studies have been published on the sodium aluminophosphate glass system [82–85]. The ^{27}Al NMR spectra of these glasses show three distinct resonances, attributable to AlO_4, AlO_5, and AlO_6 units. All of these environments are intimately connected to phosphorus species, as revealed by 2D CPMAS heteronuclear correlation and REDOR experiments [83].

A closer inspection of the 2D HETCOR cross-sections in the ^{31}P dimension suggests that the isotropic chemical shift of this resonance is correlated with the extent of Al-O-P connectivity, resulting in a tentative chemical shift scale for $Q_{m/(Al)}^{(n)}$ species (see Table 1) [83, 84]. Replacement of a P by an Al in the second coordination sphere results in upfield shift effects of 10 to 15 ppm.

Detailed $^{31}P\{^{27}Al\}$ and $^{31}P\{^{23}Na\}$TRAPDOR studies of sodium aluminophosphate glasses along the $NaAlO_2$-$NaPO_3$ join reveal that, with increasing $NaAlO_2$ content, P-O-P links are successively being replaced with P-O-Al links, whereas the magnitude of Na-P interactions is preserved [84]. Most recently, we have shown that sodium aluminophosphate glasses prepared via the sol-gel route are structurally very similar to those prepared by traditional

Table 1 Approximate ^{31}P chemical shift regions (± 5 ppm) for $Q_m^{(n)}$ species in aluminophosphate glasses. Here n refers to the number of bridging oxygen atoms and m is the number of Al atoms bonded to P

	n=0	n=1	n=2	n=3
m=0	15	0	−20	−35
m=1	5	−10	−35	
m=2	−5	−20	−50	
m=3	−15	−35		
m=4	−25			

melt quenching techniques [85]. For the glass composition 43.8% Na_2O-12.5% Al_2O_3-43.8% P_2O_5, the samples obtained by both preparation routes yield essentially identical results both in the 1D MAS and in the $^{27}Al\{^{31}P\}$ REDOR experiments.

Recently, new results have been obtained on the network connectivity of various borophosphate glass systems. Using crosspolarization methods, qualitative evidence of strong boron-phosphorus interactions was given for some lead borophosphate glasses [86]. More detailed quantitative connectivity information
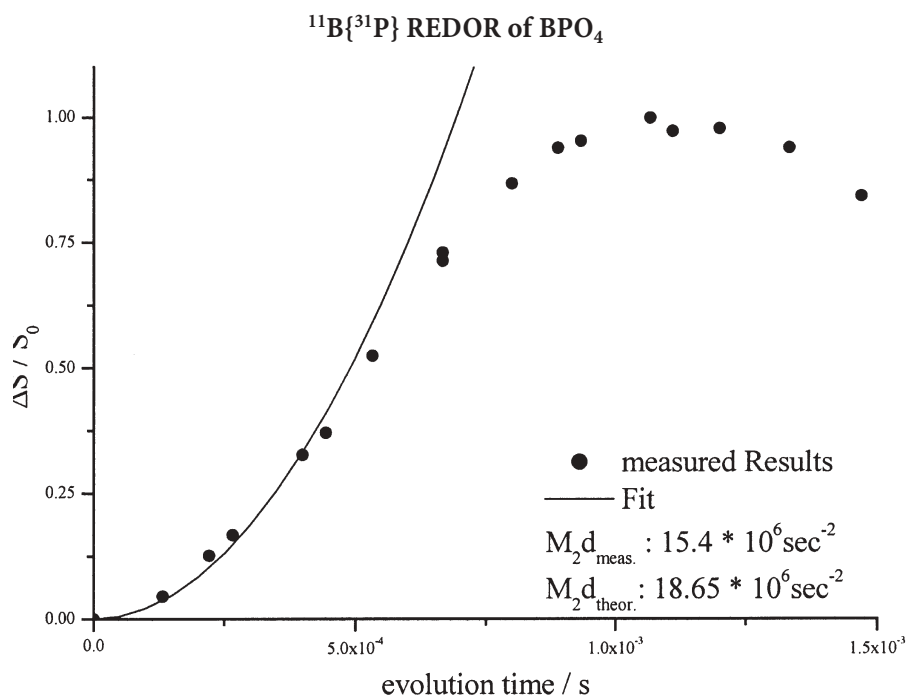
Fig. 22 $^{11}B\{^{31}P\}$ REDOR curve for crystalline boron phosphate

has been obtained recently by ^{11}B{^{31}P} REDOR spectroscopy [87]. Figure 22 shows a typical result for the crystalline model compound BPO$_4$. In the latter, each boron is tetrahedrally surrounded by four B-O-P linkages at a boron-phosphorus distance of 273 pm. Neglecting long-range contributions, these four ^{31}P spins produce a dipolar second moment of 18.4×10^6 s^{-2} at the boron site, as calculated from Eq. (4b). Experimentally, we measure 15.5×10^6 s^{-2} applying the initial curvature analysis to the ^{11}B{^{31}P} REDOR data. Figure 23 shows analogous results for a glass with composition 50 Ag$_2$O-20B$_2$O$_3$-30P$_2$O$_5$. The one-dimensional ^{11}B NMR spectrum reveals that all the boron is four-coordinated at this glass composition; however, two distinct BO$_{4/2}$ sites are differentiable [87]. The ^{11}B{^{31}P} REDOR results reveal a significant difference in the magnitude of the boron-phosphorus dipole-dipole interactions, with second moments of 15.5×10^6 s^2 and 7.4×10^6 s^2 for the two resonances at –0.5 and –2.5 ppm (vs BF$_3$-OEt$_2$). This numerical information can be translated into an estimate of the average number of B-O-P linkages for each of the boron sites, if we assume that the second nearest neighbor distances in the glass are roughly comparable to those in the crystalline model compound [87].
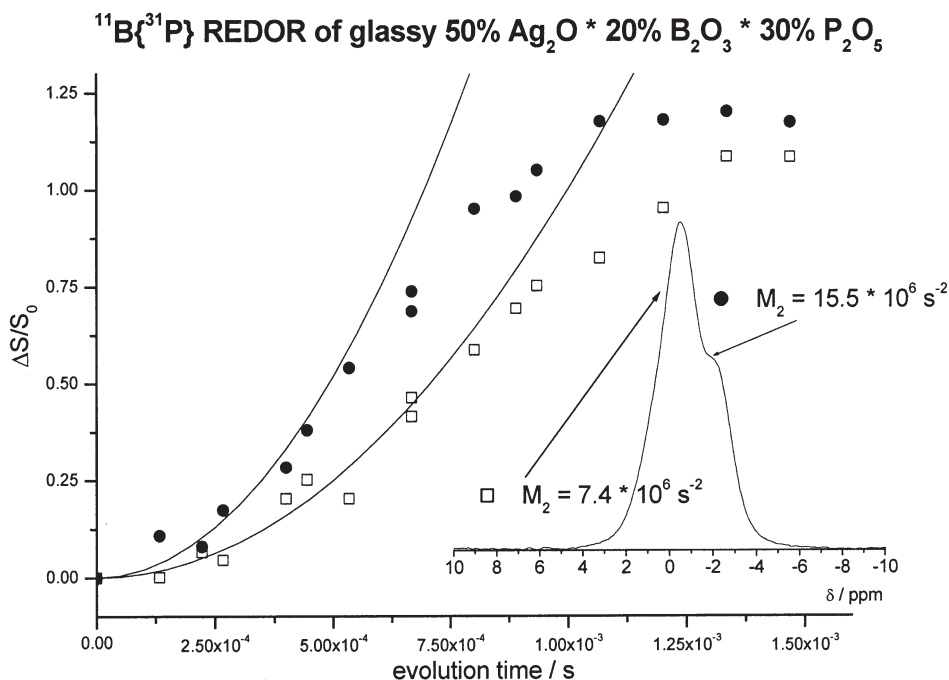
Fig. 23 Site-resolved ^{11}B{^{31}P} REDOR results on a silver borophosphate glass. The two tetrahedrally coordinated boron sites differ significantly with respect to their dipolar coupling strengths with the ^{31}P nuclei

4.4.2.3
Other Phosphate-Based Glass Systems

^{31}P{^{27}Al} and ^{31}P{^{23}Na} TRAPDOR have been used to probe the local environments of small amounts of phosphorus species introduced into sodium aluminosilicate glasses [88]. Using this approach, the authors could resolve interesting chemical shift differences between the P atoms in the vicinity of aluminum and those interacting with the sodium nuclei. In a similar vein, double resonance (REDOR and TRAPDOR) experiments proved useful to monitor the crystallization of fluoroapatite from an aluminosilicate glass matrix [89]. The precursor glass is phase separated and contains fluorine in both microphases. The composition of both microphases could be deduced on the basis of numerous dipolar recoupling experiments involving various combinations of the ^{19}F, ^{31}P, ^{27}Al, and ^{23}Na constituent isotopes. Further dipolar recoupling experiments carried out ex situ at various heating stages indicate that the crystallization of fluoroapatite is preceded by the formation of a fluoride-free sodium calcium phosphate precursor phase, which subsequently reacts with fluoride to yield fluoroapatite above 580 °C. This study is the first structural application of dipolar spectroscopy to a phase-separated glass system.

^{29}Si{^{31}P} REDOR has been used to probe silicon-phosphorus connectivity in a glass with composition Na_2O-$2SiO_2$-$3P_2O_5$ [54]. Glasses in this high-phosphorus compositional region show significant amounts of octahedrally coordinated silicon sites, which are observed at –212 ppm, in addition to regular tetrahedrally coordinated Q$^{(4)}$ sites near –120 ppm. The ^{29}Si{^{31}P} REDOR results reveal that these octahedral units must be stabilized by direct linking to phosphate groups, producing a significantly stronger dephasing than that observed for the tetrahedrally coordinated silicon atoms.

4.4.2.4
Aluminoborate Glass Systems

Aluminoborate glasses were among the first systems studied by heteronuclear X-Y double resonance techniques [90]. The most detailed results have been obtained on the system Na_2O-B_2O_3-Al_2O_3. In these glasses the great majority of the aluminium species are present as $AlO_{4/2}$ units, whereas the boron atoms occur both as trigonal $BO_{3/2}$ units and as tetrahedral $BO_{4/2}$ groups. The contribution of each structural species to the network has been quantified on the basis of detailed MAS experiments [91]. At a magnetic field strength of 11.7 T, the two boron sites are well resolved by MAS, facilitating site specific ^{11}B{^{27}Al} REDOR measurements. These studies reveal consistently that the tetrahedral boron sites are much more remote from aluminium than the $BO_{3/2}$ units [32, 90]. The apparent avoidance of $AlO_{4/2}$-$BO_{4/2}$ links can be rationalized on the basis of bond valence arguments, as both these units are formally negatively charged [92].

Two important changes are observed when the charge compensating cation is switched from sodium to calcium or magnesium: (1) the differentiation of both boron species with respect to their dipolar coupling to aluminium is lost and (2) the amount of aluminium in five- and six-coordination is substantially increased [93]. Both of these effects are likely to be connected. Indeed, ^{27}Al-^{11}B heteronuclear correlation experiments suggest that the four-coordinated boron units are preferentially interacting with these AlO_5 and AlO_6 sites [94]. In an attempt to obtain more quantitative information about boron/aluminium connectivities in sodium aluminoborate glasses, detailed ^{11}B{^{27}Al} and ^{27}Al{^{11}B} REDOR experiments have been conducted on a range of glass compositions [32]. A rigorously quantitative analysis of REDOR data is complicated by the fact that both types of nuclei are subject to strong quadrupolar interactions. Nevertheless, useful semi-quantitative information was obtained by recourse to detailed model compound calibration methods. In this manner, it was possible to analyse the REDOR data in terms of the fraction of Al-O-$BO_{4/2}$ and Al-O-$BO_{3/2}$ links. Comparison of these data with model calculations indicate that there is a distinct preference for the tetrahedral $BO_{4/2}$ and $AlO_{4/2}$ groups to be linked to neutral $BO_{3/2}$ units [32]. At high aluminium contents the glass structure seems to be organized so that the number of these links is maximized.

5
Conclusions and Outlook

In summary, the results presented above document the great power and potential of high-resolution dipolar NMR spectroscopy to provide detailed information on the structural organization of glasses at the sub-nanometer distance scale. During the past five years, a substantial amount of information has been accumulated, much of which remains at the conceptual and qualitative level at the present time. Nevertheless, the systematic composition-dependent exploration of different glass systems has only just begun, and much fundamental insight is expected to come from detailed quantitative comparison of different glass systems. In the future, we expect that this research area will also greatly benefit from the continuing improvement and refinement of the calculational and modelling approaches used to 'translate' spectroscopic observables into structural information.

Even so, there are numerous experimental and theoretical difficulties to overcome relating directly to the measurement. For example, the reliable quantification of *homonuclear* dipole-dipole interactions under high-resolution conditions (with MAS) in multispin systems is still an unsolved problem, in particular when quadrupolar nuclei are involved. Likewise, no rigorous strategy seems to be available at present for the REDOR measurement of heteronuclear dipolar coupling between two quadrupolar nuclear species. In this connection, it is of the utmost importance that NMR spectroscopy remains a vital and attractive research area in its own right. Assuredly, the continued influx of new solid state NMR technology into this research area will provide an

active stimulus for the study of increasingly sophisticated structural issues on increasingly complex materials.

References

1. Ernst RR, Bodenhausen G, Wokaun A (1987) Principles of nuclear magnetic resonance in one and two dimensions. Clarendon Press, Oxford
2. Schmidt-Rohr K, Spiess HW (1996) Multidimensional solid-state NMR and polymers. Academic Press, London
3. Eckert H (1992) Prog NMR Spectrosc 24:159; Eckert H (1994) NMR Basic Principles Prog 33:125
4. van Vleck JH (1948) Phys Rev 74:1168
5. Abragam A (1961) The principles of nuclear magnetism. Clarendon Press Oxford, p 111
6. Haase J, Oldfield E (1993) J Magn Reson A 101:30
7. Mansfield P (1965) Phys Rev A 137:961
8. Boden N, Gibb M, Levine YK, Mortimer M (1974) J Magn Reson 16:471
9. Engelsberg M, Norberg RE (1972) Phys Rev B 5:3395
10. Lathrop D, Franke D, Maxwell R, Tepe T, Flesher R, Zhang Z, Eckert H (1992) Solid State Nucl Magn Reson 1:73
11. Gee B, Eckert H (1995) Solid State Nucl Magn Reson 5:113
12. Kaplan DE, Hahn E (1958) J Phys Radium 19:821
13. Gee B, Eckert H (1996) J Phys Chem 100:3705
14. Bennett AE, Griffin RG, Vega S (1994) NMR Basic Principles Prog 33:1
15. Bennett AE, Ok JH, Griffin RG (1992) J Chem Phys 96:8624
16. Bennett AE, Rienstra CM, Griffiths JM, Zhen W, Lansbury PT Jr, Griffin RG (1998) J Chem Phys 108:9463
17. Lee YK, Kurur ND, Helmle M, Johannessen OG, Nielsen NC, Levitt MH (1995) Chem Phys Lett 242:304
18. Feike M, Demco DE, Graf R, Gottwald J, Hafner S, Spiess HW (1996) J Magn Reson A 122:214
19. Dusold S, Sebald A (2000) Ann Rep NMR Spectrosc 41:185
20. Geen H, Gottwald J, Schnell I, Spiess HW, Titman JJ (1997) J Magn Reson 125:224
21. Gullion T, Schaefer J (1989) J Magn Reson 81:196
22. Gullion T (1997) Magn Reson Rev 17:83
23. Gullion T (1998) Conc Magn Reson 10:277
24. Garbow JR, Gullion T (1991) J Magn Reson 95:442

25. Mueller KT (1995) J Magn Reson A113:81
26. Naito A, Nishimura K, Tuzi S (1994) Chem Phys Lett 229:506
27. Bertmer M, Eckert H (1999) Solid State Nucl Magn Reson 15:139
28. Chan JCC, Eckert H (2000) J Magn Reson 147:170
29. Schmidt A, Mackay RA, Schaefer J (1992) J Magn Reson 96:644
30. Hudalla C, Eckert H, Dupree R (1996) J Phys Chem100:15986
31. Bak M, Rasmussen JT, Nielsen NC (2000) J Magn Reson 147:296
32. Bertmer M, Züchner L, Chan JCC, Eckert H (2000) J Phys Chem B 104:6541
33. van Eck ERH, Janssen R, Maas WEJR, Veeman WS (1990) Chem Phys Lett 174:428
34. Grey CP, Vega, AJ (1995) J Am Chem Soc 117:8232
35. Gullion T (1995) Chem Phys Lett 246:325
36. Gullion T (1995) J Magn Reson A 117:326
37. Chopin L, Vega S, Gullion T (1998) J Am Chem Soc 120:4406
38. Pines A, Gibby MG, Waugh JS (1973) J Chem Phys 59:569
39. Hartmann SR, Hahn EL (1962) Phys Rev 128:2042
40. Caravatti P, Bodenhausen G, Ernst RR (1983) Chem Phys Lett 100:305
41. Gerstein BC, Dybowski CR (1985) Transient techniques in NMR of solids. Academic Press, p 249
42. Mehring M (1983) Principles of high resolution NMR in solids. Springer, Berlin Heidelberg New York
43. Vega AJ (1992) Solid State Nucl Magn Reson 1:32
44. Alam TM, McLaughlin J, Click CC, Conzone S, Brow RK, Boyle TJ, Zwanziger JW (2000) J Phys Chem B 104:1464
45. McLaughlin JC, Tagg SL, Zwanziger JW (2001) J Phys Chem105:67
46. Zwanziger JW, McLaughlin JC, Tagg SL (1997) Phys Rev B 56:5243
47. Ratai E, Janssen M, Eckert H (1998) Solid State Ionics 105:25
48. Isard JO (1969) J Non-Cryst Solids 1:235
49. Day DE (1976) J Non-Cryst Solids 21:343
50. Ingram MD (1987) Phys Chem Glasses 28:215
51. Bray PJ, Emerson JF, Lee D, Feller SA, Bain DL, Feil DA (1991) J Non-Cryst Solids 129:240
52. Yap ATW, Förster H, Elliott SR (1995) Phys Rev Lett 75:3946
53. Gee B, Eckert H (1996) Ber Bunsenges Phys Chem 100:1610
54. van Wüllen L, Gee B, Züchner L, Bertmer M, Eckert H (1996) Ber Bunsenges Phys Chem 100:1539; Gee B, Janssen M, Eckert H (1997) J Non-Cryst Solids 215:41
55. Gee B, Eckert H, Taillades G, Pradel A, Ribes M (1997) J Non-Cryst Solids 215:32
56. Ratai E, Chan JCC, Eckert H (2002) Phys Chem Chem Phys 4:3198
57. Janssen M (1998) PhD Thesis, University of Münster
58. Gurman SJ (1990) J Non-Cryst Solids 125:151
59. Voigt U, Epping JD, Eckert H (in preparation)
60. Janssen M, Eckert H (2000) Solid State Ionics 136/137:1007
61. Strojek W, Kalwei M, Eckert H (2004) J Phys Chem B 108:7061
62. Prabakar S, Wenslow RM, Mueller KT (2000) J Non-Cryst Solids 263/264:82
63. van Wüllen L, Eckert H, Schwering G (2000) Chem Mater 12:1840
64. Hudgens JJ, Martin SW (1993) J Am Ceram Soc 76:1691
65. Hoppe U (1996) J Non-Cryst Solids 195:138
66. Olivier L, Yuan X, Cormack AN, Jäger C (2001) J Non-Cryst Solids 293/295:53
67. Jäger C, Feike M, Born R, Spiess HW (1994) J Non-Cryst Solids 180:91
68. Alam TM, Brow RK (1998) J Non-Cryst Solids 223:1
69. Olson KK, Zwanziger JW, Hartmann P, Jäger C (1997) J Non-Cryst Solids 222:199
70. Feike M, Jäger C, Spiess HW (1998) J Non-Cryst Solids 223:200
71. Fayon F, Massiot D, Suzuya K, Price DL (2001) J Non-Cryst Solids 283:88

72. Jäger C, Hartmann P, Witter R, Braun MJ (2000) Non-Cryst Solids 263/264:61
73. Montagne L, Palavit G, Shaim A, Et-Tabirou M, Hartmann P, Jäger C (2001) J Non-Cryst Solids 293/295:719
74. Witter R, Hartmann P, Vogel J, Jäger C (1998) Solid State Nucl Magn Reson 113:189
75. Tischendorf B, Otaigbe JU, Wiench JW, Pruski M, Sales BC (2001) J Non-Cryst Solids 282:147
76. Munoz F, Pascual L, Duran A, Montagne L, Palavit G, Berjoan R, Marchand R (2003), J Non-Cryst Solids 324:142
77. Alam TM, Lang DP (2001) Chem Phys Lett 336:385
78. Wang S, Stebbins JF (1998) J Non-Cryst Solids 231:286
79. Van Wüllen L, Schwering G (2002) Solid State Nucl Magn Reson 21:134
80. van Wüllen L, Müller U, Jansen M (2000) Chem Mater 12:2347
81. van Wüllen L, Jansen M (2001) J Mater Chem 11:224
82. Chan JCC, Eckert H (1999) Phosphorus Res Bull 10:475
83. Egan JM, Wenslow RM, Mueller KT (2000) J Non-Cryst Solids 261:115
84. Lang DP, Alam TM, Bencoe DN (2001) Chem Mater 13:420
85. Zhang L, Chan JCC, Eckert H, Helsch G, Hoyer LP, Frischat GH (2003) Chem Mater 15:2702
86. Koudelka L, Mosner P, Zeyer M, Jäger C (2003) J Non-Cryst Solids 326/327:72; Jaeger C (2003) Poster, Alpine Conference on Solid State NMR, Chamonix
87. Elbers S, Eckert H, Koudelka L, Strojek W (2004) Solid State Nucl Magn Reson (in press)
88. Schaller T, Rong C, Toplis MJ, Cho H (1999) J Non-Cryst Solids 248:19; Gee B, Janssen M, Eckert H (1997) J Noncryst Solids 215:41
89. Chan JCC, Ohnsorge R, Meise-Gresch K, Eckert H, Höland W, Rheinberger V (2001) Chem Mater 13:4198
90. van Wüllen L, Züchner L, Müller-Warmuth W, Eckert H (1996) Solid State Nucl Magn Reson 6:203
91. Züchner L, Chan JCC, Müller-Warmuth W, Eckert H (1998) J Phys Chem 102:4495
92. Bunker BC, Kirkpatrick RJ, Brow RK (1991) J Am Ceram Soc 74:1425
93. Chan JCC, Bertmer M, Eckert H (1999) J Am Chem Soc 121:5238
94. Chan JCC, Bertmer M, Eckert H (1998) Chem Phys Lett 292:154

Solid-State NMR Studies of Bone

Waclaw Kolodziejski (✉)

Medical University of Warsaw, Faculty of Pharmacy, Department of Inorganic
and Analytical Chemistry, ul. Banacha 1, 02-097 Warszawa, Poland
waclaw@pluton.farm.amwaw.edu.pl

Abstract Solid-state NMR studies on bone, bone mineral standards and collagen are reviewed. NMR spectroscopy was mostly applied to the bone mineral and confirmed that the structure resembles that of calcium carbonatoapatite of type B. Apatite in bone was found to be deficient in structural hydroxyl groups. Concentration and distribution of hydrogenphosphate and carbonate ions, and of water in apatite crystals (interior vs surface and crystal defects vs structural positions) were closely investigated. The NMR characterization of the organic matrix still remains a challenge for future research.

Keywords Bone · Apatite · Structure · Solid-state NMR · Cross-polarization

List of Abbreviations and Symbols

A	Amplitude of a CP signal in Eq. (1)
A_{sb}	A measured for a sideband
A_{cb}	A measured for a centreband
ADRF	Adiabatic demagnetisation in the rotating frame
ADRF-CP	ADRF performed CP
B	Amplitude of a CP signal in Eq. (2)
BD	Bloch decay
BRU	Brushite
CHA	Carbonatoapatite
CHA-A	Carbonatoapatite of type A
CHA-B	Carbonatoapatite of type B
CHA-AB	Carbonatoapatite of type AB (mixed)
CP	Cross-polarization

CRAMPS	Multiple-pulse homodecoupling combined with MAS
CSA	Chemical shift anisotropy
CT	Contact time
D_{HH}	Dipolar coupling constant for the ^{1}H-^{1}H interaction
D_{HP}	Dipolar coupling constant for the ^{1}H-^{31}P interaction
D_{PP}	Dipolar coupling constant for the ^{31}P-^{31}P interaction
DD	Dipolar dephased (dipolar suppression)
DCP	Differential cross-polarization
DS	Dipolar suppression period
HA	Calcium hydroxyapatite
HAc	Calcined HA (dehydrated)
HAh	Hydrated HA (as-prepared)
HETCOR	Heteronuclear correlation spectroscopy
I-I*-S	Non-classical CP model – see text and Eq. (1)
I-S	Classical CP model – see text and Eq. (2)
M_2^{PP}	Second moment for the dipolar ^{31}P-^{31}P interaction
M_2^{PP} (*pulse*)	M_2^{PP} measured using Hahn spin echo with the initial ^{31}P magnetization prepared by a π/2 pulse
M_2^{PP} (*CP*)	M_2^{PP} measured using Hahn spin echo with the initial ^{31}P magnetization prepared by CP from protons
MAS	Magic-angle spinning
OCP	Octacalciumphosphate – for the chemical formula see Table 2
T_{CP}	Cross-polarization time constant for the **I-S** model
T_{df}	Proton diffusion time constant
t_f	Time period of forward CP in DCP – see text and Fig. 14
t_r	Depolarisation time period in DCP – see text and Fig. 14
T_1^P	^{31}P spin-lattice relaxation time in the laboratory frame
T_2	Cross-polarization time constant for the **I-I*-S** model
$T_{1\rho}^H$	^{1}H spin-lattice relaxation time in the rotation frame
T_2^H	^{1}H spin-spin relaxation time in the laboratory frame
RD	Recycle delay
λ	Constant in Eq. (1) – for interpretation see text
ι	Sideband pattern index
σ_i	Isotropic chemical shift
$\sigma_{11}, \sigma_{22}, \sigma_{33}$	Principal components of a chemical shift tensor
τ	Additional period of the proton spin lock prior to CP (cf. Fig. 11)
1D	One-dimensional
2D	Two-dimensional

1
Introduction

Bone is the building material of the vertebrate skeleton. The main function of the skeleton is to support the soft tissues. Bone experiences numerous complex changes over the lifetime of the organism, both natural and pathological, related to changes in other tissues. It follows that bone health status should be monitored to prevent and diagnose various diseases. In particular, it is very important to monitor the progression of osteoporosis and thus predict the risk of

bone fractures. The factors determining overall bone quality are bone mineral density (BMD) measured with densitometry, bone microarchitecture (morphology) which can be assessed using imaging techniques (X-ray Computed Tomography and MRI), and bone chemical composition and structure, which can be investigated with instrumental analytical methods, preferably spectroscopic. The latter study requires bone samples collected during surgical operations, while the former examinations are non-invasive. Alternatively, bone samples from other animals can be used as models for human bone. This article reviews high-resolution solid-state NMR studies on bone chemistry using ^{31}P, ^1H and ^{13}C nuclei.

Bone is a dynamic tissue undergoing a continuous rebuilding process. Bone turnover is associated with resorption of old tissue by osteoclasts (bone resorption cells) and formation of new tissue by osteoblasts (bone forming cells). This remarkable activity allows bone to grow and retain structural integrity, for example by healing microfractures. Simultaneously, the bone mineral serves as the main body reservoir of calcium and phosphorus. The rebuilding process itself, and the transport of elements to and from bone by means of various chemical species, are controlled by specific homeostasis, which is at least in part regulated hormonally.

Research on bone structure has been thoroughly reviewed [1–3]. From the morphological point of view, the adult skeleton is ca. 80% cortical and 20% trabecular bone. Cortical bone is compact, while trabecular bone consists of a network of interconnected plates and struts, which are 100–300 μm thick. Because of the resulting high surface area, trabecular bone is metabolically more active and responsive to influences and diseases, such as osteoporosis. The bone tissue consists of cells (ca. 2 wt%) and extracellular matter, amenable to examination by high-resolution solid-state NMR. The extracellular matter contains respectively ca. 65, 25 and 10 wt% of inorganic material, organic material and water [4]. The bone mineral is dominated by calcium apatite deposited on the organic matrix, which is ca. 90% collagen.

Intact bone is a demanding material for structural studies. Severe experimental difficulties arise from the morphological diversity of bone, from the coexistence, interrelationship and great complexity of its organic and inorganic components, and last but not least from the substantial sensitivity of bone samples to physical and chemical effects. In consequence, classical "wet" chemistry methods are often criticised as too invasive, especially if it is necessary to isolate the inorganic or organic part from whole bone. By contrast, high-resolution solid-state NMR gives us the opportunity to look specifically at selected magnetic nuclei in whole bone without any chemical pretreatment, thus avoiding interference with bone structure. ^1H and ^{31}P resonances are particularly suitable for the study of the bone mineral, while ^{13}C resonance is indispensable when observing the organic matrix. Solid-state ^1H, ^{31}P and ^{13}C NMR spectra of bone are broadened by homonuclear and heteronuclear dipolar coupling, chemical shift anisotropy (CSA) and structural disorder, which spreads chemical shifts. In order to obtain high resolution ^{13}C and ^{31}P spectra, one must use

magic-angle spinning (MAS) under high-power proton decoupling. For ^{1}H NMR, it is necessary to employ sufficiently fast MAS or multiple-pulse homodecoupling combined with MAS (CRAMPS). Bloch-decay (BD), that is conventional pulse-acquire experiments, are used for abundant nuclei (^{1}H and ^{31}P). Cross-polarization (CP) can be applied for signal enhancement (^{13}C) or for exposing protonated sites (^{31}P), for achieving 2D chemical shift correlation or for structural studies involving CP kinetics. It is useful to compare normal CP spectra with those recorded under dipolar suppression (dipolar-dephased spectra, DD), because this discloses unprotonated sites or highly mobile species. For details of the solid-state NMR techniques see [5–14].

2
Structure of Bone Components and their Model Compounds

In 1926, DeJong identified the bone mineral as calcium hydroxyapatite (HA), $Ca_{10}(OH)_2(PO_4)_6$ [15]. Pure HA crystallises in the hexagonal space group $P6_3/m$ [16] and, when super-pure and strictly stoichiometric, in the monoclinic space group $P2_1/b$ [17a]. As biological hydroxyapatites are always contaminated with various ions, we shall consider only the hexagonal form (Fig. 1). In this form, all the P atoms are crystallographically equivalent [16]. The shortest inter-phosphorus distance is 4.112 Å, which corresponds to the [31]P-^{31}P dipolar coupling of 284 Hz. The structural hydroxyl groups of HA are crystallographically equivalent and located at the edges of unit cells in the –O-H O-H O-H O-H– columns, parallel to the c-axis. They do not participate in hydrogen bonding, because the successive oxygen atoms are too distant from each other (3.44 Å). In conse-
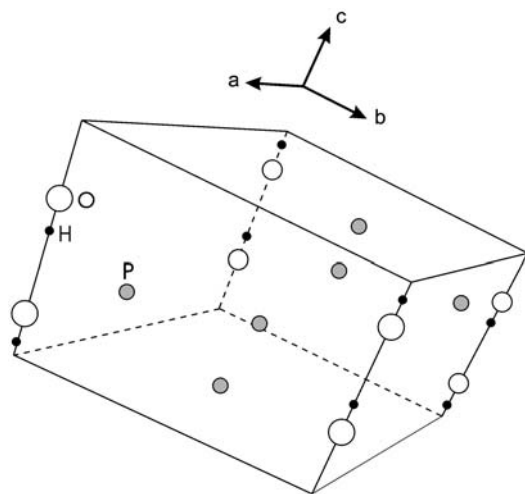
Fig. 1 Crystal unit cell of HA. Oxygen atoms of the PO_4^{3-} ions and the Ca^{2+} ions are omitted for clarity. The picture was prepared using data from [16], deposited in the Cambridge Crystallographic Data Base

quence, the ^{1}H MAS NMR peak of the structural hydroxyl groups appears at ca. 0 ppm [18]. Two neighbouring intra-column protons are 3.44 Å apart, which corresponds the ^{1}H-^{1}H dipolar coupling D_{HH}=2.951 kHz. This means that homonuclear dipolar coupling in HA (^{31}P-^{31}P and ^{1}H-^{1}H) can easily be overcome by MAS at several kilohertz. Each P atom has two proton neighbours at 3.847 Å (D_{HP}=855 Hz) and further two at 4.205 Å (D_{HP}=655 Hz), while the others are 6 Å or more away (D_{HP}<230 Hz). The latter information on heteronuclear dipolar coupling can be useful for evaluation of the ^{1}H→^{31}P CP rates.

According to the present state of knowledge, bone mineral is always non-stoichiometric calcium apatite and would be better classified as calcium carbonatoapatite of type B (CHA-B) than as HA [19, 20]. The carbonate anion, CO_3^{2-}, is the principal minor constituent of the bone mineral, estimated at 5–8 wt% [4, 19, 21, 22]. Generally, apatites are crystalline minerals with crystallographic structure similar to HA and formed by substitution of various ions into the HA lattice [19]. In particular, carbonate ions can replace hydroxyl ions or orthophosphate ions, PO_4^{3-}, leading to carbonatoapatites of type A and B, respectively. Carbonatoapatite of type A (CHA-A) and mixed (CHA-AB) are, together with CHA-B, components of dental enamel. The substitution of PO_4^{3-} by CO_3^{2-} (type B) is presumed to leave an oxygen vacancy in one of the equivalent positions, III or III′, in the crystal lattice (Fig. 2). This vacancy is positively charged (+1) and the electric imbalance in the lattice has to be compensated by a joint release of one calcium cation and one hydroxyl anion, that is by creation of a net negative charge (–1) [21]. It follows that the bone mineral should be defi-
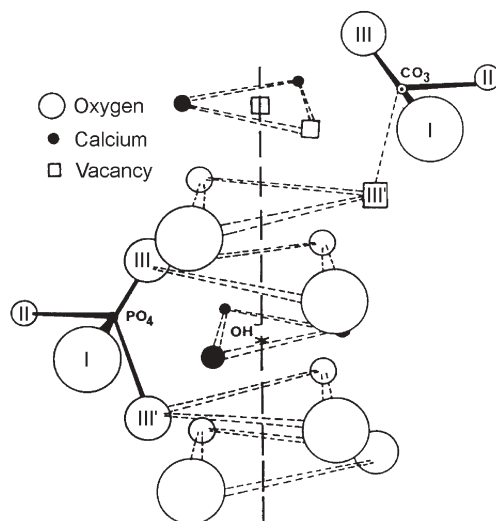
Fig. 2 Crystallographic structure of CHA-B [23]. Hydroxyl groups are located at the *c*-axis inside triangles formed by calcium. In this scheme, four tetrahedral phosphate oxygen sites, labelled I, II and III, are occupied by three oxygens of a carbonate ion, while the site III′ is vacant. Note the calcium and hydroxyl vacancies in the neighbourhood of the carbonate ion

cient in hydroxyl groups, as is indeed confirmed by IR, NMR and inelastic neutron-scattering [20, 24–28].

There were numerous attempts to find a general chemical formula for bone mineral. Legros et al. [21] proposed $Ca_{8.3}(PO_4)_{4.3}(HPO_4,CO_3)_{1.7}(OH)_{0.3}$ for mammalian species (rabbit, cat and rat) on the basis of elaborate studies involving thermogravimetric analysis, X-ray diffraction, electron diffraction, IR spectroscopy and chemical analysis. The formula reflects the mechanism of ionic substitution discussed above [21] and shows calcium and hydroxyl contents decreased to 83 and 15 mol%, respectively, compared to those in stoichiometric HA. This hydroxyl content is in agreement with a rough estimate of 21% given by Cho et al. [28]. The formula comprises two types of bivalent anions, hydrogenphosphate HPO_4^{2-} and carbonate CO_3^{2-}, the total quantity of which is constant, although their molar ratio can vary (ca. 0.7:1 for rabbit periosteal bone). This is in accordance with the generally accepted view that bone mineral contains HPO_4^{2-} [19], although negative results should also be considered [20, 29].

A reasonable model mineral for predicting NMR behaviour of HPO_4^{2-} in bone apatite is brushite (BRU), $CaHPO_4 \cdot 2H_2O$. In the monoclinic crystal lattice of BRU (space group Ia), all the P atoms are crystallographically equivalent [30]. Such equivalence also occurs for HA (see above), so both HA and BRU show single ^{31}P MAS NMR peaks [31] (Fig. 3). They have similar chemical shifts, but the latter is flanked by pronounced spinning sidebands caused by considerably larger CSA (Table 1). CSA is usually the major factor, which broadens ^{31}P phosphate lines and must be suppressed by MAS. As the MAS rate required to accomplish the high resolution has to exceed CSA given in frequency units, it depends on the resonance frequency. Assuming the ^{31}P CSA values of HA and BRU of 40 and 120 ppm, respectively (Table 1), at the ^{31}P resonance fre-
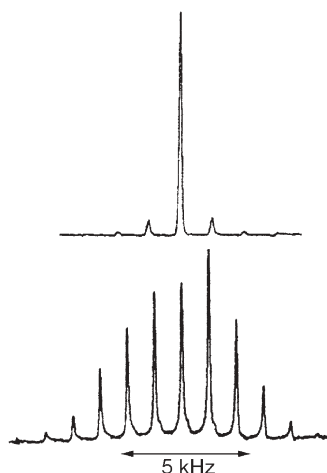
Fig. 3 Proton-decoupled ^{31}P BD/MAS NMR spectra of stoichiometric HA (*top*) and BRU (*bottom*) recorded at resonance frequency 68.4 MHz with MAS of 1.23 and 1.14 kHz, respectively (adapted from [31])

Table 1 The ^{31}P chemical shift tensors of HA and BRU [31]. The total chemical shift anisotropy $\Delta=|\sigma_{33}-\sigma_{11}|$

Phosphate	^{31}P isotropic chemical shift[a]	Principal values of ^{31}P chemical shift tensor		
		σ_{11}	σ_{22}	σ_{33}
HA[b]	2.8±0.2	19±3	4±6	−15±1
BRU	1.7±0.3	70±6	−12±6	−53±3

[a] In ppm from 85% H_3PO_4.
[b] Smaller chemical shift anisotropy of ca. 20 ppm reported in [35].

quencies of 80 and 160 MHz (200 MHz and 400 MHz for protons), this would correspond for HA to 3.2 and 6.4 kHz, respectively, and for BRU to 9.6 and 19.2 kHz, respectively. Therefore, for HPO_4^{2-} ions, high MAS rates are necessary for overcoming ^{31}P CSA in high magnetic fields.

The crystal lattice of BRU contains five kinds of equally populated hydroxyl groups located in two crystallographically inequivalent water molecules and in the HPO_4^{2-} ions [30]. The hydroxyl groups of the three species are involved in hydrogen bonds, which for the P-OH groups of HPO_4^{2-} are the strongest. The crystallographic arrangement and the molecular interactions within the crystal lattice differentiate hydroxyl protons in such a way that the two inequivalent water molecules give separate ^{1}H MAS NMR signals at 4.1 and 6.4 ppm, while the P-OH protons resonate at 10.4 ppm [20]. The strongest ^{1}H-^{31}P dipolar couplings of D_{HP}=4.6 kHz occur in the P-OH groups, while those involving water protons are below 2.5 kHz. Considering the ^{1}H-^{31}P dipolar couplings, one should expect much faster CP between these nuclei in BRU than in HA. The ^{31}P-^{31}P dipolar coupling in BRU is weak, the largest D_{PP}=354 Hz. However, the ^{1}H-^{1}H dipolar coupling in this mineral is huge compared to that in HA. It is dominated by the dipolar couplings within the inequivalent water molecules, D_{HH}=35.4 and 31.4 kHz, while other couplings are below 11.3 kHz. A contribution to the proton linewidth from chemical shift anisotropy can usually be neglected. It follows that MAS rates over 35 kHz are required to resolve the ^{1}H water peaks and ca. 12 kHz to separate the P-OH peak from a broad joint signal from water. This is demonstrated in Fig. 4, which also shows that insufficiently fast MAS can give misleading proton spectra.

The organic matrix of bone is dominated by collagen, perhaps the most abundant protein in the animal kingdom [32–34]. Its properties are diverse and remarkable. For example, collagen accounts for the strength and elasticity of tendon, the high transparency of the eye cornea and for the lubricating properties of cartilage coating the inner surface of joints. There are many severe diseases, such as some congenital malformations or rheumatoid arthritis, which are a manifestation of excessive or insufficient production of collagen, its bad hydroxylation or the aberrant arrangement of collagen fibrils in affected tissues. There are different types of collagen, but that in bone is collagen type I.
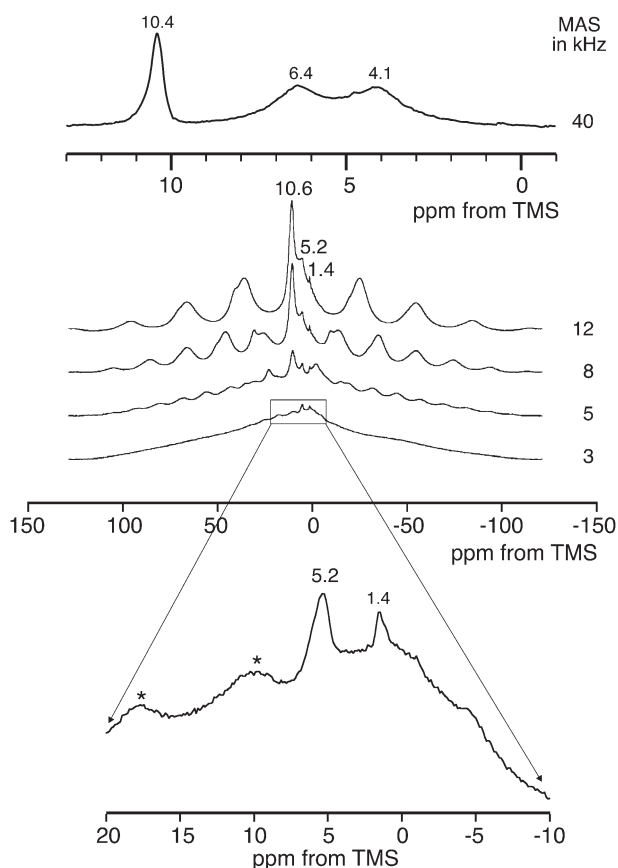
Fig. 4 Proton NMR spectra of BRU recorded with various MAS rate (*upper* at 833 MHz, *others* at 200 MHz)

Collagen structure is as follows [32–34]. A single molecular chain of collagen is composed of ca. 1000 aminoacid units and twists itself into a left-handed helix. In each turn of this helix we find glycine (Fig. 5) located near the helix axis and two other aminoacid units, which occupy the outer regions of the helix. Thus, there are about 33% glycine units, and the next most abundant species are proline (ca. 10%) and hydroxyproline (ca. 10%). Hydroxyproline is rather rare in proteins and, very unusually, is formed by hydroxylation of proline *after* the primary synthesis of collagen in fibroblasts. Then, three single molecular chains intertwine to form a right-handed supertriple-helix, called a tropocollagen molecule. Next, many tropocollagen molecules line up in a staggered fashion to form fibrils. Finally, these fibrils become organized in various, highly ordered, patterns unique for a given tissue. All these structural details should be adequately reflected in ^{1}H and ^{13}C MAS NMR spectra of bone.
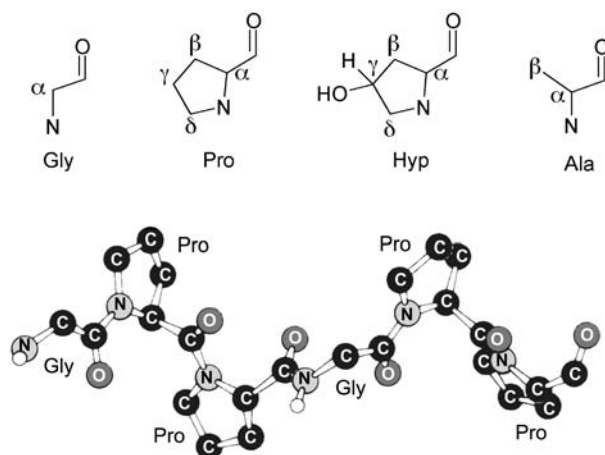
Fig. 5 Most abundant aminoacid units (*top*) and a fragment of the single molecular chain of collagen (*bottom*). Hydrogen atoms bonded to carbons have been omitted for clarity

3
Phosphorus-31 NMR

^{31}P MAS NMR spectra were measured for several kinds of bone tissue from different specimens (chicken, rat, cat, rabbit, cow and human), in some cases of various ages. Despite different MAS rates and resonance frequencies, which affect spectrum resolution, all the BD and CP spectra of bone reported so far consisted of a single, structureless and almost symmetric peak at ca. 3 ppm from 85% H_3PO_4 [20, 28, 29, 35–41] (Fig. 6). The bone matrix (demineralised bone) gives an extremely week ^{31}P MAS signal [28], which, on the basis of the chemical shift, can be assigned to residual apatite. It turns out that the peak at 3 ppm comes exclusively from the bone mineral and that various P-containing species, contributing to this resonance, have similar isotropic chemical shifts. It is difficult to obtain structural information from this single resonance. Two solutions have been proposed to deal with the problem: (i) NMR comparison of bone mineral to synthesized mineral standards and (ii) application of more advanced solid-state NMR techniques.

Following the first procedure, mineral standards were synthesized and characterized by ^{31}P MAS NMR [31, 42]. BD, CP and DD spectra of mineral standards and bone samples were compared, giving particular attention to chemical shifts (Table 2), linewidths and rotational sideband patterns [35]. A typical set of spectra, acquired for mineral standards, is given in Fig. 7. Each BD spectrum comes from all P-sites, while its CP counterpart exposes a fraction of the P-sites capable of obtaining polarization from surrounding protons. The DD experiment is performed with a time interval without proton decoupling inserted just after CP. This is called a dipolar suppression period (DS), because
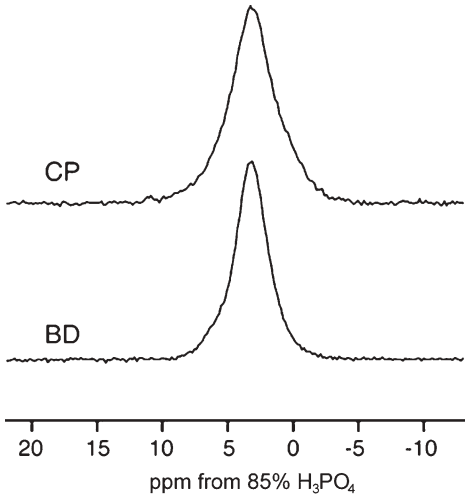
Fig. 6 Centrebands of the proton-decoupled ^{31}P CP and BD NMR spectra (81 MHz) of human trabecular bone, recorded under MAS at 3 kHz [20]. The peaks are presented with the same maximum intensities

Table 2 Isotropic ^{31}P chemical shifts of synthetic calcium phosphates (Table 1 from [42])

Compound	Chemical shift[a]
Crystalline HA	2.8
HA with 12% HPO_4^{2-}	2.8[b]
CHA-B with 3.2% CO_3^{2-}	2.8
CHA-B with 14.5% CO_3^{2-}	3.0
CHA-A[c]	5.5, 4.6, 3.8, 2.5
Amorphous HA	3.0
Octacalcium phosphate $Ca_8(HPO_4)_2(PO_4)_4 \cdot 5H_2O$ (OCP)	2.8, −0.5
Monetite $CaHPO_4$	−0.3, −1.7
BRU	1.4

[a] In ppm from 85% H_3PO_4. According to [43], the HA and BRU chemical shifts need to be corrected to 3.1 and 1.7 ppm, respectively.
[b] Inconsistent with the text [42], where a small shift of −0.5 ppm in comparison to HA was reported.
[c] Complete substitution of CO_3^{2-} for the OH$^-$ groups.

during this time any ^{31}P spins strongly coupled to adjacent protons have their signals suppressed. The DD spectra highlight those P-sites which exhibit weak dipolar ^{1}H-^{31}P couplings, but still cross-polarize from protons. In this case, CP comes from remote protons or protons located in relatively mobile chemical species. The longer the DS, the smaller the line contribution from the P-sites with immobile nearby protons.
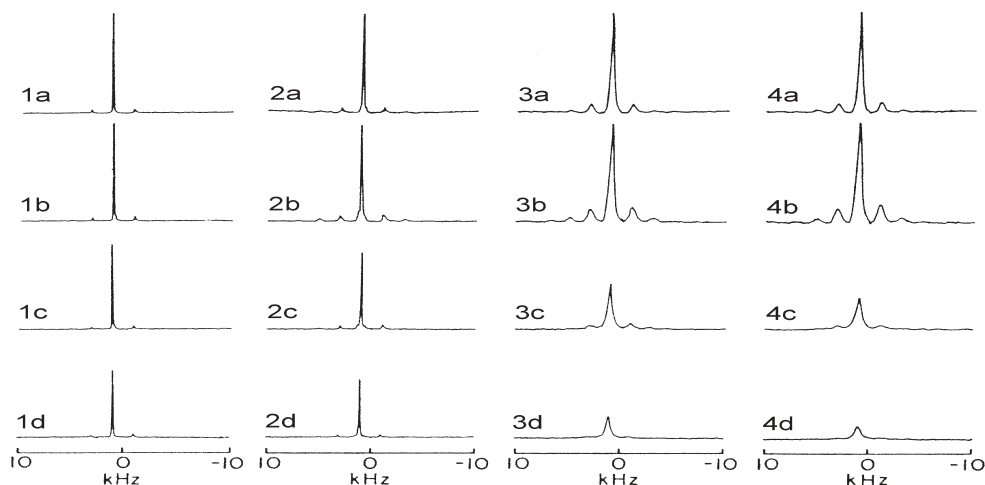
Fig. 7 Proton-decoupled ^{31}P NMR spectra (119 MHz) of apatite minerals acquired with MAS at 2 kHz (adapted from [42]). Each column presents: (a) a BD spectrum, recycle delay RD=60 s; (b) a CP spectrum, RD=10 s, contact time CT=0.5 ms; (c) and (d) DD spectra with DS of 0.5 and 1.0 ms. For comparison purposes, all the (a) and (b) graphs are presented with the same peak amplitudes, while (b)–(d) are presented on the absolute intensity scale. (1) Crystalline HA; (2) HA containing 12% of its phosphate in the form HPO_4^{2-}; (3) CHA-B containing 3.2% CO_3^{2-}; (4) CHA-B containing 14.5% CO_3^{2-}

Figure 7 shows the relative increase in sideband intensities for CP over BD as HPO_4^{2-} and CO_3^{2-} ions are introduced into the lattice and the considerable broadening of the CHA-B peaks [42]. The effect of HPO_4^{2-} ions is obvious, since they give pronounced sideband patterns and cross-polarize very efficiently. This has already been explained during the discussion of BRU. Figure 8 proves that the appearance of sideband patterns is very sensitive to the structure of the material [20]. It was found [42] that decrease in crystallinity results in considerable increase of linewidths and sideband intensities, and in dramatic reduction or disappearance of DD peaks (Fig. 9) [42]. The centreband in the CP spectrum of poorly crystalline HA looked like a superposition of a sharp line on a broader background. The CP and BD spectra of amorphous calcium phosphate were virtually identical within the experimental error. Aue et al. [42] admitted that they found no satisfactory explanation for the latter observation. Likewise, the discussion of the CO_3^{2-} effect (Fig. 7) did not go very far. It was stated that the CHA-B lines were 5–10 times broader than those from various HA samples and that this broadening showed rather small dependence on carbonate concentration. It was inferred that the introduction of CO_3^{2-} increased the CP efficiency of some PO_4^{3-} ions in the crystal lattice and imparted some changes in the PO_4^{3-} shift anisotropies. The former is questionable, because no protons were introduced into intracrystalline sites proximate to PO_4^{3-} ions and the latter acceptable, because the CHA lattice must be less ordered, at least in the
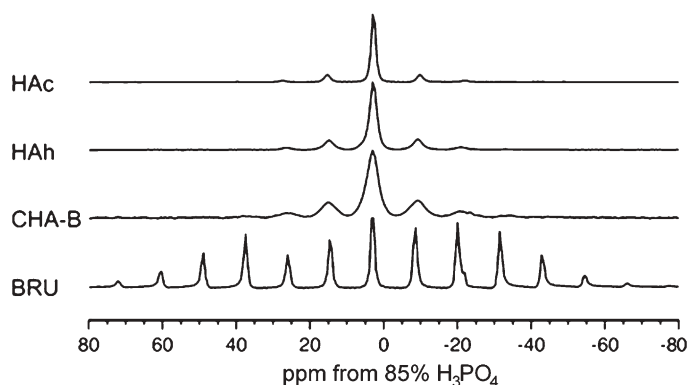
Fig. 8 Proton-decoupled ^{31}P CP NMR spectra (81 MHz) of apatites and BRU recorded with MAS at 1.00 kHz and CT=1 ms [20]. HA was studied as-prepared (hydrated denoted HAh) and calcined (heated at 1073 K denoted HAc). CHA-B contained 9 wt% CO_3^{2-}
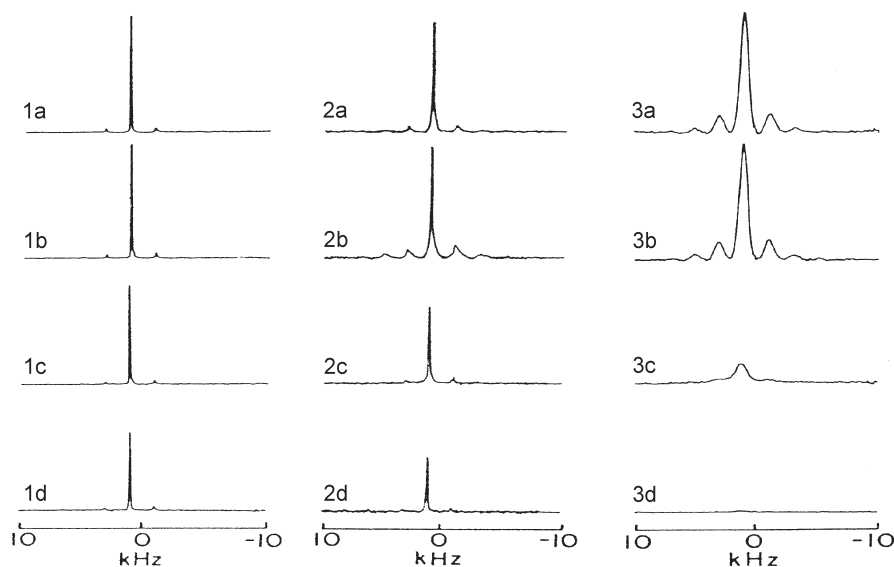
Fig. 9 Proton-decoupled ^{31}P NMR spectra (119 MHz) of phosphates acquired with MAS at 2 kHz (adapted from [42]): (1) crystalline HA; (2) poorly crystalline HA; (3) amorphous calcium phosphate. Experimental conditions for (a)–(d) are the same as in Fig. 7

vicinity of the CO_3^{2-} sites, than that of unsubstituted HA. Aue et al. [42] claimed that the difference between the BD and CP spectra of CHA-B indicates the presence of at least two types of phosphate groups in the lattice. Surface P-sites were not considered.

The studies presented in [31, 42] made it possible to identify bone mineral components by examining BD, CP and DD ^{31}P spectra. By use of spectral simu-

lation, Roufusse et al. [35] found that the CP spectra of chicken bone can be reproduced with a two-component model consisting of the unmodified CHA-B and line-broadened BRU spectra (Fig. 10a). CHA-B and BRU were supposed to contribute to the overall bone spectrum to a major and minor extent, respectively. It was suggested that "the major solid calcium phosphate mineral phase in bone is a hydroxyapatite containing ca. 5–10% CO_3^{2-} and ca. 5–10% HPO_4^{2-}, the latter in a brushite-like configuration" [35]. The HPO_4^{2-} content was reported to increase as a function of age [35], since the ratio of BRU-like HPO_4^{2-} groups to HA-like PO_4^{3-} groups in bone from 17-day-old embryo, 5-week-old and 1-year-old postnatal animals was calculated to be 0.12, 0.08 and 0.05 (all ±0.03), respectively. The latter value for the mature animal is very imprecise, because it is quite close to the standard error, and consequently may very well be equal to zero. Therefore, it is possible that no BRU-like HPO_4^{2-} ions were detected in mature human bone and that its CP spectrum was identical to synthetic CHA-B containing ca. 9 wt% of CO_3^{2-} and no intracrystalline HPO_4^{2-} ions (Fig. 10b) [20]. This is consistent with the IR estimate of the CO_3^{2-} content of 7.4 wt% [4].

The study [35] is interesting, because it presents the first attempt to quantify CO_3^{2-} and HPO_4^{2-} in bone using NMR spectroscopy. However, imitation of the HPO_4^{2-} contribution to the ^{31}P MAS NMR spectrum of bone using the spectrum of BRU (Fig. 10a) [35] nowadays seems unconvincing. Note that the HPO_4^{2-} ions have different isotropic chemical shifts in bone and in BRU [37]:
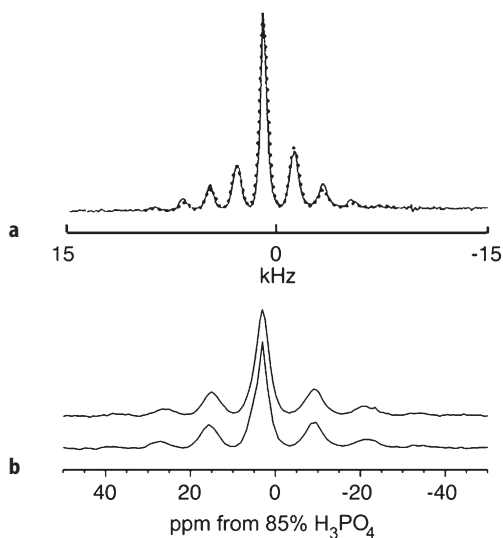
Fig. 10a,b Comparison of proton-decoupled ^{31}P CP NMR spectra of bone and mineral standards: **a** a spectrum of 17-day-old embryonic chick bone (*dotted curve*), superimposed on a computer simulated spectrum (*solid line*) of a mixture of CHA-B (3.2% CO_3^{2-}) and BRU [35]; **b** spectra of human cortical bone from a 24-year-old man (*lower curve*) and CHA-B with 9 wt% of CO_3^{2-} (*upper curve*) [20]. Experimental conditions: **a** NMR at 119 MHz, MAS at 2 kHz, CT=0.5 ms; **b** NMR at 81 MHz, MAS at 1 kHz, CT=1 ms

typically –0.4 ppm and 1.4 ppm, respectively. Another argument is that they also reside on crystal surfaces [41], where they must have different chemical (e.g. acidity) and NMR (chemical shift, relaxation, CP efficiency) properties to those inside the crystal lattice. The surface/lattice ratio for HPO_4^{2-} depends on the crystallinity of the material and cannot be properly accounted for by the two-component model consisting of unmodified CHA-B and line-broadened BRU spectra, as proposed in [35]. One should also bear in mind that the exact nature of P-containing surface species in apatites is still uncertain [20]. Closer inspection of Figs. 7 and 9 indicates that, at least in part, the ^{31}P NMR behaviour of CHA-B and bone might be rationalised by the exceptionally small crystal dimensions and resultant high specific surface areas of both materials. In respect of these properties, CHA-B and bone are very different from pure crystalline HA. It was shown (Fig. 13 in [19]) that the type B substitution of CO_3^{2-} into HA results in a dramatic decrease in the crystal size, by more than one order of magnitude, and in a morphological change from needles to rods and then to equi-axial crystals (spheroids). Mineral sites in bone, which exist as plate-like apatite structures of tens to hundreds nanometers in size, are in fact aggregates of much smaller flat crystallites, ca. 17 nm wide and 6 nm thick (diaphyseal cortical tissue from rat tibiae bones) [44]. This corresponds to the specific area of ca. 270 $m^2\ g^{-1}$ [44]. For comparison, consider pure fine-crystalline HA synthesized from aqueous solution at low temperature, where rod-like crystals were 133 nm long and 33 nm wide [45]. The specific area of that material was only 37 $m^2\ g^{-1}$ [45]. Wu et al. [41] suggested that CP predominantly samples surface phosphates. Crystal surfaces of apatite crystallites are rich in protons from adsorbed water and/or possible surface HPO_4^{2-} groups [41, 45]. This would be a rationale for high efficiency of dipolar suppression in materials with a large specific surface area, that is in amorphous calcium phosphate, CHA-B and bone (Figs. 7 and 9).

To acquire better structural information, one has to resort to more advanced solid-state NMR techniques. Here, they will be reviewed by subject rather than in chronological order. First, we shall briefly look at ^{31}P relaxation. Second, components of the $^1H{\rightarrow}^{31}P$ CP signal will be discussed. Third, much attention will be given to HPO_4^{2-} detection by differential $^1H{\rightarrow}^{31}P$ cross-polarization (DCP). Then the ^{31}P sideband pattern index and chemical shift anisotropy in the study of bone calcification will be briefly reviewed. Finally, a special ADRF-CP technique will be mentioned.

For bone, the ^{31}P spin-lattice relaxation time T_1^P is ca 100 s [36, 39] and decreases by approximately 15% from the dried to the fully hydrated sample [36]. In contrast, for synthetic HA, T_1^P is considerably shorter and varies from 1 to 22 s [31, 36]. The cited results are for differently prepared samples, different magnetic fields and different MAS rates. Homonuclear ^{31}P-^{31}P spin-spin relaxation in the solid state can be conveniently characterized by van Vleck second moments M_2^{PP} [46, 47]. Wu et al. [41] measured M_2^{PP} in bone, dental enamel and synthetic apatites, HA and CHA-B, using the ^{31}P Hahn spin echo under proton decoupling. The initial ^{31}P magnetization was prepared either by a $\pi/2$ pulse or

^{1}H$\rightarrow^{31}$P CP, giving different M_2^{PP} (pulse) and M_2^{PP} (CP) values, respectively. The reported second moments are of the order of 10^6 rad^2 s^{-2} and in all cases M_2^{PP} (CP) < M_2^{PP} (pulse). For enamel and bone M_2^{PP} (CP) was lower by 7–24% than M_2^{PP} (pulse). Note that lower M_2^{PP} corresponds to a weaker ^{31}P-^{31}P dipolar coupling. For apatite crystals this is expected for ^{31}P sites on crystal surfaces, where some near ^{31}P neighbours are intrinsically missing. This is also in accordance with common knowledge that CP "looks" rather at crystal surfaces, an environment richer in protons, e.g. from adsorbed water, than into the crystal interior. It follows that the $\pi/2$ pulse and CP preparation methods favour different crystal regions, the interior and the surface, respectively. Moreover, Wu et al. [41] postulated that a significant fraction of protonated phosphates (HPO$_4^{2-}$) are located on the surfaces of biological apatite crystals, and the concentration of unprotonated phosphates (PO$_4^{3-}$) inside the crystal lattice is elevated with respect to the surface. The assumptions may be true, although it is not yet settled whether surface PO$_4^{3-}$ ions are hydrolysed to HPO$_4^{2-}$ or are involved in H-OH$\cdots$O-PO$_3^{3-}$ hydrogen bonds, or whether both processes occur with a probability depending on various chemical and physical conditions. On the assumption that CP preferably samples surface HPO$_4^{2-}$ ions and on the basis of the M_2^{PP} (CP) values [41], one may conclude that the total concentration of the surface HPO$_4^{2-}$ ions is higher in the younger, less mature biological crystals. Wu et al. [41] optimistically suggested that their second moment measurements can be adapted to the study of bone crystals in vivo and possibly to clinical studies of human subjects. However, the method must be carefully validated and verified on many samples. Preliminary experiments in our laboratory show that ^{31}P echoes from static apatite samples decay rather within tens of microseconds of the echo time, than within ca. a millisecond as shown in Figs 2–4 in [41]. There must be some problem with those figures, because following the calculation algorithm described in [41] one obtains different numerical values of M_2^{PP} to those quoted. And lastly, many more echo-time points should be used to prove adequately that a "pseudo-FID" from the echo experiment really corresponds to a single Gaussian.

More information on the chemical structure of bone apatite can be obtained from ^{1}H$\rightarrow^{31}$P CP. First, consider the dependence of peak intensity $I(t)$ on contact time t (also denoted CT) in the conventional variable-contact time experiment (Fig. 11). Such an experiment monitors the CP kinetics, which is very specific for a particular material [12]. There are two models of the CP kinetics, **I-I***-**S** and **I-S** [12]. In this notation, the spin polarization is transferred from spins **I** to spins **S**, in our case from protons to ^{31}P, respectively.

For an isolated group of spins, CP proceeds according to the **I-I***-**S** model, where the asterisk denotes nuclei **I** in close proximity to a given nucleus **S**. Within this model, protons do not have a common spin temperature. The **I***-**S$_n$** spin pairs (n=1) or clusters (n=2, 3 …) exchange polarization in an oscillatory manner, damped by subsequent spin-diffusion with remaining protons **I**. The oscillation frequency is dependent on the **I***-**S** dipolar interaction. For rotating powders and/or overlapped signals from various chemical species, their oscil-
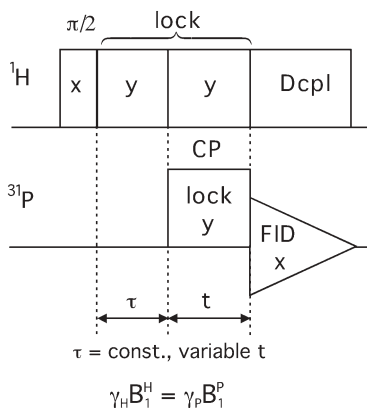
Fig. 11 The conventional CP pulse sequence with an additional period τ of the proton spin lock

lations mutually cancel out and the CP kinetic curve looks smooth and is governed by Eq. (1):

$$I(t) = A \exp(-t/T_{1\varrho}^H) \left[1 - \lambda \exp(-t/T_d) - (1-\lambda)\exp(-3t/2T_d)\exp(-t^2/2T_2^2)\right] \tag{1}$$

where t is the contact time, A is the ^{31}P signal amplitude, $T_{1\varrho}^H$ is the proton spin-lattice relaxation time in the rotating frame, T_{df} is the proton spin-diffusion time constant, and T_2 is a CP constant which reflects the ^{31}P-^1H dipolar couplings. For a rigid lattice $\lambda = (n+1)^{-1}$, where n is the number of protons in close vicinity to the observed ^{31}P nucleus. However, λ is also dependent on a molecular and/or group motion and should be treated as an adjustable parameter [12]. Equation (1) corresponds to a three-stage CP process: fast rise governed by T_2 for CP within the spin cluster, slow rise governed by T_{df} for CP controlled by proton spin diffusion from bulk protons to protons of the spin cluster, and decay due to spin-lattice relaxation governed by $T_{1\varrho}^H$.

If the I-S heteronuclear dipolar interactions are weak, e.g. reduced by molecular mobility or spacial remoteness, while the I-I homonuclear dipolar interactions are moderate or strong, then the CP kinetics is likely to follow the classical **I-S** model. In most cases, it is described by Eq. (2):

$$I(t) = B(1 - T_{CP}/T_{1\varrho}^H)^{-1}\left[\exp(-t/T_{1\varrho}^H) - \exp(-t/T_{CP})\right] \tag{2}$$

where B is signal amplitude and T_{CP} is a CP time constant dependent on dipolar interactions of the observed ^{31}P spins with protons. Equation (2) predicts double exponential behaviour of the CP intensity $I(t)$ on the contact time t. The intensity initially rises according to the T_{CP} time constant and then decreases according to the relaxation time $T_{1\varrho}^H$. The classical kinetic model is valid for ^{31}P spins, which gain polarization from a proton reservoir having a common spin temperature.

In our group, Kaflak et al. [39] studied the ^{1}H$\rightarrow$^{31}P CP kinetics for human trabecular bone under MAS at 3 kHz. In order to investigate the heterogeneity of the bone mineral with respect to $T_{1\varrho}^H$, variable-contact time experiments were performed with a variable period τ of an additional ^{1}H spin lock just before the CP contact (Fig. 11). With increasing τ the CP signal was losing intensity from sample domains with relatively fast relaxation in the rotating frame (Fig. 12). Finally, it approached the limiting case of τ=10 ms (curve C), corresponding almost exclusively to sample domains with very long $T_{1\varrho}^H$ (very slow relaxation). The kinetic curve of the fast-relaxing sample domains was obtained from the difference of the kinetic curves A and C. The slow- and fast-relaxing components of the CP signal showed different CP rates and behaved according to the **I-I*-S** and **I-S** models, respectively. Further deconvolution of the curve C was attempted and all the signal components were discussed in terms of the proton content. We hoped to assign the bone mineral domains to small regions with the same structure: HA, CHA, BRU etc. However, a thorough assignment was left until kinetic experiments on model phosphates are done. The work [39] proved the heterogeneity of bone mineral as concerns $T_{1\varrho}^H$ and CP rates, and indicated that protons of the organic matrix were not involved in the ^{1}H$\rightarrow$^{31}P polarization transfer.

The CP kinetics for BRU and various synthetic apatites were measured and interpreted [40, 48, 49]. We realized [29, 40] that the CP behaviour of bone mineral closely matches that of CHA-B, as in both cases there were two, slow and fast-relaxing, clear-cut components of the CP signal. They followed Eq. (1) and Eq. (2), respectively, with similar kinetic parameters for bone mineral and CHA-B. Figure 13 shows the deconvolution of the overall curve A from Fig. 12 into those components, while the fitted CP kinetic parameters are collected in Table 3. In view of these new experimental facts and modified computer fit-
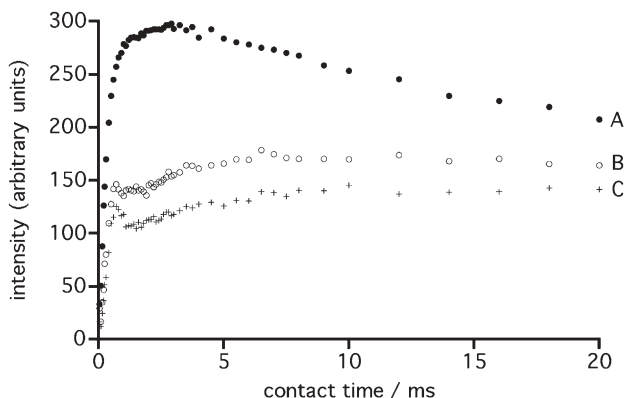
Fig. 12 Kinetics of ^{1}H$\rightarrow$^{31}P CP in lyophilised human trabecular bone under MAS at 3 kHz (81 MHz for ^{31}P) [39], studied with the pulse sequence from Fig. 11. Intensity at the maximum of the ^{31}P peak was measured as a function of the contact time. The plots A, B and C correspond to τ equal 0, 5 and 10 ms, respectively

Table 3 Parameters of the $^1H\rightarrow^{31}P$ CP kinetics for human trabecular bone, fitted for the experimental points from [39]. The slow and fast-relaxing components correspond to curves C and A-C in Fig. 13. All the time constants are reported in ms. Results of the old fittings [39] are reported in brackets

Slow-relaxing component (Eq. 1)				
A	λ	T_2	T_{df}	$T_{1\varrho}^H$
142 ± 1	0.38 ± 0.02	0.223 ± 0.007	3.4 ± 0.4	∞
$(82\pm5)^a+(60\pm4)^b$			$(3.0\pm0.3)^b$	

Fast-relaxing component (Eq. 2)		
B	T_{CP}	$T_{1\varrho}^H$
198 ± 1	0.393 ± 0.008	18.2 ± 0.4
$(198\pm2)^c$	$(0.47\pm0.02)^c$	$(17.9\pm0.8)^c$

[a] Curve E in [39]. [b] Curve F in [39]. [c] Curve D in [39].

tings, the CP results published in [39] require reinterpretation. It is now clear that both signal components come from the same carbonatoapatite-like phase. A reasonable hypothesis would be that the stronger fast-relaxing component was from the surface of apatite crystals and the weaker, slow-relaxing component from the crystal interior. The fast-relaxing component is possibly stronger because CP tends to emphasize the crystal surface over its interior and because the bone apatite interior is deficient in hydroxyl protons [20, 24, 27, 28], which could serve as the polarization source. Moreover, this component complies with the **I-S** model and gives a slower CP rate ($1/T_{CP}<1/T_2$, cf. Table 3), because surface species are usually mobile (water mobility, proton exchange, possible HPO_4^{2-} vibrations). Another supporting argument is that according to our observations, the fast-relaxing component gives more pronounced rotational sidebands than the slow-relaxing component. Stronger rotational sidebands are from P-containing species with higher chemical shift anisotropy and these tend to be located at crystal surfaces. This interpretation of the fast-relaxing component is still a hypothesis, which is currently being verified in our laboratory. The slow-relaxing component seems to comply with the **I-I*-S** model and to have a faster CP rate, because the rigidity of the crystal lattice is capable of preserving stronger heteronuclear ^1H-^{31}P couplings. This component has $T_2=0.22$ ms (Table 3), similar to various synthetic apatites [40], but twice as long as that of BRU ($T_2=0.11$ ms [48]). The quantitative assessment of both signal components is very much dependent on various factors controlling CP and on correct performance of the spectrometer hardware.

We have so far discussed centrebands of the ^{31}P CP/MAS signal from bone mineral, but rotational sidebands are also of considerable interest. The ^{31}P MAS sidebands disclose phosphorus sites with substantial chemical shift anisotropy, while CP reveals those located close to protons. In consequence, the CP rota-
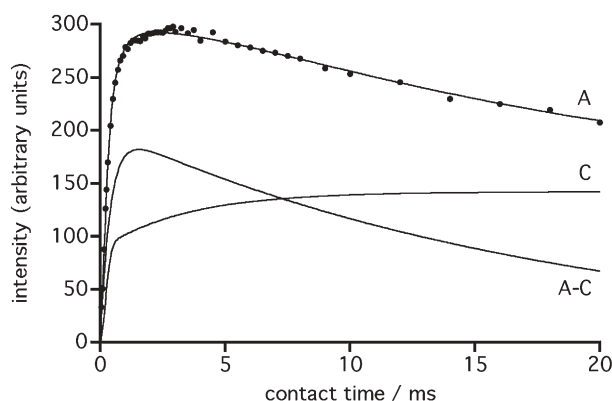
Fig. 13 Deconvolution of the variable-contact time $^1H \rightarrow ^{31}P$ CP curve (A) for human trabecular bone into slow (C) and fast-relaxing (A-C) components. First, data for $\tau=10$ ms (plot C from Fig. 11) were fitted with Eq. (1). In this fitting, a local maximum below 1 ms, left behind by damped oscillations, was neglected. Then, data for $\tau=0$ ms (plot A from Fig. 11) were fitted with a sum of Eqs. (1) and (2), using formerly computed kinetic parameters for the curve C. In this way, kinetic parameters for the curve A-C, expressed by Eq. (2) have been determined

tional sidebands should be particularly sensitive to HPO_4^{2-} ions. Consider that according to Wu et al. [41], a significant fraction of HPO_4^{2-} ions are located on the surfaces of biological apatite crystals. Then, PO_4^{3-} ions located on crystal surfaces tend to reside in disordered environments, because some near neighbours are intrinsically missing [41], and therefore they have larger chemical shift anisotropy. Their ^{31}P spins can cross-polarize from protons of adsorbed water, e.g. via $H\text{-}OH\cdots O\text{-}PO_3^{3-}$ hydrogen bonds. It follows that the surface phosphate sites probably contribute to a larger extent to CP rotational sidebands than to the CP centreband. We conclude that the sidebands of $^1H \rightarrow ^{31}P$ CP peaks must be particularly suitable for monitoring the state of apatite crystal surfaces.

They were studied in our laboratory for BRU, synthetic apatite standards and human cortical bone [20] (Table 4). The CP kinetics at MAS of 1 kHz followed either Eq. (1) or its version modified for MAS. For BRU, the CP kinetic parameters can be readily explained. Thus, one obtains $\lambda=0.5$, as expected for the rigid lattice and for the 1:1 H/P ratio in POH. The CP rate constant T_2 is ca. one order of magnitude smaller than for other samples, indicating very fast initial CP between proximate ^1H and ^{31}P nuclei. The proton spin-diffusion rate $1/T_{df}$ is also considerably higher, because BRU is much richer in protons than the other materials. Interpretation of other results in Table 4 is not straightforward. The T_2 parameters for synthetic apatites and bone are very similar (within the limits of errors), and so are the T_{df} values. This apparently indicates that the sideband CP monitors similar phosphorus sites on crystal surfaces of such different materials as HAh, HAc, CHA-B and B1-B3. Note, that these sites have very different CP kinetic parameters to BRU. Therefore, one has to conclude that BRU-like HPO_4^{2-} ions, i.e. participating in strong hydrogen bonding,

Table 4 Fitted parameters of the $^1H\rightarrow^{31}$ PCP kinetics for the first, high-frequency rotational sidebands (MAS at 1 kHz, 81 MHz for ^{31}P) of phosphate and human cortical bone samples (B1-B3) [20]. HAh and HAc denote hydrated (as-prepared) and calcined HA, respectively. The **I-I*-S** CP model has been used. The sideband amplitudes A_{sb} are in % of the absolute amplitudes A_{cb} of the corresponding centrebands. All the time constants are reported in ms

Sample	A_{sb}	λ	T_2	T_{df}	$T_{1\varrho}^H$
HAh	14.18±0.07	0.115±0.007	0.56±0.03	1.5±0.1	18.3±0.3
HAc	8.98±0.05	0.139±0.009	0.53±0.03	1.9±0.2	ca. 350
BRU	63.5±0.5	0.52±0.01	0.063±0.002	0.39±0.02	3.60±0.04
CHA-B	20.0±0.6	0.09±0.01	0.55±0.06	1.2±0.2	16.0±0.9
B1	20.5±0.2	0.07±0.01	0.45±0.03	1.8±0.3	19.3±0.6
B2	21.5±0.2	0.05±0.01	0.54±0.06	1.5±0.3	20.9±0.8
B3	20.0±0.2	0.05±0.01	0.53±0.05	1.5±0.3	20.7±0.7

do not exist in large amounts on apatite crystal surfaces. This is in accordance with proton NMR spectra of HA and bone apatite recorded under ultra-fast MAS [20] (see below). However, we cannot exclude some HPO_4^{2-} ions involved in weak molecular interactions with various species present on apatite crystal surfaces (adsorbed water and ions). As concerns surface PO_4^{3-} ions, the presence of H-OH$\cdots$O-PO_3^{3-} hydrogen bonds is likely and these bonds can mediate a proton exchange between adsorbed water and those ions. Water is certainly involved because $T_{1\varrho}^H$ is evidently dependent on hydration (cf. HAh and HAc in Table 4). The bone samples exhibit similar proton relaxation rates, although B1 was lyophilised and the others were not. It turns out that lyophilisation mostly removes bulk water, but strongly adsorbed water on crystal surfaces is less affected. The λ value decreases upon hydration from HAc to HAh, which indicates an increase in the H/P ratio within spin clusters involved in CP. The amplitudes A_{sb} are very characteristic of the materials, and probably depend on various factors, including chemical composition of crystal surfaces and their areas. The analysis of Table 4 indicates that CHA-B is most similar to bone mineral of all the reference compounds examined.

Structural function of HPO_4^{2-} ions in bone mineral and their content are of great biological interest. Concentration of these ions decreases as bone apatite matures with age [50, 51]. In order to analyse scarce HPO_4^{2-} ions in the presence of abundant PO_4^{3-} ions, one has to resort to a special CP technique proposed by Zumbulyadis [52] and X. Wu et al. [53], and applied to bone mineral by Y. Wu et al. [37]. The technique is a modified version of conventional CP (Fig. 14a) and is called differential cross-polarisation (DCP). The proton spin-lock is divided into two periods, t_f and t_r. During the first period, polarisation is transferred, as usual, from ^{1}H to ^{31}P. The phase of the ^{1}H spin-lock pulse is then reversed, which forces polarisation to transfer backwards (depolarisation), from ^{31}P to ^{1}H. The DCP experiment is performed with arbitrarily chosen, constant t_f and constant or variable t_r. The variable t_r experiment begins with CP peaks of

maximum intensity, which then decrease over the t_r time, pass through a null and finally become inverted (Fig. 14b). This DCP spectra set looks like that from the standard inversion recovery technique, but performed the other way round and based rather on the CP rate than on the spin-lattice relaxation rate. Consequently, the technique allows the determination of the T_{CP} constants. For example, the T_{CP} values for PO_4^{3-} in HA and OCP are both 560 µs, while for HPO_4^{2-} in BRU and OCP are 140 and 250 µs, respectively (162 MHz for ^{31}P, MAS at 5 kHz) [37]. It turns out that protonated and non-protonated species have markedly different CP rates and this difference can be exploited in the DCP experiments. Thus, the HPO_4^{2-} and PO_4^{3-} ions contribute to the same ^{31}P CP peak from bone mineral, but have different polarization rates. For the former, depolarisation is faster and for the latter slower, because of larger and smaller dipolar ^{1}H-^{31}P coupling, respectively. The depolarisation time t_r can be specifically selected in order to suppress the dominant PO_4^{3-} signal and expose the HPO_4^{2-} peak (Fig. 15). This technique was tested on model synthetic calcium phosphates and applied to the study of animal bone (chicken, bovine and rabbit) [37]. The HPO_4^{2-} rotational sideband pattern was correctly visualised by DCP and analysed according to the procedure of Herzfeld and Berger [54]. The ^{31}P chemical shift tensor was determined. The isotropic chemical shift of HPO_4^{2-} in bone mineral was found to be the same as in OCP (σ_i=−0.1 ppm corrected
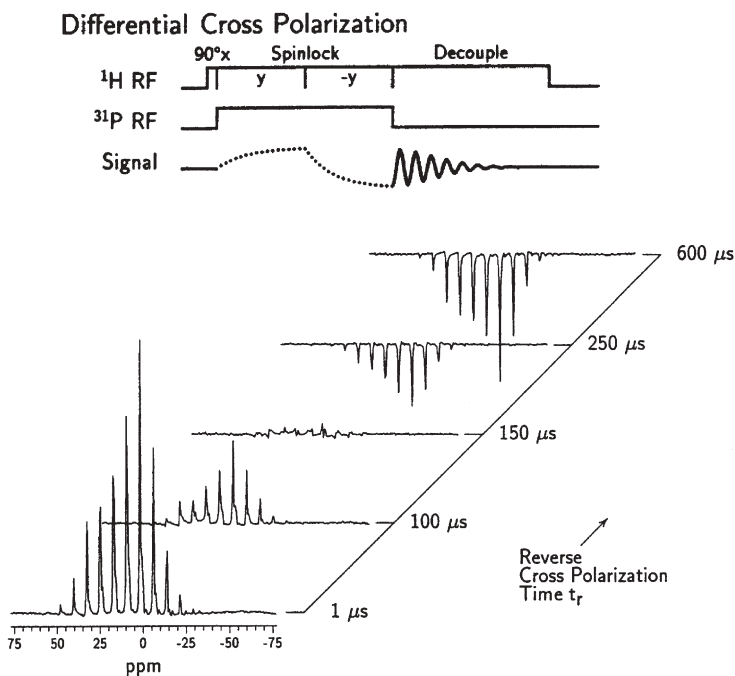
Fig. 14 The pulse sequence of the DCP experiment (*top*) and the variable t_r spectrum set (*bottom*) for BRU (162 MHz for ^{31}P, MAS at 5 kHz) (adapted from [37])

A: $t_r = 1$ μs   B: $t_r = 315$ μs   C: $t_r = 500$ μs
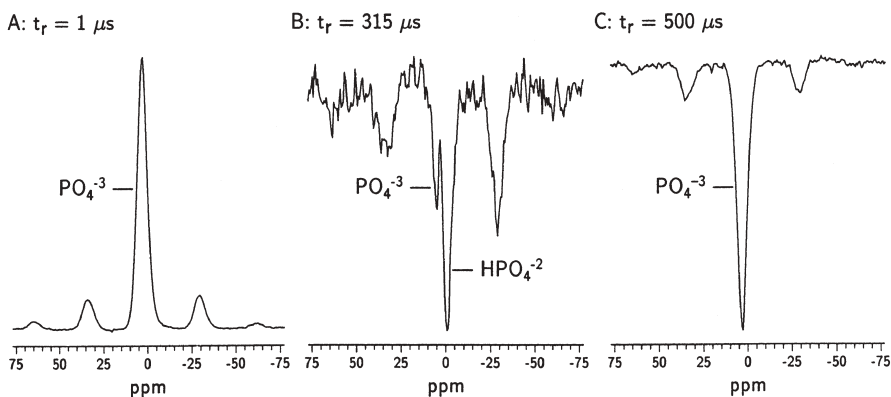
Fig. 15A–C ^{31}P DCP spectra of bone from 19-day-old chick embryo for tf=300 µs [37]: **A** t_r=1 µs. **B** t_r=315 µs. **C** t_r=500 µs. The spectrum A is essentially that of a conventional CP experiment, only the apatitic resonance is apparent. In spectrum B, the PO_4^{3-} peak is nearly nulled, and the HPO_4^{2-} spectrum centreband and sidebands are revealed. In spectrum C, the apatitic resonance is well past null, and again obscures the HPO_4^{2-} peak

value according to [43]), while the chemical shift anisotropy was close to that of BRU (Δ=116 ppm). It was concluded that "the intimate structure of the acid phosphate group in bone mineral is unique, and that none of the common synthetic calcium phosphates accounts well for all the observed solid state phosphorus-31 NMR properties of bone mineral" [37].

Conventional CP [55] and DCP [43] were then applied to the study of the mineralization process in bone. The results support the hypothesis that phosphoproteins complexed with calcium play a significant role in the initiation of bone calcification. Wu et al. [43] introduced a new parameter $\iota = \sigma_i - \sigma_{22}$, the sideband pattern index, which is related to the skew of the chemical shift tensor. The parameter ι was found to be very useful for interpreting chemical shift tensors in biological calcium phosphates. It is generally positive if the peak intensity of the first low-frequency sideband is greater than that of the first high-frequency sideband (Fig. 16). It has been noticed that the parameter ι for a phosphate group coordinating Ca^{2+} is positive, and that it is negative if Ca^{2+} is not involved (Fig. 16). The analysis has been aided by results from mean ^{31}P chemical shift anisotropy, which evidently decreases with tissue age or maturity (Fig. 17).

Finally, it is necessary to mention ^{1}H$\rightarrow^{31}$P CP between the dipolar and Zeeman reservoirs, which is performed via adiabatic demagnetisation in the rotating frame (ADRF) [56]. Distinctive, sample dependent, transient oscillations of the CP signal were observed. The technique was applied to detect HPO_4^{2-} ions in bone and tailored for in vivo ^{31}P MRI studies. It was possible to discern narrow and broad signal components for porcine bone from proton-devoid and proton-containing regions. The ADRF method was then coupled with DCP [57].
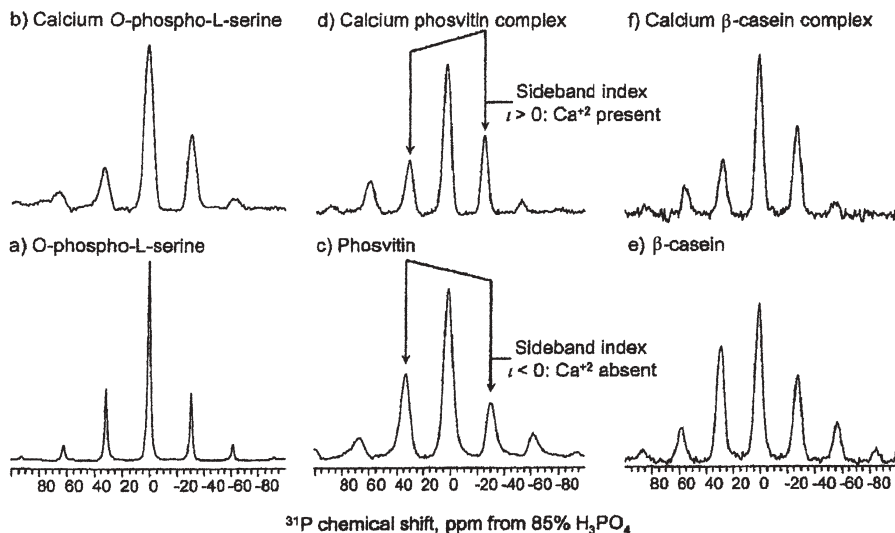
Fig. 16a–f Conventional ^{31}P CP/MAS NMR spectra of various species related to the early stages of mineralization (162 MHz for ^{31}P, MAS at 4.5–5 kHz) [43]. The spectra show that the sign of the sideband pattern index is indicative of the Ca^{2+} complexation
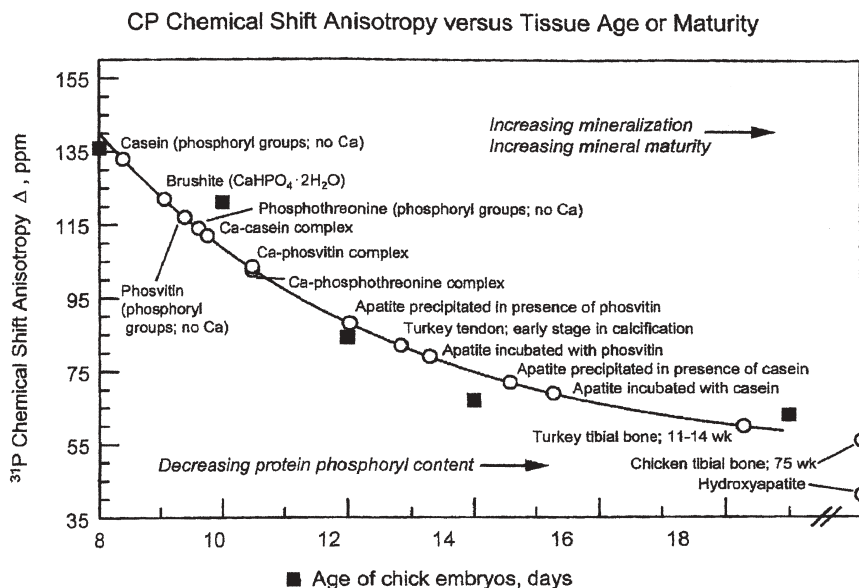
Fig. 17 ^{31}P chemical shift anisotropy Δ derived from Herzfeld-Berger analysis as a function of age of five chick embryo specimens (*filled square symbols*) [43]. There is a clear progression of Δ from large values at the early stages (initially arising from almost pure phosphoprotein) to mature mineralization (finally producing almost pure apatite). *Open circles* are located where the various model compounds, turkey tendon and bone, and adult chicken bone would fall based on their observed Δ values, following a similar progression of mineralization

4
1D Proton and 2D ^{1}H-^{31}P HETCOR NMR

The first useful proton MAS NMR spectra of mineral bone standards and dental enamel were recorded by Yesinowski and Eckert [18]. Enamel is often studied because it is thought to resemble bone mineral in structure and does not contain an organic matrix, where strong peaks obscure those of apatite. Generally, from whole bone, both inorganic and organic proton signals are expected, and this poses spectral resolution problems. Even ^{1}H CRAMPS yielded broad overlapped peaks (Fig. 18) [38]. The main collagen peak appeared at 1.3 ppm and a massive interfering water resonance at 4–6 ppm. In the collagen and bone spectra, an unassigned broad component at 7 ppm was observed. Only in the bone sample with chemically removed organics was it possible to detect a small peak at 0.2 ppm from structural hydroxyl groups of apatite. That sample had a relatively large water content, as evidenced by a huge water signal attributed to "a partially wet sample". Evidently, chemical treatment was not a remedy for interfering water and organic resonances. Moreover, it could seriously modify the bone mineral [38]. Conventional proton MAS spectra of bone, reported later by Cho et al. [28], also suffer from poor resolution caused by the overwhelming water band.

Fractional water content in bone for a single specimen varies with age, sex and progress of bone disease [58]. Water can be associated with bone mineral, organic matrix or can be free (bulk water). Bulk water fills pores in the calcified matrix. For the sake of clarity and classification purposes, consider types of water molecules in bone apatite and related materials. Santos et al. [38] made a distinction between structural (inclusion) and non-structural (adsorbed) H_2O molecules. The former participated in ^{1}H$\rightarrow^{31}$P CP and the latter did not. Funduk et al. [59] performed wide-line ^{1}H NMR studies of human enamel. They found solid-like interstitial and semiliquid-like water, characterized by a proton spin-lattice relaxation time T_2^H of 14 and 240 µs, respectively. In the same experimental conditions, the structural hydroxyl groups of enamel had $T_2^H =$ 61 µs. Both types of H_2O molecules could neither be extracted in vacuum nor exchanged upon deuteration. It was suggested that the semiliquid-like water was confined in closed pores of the enamel structure. Elliot [17b] cited several studies, which postulated lattice water located in the structural OH$^-$ positions. Greenfield et al. [60] considered H_2O molecules trapped inside lattice defects. Yesinowski and Eckert [18] assigned the proton MAS NMR peak at 5.6 ppm to surface-adsorbed water. The assignment was confirmed by the observation that the intensity of this peak decreased upon exchange with D_2O in the vapour phase. Structural water was discussed for BRU and OCP, not HA [18]. The first monolayer of surface adsorbed water on HA has a differential heat of adsorption of 23 kcal mol^{-1} [61]. This is a rather high energy for intermolecular interactions, considering that it is ca. four times larger than the energy of the hydrogen bond in liquid water. It follows that the first monolayer on HA is composed of strongly adsorbed H_2O molecules. For coverages above two
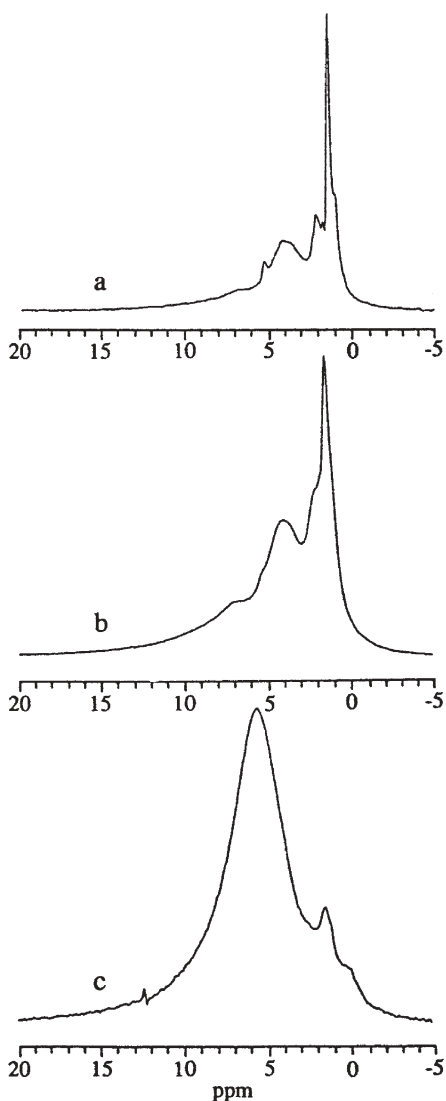
Fig. 18a–c ^{1}H CRAMPS NMR spectra of bone (200 MHz spectrometer): **a** bovine collagen; **b** animal bone standard H5 (provenance, preparation and storage conditions unstated); **c** hypochlorite-bleached animal bone (organic matrix removed from H5) [38]

monolayers there exists a liquid-like water [61]. Overall, in bone mineral one can find structural water (H_2O-for-OH^- and H_2O in lattice defects) and surface-adsorbed water (liquid-like and strongly adsorbed).

The resolution of conventional proton MAS spectra presented by Kaflak-Hachulska et al. [20] is much better than those discussed earlier (Figs. 19 and 20). For MAS at 40 kHz rotational sidebands are missing. Ultra-high speed MAS

was used to "spin out" ¹H-¹H dipolar couplings and proton CSA of less mobile H_2O and collagen molecules (¹H CSA for rigid water is ca. 20 ppm [18]). Furthermore, the bone samples were lyophilised prior to the measurements. The spectrum of human trabecular bone is very similar to that of bovine collagen type I, except that a water peak at 5.0 ppm is smaller and a minor unassigned peak appears at 2.8 ppm. For the apatites (Fig. 20), the peaks at ca. 5 and 0 ppm are from water and structural hydroxyl groups, respectively. Over heating HA loses water, so its peak decreases from HAh to HAc and moves to a lower frequency by 0.5 ppm. This shift indicates that the residual, strongly adsorbed, surface water in HAc is probably less hydrogen-bonded (forms smaller multimers or agregates) than dominant liquid-like surface-adsorbed water in HAh. The chemical shift of 3.5 ppm in CHA-B is typical of the P-OH groups on the crystal surface [62]. Assignment of the peaks ca. 1 ppm is not clear, but they can come from the structural water [20, 40].

Considering that phosphates in bone are over twice as abundant by weight than organic substances, one would expect a significant contribution from their resonances to the proton spectrum of mature human bone (Fig. 19). The organic peaks completely obscure the spectral region from ca. 1 to 6 ppm, but beyond this range any sharp inorganic peak must be clearly visible. However, there is no peak at 10.4 ppm expected from BRU-like HPO_4^{2-} anions involved in strong hydrogen bonding. Furthermore, the DCP method [37] has failed to detect such ions. Perhaps mature human bone is devoid of such ions or their concentration is too small for ¹H MAS NMR detection. However, more mobile and less hydrogen-bonded HPO_4^{2-} anions than those in BRU are not excluded, be-
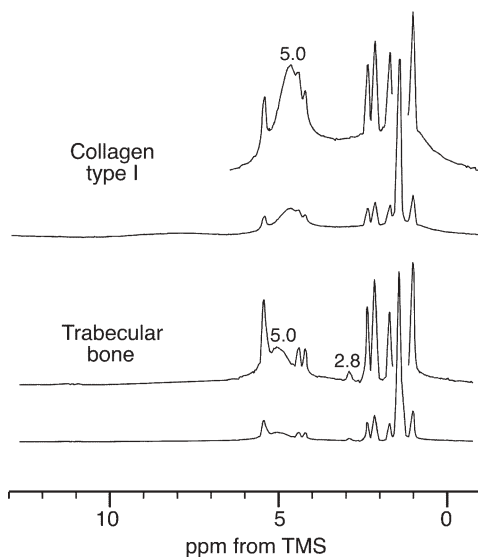
Fig. 19 ¹H NMR spectra of collagen and lyophilised human trabecular bone recorded with MAS at 40 kHz (833 MHz spectrometer) [20]

cause they would give proton signals in the spectral region covered by the organic matrix.

Another interesting result is that no proton peak was noticed at ca. 0 ppm originating from structural hydroxyl groups in bone mineral (Fig. 19). This indicates that either that bone sample was deficient in such groups [28] or they were beyond detection under ultra-high speed MAS. The observation of the structural hydroxyl groups could be hampered by structural disorder of the apatite crystal lattice or by substantial molecular motion, proton or spin exchange with correlation times on the order of the spinning rate. Cho et al. [28] insisted that an OH⁻ content equal to 21% of the HA stoichiometric value cannot produce a resolvable ^{1}H MAS NMR peak in 1D spectroscopy. Thus, considering only the feeble look of the proton 0 ppm peak from CHA-B (Fig. 20), one would expect this apatite to be a better model of bone mineral than HAc and HAh. The OH⁻ deficiency in bone mineral can affect proton NMR coherence within the –O-H O-H O-H O-H– chains, so the studies on multiple-quantum dynamics look very promising in this respect [63].

In order to remove unwanted organic peaks in the proton spectra, one has to resort to 2D ^{1}H-^{31}P heteronuclear correlation spectroscopy (HETCOR). When performed via ^{1}H→^{31}P CP, HETCOR "sees" only protons capable of providing polarization to ^{31}P spins (Figs. 21–23). It follows that these protons must
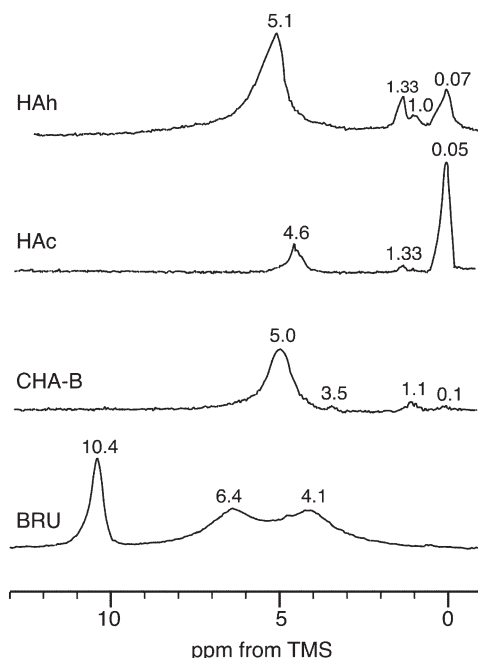
Fig. 20 ^{1}H NMR spectra of various mineral standards recorded with MAS at 40 kHz (833 MHz spectrometer) [20]. HAh and HAc denote hydrated (as-prepared) and calcined HA, respectively. CHA-B contained 9 wt% of CO_3^{2-}
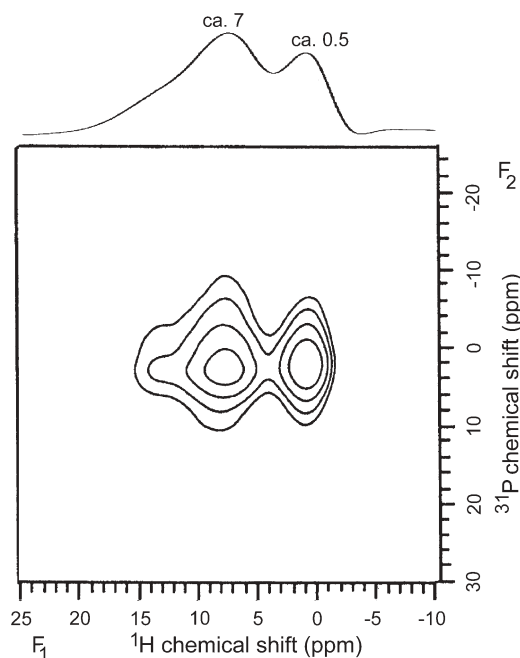
Fig. 21 The ^{1}H-^{31}P HETCOR spectrum of the animal bone standard H5 with the ^{1}H projection *at the top* (adapted from [38])

reside in bone apatite. The ^{1}H projections or cross-sections provide us with 1D proton spectra without the organic peaks. The spectra shown in Figs. 21–23 were acquired with different pulse sequences from differently prepared samples of different species, so they show different intensities of the water signal. However, it is clear that all the spectra reveal the 0 ppm peaks from the structural hydroxyl groups. On the basis of their intensities, it was concluded that bone mineral is substantially deficient in structural hydroxyl groups compared to stoichiometric HA [20, 28]. Cho et al. [28] attempted to measure the percentage of structural hydroxyl groups and quoted an approximate value of 21±1% of the stoichiometric content. This work ought to be honoured as the first NMR quantitation effort in this respect. The reported estimation was based on the "excellent fit (correlation coefficient=0.99) to a two parameter exponential" [28], which was performed for *three experimental points*. Nevertheless, the work [28] presents very interesting results on the contribution of water to the CP process. It shows, on a set of HETCOR projections recorded under the same conditions as a function of time in the spectrometer, that water capable of slow evaporation from bone, presumably liquid-like surface-adsorbed water, takes part in CP. Then, the much smaller water peak (Fig. 23b), presumably from more strongly adsorbed water, increases up to the contact time of ca. 3 ms and after that decays due to proton relaxation. Both observations indicate (al-
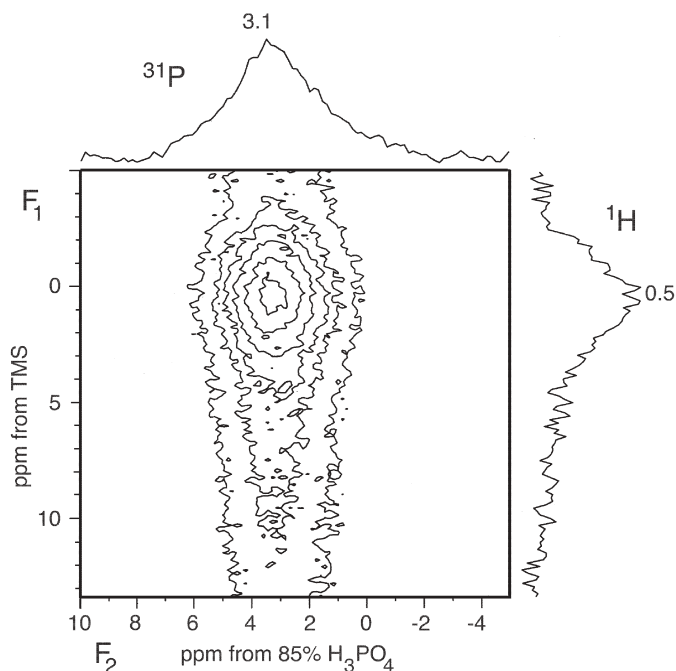
Fig. 22 The ^{1}H-^{31}P HETCOR spectrum of lyophilised human cortical bone with the ^{1}H cross-sections through the top of the peak [20]

though it has not been commented upon in these terms [28]) that polarization is transferred somehow from loosely- to tightly-bound surface water (possibly via proton exchange or spin diffusion) and that CP from the tightly-bound surface water participates in CP together with the structural hydroxyl groups. This is possibly the reason for the two components of the CP kinetics discussed in the paragraph above.

5
Carbon-13 NMR

Solid-state ^{13}C MAS NMR has been used only to study various synthetic carbonatoapatites and dental enamel [23] (Fig. 24). Chemical shifts for CO_3^{2-} in various apatite locations were determined and response of the peaks to dipolar suppression and heating was investigated. For CP, a long contact time of 10 ms was required. For BD, a recycle delay of 60 s was used. In Fig. 24, spectra A and B were recorded with and without CP. CHA-A gives a relatively sharp peak and does not cross-polarize, because CO_3^{2-} replaces OH^-, depleting the main proton source for the polarization. The spectra C and D were not adequately described in [23], so it is not sure whether BD or CP was applied. It is
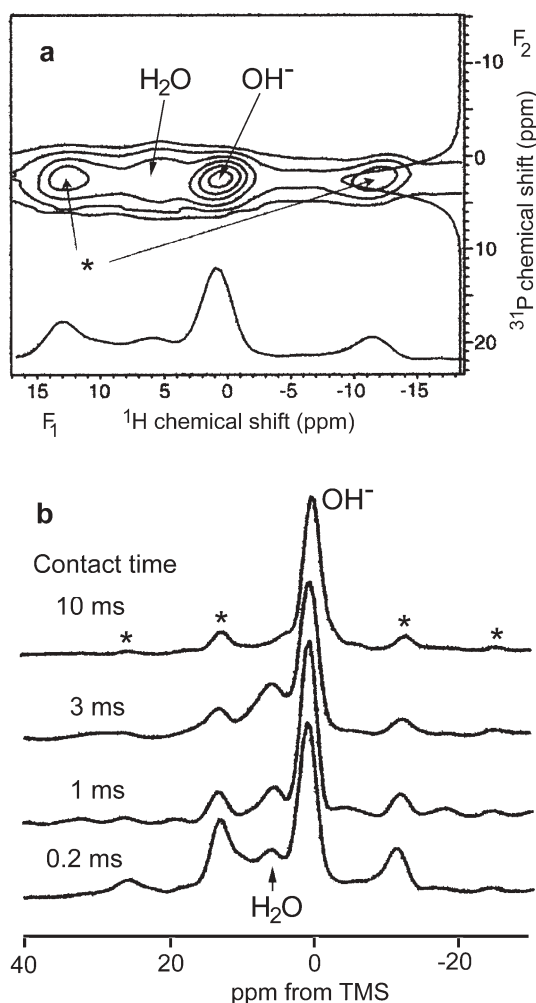
Fig. 23a, b ^{1}H-^{31}P HETCOR NMR of bovine cortical bone (adapted from [28]): **a** a 2D spectrum recorded with CT=0.2 ms; **b** [1]H projections of the 2D spectra for various contact times

more probable that the latter technique was used, since later in the text the DD experiments on CHA-B and CHA-AB are discussed. The CHA-B signal has a long low-frequency tail and consists of two overlapping components, which behave differently on heating. The CHA-AB spectrum contains peaks from CHA-A and CHA-B, while the assignment of the 168.2 ppm peak is not clear. This central peak comes from CO_3^{2-} located close to protons but, curiously, the species bearing those protons appeared resistant to heating.

Beshah et al. [23] also showed an enamel CP spectrum, in which a large CHA-B peak and a small CHA-A peak can be easily discerned. The CO_3^{2-} ions
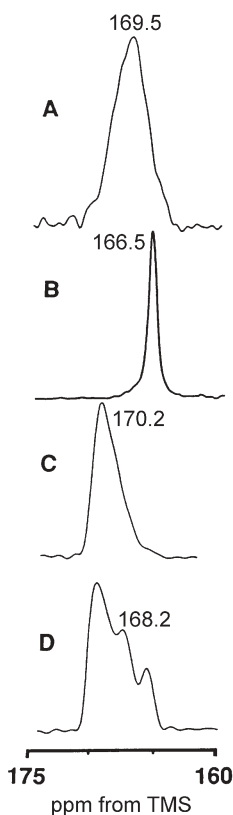
Fig. 24A–D ^{13}C MAS NMR spectra of synthetic carbonato apatites (79.9 MHz for ^{13}C, MAS at 2.0–3.4 kHz) [23]: **A** amorphous CHA; **B** CHA-A; **C** CHA-B; **D** type CHA-AB (mixed)

are very important constituents of bone mineral. The CO_3^{2-} substitution reduces crystallinity and increases the extent of dissolution of apatites [19]. Unsuccessfully, in the ^{13}C MAS spectra of bone [64] the peaks from the CO_3^{2-} ions are completely obscured by strong carbonyl resonances from the organic matrix. The spectra of bone and collagen are very similar (Fig. 25) [64] and can be assigned according to [65]. To the author's knowledge, the ^{13}C CP/MAS spectrum of bone has been presented for the first time in this review.

6
Summary and Prospects

Up to now, solid-state NMR has been almost exclusively applied to the study of bone mineral. It was confirmed that the structure of bone mineral resembles that of CHA-B. Bone apatite was found deficient in structural hydroxyl groups.
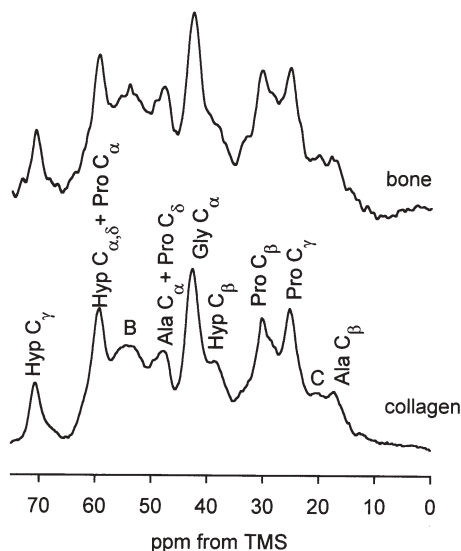
Fig. 25 ^{13}C NMR spectra of human cortical bone and collagen type I (100 MHz for ^{13}C, MAS at 7.5 kHz, CT=1.6 ms). The carbonyl region has been omitted. For assignment [65] consult Fig. 5. Peaks B and C are from minor aminoacid residues

Much work has been devoted to detection and location of HPO_4^{2-} ions. A number of problems concerning bone mineral still remain to be solved by solid-state NMR. They include reliable OH^-, CO_3^{2-} and HPO_4^{2-} counting under interference from the organic matrix, together with detection and characterization of minor ionic constituents such as Na^+, Mg^{2+}, F^-, Cl^- etc. Concentration and distribution of all those ions and water in apatite crystals (interior vs surface and crystal defects vs structural positions) as well as pertinent molecular interactions should be accurately investigated. The reason is that they affect such important material properties of bone apatite as crystal habit and size, total crystal surface area and surface adsorption, crystal lattice parameters and density, stability (internal strains), solubility and interfacial properties, mechanical performance (hardness and flexural strength), nucleation and crystal growth under physiological conditions (biomineralisation) and so on. Therefore, in order to establish characterization and diagnostic procedures for bone mineral using solid-state NMR, healthy and diseased mammalian and other animal tissue should be examined as a function of age and varying extent of pathological transformations. Various sample preparations have to be explored and their effect on NMR parameters investigated. More work on variable-contact time CP (ADRF-CP), variable-depolarisation time DCP and HETCOR is necessary, maybe coupled with selective proton irradiation and multiple-quantum approach, performed at various temperatures and MAS rates. Nuclear relaxation as a function of magnetic field and temperature can be employed. ^{13}C NMR requires special attention, because it provides access to information on

the organic matrix. Quadrupolar nuclei like ^{23}Na and ^{17}O should also be considered. Certainly, the ^{43}Ca resonance at natural nuclear abundance would be of the greatest interest and could become feasible with the progress in NMR hardware.

References

1. Man S (2002) Biomineralization. Oxford University Press, Oxford
2. Currey J (2002) Bones: structure and mechanics. Princeton University Press, Princeton
3. Bilezikian JP, Raisz LG, Rodan GA (2001) Principles of bone biology, 2nd edn. Academic Press, New York
4. LeGeros RZ (1981) Apatites in biological systems. Prog Crystal Growth Charact 4:1–45
5. Andrew ER (1971) The narrowing of NMR spectra of solids by high-speed specimen rotation and the resolution of chemical shift and spin multiplet structures of solids. Prog NMR Spectrosc 8:1–39
6. Maricq MM, Waugh JS (1979) NMR in rotating solids. J Chem Phys 70:3300–3316
7. Pines A, Gibby MG, Waugh JS (1973) Proton-enhanced NMR of dilute spins in solids. J Chem Phys 59:569–590
8. Mehring M (1983) Principles of high resolution NMR in solids. Springer, Berlin Heidelberg New York
9. Fyfe CA (1983) Solid state NMR for chemists. CFC Press, Guelph
10. Stejskal EO, Memory JD (1994) High resolution NMR in the solid state. Fundamentals of CP/MAS. Oxford University Press, Oxford
11. Samoson A (2002) Extended magic-angle spinning. In: Grant DM, Harris RK (eds) Encyclopedia of nuclear magnetic resonance, vol 9. Advances in NMR. Wiley, New York, pp 59–64
12. Kolodziejski W, Klinowski J (2002) Kinetics of cross-polarization in solid-state NMR. A guide for chemists. Chem Rev 102:613–628
13. MacKenzie KJD, Smith ME (2002) Multinuclear solid-state NMR of inorganic materials. Pergamon, Amsterdam
14. Duer MJ (ed) Solid-state NMR spectroscopy. Principles and applications. Blackwell Science, Oxford
15. DeJong WF (1926) La substance minerale dans les os. Res Trav Chim 45:445–448
16. Sudarsanan K, Young RA (1969) Significant precision in crystal structural details: Holly Springs hydroxyapatite. Acta Crystallogr B 25:1534–1543
17. a Elliott JC (1994) Studies in inorganic chemistry 18. Structure and chemistry of the apatites and other calcium orthophosphates. Elsevier, Amsterdam, pp 112–117; b pp 149–152
18. Yesinowski JP, Eckert H (1987) Hydrogen environments in calcium phosphates: ^{1}H MAS NMR at high spinning speeds. J Am Chem Soc 109:6274–6282
19. LeGeros RZ (1994) Biological and synthetic apatites. In: Brown PW, Constanz B (eds) Hydroxyapatite and related materials. CRC Press, Boca Raton, pp 3–28
20. Kaflak-Hachulska A, Samoson A, Kolodziejski W (2003) ^{1}H MAS and ^{1}H→^{31}P CP/MAS NMR study of human bone mineral. Calcif Tissue Int 73:476–486

21. Legros R, Balmain N, Bonel G (1986) Structure and composition of the mineral phase of periosteal bone. J Chem Res (S):8–9
22. Aoki H (1991) Science and medical applications of hydroxyapatite. Takayama Press, Tokyo
23. Beshah K, Rey C, Glimcher MJ, Schimizu M, Griffin RG (1990) Solid state carbon-13 and proton NMR studies of carbonate-containing calcium phosphates and enamel. J Solid State Chem 84:71–81
24. Rey C, Miquel JL, Facchini L, Legrand AP, Glimcher MJ (1995) Hydroxyl groups in bone mineral. Bone 16:583–586
25. Kaflak-Hachulska A, Zlotkowska A, Kolodziejski W (1999) Infrared study of hydroxylic groups in human bone and bone components. In: Materials of Vth International Conference on Molecular Spectroscopy from Molecules to Molecular Biological Systems and Molecular Materials: Role of Molecular Interactions and Recognition. Wroclaw-Ladek Zdrój, Poland
26. Kolodziejski W, Kaflak-Hachulska A (1999) Proton MAS NMR studies of human bone and bone components. In: Materials of the Alpine Conference on Solid-State NMR. Chamonix – Mont Blanc, France
27. Loong C-K, Rey C, Kuhn LT, Combes C, Wu Y, Chen S-H, Glimcher MJ (2000) Evidence of hydroxyl-ion deficiency in bone apatites: an inelastic neutron-scattering study. Bone 26:599–602
28. Cho G, Wu Y, Ackerman JL (2003) Detection of hydroxyl ions in bone mineral by solid-state NMR spectroscopy. Science 300(5622):1123–1127
29. Kaflak-Hachulska A, Chmielewski D, Górecki A, Kolodziejski W (2001) Phosphorus-31 CP/NMR study of bone mineral. In: Materials of the 2nd Alpine Conference on Solid-State NMR. Chamonix – Mont Blanc, France
30. Curry NA, Jones DW (1971) Crystal structure of brushite, calcium hydrogen orthophosphate dihydrate: a neutron-diffraction investigation. J Chem Soc A Inorg Phys Theor 3725–3729
31. Rothwell WP, Waugh JS, Yesinowski JP (1980) High-resolution variable temperature ^{31}P NMR of solid calcium phosphates. J Am Chem Soc 102:2637–2643
32. Ramachandran GN (ed) (1967) Treatise on collagen. Academic Press, New York
33. Traub W, Piez KA (1971) Adv Protein Chem 25:243–352
34. Nimni ME (ed) (1988) Collagen. CRC Press, Boca Raton
35. Roufosse AH, Aue WP, Roberts JE, Glimcher MJ, Grffin RG (1984) Investigation of the mineral phases of bone by solid-state phosphorus-31 magic angle sample spinning nuclear magnetic resonance. Biochemistry 23:6115–6120
36. Dawson KL, Farnan IE, Constantz BR, Young SW (1991) Solid-state phosphorus-31 nuclear magnetic resonance differentiation of bone mineral and synthetic apatite used to fill bone defects. Inv Radiol 26:946–950
37. Wu Y, Glimcher MJ, Rey C, Ackerman JL (1994) A unique protonated phosphate group in bone mineral not present in synthetic calcium phosphates. J Mol Biol 244:423–435
38. Santos AR, Wind RA, Bronnimann CE (1994) ^{1}H CRAMPS and [1]H-[31]P HetCor experiments on bone, bone mineral, and model calcium phosphate phases. J Magn Reson B 105:183–187
39. Kaflak A, Chmielewski D, Górecki A, Kolodziejski W (1998) Kinetics of [1]H→[31]P cross-polarization in human trabecular bone. Solid State NMR 10:191–196
40. Kaflak-Hachulska A (2000) The study of bone mineral using nuclear magnetic resonance spectroscopy with cross-polarization. PhD thesis. Medical University of Warsaw
41. Wu Y, Ackerman JL, Kim H-M, Rey C, Barroug A, Glimcher MJ (2002) Nuclear magnetic resonance spin-spin relaxation of the crystals of bone, dental enamel and synthetic hydroxyapatites. J Bone Miner Res 17:472–480

42. Aue WP, Roufosse AH, Glimcher MJ, Griffin RG (1984) Solid-state phosphorus-31 nuclear magnetic resonance studies of synthetic solid phases of calcium phosphate: potential models of bone mineral. Biochemistry 23:6110–6114

43. Wu Y, Ackerman JL, Strawich ES, Rey C, Kim H-M, Glimcher MJ (2003) Phosphate ions in bone: Identification of a calcium-organic phosphate complex by[31]P solid-state NMR spectroscopy at early stages of mineralization. Calcif Tissue Int 72:610–626

44. Arsenault AL, Grynpas MD (1988) Crystals in calcified epiphyseal cartilage and cortical bone of the rat. Calcif Tissue Int 43:219–225 and references therein

45. Arends J, Christoffersen J, Christoffersen MR, Eckert H, Fowler BO, Heughebaert JC, Nancollas GH, Yesinowski JP, Zawacki SJ (1987) A calcium hydroxyapatite precipitated from an aqueous solution. J Cryst Growth 84:515–532

46. van Vleck JH (1948) The dipolar broadening of magnetic resonance lines in crystals. Phys Rev 74:1168–1183

47. Abragam A (1961) The principles of nuclear magnetism. Oxford University Press, Oxford, pp 97–132

48. Kaflak-Hachulska A, Slósarczyk A, Kolodziejski W (2000) Kinetics of NMR cross-polarization from protons to phosphorus-31 in natural brushite. Solid State NMR 15:237–238

49. Kolodziejski W, Kaflak-Hachulska A (2001) Kinetics of the[1]H to ^{31}P NMR cross-polarization in minerals. In: Materials of the ISMAR 2001 Conference, Rhodes, Greece

50. Rey C, Shimizu M, Collins B, Glimcher MJ (1990) Resolution-enhanced Fourier transform infrared spectroscopy study of the environment of phosphate ion in the early deposits of a solid phase of calcium phosphate in bone and enamel and their evolution with age. I. Investigations in the v_4-PO_4^{3-} domain. Calcif Tissue Int 46:384–394

51. Rey C, Shimizu M, Collins B, Glimcher MJ (1991) Resolution-enhanced Fourier transform infrared spectroscopy study of the environment of phosphate ion in the early deposits of a solid phase of calcium phosphate in bone and enamel and their evolution with age. II. Investigations in the v_3-PO_4^{3-} domain. Calcif Tissue Int 49:383–388

52. Zumbulyadis N (1987) ^{1}H/[29]Si cross-polarization dynamics in amorphous hydrogenated silicon. J Chem Phys 86:1162–1166

53. Wu X, Zhang S, Wu X (1988) Selective polarization transfer in solid state high-resolution CP MAS NMR. J Magn Reson 77:343–347

54. Herzfeld J, Berger SE (1980) Sideband intensities in NMR spectra of sample spinning at the magic angle. J Chem Phys 73:6021–6030

55. Wu LNY, Genge BR, Dunkelberger DG, LeGeros RZ, Concannon B, Wuthier RE (1997) Physicochemical characterization of the nucleational core of matrix vesicles. J Biol Chem 272:4404–4411

56. Ramanathan C, Wu Y, Pfleiderer B, Lizak MJ, Garrido L, Ackerman JL (1996) ADRF-CP surface-coil spectroscopy of synthetic calcium phosphates and bone mineral. J Magn Reson A 121:127–138

57. Ramanathan C, Ackerman JL (1997) ADRF differential cross polarization spectroscopy of synthetic calcium phosphates and bone mineral. J Magn Reson 127:26–35

58. Timmins PA, Wall JC (1977) Bone water. Calcif Tissue Res 23:1–5

59. Funduk N, Kydon DW, Schreiner LJ, Peemoeller H, Miljkovic L, Pintar MM (1984) Composition and relaxation of the proton magnetization of human enamel and its contribution to the tooth NMR image. Magn Reson Med 1:66–75

60. Greenfield DJ, Termine JD, Eanes ED (1974) A chemical study of apatites prepared by hydrolysis of amorphous calcium phosphate in carbonate containing solutions. Calcif Tissue Res 14:131–138

61. Dry ME, Beebe RA (1960) J Phys Chem 64:1300–1304

62. Kolodziejski W, Rocha J, He H, Klinowski J (1991) High resolution solid state ^{1}H nuclear magnetic resonance spectra of organic template in hydrated aluminophosphate VPI-5. Appl Catal 77:L1–L8

63. Cho G, Yesinowski JP (1993) Multiple-quantum NMR dynamics in the quasi-one-dimensional distribution of protons in hydroxyapatite. Chem Phys Lett 205:1–5

64. Kaflak A, Kolmas J, Kolodziejski W (to be published)

65. Saito H, Yokoi M (1992) A ^{13}C NMR Study of collagens in the solid state: hydration/dehydration-induced conformational change of collagen and detection of internal motions. J Biochem 111:376–382

Natural Abundance ^{15}N and ^{13}C CP/MAS NMR of Dialkyldithiocarbamate Compounds with Ni(II) and Zn(II)

Alexander V. Ivanov [1] · Oleg N. Antzutkin [2] (✉)

[1] Far Eastern Branch of the Russian Academy of Sciences, Amur Integrated Research Institute, 675000 Blagoveschensk, Amur Region, Russia
alexander.v.ivanov@chemist.com

[2] Luleå University of Technology, Division of Chemistry, 97187 Luleå, Sweden
Oleg.Antzutkin@ltu.se

Abstract Different symmetrically substituted and cyclic dialkydithiocarbamate (R=CH$_3$, C$_2$H$_5$, C$_3$H$_7$, *i*-C$_3$H$_7$, C$_4$H$_9$, *i*-C$_4$H$_9$ and R$_2$=(CH$_2$)$_5$, (CH$_2$)$_6$, (CH$_2$)$_4$O) compounds, such as tetraalkylthiuram disulfides, mononuclear nickel(II), binuclear zinc(II) and heteropolynuclear complexes and their adducts (both non-solvated and solvated forms) with planar and non-planar N-donor organic bases, have been prepared and studied by means of natural abundance ^{13}C and ^{15}N CP/MAS NMR spectroscopy. Useful correlations between molecular structures and ^{13}C and ^{15}N chemical shifts in these compounds have been established and assignments to carbon and nitrogen sites in resolved molecular structures have been suggested. A combination of the mesomeric effect of dithiocarbamate groups and the (+)inductive effect of alkyl substituents at the nitrogen atoms has been discussed in interpretations of ^{13}C and ^{15}N chemical shifts of the studied compounds. A high sensitivity of ^{15}N chemical shift to the subtle structural differences of both dithiocarbamate groups and N-

donor molecules has been revealed. Several remarkable cases of conformational isomerism have been recognized for both dithiocarbamate complexes and their adducts.

1
Introduction

1.1
General Introduction

In 2002 NMR again, for the third time since its discovery, won the Nobel prize, and for a second time in chemistry, for achievements in structural biology. Multi-dimensional liquid state NMR, as a tool for elucidating the 3D structure of proteins, enzyme-coenzyme complexes, DNA and RNA fragments, and other bio-molecules, has reached its apogee, and this event has been faithfully recognized by the whole scientific community. It is almost generally accepted that the development and success of solid-state NMR is at least ten years behind that of NMR in liquids. We draw this conclusion from our personal impressions from discussions with colleagues during NMR conferences. This delayed development may be caused by the range of anisotropic interactions in the solid state, which broaden NMR lines, rendering the separation of interactions and analysis of data more difficult than for the liquid state, where all anisotropies are naturally averaged out by the fast tumbling and rotation of molecules facilitating high resolution in liquid state NMR. However, despite these inherent difficulties, solid state NMR is an 'explosively' developing area, thanks to the great need for studies of solid matter and materials, ranging from cement to ceramics, glass and oxides, from capacitor foils, polymers and composites to biopolymers, such as amyloid fibrils, prion deposits and plaques causing such diseases as diabetes, Alzheimer's disease and 'mad-cow' disease [1]. Particularly in the latter cases, other methods of structural study, such as single-crystal neutron and X-ray diffraction, fail because of the amorphous nature of the material. Indeed, solid-state NMR can do what was almost thought to be impossible, by measuring inter-spin distances and torsion angles with high precision, or defining other structural constraints in these amorphous or polycrystalline materials [2]. The field of solid-state NMR is currently also expanding towards studies of adsorption of both inorganic and organic molecules and metal ions on mineral surfaces from liquid solutions. Here, both solid and liquid state NMR techniques complement each other.

However, the main topic we would like to discuss here is the field of thioorganometallo-chemistry. In particular, our interest is focused on the re-

lationship between structure obtained from single-crystal X-ray diffraction and experimental data obtained from solid-state NMR and, in some cases, complemented by EPR and other techniques. Surprisingly, in most cases, there is no need for advanced solid-state NMR experiments, such as distance and torsion angle measurements, extensively described by us, for applications in biology [2]. A combination of simple chemical shift measurements, obtained by performing standard natural abundance multinuclear ^{15}N, ^{13}C, ^{31}P, ^{113}Cd CP/MAS NMR, complemented by estimations of chemical shift anisotropies from spinning sideband patterns and, in some cases by J-couplings, was shown to be sufficient to establish the required correlations with X-ray structures of organometallic complexes, their adducts with nitrogen bases and even with solvated forms of these systems. Moreover, in many cases solid-state NMR data have been used to predict molecular structures, such as mono-, bi-, tetra- and polynuclear complexation, which were then successfully confirmed by single-crystal X-ray diffraction studies. The main goal of this chapter is to review our recent progress in this field.

1.2
Applications of Dialkyldithiocarbamates

Transition metal complexes of dialkyldithiocarbamates have been in the focus of research for more than a century. These ligands, as well as *O,O´*-dialkyldithiophosphates and alkylxanthates are frequently used as reagents-collectors in the froth flotation enrichment of metal sulfide ores [3]. Dialkyldithiocarbamates are also widely used in rubber chemistry as vulcanizing agents [4], in medicine as radioprotectors and for the treatment of the chronic alcoholism [5], in mechanical engineering as additives to lubricating oils, antioxidants and inhibitors of corrosion, as well as in agriculture as fungicides and pesticides [6–8]. A number of nitrogen donor adducts of dialkyldithiocarbamates are also used in the chemical decomposition process of semiconductor M-S films [9], which are widely applied in solar cell technology [10].

It is also known that mercury, cadmium and lead are dangerous ecotoxicants [11–13]. Mercury has been shown to be highly cytotoxic, neurotoxic and immunotoxic and it bioaccumulates in the nervous system, heart and hormonal glands, causing damage to nerve cells, blood cells, DNA, and blocking the function of the hormonal system and enzymatic processes of the body's cellular metabolic system [11, 12]. Recent research on cadmium, one of the most serious environmental pollutants found in food, water and cigarette smoke [14], has shown that ions of this metal disrupt an essential DNA repair system, which is important in preventing cancer [15, 16]. Micromolar concentrations of Cd^{2+} ions, similar to those that can accumulate in organisms, markedly increase mutation rates in yeast [15]. Noting that more than 15,000 tons of cadmium are produced worldwide each year for nickel-cadmium batteries, pigments, chemical stabilizers, metal coatings and alloys [17], and that cadmium has a low excretion rate with a biological half-life of 10–30 years, research on cadmium

complexation is of great importance, and the quest for reagents capable of efficiently fixing cadmium (and mercury and lead) in stable complexes for biological inactivation is an urgent problem. Both dialkyldithiocarbamates and *O,O′*-dialkyldithiophosphates of mercury, cadmium and lead have extremely low solubility in aqueous solutions and, therefore, can be used for the biological inactivation of these hazardous metal ions.

2
Dialkyldithiocarbamates

2.1
Thiuram Disulfides

Tetraalkylthiuram disulfides, $R_2NC(S)S\text{-}S(S)CNR_2$, are oxidized forms of the dialkyldithiocarbamate ions $R_2NC(S)S^-$. Thiuram disulfides possess pronounced oxidative properties and can easily oxidize and stabilize polyvalent cations in high oxidation states (Ni(III), Cu(III), Ag(II), etc.) as well as coordinate these metal ions in the molecular form [18, 19]. Therefore, it should always be kept in mind that complexation of polyvalent cations with dialkyldithiocarbamate anions can be accompanied by a redox equilibrium of the following type:

$$(\text{Dtc})_2 \leftarrow \pm\, 2e \rightarrow 2\text{Dtc}^- \qquad\qquad\qquad\qquad (1)$$
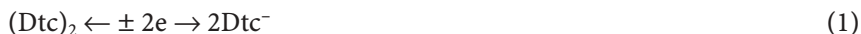
Previously, the molecular structures of many thiuram di- [20–31] (see Fig. 1), mono- [32], trisulfides [33] and thiuram disulfide derivatives, in which $R_2NC(S)S-$ groups are linked by polymethylene chains [34], have been determined by single-crystal X-ray diffraction studies. A number of polycrystalline tetralkylthiuram disulfides and their cyclic analogs have also been recently studied by means of solid-state ^{13}C and ^{15}N CP/MAS NMR [31]. Assignments and ^{13}C and ^{15}N chemical shift data for eight (**1–8**) selected thiuram disulfide compounds and initial dithiocarbamate salts are shown in Table 1. The observed differences in ^{15}N and ^{13}C isotropic chemical shifts for these molecular systems can be attributed to simultaneous manifestation of the inductive effect of alkyl substituents and to the mesomeric effect of the dithiocarbamate groups discussed below.

^{13}C resonance lines at 187–194 ppm in CP/MAS NMR spectra of thiuram disulfides (Fig. 2) can be easily assigned to carbon sites in >NC(S)S– groups, while resonance peaks at 44–66 ppm are in the range typical for carbon sites in alkyl substituents directly bonded to the nitrogen atom. These resonance lines are split as asymmetric doublets (see Fig. 2 and Table 1) because of incomplete suppression of the dipole-dipole $^{13}C\text{-}^{14}N$ interaction under magic-angle-spinning in moderate magnetic fields (^{14}N nucleus, spin I=1, $^{13}C\text{-}^{14}N$ second order quadrupolar spectral patterns) [35, 36]. Comparison of ^{13}C NMR chemical shifts of carbon sites in the thiuram disulfides and in the corresponding

Table 1 ^{13}C and ^{15}N chemical shifts[a] (ppm) of tetraalkyl substituted and cyclic thiuram disulfides and initial sodium dithiocarbamate salts [relative to TMS (^{13}C) and NH$_4$Cl (^{15}N)]

Compounds	^{13}C						^{15}N	N-C(S)S d, Å
	>NC(S)S–	>NCH$_2$– >NCH$_3$ or >NCH–	>CH–	–CH$_2$–	–CH$_2$O–	–CH$_3$	>N–	
1. [(CH$_3$)$_2$NC(S)S]$_2$	193.8 (49)[b]	48.0 (35)[b]; 44.0 (35)[b] (1:1)					106.7	1.329 [24]
2. [(C$_2$H$_5$)$_2$NC(S)S]$_2$	191.6 (45)[b]	53.3; 52.6; 48.9; 48.5 (1:1:1:1)				16.1; 15.5; 12.3 (1:1:2)	130.2 128.5 (1:1)	1.332 1.331 [24]
3. [(C$_3$H$_7$)$_2$NC(S)S]$_2$	193.9 191.8 (1:1)	60.6; 58.9; 55.1 (1:1:2)		22.0; 19.8; 18.8 (2:1:1)		13.2; 11.9; 11.3 (1:1:2)	129.7 127.3 (1:1)	1.337 1.326 [25]
4. [(i-C$_3$H$_7$)$_2$NC(S)S]$_2$	187.3 (46)[b]	58.6 (34)[b]; 53.5 (34)[b]; (1:1)				21.1; 20.5 (1:1)	142.7	1.327 [26]
5. [(i-C$_4$H$_9$)$_2$NC(S)S]$_2$	193.7 191.2 (1:1)	66.0; 61.8; 59.6 (1:2:1)	28.5; 28.0; 27.0; 26.1 (1:1:1:1)			22.4; 22.1; 21.7; 21.4; 20.9; 20.5; 20.1 (1:1:1:1:1:2:1)	121.1 120.6 (1:1)	
6. [(CH$_2$)$_5$NC(S)S]$_2$	190.7	57.4; 56.5; 54.1; 53.0 (1:1:1:1)		30.0; 27.8; 26.6; 25.7 (1:2:1:2)			121.9	1.330 1.329 [27]
7. [(CH$_2$)$_6$NC(S)S]$_2$	191.7 (43)[b]	62.5; 58.4; 54.2 (1:1:2)		30.4; 28.7; 27.6; 26.7; 26.3			127.3 121.3 (1:1)	1.336 1.333 [31]

Table 1 (continued)

Compounds	^{13}C						^{15}N	N-C(S)S d, Å
	>NC(S)S–	>NCH$_2$– >NCH$_3$ or >NCH–	>CH–	–CH$_2$–	–CH$_2$O–	–CH$_3$	>N–	
8. [(O{CH$_2$}$_4$)NC(S)S]$_2$	193.2; 190.0 (1:1)	55.9; 53.6; 50.8 (1:2:1)			68.4; 67.6 (1:1)		115.8; 109.6 (1:1)	1.381; 1.309 [29]
1a. Na{S$_2$CN(CH$_3$)$_2$}·xH$_2$O^c	209.7 (51)^b; 207.4 (43)^b	47.5 (39)^b; 47.0 (31)^b					116.7	
2a. Na{S$_2$CN(C$_2$H$_5$)$_2$}·3H$_2$O^d	206.5 (51)^b	48.6 (71)^b				13.2	139.1	
3a. Na{S$_2$CN(C$_3$H$_7$)$_2$}·H$_2$O	208.3	59.4; 57.9 (1:1)		22.3; 21.5 (1:1)		12.6; 11.5 (1:1)		
4a. Na{S$_2$CN(i-C$_3$H$_7$)$_2$}·3H$_2$O	206.6	58.6; 51.3 (1:1)				21.7; 19.8 (3:1)		
5a. Na{S$_2$CN(i-C$_4$H$_9$)$_2$}·3H$_2$O	208.2	66.7	28.0; 27.1 (1:1)			23.0; 22.4; 20.8 (1:1:2)		
6a. Na{S$_2$CN(CH$_2$)$_5$}·2H$_2$O	205.2	54.6; 53.3 (1:1)		27.4; 27.1 (2:1)			135.1	
7a. Na{S$_2$CN(CH$_2$)$_6$}·2H$_2$O	206.3	60.3; 55.5 (1:1)		29.8; 27.0; 26.2; 24.9 (1:1:1:1)			135.2	
8a. Na{S$_2$CN(CH$_2$)$_4$O}·2H$_2$O	204.8	54.6; 53.9; 53.5			67.6; 67.2		130.8	

^{a} Relative to polycrystalline adamantane (the least shielded ^{13}C resonance, 38.56 ppm) [37] and NH$_4$Cl [38, 39]; ^{b} ^{13}C–^{14}N asymmetric doublets (Hz); ^{c} "Aldrich" compound; ^{d} "Fluka" compound.
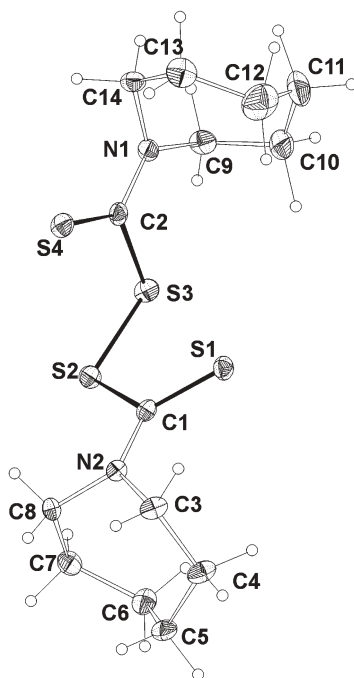
Fig. 1 ORTEP diagrams (ellipsoids at 50% probability level) of the thiuram disulfide $[(CH_2)_6NC(S)S]_2$ at 295 K [31]

sodium salts indicates that covalent bonding of two dithiocarbamate groups results in an increase of the electronic shielding of carbon nuclei in the >NC(S)S– moieties (see Table 1). Depending on the number of ^{13}C resonance lines for the >NC(S)S– groups, thiuram disulfides, $[R_2NC(S)S]_2$ fall into two groups (i) R=CH$_3$ (**1**), C$_2$H$_5$ (**2**), i-C$_3$H$_7$ (**4**), R$_2$=(CH$_2$)$_5$ (**6**) and (CH$_2$)$_6$ (**7**) with a single ^{13}C resonance line, i.e. spectrally equivalent carbon sites in the dithiocarbamate groups (Figs. 2a,b,d and Table 1) and (ii) R=C$_3$H$_7$ (**3**), i-C$_4$H$_9$ (**5**) and R$_2$=O(CH$_2$)$_4$ (**8**) with 1:1 ^{13}C doublets (Fig. 2c,e, Table 1), i.e. structurally non-equivalent carbon sites in >NC(S)S–.

Analogously, ^{15}N NMR spectra exhibit either singlets (Fig. 3a,c) or doublets (Fig. 3b,d,e) for nitrogen sites in the >NC(S)S– groups. However, there is no full correlation between ^{13}C and ^{15}N NMR spectra of thiuram disulfides. For instance, the ^{13}C NMR spectrum of compound **7**, R$_2$=(CH$_2$)$_6$ (Table 1) shows a single resonance line for carbon sites in the dithiocarbamate groups (191.7 ppm), while the ^{15}N NMR spectrum reveals their structural nonequivalence (127.3 and 121.3 ppm, Fig. 3d). Therefore, spectral equivalence of carbon sites can be combined with nonequivalence of peripheral N atoms in the >NC(S)S– groups of thiuram disulfides.

Let us consider how experimental ^{13}C and ^{15}N resonances can be assigned to particular atoms in the structures studied. It is known that the >N-C(S)S– bond
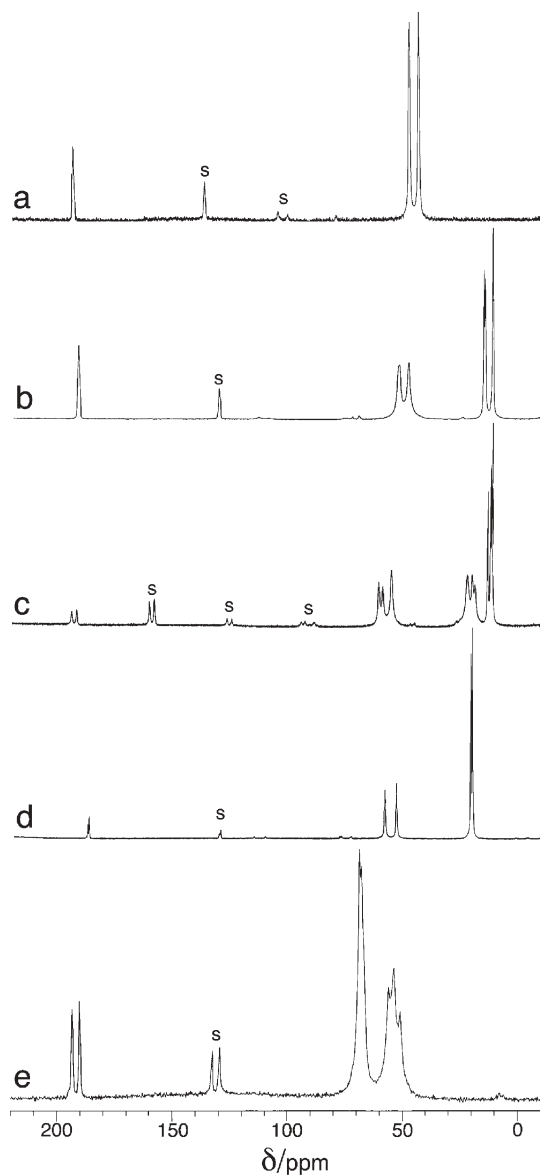
Fig. 2a–e 90.52 MHz ^{13}C CP/MAS NMR spectra (T=295 K) of the polycrystalline thiuram disulfides, [R$_2$NC(S)S]$_2$ (number of signal transients/MAS frequency (Hz)): **a** R=CH$_3$ (1660/5200); **b** R=C$_2$H$_5$ (512/5500); **c** R=C$_3$H$_7$ (5300/3000); **d** R=i-C$_3$H$_7$ (4100/5100); **e** R$_2$=(CH$_2$)$_4$O (2800/5500). 's' denotes spinning sidebands
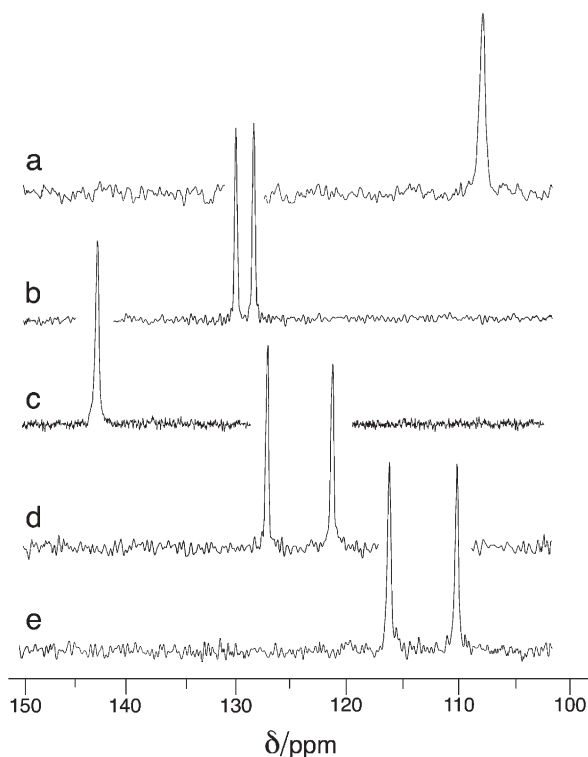
Fig. 3a–e 36.48 MHz ^{15}N CP/MAS NMR spectra (T=295 K) of the polycrystalline thiuram disulfides, $[R_2NC(S)S]_2$ (number of signal transients/MAS frequency (Hz)): **a** R=CH$_3$ (5000/5000); **b** R=C$_2$H$_5$ (1560/6000); **c** R=i-C$_3$H$_7$ (2200/5500); **d** R$_2$=(CH$_2$)$_6$ (1560/6000); **e** R$_2$=(CH$_2$)$_4$O (24300/6000)

in a dithiocarbamate group is always substantially stronger than N-C bonds involving N-alkyl substituents, because the formally single >N-C(S)S– bond is of a partially double character, i.e., molecular orbitals at the N atom are mixed sp^3- and sp^2-hybrid states. For this reason, the resonance structure of the dithiocarbamate groups in thiuram disulfides can be represented by the following two configurations (Scheme 1).
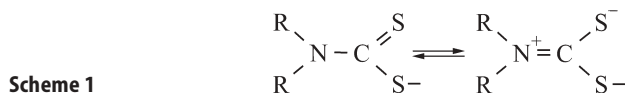
Scheme 1

Hence, four resonance configurations (two for each dithiocarbamate group) should be used for the correct description of thiuram disulfides. The resultant structure is displayed in Scheme 2.

$$\delta^- S \cdots C = \overset{\delta^+}{N} \overset{R}{\underset{R}{\diagup}}$$
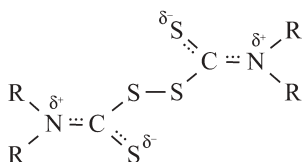
Scheme 2

Within the framework of the electron density redistribution concept, the structure of thiuram disulfide is stabilized by the mesomeric effect favored by the planar C_2N-C(S)S fragments. Obviously, the greater the contribution from the sp^2-hybrid state, the stronger is the >N-C(S)S– bond. On the other hand, a larger δ^+ surplus charge appears at these nitrogen atoms; i.e., the electron density is displaced from the N atom to make its nucleus significantly deshielded. Thus, the spectral nonequivalence of the dithiocarbamate groups can be explained by different degrees of double bonding in formally symmetrical structural fragments of thiuram disulfides. From this point of view, the poorly shielded ^{15}N resonances in the NMR spectra of thiuram disulfides should be assigned to the moiety containing the stronger >N-C(S)S– bond and vice versa.

Hence, the experimental ^{13}C and ^{15}N NMR spectra reveal both a high degree of symmetry of the >N-C(S)S– bonds in the dithiocarbamate fragments of tetramethyl-, tetraisopropyl-, and bis(cyclopentamethylene)-thiuram disulfides and the presence of some asymmetry in the other five compounds given in Table 1. For instance, ^{15}N NMR spectra of tetrapropyl- and dimorpholinethiuram disulfides show two 1:1 resonances (Fig. 3e, Table 1). According to Jian et al. [25] and Rout et al. [29], both compounds are characterized by a pronounced nonequivalence of the >N-C(S)S– bonds in the two dithiocarbamate moieties (Table 1). One of these bonds is stronger (1.326 and 1.309 Å) than the other (1.337 and 1.381 Å, in compounds **3** and **8**; see Table 1). Based on the foregoing conceptual approach, we assigned the poorly shielded ^{15}N resonances at δ=129.7 and 115.8 ppm in the NMR spectra of $[(C_3H_7)_2NC(S)S]_2$ (**3**) and $[(O\{CH_2\}_4)NC(S)S]_2$ (**8**), to nitrogen atoms in the dithiocarbamate moieties containing the stronger >N-C(S)S– bonds, i.e. with d=1.326 Å in **3** and 1.309 Å in **8**. Correspondingly, the two other, highly shielded ^{15}N resonances at δ=127.3 (**3**) and 109.6 ppm (**8**) were assigned to the N atoms with the weaker >N-C(S)S– bonds, i.e. with d=1.337 Å in **3** and 1.381 Å in **8**. Insofar as partial double bonding gives rise not only to a positive surplus charge at N atoms, but also to a negative surplus charge, $\delta(^{13}C)$, at carbon atoms in the C(S)S molecular fragment, ^{13}C resonance lines for the corresponding carbon atoms can also be assigned. In terms of our approach, the highly shielded resonances in the ^{13}C NMR spectra of compounds **3** and **8** at δ=191.8 and 190.0 ppm, were assigned to the dithiocarbamate moieties containing the stronger >N-C(S)S– bonds, while the resonances at δ=193.9 and 193.2 ppm, to the moieties with the weaker bonds.

Analysis of the experimental data (Table 1) showed that the ^{15}N chemical shifts of thiuram disulfides also depend considerably on the alkyl substituents at the N atom. This dependence does not correlate with the double-bond char-

acter at nitrogen atoms in >N-C(S)S moieties discussed above. For instance, the >N-C(S)S– bond lengths in tetramethyl- and tetraethylthiuram disulfides are virtually the same, while $\delta(^{15}N)$ values differ significantly. The same is true for tetrapropyl- and tetraisopropylthiuram disulfides. Alkyl groups are known to be σ-electron donors. For this reason, their (+)-inductive effect plays an important part, along with the mesomeric effect, in the electron density distribution in thiuram disulfide molecules. The inductive effects of alkyl substituents are quantitatively expressed in terms of the inductive Taft constants σ* [40]. Let us consider variations of the ^{15}N chemical shift in experimental NMR spectra of dialkylthiuram disulfides with the Taft constant for –CH$_3$ (σ*=0.00), –C$_2$H$_5$ (–0.10), and –CH(CH$_3$)$_2$ (–0.19) [40]. According to the latter values, the electron-donating properties of the alkyl substituents toward the nitrogen atom are enhanced from methyl to isopropyl groups. For this reason, it could be expected that ^{15}N chemical shifts would decrease in the order [(CH$_3$)$_2$NC(S)S]$_2$> [(C$_2$H$_5$)$_2$NC(S)S]$_2$>[(i-C$_3$H$_7$)$_2$NC(S)S]$_2$. However, the real order of their δ(^{15}N) values is quite the opposite. This apparent inconsistency is due to the specific inductive effect of alkyl substituents bound to the sp^2-hybridized N atoms. In this case, the electron density is displaced from the alkyl substituents to a carbon atom that is immediately behind the N atom. This electronic effect underlies the Markovnikov empirical rule. Hence, the increasing inductive effect in the series CH$_3$<C$_2$H$_5$<i-C$_3$H$_7$ is accompanied by an additional displacement of the electron density from the N atom towards the C(S)S fragment and by monotonic increase in the positive (on the N atom) and negative (on the C atom) surplus charges. Thus, the increasing electron deshielding of the nitrogen nuclei in the thiuram disulfides under discussion can be explained by the simultaneous manifestation of mesomeric and inductive effects, with the latter gradually becoming predominant.

2.2
Dialkyldithiocarbamate Nickel(II) Complexes

Among transition-metal dithiocarbamates, which show considerable structural diversity, nickel(II) complexes are characterized by the simplest type of mononuclear molecular structures, [Ni(S$_2$CNR$_2$)$_2$], [41–56] with the square-planar configuration of [NiS$_4$] chromophores. The latter is due to the dsp^2-hybrid state of the central atom (R=CH$_3$ [41], C$_2$H$_5$ [42–44], C$_3$H$_7$ [45, 46], iso-C$_3$H$_7$ [47], C$_4$H$_9$ [48], iso-C$_4$H$_9$ [49]; or R$_2$=(CH$_2$)$_5$ [50], (CH$_2$)$_6$ [51, 46], (CH$_2$)$_4$O [52]). These complexes have only the terminal type of ligand coordinated to nickel by two sulfur atoms, giving rise to planar four-membered chelates [NiS$_2$C] (Scheme 3).
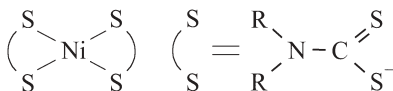
Scheme 3

To characterize the terminal chelating structural state of different dialkyl substituted and cyclic dithiocarbamate ligands, $R_2N-C(S)S^-$, various mononuclear nickel(II) complexes $[Ni(S_2CNR_2)_2]$, $R=CH_3$ (**9**), C_2H_5 (**10**) C_3H_7 (**11**), *iso*-C_3H_7 (**12**), C_4H_9 (**13**), *iso*-C_4H_9 (**14**); $R_2=(CH_2)_5$ (**15**), $(CH_2)_6$ (**16**), $(CH_2)_4O$ (**17**)) have been studied using ^{13}C and ^{15}N CP/MAS NMR spectroscopy (see Table 2).

^{13}C NMR spectra of two types of Ni(II) dithiocarbamate compounds, complexes precipitated from aqueous solutions and those recrystallized from organic solvents, have been recorded. Being spectrally identical, the latter give rise to narrower resonance lines. The NMR spectra (Figs. 4 and 5, Table 2) indicate that all complexes are individual compounds. ^{13}C NMR resonance lines can be assigned to carbon sites in >NC(S)S– moieties and in alkyl substituents at the nitrogen atom. The ^{13}C NMR spectrum of the morpholinedithiocarbamate complex also shows resonances of C-sites in –OCH_2– groups (66.4 and 67.6 ppm). Some ^{13}C resonances are represented as asymmetric doublets and can be assigned to carbon atoms directly bonded to the nitrogen atom
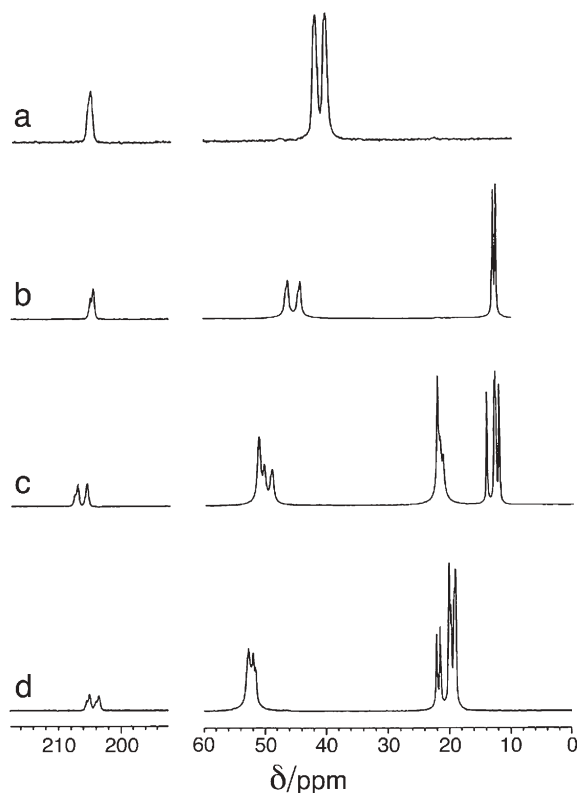
Fig. 4a–d 90.52 MHz ^{13}C CP/MAS NMR spectra of the polycrystalline dithiocarbamate nickel(II) complexes, $[Ni\{S_2CNR_2\}_2]$ (with number of signal transients given in parentheses): **a** $R=CH_3$ (3624); **b** $R=C_2H_5$ (700); **c** $R=C_3H_7$ (1220); **d** $R=i$-C_3H_7 (1200). The MAS frequency was 5500 Hz

Table 2 ^{13}C and ^{15}N chemical shifts (ppm) of dithiocarbamate nickel(II) complexes, [Ni(S$_2$CNR$_2$)$_2$], relative to TMS (^{13}C) and NH$_4$Cl (^{15}N)

Complex	^{13}C						^{15}N >N–	N-C(S)S d, Å
	>NC(S)S–	>NCH–	>NCH$_2$– or >N–CH$_3$	–CH$_2$– (–CH<)	–CH$_2$O–	–CH$_3$		
9. [Ni{S$_2$CN(CH$_3$)$_2$}$_2$]	205.3 (41.6)[a]		42.2 (31.7)[a] 40.5 (30.8)[a] (1:1)				116.3	1.349 [41]
10. [Ni{S$_2$CN(C$_2$H$_5$)$_2$}$_2$]	204.5 (41.6)[a]		46.8 (27.1)[a] 44.8 (29.8)[a] (1:1)			13.1 12.6 (1:1)	139.6	1.324 [44]
11. [Ni{S$_2$CN(C$_3$H$_7$)$_2$}$_2$]	207.2 (37.1)[a] 205.5(1:1)		51.2; 50.4; 49.1(2:1:1)	22.2; 21.8; 21.3 (2:1:1)		14.3; 13.1; 12.8; 12.3 (1:1:1:1)	136.1 128.9 (1:1)	1.33 [45] 1.313 1.319 [46]
12. [Ni{S$_2$CN(i-C$_3$H$_7$)$_2$}$_2$]	205.3 (38.9)[a] 203.8 (41.6)[a] (1:1)	53.1; 52.8; 52.0; 51.6 (2:1:1)				22.2; 21.6; 20.2; 19.8; 19.3; 19.1 (1:1:2:1:1:2)	154.9 153.0 (1:1)	1.329 1.337 [47]
13. [Ni{S$_2$CN(C$_4$H$_9$)$_2$}$_2$]	205.6		51.2	31.5; 21.6; 20.3(2:1:1)		15.3	135.2	1.329 [48]
14. [Ni{S$_2$CN(i-C$_4$H$_9$)$_2$}$_2$]	208.1; 207.5 (1:1)		57.6; 56.7 (1:1)	28.6; 27.6 (1:1)		22.2; 21.4; 21.0; 20.2; 19.7; 19.5 (2:1:2:1:1:1)	131.1 130.3 (1:1)	1.31 1.33 [49]

Table 2 (continued)

Complex	^{13}C						^{15}N >N–	N-C(S)S d, Å
	>NC(S)S–	>NCH–	>NCH$_2$– or>N–CH$_3$	–CH$_2$– (–CH<)	–CH$_2$O–	–CH$_3$		
15. [Ni{S$_2$CN(CH$_2$)$_5$}$_2$]	202.9 (45.3)[a]		49.9 (28.9)[a]	29.4; 27.5; 25.7(1:1:1)			131.2	1.327 [50]
16. [Ni{S$_2$CN(CH$_2$)$_6$}$_2$]	205.6 (32.6)[a] 205.1(1:1)		52.8 50.7 48.3 (1:2:1)	30.4; 30.0; 29.3; 28.5; 27.5; 27.3 (1:1:3:1:1:1)			136.0 134.2 (1:1)	1.35 [51] 1.317 1.322 [46]
17. [Ni{S$_2$CN(CH$_2$)$_4$O}$_2$]	208.6 (48.9)[a]		46.9; 46.2 (1:1)		67.6 66.4 (1:1)		118.0	1.328 [52]

[a] ^{13}C–^{14}N asymmetric doublets (in Hz).
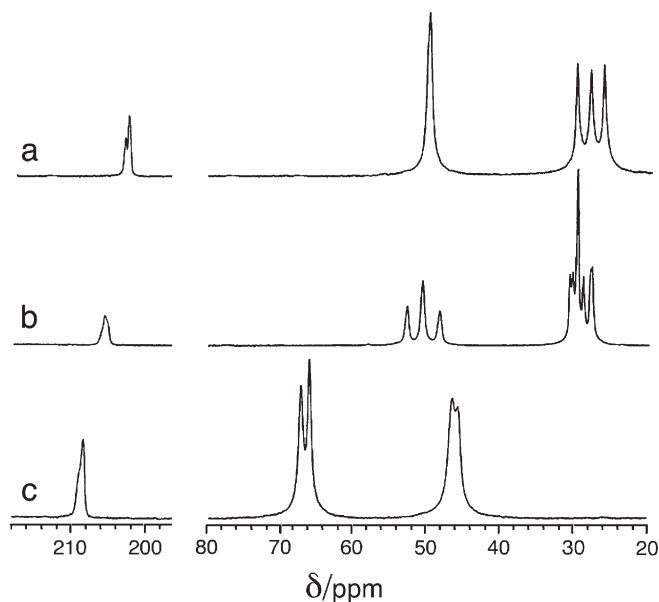
Fig. 5a–c 90.52 MHz ^{13}C CP/MAS NMR spectra of the polycrystalline dithiocarbamate nickel(II) complexes with cyclic dithiocarbamate ligands [Ni{S$_2$CNR$_2$}$_2$] (with number of signal transients given in parentheses): **a** R$_2$=(CH$_2$)$_5$ (1800); **b** R$_2$=(CH$_2$)$_6$ (1000); **c** R$_2$=(CH$_2$)$_4$O (5200). The MAS frequency was 5500 Hz

(^{13}C–^{14}N second order quadrupolar patterns [35, 36]; see Figs. 4 and 5 and Table 2).

From the most informative ^{13}C resonances that arise from >NC(S)S– moieties, Ni(II) dithiocarbamate complexes can be divided into two groups. The first group contains [Ni(S$_2$CNR$_2$)$_2$] compounds with R=CH$_3$, C$_2$H$_5$, C$_4$H$_9$ or R$_2$=(CH$_2$)$_5$, (CH$_2$)$_4$O that give rise to one ^{13}C (>NC(S)S–) resonance only (Figs. 4a,b and 5a,c). Note that ^{15}N NMR spectra of these complexes (Fig. 6a,d) also show singlets assigned to chemically equivalent nitrogen sites in the two >NC(S)S– moieties. Both these observations adequately reflect the centrosymmetric character of the molecular structures of the dithiocarbamate nickel(II) complexes studied [41–44, 48, 50, 52]. By contrast, 1:1 doublets in both ^{13}C and ^{15}N NMR spectra of the nickel complexes with dipropyl-, di-*iso*-propyl-, di-*iso*-butyl- and hexamethylene-dithiocarbamate ligands (Figs. 4c,d, 6b,c and 6e and Table 2) point to a structural nonequivalence of the two >NC(S)S– molecular fragments. However, this nonequivalence can be either intra- (i.e. between ligands in the same molecule) or intermolecular (i.e. two different but centrosymmetric molecules in the unit cell). To distinguish between these different structural situations let us refer to the reported single crystal X-ray diffraction data for complexes in the second group [45, 47, 49, 51]. The unit cell of complexes **12** and **14** comprises two structurally nonequivalent cen-
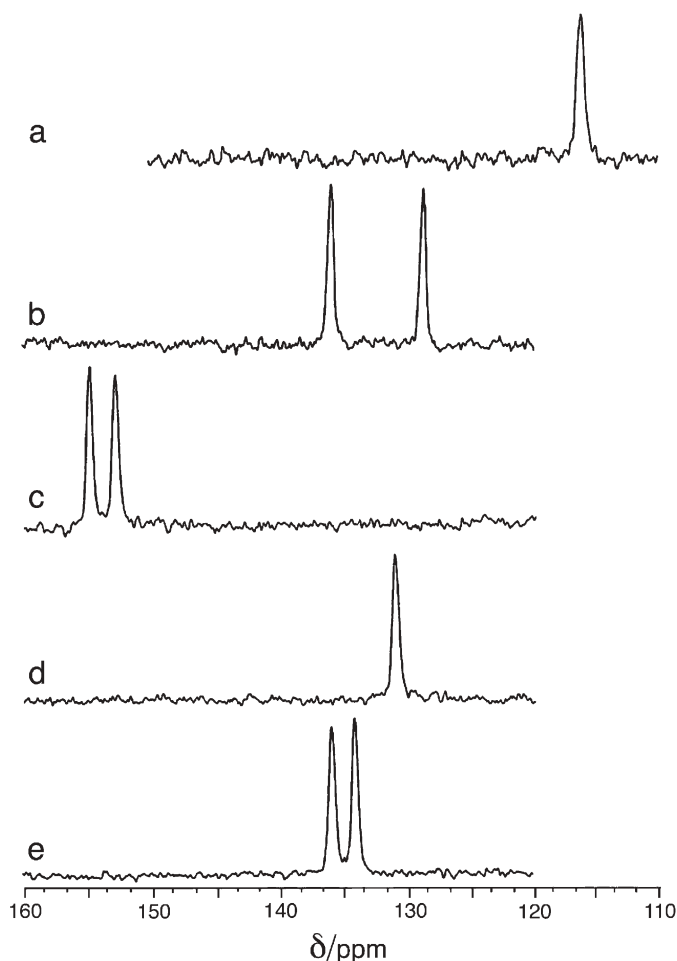
Fig. 6a–e 36.48 MHz ^{15}N CP/MAS NMR spectra of the polycrystalline dithiocarbamate nickel(II) complexes [Ni{S$_2$CNR$_2$}$_2$] (with number of signal transients given in parentheses): **a** R=CH$_3$ (4600); **b** R=C$_3$H$_7$ (1600); **c** R=*i*-C$_3$H$_7$ (4100); **d** R$_2$=(CH$_2$)$_5$ (6500); **e** R$_2$=(CH$_2$)$_6$ (2200). The MAS frequency was 5500 Hz

trosymmetric molecules [Ni(S$_2$CNR$_2$)$_2$], R=*i*-C$_3$H$_7$ [47] and *i*-C$_4$H$_9$ [49]. At the same time, in **16**, the hexamethylenedithiocarbamate ligands incorporated in the same [Ni{S$_2$CN(CH$_2$)$_6$}$_2$] molecule are structurally nonequivalent [46, 51]. ^{13}C and ^{15}N NMR data on [Ni{S$_2$CN(C$_3$H$_7$)$_2$}$_2$] (**11**) (Figs. 4c, 5b and Table 2) are inconsistent with the conclusion from X-ray crystallography for this compound [45], that the complex exists in only one centrosymmetric molecular form. However, our recent single-crystal X-ray diffraction study on the latter complex (motivated by inconsistencies between the old X-ray diffraction and novel solid-state ^{13}C and ^{15}N NMR data) [46] revealed two structurally nonequivalent
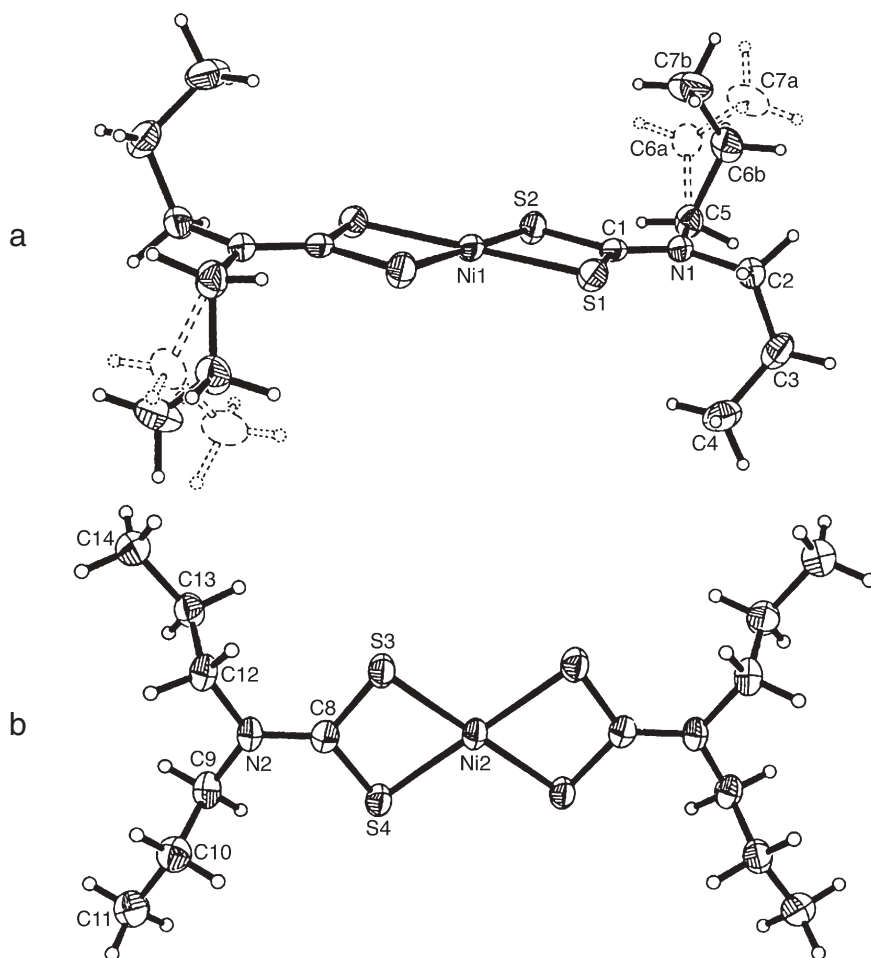
Fig. 7a, b ORTEP diagrams (ellipsoids at 50% probability level) of the two molecular forms of [Ni{S$_2$CN(C$_3$H$_7$)$_2$}$_2$] at 173 K

centrosymmetric molecules of [Ni{S$_2$CN(C$_3$H$_7$)$_2$}$_2$] in the unit cell (see Fig. 7). This example points to the power of solid-state NMR to predict new, or to re-evaluate known, structures of Ni(II) dithiocarbamate compounds.

Although ^{13}C and ^{15}N NMR spectra of Ni(II)-dithiocarbamate complexes are mutually consistent (Figs. 4, 5 and 6), a spectral nonequivalence of dithiocarbamate groups is more pronounced in ^{15}N spectra, for example for R=C$_3$H$_7$ in >NC(S)S– groups $\Delta\delta_{iso}(^{15}$N)=7.2 ppm compared to $\Delta\delta_{iso}(^{13}$C)=1.7 ppm for ^{13}C resonances. This points to a higher sensitivity of ^{15}N chemical shifts (compared to ^{13}C) to subtle structural differences.

2.2.1
Assignment of ^{13}C and ^{15}N Resonances

Here we consider the possibility of assigning 1:1 doublets in both ^{13}C and ^{15}N NMR spectra of Ni(II)-dialkyldithiocarbamate complexes, classified by us as belonging to the second group. This assignment is based on known single crystal structures for these compounds. As discussed above for thiuram disulfide compounds, the >NC(S)S– group is always characterized by a considerable contribution of a double bond character to the formally single N-C bond through the mixing of the sp^2 to sp^3 hybrid state of the nitrogen atom [57]. The larger the sp^2 contribution, the stronger the >N-C(S)S– bond, and the larger the electron density displacement from the nitrogen atom (i.e., the lower the degree of electronic shielding of the nucleus). This results in a greater positive surplus charge δ^+ on the N-atom. Therefore the ^{15}N resonances with the larger chemical shifts of 136.1, 154.9, and 136.0 ppm (Table 2) in ^{15}N NMR spectra of dipropyl-, di-*iso*-propyl- and hexamethylene-dithiocarbamate complexes (compounds **11**, **12**, and **16**) should be assigned to the dithiocarbamate ligands with a shorter >N-C(S)S– bond, 1.313 [46], 1.329 [47], and 1.317 Å [46] in **11**, **12** and **16**. Correspondingly, ^{15}N resonances at 128.9, 153.0, and 134.2 ppm can be assigned to the dithiocarbamate ligands with the weaker (longer) C-N bond, 1.319 (in **11**) [46], 1.337 Å (in **12**) [47], and 1.322 Å (in **16**) [46]. ^{13}C resonances can be also assigned by the same approach. However, in this case, a stronger >N-C(S)S– bond corresponds to a larger electron-density transfer to the carbon atom, and thus to a larger negative surplus charge, δ^-. Hence, ^{13}C NMR signals with lower chemical shifts, 205.5, 203.8, and 205.1 ppm, should be assigned to ligands with a stronger (shorter) C-N bond in compounds **11**, **12** and **16**.

Although chemical shifts do not always correlate with bond strength due to other contributions (for example, the paramagnetic part of the chemical shift), consideration of this factor is often appropriate since the diamagnetic part of the chemical shift interaction, in the molecular systems under discussion, is dominating. For example, a definite difference in the C=O bond strength was argued to be the main reason behind the difference in the ^{13}C chemical shifts of ^{13}C^{16}O and ^{13}C^{17}O molecules [58].

It is noteworthy that ^{15}N chemical shifts of the dithiocarbamate ligands in nickel(II) complexes also depend on alkyl substituents at the nitrogen atom (Table 2). This dependence does not correlate with the dependence of δ(^{15}N) values of dithiocarbamate moieties on the >N-C(S)S– bond length discussed above. For example, these bonds in [Ni(S$_2$CNR$_2$)$_2$] complexes with R=i-C$_3$H$_7$ and R$_2$=(CH$_2$)$_5$ and (CH$_2$)$_4$O are rather similar (Table 2). Nevertheless, the ^{15}N chemical shifts of these compounds are considerably different. In the order of increasing δ(^{15}N) of the complexes, the dialkyldithiocarbamate ligands form the following series (1): CH$_3$ (116 ppm)≈(CH$_2$)$_4$O (118)<i-C$_4$H$_9$ (131)≈(CH$_2$)$_5$ (131)≈C$_3$H$_7$ (132)<(CH$_2$)$_6$ (135)≈C$_4$H$_9$ (135)<C$_2$H$_5$ (140)<i-C$_3$H$_7$ (154). Obviously, this series is in formal conflict with the increase in the (+)inductive effect of the alkyl substituents described by Taft's inductive constants, σ^*, that

Scheme 4

$$R\diagdown N-C\diagup S^{-} \longleftrightarrow R\diagdown N^{+}=C\diagup S^{-} \longleftrightarrow R\diagdown N-C\diagup S$$
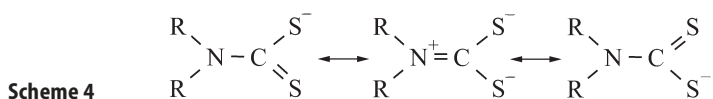
quantitatively reflect the inductive effect of alkyl substituents [40] –CH$_3$ (σ^{*}=0.00), C$_2$H$_5$ (–0.10) and –CH(CH$_3$)$_2$ (–0.19). A decrease in ^{15}N chemical shift along the series of the MDtc, EDtc, *i*-PDtc Ni(II) dithiocarbamate complexes would be expected. However, the situation is quite the opposite, because of the additional mesomeric (resonance) effect. The following three canonical resonance structures of the dialkyldithiocarbamate ligands must be taken into account (Scheme 4).

Thus, the averaged effective structure of the dithiocarbamate ligands can be represented by Scheme 5.

Scheme 5

$$R\diagdown N \overset{\delta^{+}}{\cdots} C \overset{\delta^{-}}{\cdots} S$$

The mesomeric effect stabilizes the planar structure of the C$_2$N-C(S)S– moiety, because the molecular orbitals of the nitrogen and carbon atoms have a considerable contribution from the sp^2 hybridization state.

From this standpoint, the decrease in electronic shielding of nitrogen nuclei in the above-mentioned series (1) of Ni(II)-dithiocarbamate complexes can be explained by a specific manifestation of the inductive effect of alkyl substituents bonded to the sp^2-hybridized nitrogen atom. In this case, electron density is transferred not to the nitrogen atom bearing alkyl groups but to the next carbon atom. (Markovnikov's rule is based precisely on this electronic effect.) Therefore, the increase in the inductive effect of alkyl substituents in the series CH$_3$, C$_2$H$_5$, *i*-C$_3$H$_7$ results in a progressively larger additional displacement of electron density in the R$_2$N-C(S)S– moiety from the nitrogen atom towards the carbon atom. Thus, the decrease in electronic shielding of nitrogen nuclei along the series [Ni{S$_2$CN(CH$_3$)$_2$}$_2$], [Ni{S$_2$CN(C$_2$H$_5$)$_2$}$_2$], [Ni{S$_2$CN(*i*-C$_3$H$_7$)$_2$}$_2$] is accounted for by the interplay of the mesomeric effect of the dithiocarbamate groups and the inductive effect of the alkyl substituents, with a progressively increasing role for the latter effect.

2.3
Dialkyldithiocarbamate Zinc(II) Complexes

Molecular structures of dithiocarbamate zinc(II) complexes are of particular interest because of the unusual mode of formation of binuclear compounds, [Zn$_2$(S$_2$CNR$_2$)$_4$], with symmetric linear/branched alkyl groups: R=CH$_3$ [59, 60], C$_2$H$_5$ [61, 62], C$_3$H$_7$ [63], *iso*-C$_3$H$_7$ [64], –CH$_2$CH=CH$_2$ [65], C$_4$H$_9$ [66], or cyclic/asymmetric alkyl chains: R$_2$=(CH$_2$)$_4$ [67], (CH$_2$)$_6$ [68], (CH$_3$, C$_2$H$_5$), (CH$_3$, C$_3$H$_7$), (CH$_3$, *iso*-C$_3$H$_7$), (CH$_3$, C$_4$H$_9$) [69], (C$_2$H$_5$, *cyclo*-C$_6$H$_{11}$) [70]. In these com-
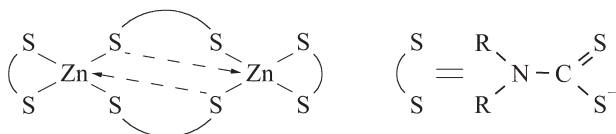
Scheme 6

pounds, pairs of ligands have different structural functions. Two of them are terminal ligands, bidentately coordinated to the metal atom, forming planar four-membered metallacycles [ZnS$_2$C]. The other two ligands act as bridges, which link neighboring zinc atoms into a dimer. They are involved in the extended non-planar eight-membered [Zn$_2$S$_4$C$_2$] metallacycle in 'chair' [61–65, 67–70] or 'boat' [59, 60, 66] conformations. Therefore, each zinc atom has a distorted tetrahedral or trigonal-bipyramidal environment of four or five sulfur atoms. (The fifth Zn-S bond is usually relatively weak (Scheme 6).)

The only exception from the binuclear type of coordination of zinc(II) dithiocarbamate complexes is the mononuclear di-*cyclo*-hexyldithiocarbamate-zinc(II), [Zn{S$_2$CN(*c*-C$_6$H$_{11}$)$_2$}$_2$], with a tetrahedral structure [70]. The presence of two bulky cyclic alkyl substituents in the ligand renders the formation of the binuclear molecular structure sterically impossible[1].

To assign dithiocarbamate ligands, which play different structural functions in the aforementioned binuclear complexes, zinc(II) compounds with nine symmetric N,N-dialkylsubstituted and cyclic dithiocarbamate ligands –S(S)C-NR$_2$, R=CH$_3$ (**18**), C$_2$H$_5$ (**19**), C$_3$H$_7$ (**20**), *iso*-C$_3$H$_7$ (**21**), C$_4$H$_9$ (**22**), R$_2$=(CH$_2$)$_5$ (**23**), (CH$_2$)$_6$ (**24**), (CH$_2$)$_4$O (**25**) and *iso*-C$_4$H$_9$ (**26**) have been prepared and studied by both ^{13}C and ^{15}N CP/MAS NMR.

^{13}C CP/MAS NMR spectra of dithiocarbamate zinc(II) complexes (both those precipitated from water solutions and those recrystallized from organic solvents) reveal the individual character of all the prepared compounds. In contrast to mononuclear nickel(II) dithiocarbamate compounds with only terminal type ligands with almost equivalent >NC(S)S– carbon sites, experimental NMR spectra of the zinc complexes **18–25** show pairs of ^{13}C resonances assigned to >NC(S)S– moieties and sets of resonance lines assigned to alkyl (alkoxyl in **25**) substituents at the nitrogen atom in the bridging (two sites) and the terminal (two almost equivalent sites) type of dithiocarbamate ligands (Figs. 8 and 9 and Table 3). Only two exceptions can be noted: [Zn$_2${S$_2$CN(CH$_3$)$_2$}$_4$] (compound **18**) and [Zn$_2${S$_2$CN(*i*-C$_3$H$_7$)$_2$}$_4$] (**21**) (Fig. 8b) show quartets (1:1:1:1) of ^{13}C resonances from sites in the >NC(S)S– moieties of the ligands and thus a structural difference in all dithiocarbamate ligands (terminal and bridging) in these two zinc(II) dithiocarbamate complexes can be suggested. As in thiuram disulfides and nickel(II) dithiocarbamate compounds, carbon atoms directly bonded to the nitrogen atom usually show asymmetric doublets in experimental NMR spectra of the zinc complexes, due

---

[1] Analogous steric effects of bulky substituents at the nitrogen atom have been also reported for copper(II) dithiocarbamate complexes [71].

Table 3 ¹³C and ¹⁵N chemical shifts (ppm) of binuclear dithiocarbamate zinc(II) complexes, [Zn₂(S₂CNR₂)₄], relative to TMS (¹³C) and NH₄Cl (¹⁵N)

Complex	¹³C						¹⁵N
	>NC(S)S–	>N–CH< >N–CH₂– or >N-CH₃	>CH–	–CH₂–	–CH₂O–	–CH₃	>N–
18. [Zn₂{S₂CN(CH₃)₂}₄]	203.1 (35)ᵃ; 202.8; 202.6; 202.4 (1:1:1:1)	48.5; 48.2; 47.8; 47.4; 46.7; 46.6					122.8; 112.3 (1:1)
19. [Zn₂{S₂CN(C₂H₅)₂}₄]	202.3 (44)ᵃ; 199.7 (42)ᵃ (1:1)	50.8; 50.0 (3:5)				14.6; 13.2; 12.9; 12.7 (1:1:1:1)	149.6; 136.6 (1:1)
20. [Zn₂{S₂CN(C₃H₇)₂}₄]	204.5; 202.2 (1:1)	60.6; 60.0; 56.7; 56.5 (1:1:1:1)		21.8; 20.9; 20.5 (2:1:1)		13.9; 13.4; 13.2; 12.0 (1:1:1:1)	148.2; 130.2 (1:1)
21. [Zn₂{S₂CN(i-C₃H₇)₂}₄]	203.0 (50)ᵃ; 202.8; 199.7 (46)ᵃ; 199.6 (1:1:1:1)	61.8 (27)ᵃ; 59.8 (31)ᵃ; 52.6 (32)ᵃ; 50.8 (36)ᵃ (1:1:1:1)				21.9; 21.7; 21.5; 21.2; 20.5; 20.3; 20.2 (1:1:1:1:1:2)	161.0; 146.6 (1:1)
22. [Zn₂{S₂CN(C₄H₉)₂}₄]	203.4; 200.4 (34)ᵃ (1:1)	61.5; 58.6 (1:3)		33.8; 32.9; 31.3; 30.0 (1:3:2:2); 22.0; 21.4; 21.0 (2:3:3)		16.2; 14.7; 14.5; 14.1 (1:1:1:1)	150.0; 131.6 (1:1)

Table 3 (continued)

Complex	^{13}C						^{15}N
	>NC(S)S–	>N–CH< >N–CH$_2$– or >N–CH$_3$	>CH–	–CH$_2$–	–CH$_2$O–	–CH$_3$	>N–
23. [Zn$_2$\{S$_2$CN(CH$_2$)$_5$\}$_4$]	201.8 200.3 (1:1)	55.7; 55.3; 54.4; 52.0 (1:1:1:1)		28.4; 27.1 (3:1) 26.0; 25.2 (1:1)			142.2 142.0 128.0 (1:1:2)
24. [Zn$_2$\{S$_2$CN(CH$_2$)$_6$\}$_4$]	203.6 201.6 (1:1)	57.3; 55.9; 54.6; 54.4 (1:1:1:1)		29.7; 28.7; 27.7; 27.6; 26.0 (2:2:1:1:2)			144.0 131.9 (1:1)
25. [Zn$_2$\{S$_2$CN(CH$_2$)$_4$O\}$_4$]	200.4 (61)[a] 199.7 (60)[a] (1:1)	54.3; 53.6; 52.8; 50.8 (1:1:1:1)			67.4; 67.1 (1:3)		138.5 124.9 (1:1)
26a. [Zn$_2$\{S$_2$CN(i-C$_4$H$_9$)$_2$\}$_4$]	204.3; 203.7; 201.9 (34)[a] 201.6 (1:1:1:1)	66.4, 66.2; 65.4, 64.8 (1:1:1:1)	28.3, 28.0; 27.9, 27.8			24.0, 23.5; 22.8, 22.7; 22.2, 22.1; 22.0, 21.5	145.2; 143.5; 125.8; 124.1 (1:1:1:1)
26b. [Zn\{S$_2$CN(i-C$_4$H$_9$)$_2$\}$_2$]	205.8 (40)[a]	62.3, 60.7 (1:3)	27.5, 26.8			21.3, 21.0; 20.8, 20.0	133.4, 132.6 (1:1)

[a] ^{13}C–^{14}N asymmetric doublets (in Hz).
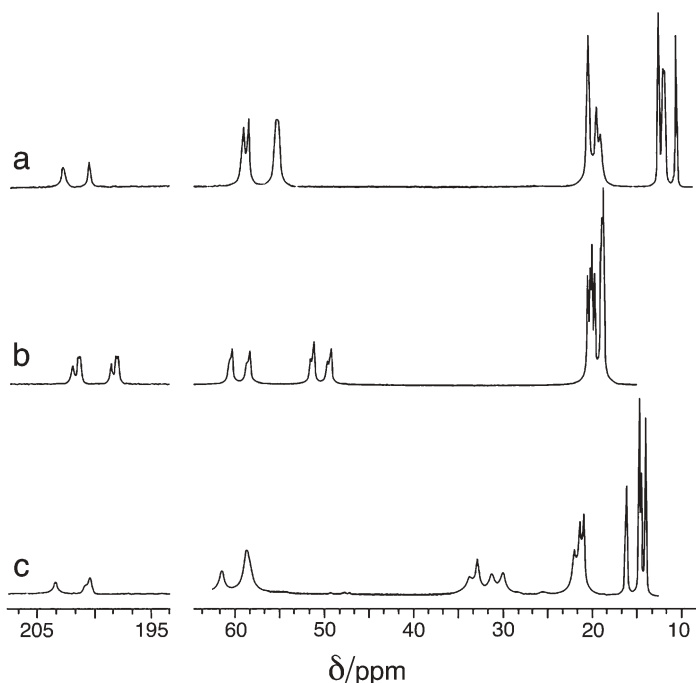
Fig. 8a–c 90.52 MHz ^{13}C CP/MAS NMR spectra of the polycrystalline binuclear zinc complexes with dialkyl-substituted dithiocarbamate ligands, [Zn$_2$(S$_2$CNR$_2$)$_4$] (number of signal transients/MAS frequency (Hz)): **a** R=C$_3$H$_7$ (512/4500); **b** R=*i*-C$_3$H$_7$ (1024/5500); **c** R=C$_4$H$_9$ (2200/3000)

to the dipole-dipole interaction between ^{13}C and the quadrupolar ^{14}N (I=1) nuclei (see Figs. 8, 9 and Table 3).

A common specific feature of ^{15}N CP/MAS NMR spectra of the zinc complexes under investigation, is the presence of pairs of signals (1:1) (Fig. 10, Table 3) consistent with their binuclear structure. A spectral nonequivalence of the >NC(S)S– groups in the terminal and the bridging type of ligand is more pronounced in ^{15}N NMR spectra: $\Delta\delta_{iso}(^{15}$N)=10.5–18.5 ppm compared with $\Delta\delta_{iso}(^{13}$C)=0.5–3.3 ppm in ^{13}C NMR spectra for the same compounds. Therefore, despite both ^{13}C and ^{15}N solid-state NMR data adequately reflecting the binuclear structural organization of the dithiocarbamate zinc(II) complexes, ^{15}N NMR is more sensitive than ^{13}C NMR to subtle structural differences.

2.3.1
Assignment of ^{13}C and ^{15}N NMR Signals

Consider the origin of the NMR spectral nonequivalence of dithiocarbamate ligands with different structural functions, as well as the possibility of assigning ^{13}C and ^{15}N NMR resonances to the structural positions of corresponding
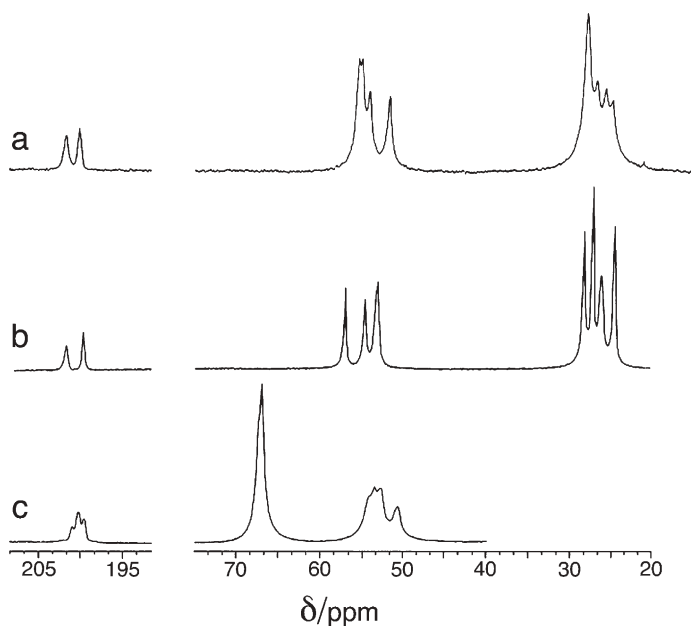
Fig. 9a–c 90.52 MHz ^{13}C CP/MAS NMR spectra of the polycrystalline binuclear zinc complexes with cyclic dithiocarbamate ligands, $[Zn_2(S_2CNR_2)_4]$ (number of signal transients/MAS frequency (Hz)): **a** $R_2=(CH_2)_5$ (2260/4900); **b** $R_2=(CH_2)_6$ (512/5300); **c** $R_2=(CH_2)_4O$ (2048/5500)

atoms in known molecular structures. Reported single-crystal X-ray diffraction structures for zinc dithiocarbamate complexes show that N-C(S)S chemical bonds have lengths intermediate between those for the single N-C and the double N=C chemical bonds in both the terminal and the bridging ligands. Thus, as with the analysis of the nickel(II) dithiocarbamate compounds given above, three chemical resonance structures are required to describe adequately shifts of electron densities in the dithiocarbamate ligands.

It is important to notice that the zinc(II) complexes under consideration are characterized by shorter N-C bonds in the bridging ligands (from X-ray diffraction data). This points to a systematically larger contribution of the double bond character to the N-C bond in the bridging compared to the terminal ligands. Therefore, in the bridging ligands the mixture of the sp^2 to the sp^3 hybrid state of the nitrogen atom is larger. Considering the mesomeric effect[2] this structural situation also corresponds to a larger electron density transfer from the nitrogen atom towards the –C(S)S-moiety. Hence, it is clear that stronger >N-C(S)S– chemical bonds in the bridging ligands predetermine the lower de-

---

[2] The mesomeric effect is favored by the planar structure of the C_2N-C(S)S moiety, which is caused by a nearly sp^2 hybrid state of the nitrogen and carbon atoms.
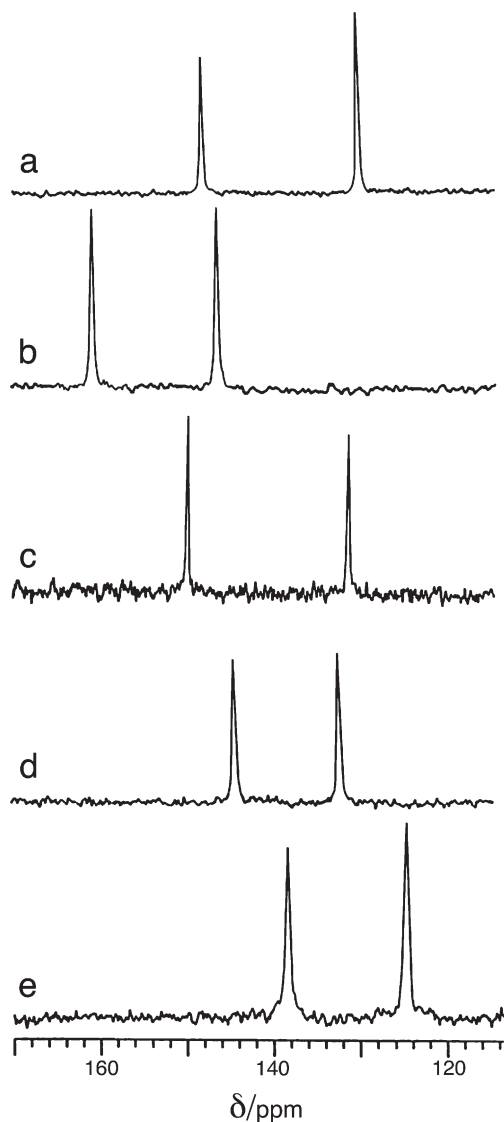
Fig. 10a–e 36.48 MHz ^{15}N CP/MAS NMR spectra of the polycrystalline binuclear dithio-carbamate zinc complexes, $[Zn_2(S_2CNR_2)_4]$ (number of signal transients/MAS frequency (Hz)): **a** R=C_3H_7 (2800/4100); **b** R=i-C_3H_7 (2400/4500); **c** R=C_4H_9 (2600/3000); **d** R_2=$(CH_2)_6$ (7000/2500); **e** R_2=$(CH_2)_4O$ (9800/5500)

gree of electronic shielding of the nitrogen nucleus (i.e., the larger ^{15}N NMR chemical shift). For example, in the binuclear molecule of complex **22** [66] (see Fig. 11) N-C bond lengths in the >NC(S)S– moiety of the bridging and the terminal ligands are 1.313 and 1.330 Å, respectively. The ^{15}N CP/MAS NMR spectrum of **22** (Fig. 10c) shows two resonance lines at δ(^{15}N) 150.0 and 131.6 ppm.
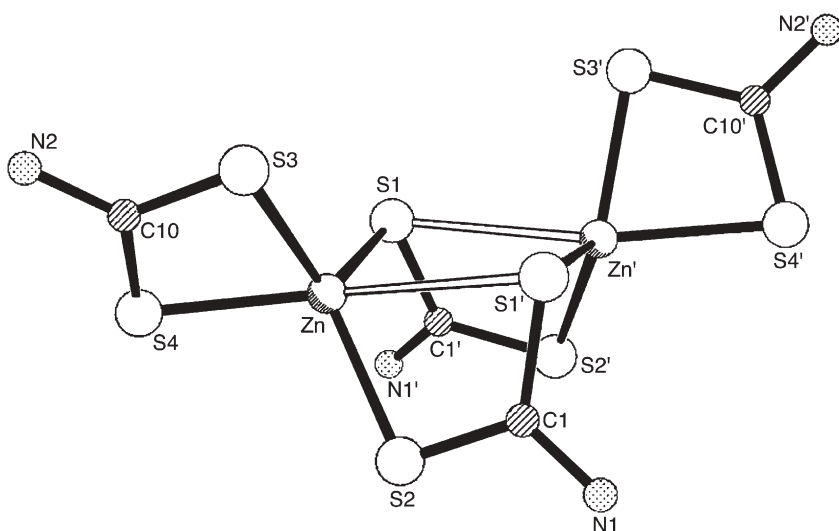
Fig. 11 The central fragment of the molecular structure of $[Zn_2\{S_2CN(C_4H_9)_2\}_4]$

In terms of the approach suggested, the resonance with the larger chemical shift (150.0 ppm) should be assigned to the bridging ligands while the signal at 131.6 ppm will be from the terminal ligands. This approach also allows us to assign ^{13}C NMR resonance lines. In this case, the electron-density transfer from the nitrogen to the carbon atom is also more pronounced in the bridging ligands. Therefore, carbon sites with the smaller chemical shift δ=200.4 ppm should be assigned to the bridging ligands, while the resonance at δ=203.4 ppm corresponds to the terminal ligands. Using this line of reasoning, all ^{15}N and ^{13}C resonances in the spectra of dithiocarbamate zinc(II) complexes with known molecular structures [59–65, 67–70] can be assigned.

Table 3 shows that the ^{15}N chemical shifts of the dithiocarbamate ligands in the zinc complexes are determined not only by their structural function (terminal or bridging) but also depend on the nature of the alkyl substituents at the nitrogen atom. This dependence does not correlate with the relationship discussed above between $\delta_{iso}(^{15}N)$ and the N-C(S)S bond length. For example, differences between the corresponding bond lengths in the terminal (1.335, 1.329 Å) and bridging (1.329, 1.321 Å) ligands in $[Zn_2(S_2CNR_2)_4]$ complexes (R=C_3H_7 [63], iso-C_3H_7 [64]) are relatively small. However, $\delta_{iso}(^{15}N)$ values for these compounds (**20, 21**) are significantly different. In order of increasing mean chemical shift (four N-sites in the same compound), $(\delta_{term}+\delta_{brid})/2$, in the zinc(II) dithiocarbamate complexes, the dialkyl-substituted dithiocarbamate ligands form the following series: *CH$_3$* (118 ppm)<*(CH$_2$)$_4$O* (132)<*(CH$_2$)$_5$* (135)<*(CH$_2$)$_6$* (138)≈*C$_3$H$_7$* (139)<*C$_4$H$_9$* (141)<*C$_2$H$_5$* (143)<*iso-C$_3$H$_7$* (154). Inasmuch as this series reflects a successive decrease in the electronic shielding of nitrogen nuclei, this is in formal contradiction to the increase in the (+)in-

ductive effect of alkyl substituents in the series $-CH_3$ (0.00), $-C_2H_5$ (–0.10), $-CH(CH_3)_2$ (–0.19) (Taft's inductive constants σ^*, which are a quantitative measure of the inductive effect of alkyl substituents, are given in parentheses [40]). According to these σ^* values, a decrease in the ^{15}N chemical shift along the series of dimethyl-, diethyl-, and di-*iso*-propyl-dithiocarbamate zinc(II) complexes is anticipated. However, the actual trend is quite the reverse of that expected, because the mesomeric (resonance) effect, discussed above, in the dithiocarbamate moieties manifests itself, together with the inductive effect of the alkyl substituents. The fact is, that the alkyl substituents in the dithiocarbamate ligands are bound to the nitrogen atom with a large admixture of sp^2-hybridization. In this case, the electron density is transferred, not to the nitrogen atom bearing alkyl groups, but to the adjacent carbon atom in the >NC(S)S moiety. Therefore, the increase in the inductive effect of the alkyl substituents in the series dimethyl-, diethyl- and di-*iso*-propyl-dithiocarbamate complexes results in a progressively larger additional transfer of the electron density in the $R_2N-C(S)S$ moiety from the nitrogen atom towards the carbon atom. Thus, the decrease in the electronic shielding of nitrogen nuclei along the series $[Zn_2\{S_2CN(CH_3)_2\}_4]$, $[Zn_2\{S_2CN(C_2H_5)_2\}_4]$, $[Zn_2\{S_2CN(iso\text{-}C_3H_7)_2\}_4]$ is caused by a progressive increase in the inductive effect of alkyl substituents, which manifests jointly with the mesomeric effect of dithiocarbamate groups.

However, among dithiocarbamate zinc compounds, *N,N*-di-*iso*-butyldithiocarbamato-zinc(II) complex (**26**) is the most interesting case in terms of both ^{13}C and ^{15}N CP/MAS NMR spectroscopy [72]. The ^{13}C CP/MAS NMR spectrum of this complex (Fig. 12a) shows groups of resonance lines (with relative integral intensities 1:2:2:4) that arise from carbon sites in $-S(S)CN<$, $>NCH_2-$, $>CH-$, and $-CH_3$ groups (Table 3). The most spectrally informative is the first set of ^{13}C resonances ($-S(S)CN<$). The pattern of this set of resonance lines (2:1:1:1:1) indicates the presence of six nonequivalent dithiocarbamate groups in **26**. The ^{15}N NMR spectrum (Fig. 12b) is consistent with this assignment and also shows six resonance lines of equal intensity (1:1:1:1:1:1). Additional ^{15}N CP/MAS NMR experiments on the melt of **26** (prone to supercooling) during the course of slow crystallization revealed different rates of accumulation of the outer doublets with respect to the two central resonance lines. The presence of two types of structurally different molecular forms in *N,N*-di-*iso*-butyldithiocarbamate zinc(II) complex in the same polycrystalline sample can be suggested, i.e., both binuclear and mononuclear forms of complex **26**, in which all ligands are structurally nonequivalent. The outer ^{15}N NMR doublets have been assigned to the binuclear form of the complex. (An analogous character of ^{15}N NMR spectral nonequivalence between the terminal and the bridging ligands has been found in $[Zn_2\{S_2CN(CH_2)_5\}_4]$ (see Table 3).) The central doublet arises from the mononuclear form, $[Zn\{S_2CN(i\text{-}C_4H_9)_2\}_2]$, which has similar ^{15}N chemical shifts to the mononuclear nickel(II) complex, $[Ni\{S_2CN(i\text{-}C_4H_9)_2\}_2]$ (see Table 2) containing only the terminal ligands. Therefore, NMR results have permitted us to suggest that at the molecular level complex **26** concurrently exists as a 1:1 combination of mono- and binuclear species.
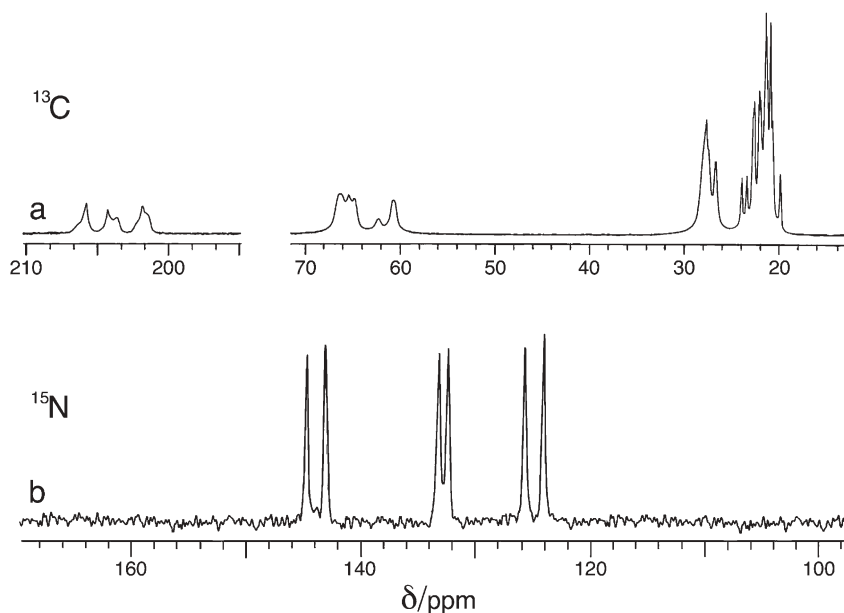
Fig. 12a,b 90.52 MHz ^{13}C and 36.48 MHz ^{15}N CP/MAS NMR spectra of the polycrystalline *N,N*-di-*iso*-butyldithiocarbamate zinc(II) complex, [Zn$_2${S$_2$CN(*i*-C$_4$H$_9$)$_2$}$_4$][Zn{S$_2$CN(*i*-C$_4$H$_9$)$_2$}$_2$] (number of signal transients/MAS frequency (Hz)): **a** ^{13}C (3000/5000); **b** ^{15}N (20600/3000)

To verify this conclusion, the structure of di-*iso*-butyldithiocarbamate zinc(II) complex has been determined using single-crystal X-ray diffraction, and indeed, the unit cell of this compound does include simultaneously both the mononuclear, [Zn{S$_2$CN(*i*-C$_4$H$_9$)$_2$}$_2$] and the binuclear, [Zn$_2${S$_2$CN(*i*-C$_4$H$_9$)$_2$}$_4$] molecular forms of **26** (see Fig. 13).

2.4
Heteropolynuclear Zinc(II)-Nickel(II) Dialkyldithiocarbamate Complexes

Supramolecular heteronuclear complexes [Zn$_2$(S$_2$CNR$_2$)$_4$·nNi(S$_2$CNR$_2$)$_2$] (n=1–4) can be formed through chemical interaction between zinc(II) and nickel(II) dithiocarbamate complexes, as shown by both ^{13}C and ^{15}N CP/MAS NMR spectroscopy [73]. Note that this system is not amenable to single-crystal X-ray diffraction studies because of its amorphous nature on the microscopic scale. Figure 14 shows ^{13}C and ^{15}N CP/MAS NMR spectra of a polynuclear complex [Zn$_2${S$_2$CN(C$_2$H$_5$)$_2$}$_4$·2Ni{S$_2$CN(C$_2$H$_5$)$_2$}$_2$] (**27**). It can be seen that both the ^{13}C and ^{15}N sites of the 'binuclear' part of this polynuclear complex have chemical shifts which are very close to those of the corresponding sites of the zinc(II) diethyldithiocarbamate complex, [Zn$_2${S$_2$CN(C$_2$H$_5$)$_2$}$_4$] (see Table 3). However, two new ^{13}C (205.8 and 43.9 ppm) and ^{15}N (131.6 and 133.9 ppm) res-

Fig. 13a,b ORTEP diagrams (ellipsoids at 30% probability level) of: **a** the binuclear [Zn$_2${S$_2$CN(i-C$_4$H$_9$)$_2$}$_4$]; **b** the mononuclear [Zn{S$_2$CN(i-C$_4$H$_9$)$_2$}$_2$] molecular forms of the N,N-di-iso-butyldithiocarbamate zinc(II) complex

Scheme 7

onances of the above complex can be assigned neither to the pure nickel(II) nor to the zinc(II) complexes. These resonance lines have been assigned to the ^{13}C and ^{15}N sites of the dithiocarbamate groups and to the ^{13}C sites of the methylene groups of diethyldithiocarbamate ligands in $[Ni\{S_2CN(C_2H_5)_2\}_2]$ square-planar molecules, which are coordinated with the sulfur atoms in the terminal ligands of the binuclear zinc(II) dithiocarbamate part of the heteronuclear complex (see Scheme 7). It is known that additional coordination of an electron donor atom to the axial position of a square-planar complex of dithiocarbamato-Me(II) (Me is a transition metal, Cu, Zn, Ni, Cd, Hg, etc) yields a decrease in the partial-double-bond character in the >NC(S)S moiety. As a result of that, displacement of the electron density to the nitrogen from the carbon atom in the chelate cycle is expected [57]. In our case, coordination of a sulfur atom in $[Zn_2\{S_2CN(C_2H_5)_2\}_4]$ with the axial position of $[Ni\{S_2CN(C_2H_5)_2\}_2]$ leads to an increase of the ^{13}C chemical shift by 1.6 ppm and to a decrease of the ^{15}N shifts by 6.7 ppm (on average) at the carbon and nitrogen sites of the >NC(S)S moi-

ety. A decrease in the nitrogen surplus charge δ^+ also results in an increased shielding of methylene ^{13}C nuclei and therefore to a decrease in their chemical shifts (by 2.3 ppm). Note also the appearance of two (1:1) structurally non-equivalent ^{15}N sites (131.6 and 133.9 ppm) in the 'nickel' part of the heteropolynuclear complex. This means that the nitrogen atoms of the two dithiocarbamate ligands in the $[Ni\{S_2CN(C_2H_5)_2\}_2]$ part of the complex have different electronic environments. The most probable explanation for this structural nonequivalence is the formation of a hydrogen bond between one of nitrogen atoms of $[Ni\{S_2CN(C_2H_5)_2\}_2]$ and a methylene group of one of the terminal ligands in the binuclear part, $[Zn_2\{S_2CN(C_2H_5)_2\}_4]$, of the heteropolynuclear complex (see Scheme 7). The result of this interaction is an increase in the ^{15}N chemical shift by 2.3 ppm, which reflects the decrease of shielding of the corresponding nitrogen atom compared to the other. The hydrogen bond formation is sterically allowed since the four-membered chelate ring of the dinuclear zinc(II) molecule is aligned perpendicular to the plane of the square-planar nickel(II) complex. The other nitrogen atom of the 'nickel' part of the heteropolynuclear complex is in a different environment, since the binuclear zinc molecule is non-planar. The dihedral angle between the CS_2Zn plane of the four-membered ring and the S_2Zn plane of the eight-membered ring is most probably close to 90° because of the tetrahedral coordination of the zinc atoms in the S_2ZnS_2 moieties.

2.5
Bis(dialkyldithiocarbamato)zinc(II) Adducts with Nitrogen Bases

Transition metal atoms coordinated by dithiocarbamate ligands through four sulfur atoms have both electronic (free *d*-orbitals) and steric (free octahedral sites) propensity to form adducts with nitrogen bases, since nitrogen atoms have one sp^3-hybrid orbital, which is occupied by the lone pair of stereochemically active electrons. To characterize newly prepared adducts of dimethyl-, diethyl- and morpholinedithiocarbamate zinc(II) complexes with cyclic N-donor bases, such as pyridine, piperidine, hexamethyleneimine and morpholine, compounds **28–35** have been prepared and studied by ^{13}C and ^{15}N CP/MAS NMR (see Table 4) [74–77, 82, 83, 85]. Among adducts of dialkyldithiocarbamate zinc(II) complexes with cyclic N-donor bases, *bis*(dimethyldithiocarbamato)pyridinezinc(II), compound **28**, and *bis*(morpholinedithiocarbamato)hexamethyleneiminezinc(II) (**32**) showed the simplest structural situations. Both ^{13}C and ^{15}N NMR spectra of these compounds are characterized by two distinct groups of resonance lines from dithiocarbamate ligands and coordinated pyridine or hexamethyleneimine molecules (see Figs. 15a, 16a, 17c, and 18c). Single ^{13}C and ^{15}N resonances assigned to >NC(S)S– groups in dithiocarbamate ligands suggest their possible structural equivalence in both $[Zn(C_5H_5N)\{S_2CN(CH_3)_2\}_2]$, **28**, and $[Zn\{(CH_2)_6NH\}\{S_2CN(CH_2)_4O\}_2]$, **32**, molecular systems. NMR chemical shift data reported earlier for organic compounds [78], permitted us to assign the group of ^{13}C resonance lines (149.5, 143.0 and

Table 4 ^{13}C and ^{15}N chemical shifts (ppm) of adducts (**28–33**) of dialkyldithiocarbamate zinc(II) complexes with cyclic N-donor bases [relative to TMS (^{13}C) and NH_4Cl (^{15}N)]

Complex	-S(S)CNR₂ (R=CH₃, C₂H₅; R₂=(CH₂)₄O)					C₅H₅N, (CH₂)₆NH, (CH₂)₅NH, O(CH₂)₄NH			
	>NC(S)S-	-CH₂O-	>NCH₂- or >NCH₃	-CH₃	>N-	o-CH₍₂₎-	m-CH₍₂₎-	p-CH₍₂₎-	>N-
28. [Zn(C₅H₅N){S₂CN(CH₃)₂}₂] [74]	204.7 (43)ᵃ		47.8; 45.9 (1:1)		106.8	149.5	127.9	143.0	218.5
29. [Zn{(CH₂)₆NH}{S₂CN(CH₃)₂}₂] [77]	205.9 (52)ᵃ 204.2 (46)ᵃ (1:1)		46.6 (33)ᵃ 46.2; 45.9 (31)ᵃ (1:2:1)	13.3 12.7 (1:1)	104.8 102.5 (1:1)	49.5	32.1 29.6 (1:1)	29.4 25.7 (1:1)	1.6
30. [Zn{(CH₂)₅NH} {S₂CN(C₂H₅)₂}₂] [75]	205.9 204.4 (37)ᵃ (1:1)		49.7 48.6 (1:1)	13.3 12.7 (1:1)	133.7 129.1 (1:1)	47.3	28.8	25.2	7.0
31. [Zn{(CH₂)₆NH} {S₂CN(C₂H₅)₂}₂] [77]	205.9 204.4 (1:1)		50.3 48.9 (1:1)	12.9	133.7 128.6 (1:1)	49.5	31.4	28.0	10.0
32. [Zn{(CH₂)₆NH} {S₂CN(CH₂)₄O}₂] [77]	204.9	67.3 66.5 (1:1)	52.7 51.7 (1:1)		116.4	49.3	31.6 30.5 (1:1)	27.4	3.6
33. [Zn{O(CH₂)₄NH} {S₂CN(CH₂)₄O}₂] [76, 93]	206.5 204.5 (1:1)	66.1	52.7; 51.5; 50.9 (1:1:2)		117.8 116.4 (1:1)	66.6; 65.2 (1:1) -CH₂O-	48.3; 46.5 (1:1) >NCH₂-		-7.2

Table 4 (continued)

Complex	-S(S)CNR$_2$ (R=CH$_3$, C$_2$H$_5$; R$_2$=(CH$_2$)$_4$O)				>N-	C$_5$H$_5$N, (CH$_2$)$_6$NH, (CH$_2$)$_5$NH, O(CH$_2$)$_4$NH			
	>NC(S)S	-CH$_2$O-	>NCH$_2$- or >NCH$_3$	-CH$_3$	>N-	o-CH$_{(2)}$-	m-CH$_{(2)}$-	p-CH$_{(2)}$-	>N-
α,β-34. [Zn(C$_5$H$_5$N){S$_2$CN(C$_2$H$_5$)$_2$}$_2$] [82]	204.4		51.4; 51.6; 50.7; 49.5	15.5;14.5; 13.3; 12.9; 12.6; 12.1; 11.8; 11.2 (1:1:1:1: 1:1:1:1)	133.9 132.2 131.3 (1:2:1)	150.7 148.7	126.5 125.8	140.3	231.7 228.9
γ-34. [Zn(C$_5$H$_5$N){S$_2$CN(C$_2$H$_5$)$_2$}$_2$]	205.0 202.8 (3:1)		50.8; 48.6 (1:1)	14.9; 14.6; 13.8; 12.8; 12.0; 11.2 (1:1:2:1:2:1)	136.6 131.1 130.6 (1:2:1)	150.9 148.8 (1:3)	126.1	139.7	230.8 [83]
35. [Zn{O(CH$_2$)$_4$NH} {S$_2$CN(C$_2$H$_5$)$_2$}$_2$] [84, 85]	205.8 204.5 203.9		49.7	14.5; 13.4; 12.6; 12.3	132.7 131.5 127.2 126.7	67.8 -CH$_2$O-	51.2 >NCH$_2$-	-2.3 -7.5	

^{a} ^{13}C–^{14}N asymmetric doublets (in Hz).

Fig. 15a–c 90.52 MHz ^{13}C CP/MAS NMR spectra of the polycrystalline adducts of dithiocarbamate zinc(II) complexes with cyclic N-donor bases (number of signal transients/MAS frequency (Hz)): **a** [Zn(C$_5$H$_5$N){S$_2$CN(CH$_3$)$_2$}$_2$] (2000/6100); **b** [Zn{(CH$_2$)$_5$NH}{S$_2$CN (C$_2$H$_5$)$_2$}$_2$] (2048/5500); **c** [Zn{O(CH$_2$)$_4$NH}{S$_2$CN(CH$_2$)$_4$O}$_2$] (4100/5500). Spinning sidebands are marked by 's'

127.9 ppm with relative integral intensities 2:1:2) in the central region of the ^{13}C CP/MAS NMR spectrum of the adduct **28** (see Fig. 15a) to *o*-, *p*-, and *m*-carbon atoms, respectively, in the coordinated pyridine molecule. The resonances from *o*- and *m*-C atoms are substantially broader than those from *p*-carbon atom. This line broadening can be explained in terms of molecular dynamics, i.e., by either rotations or large-angle vibrations of the pyridine molecule about the Zn-N(Py) bond [79–81]. (The broadening may also be due to partial statistical disorder of the heterocycle over several structurally close positions.) Clearly, dynamics of this type bring about a scatter of the ^{13}C chemical shifts of carbon atoms in the *o*- and *m*-positions, but virtually does not change the nearest chemical surroundings of the carbon atom occupying the *para*-position, and hence does not affect its linewidth.

Both ^{13}C and ^{15}N NMR spectra of other adducts, **29–31** and **33**, show double resonance lines with relative intensities 1:1 (see Figs. 15–18 and Table 4) assigned to C and N sites, in the >NC(S)S– groups. The latter indicates the structural nonequivalence of the dithiocarbamate ligands in these compounds. The
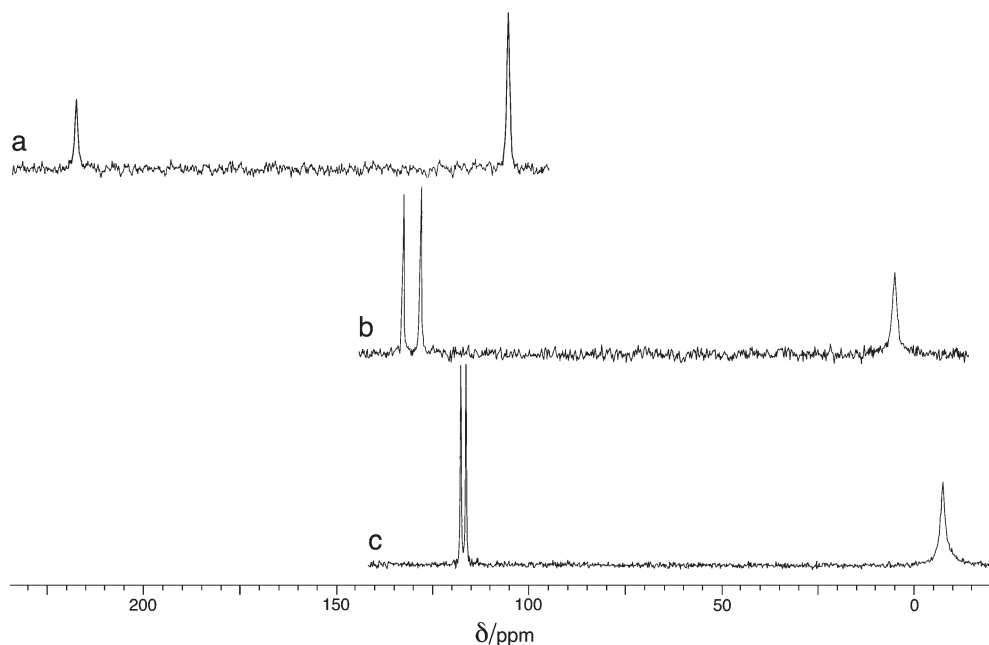
Fig. 16a–c 36.48 MHz ^{15}N CP/MAS NMR spectra of the polycrystalline adducts of dithio-carbamate zinc(II) complexes with cyclic N-donor bases (number of signal transients/MAS frequency (Hz)): **a** [Zn(C$_5$H$_5$N){S$_2$CN(CH$_3$)$_2$}$_2$] (18600/5500); **b** [Zn{(CH$_2$)$_5$NH}{S$_2$CN (C$_2$H$_5$)$_2$}$_2$] (2500/4400); **c** [Zn{O(CH$_2$)$_4$NH}{S$_2$CN(CH$_2$)$_4$O}$_2$] (21400/5500)

^{15}N chemical shift values of nitrogen sites in the >NC(S)S– groups of adducts **28–33** show a strong dependence on alkyl substituents at the nitrogen atom (see Table 4), similar to those in the previously discussed dithiocarbamate nickel(II) and zinc(II) complexes.

Compared to other N-donor bases, (CH$_2$)$_6$NH, (CH$_2$)$_5$NH and O(CH$_2$)$_4$NH, the coordinated pyridine molecule is characterized by the largest value of ^{15}N chemical shift (218.5–231.5 ppm) because of the aromatic character of the system, i.e., an additional shift of the electron density from the nitrogen nucleus to the conjugating system of the heterocycle (see Table 4). It is worth noting that the ^{15}N chemical shift of a free pyridine molecule is equal to –83.0 ppm in the absolute scale [38, 39] or 258 ppm relative to solid NH$_4$Cl [38, 39], i.e., adduct formation leads to additional shielding of the nitrogen site of the donor molecule by ca. 30 ppm. This is due to the formation of an additional chemical bond of the nitrogen atom with zinc characterized by a low electronegativity.

Let us now discuss two representative examples, adducts [Zn(C$_5$H$_5$N){S$_2$CN(C$_2$H$_5$)$_2$}$_2$] **34**, and [Zn{O(CH$_2$)$_4$NH}{S$_2$CN(C$_2$H$_5$)$_2$}$_2$], **35,** in the light of solid state NMR predicting the type of molecular structure, which were later confirmed by the direct method of single crystal X-ray diffraction analysis. The ^{15}N CP/MAS NMR spectra of the polycrystalline adducts **34** and **35,** together
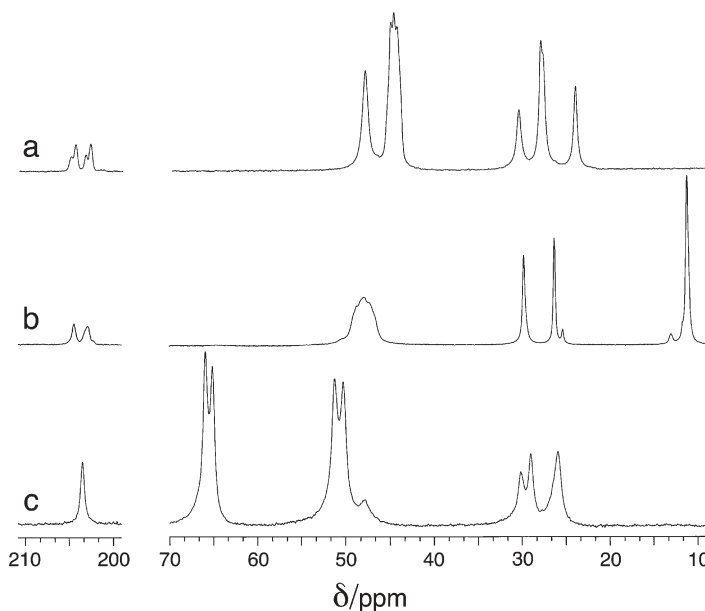
Fig. 17a–c 90.52 MHz ^{13}C CP/MAS NMR spectra of the polycrystalline adducts of dithio-carbamate zinc(II) complexes with hexamethyleneimine (number of signal transients/MAS frequency (Hz)): **a** [Zn{(CH$_2$)$_6$NH}{S$_2$CN(CH$_3$)$_2$}$_2$] (900/5500); **b** [Zn{(CH$_2$)$_6$NH}{S$_2$CN(C$_2$H$_5$)$_2$}$_2$] (1480/5200); **c** [Zn{(CH$_2$)$_6$NH}{S$_2$CN(CH$_2$)$_4$O}$_2$] (1080/6200)

with the initial zinc(II) diethyldithiocarbamate complex, [Zn$_2${S$_2$CN(C$_2$H$_5$)$_2$}$_4$] (**19**), are shown in Fig. 19. Nitrogen sites in the >NC(S)S– groups have chemical shifts in the range 126.7–134 ppm in both adducts **34** and **35**. These values are close to the 136.6 ppm assigned to nitrogen sites in the terminal ligands of the initial binuclear complex [Zn$_2${S$_2$CN(C$_2$H$_5$)$_2$}$_4$] **19** (bridging sites have $\delta(^{15}$N)=149.6 ppm, see Table 3). Thus the existence of only the terminal type of dithiocarbamate ligand in the adduct molecules can be suggested. Moreover, three (1:2:1) or four (1:1:1:1) resonance lines assigned to nitrogen sites in the >NC(S)S– groups of **34** and **35** suggest the existence of at least two structurally distinct monomer molecules of the adducts in the unit cell. This conclusion is additionally supported by the observation that both a pyridine resonance (around 230 ppm) in **34** and a morpholine resonance (around –5 ppm) in **35** are distinctly split in symmetric doublets with relative peak intensities of 1:1 (see Fig. 19b,c). The ^{13}C CP/MAS NMR spectra of compounds **19**, **34**, and **35**, though less representative, also support the aforementioned hypothesis about two polymorphs of adducts **34** and **35** in the unit cell (for example, *ortho*- and *meta*-C sites of pyridine in **34** and OCH$_2$ sites of morpholine molecules in **35** are also split into doublets (1:1), see Fig. 20b,c and Table 4).

The existence of two isomers of both *bis*(diethyldithiocarbamato)-pyridinezinc(II), **34**, and *bis*(diethyldithiocarbamato)morpholinezinc(II), **35**, in the asymmetric units has been confirmed by direct structural single-crystal X-
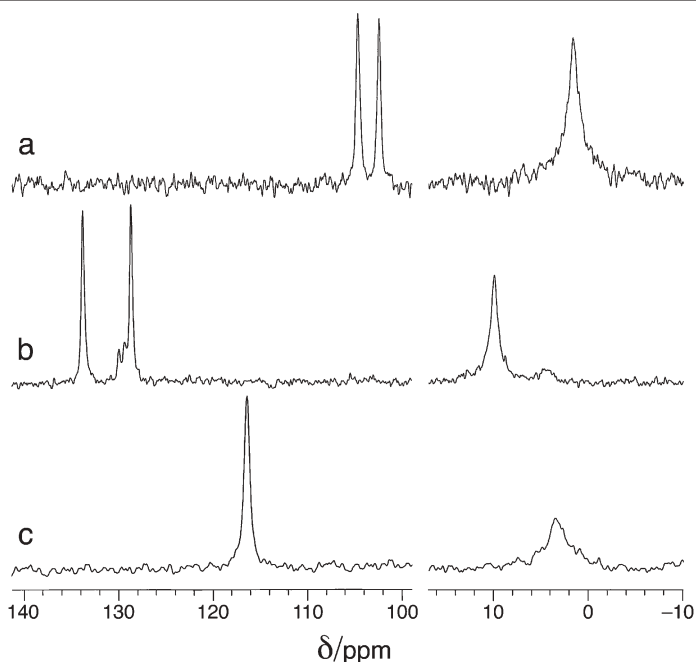
Fig. 18a–c 36.48 MHz ^{15}N CP/MAS NMR spectra of the polycrystalline adducts of dithio-carbamate zinc(II) complexes with hexamethyleneimine (number of signal transients/MAS frequency (Hz)): **a** [Zn{(CH$_2$)$_6$NH}{S$_2$CN(CH$_3$)$_2$}$_2$] (8800/5250); **b** [Zn{(CH$_2$)$_6$NH}{S$_2$CN(C$_2$H$_5$)$_2$}$_2$] (2700/3100); **c** [Zn{(CH$_2$)$_6$NH}{S$_2$CN(CH$_2$)$_4$O}$_2$] (19200/4800)

ray diffraction analysis. Figure 21 (see also Fig. 29a,b) shows the molecular structures of the α- and β-forms of **34**. α-**34** and β-**34** have very similar structures (bond lengths and angles) [82, 83] with the main differences in (i) Zn-N chemical bonds (2.072(5) in the α-form and 2.079(5) Å in the β-form), (ii) the acute angles of the planes of the pyridine molecules relative to the most weak Zn-S bond (torsion angles S(6)-Zn(1)-N(5)-C(17) and S(5)-Zn(2)-N(1)-C(6) in Fig. 29a,b) which are equal to 52.7 and –45.6 ° in α-**34** and β-**34**. In spite of very marginal differences in the molecular structures of α- and β-**34**, the ^{15}N chemical shifts of the coordinated pyridine molecules differ by 2.7 ppm, which points to a very high sensitivity of this magnetic interaction to structural differences in α- and β-[Zn(C$_5$H$_5$N){S$_2$CN(C$_2$H$_5$)$_2$}$_2$]. Moreover, the resonance at 231.5 ppm can be assigned to the nitrogen atom of the pyridine molecule in the β-conformer (somewhat weakly bonded Py molecule), while the other resonance at 228.8 ppm corresponds to the α-**34**. This assignment is based on the previously mentioned conclusion, that adduct formation (with pyridine) leads to additional shielding of the nitrogen sites of the donor aromatic molecule.

Figure 22 represents the two isomorphs in the asymmetric unit of **35** [84, 85]. Compared with the previously discussed adduct **34,** with aromatic and planar molecules of pyridine, compound [Zn(O(CH$_2$)$_4$NH){S$_2$CN(C$_2$H$_5$)$_2$}$_2$] contains
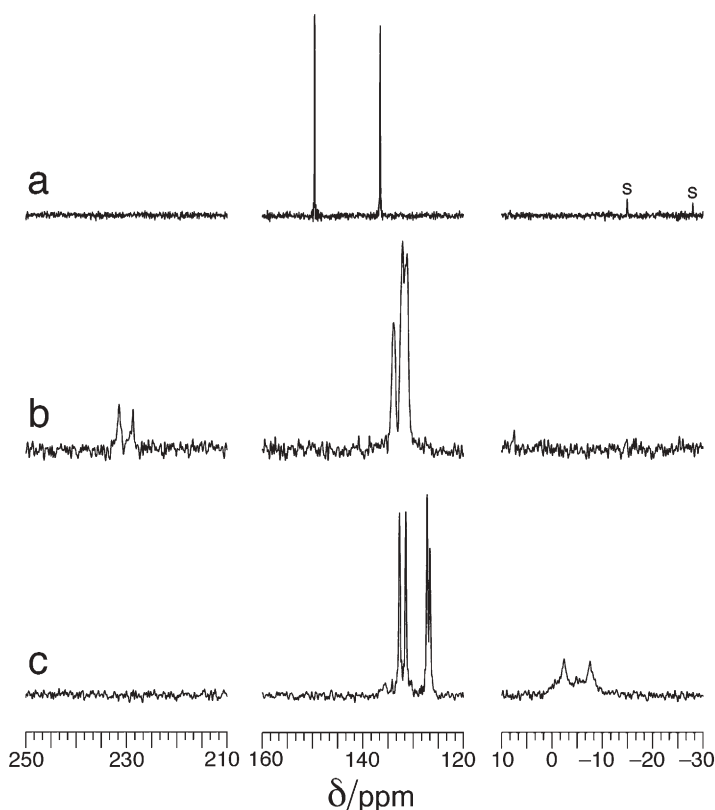
Fig. 19a–c 36.48 MHz ^{15}N CP/MAS NMR spectra of the polycrystalline systems (number of signal transients/MAS frequency (Hz)): **a** [Zn$_2$\{S$_2$CN(C$_2$H$_5$)$_2$\}$_4$] (3740/6000); **b** [Zn\{C$_5$H$_5$N\}\{S$_2$CN(C$_2$H$_5$)$_2$\}$_2$] (17600/6000); **c** [Zn\{NH(CH$_2$)$_4$O\}\{S$_2$CN(C$_2$H$_5$)$_2$\}$_2$] (41027/6000). Spinning sidebands are marked by 's'

non-aromatic and non-planar (the 'chair' formation) morpholine molecules coordinated to zinc atoms in the two isomorphs. Note that the structures of α- and β-**35** are very different (see Fig. 22) (i) the α-isomer has an almost square-pyramidal geometry, while the β-isomer exhibits a pronounced distortion towards a trigonal bipyramidal coordination, (ii) the Zn-N chemical bonds are significantly different (2.077(5) in the α-form and 2.106(5) Å in the β-form), (iii) in spite of both coordinated morpholine molecules adopting the expected chair formation, the spatial orientation modes of these molecules are very different. In the α-isomer, the bisecting plane passing through atoms C2, Zn1, N1 and C1 is almost perpendicular (85.4(4)°) to the plane defined by C11, C12, C13, and C14 (see Fig. 22a), while the analogous planes of the β-isomer form an acute angle of only 9.7(4)°. This conformational isomerism with the two forms of adduct **35** correlated as rotation isomers has been clearly revealed by ^{15}N CP/MAS NMR, as two somewhat broadened resonance lines (1:1) with chem-
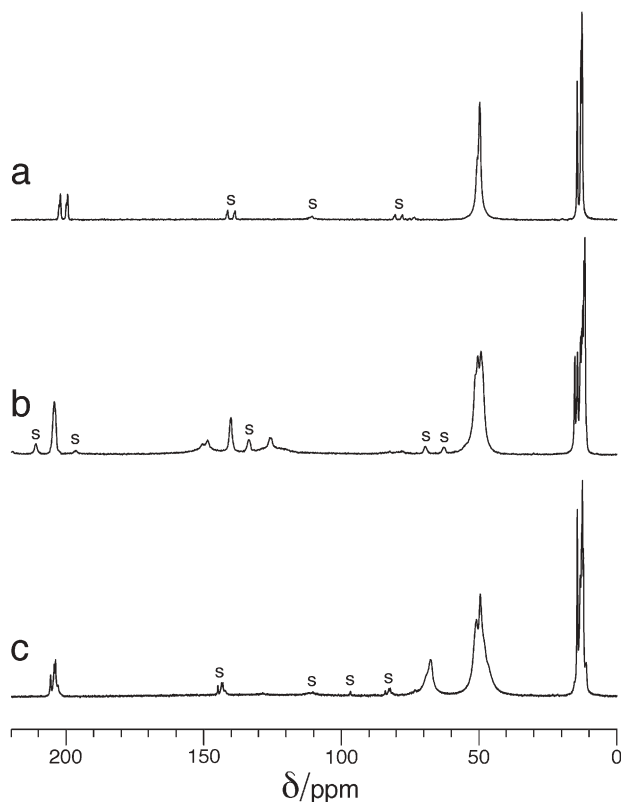
Fig. 20a–c 90.52 MHz ^{13}C CP/MAS NMR spectra of the polycrystalline systems (number of signal transients/MAS frequency (Hz)): **a** [Zn$_2${S$_2$CN(C$_2$H$_5$)$_2$}$_4$] (256/5500); **b** [Zn{C$_5$H$_5$N} {S$_2$CN(C$_2$H$_5$)$_2$}$_2$] (1536/6400); **c** [Zn{NH(CH$_2$)$_4$O}{S$_2$CN(C$_2$H$_5$)$_2$}$_2$] (2048/5500). Spinning sidebands are marked by 's'

ical shifts equal to –2.3 and –7.5 ppm can be putatively assigned to α- and β-isomers, respectively (note that the ^{15}N chemical shift of pure liquid morpholine is equal to –8.9 ppm [113]). This assignment has been made on the observed empirical correlation between the Zn-N bond length and ^{15}N chemical shift of the nitrogen site of the coordinated morpholine molecule in adduct **35** and its solvates (see the following section and Table 6). The degree of deshielding increases with a decrease in the Zn-N bond length (for example, for compound **44**, the Zn-N bond length is equal to 2.061(6) Å and δ(^{15}N)=0.5 ppm [85]).
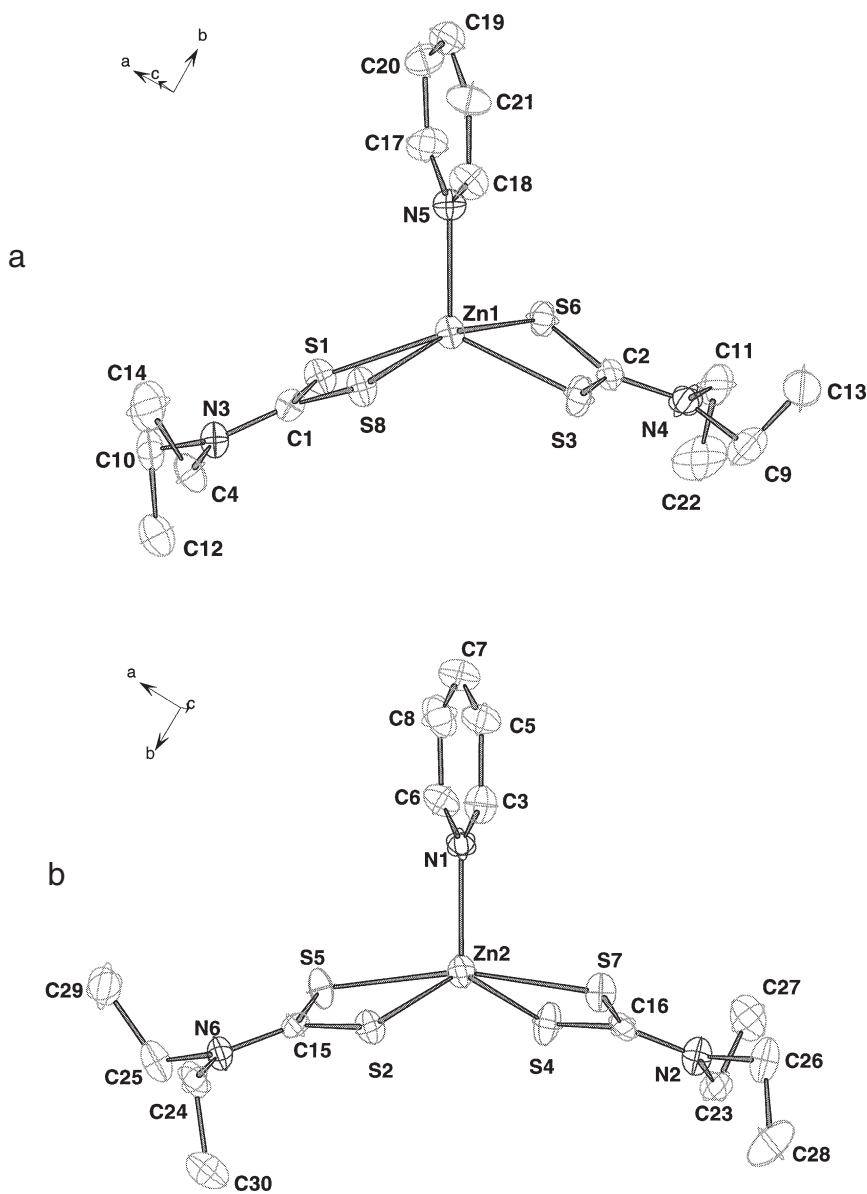
Fig. 21a, b ORTEP diagrams (ellipsoids at 50% probability level) of $[Zn\{C_5H_5N\}\{S_2CN(C_2H_5)_2\}_2]$: **a** α-form; **b** β-form
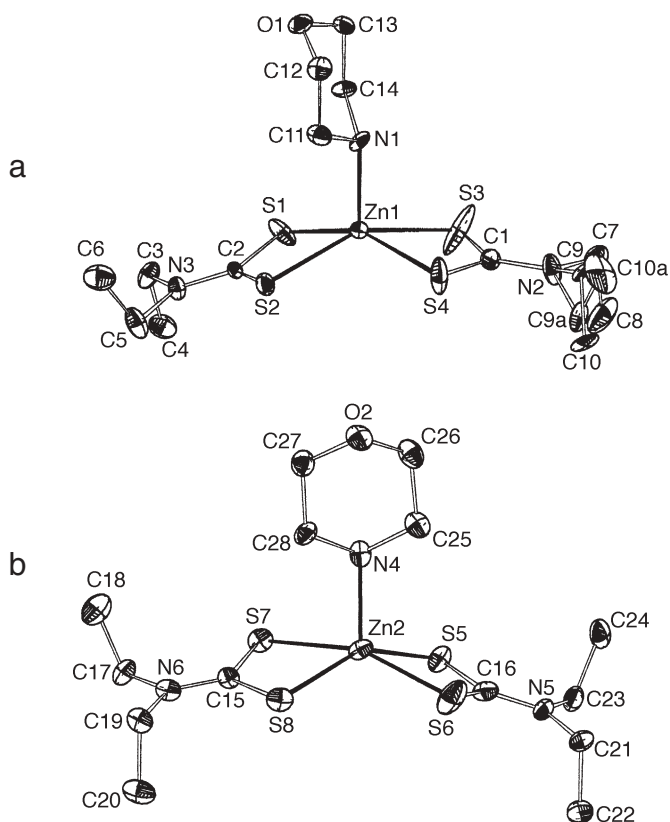
Fig. 22a, b ORTEP diagrams (ellipsoids at 50% probability level) of [Zn{NH(CH$_2$)$_4$O}{S$_2$CN (C$_2$H$_5$)$_2$}$_2$]: **a** α-isomer; **b** β-isomer

2.6
Solvated Forms of Adducts of Dialkyldithiocarbamate Zinc(II) Complexes

Our recent studies [74–76, 85–93] show that almost all prepared polycrystalline adducts of zinc(II)-dithiocarbamates (see previous section) may form solvates, i.e. incorporating small 'guest' molecules such as benzene, various chlorohydrocarbons and N-donor bases, which are held by van-der-Waals forces between molecules of the 'host' compound. X-ray diffraction studies [85–91, 93] have revealed an ordered system of molecular channels occupied by outer-sphere guest molecules in the crystal lattice of solvated forms of the adducts (see Fig. 23), i.e., clathrate type structures.

Persistent interest in studying the clathrate systems is largely caused by the great diversity of areas of their practical application. They can be used in efficient fine purification of substances, in isomer separation [95, 96], in the development of energy-saving water desalination technologies, etc. In recent
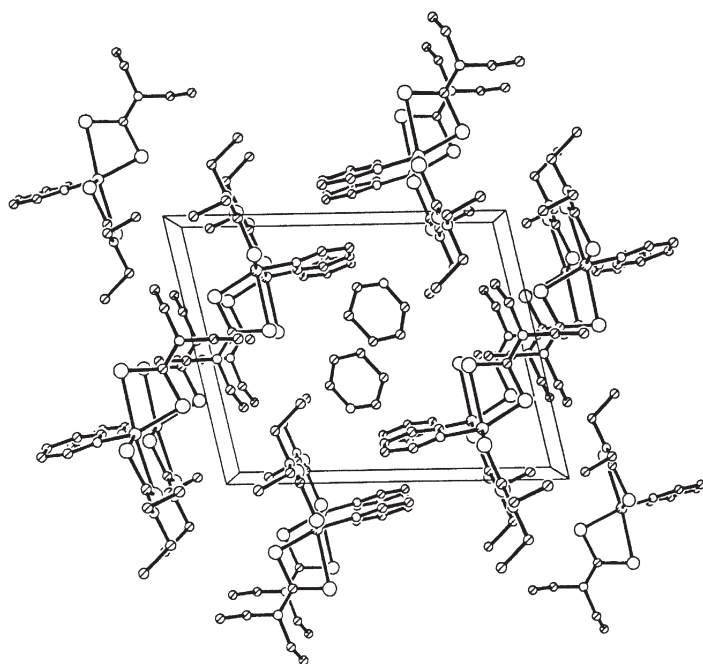
Fig. 23 Perspective view of the molecular channel populated by outer-sphere solvating pyridine molecules in the structure of $[Zn(C_5H_5N)\{S_2CN(C_2H_5)_2\}_2]\cdot C_5H_5N$

years, this interest has been stimulated by the practice of using clathrate-type compounds in the exploitation of gas deposits, and by the associated problems of gas pipeline maintenance under northern conditions. Clathrate structures at the molecular level, or in a host crystal structure, are generally characterized by the presence of ordered molecular cavities for the accommodation of guest molecules, where the latter are held by the hydrogen bonds [97, 98] or/and relatively weak van der Waals forces [99]. Moreover, the formation of clathrates can also substantially modify the physicochemical characteristics of the guest molecules [100]. As for the effect of guest molecules on the structure of the hosts at a molecular level, this problem has been very poorly investigated to date.

To study the perturbing effect of solvating molecules, such as C_6H_6, CH_2Cl_2, $CHCl_3$, CCl_4, $1,2-C_2H_4Cl_2$, C_5H_5N and $O(CH_2)_4NH$, on the molecular and crystal structures of adducts, solvated forms of a variety of zinc(II) dithiocarbamate adducts (see Tables 5 and 6) have been prepared and investigated by means of CP/MAS ^{13}C and ^{15}N NMR spectroscopy, and by single-crystal X-ray diffraction [74–76, 85–93]. These studies have shown that crystalline *bis*(diethyldithiocarbamato)pyridinezinc(II) (compound **34**) can easily form various solvated complexes, $[Zn(C_5H_5N)\{S_2CN(C_2H_5)_2\}_2]\cdot L$ (compounds **36–42**, see Table 5), where L are outer-sphere solvating molecules. Interestingly, compared with the original adduct **34**, its solvated forms are characterized by simpler ^{13}C and ^{15}N

Table 5 ^{13}C and ^{15}N chemical shifts (ppm) of solvated forms of *bis*(diethyldithiocarbamato)pyridinezinc(II), [Zn{C$_5$H$_5$N}{S$_2$CN(C$_2$H$_5$)$_2$}$_2$]·L, relative to TMS (^{13}C) and NH$_4$Cl(^{15}N)

Complex	–S(S)CN(C$_2$H$_5$)$_2$				C$_5$H$_5$N				L
	>NC(S)S–	>NCH$_2$–	–CH$_3$	>N–	o-CH–	m-CH–	p-CH–	>N–	=C=
36. [Zn(C$_5$H$_5$N){S$_2$CNR$_2$}$_2$]· C$_5$H$_5$N [87]	203.1 (70)^a	49.4 (55)^a (1:1)	13.0; 12.4; 11.6 (1:2:1)	134.9 132.7 (1:1)	150.0 150.0	126.3 123.9 (1:1)	140.8 135.3 (1:1)	227.1 279.7	
37. [Zn(C$_5$H$_5$N){S$_2$CNR$_2$}$_2$]· C$_6$H$_6$ [86]	203.4 (70)^a 202.4 (1:1)	49.6 (60)^a	12.2; 11.4 (3:1)	135.0 132.8 (1:1)	149.7	125.5	140.3	226.9	128.4
38. [Zn(C$_5$H$_5$N){S$_2$CNR$_2$}$_2$]· CH$_2$Cl$_2$ [88]	203.1	49.1	13.1; 12.5; 11.9	135.7 131.3 (1:1)	150.4	126.4	140.4	225.2	55.0
39. [Zn(C$_5$H$_5$N){S$_2$CNR$_2$}$_2$]· 1/2 CHCl$_3$ [88]	202.5 (75)^a	48.8 (40)^a	13.5; 12.9; 12.0 (1:2:1)		150.1	127.2	140.5		81.0
40. [Zn(C$_5$H$_5$N){S$_2$CNR$_2$}$_2$]· CHCl$_3$ [88]	202.9	49.1	13.0, 12.1	136.2 131.6 (1:1)	149.9	126.7	140.2	226.1	80.8
41. [Zn(C$_5$H$_5$N){S$_2$CNR$_2$}$_2$]· 2CCl$_4$ [90, 91]	201.6 (38)^a	50.7; 49.8 (1:1)	14.0; 12.9 (1:1)	134.7	148.4	127.2	144.0	228.6	96.9

Table 5 (continued)

Complex	-S(S)CN(C₂H₅)₂				C₅H₅N				L =C=
	>NC(S)S-	>NCH₂-	-CH₃	>N-	o-CH-	m-CH-	p-CH-	>N-	=C=
42. [Zn(C₅H₅N){S₂CNR₂}₂]· 1,2-C₂H₄Cl₂ [89]	205.6 203.8 (1:1)	49.6; 49.2 (1:1)	14.9; 13.2; 12.4 (1:2:1)	130.4 128.4 (1:1)	150.2	126.2	141.8	225.6	52.9 52.1 (1:1)
C₅H₅N [78]					149.7	123.6	135.5	258.0[b]	128.5
C₆H₆ [94]									54.0
CH₂Cl₂ [94]									77.2
CHCl₃ [94]									96.0
CCl₄ [94]									

[a] ¹³C-¹⁴N asymmetric doublets (in Hz).
[b] On the absolute ¹⁵N scale, δ(¹⁵N, pyridine) = –83.0 ppm [38, 39], which corresponds to 258.0 ppm from NH₄Cl.

Table 6 ^{13}C and ^{15}N chemical shifts (ppm) of solvated forms of *bis*(dialkyldithiocarbamato)zinc(II) adducts with cyclic N-donor bases, [ZnB{S$_2$CNR$_2$}$_2$]·L, relative to TMS (^{13}C) and NH$_4$Cl (^{15}N)

Complex	–S(S)CNR$_2$					C$_5$H$_5$N, (CH$_2$)$_5$NH, O(CH$_2$)$_5$NH						C$_6$H$_6$ =C=
	>NC(S)S–	>NCH$_2$– or >NCH$_3$	–CH$_2$O–	–CH$_3$	>N–	o–C	m–C	p–C	>NCH$_2$–	–CH$_2$O–	>N–	
43. [Zn(C$_5$H$_5$N){S$_2$CN(CH$_3$)$_2$}$_2$]· 1/2 C$_6$H$_6$ [74]	204.9	47.7, 45.8, 44.4 (1:2:1)			105.7, 105.0 (1:1)	145.9	127.7	142.9, 140.0			226.8	130.3
44. [Zn{O(CH$_2$)$_4$NH}{S$_2$CN(C$_2$H$_5$)$_2$}$_2$]· C$_6$H$_6$ [85]	202.9 (38)^a	49.7		13.0, 12.2, 11.4	135.9, 133.0 (1:1)				46.8	68.9, 68.3	0.5	129.2
45. [Zn{O(CH$_2$)$_4$NH}{S$_2$CN(C$_2$H$_5$)$_2$}$_2$]· O(CH$_2$)$_4$NH [85]	203.2 (46)^a	49.3		13.0, 12.5, 11.5, 11.3	135.6, 131.3 (1:1)				49.7, 46.8 (1:1)	69.1, 67.5 (1:1)	–5.0, –6.3 (1:1)	
46. [Zn{O(CH$_2$)$_4$NH}{S$_2$CN(C$_2$H$_5$)$_2$}$_2$]· C$_5$H$_5$N [92]	203.3	49.2		13.0, 12.6, 11.2	135.2, 131.1 (1:1)	150.2	124.4	135.2	47.1	68.4	271.2, –5.4	
47. [Zn(C$_5$H$_5$N){S$_2$CN(C$_2$H$_5$)$_2$}$_2$]· O(CH$_2$)$_4$NH [92]	203.3	49.2		13.0, 12.6, 11.2	135.4, 131.2 (1:1)	150.4, 149.8	124.5	139.1	46.8	68.8, 67.7	227.6, –5.8	
48. [Zn{(CH$_2$)$_5$NH}{S$_2$CN(C$_2$H$_5$)$_2$}$_2$]· C$_6$H$_6$ [75]	203.4 (46)^a 202.6	49.3		12.5, 12.0, 11.0	135.8, 132.6 (1:1)	46.9	28.2	25.2			7.5	128.7

Table 6 (continued)

Complex	-S(S)CNR₂					C₅H₅N, (CH₂)₅NH, O(CH₂)₅NH						C₆H₆ =C=
	>NC(S)S-	>NCH₂- or >NCH₃	-CH₂O-	-CH₃	>N-	o-C	m-C	p-C	>NCH₂-	-CH₂O-	>N-	
49. [Zn{(CH₂)₅NH}{S₂CN(C₂H₅)₂}₂]·C₅H₅N [75]	202.8 (44)ᵃ	48.8		13.1 12.6 12.0 10.5	135.0 132.1 (1:1)	46.8 150.3	27.1 124.3	25.8 136.8	49.0			-3.7 271.5
50. [Zn{(CH₂)₅NH}{S₂CN(C₂H₅)₂}₂]·O(CH₂)₄NH [75]	203.4	49.0		12.6 12.2 11.6 11.0	135.4 131.0 (1:1)	47.3	28.6	26.3	49.0	68.8 67.6	-4.9 -1.0	
51. [Zn{O(CH₂)₄NH}{S₂CN(CH₂)₄O}₂]·O(CH₂)₄NH [93]	205.4 203.9 (1:1)	53.2 52.4 (3:1)	68.5 67.7 (1:1)		118.8 112.3 (1:1)				47.9 47.3 (1:1)	66.5 65.8 (1:1)	-8.0 -2.2 (1:1)	

ᵃ ¹³C–¹⁴N asymmetric doublets (in Hz).
ᵇ On the absolute ¹⁵N scale δ(¹⁵N) = −83.0 ppm for pyridine [38, 39], which corresponds to 258.0 ppm from NH₄Cl.
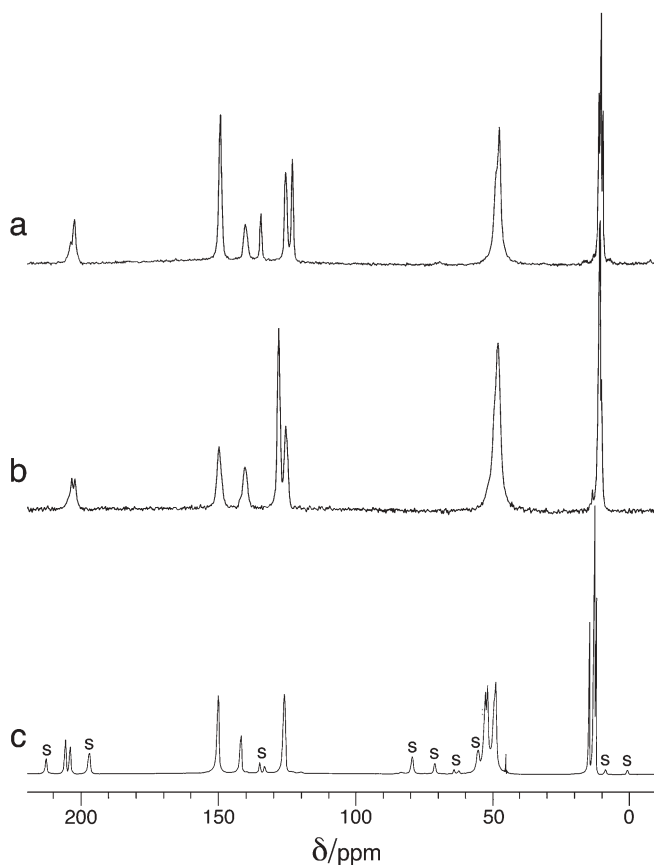
Fig. 24a–c 90.52 MHz ^{13}C CP/MAS NMR spectra of the polycrystalline solvated forms of *bis*(diethyldithiocarbamato)pyridinezinc(II) (number of signal transients/MAS frequency (Hz)): **a** [Zn(C$_5$H$_5$N){S$_2$CN(C$_2$H$_5$)$_2$}$_2$]·C$_5$H$_5$N (18400/6000); **b** [Zn(C$_5$H$_5$N){S$_2$CN(C$_2$H$_5$)$_2$}$_2$]· C$_6$H$_6$ (18400/6000); **c** [Zn(C$_5$H$_5$N){S$_2$CN(C$_2$H$_5$)$_2$}$_2$]· 1,2-C$_2$H$_4$Cl$_2$ (1540/6400). Spinning sidebands are marked by 's'

CP/MAS NMR spectra (see Figs. 24, 25, and 26). ^{13}C NMR spectra of polycrystalline compounds **36–42** (Figs. 25 and 26) show resonance signals from the >NC(S)S–, –CH$_2$– and –CH$_3$ groups of diethyldithiocarbamate ligands, the aromatic carbon sites of the coordinated pyridine molecules (*ortho* : *para* : *meta*=2:1:2) and the C-sites of solvating outer-sphere molecules of either benzene, pyridine or various chlorohydrocarbons. Either one or two closely spaced ^{13}C resonance lines assigned to carbon sites in >NC(S)S– groups, point to a possible structural equivalence or similarity of the ligands (see Figs. 24 and 25). In some spectra (Figs. 25a,c), ^{13}C resonances from *ortho*- and *meta*-carbon atoms of the coordinated pyridine molecules are considerably broader than the resonance line assigned to carbon sites in the *para*-position. Observed broadening can be caused by molecular dynamics, rotations or large-angle librations of
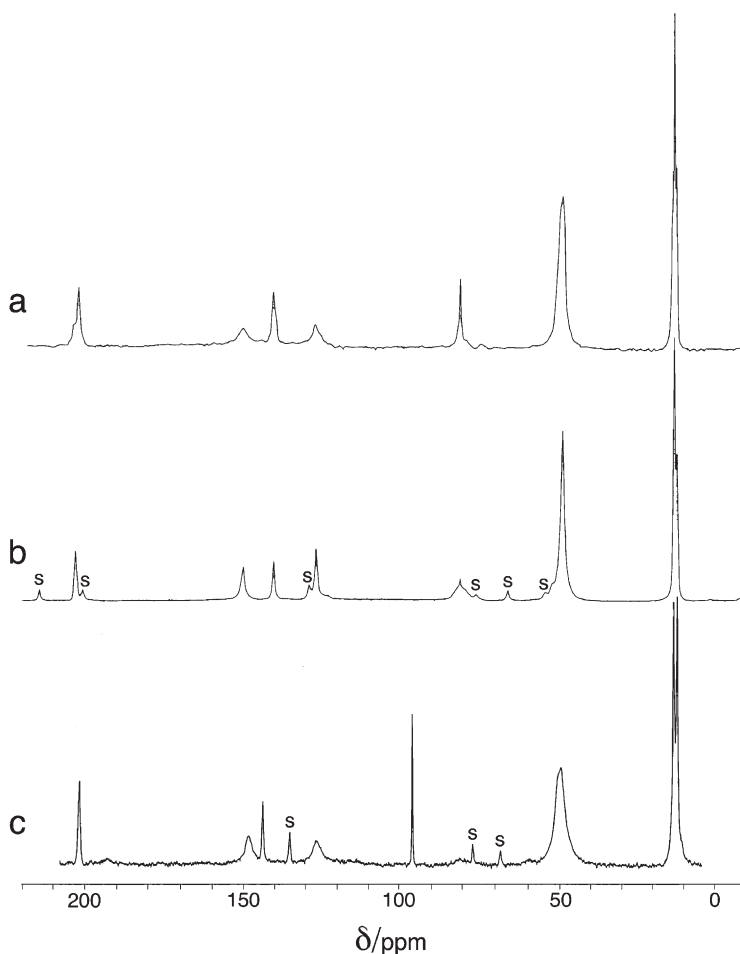
Fig. 25a–c 90.52 MHz ^{13}C CP/MAS NMR spectra of the polycrystalline solvated forms of *bis*(diethyldithiocarbamato)pyridinezinc(II) (number of signal transients/MAS frequency (Hz)): **a** [Zn(C$_5$H$_5$N){S$_2$CN(C$_2$H$_5$)$_2$}$_2$]·(1/2)CHCl$_3$ (9200/6700); **b** [Zn(C$_5$H$_5$N){S$_2$CN(C$_2$H$_5$)$_2$}$_2$]· CHCl$_3$ (2560/6000); **c** [Zn(C$_5$H$_5$N){S$_2$CN(C$_2$H$_5$)$_2$}$_2$]·2CCl$_4$ (2056/4000). Spinning sidebands are marked by 's'

the pyridine heterocycle about the Zn-N bond at 295 K. It should also be noted that the ^{13}C chemical shift of the *para*-carbon atom is the most sensitive to the formation of the Zn-N bond (see Table 5).

The ^{15}N CP/MAS NMR spectra of the solvated adducts **36–42** (see Fig. 26) show one or two resonance lines assigned to nitrogen sites in diethyldithio-carbamate ligands (128.4–136.2 ppm) and single N-resonances from coordi-nated pyridine molecules (225.2–228.6 ppm). Therefore, diethyldithiocarba-mate ligands are spectrally slightly nonequivalent in most of the solvated forms of the adducts, with the single exception of [Zn(C$_5$H$_5$N){S$_2$CN(C$_2$H$_5$)$_2$}$_2$]·2CCl$_4$,
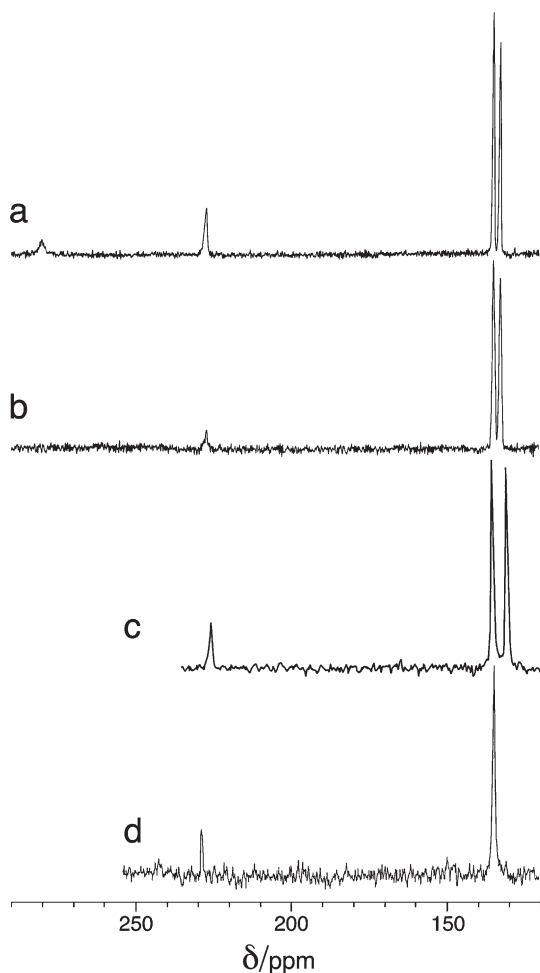
Fig. 26a–d 36.48 MHz ^{15}N CP/MAS NMR spectra of the polycrystalline solvated forms of *bis*(diethyldithiocarbamato)pyridinezinc(II) (number of signal transients/MAS frequency (Hz)): **a** [Zn(C$_5$H$_5$N){S$_2$CN(C$_2$H$_5$)$_2$}$_2$]·C$_5$H$_5$N (17600/6000); **b** [Zn(C$_5$H$_5$N){S$_2$CN(C$_2$H$_5$)$_2$}$_2$]· C$_6$H$_6$ (17600/6000); **c** [Zn(C$_5$H$_5$N){S$_2$CN(C$_2$H$_5$)$_2$}$_2$]·CHCl$_3$ (25200/6000); **d** [Zn(C$_5$H$_5$N){S$_2$CN (C$_2$H$_5$)$_2$}$_2$]·2CCl$_4$ (15300/6000)

compound **41**. A considerable decrease in the ^{15}N chemical shift of the pyridine molecule by 30–33 ppm (compared to liquid pyridine) upon formation of the Zn-N bond in both the non-solvated and solvated forms of the adducts, points to an increase of electronic shielding of the nitrogen nucleus in the coordinated pyridine molecules, as discussed previously. ^{15}N NMR data for compound **36**, [Zn(C$_5$H$_5$N){S$_2$CN(C$_2$H$_5$)$_2$}$_2$]·C$_5$H$_5$N, which includes both coordinated and solvating pyridine molecules, permitted us to denote a large difference (by more than 50 ppm) in the ^{15}N chemical shift values of the two structurally different

Py molecules. The nitrogen nucleus of the solvating molecule is essentially more deshielded compared to both coordinated and free pyridine. Therefore, ^{15}N NMR shows a very high sensitivity to different structural functions of pyridine molecules in adduct and solvate compounds.

From the analysis of both ^{13}C and ^{15}N NMR spectra, one can conclude that the solid-state solvation of compound **34**, [Zn(C$_5$H$_5$N){S$_2$CN(C$_2$H$_5$)$_2$}$_2$] leads to a profound structural reorganization of the original adduct at the molecular level. This includes the structural unification of two rotation isomers of adducts yielding a qualitatively new structural state. The single-crystal X-ray diffraction analysis has clarified the essence of this structural reorganization. As expected, all solvated forms of *bis*(diethyldithiocarbamato)pyridinezinc(II), **36–42**, exist as a single molecular form, in contrast to the two isomeric forms of the original crystalline non-solvated adduct **34** (see Figs. 21, 27, 28 and 29). XRD results obtained for the original adduct **34** and its solvated forms **36–42** allow one to conclude that solvation brings about a profound structural reorganization at several levels: (i) supramolecular, (ii) molecular, and (iii) local. These are described in more detail below:

(i) The course of solvation in the crystal lattice of the original adduct **34** is accompanied by the formation of a system of ordered molecular channels occupied by the outer-sphere solvating molecules (see Fig. 23), i.e., lattice structures of the clathrate type. The solvation of [Zn(C$_5$H$_5$N){S$_2$CN (C$_2$H$_5$)$_2$}$_2$] substantially simplifies the unit cell structure. The Z value decreases from 8 (in **34**) to 2–4 (in solvated forms **36–42**) and renders all molecules of the host complex structurally equivalent.
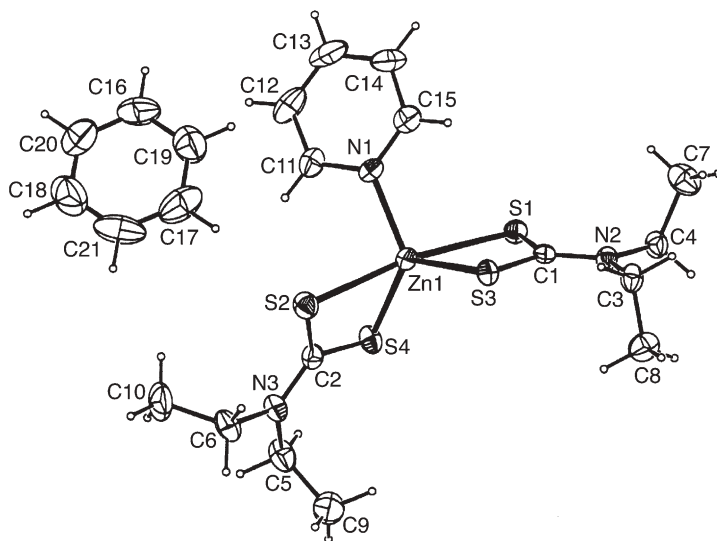
Fig. 27 Molecular structure of [Zn(C$_5$H$_5$N){S$_2$CN(C$_2$H$_5$)$_2$}$_2$]·C$_6$H$_6$ (ellipsoids at 50% probability level)
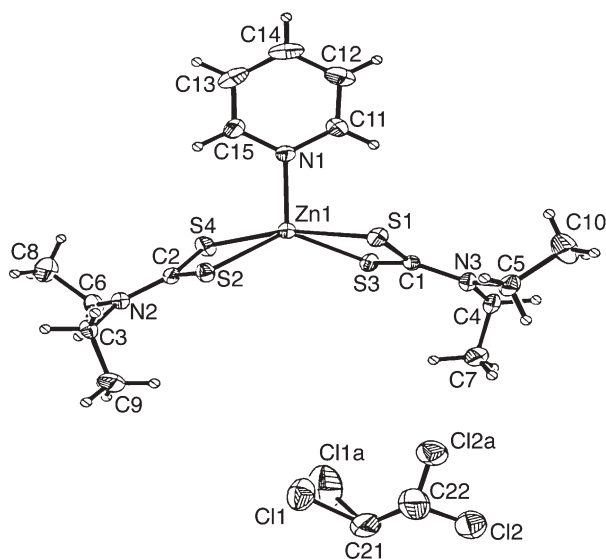
Fig. 28 Molecular structure of $[Zn(C_5H_5N)\{S_2CN(C_2H_5)_2\}_2]\cdot1,2\text{-}C_2H_4Cl_2$ (ellipsoids at 50% probability level)

(ii) At the molecular level, solvation results in the unification of the molecular structures of the two isomeric forms of the original non-solvated adduct **34,** leading to the transition of this molecular system to qualitatively new structural states (see Figs. 27–29).

(iii) The local level is characterized by the reorientation of the pyridine ring plane from the position nearly perpendicular to the root-mean-square bisecting plane (in **34**) (Figs. 29a,b) to a position, which is either nearly coplanar with the aforementioned bisecting plane (in compound **42**) (Fig. 29d) or adjusts to intermediate positions (in compounds **36–41**, see Fig. 29c).

Compared to adduct **34,** which forms two isomeric molecules in the crystalline state, its dimethyl substituted analog, $[Zn(C_5H_5N)\{S_2CN(CH_3)_2\}_2]$ (**28**), exists as only one and is a highly symmetrical molecule with two structurally equivalent dimethyldithiocarbamate ligands [74] (see Fig. 16a and Table 4). However, the solvation of this adduct with benzene, $[Zn(C_5H_5N)\{S_2CN(CH_3)_2\}_2]\cdot(1/2)C_6H_6$ (**43**), yields some structural nonequivalence of dithiocarbamate ligands (see Table 6, >N– sites) and an increase of the ^{15}N chemical shift of coordinated pyridine molecules by more than 8 ppm (see Tables 4 and 6).

As already discussed, like the crystalline adduct of *bis*(diethyldithio carbamato)zinc(II) with pyridine, $[Zn\{C_5H_5N\}\{S_2CN(C_2H_5)_2\}_2]$ (**34**), a corresponding adduct with a non-planar N-donor morpholine molecule, $[Zn\{O(CH_2)_4NH\}\{S_2CN(C_2H_5)_2\}_2]$ (**35**), exists as two conformers which are cor-
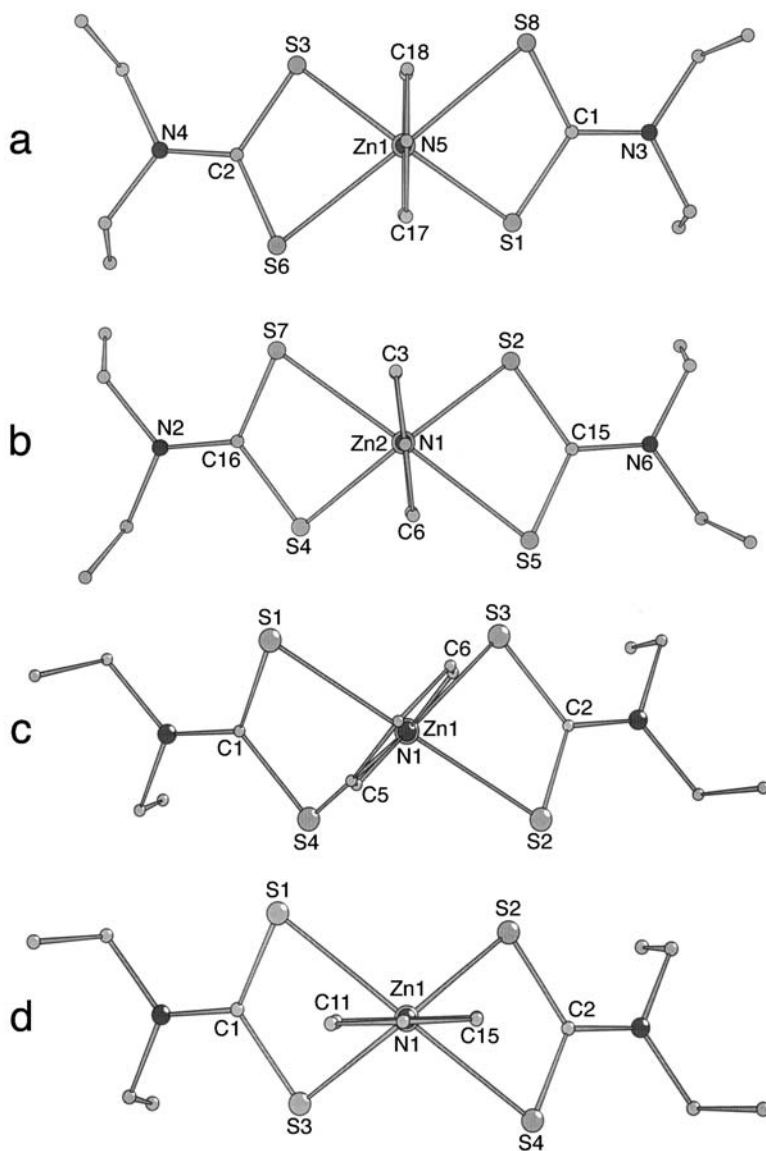
Fig. 29a–d Projections of the molecular structures of: **a** α-form; **b** β-form of the adduct [Zn(C$_5$H$_5$N){S$_2$CN(C$_2$H$_5$)$_2$}$_2$], and its solvated forms: **c** [Zn(C$_5$H$_5$N){S$_2$CN(C$_2$H$_5$)$_2$}$_2$]·C$_5$H$_5$N; **d** [Zn(C$_5$H$_5$N){S$_2$CN(C$_2$H$_5$)$_2$}$_2$]·1,2-C$_2$H$_4$Cl$_2$ onto the plane perpendicular to the vector of the N-Zn bond

related as rotation isomers. Solvation of the adducts studied in the solid state, using benzene (**44**) and morpholine (**45**), leads to significant structural reorganization at the molecular level, i.e. their structural unification yields qualitatively new structural states, which are characterized principally by different ^{13}C and ^{15}N NMR spectra (see Fig. 30 and Fig. 31). Each of these spectra includes a single ^{13}C resonance line (Fig. 30) and two ^{15}N resonance lines (Fig. 31), assigned to carbon and nitrogen sites in >NC(S)S– groups, and a single ^{15}N resonance line from the coordinated morpholine molecules. Additionally, ^{13}C and /or ^{15}N NMR spectra show a ^{13}C resonance line from six structurally equivalent carbon atoms of guest benzene molecules in **44** (129.2 ppm, Fig. 30b, Table 6) and an additional ^{15}N resonance line from solvating morpholine molecules in **45** (Fig. 31a, Table 6). This proves the existence of solvated forms of *bis*(diethyldithiocarbamato)morpholinezinc(II) with outer-sphere molecules of benzene or morpholine, (compounds **44** and **45**) in unique molecular forms.

Compared to the original adduct **35**, single-crystal X-ray diffraction studies of its solvated forms **44** and **45,** revealed clathrate type structures, i.e., the pres-
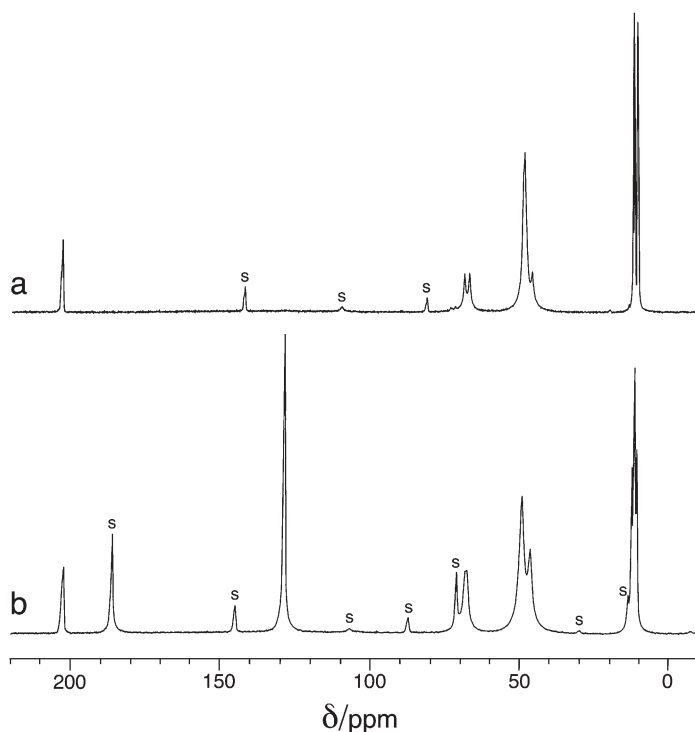
Fig. 30a, b 90.52 MHz ^{13}C CP/MAS NMR spectra of the polycrystalline solvated forms of *bis*(diethyldithiocarbamato)morpholinezinc(II): **a** [Zn{O(CH$_2$)$_4$NH}{S$_2$CN(C$_2$H$_5$)$_2$}$_2$]·O(CH$_2$)$_4$NH; **b** [Zn{O(CH$_2$)$_4$NH}{S$_2$CN(C$_2$H$_5$)$_2$}$_2$]·C$_6$H$_6$. The MAS frequency was 5.5 kHz. The number of signal transients was 2048. Spinning sidebands are marked by 's'
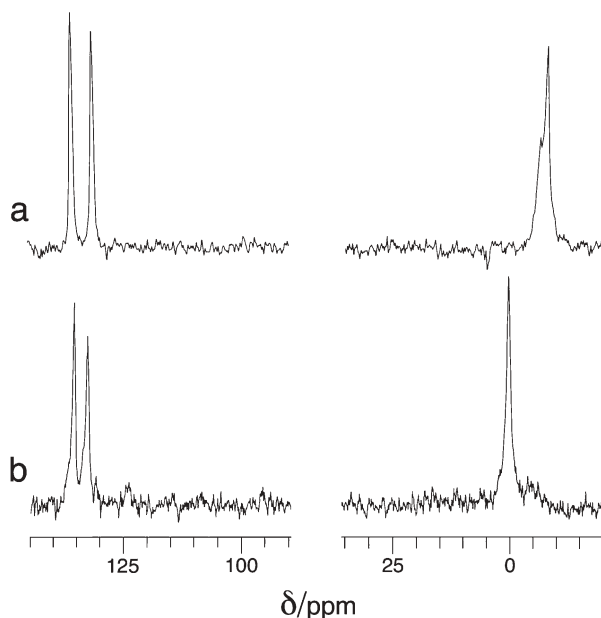
Fig. 31a,b 36.48 MHz ^{15}N CP/MAS NMR spectra of the polycrystalline solvated forms of *bis*(diethyldithiocarbamato)morpholinezinc(II): **a** [Zn{O(CH$_2$)$_4$NH}{S$_2$CN(C$_2$H$_5$)$_2$}$_2$]· O(CH$_2$)$_4$NH; **b** [Zn{O(CH$_2$)$_4$NH}{S$_2$CN(C$_2$H$_5$)$_2$}$_2$]·C$_6$H$_6$ (sum of 15200 (a) and 16800 (b) signal transients). The MAS frequency was equal to 6.0 kHz

ence of molecular channels populated by the outer-sphere solvating molecules of benzene or morpholine in the crystalline lattice. Moreover, at the molecular level, the following structural differences in compounds **35** (Fig. 22), **44** (Fig. 32), and **45** (Fig. 33) have been established: (i) different lengths of the Zn-N bond, (ii) reoriented position of the heterocyclic ring of the coordinated morpholine molecule, and (iii) enhanced contribution of the trigonal-bipyramidal character to the geometry of the coordination polyhedra of the central atom (from 7.5 and 22.7% – in the two polymorphs of the original adduct **35** to ~75% – in the solvated compounds **44** and **45**). The geometry of the coordination polyhedra in the solvated forms of the adduct is intermediate between the trigonal bipyramid – D$_{3h}$ and the square pyramid – C$_{4v}$.

The solvation of adduct **33** [Zn{O(CH$_2$)$_4$NH}{S$_2$CN(CH$_2$)$_4$O}$_2$] with morpholine also produces an increase in the structural nonequivalence of morpholinedithiocarbamate ligands in the solvated adduct **51**, [Zn{O(CH$_2$)$_4$NH} {S$_2$CN(CH$_2$)$_4$O}$_2$]·O(CH$_2$)$_4$NH (Table 6) [93]. Note that in compound **51,** there are three types of morpholine molecules/groups, which have different structural functions (i) as morpholinedithiocarbamate ligands (ii) as morpholine coordinated to zinc and (iii) as guest molecules of morpholine in the solvated adduct. All these types of functionally different morpholine molecules have been readily distinguished and assigned by ^{15}N CP/MAS spectroscopy (see Table 6).
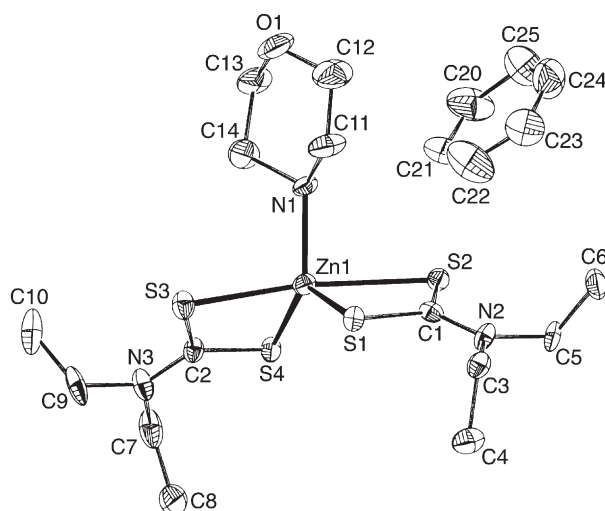
Fig. 32 ORTEP diagram (ellipsoids at 50% probability level) of [Zn{O(CH$_2$)$_4$NH}{S$_2$CN(C$_2$H$_5$)$_2$}$_2$]·C$_6$H$_6$

Like benzene and various chlorohydrocarbon molecules, N-donor bases also participate in the solvation of different crystalline adducts [85, 87, 93]. For example, crystalline solvated adducts [Zn{C$_5$H$_5$N}{S$_2$CN(C$_2$H$_5$)$_2$}$_2$]·C$_5$H$_5$N (**36**) [87], [Zn{O(CH$_2$)$_4$NH}{S$_2$CN(C$_2$H$_5$)$_2$}$_2$]·O(CH$_2$)$_4$NH (**45**) [85] and [Zn{O(CH$_2$)$_4$NH}{S$_2$CN(CH$_2$)$_4$O}$_2$]·O(CH$_2$)$_4$NH (**51**) [93] have been successfully synthesized. The bases in these solvated forms of adducts have different structural functions; one of the molecules is directly coordinated to the central atom,
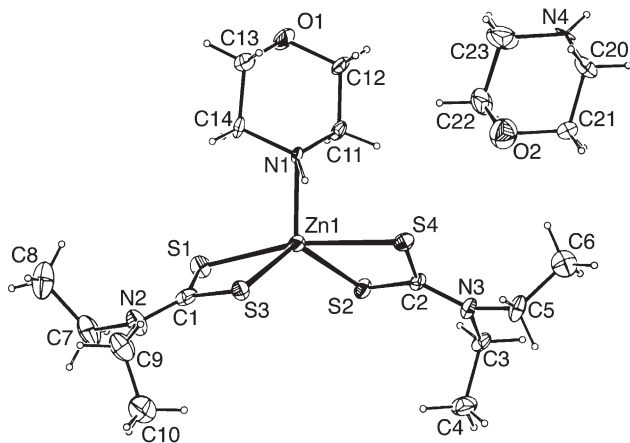
Fig. 33 ORTEP diagram (ellipsoids at 50% probability level) of [Zn{O(CH$_2$)$_4$NH}{S$_2$CN(C$_2$H$_5$)$_2$}$_2$]·O(CH$_2$)$_4$NH

while the second molecule is in the outer sphere. In the course of preparation, introduction of different base molecules into the composition of solvated adducts may give rise to samples with different variants of distribution of these molecules between the inner and outer coordination spheres (compounds **46**, **47**, **49** and **50**, see Table 6). Similar compounds incorporating the same pair of bases, which are different in their structural function, are called solvation isomers (**46, 47**). The best way to prepare this type of solvated adduct is to use an additional quantitative absorption of N-donor bases by the polycrystalline samples of the initial adducts $[Zn(B)\{S_2CN(C_2H_5)_2\}_2]$ (B=C_5H_5N, $O(CH_2)_4NH$, $(CH_2)_5NH$). Solvates of the composition $[Zn(B)\{S_2CN(C_2H_5)_2\}_2]\cdot B'$ (B'=C_5H_5N, $O(CH_2)_4NH$) have been prepared using this method [92] (see Table 6). Experimental NMR spectra of these adducts include resonances from both inner-sphere coordinated and outer-sphere solvating molecules of nitrogen-containing bases (Table 6). Figure 34 shows the ^{15}N CP/MAS NMR spectrum of a polycrystalline sample of $[Zn\{(CH_2)_5NH\}\{S_2CN(C_2H_5)_2\}_2]\cdot C_5H_5N$ (**49**) which indicates four different nitrogen sites. Two intermediate ^{15}N resonances (132.1 and 135.0 ppm) arise from structurally different nitrogen sites in >NC(S)S– groups. The other two resonance lines can be assigned to the nitrogen site in the coordinated piperidine molecule (highly shielded, –3.7 ppm) and to N-atoms in the solvating pyridine molecule (poorly shielded, 271.5 ppm).

It is important to note the different chemical shift ranges for the coordinated and solvating pyridine molecules. ^{15}N CP/MAS NMR studies of 14 various solvated and non-solvated pyridine containing adducts permitted us to determine the range of ^{15}N chemical shifts of the coordinated pyridine molecules, $\delta_{iso}(^{15}N)$=225.2–231.7 ppm. While in outer-sphere solvating pyridine molecules, the nitrogen nucleus is considerably less shielded: $\delta(^{15}N)$=271.2–279.7 ppm. Thus, the ^{15}N chemical shift is characterized by high sensitivity to different structural functions of pyridine molecules incorporated into zinc(II)-dialkyldithiocarbamate compounds. This makes it possible to assign both coor-
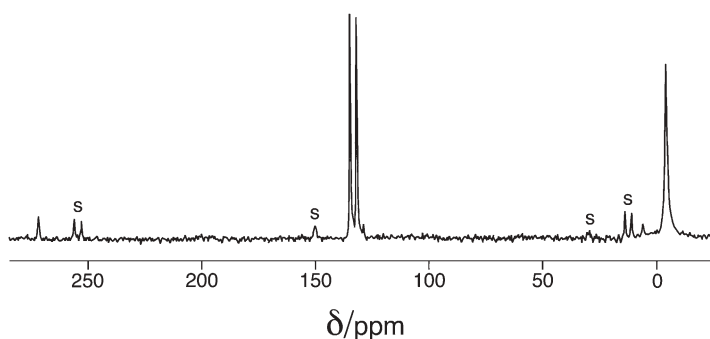
Fig. 34 36.48 MHz ^{15}N CP/MAS NMR spectra of the polycrystalline solvated adduct $[Zn\{(CH_2)_5NH\}\{S_2CN(C_2H_5)_2\}_2]\cdot C_5H_5N$ (sum of 11000 signal transients). The MAS frequency was 4400 Hz. Spinning sidebands are marked by 's'

dinated and solvated pyridine molecules unambiguously using ^{15}N CP/MAS NMR spectroscopy.

2.7
Hysteresis in the Formation Reaction of the Adduct [Zn(C$_5$H$_5$N){S$_2$CN(C$_2$H$_5$)$_2$}$_2$]

As already discussed, the adduct [Zn(C$_5$H$_5$N){S$_2$CN(C$_2$H$_5$)$_2$}$_2$], **34**, has two rotation isomers in the asymmetric unit, assigned as α- and β-conformers [82]. It has been found that the adduct crystallizes in the orthorhombic space group $P2_12_12_1$ (No. 19), based on monomeric units in which the zinc atom coordinates four sulfur (two dithiocarbamate groups) and one nitrogen (pyridine molecule) atoms, forming a coordination polyhedron close to trigonally bipyramidal [82]. Surprisingly, O'Brien et al. have reported that the same adduct, [Zn(C$_5$H$_5$N){S$_2$CN(C$_2$H$_5$)$_2$}$_2$], crystallizes in the other monoclinic space group $P2_1/c$, and is characterized by a unique molecular form [101] with slightly different bond lengths and bond angles from those in the α- and β-**34** rotation isomers. This polymorphism has been clarified by our recent study [83] and the pathway of physico-chemical conditions, in which each of the aforementioned isomers can be prepared, has been identified.

α- and β-**34** isomorphs can be prepared by dissolving equimolar quantities of pyridine and the initial binuclear zinc(II) complex in a minute volume of toluene and isolated by slow evaporation of the solvent [82]. In contrast, O'Brien et al. prepared [Zn(C$_5$H$_5$N){S$_2$CN(C$_2$H$_5$)$_2$}$_2$] by reaction of 2,4,6-C$_6$H$_2$(CH$_3$)$_3$SZnS$_2$CN(C$_2$H$_5$)$_2$ with excess pyridine, from which the adduct was recrystallized [101]. However, it is known that recrystallization of the initial complex [Zn$_2${S$_2$CN(C$_2$H$_5$)$_2$}$_4$] (**19**) from pure pyridine, as well as absorption of C$_5$H$_5$N from the gaseous phase by crystalline samples of **19** in the molar ratio 4:1, both lead to formation of the solvated form of the adduct with an outersphere pyridine molecule, [Zn(C$_5$H$_5$N){S$_2$CN(C$_2$H$_5$)$_2$}$_2$]·C$_5$H$_5$N, **36** [87]. Solvated adduct **36** crystallizes in the same monoclinic space group, $P2_1$ [87], as the adduct [Zn(C$_5$H$_5$N){S$_2$CN(C$_2$H$_5$)$_2$}$_2$] reported by O'Brien et al. [101]. It is noteworthy that the solvated form **36** is not very stable and that a slow desorption of guest pyridine molecules cannot be avoided at room temperature, if crystals of the solvate are not protected by a thin film of glue during X-ray data collection. (The structure of **36** was resolved from X-ray diffraction measurements at 170 K with crystals protected by films of an epoxy glue [87], while O'Brien et al. performed X-ray measurements at 293 K without any particular protection of the crystals [101].) It has been suggested [83] that the [Zn(C$_5$H$_5$N){S$_2$CN(C$_2$H$_5$)$_2$}$_2$] reported by O'Brien et al. is, in fact, a special structural state of the adduct formed from solvate **36**, which has lost, either a large part of or all, its guest pyridine molecules. Interestingly, ^{15}N CP/MAS NMR has played a crucial role in the elucidation of the chemical hysteresis in adduct formation of [Zn(C$_5$H$_5$N){S$_2$CN(C$_2$H$_5$)$_2$}$_2$] (**34**) as will be discussed below.

Figure 35 shows ^{15}N CP/MAS NMR spectra of the polycrystalline zinc(II) diethyldithiocarbamate complex, its adducts and the solvated form with pyridine.

Figure 35a represents the spectrum of the initial polycrystalline binuclear diethyldithiocarbamate zinc(II) complex, $[Zn_2\{S_2CN(C_2H_5)_2\}_4]$, **19**. Two resonances have been assigned previously to two pairs of magnetically equivalent nitrogen sites in bridging (149.6 ppm) and terminal (136.6 ppm) diethyldithiocarbamate ligands [73, 83]. The adduct α/β-**34**, $[Zn(C_5H_5N)\{S_2CN(C_2H_5)_2\}_2]$, recrystallized from toluene, has only terminal ligands (131.3, 132.2, and 133.9 ppm) and two distinct resonances of the adduct pyridine molecules (231.7 and 228.9 ppm, see Fig. 35b), which correspond to two different isomers, α-**34** and β-**34**, in the asymmetric unit cell, as discussed previously (Figs. 21, 29a,b) [82]. After further absorption of pyridine molecules by α/β-**34** (or by recrystallization of **19** from pure pyridine), up to a molar ratio of zinc-to-pyridine equal to 1:2, the solvated species of the adduct, $[Zn(C_5H_5N)\{S_2CN(C_2H_5)_2\}_2]\cdot C_5H_5N$, **36**, is formed. Figure 35c shows the spectrum of **36** with four well resolved nitrogen resonances at 132.7, 134.9 ppm (nitrogen sites in the >NC(S)S groups), 227.1 ppm (coordinated pyridine molecules) and at 279.7 ppm (solvating pyridine molecules, see also Table 5) [83, 87]. X-ray diffraction analysis revealed only one adduct molecule in the unit cell that faithfully correlates with the ^{15}N CP/MAS NMR spectrum of **36** (a single resonance for the coordinated pyridine molecule) [87]. Figure 35d depicts the spectrum of a sample of **36** after partial desorption of pyridine, which was achieved by gentle heating of the sample. The resonance of solvating pyridine molecules at 279.7 ppm has disappeared, and the resonance line of the other (coordinated by Zn) pyridine molecule is shifted from 227.1 (in the solvate **36**) to 230.8 ppm. The latter is close to the mean value of chemical shifts of nitrogen sites in pyridine of the two α- and β-isomers of adduct **34** (compare also with Fig. 35b and Table 4). Furthermore, the chemical shifts of nitrogen sites in diethyldithiocarbamate groups after desorption of pyridine are substantially different from those for both adduct **34** and for the solvated form **36**. It has been suggested [83] that the spectrum shown in Fig. 35d corresponds to the adduct γ-$[Zn(C_5H_5N)\{S_2CN(C_2H_5)_2\}_2]$, with the X-ray diffraction structure reported earlier by O'Brien and co-workers [101]. The presence of a single nitrogen resonance of adduct pyridine in this ^{15}N NMR spectrum suggests a single rotation isomer of **34** in the asymmetric unit. An almost identical ^{15}N NMR spectrum (as in Fig. 35d) has been produced by a sample of **19** after equimolar absorption of pyridine from the gaseous phase, suggesting that the same compound γ-**34** has been formed. However, it is worth noting that three resonance lines ((1:2:1) 130.6, 131.1 and 136.6 ppm) assigned to nitrogen sites in the >NC(S)S moieties suggest the presence of at least two molecules in an asymmetric unit with some nonequivalence of one of the four (in the two molecules) dithiocarbamate ligands. This conclusion is also in accordance with the ^{13}C CP/MAS NMR spectrum for the same compound (see Table 4). Nevertheless, as follows from the assignment of a single resonance line (230.8 ppm) to nitrogen sites in the coordinated C_5H_5N, both orientations of pyridine rings and Zn-N bond lengths in these molecules are, probably, almost identical. This probably misled O'Brien and co-workers to the conclusion that there is only one centrosymmetric mol-
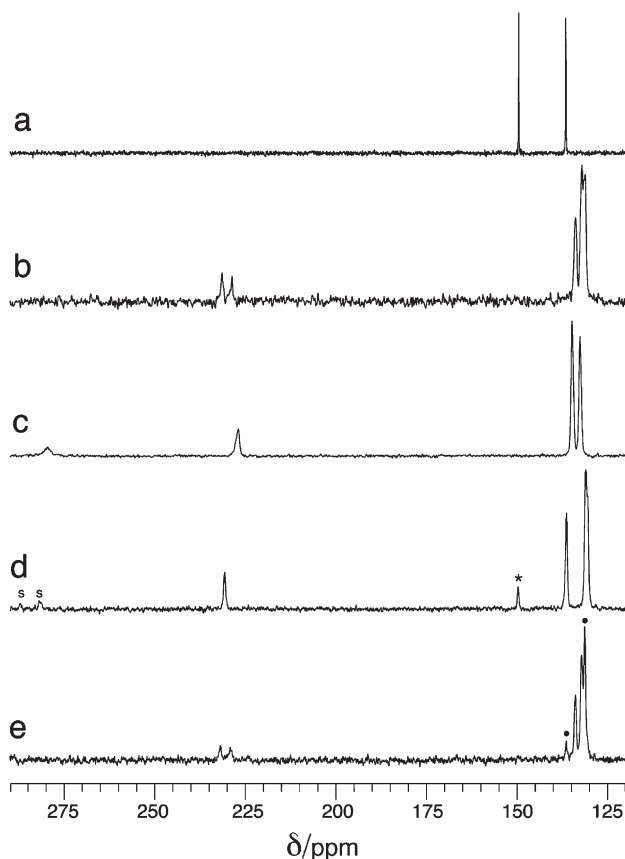
Fig. 35a–e 36.48 MHz ^{15}N CP/MAS NMR spectra of powder samples of the polycrystalline: **a** [Zn$_2$\{S$_2$CN(C$_2$H$_5$)$_2$\}$_4$] (**19**); **b** α,β-[Zn\{C$_5$H$_5$N\}\{S$_2$CN(C$_2$H$_5$)$_2$\}$_2$] (**34**); **c** [Zn\{C$_5$H$_5$N\}\{S$_2$CN (C$_2$H$_5$)$_2$\}$_2$]·C$_5$H$_5$N (**36**); **d** [Zn\{C$_5$H$_5$N\}\{S$_2$CN(C$_2$H$_5$)$_2$\}$_2$]·C$_5$H$_5$N after a partial desorption of pyridine giving rise to γ-**34; e** following recrystallization from the melt giving rise to α,β-**34**. The MAS frequency was 6.0 kHz in (a), (b), (c) and (e) or 5.5 kHz in (d). The number of transients and cross-polarization times were, respectively: (3740, 1.25 ms) (a); (17600, 3.5 ms) (b); (25000, 3.5 ms) (c); (77702, 1.2 ms) (d); and a sum of two spectra with (50000, 1.2 ms) and (25000, 2.4 ms) (e). An admixture of the initial complex (**19**) in (d) and the adduct (γ-**34**) in (e) are labeled as (*) and (·), respectively. 's' in (d) denotes spinning sidebands

ecule of γ-**34** in the asymmetric unit, since X-ray diffraction analysis is still a model dependent method, which encounters difficulties if there is a statistical distribution of different conformations of alkyl groups in these and similar systems. Finally, a simple recrystallization of γ-**34** from the melt has produced a more stable state of the adduct with the two isomers in the asymmetric unit, α- and β-**34**, as can be seen in Fig. 35e.

These results are summarized in the diagram in Fig. 36. The metastable state of the adduct, γ-**34**, is formed by either absorption of pyridine by the initial

complex **19** or by desorption of guest molecules of pyridine from the solvated form **36**. The other state of the adduct with two isomers in the asymmetric unit, α/β-**34**, can be prepared by either slow evaporation of an equimolar solution of **19** and pyridine from toluene or by recrystallization of γ-**34** from the melt. In the latter process, γ-**34**→α/β-**34** (as well as α/β-**34**→**36**) is not directly reversible, since γ-**34** can be obtained from α/β-**34** only through the solvated form **36** (or through the initial complex **19**). This points to chemical hysteresis in the formation of the adduct $[Zn(C_5H_5N)\{S_2CN(C_2H_5)_2\}_2]$.

2.8
Cd(II) and Hg(II) Diethyldithiocarbamate Complexes

Looking at the Periodic Table of elements, it is logical to explore Cd(II) and Hg(II) dithiocarbamate systems next after the Ni(II) and Zn(II) compounds described in the previous sections of this chapter. Interestingly, solid-state NMR opens new possibilities for studies of these systems, since [113]Cd, [111]Cd and [199]Hg are 'magnetic' nuclei (nuclear spin I=1/2) with sufficiently large magnetic moments and relatively high natural abundances (12.75, 12.26, and 16.84 at.%, respectively). From the point of view of coordination chemistry in the solid state, these systems show a larger diversity and polymorphism: dithiocarbamate ligands can form polynuclear, binuclear and/or mononuclear complexes with Cd(II) and Hg(II), depending on alkyl substituents at the nitrogen atom and on solvent properties [102–111]. For example, Fig. 37 shows ^{15}N CP/MAS NMR spectra of mononuclear, $[M\{S_2CN(C_2H_5)_2\}_2]$, M(II)=Ni or Hg, or binuclear, $[M_2\{S_2CN(C_2H_5)_2\}_4]$, M(II)=Zn, Cd or Hg complexes, where nitrogen sites in the terminal dithiocarbamate ligands have chemical shifts around 135–138 ppm, while those in the bridging ligands are less shielded (148–150 ppm). Note also a characteristic splitting of ^{15}N resonances in the spectra of polycrystalline Cd(II) and Hg(II) dithiocarbamate complexes (Fig. 37c–e). Central resonance lines are flanked by doublets due to the J-coupling interaction ($^3J\{^{15}$N-$^{111/113}$Cd\}=28.1 and 17.9 Hz for terminal and bridging ligands in the binuclear cadmium complex $[Cd_2\{S_2CN(C_2H_5)_2\}_4]$ (Fig. 37c); $^3J\{^{15}$N-^{199}Hg\}=64.2 Hz (terminal) and 48.5 Hz (bridging) in the binuclear compound $[Hg_2\{S_2CN(C_2H_5)_2\}_4]$ (Fig. 37d) and $^3J\{^{15}$N-^{199}Hg\}=52.2 Hz for terminal ligands in the mononuclear mercury complex $[Hg\{S_2CN(C_2H_5)_2\}_2]$ [108] (Fig. 37e)). Relative integral intensities of these satellites normalized to the total integral intensity of the spectra (ca. 0.25 and 0.165) are also in accord with the known relative abundances of the 'magnetic' nuclei ([111]Cd plus [113]Cd, 25.01 at.%, having very close values of magnetic moments, and [199]Hg, 16.84 at.%, respectively).

Representative [113]Cd CP/MAS NMR spectra of two Cd(II) dithiocarbamate complexes, $[Cd_2\{S_2CN(C_2H_5)_2\}_4]$ and $[Cd\{S_2CN(CH_3)_2\}_2]_n$ at a moderate spinning of 5.5 kHz are shown in Fig. 38. A remarkable difference in the number and intensity of spinning sidebands in these two spectra can be seen. Therefore cadmium sites in the binuclear complex (R=C_2H_5) have much larger chemical shift anisotropies ($\delta_{aniso}=\delta_{zz}-\delta_{iso}$=379.8±3.5 ppm, $\eta=(\delta_{yy}-\delta_{xx})/\delta_{aniso}$=0.404±
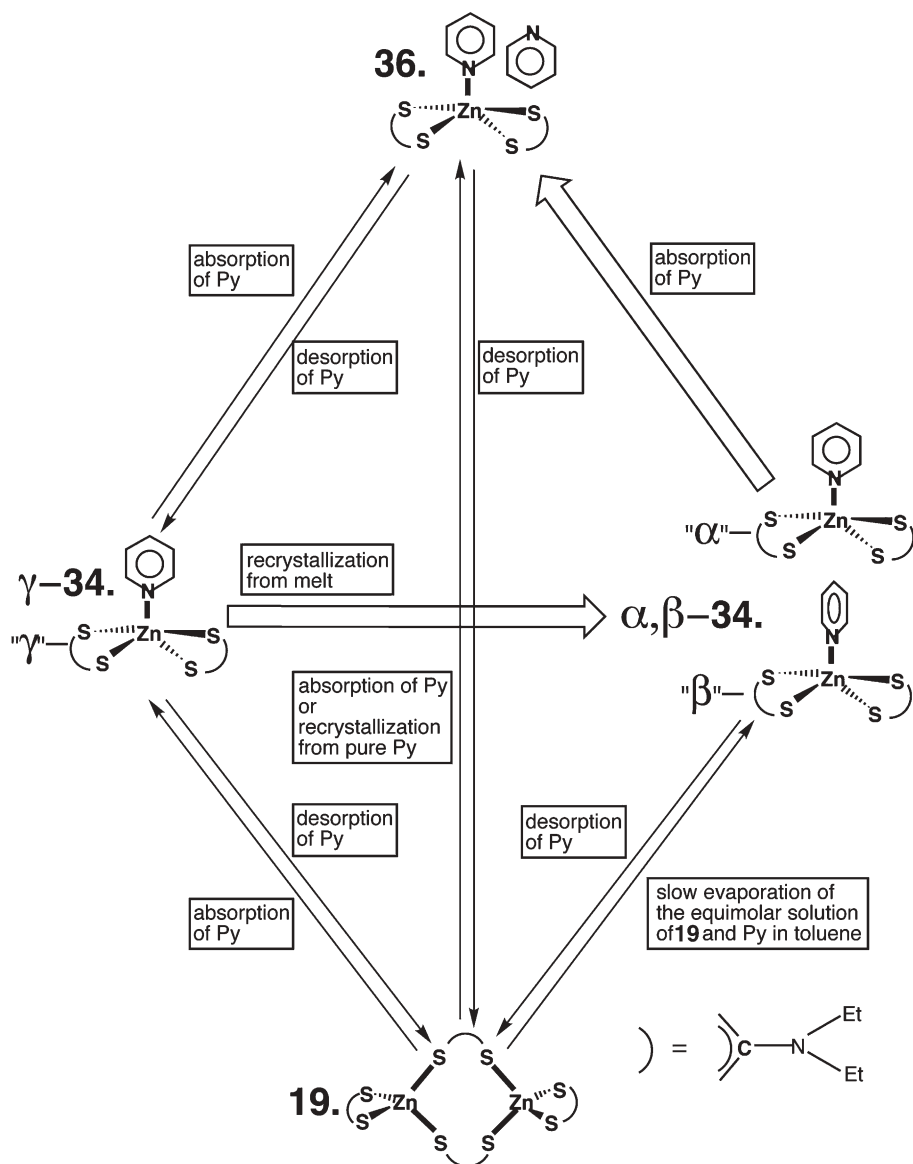
Fig. 36 Chemical pathways for bis(diethyldithiocarbamato)zinc(II), [Zn$_2${S$_2$CN(C$_2$H$_5$)$_2$}$_4$] (compound **19**), its adduct with pyridine, [Zn{C$_5$H$_5$N}{S$_2$CN(C$_2$H$_5$)$_2$}$_2$] (compound α,β-**34**, α- and β- are two isomorphs); the solvated form of the adduct with guest molecules of pyridine, [Zn{C$_5$H$_5$N}{S$_2$CN(C$_2$H$_5$)$_2$}$_2$]·C$_5$H$_5$N (compound **36**) and the meta-stable state of the adduct, γ-[Zn{C$_5$H$_5$N}{S$_2$CN(C$_2$H$_5$)$_2$}$_2$] (compound γ-**34**)
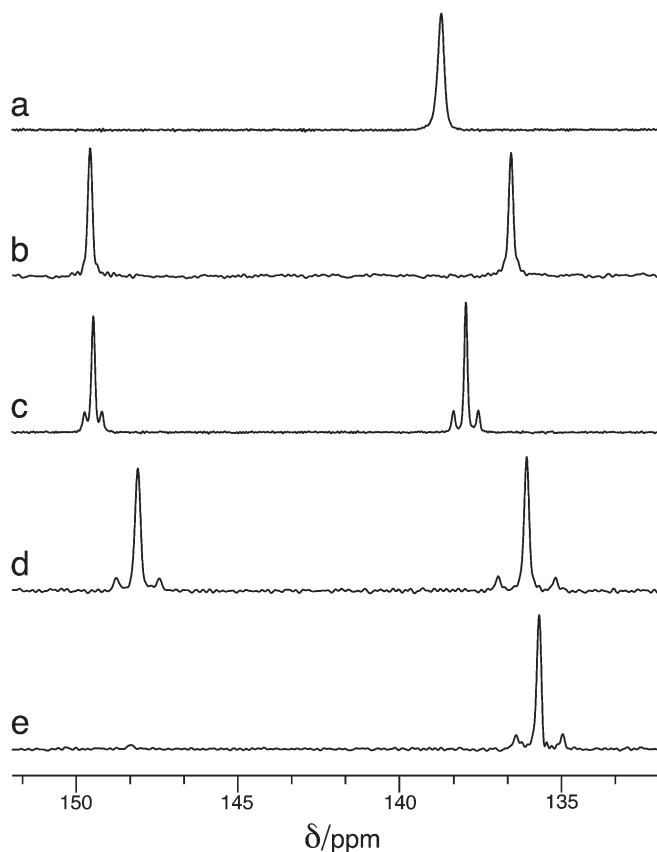
Fig. 37a–e 36.48 MHz ^{15}N CP/MAS NMR spectra of: **a** the polycrystalline mononuclear [Ni{S$_2$CN(C$_2$H$_5$)$_2$}$_2$] (**10**); **b** the binuclear [Zn$_2${S$_2$CN(C$_2$H$_5$)$_2$}$_4$] (**19**); **c** [Cd$_2${S$_2$CN(C$_2$H$_5$)$_2$}$_4$]; **d** [Hg$_2${S$_2$CN(C$_2$H$_5$)$_2$}$_4$]; **e** the mononuclear [Hg{S$_2$CN(C$_2$H$_5$)$_2$}$_2$] complexes. The MAS frequency and number of signal transients were (2400 Hz/12700) in (a), (6000 Hz/3740) in (b), (5000 Hz/46316) in (c), (6000 Hz/13300) in (d) and (3500 Hz/17164) in (e)

0.013)[3] compared with Cd nuclei in the polynuclear complex (R=CH$_3$, δ_{aniso}=77.6±0.5 ppm and η=0.677±0.020). An almost spherically symmetric ^{113}Cd chemical shift tensor in the [Cd{S$_2$CN(CH$_3$)$_2$}$_2$]$_n$ complex with only the bridging type of ligands points to a putatively high tetrahedral symmetry of the chemical surroundings (Cd-S bonds and S-Cd-S bond angles) around cadmium sites in the polynuclear complexes, while the S$_2$CdS$_2$ moiety in the binuclear complex has a larger distortion from tetrahedral symmetry leading to larger ^{113}Cd chemical shift anisotropy. However, these preliminary conclusions must

---

[3] CSA parameters estimated from spinning sideband amplitudes using a simulation program in the Mathematica front end [114].
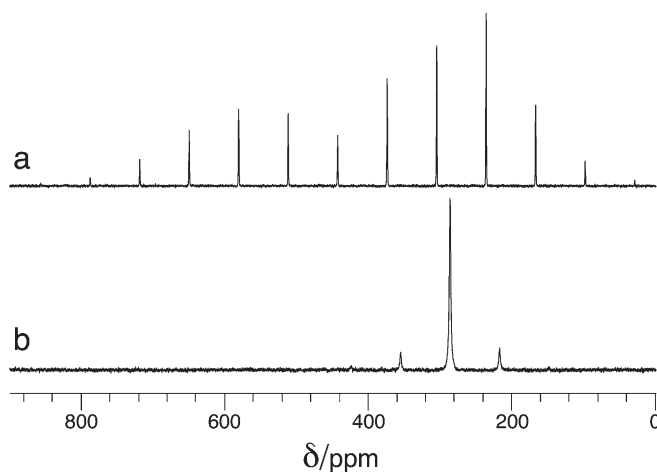
Fig. 38a, b 79.86 MHz ^{113}Cd CP/MAS NMR spectra of the polycrystalline complexes: **a** the binuclear $[Cd_2\{S_2CN(C_2H_5)_2\}_4]$; **b** the polynuclear $[Cd\{S_2CN(CH_3)_2\}_2]_n$. The MAS frequency was 5500 Hz. Number of signal transients was 240 (a) and 120 (b). The centreband in (a) is at 376 ppm

be proven by direct crystallographic methods, single crystal X-ray or neutron diffraction studies.

3
Concluding Remarks

It is amazing to contemplate the variety and complexity of dithiocarbamate systems in the solid state, ranging from simple thiuram disulfides, metal(II)-dithiocarbamate complexes, their adducts with nitrogen containing bases and, finally, to the solvated forms of these adducts. Each class of systems in this list is a 'new dimension' for exciting discoveries when multinuclear solid-state NMR is used in combination with other methods, in particular, direct single-crystal X-ray diffraction analysis. Another dimension to explore is comparing NMR experimental data with *ab-initio* quantum mechanical calculations based on the known structures of these systems. For this, full chemical shift tensors of carbon and nitrogen sites in the dialkyldithiocarbamate groups have to be experimentally measured and compared with theoretical calculations to elucidate interesting and useful correlations between the structure and magnetic properties of the dithiocarbamate systems. Work along these lines has already achieved notable success for Ni(II), Zn(II), and Pb(II) dithiophosphate complexes [112], and we plan to extend these ideas to the dithiocarbamate compounds discussed in this chapter.

References

1. Duer MJ (ed) (2002) Solid-state nuclear magnetic resonance spectroscopy, principles and applications. Blackwell Science, Oxford
2. Antzutkin ON (2002) Molecular structure determination: application in biology. In: Duer MJ (ed) Solid-state nuclear magnetic resonance spectroscopy, principles and applications. Blackwell Science, Oxford, p 280
3. Abramov AA (1993) Froth flotation methods of enrichment. Nedra, Moscow
4. McCleverty JA, Spencer N, Bailey NA, Shackleton SL (1980) J Chem Soc Dalton Trans 9:1939
5. Byr'ko VM (1984) Dithiocarbamates. Nauka, Moscow
6. Lawton SL, Kokotailo GT (1969) Inorg Chem 8:2410
7. Harrison PG, Begley MJ, Kikabhai T, Killer F (1986) J Chem Soc Dalton Trans 925
8. Haiduc I, Bryan-Sowerby D, Shao-Fang Lu (1995) Polyhedron 14:3389
9. O'Brien P (1992) Precursors for electronic materials. In: Bruce DW, O'Hare D (eds) Inorganic materials. Wiley, New York, p 491
10. Hovel HJ (1975) Semiconductors/semimetals: solar cells, vol 11. Academic Press, New York
11. World Health Organization (WHO) (1991) Environmental health criteria 118, inorganic mercury, Geneva
12. Agency for Toxic Substances and Disease Registry, U.S. Public Health Service (1999) Toxicological profile for mercury, March
13. Groten JP, van Bladeren PJ (1994) Food Sci Technol 5:50
14. Cadmium (1993) In: IARC monographs on the evaluation of carcinogenic risks to humans. IARC, Lyon, France, p 119
15. Jin YH, Clark AB, Slebos RJC, Al-Refai H, Taylor JA, Kunkel TA, Resnick MA, Gordenin DA (2003) Nat Genet 34:326
16. McMurray CT, Tainer JA (2003) Nat Genet 34:239
17. Hayes RB (1997) Cancer Causes Control 8:371
18. Golding RM, Tennant WC (1972) Mol Phys 24:301
19. Jian FF, Wang ZX, Chen W, Bai ZP, Zang KK, You XZ (1999) Polyhedron 18:2219
20. Maroy K (1965) Acta Chem Scand 19:1509
21. Ymen I (1983) Acta Chem Scand 37:70
22. Wang Y, Liao JH (1989) Acta Crystallogr B45:65
23. Karle IL, Estlin JA, Britts K (1967) Acta Crystallogr 22:273
24. Wang Y, Liao JH, Ueng CH (1986) Acta Crystallogr C42:1420
25. Jian FF, Jiang L, Fun H-K, Chinnakali K, Abdul Razak I, You X (1999) Acta Crystallogr C55:573
26. Kumar V, Aravamudan G, Seshasayee M (1990) Acta Crystallogr C46:674
27. Dix MF, Rae AD (1973) Cryst Struct Commun 2:159
28. Polyakova IN, Starikova ZA (1990) Zh Strukt Khim 31:148
29. Rout GC, Seshasayee M, Aravamudan G (1982) Cryst Struct Commun 11:1389.

30. Yamin BM, Suwandi SA, Fun HK, Sivakumar K, Bin Shawkataly O (1966) Acta Crystallogr C52:951
31. Ivanov AV, Zinkin SA, Forsling W, Antzutkin ON, Kritikos M (2003) Russ J Coord Chem (Engl Transl) 29:142
32. Colapietro M, Domenicano A, Vaciago A (1976) Acta Crystallogr 32:2581
33. Husebye S (1973) Acta Chem Scand 27:756
34. Jian FF, Zhu D, Fun HK, Chinnakali K, Abdul Razak I, You XZ (1999) Acta Crystallogr C55:940
35. Hexem JG, Frey MH, Opella SJ (1982) J Chem Phys 77:3847
36. Harris RK, Jonsen P, Packer KJ (1985) Magn Reson Chem 23:565
37. Earl WL, VanderHart DL (1982) J Magn Reson 48:35
38. Ratcliffe CI, Ripmeester JA, Tse JS (1983) Chem Phys Lett 99:177
39. Mason J (1996) In: Grant DM, Harris RK (eds) Encyclopedia of nuclear magnetic resonance. Wiley, New York, vol 5, p 3222
40. Hauptmann S, Graefe J, Remane H (1976) Lehrbuch der organischen Chemie. VEB Deutscher Verlag für Grundstoffindustrie, Leipzig
41. Lokaj J, Garaj J, Kettmann V, Vrabel V (1980) Coll Czech Chem Commun 45:2147
42. Bonamico M, Dessy G, Mariani C, Vaciago A, Zambonelly L (1965) Acta Crystallogr 19:619
43. Khan MNI, Fackler JP, Murray HH, Hienrich DD (1987) Acta Crystallogr C43:1917
44. Selvaraju R, Panchanatheswaran K, Thiruvalluvar A, Parthasarathi V (1995) Acta Crystallogr C51:606
45. Peyronel G, Pignedoli A (1967) Acta Crystallogr 23:398
46. Ivanov AV, Ivakhnenko EV, Forsling W, Gerasimenko AV, Bukvetskii BV (2002) Russ J Inorg Chem (Engl Transl) 47:410
47. Newman PWG, White AH (1972) J Chem Soc Dalton Trans 20:2239
48. Lokaj J, Vrabel V, Kello E (1984) Chem Zvesti 38:313
49. Raston CL, White AH (1976) Austr J Chem 29:523
50. Radha A, Seshasayee M, Aravamudan G (1988) Acta Crystallogr C44:1378
51. Starikova ZA, Shugam EA, Agre VM, Oboznenko JV (1972) Krystallogr 17:111
52. Herring FG, Park JM, Rettig SJ, Trotter J (1979) Can J Chem 57:2379
53. Cox MJ, Tiekink ERT (1999) Z Kristallogr 214:242
54. Martin JM, Newman PWG, Robinson BW, White AH (1972) J Chem Soc Dalton Trans 20:2233
55. Ramalingam K, Radha A, Aravamudan G, Mahadevan C, Subramanyam C, Seshasayee M (1984) Acta Crystallogr C40:1838
56. Christidis PC (1986) Acta Crystallogr C42:781
57. Higgins GMC, Saville B (1963) J Chem Soc 3:2812
58. Hope PT (1995) Nuclear magnetic resonance. Oxford University Press, Oxford, p 37
59. Klug HP (1966) Acta Crystallogr 21:536
60. Ramalingam K, bin Shawkataly O, Fun HK, Abdul Razak I (1998) Z Kristallogr 213:371
61. Bonamico M, Dessy G, Mazzone G, Mugnoly A, Vaciago A, Zambonelly L (1963) Atti Accad naz Linc Rend Cl Sc Fic mat e natur 35:338
62. Bonamico M, Mazzone G, Vaciago A, Zambonelly L (1965) Acta Crystallogr 19:898
63. Sreehari N, Varghese B, Manoharan PT (1990) Inorg Chem 29:40
64. Miyamae H, Ito M, Iwasaki H (1979) Acta Crystallogr B35:1480
65. Kellö E, Vrabel V, Kettmann V, Garaj J (1983) Coll Czech Chem Commun 48:1272
66. Ivanov AV, Ivakhnenko EV, Gerasimenko AV, Forsling W (2003) Russ J Inorg Chem (Engl Transl) 48:45
67. Franceti V, Leban I (1979) Vestn Slov Kem Drus 26:113
68. Agre VM, Shugam EA (1972) Zhurn Struct Khim 13:660

69. Motevalli M, O'Brien P, Walsh JR, Watson IM (1996) Polyhedron 15:2801
70. Cox MJ, Tiekink ERT (1999) Zeitsch Kristallogr 214:184
71. Boyd PDW, Mitra S, Raston CL, Rowbottom GL, White AH (1981) J Chem Soc Dalton Trans 1:13
72. Ivanov AV, Ivakhnenko EV, Forsling W, Gerasimenko AV (2003) Dokl Chem (Proc Russ Acad Sci) (Engl Transl) 390:162
73. Ivanov AV, Rodyna TA, Antzutkin ON (1998) Polyhedron 17:3101
74. Ivanov AV, Lutsenko IA, Forsling W (2002) Russ J Coord Chem (Engl Transl) 28:57
75. Ivanov AV, Forsling W, Antzutkin ON, Novikova EV (2001) Russ J Coord Chem (Engl Transl) 27:158
76. Ivanov AV, Leskova SA, Mel'nikova MA, Rodina TA, Lund A, Antzutkin ON, Forsling W (2001) Russ J Inorg Chem (Engl Transl) 48:415
77. Ivanov AV, Novikova EV, Leskova SA, Forsling W (2004) Russ J Inorg Chem (Engl Transl) 49 (in press)
78. Johnson LRF, Jankowski WC (1972) Carbon-13 NMR spectra. A collection of assigned, coded and indexed spectra. Wiley, New York
79. Rice DM, Wittebort RJ, Griffin RG et al. (1981) J Am Chem Soc 103:7707
80. Frey MH, Opella SJ, Rockwell AL, Gierasch LM (1985) J Am Chem Soc 107:1946
81. Frey MH, DiVerdi JA, Opella SJ (1985) J Am Chem Soc 107:7311
82. Ivanov AV, Mitrofanova VI, Kritikos M, Antzutkin ON (1999) Polyhedron 18:2069
83. Ivanov AV, Antzutkin ON (2002) Polyhedron 21:2727
84. Ivanov AV, Forsling W, Kritikos M, Antzutkin ON, Novikova EV (1999) Dokl Chem (Proc Russ Acad Sci) (Engl Transl) 369:268
85. Ivanov AV, Kritikos M, Antzutkin ON, Forsling W (2001) Inorg Chim Acta 321:63
86. Ivanov AV, Kritikos M, Antzutkin ON, Lund A, Rodina TA (1998) Russ J Inorg Chem (Engl Transl) 43:1368
87. Ivanov AV, Kritikos M, Antzutkin ON, Lund A, Mitrofanova VI (1998) Russ J Coord Chem (Engl Transl) 24:645
88. Ivanov AV, Kritikos M, Antzutkin ON, Forsling W, Lund A, Lutsenko IA (1999) Russ J Coord Chem (Engl Transl) 25:543
89. Ivanov AV, Kritikos M, Antzutkin ON, Lund A (1999) Russ J Inorg Chem (Engl Transl) 44:1605
90. Ivanov AV, Forsling W, Antzutkin ON, Kritikos M, Rodina TA, Lutsenko IA (1999) Dokl Chem (Proc Russ Acad Sci) (Engl Transl) 366:142
91. Ivanov AV, Forsling W, Kritikos M, Antzutkin ON (2000) Russ J Coord Chem (Engl Transl) 26:53
92. Ivanov AV, Novikova EV, Antzutkin ON, Forsling W (2001) Russ J Inorg Chem (Engl Transl) 46:1832
93. Ivanov AV, Leskova SA, Kritikos M, Forsling W (2004) Russ J Inorg Chem (Engl Transl) 49 (in press)
94. Levy GC, Lichter RL, Nelson GL (1980) Carbon-13 Nuclear Magnetic Resonance Spectroscopy. Wiley, New York
95. Schaeffer WD, Dorsey WS, Skinner DA, Christian CG (1957) J Am Chem Soc 79:5870
96. Williams FV (1957) J Am Chem Soc 79:5876
97. Hardy ADU, MacNicol DD, McKendric JJ, Wilson DR (1975) Tetrahedron Lett 52:4711
98. Hardy ADU, McKendric JJ, MacNicol DD, Wilson DR (1979) J Chem Soc Perkins Trans II 6:729
99. Candeloro De Sanctis S, Giglio E (1979) Acta Cryst B35:2650
100. Harata K (1993) J Chem Soc Chem Commun 6:546
101. Malik MA, Motevalli M, O'Brien P (1999) Polyhedron 18:1259
102. Domenicano A, Torelli L, Vaciago A, Zambonelli L (1968) J Chem Soc (A) 2:1351

103. Cox MJ, Tiekink ERT (1999) Z Kristallogr 214:670
104. Jian F-F, Wang Z-X, Fun H-K, Bai Z-P, You X-Z (1999) Acta Crystallogr C55:174
105. Casas JS, Sánchez A, Bravo J, García-Fontán S, Castellano EE, Jones MM (1989) Inorg Chim Acta 158:119
106. Agre VM, Shugam EA (1972) Krystallogr 17:303
107. Cox MJ, Tiekink ERT (1997) Z Kristallogr 212:542
108. Iwasaki H (1973) Acta Crystallogr B29:2115
109. Ito M, Iwasaki H (1979) Acta Crystallogr B35:2720
110. Cox MJ, Tiekink ERT (1999) Z Kristallogr 214:571
111. Chieh C, Cheung SK (1981) Can J Chem 59:2746
112. Larsson A-C, Ivanov AV, Forsling W, Antzutkin ON, Abraham AE, de Dios AC (2004) J Am Chem Soc (accepted)
113. Martin GJ, Martin ML, Goueshard J-P (1981) ^{15}N NMR spectroscopy. Springer, Berlin Heidelberg New York
114. Antzutkin ON, Lee YK, Levitt MH (1998) J Magn Reson 135:144

Author Index Volumes 201–246

The volume numbers are printed in italics

Subject Index